Lecture Notes in Civil Engineering

Sumanta Haldar
Shantanu Patra
Ravindra K. Ghanekar *Editors*

Advances in Offshore Geotechnics

Proceedings of ISOG2019

Springer

Lecture Notes in Civil Engineering

Volume 92

Lecture Notes in Civil Engineering (LNCE) publishes the latest developments in Civil Engineering - quickly, informally and in top quality. Though original research reported in proceedings and post-proceedings represents the core of LNCE, edited volumes of exceptionally high quality and interest may also be considered for publication. Volumes published in LNCE embrace all aspects and subfields of, as well as new challenges in, Civil Engineering. Topics in the series include:

- Construction and Structural Mechanics
- Building Materials
- Concrete, Steel and Timber Structures
- Geotechnical Engineering
- Earthquake Engineering
- Coastal Engineering
- Ocean and Offshore Engineering; Ships and Floating Structures
- Hydraulics, Hydrology and Water Resources Engineering
- Environmental Engineering and Sustainability
- Structural Health and Monitoring
- Surveying and Geographical Information Systems
- Indoor Environments
- Transportation and Traffic
- Risk Analysis
- Safety and Security

To submit a proposal or request further information, please contact the appropriate Springer Editor:

– Mr. Pierpaolo Riva at pierpaolo.riva@springer.com (Europe and Americas);
– Ms. Swati Meherishi at swati.meherishi@springer.com (Asia - except China, and Australia, New Zealand);
– Dr. Mengchu Huang at mengchu.huang@springer.com (China).

All books in the series now indexed by Scopus and EI Compendex database!

More information about this series at http://www.springer.com/series/15087

Sumanta Haldar · Shantanu Patra ·
Ravindra K. Ghanekar
Editors

Advances in Offshore Geotechnics

Proceedings of ISOG2019

Springer

Editors
Sumanta Haldar
School of Infrastructure
Indian Institute of Technology Bhubaneswar
Jatni, Odisha, India

Shantanu Patra
School of Infrastructure
Indian Institute of Technology
Bhubaneswar
Jatni, Odisha, India

Ravindra K. Ghanekar
Institute of Engineering
and Ocean Technology
ONGC
Navi Mumbai, Maharashtra, India

ISSN 2366-2557 ISSN 2366-2565 (electronic)
Lecture Notes in Civil Engineering
ISBN 978-981-15-6831-2 ISBN 978-981-15-6832-9 (eBook)
https://doi.org/10.1007/978-981-15-6832-9

This Springer imprint is published by the registered company Springer Nature Singapore Pte Ltd.
The registered company address is: 152 Beach Road, #21-01/04 Gateway East, Singapore 189721, Singapore

Committees

Organizing Committee

R. V. Rajakumar (Patron), IIT Bhubaneswar
R. K. Panda (Chairman), IIT Bhubaneswar
S. K. Mahapatra (Co-chairman), IIT Bhubaneswar
Sumanta Haldar (Organizing Secretary), IIT Bhubaneswar
Shantanu Patra (Co-organizing Secretary), IIT Bhubaneswar
Ravindra K. Ghanekar (Chief Advisor), IEOT, ONGC
Arindam Sarkar, IIT Bhubaneswar
Suresh R. Dash, IIT Bhubaneswar
Goutam Mondal, IIT Bhubaneswar
Akanksha Tyagi, IIT Roorkee
B. Hanumantha Rao, IIT Bhubaneswar
Tushar Kanti Roy, IEOT, ONGC

Advisory Committee

G. L. Sivakumar Babu, India
J. T. Shahu, India
Nilanjan Saha, India
C. R. Parthasarathy, India
Rupam Mahanta, India
Kaushik Mukherjee, Malayasia
Subrata Chakraborty, India
Amir M. Kaynia, Norway
Masayuki Hyodo, Japan
Dileep Dewaikar, India
Debasis Roy, India

Domenico Lombardi, UK
Christophe Gaudin, Australia
Subhamoy Bhattacharya, UK
Dipanjan Basu, Canada
Amin Barari, Denmark
M. R. Madhav, India
B. K. Maheshwari, India

Preface

This is the first Indian Symposium on Offshore Geotechnics (ISOG 2019)—the first event exclusively dedicated to offshore geotechnical engineering in India.

Although India started its efforts in petroleum exploration and production in 1970s, Indian academics (mainly in IIT Delhi) and in-house R&D facilities of oil companies (mainly IEOT, ONGC) started developing expertise in this area mainly in 1980s and 1990s. The academic endeavour declined later due to many reasons. The in-house efforts in ONGC continued through in-house efforts and external cooperation, both formal and informal, due to their obvious and essential practical needs. This situation continued till very recently when academic institutions also initiated work on issues related to offshore geotechnical engineering.

India is now venturing into deep and ultra-deep waters for petroleum exploration and production. Alternative offshore energy—especially offshore wind—is on the very focus of the Government of India. These both pose special challenges to geotechnical engineers as far as site investigation and foundation design are concerned. In addition, there are many issues related to shallow water areas which also need review, update and further research.

There is hence a need to not only accelerate academic efforts in the area but also to put emphasis on industry–academia interaction and cooperation—both nationally and internationally—to address the need for solutions to problems specific to Indian offshore scenario. This symposium is a step towards giving impetus to the efforts to achieve both these goals.

The format of the symposium is consciously chosen so that there are no parallel sessions, and only the invited keynote lectures from Indian and overseas experts and selected papers from Indian delegates are orally presented. Other entries have been included in the poster session. Being the first event on offshore geotechnics in India after a very long time, this format allows everybody to listen to all presentations and allows constructive and valuable interaction on all aspects.

The keynote and other theme papers in this symposium pertain to the themes of offshore site characterization, offshore shallow and deep foundations, offshore anchoring systems, geotechnics for offshore wind energy converters, geotechnical

issues related to gas hydrate exploitation and another important research aspect related to the establishment and use of onshore test sites for offshore applications.

We realize that we have not received contributions for all the themes initially envisaged for the symposium but we are very hopeful that in the following such symposia in future, other envisaged themes shall also find representation as more and more work is performed in India on these issues.

The technical substance to the symposium is basically due to the contribution of authors of invited and other theme papers (presented orally or in poster session). We acknowledge that their contribution is what made this symposium possible. Each paper included in the proceedings has been peer reviewed, and we also express our gratitude to the reviewers for their efforts.

We are grateful to the members of the organizing committee for their efforts and also to the advisory committee members for their timely and constructive advice in planning and conduct of this symposium.

We are also grateful for the support rendered by Scheme for Promotion for Research Collaboration, Ministry of Human Resource Development (MHRD) of Government of India. The support of Technical Committee TC 209 of International Society for Soil Mechanics and Geotechnical Engineering (ISSMGE) and local chapter of Indian Geotechnical Society (IGS) is also gratefully acknowledged under whose aegis this symposium is organized.

We also acknowledge gratefully the financial support extended by our industry sponsors and well-wishers which made it possible to host this symposium.

We are also thankful to the publishers of these proceedings for their editorial efforts and extensive cooperation.

Jatni, India — Sumanta Haldar
Jatni, India — Shantanu Patra
Navi Mumbai, India — Ravindra K. Ghanekar
December 2019

Reviewers

Goutam Mondal, IIT Bhubaneswar
Bappaditya Manna, IIT Delhi
Anindya Pain, CBRI, Roorkee
Manash Chakraborty, IIT BHU
Sarat Kumar Dash, IIT (ISM), Dhanbad
Nilanjan Saha, IIT Madras
Akanksha Tyagi, IIT Roorkee
M. R. Madhav, JNT University, Hyderabad
Rupam Mohanta, IEOT, ONGC, Mumbai
Kaushik Mukherjee, Petronas, Malaysia
Sumanta Haldar, IIT Bhubaneswar
Shantanu Patra, IIT Bhubaneswar

Contents

About the Editors

Dr. Sumanta Haldar is currently an associate professor at IIT Bhubaneswar. He has over 15 years of research experience in the field of offshore geotechnics, soil-structure interaction and dynamics of soils and foundations. Dr. Haldar is working on offshore geotechnics, foundations for renewable energy devices and soil-structure interaction problem. During his doctoral research at the Indian Institute of Science, Bangalore, he worked on static and dynamic soil structure interaction and risk-reliability based design of pile foundation. His current research aims at developing theoretical models of various geotechnical structures with a goal of producing more rational design solutions and considering reliability concepts. The focus of his research is on the application of the fundamental principles of mechanics and mathematics in the experimental and computational aspects of geotechnical engineering. He has more than 50 peer reviewed international and national journal and conference publications and book chapters.

Dr. Shantanu Patra is currently an Assistant Professor at IIT Bhubaneswar. He pursued his Ph.D. from IIT Delhi on experimental and numerical analysis of reinforced soil behavior under the oblique pullout force. He did his postdoctoral research which was specifically on physical and numerical modeling of the foundation for offshore wave energy devices at the University of Dundee, United Kingdom. During this period, Dr. Patra gained experience in geotechnical centrifuge modeling and developed a scalable actuator control system for Dundee centrifuge. Currently, Dr. Patra is working on application of the screw pile foundation for offshore and onshore renewable energy devices, railway geotechnics, reinforced soil technology, and is guiding Ph.D. scholars. Dr. Patra has more than 30 peer-reviewed international and national journal and conference publications and book chapters.

Mr. Ravindra K. Ghanekar is currently heading the Geotechnical section of IEOT, ONGC. He obtained his Master's degree in structural engineering from University of Roorkee, India in 1983 and has since been working in India's premier oil company Oil and Natural Gas Corporation Limited (ONGC). He has over 25

years of experience in the field of offshore geotechnics and offshore structural engineering - including shallow and deepwater offshore soil investigations; design of offshore structures and foundations, and installation engineering. Over the years, he has played a key-role in developing the technical capabilities of Institute of Engineering and Ocean Technology (IEOT), ONGC in the field of offshore geotechnics. He has also been active in promoting offshore geotechnics within India. He has more than 35 technical publications in national and international forums.

Design of Anchoring Systems for Deep Water Soft Sediments

Mark F. Randolph

1 Introduction

With the transition from fixed structures founded in shallow water, to floating production systems in much deeper water, the offshore oil and gas industry have relied increasingly on anchoring systems. The choice of anchor depends on both the floating system and the design of the mooring system. In early deep water developments in the 1990s, tension leg platforms like at Auger, Mars, Ursa, etc., in the Gulf of Mexico were a common choice, secured to the seabed by long-driven piles loaded primarily in vertical tension (Doyle 1994; Garside et al. 1997). However, novel types of floating platforms such as SPARs, floating production, storage and offloading (FPSO) vessels and semi-submersible floating production systems were soon developed and these required anchors that needed to withstand quasi-horizontal loading, generally with a much lower vertical component (Randolph and Gourvenec 2011).

Increasing water depth became an important driver for novel anchoring solutions. Only recently have underwater hammers been capable of operating at ultra-deep (>2000 m) water depths, so there were incentives for alternative means of anchor installation. This led to a wide range of alternative anchor types, ranging from suction caissons to different forms of plate anchors and gravity installed (e.g. torpedo) anchors. In most cases, the chain attachment to these anchors was embedded well below the soil surface, in order to maximize the holding capacity of the anchor.

Another consideration in deep water was the lateral spread of the mooring system. For moderate water depths, catenary mooring systems are economic without either undue quantities of chain or excessive horizontal extent of the overall system. However, in deep water, although a catenary mooring system may still be used (for example, for the Na Kika FPS in 2200 m of water, where the mooring system extended over a diameter of more than 5 km at the seabed—Newlin 2003), semi-taut

M. F. Randolph (✉)
Centre for Offshore Foundation Systems, University of Western Australia, Perth, Australia
e-mail: mark.randolph@uwa.edu.au

S. Haldar et al. (eds.), *Advances in Offshore Geotechnics*, Lecture Notes in Civil Engineering 92, https://doi.org/10.1007/978-981-15-6832-9_1

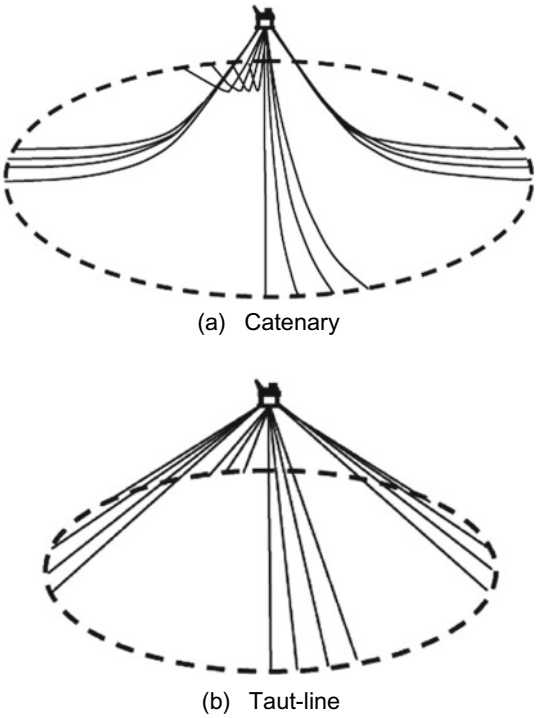

Fig. 1 Catenary and taut-wire mooring configurations

and taut systems are more common (see Fig. 1, after Randolph and Gourvenec 2011). Generally, a high proportion of the mooring line will comprise polyester cable, with chain used at the connection with the vessel, and for the section embedded within the seabed. The consequence of semi-taut or taut mooring systems is that the loads on the anchors have a much higher vertical component compared with a catenary system.

This paper presents a brief summary of different types of anchor, from drag anchors to piles, suction caissons, torpedo anchors and various forms of plate anchor. Particular focus is on design strategies for suction caissons with respect to the trenching phenomonen that has come to light in the last five years, and also the attractive potential of anchors that are designed to continue to embed as they are loaded.

2 Drag Anchors

Historically, drag anchors that embed themselves have been by far the most common form of anchor for relative low mooring loads. Typically, maximum 'efficiencies', i.e. the ratio of holding force to the anchor weight, are in the range 20–50, although

higher efficiencies have been quoted for more recent designs. The lower end of this range is applicable for soft clays, while the upper end is applicable for sands. Thus, for anchors weighing up to 32 tonnes, maximum loads of around 6 MN (soft clay) to over 15 MN (sand) are possible in principle.

In practice, however, such high efficiencies require significant anchor embedment and correspondingly large drag distances. In addition, layering within the soil stratigraphy, for example, the presence of lightly cemented layers in carbonate sands, may impede embedment of an anchor, limiting the efficiencies that can be mobilized to much lower values. Chow et al. (2017) showed field data from the North-West Shelf of Australia where efficiencies under monotonic loading were as low as 15–17, and reduced further to around 10 under cyclic loading.

In soft sediments such as predominate in deep water developments, anchor capacity will increase with time because of consolidation effects, but will also be susceptible to reduction under cyclic loading. O'Neill et al. (2010) outlined a methodology for assessing the net effects on anchor capacity.

The shift towards semi-taut or taut mooring systems in deep water requires an increasing vertical component of load to be resisted by the anchor. That has led to novel anchor designs (referred to as VLAs—vertically loaded anchors) such as the Bruce Dennla and Vryhof Stefmanta, where the angle of the chain relative to the anchor fluke can be increased following the embedment process. This causes the anchor to embed further during operational loading, but also increases the capability to withstand higher inclinations of loading. The conditions that cause an anchor to embed deeper as it is loaded are considered further later in the paper (Fig. 2).

Fig. 2 Bruce Dennla VLA (www.bruceanchor.co.uk)

3 Anchor Piles

Anchor piles are a relatively expensive form of anchor because of their cost of installation, especially in deep water. However, they still play a role in intermediate water depths where either the required anchor loads are high, or the seabed conditions prohibit other forms of anchor. The latter may pertain in profiles containing layers of dense sands or cemented material, for example, in cemented calcareous sands off the north-west coast of Australia (Erbrich 2004; Erbrich et al. 2017; Frankenmolen et al. 2017).

The ideal design configuration for an anchor pile would be for a failure mode where two plastic hinges form, as illustrated in Fig. 3 (after Neubecker and Randolph 1995a). The anchor chain is attached at a depth h such that the overlying soil has sufficient lateral resistance to generate a plastic moment M_p at the padeye under the ultimate anchor load. In practice, however, that would imply rather deep padeye locations.

Assuming lateral sol resistance increasing proportionally with depth at a rate of p'_u (units of nominal lateral pressure per metre, kPa/m), the normalized padeye depth would be

$$\frac{h}{D} = \left(6\frac{M_p}{p'_u D^4}\right)^{1/3} \tag{1}$$

As an example, consider a soil resistance gradient of $p'_u = 30$ kPa/m and a steel yield stress of 350 MPa. Assuming a pile wall thickness of 70 mm, typical padeye depths would range from 24 to 29 m as the pile diameter increases from 3 to 5 m.

Another consideration is the tensile capacity of the pile, since a deep padeye implies a high angle of the anchor chain at the padeye (Neubecker and Randolph 1995b). In sediments such as carbonate sands, where anchor piles might need to be used in preference to suction caissons, the padeye is generally placed near the surface in order to limit the vertical component of load (Erbrich 2004; Finnie et al. 2019).

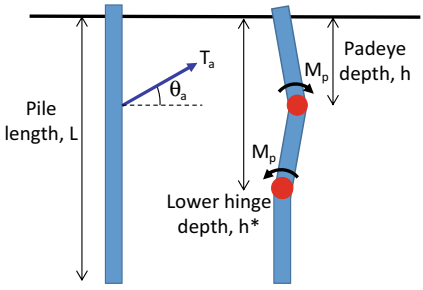

Fig. 3 Optimum configuration for anchor pile

4 Suction Caissons

Suction caissons are the most common form of anchor used in deep water applications, mostly in relatively soft sediments although they have also been used in overconsolidated glacial tills with shear strengths estimated to be as high as 400 kPa (Håland 2002). A summary of suction caisson applications up to 2004 was provided by Andersen et al. (2005). In addition to anchoring mooring lines, suction caissons are used extensively in deep water applications to restrain pipeline movements and as foundations for manifolds. Example suction caissons used as anchors for the Laminaria FPSO are shown in Fig. 4 (Erbrich and Hefer 2002).

Design of suction caissons comprises two main aspects: installation and operation. The first aspect has become relatively routine, with embedment by self-weight typically by about half the final embedment, followed by pumping out the water from within the caisson, creating a net force to embed the caisson further into the seabed. The thin-walled nature of suction caissons, often with D/t ratios of 150–200, coupled with the use of suction installation, entails that the external shaft friction remains low, even after full consolidation (Andersen and Jostad 2002). The consolidation process itself is relatively short, however, (Randolph 2013).

During installation, it is necessary to establish (a) that the caisson will not buckle (implode) under the required suction, and (b) that the soil plug will not fail upwards, rather than force the caisson downwards. For the latter, given that the internal shaft friction contributes both to installation resistance and also plug upheaval resistance, an appropriate design approach to assess the risk of plug upheaval is to factor the external resistance up by the required partial factor and the plug reverse end-bearing capacity at tip level downwards by the same factor (Andersen et al. 2005).

Fig. 4 Suction caissons: 5.5 m diameter by 13.5 long

In stratified soil conditions, interbedded sand layers can lead to water accumulating within the soil plug due to upward movement of overlying clay in the plug during penetration of the caisson tip through the sand layer. This may lead to a need to pressure grout within the caisson at the end of installation. Risks of heterogeneity within the sediments, leading to tilt of the caisson during installation, may be allowed for by dividing the caisson internally into separate chambers, allowing application of differential pumping pressures to maintain verticality (Frankenmolen et al. 2017).

4.1 Operational Capacity of Suction Caissons

Suction caissons as mooring anchors are generally designed with an embedded padeye, as indicated in Fig. 5 (after Randolph and House 2002). The line of action of the design loading crosses the caisson axis at centre-line intercept depth z_{cl}, which is chosen such that the caisson translates without rotation. The capacity of the caisson may then be determined conveniently using the upper bound solution of Murff and Hamilton (1993), which comprises a conical wedge of failing soil, above a 'full-flow' confined failure region, as shown in Fig. 6a. Software such as AGSPANC (2001) was developed on the basis of the Murff-Hamilton solution.

In general, the anchor fails by rotation about a point at depth h, which may lie below (Fig. 6a) or above (Fig. 6b) the caisson tip. Although the Muff-Hamilton upper bound solution is not exact, because of the top and bottom bounding planes of the full flow region, it becomes exact for the mechanism shown in Fig. 6b, where the base failure scoop wraps around to intersect the caisson at the base of the conical wedge. Depending on the soil strength profile, the optimal centre-line intercept at z_{cl} is typically at a depth of around 70% of the caisson embedment, L.

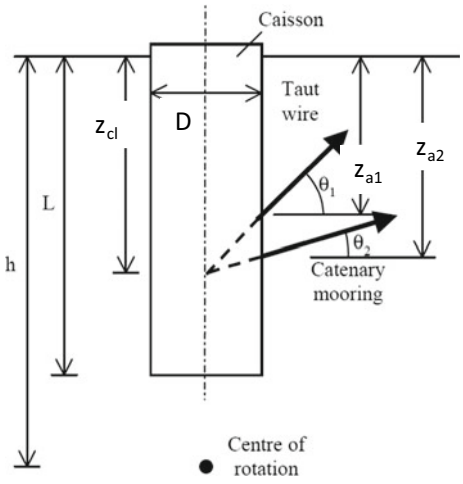

Fig. 5 Optimum configuration for anchor pile

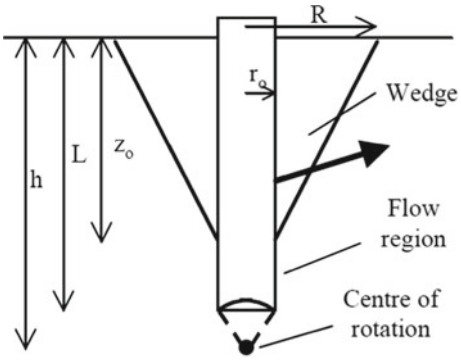

(a) General failure mechanism

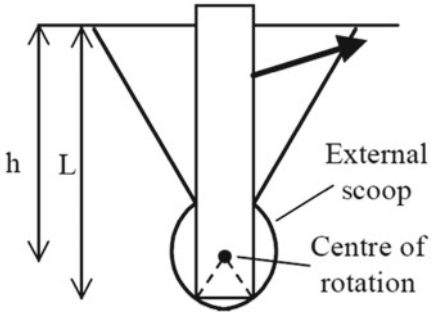

(b) Failure mechanism with increased rotation

Fig. 6 Murff-Hamilton failure mechanism

Supachawarote et al. (2004, 2005) presented design charts for failure envelopes in vertical–horizontal (H-V) load space, for pure translational failure, also considering potential gap formation. The failure envelopes were expressed as

$$\left(\frac{H}{H_{ult}}\right)^a + \left(\frac{V}{V_{ult}}\right)^b = 1$$

with

$$a = 0.5 + L/D; \quad b = 4.5 - L/3D \tag{2}$$

As a first approximation, the ultimate horizontal capacity for intermediate length caissons ($L/D \sim 3$) may be estimated as about $10 s_u LD$, while vertical capacity corresponds to the sum of shaft (e.g. friction of $\tau_s = \alpha s_u$) and base resistance ($q_{bu} \sim 9 s_u$).

Depending on the soil strength ratio (s_u/σ'_{v0}), a gap may open behind the caisson as it fails, in which case a one-sided wedge mechanism pertains, reducing the plastic work but now with additional work required due to the upward motion of the front wedge. To help avoid this, most designs adopt a centre-line intercept depth which is marginally below the pure translation point, so that the caisson rotates backward

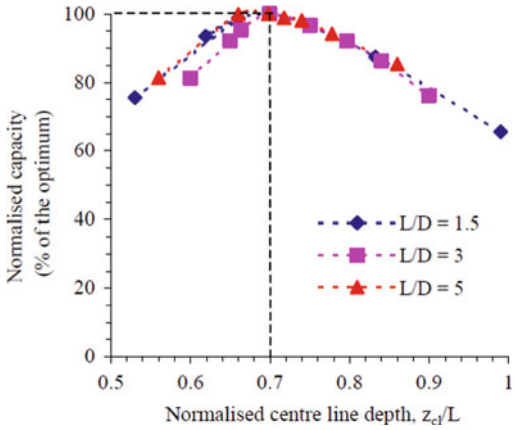

Fig. 7 Effect of non-optimal loading intercept z_{cl}

during failure. Minor reductions in capacity occur as a result of varying the z_{cl} value, as shown in Fig. 7.

A more extensive study of caisson capacity was presented by Kay and Palix (2010) and Palix et al. (2010), who investigated a wide range of loading conditions for caissons with *L*/*D* from 1.5 to 5 and for three different profiles of soil strength. Adopting the load reference point at mudline on the caisson axis, failure envelopes in *H*-*M*-space were shown to take an elliptical form, as illustrated in Fig. 8, where the mudline load H_0 and moment M_0 have been normalized as:

$$H^* = \frac{H_0}{LDs_{u,\text{avg}}}; \quad M^* = \frac{M_0}{LD^2 s_{u,\text{avg}}} \tag{3}$$

Detailed relationships for the failure envelopes were provided, allowing for the caisson dimensions and soil strength profile. However, for soil with strength proportional to depth, they may be approximated as

$$\begin{aligned} H*(t) &= N_{p,\text{fixed}} \cos t + 0.31 N_{p,\text{free}} \sin t \\ M*(t) &= 0.67 N_{p,\text{fixed}} \cos t - 0.46 N_{p,\text{free}} \sin t \end{aligned} \tag{4}$$

where $N_{p,\text{ fixed}}$ and $N_{p,\text{ free}}$ are the values of H^* for zero rotation and zero moment, respectively (Fig. 9).

4.2 Embedded Anchor Chain and Tension Profiles

The embedded section of an anchor chain will form an inverse catenary through the soil, from an angle θ_a at the padeye to θ_m at the mudline. For a catenary mooring, the latter will be zero, but the padeye anchor angle may still be 20–25° relative

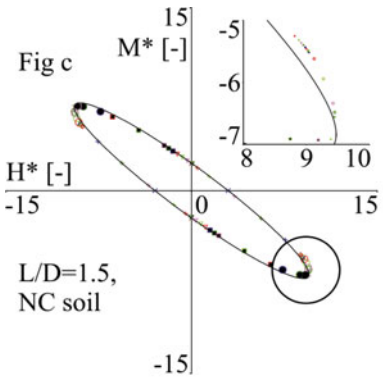

(a) $L/D = 1.5$

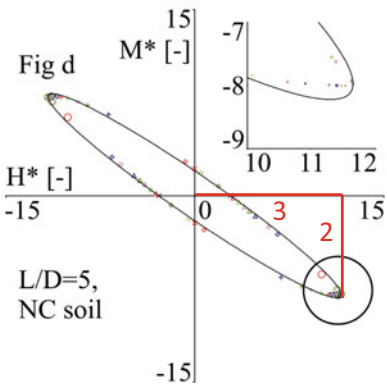

(b) $L/D = 5$

Fig. 8 Design charts from Kay and Palix (2010)

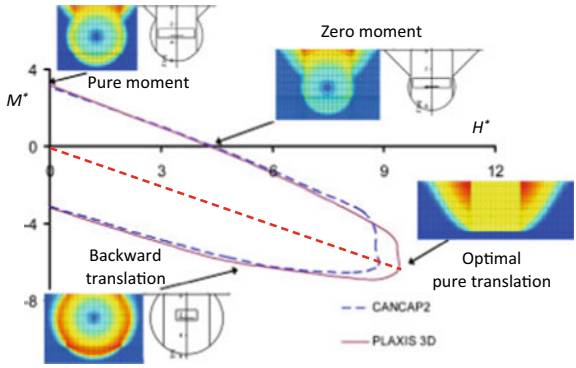

Fig. 9 Failure mechanisms for different loading conditions for $L/D = 1$ (after Palix et al. 2010)

to horizontal. The change in angle of the chain between padeye and mudline is determined by the chain tension and the bearing Q and frictional F resistance per unit length provided by the soil. An approximate, but remarkably robust, solution for the chain shape through the soil may be expressed as (Neubecker and Randolph 1995b):

$$\frac{T_a}{2}\left(\theta_a^2 - \theta^2\right) = \int_z^{z_a} Q \mathrm{d}z \tag{5}$$

where T_a is the chain tension at the padeye (depth z_a) and Q is the normal resistance from the soil.

A corresponding expression was given for the change of load between mudline (T_m) and padeye, as

$$\frac{T}{T_a} = e^{\mu(\theta_a - \theta)} \tag{6}$$

where μ is the friction ratio for the chain, i.e. the ratio of frictional resistance F to normal resistance Q. These quantities may be derived for anchor chains in soil of a given shear strength using relationships proposed by Degenkamp and Dutta (1989).

However, for a fixed anchor such as a suction caisson, where the chain originally lies along the side of the caisson during installation, and is then tensioned to form the inverse catenary shape, recent studies have shown that Eq. (6) considerably overestimates the variation of tension along the chain. Sun et al. (2019a) presented detailed 3D finite element analyses of chain tensioning for a fixed padeye location. They showed that, even for non-softening soil, the change in tension between mudline and padeye was less than 5% (equivalent to $\mu \sim 0.07$), for conditions of a 9 m deep padeye, soil shear strength profile of $s_u = 2 + 1.2z$ kPa, and a simulated chain with a friction ratio of $\mu = 0.34$.

Figure 10 compares tension profiles from the Neubecker–Randolph solution with those from the FE analyses. The much lower change in tension from the numerical analyses resulted from low mobilized friction along the chain, particularly at depth, as a result of (a) interaction between the frictional and bearing resistance from the soil, and (b) limited 'sliding' chain movement because of the fixed padeye. Further studies for softening soil showed that, for typical marine soil sensitivities of 3–5, the tension loss through the soil is only 2–3%; the inverse catenary profiles of the chain were still well predicted by Eq. (5) (Sun et al. 2019b).

These are important results that have revealed the unconservative nature of current design practice, where relationships such as Eq. (6) (or equivalent from solving the chain equations numerically) are applied, with μ typically taken in excess of 0.3 for fine-grained soil.

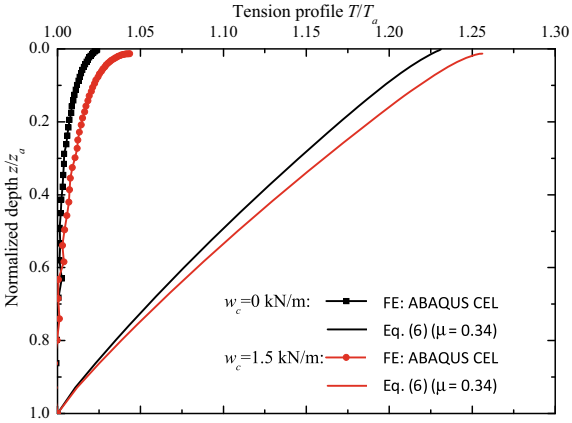

Fig. 10 Comparison of chain tension profiles after chain tensioning to $\theta_a = 35°$ (after Sun et al. 2019a)

4.3 Trenching

Semi-taut mooring configurations are often favoured in deep water, as discussed previously. However, an important phenomenon associated with such mooring designs has come to light in recent years, which is the development of significant trenching in front of the anchor. This first came to light from surveys of the Serpentina FPSO moorings (Bhattacharjee et al. 2014). A schematic illustration of the surveyed trenches is shown in Fig. 11.

The mechanisms involved in trench formation are relatively well understand, although quite difficult to quantify (Sassi et al. 2017; Versteele et al. 2017; O'Neill et al. 2018). For a semi-taut mooring with a suction caisson anchor, the chain will

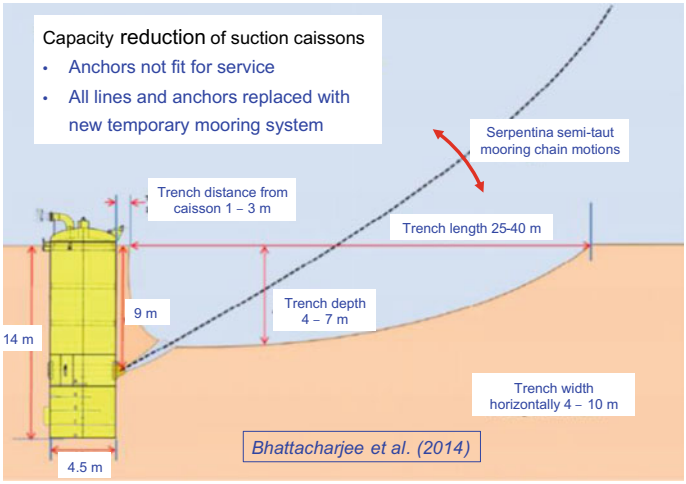

Fig. 11 Summary of trench geometries at Serpentina

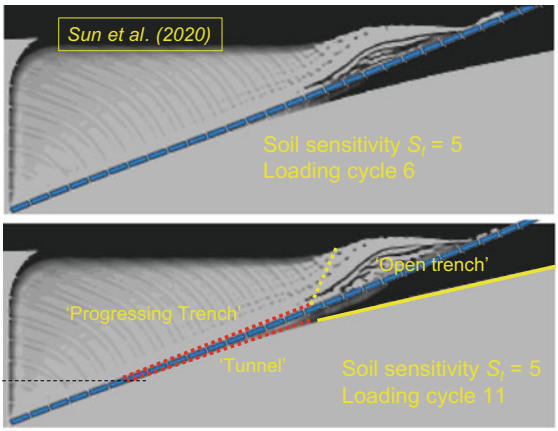

Fig. 12 Trench development with number of cycles

initially be tensioned, creating a wound in the seabed sediments. Typical 'ambient' loading conditions will involve a chain angle in the range 10–20° at mudline. During storm events, though, that angle will increase to 25–35°, possibly accompanied by 'out of plane' displacements. The alternating lifting (and tautening), followed by relaxing to the ambient condition, will work the soil in the path of the chain, remoulding it and facilitating water entrainment to further soften it. Additional mechanisms such as erosion and trench collapse may also contribute to the trench formation.

Numerical analysis of trench development using large deformation finite element analysis is presented by Sun et al. (2020) for soft clay with a sensitivity of 5. The high computational cost of the analysis limited the number of cycles to 11, but it may be seen from Fig. 12 that the main trench, and a narrow water filled 'tunnel' extending towards the padeye, continue to grow with increasing number of cycles. The form of trench is quite similar to that illustrated in Fig. 11, particularly once allowance is made for other contributing mechanisms such as erosion, water entrainment and out of plane motion of the chain.

A summary of trenches observed in the Gulf of Guinea (Colliat et al. 2018) showed that the trench widths at seabed level were generally similar to the maximum trench depth. The latter ranged between 25% and 100% of the padeye depth, although the maximum depth did not generally occur adjacent to the caisson. From observations at different periods of operation, the authors suggested that full trench development takes 8–10 years to complete, with more severe trenches occurring for more heavily loaded anchors (for which the maximum chain angle at mudline will be greater).

It appears that the open trenches observed in the Gulf of Guinea may be associated with the strength intercept of 10–15 kPa that occurs at many locations there (Kuo and Bolton 2014). For example, similar trenches have not been observed in the Gulf of Mexico, where the seabed sediments do not exhibit any significant strength intercept. However, it is still possible that the soil in the vicinity of the moving anchor chain has been severely softened, but without an open trench being formed.

Predictive models of the timescale and magnitude of trench development for different mooring configurations are still being developed. In the meantime, a key question for design is how best to take into account a possible trench. Preliminary studies (Sassi et al. 2018) have indicated that:

- A gap does not develop behind the caisson, even where a trench exists.
- The caisson capacity under including (30°) loading was reduced by only 11% (model tests) to 19% (FE modelling).

Other studies (Feng et al. 2019) have shown rather larger reductions in horizontal translational capacity. For full (caisson) width trenches extending down to the padeye, the capacity reduction ranged between 40%, for full suction capacity of the rear face of the caisson, and 70%, where a gap was allowed to develop.

In the light of such reductions in capacity, a possible design approach would be to reduce the depth of the padeye (hence limiting the size of trench and resulting loss of capacity) accepting some forward motion of the caisson and in consequence a capacity that is less than the ideal translational capacity. This is illustrated in Fig. 13. The optimal padeye depth is then obtained as a compromise between the two competing factors: loss of soil resistance due to the trench, and reduction in caisson capacity due to forward rotation.

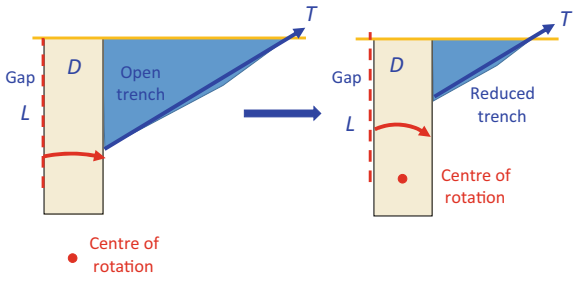

(a) Reduction of padeye depth and trench size

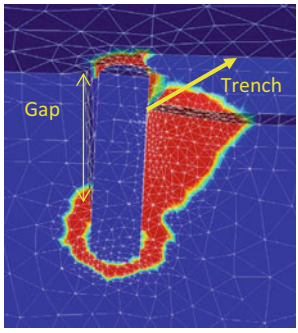

(b) Failure mechanism with shallow padeye

Fig. 13 Design strategy of reducing padeye depth

5 Gravity Installed Torpedo Anchors

Gravity installed anchors were developed originally as a low-cost anchoring system suitable for deep water applications. Two slightly different geometries were proposed: a 'deep penetrating anchor' (Lieng et al. 1999, 2010); and a 'torpedo' anchor (Medeiros 2001; Araujo et al. 2004—see Fig. 14a and 15). Both of these comprise a 10–17 m long rocket- or torpedo-shaped anchor with side fins (referred to as flukes) towards the upper end of the anchor, with masses in the range 24–98 tonnes. The anchor is installed by releasing it from a given height above the seabed, allowing it to fall freely through the water column, reaching a terminal velocity of 15–30 m/s at impact with the seabed. Typical (tip) burial depths are around 2–3 times the anchor length.

A more complex 'OMNI-Max' anchor was developed by Delmar (Shelton 2007; Zimmerman et al. 2009—see Fig. 14b and Fig. 15). It is about 60% of the length

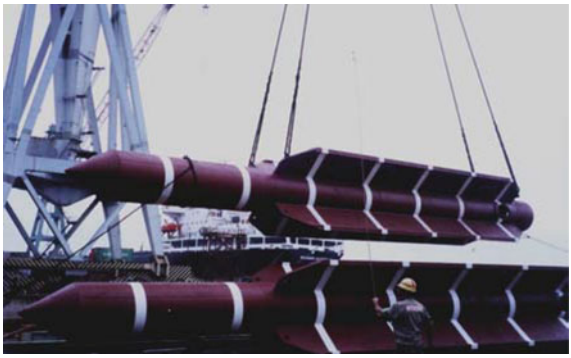

(a) Torpedo anchor (Araujo et al. 2004)

(b) Delmar's OMNI-Max (Shelton 2007)

Fig. 14 Contrasting gravity-installed anchors

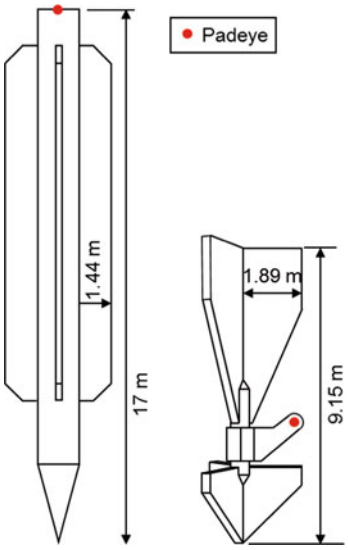

Fig. 15 Torpedo anchor (98 t) and OMNI-Max (39 t)

and 40% of the weight of a large (e.g. T-98, Brandao et al. 2006) torpedo anchor, and has small fins near the tip in addition to those at the tail. A shank that is free to rotate around the shaft is located between the two sets of fins. The key aspect of the OMNI-Max is that it is designed to 'dive' as the load is increased, a concept that will be discussed in greater detail later in the paper.

Gravity-installed anchors have mostly been used for temporary mooring of drilling vessels, although the large T-98 torpedo anchor shown here was used for permanent anchoring of the P-50 FPSO in Brazilian waters (Brandao et al. 2006). As part of the qualification process for the anchor, actual installation depths and orientation were carefully monitored and finite element analyses were undertaken to evaluate anchor capacity for different relative angles of anchor and chain load.

Figure 16 shows the computed load responses for different combinations of anchor tilt and loading direction. The fins attached to the anchor lead to quite similar capacities under pure axial and pure lateral (for load applied at the head of the anchor) loading, with 'efficiencies' of 8–9, although the horizontal capacity takes greater displacement to be mobilized. There is also an optimum capacity where the relative angle between anchor axis and loading direction is around 35–45° (see also de Aguiar et al. 2009).

The anchor tip embedment depth is a critical quantity in determining the load capacity, since (for most deep water deposits) the soil strength increases proportionally with depth according to $s_u \sim kz$. Results from centrifuge model tests and available field data suggest that anchor embedment may be expressed in terms of the total energy E (sum of kinetic energy at seabed impact plus the change in potential energy during embedment) according to (O'Loughlin et al. 2013)

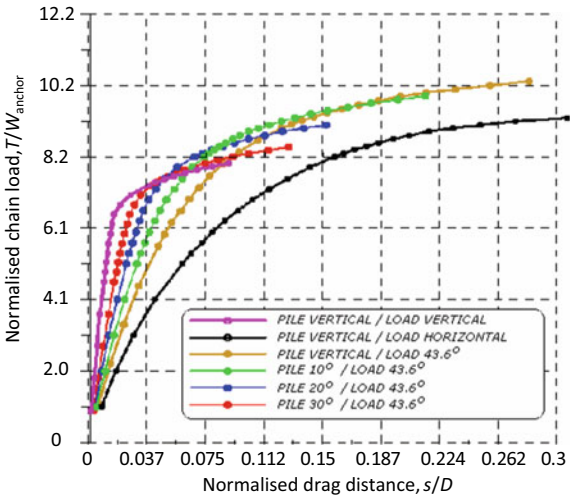

Fig. 16 Computed load response of T-98 anchors (after Brandao et al. 2006)

$$\frac{z_{\text{tip}}}{D_{\text{eff}}} \sim \left(\frac{E_{\text{total}}}{kD_{\text{eff}}^4}\right)^{1/3} \tag{7}$$

This is shown in Fig. 17.

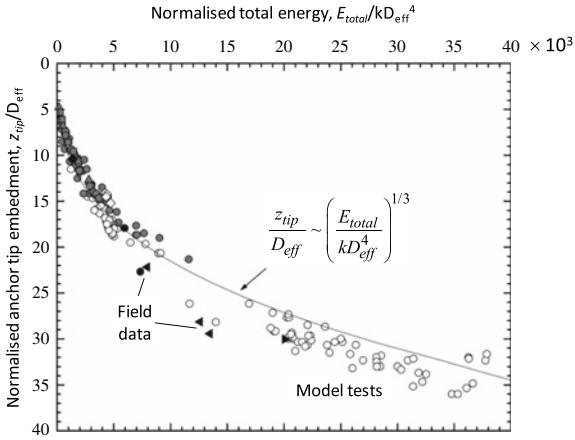

Fig. 17 Energy relationship for anchor embedment (after O'Loughlin et al. 2013)

6 Plate Anchors

6.1 Suction Embedded Plate Anchors

The final anchor types to be considered are different forms of plate anchor. The main one of these is the suction embedded plate anchor (SEPLA) developed by Intermoor (Dove et al. 1998; Wilde et al. 2001). The anchor takes the form of a main (rectangular) fluke, to which is attached a 'keying flap'. The shank and padeye are located centrally within the main fluke. A SEPLA is installed by means of a suction caisson, which is then withdrawn leaving behind the anchor and attached chain. Figure 18 shows a SEPLA being inserted into the slot at the tip of a suction caisson. Typically, the keying flap represents around 20% of the total anchor area, and the length (normal to the caisson slot) is just under double the overall anchor dimension parallel to the slot, with overall areas of fluke plus keying flap of up to 40 m^2.

On first introduction, SEPLAs were used only for temporary moorings, such as for drilling vessels, but their use was eventually extended to permanent anchoring, following a pre-qualification exercise involving physical and numerical modelling (Wong et al. 2012).

Fig. 18 SEPLA being inserted into suction caisson slot

6.1.1 Keying Flap

The intention of the keying flap was to limit the loss of embedment of the anchor during 'keying', i.e. application of pre-tension following installation. Inevitably, as tension is applied, there will be a tendency for the plate anchor to move upwards as it starts to rotate, partly due to the presence of soil that has been disturbed and partially remoulded during penetration, and then extraction, of the caisson. In that respect, there is benefit in delaying pre-tensioning until reconsolidation has occurred (Gaudin et al. 2006).

The keying flap is configured so that it can rotate away from the anchor shank (as evident in Fig. 18) up to a limit of 20°, but not towards the shank. The hinges are eccentric, on the side of the shank, to encourage rotation under the action of friction along the flap as it moves upwards; rotation would then increase the area projected normal to travel parallel to the anchor fluke.

However, detailed experimental studies (Gaudin et al. 2010), supported by small and large strain finite element analyses (Tian et al. 2013, 2014) have shown that the moment on the flap hinges during keying is dominated by pressure on the back of the flap (reverse side from the shank) as it rotates. As such, the flap does not rotate at all during keying, and only opens once the main anchor plate has rotated to become near normal to the chain. This is illustrated in Fig. 19. An improved design would allow the keying flap to rotate *towards* the shank, but not away from the shank. This would result in the flap opening during keying but closing under operational loading, hence maximizing the anchor capacity (Tian et al. 2014).

An important aspect of the SEPLA design, which originates from the addition of a keying flap, is that the padeye is offset from the overall centre of the anchor.

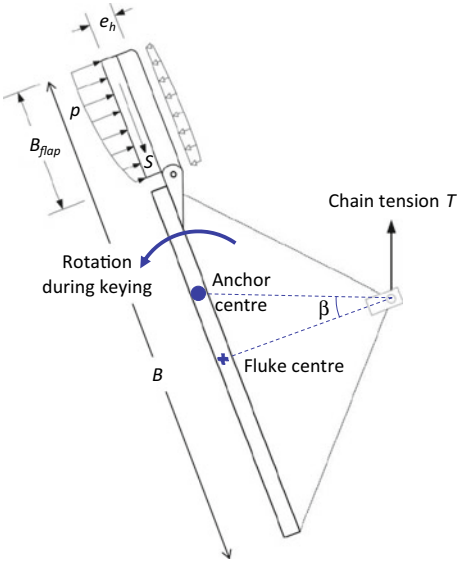

Fig. 19 Anchor geometry showing pressure on back face of flap due to rotation during keying

The resulting 'offset ratio' $\eta = \tan \beta$ (see Fig. 19) has consequences for the anchor kinematics during failure, which is discussed in more detail later.

6.1.2 Design Principles

One of the advantages of the SEPLA by comparison with other plate anchors is that the depth of installation is known deterministically according to the embedment length of the suction caisson. As such, the average shear strength of the soil in the vicinity of the as-installed anchor may be assessed from site investigation data. The ideal bearing capacity of a plate anchor for a given shear strength s_u may be expressed as $N_p s_u$, where N_p may be taken as 13.5 for a rectangular plate with length-to-breadth ratio of around 2 (Wang et al. 2010).

However, this capacity must then be modified to allow for a number of factors f, including

- Loss of embedment during keying f_z
- Reduction in capacity due to strain-softening of the soil as failure develops around the anchor f_s
- A geometry factor associated with the offset ratio of the padeye relative to the anchor centre f_g
- Potential increase in anchor capacity due to consolidation under sustained loading f_{cons}
- Reduction in capacity due to cyclic loading f_{cyc}.

The pre-qualification study described by Wong et al. (2012), with particular application to West African offshore soils, led to recommendations for the bearing response under monotonic loading of

$$N_{c,\text{design}} = f_z f_s f_g N_p = 9.7 \tag{8}$$

It was found that sustained loading gave rise to significant gain in capacity, for example, with 50% increase under a sustained load of 60% of the undrained failure value. Recent studies have quantified this increase in terms of a simple critical state approach (Zhou et al. 2020). However, in the absence of prior gain in capacity due to consolidation, upper limits of sustained loading and maximum levels of cyclic loading were found to be 80% and 75%, respectively, of the design capacity factor in Eq. (8) (Wong et al. 2012).

6.2 Dynamically Embedded Plate Anchors

An alternative method to embed plate anchors was proposed by O'Loughlin et al. (2014). The concept, which is illustrated in Fig. 20, is to use a removable 'torpedo' as the means to install a cruciform plate anchor in the form of two perpendicular circular

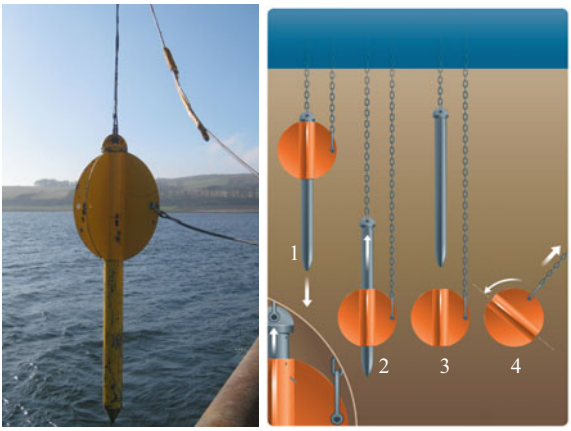

Fig. 20 Small field version and concept of DEPLA

fins of diameter D_{plate}. After dynamic installation, the torpedo mandrel is withdrawn and the anchor may then be tensioned through the attached chain. A retrieval line (not shown) may also be attached to the top of the plate anchor (near the axis) to facilitate removal.

A simple design procedure for the so-called dynamically embedded plate anchor (DEPLA) was developed (O'Loughlin et al. 2016). The procedure combines an estimate of the torpedo tip penetration using Eq. (7), from which the plate centroid embedment can be deduced, and an estimate of embedment loss during keying. The final bearing capacity Q_u is estimated in terms of the average bearing pressure q_u as

$$q_u = \frac{Q_u}{A_{\text{plate}}} = N_{c,\text{plate}} s_{\text{uf}} \tag{9}$$

where A_{plate} is the projected cross-sectional area of the anchor, s_{uf} is the local shear strength at the final (post-keying) embedment depth of the anchor centroid, and $N_{c,\text{plate}}$ is a bearing factor. A value of 14.9 was recommended for the latter for embedment depths exceeding $2.5D_{\text{plate}}$ based on field and centrifuge model test data, although this is rather higher than the range of 14.2–14.4 deduced from numerical analyses for the relevant plate thickness (Wang et al. 2010; Wang and O'Loughlin 2014), or the plasticity solution of 13.1 for an infinitely thin circular plate (Martin and Randolph 2001).

The design approach is essentially similar to that for SEPLAs, as in Eq. (8), although, in this case, the shear strength is that estimated at the post-keying depth, rather than the original (dynamic) embedment depth. The reduction term N_s due to the soil sensitivity should be incorporated, although the geometry term N_g will be unity for a padeye located at on the plane of symmetry.

As originally designed, the DEPLA will suffer a small amount of embedment loss during keying, estimated as around one plate diameter, prior to developing its ultimate capacity. However, it is evident that the design could be improved by relocating the

padeye to an offset ratio (as defined in Fig. 19) that will cause the anchor to dive, similar to the OMNI-Max anchor (Tian et al. 2015a). The optimum position of the padeye for plate anchors, and hence the maximum potential embedment depth and capacity, is considered below.

6.3 Ultimate Embedment Depth of Diving Anchors

The potential diving behaviour of anchors was demonstrated at full scale for the OMNI-Max anchor as a result of mooring line failures during Hurricane Gustav in the Gulf of Mexico (Zimmerman et al. 2009). The loss of certain mooring lines caused overloading of the remaining anchors until eventually only a single lightly loaded line remained intact. Post-hurricane retrieval of the anchors showed that three of the anchors had dived, increasing their initial embedment depths of 15.9–17.7 m to a final depth range of 32.9–36.6 m, essentially doubling their initial embedment.

Estimation of anchor kinematics and hence the ultimate embedment depth during diving may be assessed through the use of a three-dimensional failure envelope in normal, shear and moment load space. In terms of normalized bearing factors, the failure envelope may be expressed as (see Fig. 21)

$$\left(\frac{N_n}{N_{n,\max}}\right)^q + \left[\left(\frac{|N_m|}{N_{m,\max}}\right)^m + \left(\frac{|N_s|}{N_{s,\max}}\right)^n\right]^{\frac{1}{p}} = 1 \tag{10}$$

The form of the failure envelope is adapted from Murff (1994), with the separate capacity factors normalized by their ultimate values in normal $N_{n,\max}$, shear $N_{s,\max}$- and moment $N_{m,\max}$-. To maintain convexity, the value of the power p should not exceed the lower of powers m and n. Tian et al. (2015b) quoted typical values of the powers for plate anchors of:

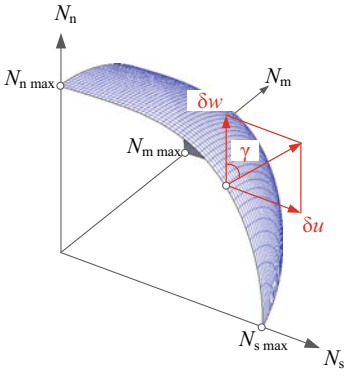

Fig. 21 Failure envelope for plate anchor

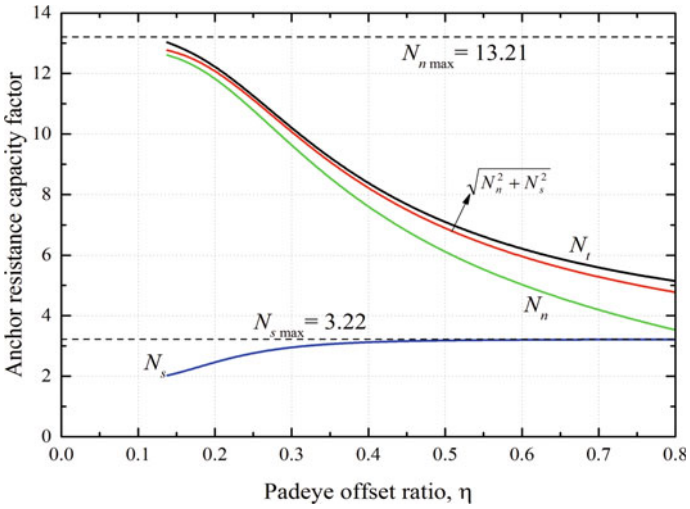

Fig. 22 Effect of padeye offset ratio on capacity factors

$$m \sim p \sim 1.1 - 1.4, n \sim 3.8 - 4.2, q \sim 3.3 - 4$$

It may be noted in passing that the value of m does not affect the final anchor kinematics, since the moment tends to zero during steady-state conditions.

The values of the maximum capacity factors need to be determined from numerical analysis for any given anchor geometry. This will generally require quite complex 3D FE analysis, such as described for the OMNI-Max anchor (Wei et al. 2015). The factors are also affected by the padeye offset ratio, $\eta = \tan\beta$, as illustrated in Fig. 22. Increasing the offset angle of the padeye relative to the anchor centroid of resistance leads to a significant reduction in the normal and moment capacity factors, accompanied by a slight increase in the shear capacity factor.

Balancing the decrease in the normal capacity factor is the tendency for the anchor to dive, embedding into stronger soil. As it does so, the padeye chain angle θ_a will increase, relative to the mudline chain angle, according to the chain geometry (Eq. 5). This will also cause the anchor to continue to rotate, always seeking to minimize the moment acting on the anchor. Eventually, steady-state conditions will be reached, with the ultimate embedment and anchor capacity achieved (Tian et al. 2015b).

The effect of the padeye offset ratio on the normalized embedment is shown for square anchors of width B in Fig. 23 for mudline chain angles θ_m between 0 and 50°. The failure envelope powers n and q were taken at the upper end of the range quoted earlier, while p was taken at the lower end. Although the magnitude of the maximum embedment varies markedly with θ_m, optimum padeye ratios fall in a narrow range of around 0.2–0.35.

Application of these principles for the SEPLA geometry were reported by Tian et al. (2015b), assuming a mudline chain angle of 30° and soil strength proportional to depth according to $s_{u-} = kz$ and typical chain dimensions relative to the anchor

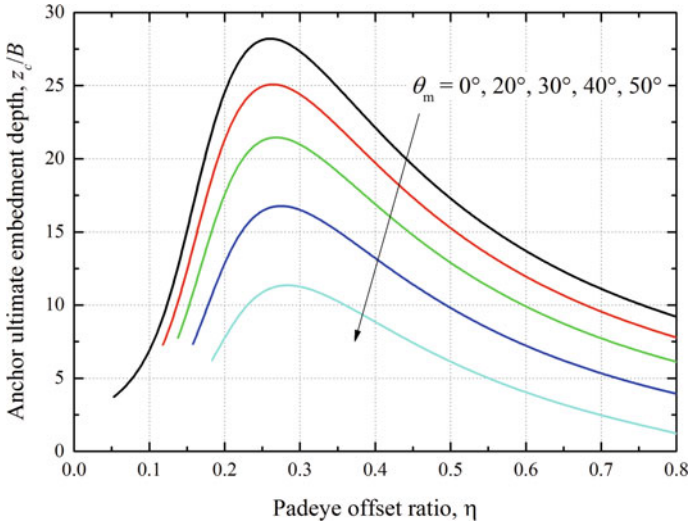

Fig. 23 Variation of ultimate depth with offset ratio

size. For that case, failure envelope powers n and q were taken at the lower end of the range quoted earlier, and p at the upper end (following Wei et al. 2015).

The resulting normalized ultimate embedment depth z_c/B and anchor capacities T_a/kB^3 (anchor) and T_m/kB^3 (mudline) are shown in Fig. 24. The combination of failure envelope powers leads to rather lower ultimate embedment depths than shown

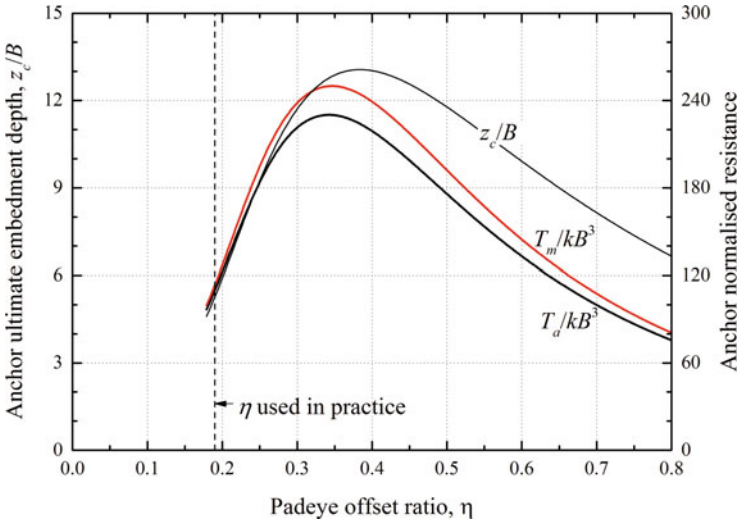

Fig. 24 Application to SEPLA geometry

in Fig. 23, and also an increase in the optimum range of offset ratios to between 0.3 and 0.4. This emphasizes the importance of adjusting the failure envelope for the particular anchor geometry.

Importantly, however, the results suggest that the current SEPLA geometry is non-optimal, since the relative sizes of the keying flap and main fluke (and shank) lead to a padeye offset ratio of $\eta = 0.19$. Increasing the size of the keying flap so that the offset ratio is around 0.3 would effectively double the potential anchor capacity.

Of course, as the anchor geometry is optimized to provide increased capacity, the size of the anchor chain would need to be increased, and that would decrease the ultimate embedment depth. As such, choice of optimum anchor geometry and design holding capacity requires an iterative procedure, although this does not change the main principles outlined here.

7 Discussion and Concluding Remarks

It is useful to compare the relative merits of different forms of deep water anchor, considering not just the potential holding capacity but also cost (fabrication, transport and installation) and reliability (robustness of design, sensitivity to variations in soil parameters and to installation conditions). As noted previously, vertically loaded drag embedment anchors (VLAs) have generally been used for moderate anchor loads (<5 MN), whereas suction caissons have been designed to withstand factored loads of up to 15 MN (e.g. Diana, and also Mad Dog—Schroeder et al. 2006). Suction-embedded plate anchors (SEPLAs) have been designed for intermediate load levels, for example, the 37 m^2 model SEPLA discussed by Wong et al. (2012), which showed failure loads of 7.7–10.7 MN for different pullout directions from an initial embedment of just over 20 m.

While suction caissons are installed to a known (and fixed) embedment, other anchors such as the OMNI-Max, the streamlined 'fish' anchor (Chang et al. 2018) and plate anchors (statically embedded SEPLAs and dynamically embedded DEPLAs) are capable, at least in principle, of diving to much greater depths than the initial installation depth. To date, advantage has not been taken of this in design. O'Loughlin et al. (2017) considered the relative merits of different forms of plate anchor, noting the 'self-adjusting' nature of the DEPLA and other forms of dynamically installed anchors with respect to the soil strength: stronger soil would reduce the embedment depth, but that would be compensated by increased capacity at that depth.

Typical initial embedment ratios for SEPLAs and DEPLAs are around 4–5 times the anchor width or diameter. Given potential maximum embedment ratios in excess of 10 indicated in Figs. 23 and 24, it seems logical to modify current designs for both types of plate anchor in order to maximize their potential. As an example, suppose that diving depths of 10 times the width of a 40 m^2 SEPLA were shown to be achievable in field trials, the holding capacity in soil with a shear strength gradient of 1.25 kPa/m would exceed 18 MN, even after allowing for detrimental effects of cyclic loading. Structural considerations would no doubt come into play for such a

design, both for the anchor (increasing the plate thickness) and the chain (increasing the bar diameter, which would reduce the potential embedment). However, there still seems significant potential for advancing the current state of practice in anchor design, taking advantage of modern techniques in physical and numerical modelling in order to evolve new designs prior to validation at field scale.

One final comment concerns the role of numerical analysis in design of anchors for deep water applications. Of the various anchor types reviewed here, in most cases the design approaches have been developed by synthesizing results from detailed numerical analyses, mostly finite element based. For a given application, the main design process itself, comprising choice of anchor type and preliminary sizing, relies on such conceptual models, often using simplified soil profiles. Numerical analysis may then be used to validate a final design, incorporating site-specific soil properties and other relevant boundary conditions. This allows fine tuning and validation of the design.

References

AGSPANC (2001) AGSPANC: Suction pile analysis code: Users' Manual, Version 3.0. Advanced Geomechanics (now Fugro)

Andersen KH, Jostad HP (2002) Shear strength along outside wall of suction anchors in clay after installation. In: Proceedings of 12th international offshore and polar engineering conference, Kitakyushu, Japan, 785–794

Andersen KH, Murff JD, Randolph MF, Clukey E, Erbrich CT, Jostad HP, Hansen B, Aubeny CP, Sharma P, Supachawarote C (2005) Suction anchors for deepwater applications. In: Proceedings of international symposium on frontiers in offshore Geotech, Perth, pp 3–30

Araujo JB, Machado RD, Medeiros CJ (2004) High holding power torpedo pile—results for the first long term application. In: Proceedings of 23rd International Conference on Offshore Mechanics and Arctic Engineering, ASME, Vancouver, OMAE2004-51201

Bhattacharjee S, Majhi SM, Smith D, Garrity R (2014) Serpentina FPSO mooring integrity issues and system replacement: unique fast track approach. In: Proceedings of offshore technology conference, Houston, OTC 25449

Brandao FEN, Henriques CCD, Araujo JB, Ferreira OCG, Amaral CDS (2006) Albacora Leste field development: FPSO P-50 mooring system concept and installation. In: Proceedings of offshore technology conference, Houston, OTC 18243

Chang K, Hossain MS, Kim YH, Randolph MF, Wang D (2018) Novel dynamically installed fish anchor—diving upon pullout in calcareous silt. In: Proceedings of offshore technology conference, Houston, OTC 28901

Chow FC, Banimahd M, Tyler S, Rathmell A, Ostojic M, Holland BJ (2017) Investigating drag anchor behaviour in calcareous materials on the North West Shelf of Australia. In: Proceedings of 8th international conference on offshore site investigation and geotechnics, Society for Underwater Technology, London, pp 1206–1213

Colliat J-L, Safinus S, Boylan N, Schroeder K (2018) Formation and development of seabed trenching from subsea inspection data of deepwater Gulf of Guinea moorings. In: Proceedings of Offshore Technology Conference, Houston, OTC 29034

de Aguiar CS, de Sousa JRM, Ellwanger GB, Porto EC, de Medeiros Junior CJ, Foppa D (2009) Undrained load capacity of torpedo anchors in cohesive soils. In: Proceedings of 28th international conference on offshore mechanics and Arctic engineering, ASME, Honolulu, OMAE2009-79465

Degenkamp G, Dutta A (1989) Soil resistances to embedded anchor chain in soft clay. J Geot Eng Div ASCE 115(10):1420–1438

Dove P, Treu H, Wilde B (1998) Suction embedded plate anchor (SEPLA): a new anchoring solution for ultra-deepwater mooring. In: Proceedings of deep offshore technology conference, New Orleans

Doyle EH (1994) Geotechnical considerations for foundation design of the Auger and Mars TLPs. In: Proceedings of international conference on behaviour of offshore structures, BOSS '94, Massachusetts Institute of Technology, Boston

Erbrich CT (2004). A new method for the design of laterally loaded anchor piles in soft rock. In: Proceedings of offshore technology conference, Houston, OTC 16441

Erbrich CT, Hefer PA (2002) Installation of the Laminaria suction piles—a case history. In: Proceedings of offshore technology conference, Houston, OTC 14240

Erbrich CT, Lam SY, Zhu H, Derache A, Sato A, Al-Showaiter A (2017) Geotechnical design of anchor piles for Ichthys CPF and FPSO. In: Proceedings 8th international conference on offshore site investigation and geotechnics, Society for Underwater Technology, London, pp 1186–97

Feng X, Gourvenec S, White DJ (2019) Load capacity of caisson anchors exposed to seabed trenching. Ocean Eng 171:181–192

Finnie I, Gillinder R, Richardson M, Erbrich CT, Wilson M, Chow F, Banimahd M, Tyler S (2019) Design and installation of mobile offshore drilling unit mooring piles using innovative drive-drill-drive techniques. In: Proceedings of 13th Australia New Zealand conference on geomechanics, Perth, pp 623–634

Frankenmolen S, Erbrich CT, Fearon R (2017) Successful installation of large suction caissons and driven piles in carbonate soils. In: Proceedings of 8th international conference on offshore site investigation and geotechnics. Society for Underwater Technology, London, pp 539–548

Garside R, Bowen KG, Stevens JW, Doyle EH, Henry DM, Romijn E (1997) Proceedings of offshore technology conference, Houston, OTC 8373

Gaudin C, O'Loughlin CD, Randolph MF, Lowmass A (2006) Influence of the installation process on the performance of suction embedded plate anchors. Géotechnique 56(6):381–391

Gaudin C, Simkin M, White DJ, O'Loughlin CD (2010) Experimental investigation into the influence of a keying flap on the keying behaviour of plate anchors. In: Proceedings of 20th International offshore and polar engineering conference, Beijing, China

Håland G (2002) Pros and cons of foundations used for the Åsgard field development. In: Proceedings of 5th international conference on offshore site investigation and geotechnics, Society for Underwater Technology, London, pp 93–105

Kay S, Palix E (2010) Caisson capacity in clay: VHM resistance envelope—Part 2: VHM envelope equation and design procedures. In: Proceedings of 2nd international symposium on frontiers in offshore geotechnics, vol 1, pp 741–746

Kuo MY-H, Bolton MD (2014) The nature and origin of deep ocean clay crust from the Gulf of Guinea. Géotechnique 64(4):249–257

Lieng JT, Hove F, Tjelta TI (1999) Deep penetrating anchor: subseabed deepwater anchor concept for floaters and other Installations. In: Proceedings of 9th international offshore and polar engineering conference, Brest, pp 613–619

Lieng JT, Tjelta TI, Skaugset K (2010) Installation of two prototype deep penetrating anchors at the Gjoa field in the North Sea. In: Proceedings of offshore technology conference, Houston, OTC 20758

Martin CM, Randolph MF (2001) Applications of the lower and upper bound theorems of plasticity to collapse of circular foundations. In: Proceedings of 10th international conference of international association of computer methods and advances in geomech (IACMAG), Tucson, 2, pp 1417–1428

Medeiros CJ (2001) Torpedo anchor for deep water. In: Proceedings of deep offshore technology conference, Rio de Janeiro

Murff JD (1994) Limit analysis of multi-footing foundation systems. In: Proceedings of 8th International Conference on International Association on computer methods and advances in Geomech (IACMAG), West Virginia, vol 1, pp 233–244

Murff JD, Hamilton JM (1993) P-ultimate for undrained analysis of laterally loaded piles. J Geotech Eng Div ASCE 119(1):91–107

Neubecker SR, Randolph MF (1995a) Performance of embedded anchor chains and consequences for anchor design. In: Proceedings of offshore technology Conference, Houston, OTC 7712

Neubecker S.R. and Randolph M.F. 1995b. Profile and frictional capacity of embedded anchor chain. J. Geot. Eng. Div., ASCE, 121(11), 787–803

Newlin JA (2003) Suction anchor piles for the Na Kika FDS mooring system. Part 1: site characterisation and design. Part 2: installation performance. In: Proceedings of international symposium on deepwater mooring systems, Houston

O'Loughlin CD, Richardson MD, Randolph MF, Gaudin C (2013) Dynamic anchor embedment in clay. Géotechnique 63(11):909–919

O'Loughlin CD, Blake A, Richardson MD, Randolph MF, Gaudin C (2014) Installation and capacity of dynamically embedded plate anchors as assessed through centrifuge tests. Ocean Eng 88:204–213

O'Loughlin CD, Blake AP, Gaudin C (2016) Towards a design method for dynamically embedded plate anchors. Géotechnique 66(9):741–753

O'Loughlin CD, White DJ, Stanier SA (2017) Plate anchors for mooring floating facilities—a view towards unlocking cost and risk benefits. In: Proceedings of 8th international conference on offshore site investigation and geotechnics, Society for Underwater Technology, London, pp 978–86

O'Neill MP, Neubecker SR, Erbrich CT (2010) Installation and in-place assessment of drag anchors in carbonate soil. In: Proceedings of 2nd international symposium on frontiers in offshore geotechnics, vol 1, pp 747–752

O'Neill MP, Erbrich CT, McNamara A (2018) Prediction of seabed trench formation induced by anchor chain motions. In: Proceedings of offshore technology conference, Houston, OTC 29068

Palix E, Willems T, Kay S (2010) Caisson capacity in clay: VHM resistance envelope—Part 1: 3D FEM numerical study. In: Proceedings of 2nd international symposium on frontiers in offshore geotechnics, vol 1, pp 753–758

Randolph MF (2013) 2nd McClelland lecture: analytical contributions to offshore geotechnical engineering. In: Proceedings of 18th international conference on soil mechanics and geotechnical engineering, Paris, pp 85–105

Randolph MF, Gourvenec SM (2011) Offshore geotechnical engineering. Taylor & Francis, London

Randolph MF, House AR (2002) Analysis of suction caisson capacity in clay. In: Proceedings of offshore technology conference, Houston, OTC 14236

Sassi K, Kuo MY-H, Versteele H, Cathie DN, Zehzouh S (2017) Insights into the mechanisms of anchor chain trench formation. In: Proceedings of 8th international conference on offshore site investigation and geotechnics, Society for Underwater Technology, London, pp 963–70

Sassi K, Zehzouh S, Blanc M, Thorel L, Cathie D, Puech A, Colliat-Dangus J-L (2018) Effect of seabed trenching on the holding capacity of suction anchors in soft deepwater Gulf of Guinea clays. In: Proceedings of offshore technology conference, Houston, OTC 28756

Schroeder K, Andersen KH, Tjok K-M (2006) Laboratory testing and detailed geotechnical design of the Mad Dog anchors. In: Proceedings of offshore technology conference, Houston, OTC 17949

Shelton JT (2007) OMNI-max anchor development and technology. In: Proceedings of 2007 Oceans Conference, Vancouver, Canada

Sun C, Feng X, Bransby MF, Randolph MF, Gourvenec S (2019a) Numerical study of mobilised friction along embedded catenary mooring chains. J Geot GeoEnv Eng ASCE 145(10): 04019081

Sun C, Feng X, Bransby MF, Randolph MF, Gourvenec S (2019b) Numerical investigations of the effect of strain softening on the behaviour of embedded mooring chains. Appl Ocean Res 92:101944

Sun C, Feng X, Bransby MF, Randolph MF, Gourvenec S (2020) Numerical investigations into development of seabed trenching in semi-taut moorings. Under review
Supachawarote C, Randolph MF, Gourvenec S (2004) Inclined pull-out capacity of suction caissons, ISOPE, Toulon, vol 2, pp 500–506
Supachawarote C, Randolph MF, Gourvenec S (2005) The effect of crack formation on the inclined pull-out capacity of suction caissons. In: Proceedings of IACMAG-05, Torino, pp 577–584
Tian Y, Cassidy MJ, Gaudin C, Randolph MF (2013) Considerations on the design of keying flap of plate anchors. J Geot and GeoEnv Eng ASCE 139(7):1156–1164
Tian Y, Gaudin C, Cassidy MJ (2014) Improving plate anchor design with a keying flap. J Geot GeoEnv Eng ASCE 140(5):04014009
Tian Y, Gaudin C, Randolph MF, Cassidy MJ (2015a) The influence of padeye offset on the bearing capacity of three dimensional plate anchors. Can Geotech J 52(6):682–693
Tian Y, Randolph MF, Cassidy MJ (2015b) Analytical solution for ultimate embedment depth and potential holding capacity of plate anchors. Géotechnique 65(6):517–530
Versteele H, Kuo MY-H, Cathie DN, Sassi K, Zehzouh S (2017) Anchor chain trenching–numerical simulation of progressive erosion. In: Proceedings of 8th international conference on offshore site investigation and geotechnics, Society for Underwater Technology, London, pp 971–977
Wang D, O'Loughlin CD (2014) Numerical study of pull-out capacities of dynamically embedded plate anchors. Can Geotech J 51(11):1263–1272
Wang D, Hu Y, Randolph MF (2010) Three-dimensional large deformation finite element analysis of plate anchors in uniform clay. J Geot GeoEnv Eng ASCE 136(2):355–365
Wei Q, Cassidy MJ, Tian Y, Gaudin C (2015) Incorporating shank resistance into prediction of the keying behaviour of SEPLAs. J Geot GeoEnv Eng ASCE 141(1):04014080
Wilde B, Treu H, Fulton T (2001) Field testing of suction embedded plate anchors. In: Proceedings of 11th international offshore and polar engineering conference, Stavanger, pp 544–551
Wong P, Gaudin C, Randolph MF, Cassidy MJ, Tian Y (2012) Performance of suction embedded plate anchors in permanent mooring applications. In: Proceedings of 22nd international offshore and polar engineering conference (ISOPE), Rhodes, ISOPE2012-TPC-0855
Zhou Z, O'Loughlin CD, White DJ, Stanier SA (2020) Improvements in plate anchor capacity due to cyclic and maintained loads combined with consolidation. Géotechnique, under review
Zimmerman EH, Smith M, Shelton JT (2009) Efficient gravity installed anchor for deepwater mooring. In: Proceedings of offshore technology conference, Houston, OTC 20117

Use of Onshore Test Sites for Offshore Geotechnical Problems

T. Lunne, NGI Oslo, S. Sharma, and R. K. Ghanekar

1 Introduction

The term reference site, or test site, as used in this paper means a site that is well-characterized and that can be used to compare measurements or observations made by different techniques or methods. This means that a test site has to be well-defined in terms of geological history, soil classification parameters and strength, deformation and flow parameters. Other requirements or specification for a test site usually include, but are not necessarily limited to:

- Representative for an area or project type
- Easily accessible
- Available over a certain time period
- Large enough so that, for instance, tests on model foundations can be performed and that it can be available for a number of applications over time before it is used up
- Relevant infrastructure is in place, e.g. access road, water supply and electricity
- Security from vandalism.

For the offshore industry, the use of onshore test sites has special advantages since use of advanced soil characterization methods and testing out model innovative foundations can be done at significantly lower costs and also frequently with higher accuracy. But, it is of course important that the soil conditions for the onshore test site are similar to the soil conditions for the offshore site where field development is to take place.

T. Lunne · N. Oslo · S. Sharma (✉)
NGI Perth, Perth, Australia
e-mail: shambuhu.sharma@ngi.no

R. K. Ghanekar
Institute of Engineering and Ocean Technology, ONGC, Panvel, Navi Mumbai, India

S. Haldar et al. (eds.), *Advances in Offshore Geotechnics*, Lecture Notes in Civil Engineering 92, https://doi.org/10.1007/978-981-15-6832-9_2

The purpose of this paper is to give examples of international test sites which have been important for developments of offshore geotechnics, and to give recommendations for the establishment of test site(s) in India.

2 International Test Sites

There are a large number of papers describing international test sites. In the following, some well-published examples will be described.

2.1 UK National Test Soft Clay Site at Bothkennar and Glacial Test Site in Cowden

The Bothkennar soft clay test site was owned, funded and managed by the UK Government through the Science and Engineering Research Council (SERC). A very comprehensive soil characterization programme was carried out in the period between 1988 and 1992 by a number of universities and research organizations. The results of the characterization were published in a volume of Géotechnique (1992) as a Symposium in print with a total of 380 pages. After 1992, Bothkennar has been used as a national test site for both industry and academia. A summary of the characterization was presented at an International Workshop in Singapore, published in a two volume proceedings (Hight et al. 2003).

The Cowden test site was established in 1976 because the clays are similar to clays found offshore east of the UK (see Fig. 1). The glacial clays at Cowden comprise

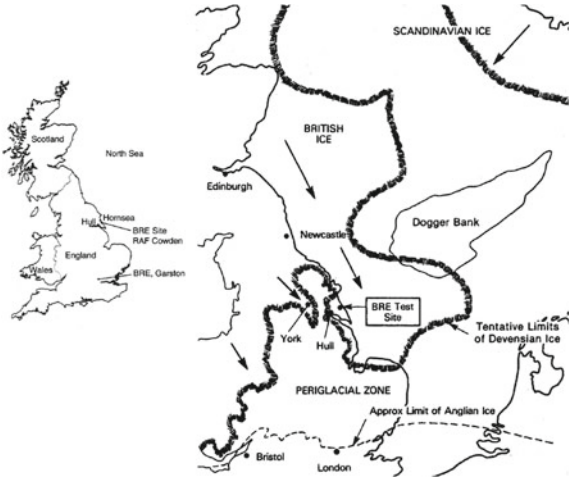

Fig. 1 Location of Cowden test site in: **a** within the UK, **b** approximate limits of Quaternary Ice sheets (Powell and Butcher 2003)

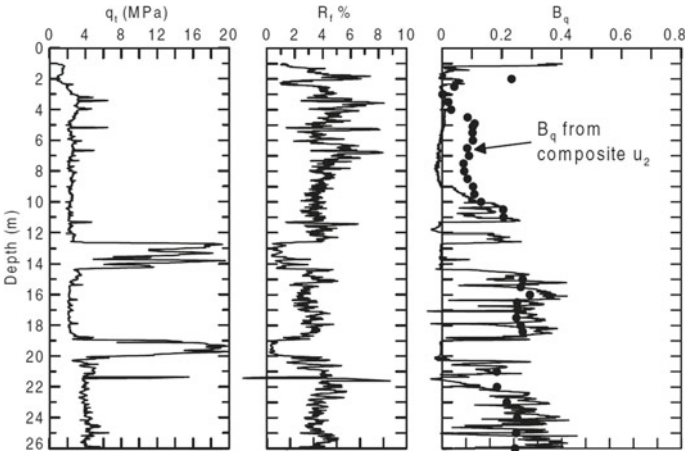

Fig. 2 CPTU profile at Cowden test site, from Powell and Butcher (2003)

tills of low plasticity, and they are overconsolidated with Ko values around 1 through much of the profile. The test site has for several decades been extensively investigated using a wide range of sampling, in situ and laboratory techniques. Figure 2 shows the results of a CPTU profile at Cowden test site. Powell and Butcher (2003) describe the information gathered and compare the results of the various techniques used. The site has also been used for assessing full-scale performance of various offshore pile types and techniques, model shallow foundations as well as coastal cliff stability.

2.2 National Geotechnical Experimentation (NGES) Sites in USA

The National Geotechnical Experimentation Sites (NGES) was established after funding was secured in 1992 by a joint partnership between the NSF (National Science Foundation) and the Federal Highway Administration (FHWA) in the USA. The history, scope, testing programme, and results of the NGES are described in detail in ASCE (2000). Two Level I (most thoroughly investigated) sites and four Level II (somewhat less thoroughly investigated) sites were established as shown in Table 1. The work performed at the established sites included a relatively large body of site characterization data and a number of industry backed, full-scale testing projects.

Table 1 Level I and II sites established in the USA through the NGES project

Site location	Site level	Soil conditions
Treasure Island, CA	Level I	Sand fill over soft clay (SFBM), liquefaction
Texas A&M, TX	Level I	Both a stiff CLAY and a SAND site
Northwestern University, IL	Level II	Soft to medium glacial CLAY
University of Houston, TX	Level II	Very stiff CLAY
University of Massachusetts Amherst	Level II	Soft lacustrine varved CLAY
Spring Villa, Alabama	Level II	Very stiff CLAY, residual soil
Fairbanks, Alaska	Added in 2003	Permafrost field site

2.3 National Soft Soil Field Testing Facility (NFTF) Australia

A national geotechnical soft soil field testing facility was established near the town of Ballina (New South Wales, Australia) for the purpose of reducing cost and risk of infrastructure construction on low-strength, poor-quality onshore and offshore soft soils (Pineda et al., 2019). The facility is being operated by the Australian Research Council's Centre of Excellence for Geotechnical Science and Engineering (CGSE) which is a collaboration between the universities of Newcastle, Wollongong and Western Australia as well as industry partners. The need for a national soft soil field testing facility was first identified by the Ballina Bypass Alliance (BBA). The alliance, comprising of NSW Roads and Maritime Services of (RMS), Leighton Contractors, Aecom, Coffey Geotechnics and SMEC, constructed the Ballina Bypass motorway over deep deposits of soft estuarine clay. During construction, settlements up to 6.5 m were recorded. Figure 3 shows how uniform the Ballina test site is.

2.4 Norwegian Test Sites

Norwegian Geotechnical Institute (NGI) has in its 60 years history made use of a number of test sites. A list of the most referenced ones is given in Table 2. Most of the sites have been on soft clays, with varying sensitivity and plasticity. But the sand site at Holmen in Drammen has also been used a lot. The test site in Longyearbyen, Svalbard, has only been used on a few occasions. The silt site at Halsen was operated by the Technical University in Trondheim and has also been used by NGI.

As an example, the Onsøy test site will be described in the following. Onsøy will also be used to illustrate the use of a test site in offshore engineering practice.

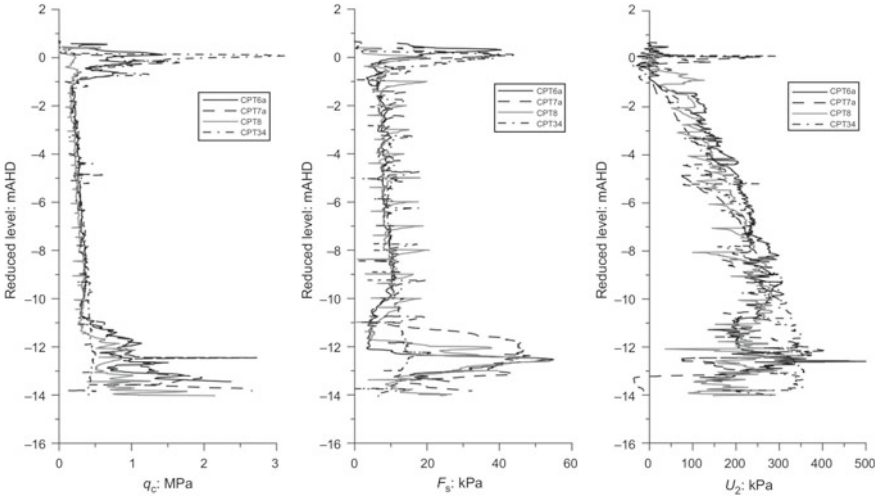

Fig. 3 Results of 4 CPTUs demonstrating the uniformity of the soft clay layer (Kelly et al. 2016)

Table 2 Overview of Norwegian test sites

Site	Soil profile	Operator	Reference
Onsøy	Lightly OC marine clay	NGI	Lunne et al. (2003a)
Drammen	Lightly OC marine clay	NGI	Lunne and Lacasse (1999)
Holmen	Loose to medium dense sand	NGI	Lunne et al. (2003b)
Lierstranda	Lightly OC marine clay	NGI	Lunne (2002)
Emmerstad	Quick clay	NGI	Lacasse et al. (1985)
Haga	Overconsolidated clay	NGI	Andersen and Stenhamar (1982)
Lysaker	Lightly OC marine clay	NGI	Dyvik et al. (1993)
Longyearbyen	Permafrost	NGI	Ladanyi et al. (1995)
Halsen	Silt	NTNU	Sandven (2003)
Tiller	Quick clay	NTNU	Sandven et al. (2004)
Glava	OC clay	NTNU	Sandven and Sjursen (1998)

2.4.1 Detailed Description of Onsøy Soft Clay Site

Due to the thickness of the clay deposit and its highly uniform nature, the Onsøy site has been used for research purposes by NGI for many years. The site is located in south-eastern Norway, about 100 km from Oslo just north of the city of Fredrikstad. The test site is located in an almost flat area that slopes gently towards the Seut River. The water table is very near to the ground level. The deposit at Onsøy consists of a weathered crust less than 1 m thick underlain by 8 m of soft marine clay with iron spots, organic matter, and shell fragments and then >30 m of homogenous soft

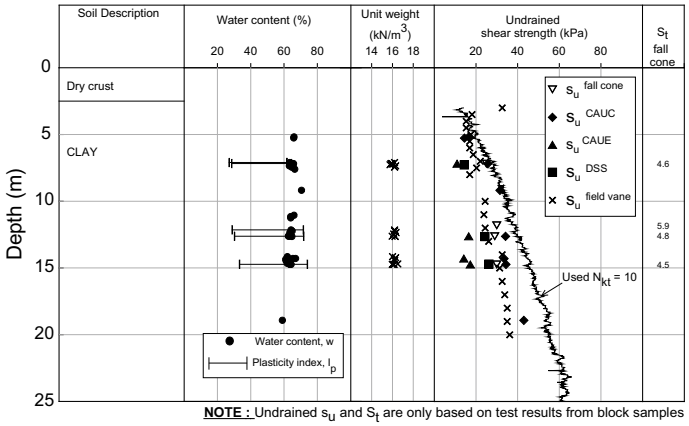

Fig. 4 Soil profile with results of advanced tests at Onsøy (Lunne et al. 2006)

medium-plastic clay over bedrock. Results of soil index testing are shown in Fig. 5. The clay has never experienced a higher vertical stress than today, but it has an apparent preconsolidation due to ageing effects. Results of constant rate of strain (CRS) oedometer tests on block samples indicate an OCR decreasing from 1.9 to 1.4 between 7 and 15 m depth below ground level. The average sensitivity as measured by the fall cone test is about 4.5 to 6.0. Several research programmes have been carried out at the Onsøy test site since 1970. A summary of the engineering geology, soil properties, in situ and laboratory tests, and model and full-scale tests is given by Lunne et al. (2003a).

Benchmarking of strength and deformation parameters has been done by taking high-quality Sherbrooke block samples and by doing triaxial, direct simple shear (DSS) and oedometer tests; see Fig. 4.

2.4.2 Similarity with Several Offshore Deepwater Fields

The Onsøy clay was deposited after the last glaciation as a marine clay, and it has never been subjected to vertical effective stresses higher than today. It is very similar to several clay deposits found in oil and gas fields offshore Norway. One example is the large Troll field in the Norwegian Trench in the North Sea at a water depth of 320–350 m. Another example is the Luva (later named Aasta Hansten) field in the Norwegian Sea at a water depth of 1200 m. Figure 5 shows these sites and the Onsøy site. A detailed study showed that the geological setting and the soil parameters at these offshore sites are very similar to the Onsøy site. Figure 6 illustrates the similarities in terms of plasticity index and OCR, and Fig. 7 compares corrected cone resistance and penetration pore pressure as measured with CPTUs.

The fact that the soil conditions at Onsøy are so similar to several offshore sites has triggered a lot of R&D activities, in terms of improving soil characterization

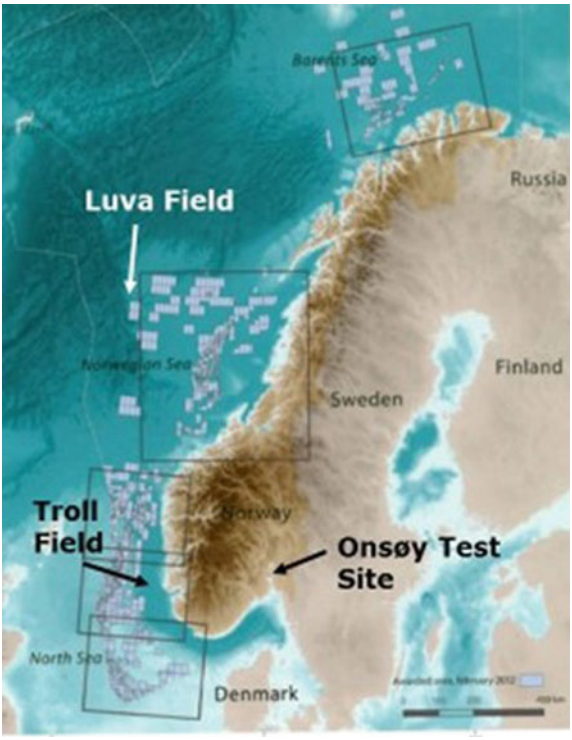

Fig. 5 Locations of Onsøy, Troll and Luva sites

methods and also verifying new foundation solutions, sponsored by the oil and gas industry. Examples are included in a later section.

2.5 Other International Test Sites

Two very well-organized international workshops were held in Singapore in 2002 and 2006 (proceedings published in 2003 and 2006 by Tan et al.). The purpose of these workshops was to describe a number of sites with a wide range of soil conditions following a set of instructions given to the authors:

- Description of engineering geology
- Composition of the soil types encountered
- State and index properties
- Soil structure
- Engineering properties
- Evaluation of quality of data
- Examples of use for engineering purposes.

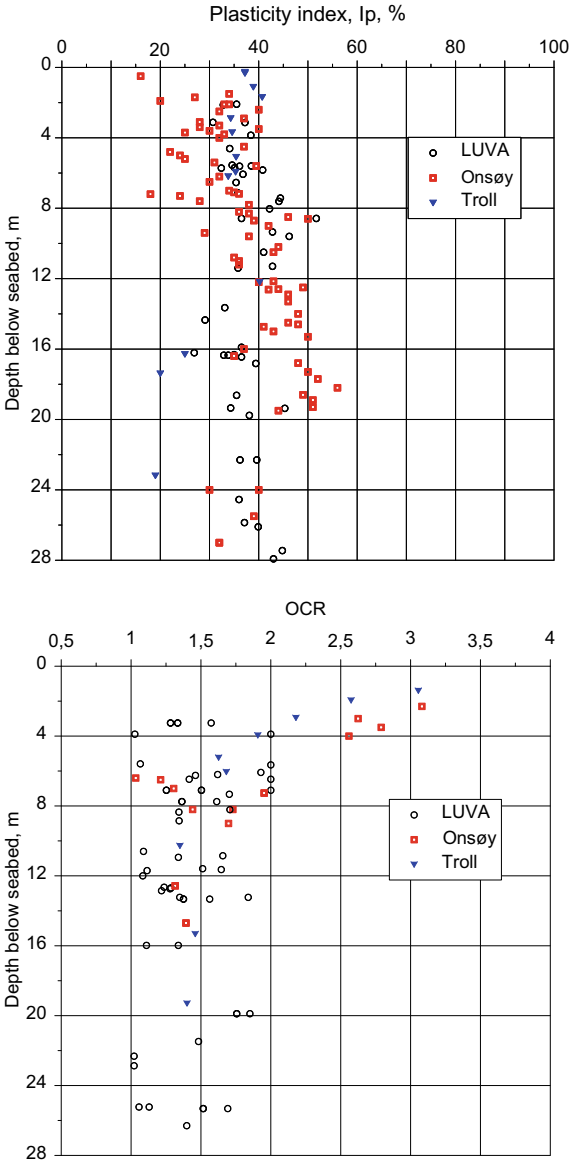

Fig. 6 Comparative values of plasticity index and OCR for Onsøy, Troll and Luva sites (Lunne et al. 2012)

The result of the workshop was published in four volumes with 58 well-structured high-quality papers on characterization of wide range of soil types. The proceedings represent a very valuable reference source for description of soil behaviour for a wide range of soil conditions.

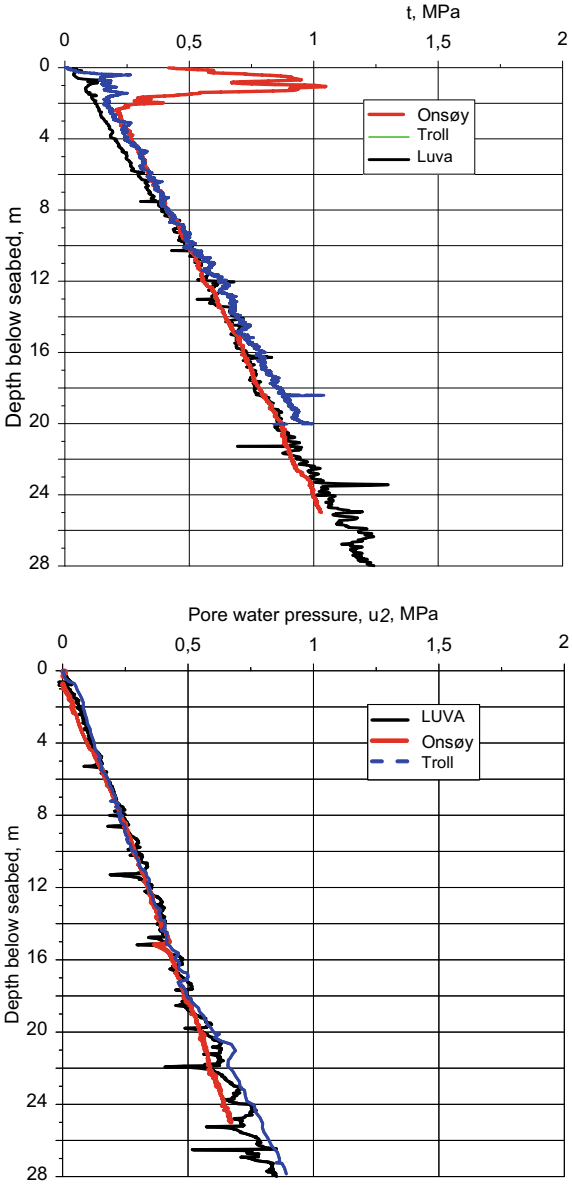

Fig. 7 Comparative CPTU results for Onsøy, Troll and Luva sites (Lunne et al. 2012)

3 Examples of Practical Use of Test Sites

3.1 Developing Soil Characterization Equipment and Procedures

3.1.1 Establishment of Sample Disturbance Criteria in Soft Clay

The issue of sample disturbance has always been important in connection with soil characterization in soft Norwegian clays. Figure 8 shows the results of two sets of CAUC and CAUE triaxial tests, in terms of stress–strain curves. One set of the tests is from a thick-walled 54-mm-piston sampler that has been used routinely for many years. The other set is from the Sherbrooke block sample which has proved to give the highest sample quality in Norwegian clays (Lacasse et al. 1985). It can be observed that there is a large difference in the results, the peak shear stress, or the undrained shear strength is more than 25% higher for the block sampler. In addition, the post-peak strain softening response was more pronounced with significantly lower shear stress mobolized at large strain for the block sampler. Due to higher cost, the use of block sampler is often limited to very important onshore projects. A need was felt to develop a scheme for evaluating sample quality especially due to the soft clays encountered in most deepwater oil and gas field developments offshore Norway.

A project was carried out at NGI with the purpose of finding the best way for quantifying sample quality (Lunne et al. 2006). Using high-quality Sherbrooke block samples of Onsøy clay, it was found that the most reliable method was to consider the volume change as measured in an oedometer test when consolidating a sample to the best estimate in situ effective stresses. This can also be measured in the consolidation phase of a CAU triaxial and DSS tests. The change in volume can be represented by the change in void ratio (Δe) normalized with the initial void ratio, e_0. Figure 9 shows

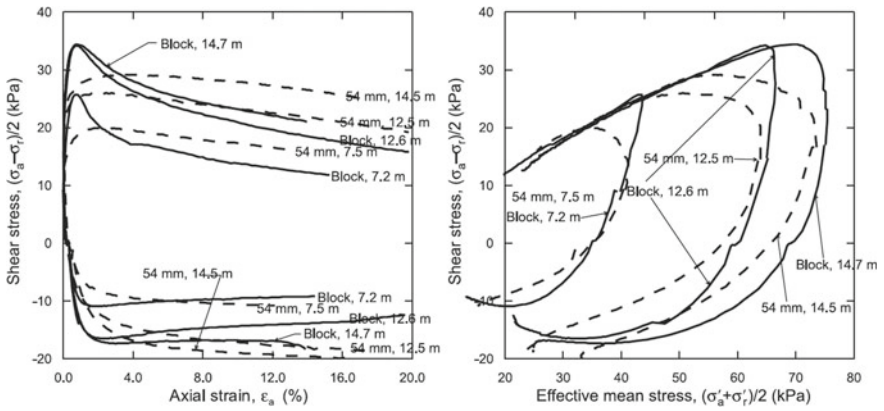

Fig. 8 Results of CAUC triaxial tests on 54 mm piston sample and Sherbrooke block sample (Lunne et al. 2006)

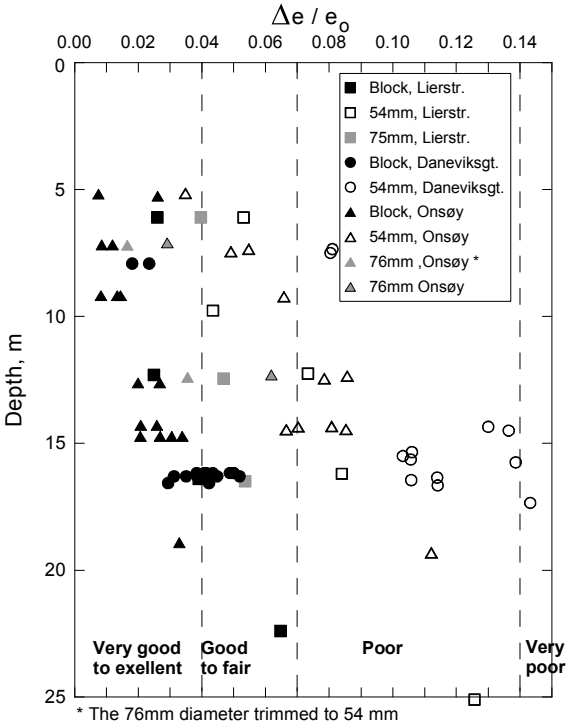

Fig. 9 Plot of $\Delta e/e_0$ form CAU tests vs depth for Lierstranda, Daneviksgate and Onsøy clays (Lunne et al. 2006)

the results from both CAU triaxial and CRS oedometer tests on samples retrieved employing various samplers at Onsøy and also at two others of NGI's test sites, Lierstranda and Daneviksgata (Drammen).

It can be seen that the $\Delta e/e_0$ values for the block samples are much lower compared to the 54 mm samples and that the 75 mm piston samples are in between. Based on the plot in Fig. 8, and also some other results, a set of criteria for quantifying sample quality was established as given in Table 3.

These criteria are now used in connection with soil investigations in Norway, both onshore and offshore. It has also been adopted in the ISO standard for Marine Soil Investigations (ISO 19901-8: 2014). Practical examples of the use of these criteria are given in the next subsection. It should be borne in mind that these criteria are

Table 3 Criteria for evaluation of sample quality of soft lightly overconsolidated clays (Lunne et al. 2006)

Overconsolidation ratio	$\Delta e/e_o$			
	Very good to excellent*	Good to fair*	Poor*	Very poor*
1–2	<0.04	0.04–0.07	0.07–0.14	>0.14
2–4	<0.03	0.03–0.05	0.05–0.10	>0.10

based on tests on Norwegian marine clays with OCR < 4 in the upper 20 m. The criteria are not valid for overconsolidated clays or clays with high silt content.

3.1.2 Development of New Sampler in Soft Clay

In the beginning of 2000, the oil companies operating in deepwater offshore Norway requested NGI to come up with a design for a new sampler that would give long seabed samples of high quality.

The criteria for the development of the new sampler for softer clays were the following: 15–20 m penetration below seafloor in down to 2000 m of water, minimum 95% recovery, and sample quality comparable to that of a thin wall piston sampler in the drilling mode. Lunne et al. (2008) presented the main aspects influencing sample quality and made recommendations for an "ideal" design. The most important characteristics were:

- Stationary piston
- Sharp cutting shoe: with an angle of 5° for soils susceptible to sample disturbance
- Area ratio smaller than 17%, combined with a length sufficient to satisfy this criterion for enlarged diameters
- Inside friction as small as possible
- Steady speed penetration of sampler
- Accurate measurement of penetration to ensure that a reliable calculation of the sample recovery ratio can be made.

The new sampler was tested both onshore (Fig. 10) and offshore, and penetration was modelled with finite element analyses.

Fig. 10 Testing out DWS in Onsøy test site

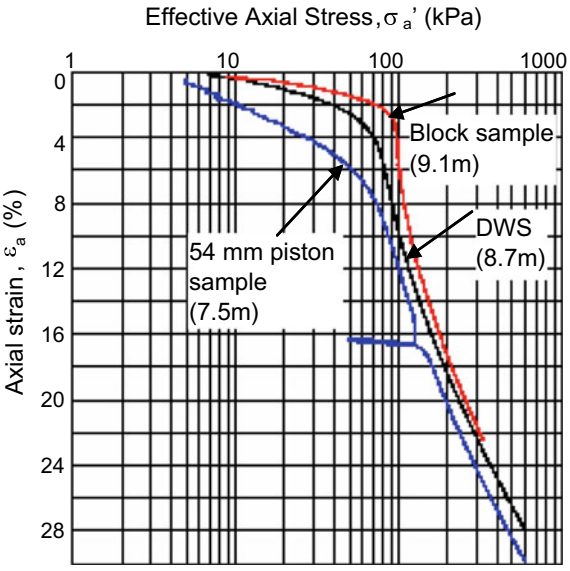

Fig. 11 Oedometer test results with deepwater sampler (DWS) at Onsøy (Lunne et al. 2008)

The deepwater sampler (DWS) was shown to provide high-quality samples. Figure 11 presents the results of constant rate of strain oedometer tests illustrating the quality of the samples recovered (from onshore testing out of sampler at Onsøy) compared with the results for high-quality block samples and 54-mm-piston samples. The stress–strain response for the DWS sample was comparable to that of block sample indicating that the quality of the DWS samples is very good.

Later offshore trials at the Troll field confirmed that the sampler worked well and could give sufficiently long high-quality samples (Lunne et al. 2008).

Another example of use of Onsøy test site for verifying the quality that can be achieved using a new offshore piston sampler is given by Santos et al. (2015).

3.1.3 N-Factors for Full-Flow Probes

The so-called full-flow penetrometers were introduced to offshore soil investigation about 20 years ago (Randolph et al. 1998). Figure 12 shows the two full-flow probes, the *T*-bar and the ball penetrometer, that are used in practice. The standard size of ball and *T*-bar (as given in the ISO standard for Marine Soil Investigation, ISO 2014) is indicated in Fig. 13, giving a cross-sectional area of 100 cm^2, or 10 times the area of the cone penetrometer. One advantage of the full-flow penetrometers is that the area is much larger than for the CPT, so that the resolution of the measurement is higher.

In order to use the results of *T*-bar or ball tests to determine undrained shear strength, the N-factors need to be determined.

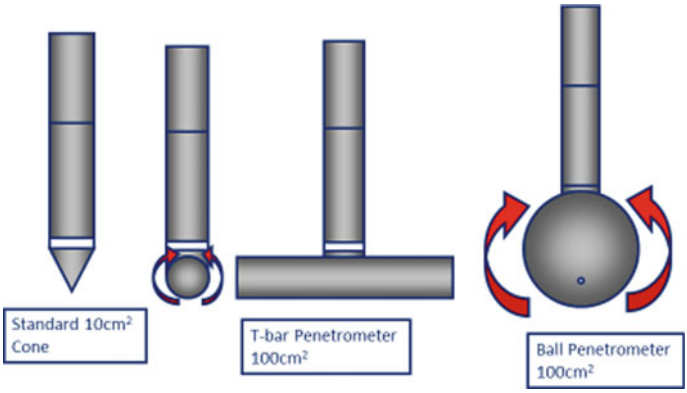

Fig. 12 Principles of T-bar and ball full-flow penetrometers

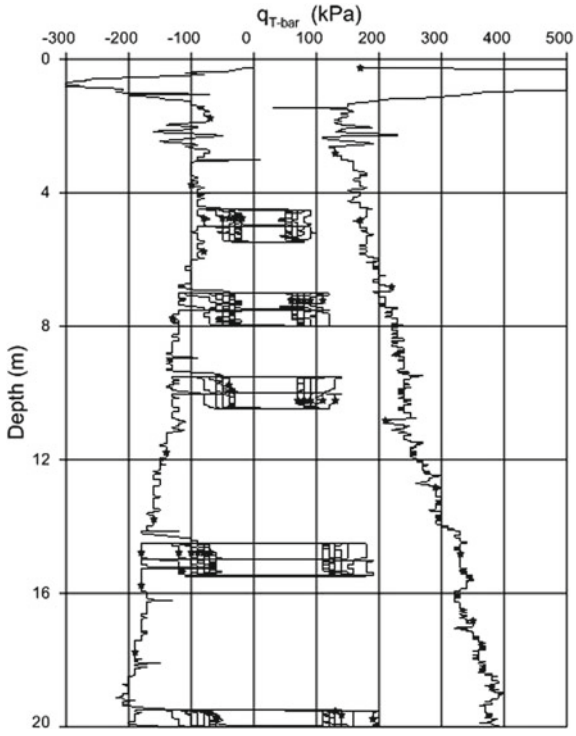

Fig. 13 Results of$T$-bar tests in Onsøy clay including $q_{T\text{-bar}}$ during penetration, extraction and cycling

$$s_u = q_{T\text{-bar}}/N_{T\text{-bar}} \quad s_u = q_{\text{Ball}}/N_{\text{Ball}}$$

Table 4 Recommended N-factors in soft clay (from Low et al. 2010)

N-factor	Definition	Recommended N-factor	
		Mean	Range
$N_{kt,suc}$	q_{net}/s_{uc}	12.0	10.0–14.0
$N_{\Delta u}$	$(u_2 - u_0/s_{uc}$	6.0	4.0–9.0
$N_{T\text{-bar,suc}}$	$q_{T\text{-bar}}/s_{uc}$	10.5	8.5–12.5

The Onsøy test site is ideal for developing N-factors due to the uniform soil conditions and due to the similarity of the soil conditions to many offshore sites as mentioned above.

Figure 13 shows the results of a T-bar test in Onsøy clay, showing measurements of the T-bar resistance, $q_{T\text{-bar}}$, during penetration, extraction and also during cycling. The latter measurements can be used to find the remoulded shear strength. Based on the measurements and results from several onshore and offshore sites recommended N-factors for CPTU and T-bar penetration tests were published as given in Table 4 by Low et al. (2010).

4 Use of Test Sites for Verifying Foundation Solutions

Over the years, a large number of field model tests have been carried out at test sites in many countries. It is not possible to describe all the above cases in detail, but three examples are chosen for description in the following.

4.1 Snorre Tension-Leg Platform

The Norwegian oil company Saga Petroleum in 1990 decided to install a tension-leg platform (TLP) at the Snorre field in the North Sea in a water depth of 310 m. The platform was to be tethered to suction anchors installed in the soft clay of the seabed (Fig. 14). These suction anchors had geometries and loading conditions quite different from other platforms used at that time, such as gravity base structures or jackets with piles.

Since there was very little practical and theoretical experience with this type of foundation Saga Petroleum contracted NGI to perform a series of model tests to simulate the basic configuration and loading conditions for a suction anchor. The primary intention of the project was not to extrapolate results directly to the prototype, but instead to provide results that could be compared to predictions made for these tests by analytical foundation design procedures that had been developed by NGI (Andersen et al. 1993). The purpose was then that the comparison would provide a means for checking the validity of these design procedures for suction anchors before these procedures were used in the final design for an actual TLP.

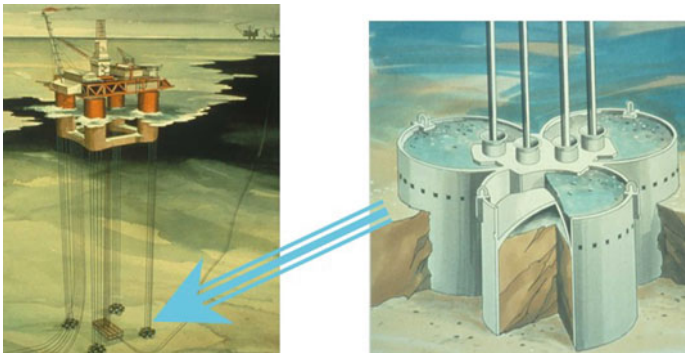

Fig. 14 Snorre TLP with detail of anchor (Andersen et al. 1993)

NGI found a site in Lysaker, Oslo, where the soil conditions were quite similar to the conditions at the offshore Snorre site. It was decided to build a model with scale 1:10 of the foundation and impose loading conditions that could simulate wave loading for the offshore conditions. The clay at the Lysaker site was characterized with high-quality sampling and laboratory tests including both monotonic and cyclic triaxial and DSS tests to provide soil parameters for detailed foundation analyses of the model subjected to cyclic loading conditions.

To simulate the conditions at the Snorre field, the upper layer (1.8 m) of the soil was removed. Before conducting the actual field model tests, a so-called class A prediction (made before the event) was carried out and the results presented in a sealed envelope to the client.

The field testing is described by Dyvik et al. (1993). The analyses carried out as well as predicted results and comparison with the measured test results are covered by Andersen et al. (1993). The test model was well-instrumented so that the failure mode could be documented. Figure 15 shows the clay surface after cyclic model test and the ratio of the predicted to measured failure loads.

Figure 16 shows predicted and measured cyclic displacements as a function of rotation.

The predicted failure loads were within 6% of the measured ones. The type and location of the failure modes were reasonably consistent with predicted failure

Test No.	Test type	Predicted/measured failure load
1	Monotonic	1.00
2	Cyclic	1.05
3	Cyclic	1.06
4	Cyclic	1.01

Fig. 15 Observed failure modes for the four tests carried out and also ratio of the predicted to measured failure loads (Andersen et al. 1993)

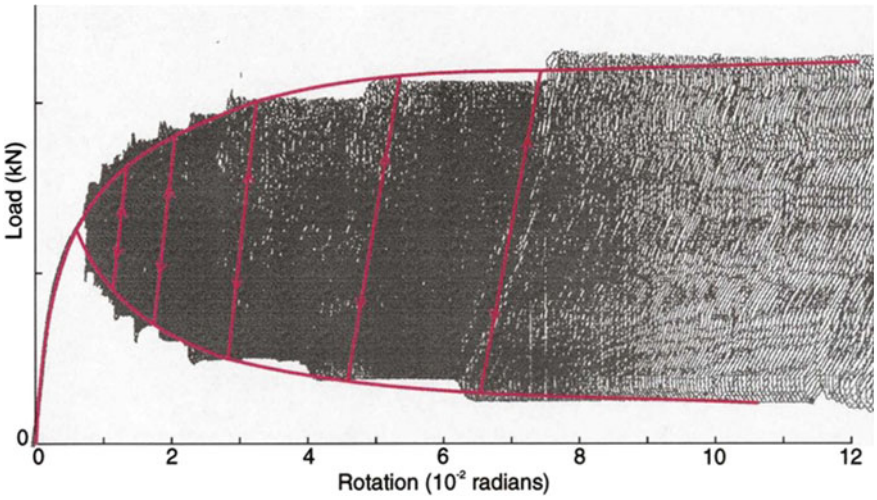

Fig. 16 Predicted and measured cyclic displacements as a function of rotation (Andersen et al. 1993)

surfaces. The predicted rotational, horizontal and vertical mode displacements were in good agreement with the measured displacements.

These model tests confirmed very well that the calculation procedures used were well-suited for the TLP suction anchors, and the client was reassured.

Finally, it should be mentioned that the Snorre TLP was successfully installed in the offshore field in 1992.

4.2 Developing Procedures for Lateral Capacity of Monopiles for Offshore Wind in the UK

As mentioned in Sect. 2.1 areas with boulder clay offshore East coast of UK are of the same geological origin as the clay at the Cowden test site. A foundation solution that has been found attractive for offshore wind farms is to use one single *monopile* which can be up to 9 m in diameter and 30–40 m long. Since procedures for evaluating lateral capacity for standard jacket piles (e.g. API) are not really suitable for the large diameter monopoles, a Join Industry Project (JIP) called PISA was launched in the UK some years ago (Byrne et al. 2015).

Field testing at the Cowden site was a very important part of this project as can be seen from Fig. 17.

Figure 18 shows the set up for the field testing at Cowden.

Based on the results of the field testing and 3D FE analysis, the so-called PISA analyses model was developed. This model is now used widely for evaluating lateral loading of large diameter monopiles (Byrne et al. 2015).

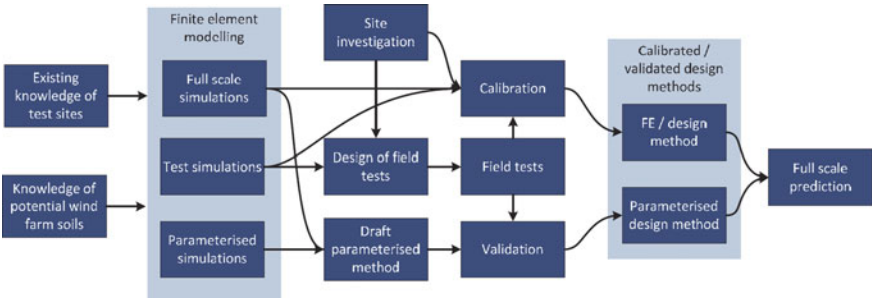

Fig. 17 Overview of activity for the PISA project (Byrne et al. 2015)

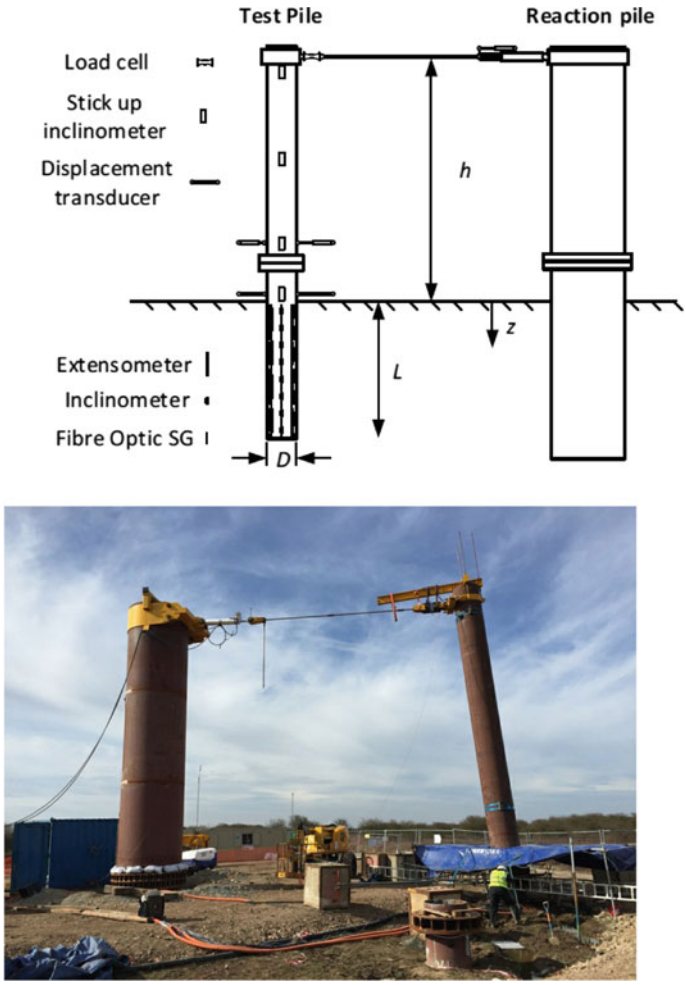

Fig. 18 Set up for testing of lateral capacity of monopiles (Byrne et al. 2015)

Fig. 19 Testing out torpedo-anchor with piezocone at Sarapui site (Porto et al. 2010)

4.3 Use of Torpedo-Anchors with Piezocone for Deepwater Floating Structures

The soils in deepwater offshore Brazil are very soft, and it has been found convenient to use the test site Sarapui in Rio operated by COPPE, Federal University of Rio de Janeiro for research on such soils (Jannuzzi et al. 2015; Danziger et al. 2019).

The need for deep penetration in deepwaters combined with the need for reducing the cost of geotechnical investigations led PETROBRAS to the development of a piezocone to be installed at the tip of a torpedo-pile, also called torpedo-anchor (Medeiros 2002). The corresponding probe was designated as torpedo-piezocone. It was decided that the torpedo-piezocone would measure cone resistance (q_c), sleeve friction (f_s), pore pressure at the cone face (u_1) and cone shoulder (u_2) as well as cone temperature during free-fall and sometime after final stop. The main dimensions of the torpedo-piezocone would be the same as in the regular piezocone, i.e. 60° cone, with 10 cm^2 base area and a 150 cm^2 friction sleeve.

In order to characterize the seabed before actually installing the torpedo-piles, a special torpedo-piezocone was developed and tested out at Sarapui site (Porto et al. 2010).

Figure 19 shows the torpedo-anchor with piezocone mounted being tested out at Sarapui site.

5 Some Suggestions for Indian Scenario

India has ventured into eastern Indian deepwaters for oil and gas production and is also planning to harness offshore wind energy in shallower Indian waters. It is also encouraging that reputed Indian academic institutions are putting in efforts to

develop expertise in offshore geotechnics which were generally lacking till a few years back.

It is also known that in both eastern and western Indian offshore, problematic calcareous sands are encountered in relatively shallow waters. These soils in some areas have very high carbonate content varying level of cementation. Also, eastern offshore area, especially the deepwater area, has very soft marine clays to considerable depths below seafloor. In some areas of western offshore also very soft to soft clays are encountered near seafloor. To the best of authors knowledge, no research test site has been established in India. It is hence suggested that the establishment of research onshore tests sites covering different types of sediments from soft marine clays to carbonate sediments can prove very useful for research and subsequent practical applications in offshore as well as onshore areas.

The first step after locating such potential sites would be to verify that the important soil characteristics are similar to the offshore sites in general. Based on that evaluation, the identified sites will have to be selected and finally established.

The type of research which can be undertaken at these research test sites and resulting benefits have already been indicated in the examples given in the paper. Some of the potential areas of research include:

- Develop sampling technique and sample quality assessment methods for calcareous sands: As noted earlier in the paper, quality of the recovered sample is one of the key areas of site characterization. It is well-documented that calcareous sediments such as those found in the offshore India are very difficult to recover in their natural state. This area of research could be very beneficial for the Indian offshore industry.
- Large-scale field tests: It is known that presently Indian academics are working on free-fall penetrometers and free-fall anchors for offshore use. The work primarily appears to be focused on analytical and/or laboratory-scale tests. Large-scale field tests using such devices on different test sites can enhance the value of the research through validation of the analytical and laboratory-scale test results.
- Model tests on large diameter monopile foundations: As another practical possibility, the capacity of large diameter monopile foundations for offshore wind energy turbines in Indian calcareous sands (found in shallower Indian waters where the wind farms shall mostly be coming up) can very well be investigated and validated on such sites through field tests.

In authors opinion, possibilities for research and development through such test sites in India are numerous and very promising.

Establishment of such research test site, in its proper sense, is itself a significant academic achievement on which future research is possible.

Such well-established and characterized sites can greatly help in increasing inter-institutional cooperation within India and also international research cooperation with Indian institutions.

Establishment of such test sites in India will also give the Indian students and researchers invaluable experience in, and, opportunity of planning, performing and interpreting large-scale 1-g field model tests. Proper management and record-keeping

of all investigations and, research results performed at such sites will help create an extremely useful database in India over the years which can inspire further research and publications.

About two decades ago, IEOT searched and identified a suitable marine clay site near Panvel, Maharashtra, but unfortunately, due to some unavoidable reasons, the site finally could not be established. The experience, however, was encouraging and generates confidence that such research test sites can be located and established in the Indian scenario.

6 Summary and Conclusions

Throughout the history of soil mechanics the use of the test site has been very important, in a range of soil types. The reference test sites have been used for developing new and improved equipment and methods for soil characterization in terms of in situ testing, sampling and laboratory testing. The test sites have also been very useful for trying out or verifying new foundation solutions by large-scale testing. The paper has reviewed some international experience and then showed selected examples of the practical use of the test sites in Norway and other countries for offshore applications. It has been argued that the establishment of Indian onshore test sites for offshore application will be very beneficial both for the industry and for academia.

References

Almeida MSS, Marques MES (2002) The behaviour of Sarapuí soft clay. In: Proceedings of the international workshop on the characterisation and engineering properties of natural soils, Singapore, vol 1, pp 477–504

Andersen KH, Stenhamar P (1982) Static plate loading tests on overconsolidated clay. Am Soc Civil Eng J Geotechn Eng 108(GT 7):918–934

Andersen KH, Dyvik R, Schrøder K, Bysveen S (1993) Field tests of anchors in clay. II: prediction and interpretation. J Geotechn Eng ASCE 119(10): 1532–1549

ASCE (2000) In: Benoit J, Lutenegger AJ (eds) National geotechnical experimentation sites. Geotechnical Special Publication No. 93. 397 p

Byrne BW, McAdam R, Burd HJ, Houlsby GT, Martin CM, Zdravkovic L, Skov Gretlund J (2015) New design methods for large diameter piles under lateral loading for offshore wind applications. In: Proceedings of 3rd international symposium of frontiers in offshore Geotechnics, Oslo

Danziger FAB, Januzzi GMF, Martins ISM (2019) The relationship between sea-level change, soil formation and stress history of a very soft clay deposit. AIMS Geosci 5(3):461–479

DeGroot DJ, Lunne T, Ghanekar R et al (2019) Engineering properties of low to medium overconsolidation ratio offshore clays. AIMS Geosci 5:535–567

Dyvik R, Andersen KH, Hansen SB, Christophersen HP (1993) Field tests of anchors in clay. I: description. J Geotech Eng ASCE 119(10):1515–1531

Géotechnique (1992) Bothkennar soft clay test site: characterization and lessons learnt. Eight Geotechnical Symposium in Print. vol XLII, Number 2, June 1992, 380 p

Guimarães G (2015) Horizontal load test on instrumented model torpedo-pile in soft clay. Ph.D. thesis: COPPE, Federal University of Rio de Janeiro

Hight D, Paul MA, Barras BF, Powell JJM, Nash DFT, Smith PR, Jardine RJ, Edwards DH (2003) The characterization of Bothkennar clay. In: Tan TS et al (eds) Characterisation and engineering properties of natural soils. Balkema 2003. Proceedings of the International Workshop, Singapore, vol 1, pp 543–598

ISO (2014) Petroleum and natural gas industries—specific requirements for offshore structures—Part 8: marine soil investigations. International Standard ISO 19901-8:2014

Jannuzzi GMF, Danziger FAB, Martins ISM (2015) Geological–geotechnical characterisation of Sarapuí II clay. Eng Geol 190:77–86

Kelly RB, Pineda JA, Bates L, Suwal LP, Fitzallen A (2016) Site characterisation for the Ballina filed testing facility, Géotechnique, Sept 2016

Lacasse S, Berre T, Lefebvre G (1985) Block sampling of sensitive clays. In: Proceedings of 11th ICSMFE, San Francisco, vol 2, pp 887–892

Ladanyi B, Lunne T, Vergobbi P, Lhuillier B (1995) Predicting creep settlements of foundations in permafrost from the results of cone penetration tests. CGJ 32(4):835–847

Li JH, Huang J, Cassidy MJ, Kelly R (2014) Spatial variability of the soil at the Ballina National field test facility. Austral Geomech 49(4):41–48

Low HE, Lunne T, Andersen KH, Sjursen MA, Li X, Randolph MF (2010) Estimation of intact and remoulded undrained shear strengths from penetration tests in soft clays. Géotechnique 60(11):843–859

Lunne, T., Lacasse, S. (1999). Geotechnical characteristics of low plasticity Drammen clay. International symposium on characterization of soft marine clays—Bothkennar, Drammen, Quebec and Ariake Clays. Yokosuka, Japan 1997. Proceedings, pp 33–56

Lunne T (2002) Engineering properties of lean Lierstranda clay. In: Proceedings of international symposium coastal engineering in practice, Yokohama September 2000, vol 2, pp 177–186

Lunne T, Long M, Forsberg CF (2003a) Characterization and engineering properties of Onsøy clay. Characterization and engineering properties of natural soils. In: Tan TS et al (eds) Balkema 2003. Proceedings of the International Workshop, Singapore 2002, vol 1, pp 395–427

Lunne T, Long M, Forsberg CF (2003b) Characterization and engineering properties of Holmen, Drammen sand. In: Tan TS et al (eds) Characterization and engineering properties of natural soils. Balkema 2003. Proceedings of the International Workshop, Singapore 2002, vol 2, pp 1121–1148

Lunne T, Berre T, Andersen KH, Strandvik S, Sjursen S (2006) Effects of sample disturbance and consolidation procedures on measured shear strength of soft marine Norwegian clays. Can Geotech J 43:726–750

Lunne T, Tjelta TI, Walta A, Barwise A (2008) Design and testing out of deepwater seabed sampler. In: Offshore technology conference, 38. Houston 2008. Proceedings paper 19290, 12p

Lunne T, Andersen KH, Yang SL, Tjelta TI, Strøm PJ (2012) Undrained shear strength for foundation design at the Luva deep water field in the Norwegian Sea. Geotech Geophys Site Charact 4(1):157–166

Medeiros CJ Jr (2002) Low cost anchor system for flexible risers in deep waters. In: Proceedings of the offshore technology conference, Paper No. OTC 14151, Houston

Pineda JA, Kelly RB, Suwal L, Bates L, Sloan SW (2019) The Ballina soft soil field testing facility. AIMS Geosci 5:509–534

Powell JJM, Butcher AP (2003) Characterisation of a glacial clay till at Cowden, Humberside. In: Hight et al (eds) Characterisation and engineering properties of natural soils. Balkema 2003. Proceedings of the International Workshop, Singapore 2002, vol 2, pp 983–1020

Porto EC, Medeiros CJ Jr et al (2010) The development of the torpedo-piezocone. In: Proceedings of the 29th international conference on Ocean, Offshore And Arctic Engineering, OMAE 2010, American Society of Mechanical Engineers, New York

Randolph MF, Hefer PA, Geise JM, Watson PG (1998) Improved seabed strength profiling using *T*-bar penetrometer. In: Proceedings of International Conference on Offshore Site Investigation

and Foundation Behaviour—'New Frontiers', Society for Underwater Technology, London, pp 221–235
Sandven R (2003) Geotechnical properties of a natural silt deposit obtained from field and laboratory tests. Characterisation and engineering properties of natural soils. In: Tan TS et al (eds) Balkema 2003. Proceedings of the International Workshop, Singapore 2002, vol 2, pp 1237–1276
Sandven R, Ørbech T, Lunne T (2004) Sample disturbance in highly sensitive clay. In: Proceedings of 2nd international conference on geotechnical and geophysical site characterization—ISC'2, Millpress, Rotterdam, Netherlands, pp 1861–1868
Sandven R, Sjursen M (1998) Sample disturbance in soils-results from investigations in an over consolidated marine clay. In: Proceedings of 1st international conference on geotechnical site characterization, A. A. Balkema, Rotterdam, Netherlands, pp 409–417
Santos RS, Alexander M, Barwise A, Walta A, Solhjell E, Lunne T (2015) A new piston sampler for a remotely operated drilling system. In: Proceedings 3rd international symposium on frontiers in offshore geotechnics (ISFOG 2015), Oslo, Norway, pp 1103–1108
Tan TS, Phoon KK, Hight DW, Leroueil S (2003) Characterization and engineering properties of natural soils. In: Proceedings, vols 1 and 2 of a workshop held in Singapore, Dec 2002, 1535 p
Tan TS, Phoon KK, Hight DW, Leroueil S (2006) Characterization and engineering properties of natural soils. In: Proceedings, vols 3 and 4 of a workshop held in Singapore November/December 2006, 1255 p

Optimising Geotechnical Engineering Models (GEMs)

N. Ramsey

Symbols and Abbreviations

BPT	Ball probe test
c_v	Coefficient of consolidation
CPT	Cone penetration test
C_s	Coefficient of swelling
DSS	Direct simple shear test
d	Diameter of object
e	Void ratio
e_o	Initial void ratio
G	Shear modulus
G_{max}	Low strain shear modulus
G_{50}	Shear modulus at half the maximum deviator stress
$G_{50(UU)*}$	G_{50} inferred from a UU triaxial test, corrected for the change in shear stiffness caused by the difference in shear strain rate of resonant column and UU triaxial tests
G_s	Specific gravity (particle density) of soil
I_r	Rigidity index (G/s_u)
LV	Laboratory vane test
N_{kt}	Defined as the ratio q_{net}/s_u
OCR	Overconsolidation ratio (or yield stress ratio in soils that have not been mechanically overconsolidated)
q_{net}	Net cone resistance, defined as the total cone resistance, corrected for geometric and pore-water effects minus the total overburden pressure
Q_t	Normalised cone resistance. Defined as q_{net}/σ_v' (the ratio of net cone resistance to effective vertical stress)

N. Ramsey (✉)
Fugro, Perth, Australia
e-mail: n.ramsay@fufgro.com

S. Haldar et al. (eds.), *Advances in Offshore Geotechnics*, Lecture Notes in Civil Engineering 92, https://doi.org/10.1007/978-981-15-6832-9_3

RC	Resonant column
s_u	Undrained shear strength
s_{ud}	Undrained shear strength measured by DSS
s_{uu}	Undrained shear strength measured by UU triaxial test
$s_{uu(CPT)}$	S_{uu} inferred from CPT data
TBT	T-bar test
UU	Unconsolidated Undrained (triaxial test)
v	Velocity of penetration
V	Normalised velocity ($v{\cdot}d/c_v$)
V&B	Vardanega and Bolton (authors)
w	Water content
α	Factor used to model degradation of stiffness with increasing shear strain
χ	Stiffness correction factor, to account for changes in shear stiffness caused by changes in shear strain rate
Δe	Change in void ratio
ε_{50}	Vertical strain at half the maximum deviator stress, measured in UU triaxial test
γ	Shear strain
γ_{ref}	Reference shear strain for stiffness degradation assessments
σ'_v	Effective vertical stress in situ
σ'_{vc}	Effective vertical stress after consolidation
σ'_{vmax}	Maximum previous effective vertical stress

1 Introduction

The GEM funnel, shown in Fig. 1, is intended to illustrate that developing a reliable Geotechnical Engineering Model (GEM) is an iterative process, involving contributions from many sources, with the process being supported by a combination of "precedent, empiricism and well-winnowed experience" (Burland 1987). The GEM funnel highlights the progressively closer alignment of the "four Gs" (Geology, Geomorphology, Geophysics and Geotechnics) that occurs as new information is integrated into the GEM.

The quality of the GEM may be visualised by the gauge of the mesh at the base of the funnel, upon which the GEM rests. A non-optimised GEM is more likely to result in a coarse-mesh that allows potentially important information to slip through, whereas an optimised (i.e. robust fit-for-purpose) GEM results in a fine-mesh that catches all relevant information. The objective of this paper is to highlight some of the GEM optimisation opportunities that occur, as the work progresses.

Optimised GEMs can only be developed by iteratively integrating the complementary geomorphological, geological and geophysical datasets, and taking account of the proposed engineering applications. Consequently, the first GEM optimisation

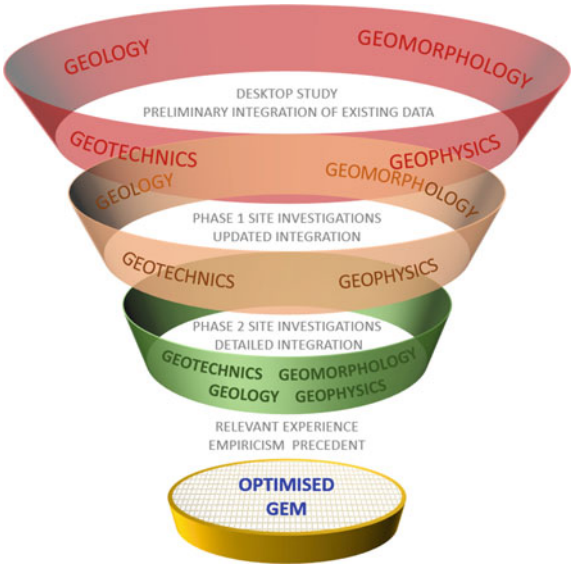

Fig. 1 GEM funnel

opportunity is to assemble a suitably experienced team of geomorphologists, geologists, geophysicists and geotechnical engineers, to contribute to the GEM, rather than expect non-specialists to make specialist assessments.

2 A Brief Review of the Four Gs

2.1 General

As previously noted by Ramsey (2018), this section reiterates the key contributions of the "four Gs" (Geomorphology, Geology, Geophysics and Geotechnics) when developing an optimised GEM. Due to space limitations, it is only possible to present single examples to highlight the significant contributions of geomorphology, geology and geophysics—for more details on these aspects, refer to Thomas (2017).

2.2 Geomorphology

Ramsey (2018) notes that the seabed topography provides vital clues on the ground conditions beneath. Figure 2 (Ramsey 2018) illustrates the seabed topography at an

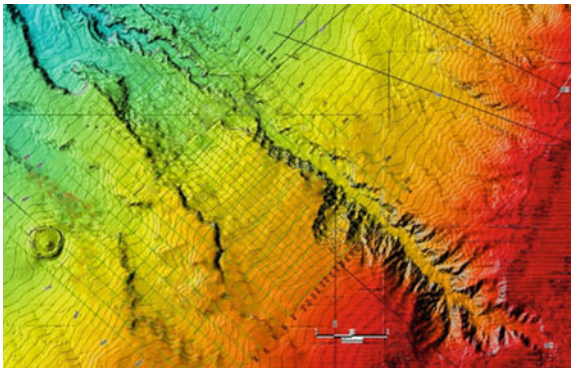

Fig. 2 Geomorphological assessment is essential

offshore deepwater site, over an area of approximately 1200 km^2. Observable geohazards include a mud volcano and multiple large slope failures. Figure 2 implicitly emphasises that borehole/testing locations chosen without considering the geomorphology would be highly unlikely to characterise the full range of ground conditions. Clearly, therefore, geomorphological assessments provide an early optimisation opportunity—particularly if they are performed by a specialist Geomorphologist or suitably experienced Engineering Geologist.

Figure 2 also highlights the importance of including time as a fourth dimension, when developing a GEM, as geohazards provide evidence of time-dependent variations at a site. Consequently, identifying the probability of activation or recurrence of a geohazard during a project-lifetime is a key optimisation opportunity. Detailed discussion of this aspect is outside the remit of this paper—for further details refer to Thomas (2017).

2.3 Geology

Geology provides a reference framework for predicting the ground conditions and geohazards likely to be encountered at and around a project site. As noted previously, space limitations preclude detailed discussion of the vital importance of understanding the geological framework—but this aspect will, no doubt, be discussed in other papers presented at this conference. However, as a simple example of the importance of understanding the geology of an area, the Godavari River is a monsoon-driven river with a high sediment loading that discharges into the Bay of Bengal. This geological setting might easily be used to predict the possible presence of areas where the rate of sediment loading exceeds the rate of consolidation of the soils, resulting in the presence of pore-water pressures in excess of hydrostatic pressure.

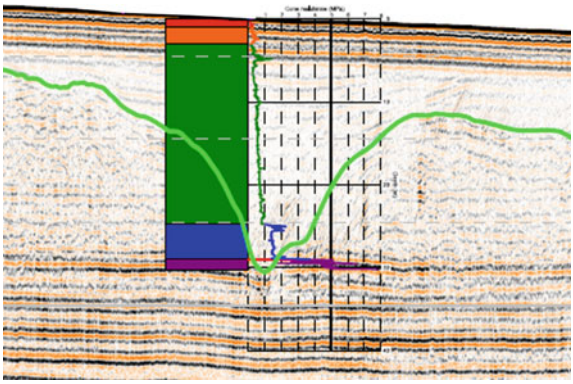

Fig. 3 Geophysical identification of buried channels

2.4 Geophysics

Geophysics provides a means to identify and define geophysical boundaries both vertically and laterally. For example, the geophysical cross section presented in Fig. 3 indicates the presence of a buried channel feature and, as can be seen in the figure, this is confirmed by a cone penetration test (CPT). Geophysical investigation is a key opportunity to optimise GEMs, as high-quality targeted geophysical investigations provide opportunities to minimise data gaps. Furthermore, some geophysical techniques, such as geophysical refraction, enable tentative predictions of geotechnical parameters. For more information on optimising geophysical site, investigations refer to Campbell et al. (2008, 2015).

2.5 Geotechnics

Ramsey (2018) notes that the significant optimisation opportunity offered by geotechnics is that geotechnical fieldwork and laboratory testing enable direct assessments of soil type and geotechnical behaviour. Conversely, the significant disadvantage of offshore geotechnical fieldwork is that each borehole or in situ test provides only a tantalising one-dimensional glimpse of the soil conditions at a single point on a map, rather than an indication of the complete range of soil conditions across a site. Nevertheless, geotechnical site investigation calibrates and supplements the geomorphological, geological and geophysical assessments.

3 Geotechnical Assessments

3.1 General

This section presents more details on the geotechnical aspects of creating GEMs and GEM optimisation opportunities.

3.2 Geotechnical Fieldwork

3.2.1 In Situ Testing (IST)

Ramsey (2018) notes that a borehole or in-situ test only provides a one-dimensional glimpse of the soil conditions at a single point on a map. So, an early GEM optimisation opportunity is to ensure that the chosen borehole/testing locations are positioned in a manner that enables a representative range of soil conditions to be evaluated. This opportunity can generally only be achieved by performing appropriate geomorphological, geological and geophysical assessments, prior to the geotechnical fieldwork. Figure 4 illustrates the unrivalled profiling capability of in situ tests, such as the cone penetration test (CPT), T-bar test (TBT) and ball probe test (BPT). Furthermore, IST provides the opportunity to predict continuous undrained shear strength profiles that are invaluable when assessing characteristic profiles. However, like all geotechnical fieldwork techniques, IST has limitations, as well as advantages. For example, IST equipment can have difficulty penetrating through some soils, particularly soils containing inclusions that are larger than the diameter of the probe. In these cases, the IST results might be misinterpreted. For example, a CPT might indicate very high cone resistances, potentially leading to premature refusal, in a gravelly soil, and this might be misinterpreted as indicating extremely dense or cemented ground conditions. However, even loose gravel particles that are greater than the diameter of the cone can cause very high cone resistance. These types of misinterpretations can, of course, be avoided by "integrated thinking" (Ramsey 2018) as a good quality geological review would be likely to highlight the possible presence of gravelly soils that might lead to sudden CPT refusal.

In summary, IST offers GEM optimisation opportunities, by providing:

- precise boundary elevations often missed by drilling and sampling techniques,
- accurate profiling information, including the proportion of soil inclusions and the proportion of intermittent layers of higher permeability,
- information on the natural soil variability within geological units.
- information on the characteristics of the soil matrix.

Conversely, IST does not provide optimisation opportunities relating to:

- the effect of the foundation dimensions and loading on soil behaviour.

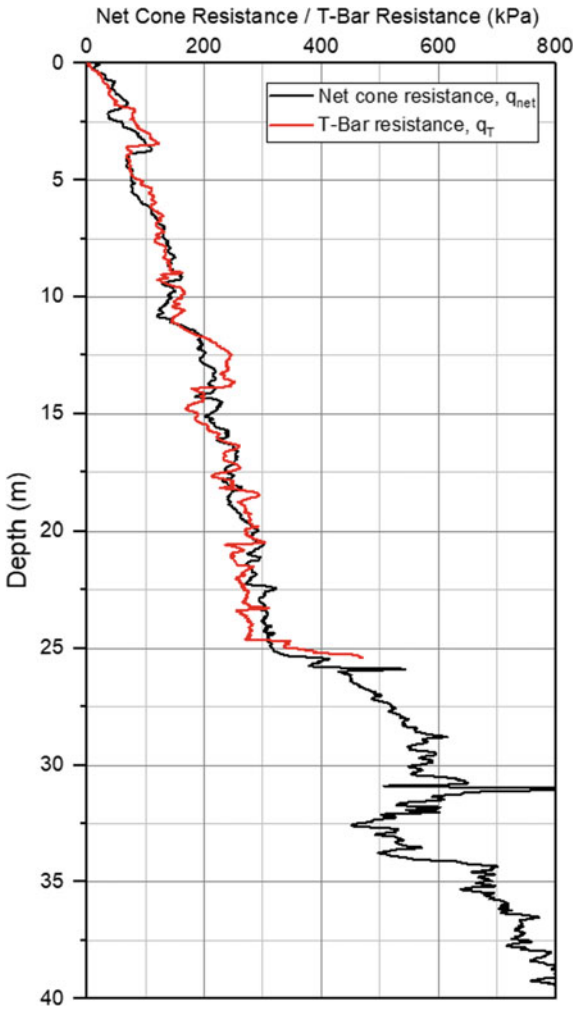

Fig. 4 Continuous profiling capability of in situ tests offers a significant GEM optimisation opportunity

- the effect of different rates of loading on soil behaviour (although could become an optimisation opportunity if tests were performed at a range of penetration rates).
- soil behaviour under cyclic loading conditions.

3.2.2 Laboratory Testing

Laboratory testing confirms and calibrates IST results; and offers several GEM optimisation opportunities, such as

- Soil samples can be reconsolidated to mitigate the effects of sampling disturbance or take account of the effects of foundation loading.

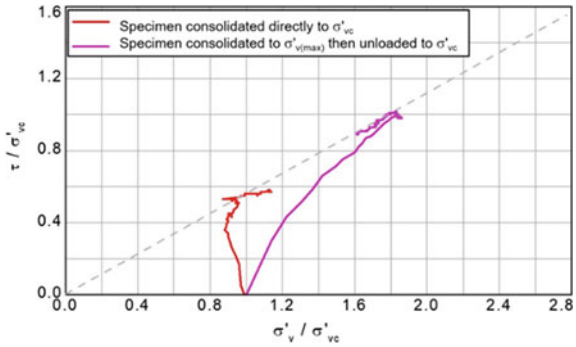

Fig. 5 Effect of consolidation on measured soil behaviour (Ramsey 2018)

- The effects of increasing strain levels on strength and stiffness can be assessed.
- The effects of rate of loading, on strength and stiffness can be assessed.
- Soil behaviour under cyclic/dynamic loading conditions can be assessed.

On the other hand, laboratory testing does have some disadvantages, including:

- A much smaller amount of soil is being tested so macro effects may not be representative of macro-behaviour.
- Laboratory tests typically take much longer to perform than in situ testing.

Furthermore, laboratory test results are significantly affected by the method of specimen preparation, the method of specimen saturation, the consolidation stresses applied to the test specimen, the direction of shearing, the rate of shearing and the drainage conditions during shearing. Consequently, integrated thinking should be applied to each of these aspects when developing an optimised laboratory testing programme.

Figure 5 presents an example of the importance of understanding the geological history at a site—in the example one direct simple shear (DSS) test specimen was consolidated directly to the final vertical effective vertical stress (σ'_{vc}). The other DSS test specimen was consolidated to the estimated maximum previous effective vertical stress ($\sigma'_{v\max}$) before unloading to σ'_{vc}. The impact of applying these different consolidation conditions on measured post-consolidation shear behaviour is clearly significant.

3.3 Accounting for Engineering Application

Ramsey (2018) notes that laboratory testing programmes need to take account of the proposed size and geometry of a foundation, and the type and magnitude of loading. Understanding the drainage conditions around the foundation during loading also offers optimisation opportunities. Figure 6 (Randolph and Hope 2004) illustrates that the resistance to penetration of an object through soil is influenced by the velocity

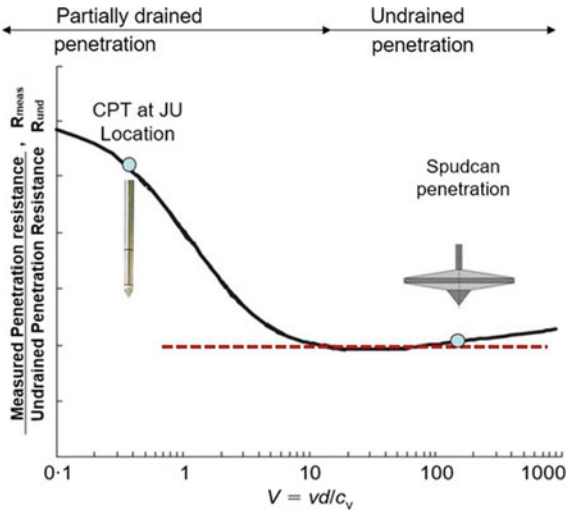

Fig. 6 Importance of understanding drainage conditions (Randolph and Hope 2004)

of penetration (v), the diameter of the object (d) and the coefficient of consolidation (cv) of the soil. The figure indicates that when the normalised velocity, V ($v \bullet d/c_v$) is greater than 30–100 soil behaviour tends to be undrained and when $V < 0.01$–0.03 the soil behaviour tends to be drained. Consequently, to optimise the GEM for installation assessments, it is important to assess whether the normalised velocities of the in situ tests are similar to the normalised velocity of the proposed foundations during installation. For example, Fig. 6 illustrates that a CPT performed at a proposed Jack-Up (JU) location might indicate relatively high resistance, due to partially drained soil conditions occurring around the cone (which is typically around 0.036 m diameter). In contrast, due to the much larger drainage path around a JU spudcan (which might be tens of metres in diameter at its widest point) the soil might behave in an undrained manner during JU installation leading, leading to a much lower penetration resistance.

3.4 Understanding Uncertainty

Figure 7 (Phoon and Kulhawy 1999) summarises the many sources of uncertainty encountered when estimating soil parameter values. When optimising GEMs, it is important to understand and take account of the likely errors and limitations of a chosen "conversion model" (which is a model used to convert a measurement into a soil parameter value) and/or "transformational model" (which is a model used to convert one soil parameter value into another soil parameter value).

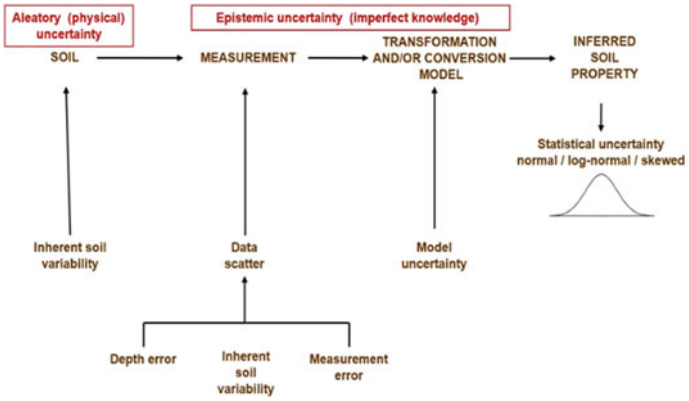

Fig. 7 Estimating uncertainties (Phoon et al. 1999)

3.5 Sample Disturbance

3.5.1 General

Sample disturbance—which is defined as an action that causes the soil to be changed from its state in situ—is inevitable. In most cases, soil disturbance tends to result in lower stiffness and maximum shear resistance—so, reducing sampling disturbance, or recognising when a sample is disturbed, is an excellent opportunity to optimise a GEM.

The degree of sample disturbance is heavily influenced by:

- Drilling equipment and/or procedures.
- Sampling equipment and/or procedures.
- Storage and transportation equipment and/or procedures.
- Method of removing soil from sample tubes.
- Preparation of test specimens.
- Method of installing test specimens in testing apparatus.
- Specimen consolidation.

Most of the sources of sample disturbance can be minimised by using appropriate drilling and sampling equipment and procedures. However, one source of inevitable disturbance is the swelling that occurs when a soil sample is extracted from its in situ state and stored at atmospheric pressure, before being tested in an onshore laboratory. This inevitable disturbance is often wrongly attributed to poor drilling and/or sampling.

The inclusion of specimen consolidation in the list above might seem controversial. It has been included, however, because inappropriate consolidation, i.e. consolidation that causes the soil to be changed from its state in situ, is a form of controlled disturbance.

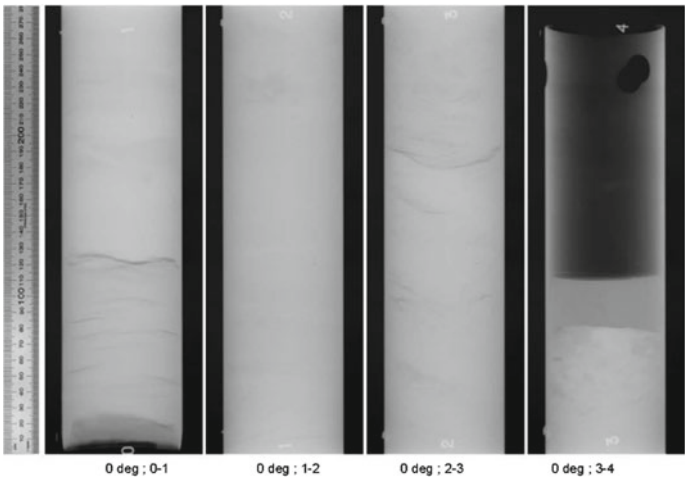

Fig. 8 X-ray of soil sample bottom-left to top-right

An excellent opportunity for optimising GEMs is to be able to recognise sample disturbance, as this enables test results on disturbed samples to be given lower credibility when assessing characteristic profiles. This section, therefore, concentrates on methods of recognising and/or assessing sample disturbance.

3.5.2 X-ray Photographs

The X-ray photograph, shown in Fig. 8, reveals the details of soil structure that provide insight on the geological history. Just as importantly, the darker zones, close to the top and bottom of the sample, reveal zones of lower density material. The top of a sample is particularly prone to drilling-induced disturbance, and the base is inevitably disturbed, to some extent, by the tensile stresses that occur at the base when the sample-tube is pulled from the ground. Review of X-ray photographs, therefore, enables testing to be allocated to the least visually disturbed portion of a sample. Consequently, X-ray photography is considered a relatively simple and low-cost method of optimising a GEM by ensuring tests are not performed on clearly disturbed soil specimens.

3.5.3 Sample Quality Assessments Based on Consolidation Behaviour of Test Specimens

ISO 19901-8 (2014) recommends using the method proposed by Lunne et al (2006) to assess sample quality, by measuring the volume changes that occur during consolidation of laboratory test specimens. The Lunne et al (2006) method was developed

by assessing the consolidation behaviour of tests performed on marine clays less than 24.4 m below seafloor, with water contents (w) ranging from 20 to 67% and plasticity indices (PI) varying from 6 to 43%. Lunne et al (2006) were careful to point out the limits of their data set and advise that outside these limits the method should only be used with caution. However, in practice, the method is often applied to all consolidated soil specimens on a project, and there are many situations—for example deepwater offshore India—where the water content and/or the plasticity indices may be outside the Lunne et al (2006) data set.

Recognising that, even for perfect samples, some volume change is inevitable as the soil specimen is consolidated back to the in situ effective vertical stress the author has developed a modified formula that includes a "depth correction" based on the swelling index measured during oedometer tests to decouple void ratio changes (due to the reconsolidation to the in situ vertical stress) from those induced by sample disturbance. The author's modified formula is:

$$\Delta e/e_o \text{ at } \sigma_v' \text{ (corrected)} = \Delta e/e_o \text{ at } \sigma_v' \text{(measured)} - C_s \times \log 10\,(\,\sigma_v'/10)/e_o$$

It may be seen, in the preceding formula, that the effective vertical stress in situ has been normalised using a 10 kPa "reference stress". It is recognised that this reference stress is somewhat arbitrary, as it is merely based on the initial effective stress reported by Lunne et al (2006) for their tests on Lierstranda Clay (and because it is a typical initial effective stress). Although the proposed correction has not been comprehensively verified, the general principles, on which the correction is based, are considered to be sound.

A shortfall of the Lunne et al (2006) method is that the sample quality is only assessed retrospectively, after the test specimen has been selected, prepared, consolidated and tested. A method of assessing soil disturbance during the offshore fieldwork would, therefore, be a GEM optimisation opportunity.

3.5.4 New Sample Quality Assessment (SQA) Method

Figure 9 presents example UU triaxial results from a deepwater site offshore India. It might be tempting to make a qualitative assessment of the sample quality simply by examining the shape of the stress–strain curve. However, one of the limitations of this approach is that the initial specimen stiffness (typically expressed via the proxy term ε_{50}, the strain at half the maximum deviator stress) tends to increase with increasing overconsolidation ratio, OCR. This example highlights that although ε_{50} is a good starting point, any assessment of sample disturbance needs to take account of several additional factors, the most important of which are the maximum stiffness, the reduction in maximum shear modulus with increasing OCR, the rate of reduction of shear modulus with increasing shear strain and rheological effects.

Consequently, the author has developed a new method for assessing sample disturbance that takes account of the above factors. The new method is based on a comparison of predicted and measured $G_{50}/G_{\max}$ values from UU and resonant column

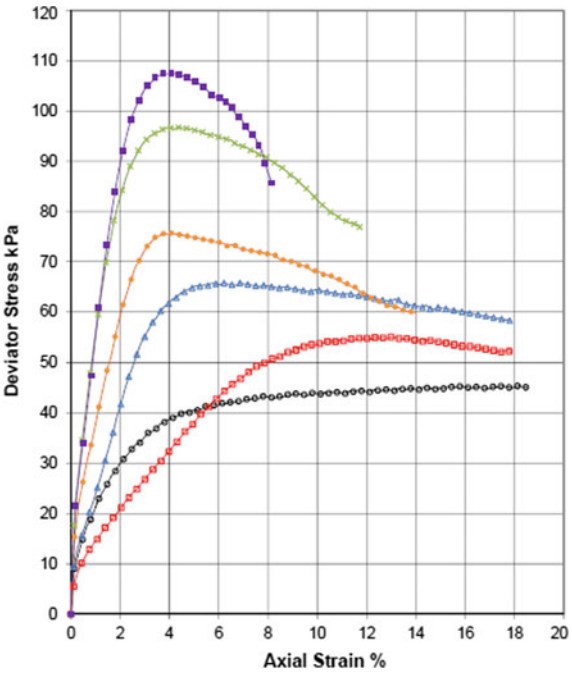

Fig. 9 UU triaxial results example

measurements, or where resonant column measurements are unavailable, using a new formula for predicting G_{max} from CPT data. A detailed description of the methodology, including the new formula for predicting G_{max}, is presented in Appendix 2—the remainder of this section presents some example results and discusses some potential advantages of the new method.

The new SQA method is intended to be used during two stages of a geotechnical site investigation.

- The first stage is during the offshore fieldwork, where the new method can be used to provide preliminary predictions of SQA. This offers the opportunity for significant optimisation as, by enabling the sample quality to be assessed as the fieldwork proceeds, it offers the opportunity to assess mitigation methods in cases where the SQA consistently predicts poor quality. As the new SQA method is based on UU triaxial test and CPT results, it is essential that the UU tests are performed and processed as soon as possible after the samples are retrieved to deck. Expediting the UU testing enables SQA predictions to be made as the work progresses, but also avoids the time-dependent reductions in UU shear strength and stiffness that occur in most soils with time (Graham et al. 1990) which reduces the SQA prediction.
- The second stage is intended to occur onshore, when advanced laboratory testing onshore (particularly oedometer testing, resonant column testing and "standard" and "rapid" direct simple shear testing) can be used to improve the reliability

of the G_{max}, γ_{ref} and χ assessments and develop site-specific relationships that improve the SQA (refer to Appendix 2 for more details).

Note that one limitation of using the new SQA method offshore is that heavily overconsolidated low plasticity soil samples can, in some cases, exhibit temporary increases in shear strength and stiffness, above those existing in situ—this type of sampling disturbance would not be recognised. Another limitation of the method is that fissuring (or other forms of significant soil fabric) can cause unreliable SQA predictions. However, both these limitations can be mitigated somewhat by visual assessments and onshore laboratory testing.

Figure 10 presents G_{50}/G_{max} profiles (as G_{50}/G_{max} measurements provide the basis for predicting SQA in the new method) and s_u profiles at Site A. Two adjacent boreholes were performed at the site, the first containing continuous sampling and

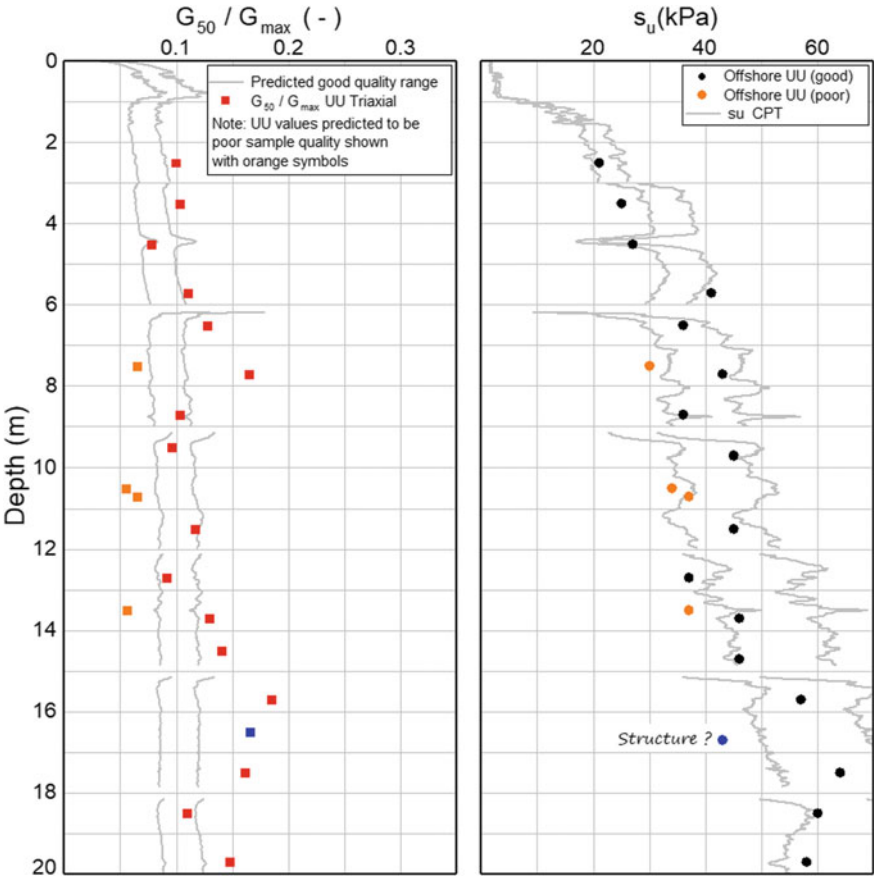

Fig. 10 New method for assessing sample disturbance—offshore test results—Site A—shallow-water (<170 m)—not offshore India—Contractor 1

the second containing "continuous" CPTs. The left-plot on Fig. 12 indicates that most of the G_{50}/G_{max} ratios inferred from the offshore UU triaxial results were of "good quality" or better. However, several G_{50}/G_{max} values, inferred from UU triaxial tests in the depth range 7.5–13.5 m, were predicted to be poor sample quality. As would be expected, the right-plot indicates that the associated UU undrained shear strength values plotted below the general trend. Unfortunately, no onshore testing was performed at Site A to confirm the Stage 1 SQA predictions, but it is notable that removing the four samples considered to be of poor quality could potentially lead to an increase in the low estimate characteristic undrained shear strength profile.

It is also noteworthy, in Fig. 10, that one sample, at approximately 16.5 m, predicted by the SQA to be better than good quality indicated a relatively low undrained shear strength. A review of the individual test specimen details suggested that the low shear strength was probably due to slickensiding—therefore, highlighting the need to review, and take account of, the UU sample descriptions and failure modes as part of the SQA process.

A second example, containing both offshore and onshore review, is presented in Figs. 11 and 12. As in the first example, two adjacent boreholes were performed at Site B; one containing continuous sampling and the other containing "continuous"

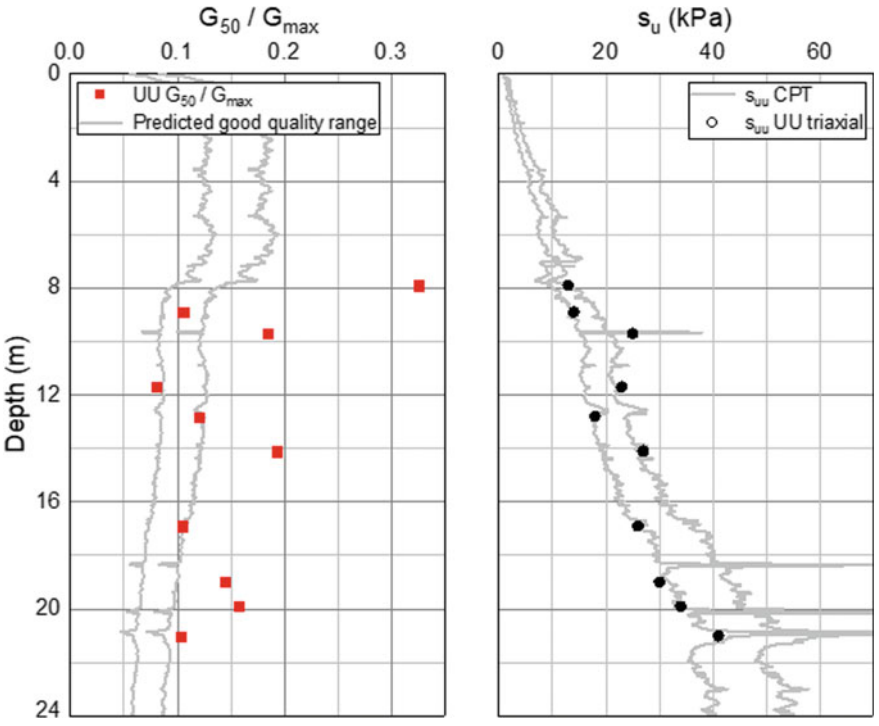

Fig. 11 New method for assessing sample disturbance—offshore results—Site B—deepwater (>170 m)—offshore India—Contractor 2

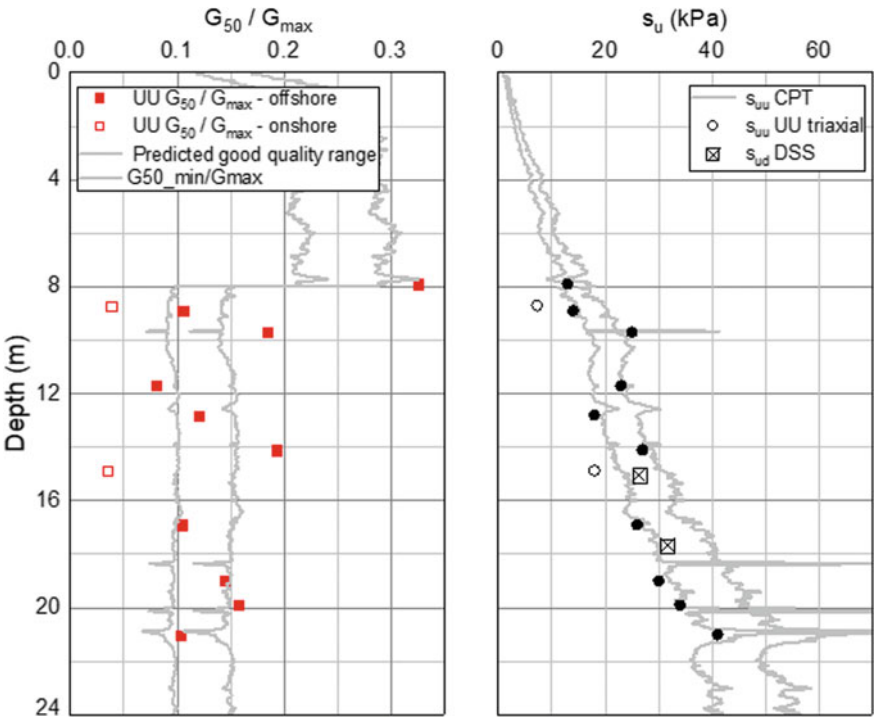

Fig. 12 New method for assessing sample disturbance—offshore test results—Site B—deepwater (>170 m)—offshore India—contractor 2

CPTs. Figure 11 presents the offshore SQA predictions, in terms of the G_{50}/G_{max} data on the left-plot, whilst the right-plot presents corresponding s_u profiles.

It may be seen on the right-plot that there are two general soil units; a surficial essentially normally consolidated drape to approximately 8 m, overlying a lightly overconsolidated unit that was considered likely to be a mass transport deposit (MTD). The preliminary SQA predicts good quality, or better, sampling at all but one the UU depths, and the one sample predicted to be of lower quality did not indicate a complementary low undrained shear strength value. This behaviour is considered to suggest that the samples were of generally good quality or better—but the very high-quality values might indicate that the average values used to generate the offshore reference profiles could require amendment after the onshore advanced laboratory testing programme (See Appendix 2 for details of the new SQA method).

Figure 12 presents updated reference curves based on onshore oedometer, resonant column and rheological testing. It may be seen on the plot on the left that the onshore testing has led to a significant difference between the SQA profiles in the drape and MTD units (in this case, predominantly due to a higher than typical increase in the rheological behaviour of the MTD unit). However, this has made no significant

difference to the sample quality assessment; i.e. the one sample predicted to be of poor-quality offshore is still predicted to be of low quality.

The plot on the left of Fig. 12 also presents sample quality assessments made on two UU tests performed onshore. It may be seen that the predicted quality of these two samples is much lower than the offshore samples. Based on the author's experience and other research (e.g. Graham et al. 1992), this behaviour was expected. Furthermore, the corresponding undrained strength measurements were lower than the general offshore trend. Consequently, performing additional onshore triaxial testing without attempting to reinstate the effective stresses in situ is not recommended.

The results of two onshore DSS tests are also presented in the right-plot of Fig. 12. These soil specimens were consolidated to the estimated in situ conditions. It may be seen that the results of these tests are, as would be expected, much higher than the onshore UU tests, and in generally good agreement with the good quality or better offshore UU tests.

The final example, presented in Figs. 13 and 14, is for much more challenging ground conditions. Site C is in deepwater, offshore India. At this site, the static pore-water pressure in situ is, in some zones, greater than hydrostatic pressure. This condition is particularly challenging for drilling and sampling, so samples are much

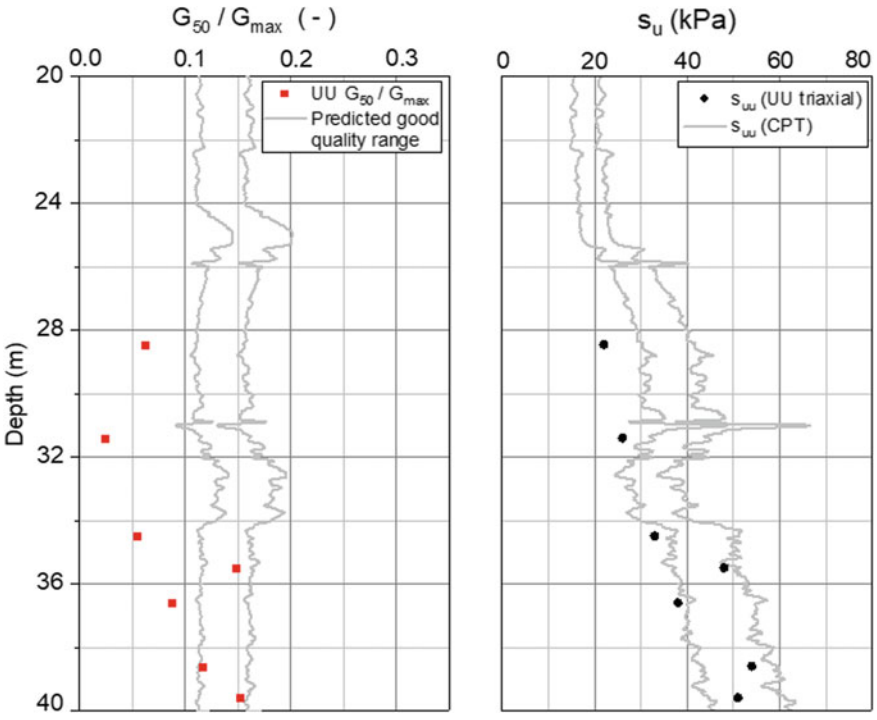

Fig. 13 New method for assessing sample disturbance—offshore test results—Site C—deepwater (>170 m)—offshore India—contractor 2

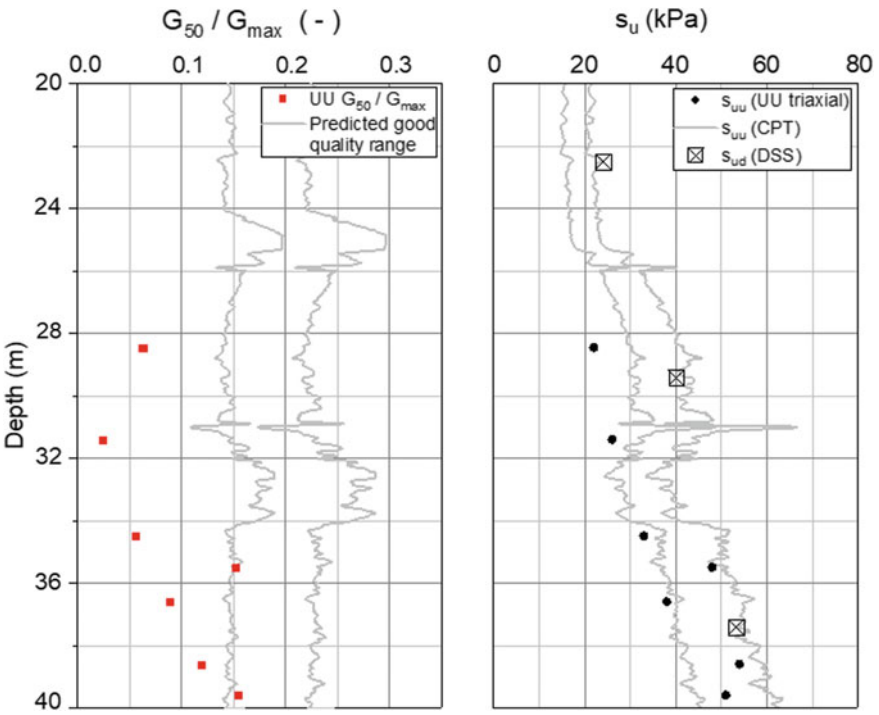

Fig. 14 New method for assessing sample disturbance—deepwater site offshore India—onshore assessments

more prone to disturbance—and, in some cases, sample disturbance is practically unavoidable.

For clarity, Fig. 13 presents offshore test results only for a depth range of 28–40 m. The SQA presented on the left-plot predicts poor sample quality at four depths, based on the offshore UU triaxial results. As in the previous example, these low G_{50}/G_{max} ratios generally coincide with UU strengths that are lower than the s_u profiles predicted using the CPT data (which used site-wide N_{kt} ranges). As several consecutive s_u values are low they are more likely to influence a chosen low estimate characteristic profile. In this case, the new method enables the preliminary LE characteristic profile to be optimised, by providing a quantitative means of differentiating poor-quality and good-quality samples and hence tests more likely to provide representative undrained shear strength values. Furthermore, as noted previously, the new method enables optimal selection of samples for additional onshore laboratory testing.

Figure 14 presents an amended assessment of sample disturbance, using advanced laboratory testing performed onshore to develop site-specific G_{max}, γ_{ref}, α and χ correlations (see Appendix 2 for more details). It may be seen that the G_{50}/G_{max} for good quality results has increased at this site (primarily due to γ_{ref}, being higher

than the average value predicted using the Vardanega and Bolton (2011) formula for assessing γ_{ref} from water content measurements. This significant change has resulted in one more test being downgraded (at a test depth of approximately 38.5 m). However, the UU test at this depth did not indicate an anomalously low shear strength, so there would be no effect on chosen characteristic profiles. It may also be seen that the two UU triaxial results on "Predicted Good Quality" samples are in good agreement with the results of a nearby direct simple shear (DSS) test (consolidated taking account of the predicted excess pore-water pressures).

At the time of writing this paper, the new SQA method has been applied on a relatively small number of projects—however, in all cases, the results have been very encouraging.

It is important to emphasise that this new method is intended as a tool to enable GEMs to be optimised by allowing more reliable assessments of characteristic soil parameter values and profiles. The new method should not be included within contracts, as a minimum measure of sample quality. This is because there are several factors that can cause misleading results such as soil structure and mineralogy—and there are ground conditions that almost inevitably lead to sample disturbance using standard offshore investigation methods: for example, soils with significant excess pore-water pressures. Even in cases where a significant proportion of samples are classified of poor quality, the new method can be used to optimise targeting of samples for advanced laboratory testing, which can be used, via appropriate consolidation, to reduce the impact of poor-quality sampling.

3.6 Geotechnical Unitisation

3.6.1 General

A "Geotechnical Unit" is a systematic three-dimensional grouping of soils, containing soils with similar geotechnical properties, and comparable boundary elevations, for a defined engineering application. Geotechnical units should, if possible, be compatible with corresponding geological and geophysical units. As geotechnical units are also dependent on engineering application, they are not constrained to be equal to the geophysical and geological units—but any discrepancies should be clearly noted in the geotechnical interpretive report.

Geotechnical unitisation enables more reliable geotechnical units and site-wide correlations to be developed based on all information at the site, rather than information obtained at a single borehole or test location. This process offers a significant GEM optimisation opportunity, as geotechnical unitisation enables interpolation and extrapolation of geotechnical soil parameters, particularly when there is geophysical continuity. Although geotechnical unitisation often requires some minor simplifications of soil properties, these simplifications are typically more than justified by the benefits, in terms of increasing the effective data set at individual locations and enabling more reliable predictions of the expected range of soil behaviour.

3.6.2 Assessing Geotechnical Units

The main differentiators between geotechnical units at a site are often strength and particle size distribution, as they strongly influence other soil properties. However, there are many other potential differentiators such as carbonate content, organic content, plasticity, structure ("fissured", "slickensided", etc.) and "gassy and/or expansive" soils.

Typically, CPTs are the optimal method for differentiating geotechnical units because, as noted earlier, CPTs provide excellent continuous soil profiling data, which can be used to identify characteristic "cone signatures" (a useful application of statistics) even when tests are widely separated. Furthermore, CPTs can often be used to define geotechnical unit boundaries, even when the changes in cone behaviour are relatively subtle. Laboratory test data can be used to optimise the process by confirming, and potentially refining, the CPT-derived geotechnical unit boundaries.

Ramsey (2018) notes that—in the author's opinion—composite plots are often incorrectly used to characterise several geotechnical units on a single figure. However, soil boundary elevations often vary laterally, so composite plots presented in this way can give a misleading impression of unit thicknesses. For example, Fig. 15 presents composite plots of four cone penetration tests—and, on this basis, Unit IV is inferred to be approximately 3.7 m thick. Furthermore, the relatively soft nature of the unit is not plainly apparent. In contrast, Fig. 16 presents cross-sectional plots of total cone resistance at the same four locations. The shaded areas on Fig. 16 highlight

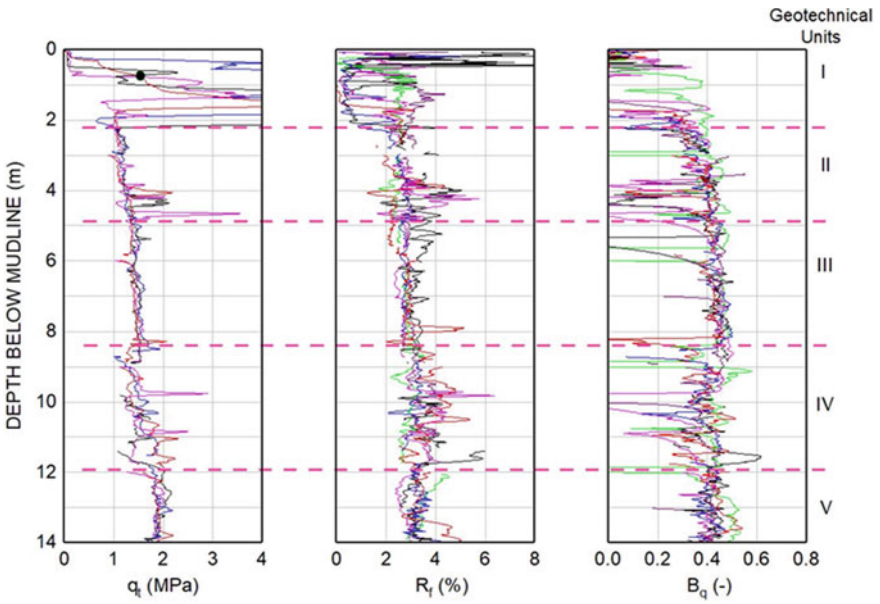

Fig. 15 Estimating geotechnical units by composite plot (use with care)

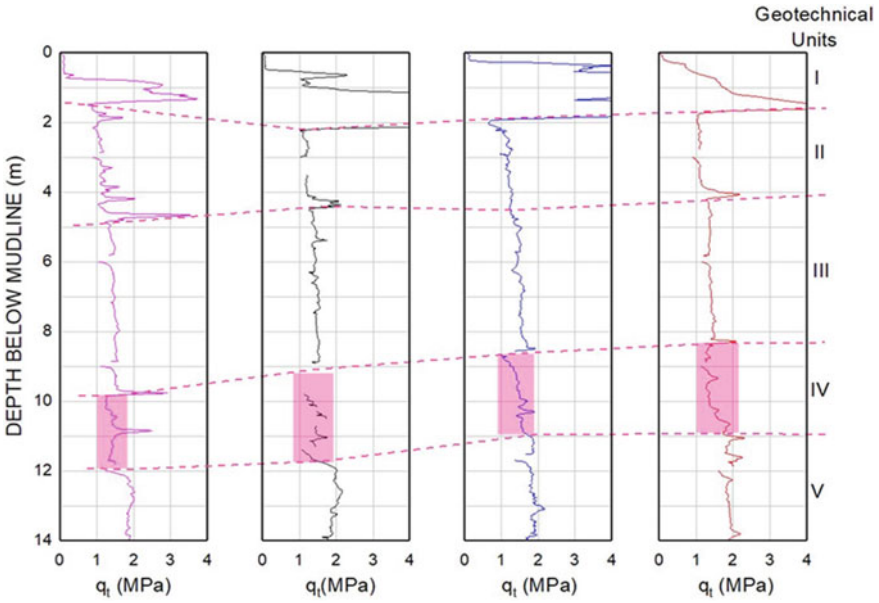

Fig. 16 Estimating geotechnical units by cross-sectional plot (generally recommended)

the variations in boundary elevation and thickness of Unit IV, which is shown to have a maximum thickness of 2.7 m, and the softer nature of the unit is much easier to discern. Consequently, producing cross-sectional plots to assess continuity of geotechnical units is a simple and quick optimisation opportunity.

3.7 Applying Statistics

It may be tempting to use automated statistical techniques as a GEM optimisation technique. However, in the author's opinion, the application of statistics always requires careful judgement, as automated techniques can lead to conclusions that are misleading, or even completely incorrect.

Figure 17 presents an example of an appropriate use of statistics for a deepwater site offshore India.

The histogram and cumulative frequency curves, which were based on more than 100 measurements across the site confirmed the N_{kt} distribution (where N_{kt} is defined as the ratio between the net cone resistance and the corresponding undrained shear strength) followed standard trends. One of the advantages of assessing N_{kt} via statistics (when there is no obvious depth dependency) is that the data are normalised; i.e. they become independent of depth. Consequently, an optimisation opportunity can be exploited by performing separate assessments of N_{kt} for different methods of

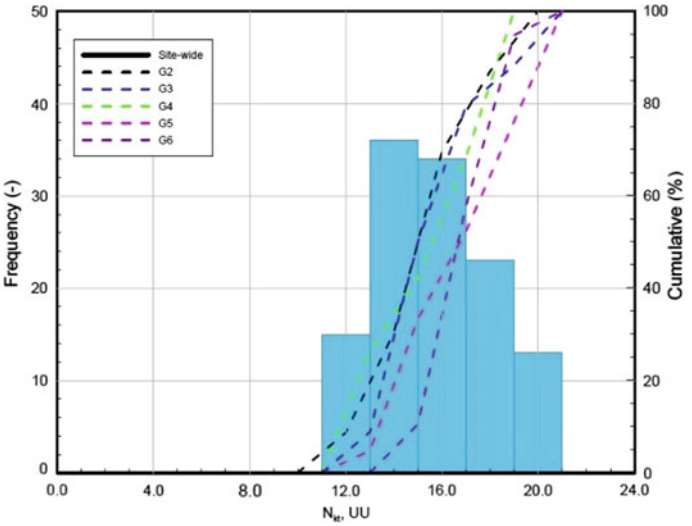

Fig. 17 Example—optimising GEMs using statistics

assessing undrained shear strength. By comparing the ratios of the N_{kt} factors, it then becomes possible to assess strength anisotropy via a much larger database than the typical approach of performing a small number of comparative tests on adjacent test specimens. Another optimisation opportunity occurs when estimating N_{kt} values—typically N_{kt} is assessed from all measured values. However, this assessment can easily be optimised by only taking account of good quality correlations, where good quality is defined as:

- A net cone resistance profile varying by less than $\pm 10\%$ in the vicinity of the corresponding undrained shear strength value.
- SQA predicted to be good or better.
- The maximum vertical consolidation pressure (for consolidated triaxial and simple shear tests) has not exceeded 90% of the preconsolidation pressure estimated from oedometer and/or CPT data.

3.8 Estimating Characteristic Values and Profiles

Ramsey (2018) notes that the choice of characteristics should be straightforward, providing robust integration of the geomorphological, geological, geophysical and geotechnical datasets has occurred, and the proposed engineering application has been considered during the development of the GEM. Conversely, if significant empiricism, precedent and well-winnowed experience are needed to assess characteristic value and profiles, then this is likely to be a sign that the GEM has not been sufficiently optimised.

Although the best estimate (most probable) value or profile will only occasionally be a characteristic, the best estimate provides a useful reference for assessing the low estimate and high estimate values or profiles, which are more typically presented as characteristics. It is important to note that the exact purpose, or range of purposes, must always be defined when presenting a characteristic value, or profile.

4 Assessing Gem Optimisation

The GEM checklist, presented in Appendix 1, is a useful means of assessing GEM optimisation. If the answers to all the items in the GEM checklist are positive, then the GEM is likely to be optimised for the level of work required.

Another simple approach for assessing GEM optimisation is to remove one or more of the geotechnical boreholes and in situ tests and then request a third party to predict the ground conditions at the missing locations.

5 Conclusions

- Developing a GEM is not a linear process—it is an iterative process in which all new data are used to improve the GEM, either by increasing its reliability or by amending the GEM to fit the new data.
- The quality of the GEM may be visualised by the gauge of the mesh at the base of the GEM funnel. A non-optimised GEM is more likely to result in a coarse-mesh that allows potentially important information to slip through, whereas an optimised (robust fit-for-purpose) GEM can be visualised as a fine-mesh that catches all relevant information.
- The first GEM optimisation opportunity is to gather a suitably experienced team of geomorphologists, geologists, geophysicists and geotechnical engineers, to contribute to the GEM, rather than expect non-specialists to make specialist assessments.
- An early GEM optimisation opportunity is to ensure that the chosen borehole/testing locations are positioned in a manner that enables a representative range of soil conditions to be evaluated. This opportunity can generally only be achieved by performing appropriate geomorphological, geological and geophysical assessments, prior to the geotechnical fieldwork.
- Assessing, and allowing for sample quality, is a significant opportunity to optimise a GEM. A new sample quality assessment (SQA) method is proposed. Details are presented in Appendix 2, and several examples are presented and discussed. Although the new method has only been applied to a limited number of projects, so far, the success of the method in predicting sample disturbance has, in all cases, been very encouraging.

- A new formula for predicting G_{max} is proposed. The advantage of the new proposed formula is that it accounts for the effect of OCR on G_{max}: $G\max = 40 \cdot q_{net} \cdot \left\{1 - \exp\left[2.46 \cdot \sqrt{(\ln(Q_t/3))} - 4.76\right]\right\}$.
- Geotechnical unitisation offers a significant GEM optimisation opportunity, as geotechnical unitisation enables interpolation and extrapolation of geotechnical soil parameters, particularly when there is geophysical continuity.
- If a GEM is optimised, then assessing characteristic values, or profiles, should be relatively straightforward—if this is not the case, then it is likely that there are deficiencies in the GEM.
- The GEM checklist, presented in Appendix 1, is a useful means of assessing GEM optimisation. If the answers to all the items in the GEM checklist are positive, then the GEM is likely to be optimised for the level of work required.

Appendix 1: Geotechnical Engineering Model (GEM) Checklist

Check Item

Is the scope of work consistent with the proposed engineering applications?

Are the geomorphology and geology understood?

Have all potential geohazards been identified?

Is there enough information to develop a reliable GEM?

Is the soil investigation coverage adequate?

Has a sample quality assessment (SQA) been performed and do the results confirm the samples of good quality?

Have all anomalous data been reviewed and discussed in the report text?

Is the acquired geotechnical information fit-for-purpose?

Has enough information been gathered in all significant geotechnical units?

Is the GEM consistent with the geological, geophysical and geomorphological datasets?

Have the ranges of applicability of all characteristic values been clearly defined?

Check Item commentary

The scope of work must enable the project objectives to be achieved—so proposed foundation types, geometries and loadings should be defined.

It is essential vital to understand the geomorphology and geology of the site, as these provide essential frameworks for GEM development.

Consider geology; near-field topography; far-field topography; mineralogy; project-induced changes.

A reliable GEM needs adequate geological; geophysical, geomorphological and geotechnical information.

Ensure sufficient investigation is performed for the project requirements—noting that geohazards may be located outside the project area.

High-quality numerical analyses need high-quality input data.

Consider the possibility of aleatory, epistemic, transformational and measurement errors, and whether the GEM needs to be amended.

Consider geology; magnitude, direction and rate of loading; temperature and salinity; and drainage conditions under loading.

Consider vertical and lateral variability; possible weak zones; possible strong zones, peak strength and post-peak behaviour; stiffness degradation; cyclic/dynamic behaviour; and potential change in material properties with loading and/or time.

If, for engineering reasons, the GEM is inconsistent with the geomorphological or geological or geophysical datasets, then the reason for each inconsistency should be clearly highlighted in the report.

Consider the consolidation behaviour of the soil, drainage length, intended design purpose, design life of the structure, magnitudes and durations of static and dynamic loadings, rates and directions of loading and time-dependent changes (e.g. scour).

Appendix 2: Details of New Sample Quality Assessment (SQA) Method

Stage 1—offshore predictions (assuming no previous experience at the site)

1. Calculate $G_{\max}$ from shear-wave velocity measurements, if available.
2. If no shear-wave velocity measurements or existing experience available at the site, then predict the $G_{\max}$ profile using the equation:

$$G_{\max} = 40 \cdot q_{net.}\{1 - \exp\left[2.46 \cdot \sqrt{(\ln(Q_t/3))} - 4.76\right]\}$$

where q_{net} is the net cone resistance Q_{t} is the normalised cone resistance, $q_{\text{net}}/\sigma'_{\text{v}}$, σ'_{v} is the corresponding effective vertical stress and all values are in kPa.

The equation above has been developed by the author assuming the relationship between I_{r} and OCR plotted below, OCR $= Q_t/3$ (Mayne 2014) and $3 \leq Q_{\text{t}} \leq 90$.

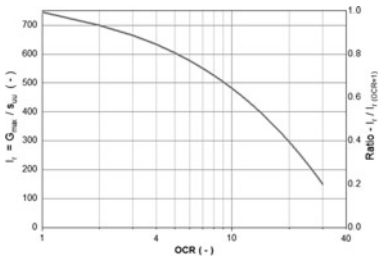

Total and effective unit weight values (required for q_{net} and σ'_v profiles) can be based on UU triaxial results, or published relationships, such as Robertson and Cabal (2010).

3. Calculate "rate-corrected" $G_{50(UU)*}$ values using the equation:

$$G_{50(UU)*} = [s_{uu}/(3 * \varepsilon_{50})] \cdot \chi$$

where s_{uu} is the undrained shear strength measured in the UU triaxial test, ε_{50} is the vertical strain at half the maximum deviator stress and χ is a stiffness correction factor to account for the change in stiffness caused by the differing shear strain rates of resonant column (typically 30%/s) and UU triaxial tests (typically 0.025%/s). For these typical values, the strain-rate difference is 3.08 $\log_{10}$ cycles—so, for a typical increase in stiffness of 5% per $\log_{10}$ cycle, the stiffness correction factor, χ, is:

$$\chi = (1 + 0.05)^{3.08} = 1.16$$

4. Divide the $G_{50(UU)*}$ values by the corresponding G_{max} value to estimate the ratio $G_{50(UU)*}/G_{max}$.
5. Predict the OCR profile using the equation (Mayne 2014):

$$\text{OCR} = Q_t/3$$

6. Estimate LE and BE γ_{50} profiles using the equation below (based on Hight et al. 1985):

$$\gamma_{50} = \beta * 1.5 * \left[0.5 + 1.177 \cdot \log_{10}(\text{OCR})\right]$$

where $\beta(\text{LE}) = 0.75$ and $\beta(\text{HE}) = 1.25$.

7. Generate the γ_{ref} profile using the equation below (based on V&B 2011)—assuming $G_s = 2.7$ and using measured UU water contents, or water contents inferred from the σ'_v profile:

$$\gamma_{ref} = 0.56 * (w * G_s)/1000$$

8. Predict LE and HE G_{50}/G_{max} profiles using the equation below (based on V&B 2011):

$$G_{50}/G\text{max} = 1/(1 + (\gamma_{50}/\gamma_{ref})^{\alpha}$$

using the γ_{50} and γ_{ref} profiles calculated in Steps 6 and 7, and assuming $\alpha = 0.97$ (based on V&B 2011).

9. Plot the $G_{50(UU)*}/G_{max}$ values and G_{50}/G_{max} profiles and compare the results. If the $G_{50(UU)*}/G_{max}$ values lie within or above the G_{50}/G_{max} profiles, then the samples are predicted to be of good, or better than good, quality.
10. If the $G_{50(UU)*}/G_{max}$ values plot below the G_{50}/G_{max} profiles, then the samples are predicted (not stipulated) to be of poor quality. If so, then potential reasons for the predicted low sample quality should be considered, and operational changes made if deemed appropriate. Potential reasons might include, but not be limited to, drilling-induced disturbance, sampling induced disturbance, soil structure effects, poor-quality UU testing, or excess pore-water pressure in situ.

Stage 2—onshore predictions.

The offshore predictions can be confirmed onshore, using laboratory testing to confirm the key assumed parameters, i.e. OCR, χ, γ_{ref} and α. These parameters can be measured using the following onshore tests:

1. Resonant Column (RC) testing enables direct assessments of γ_{ref} and α.
2. Varying rate of strain Direct Simple Shear (DSS) testing enables site-specific χ correlations to be developed.
3. Oedometer testing enables OCR to be estimated more reliably and—if further optimisation is required—enables site-specific correlations to be developed between OCR and ε_{50}, and OCR and Q_t.

Based on the author's experience, so far, onshore assessments of sample quality have generally yielded similar results to offshore predictions.

References

Burland JB (1987) Kevin Nash Lecture, The teaching of soil mechanics—a personal view. In: Proceedings of the 9th European conference on soil mechanics and foundation engineering, Dublin, vol 3, pp 1427–1447

Campbell KJ et al (2008) Modern deepwater site investigation: getting it right the first time. OTC Paper 19535

Campbell KJ et al (2015) AUV technology for seabed characterization and geohazards assessment, the leading edge, vol 34, no. 2. Society for Exploration Geophysicists

Graham J, Jamieson MR, Ho DY, Azizi F (1990) Influence of storage and reconsolidation procedures on clay properties. Geotech Test J GTJODJ 13(4):280–290

Hight DW, Gens A, Jardine RJ (1985) Evaluation of geotechnical parameters from triaxial tests on offshore clay. In: Proceedings offshore site investigation 85, London, Mar 1985

ISO/DIS 19901-8 (2014) Petroleum and natural gas industries—specific requirements for offshore structures—Part 8: Marine soil investigations

Lunne T, Berre T, Andersen KH, Strandvik S, Sjursen M (2006) Effects of sample disturbance and consolidation procedures on measured shear strength of soft marine Norwegian clays. Can Geotech J 43:726–750

Mayne PW (2014) Interpretation of geotechnical parameters from seismic piezocone tests. In: Proceedings, 3rd international symposium on cone penetration testing (CPT'14), Las Vegas, Nevada

Phoon K-K, Kulhawy FH (1999) Characterization of geotechnical variability. Can Geotech J 36(4):612–624

Ramsey N (2018) A philosophy for developing geotechnical engineering models. In: Proceedings first Vietnamese symposium on offshore engineering

Randolph M, Hope S (2004) Effect of cone velocity on cone resistance and excess pore pressures. In Matsui T, Tanaka Y, Mimura M (eds) Proceedings of the IS Osaka—engineering practice and performance of soft deposits (Osaka, Japan ed., pp 147–152). Yodogawa Kogisha Co. Ltd, Osaka, Japan

Robertson PK, Cabal KL (2010) Estimating soil unit weight from CPT. In: 2nd International symposium on cone penetration testing (CPT'10). Huntington Beach, California

Thomas S (2017) A phased and integrated data interpretation approach to site characterization. In: Proceedings of the 8th international conference on offshore site investigation and geotechnics, 12–14 Sept 2017, pp 71, 87

Vardanega PJ, Bolton M (2011) Practical methods to estimate the non-linear shear stiffness of clays and silts. In: C-K Chung, H-K Kim, J-S Lee, Y-H Jung, D-S Kim (eds) Deformation characteristics of geomaterials: proceedings of the fifth international symposium on deformation characteristics of geomaterials, IS-Seoul 2011, vol 1, pp 372–379

Lattice Leg–Soil Interaction Effects in Deeply Embedded Spudcan Foundations

Fook-Hou Lee, Yong Fu, Yuping Li, Jiangtao Yi, and Xi-Ying Zhang

1 Introduction

Jack-up rigs are widely used in offshore hydrocarbon exploration and short-term drilling. They are usually supported by three lattice legs, each of which rests on a spudcan footing. A typical lattice leg consists of three or four vertical chords with inclined and horizontal braces (Bennett et al. 2005). Typical brace arrangements include X-brace, K-brace and reversed-K-brace. The diameter of each chord and brace member usually ranges from 0.25 to 1 m (SNAME 2008). Figure 1 shows the plan view of typical three- and four-chord lattice legs. During installation into soft deposits, the spudcan can penetrate up to a depth of two to three times its diameter (Endley et al. 1981). In such situations, a substantial length of the lattice will be embedded within the soft clay layer and interaction between lattice leg and soil may affect spudcan foundation behaviour significantly.

Leg–soil interaction is typically ignored in current spudcan design and the spudcan foundation is taken to be just a footing. The implied assumption is that the interaction between lattice leg and soil is negligible, even in situations, wherein the lattice leg is

F.-H. Lee (✉)
Department of Civil & Environmental Engineering, National University of Singapore, Singapore, Singapore
e-mail: leefookhou@nus.edu.sg

Y. Fu
Department of Ocean Science and Engineering, Southern University of Science and Technology, Shenzhen, China

Y. Li
Geotechnical Research Institute, Hohai University, Nanjing, Jiangsu, China

J. Yi
School of Civil Engineering, Chongqing University, Chongqing, China

X.-Y. Zhang
American Bureau of Shipping, Houston, TX, USA

S. Haldar et al. (eds.), *Advances in Offshore Geotechnics*, Lecture Notes in Civil Engineering 92, https://doi.org/10.1007/978-981-15-6832-9_4

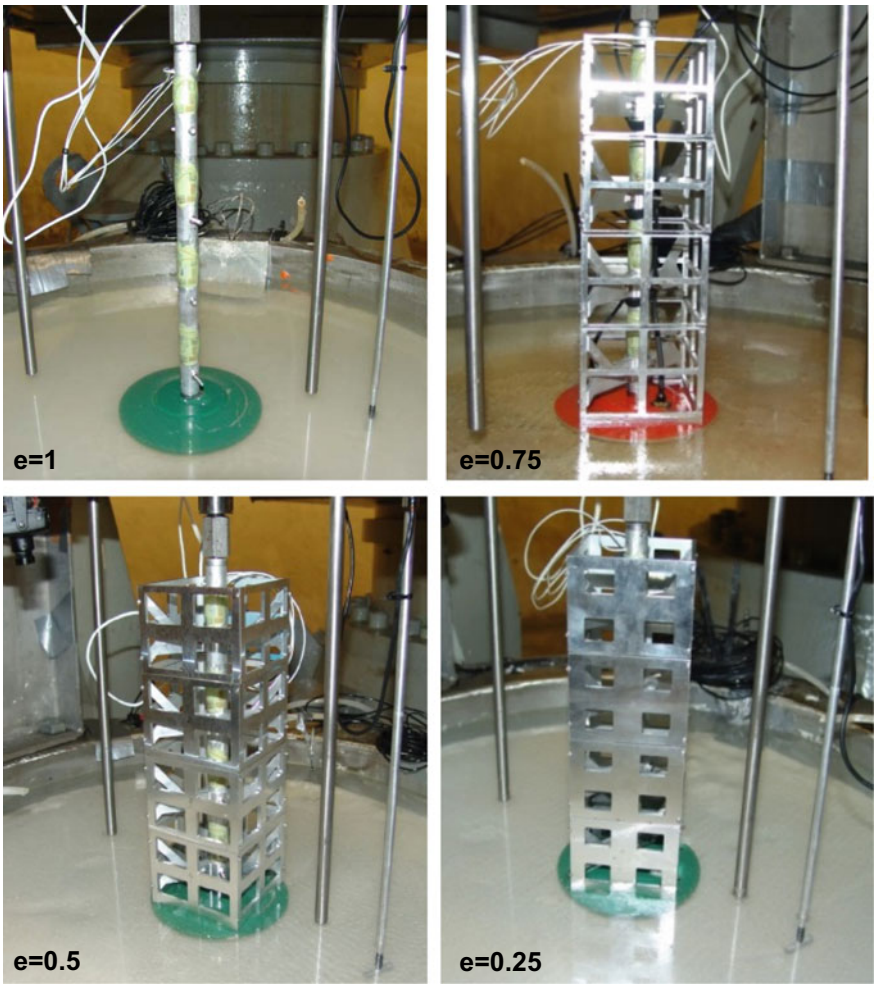

Fig. 1 Configurations of centrifuge model legs

deeply embedded in the soil. In this paper, findings from research conducted in NUS over the past few years on lattice leg–soil interaction will be summarized. These findings show interaction effects between lattice leg and soil which can affect the overall behaviour of the spudcan foundations.

2 Soil Backflow and Bearing Behaviour

Soil backflow on top of deeply penetrated spudcan footings can affect bearing capacity (Menzies and Roper 2008) and lateral resistance (Springman and Schofield

1998), as well as combined load capacity (Zhang et al. 2011). For fully embedded large diameter spudcans, the cavity depth may also significantly affect spudcan uplift resistance (BSI 2012), as the soil weight above spudcan footing can contribute significantly to the uplift resistance. In the standard BS EN ISO 19905-1 (BSI 2012) method for estimating cavity depth above the spudcan, the influence of lattice legs is not considered.

The influence of lattice legs on soil backflow and cavity depth was investigated by Li et al. (2017) using centrifuge model tests (Fig. 1) and coupled Eulerian-Lagrangian (CEL) finite element analyses with ABAQUS (Fig. 2). Their results show that, for normally consolidated clay, the effect of the lattice leg on the soil flow and cavity profile is insignificant when the depth of penetration less than approximately 0.31 times the spudcan diameter. For larger penetration depths, lattice leg effect becomes more evident. In the absence of the lattice leg, laterally inward soil flow on top of the spudcan leads to the creation of a shallow cavity. The effect of the lattice leg is to restrict the lateral soil flow to the zone outside the lattice cage. Within the lattice cage, soil flow is predominantly vertical, with the soil moving downwards together with the lattice leg. Soil ingress into the lattice cage occurs largely by cavity collapse through the lattice openings above the backflow region, Fig. 3a.

For over-consolidated clay, the restricting effect of the lattice on cavity collapse at the upper part of the cavity is more significant, resulting in a deeper, steep-sided

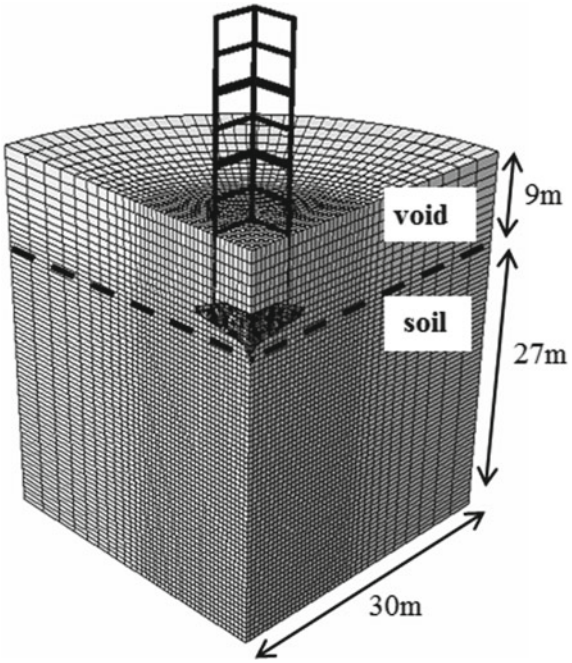

Fig. 2 Coupled Eulerian-Lagrangian finite element mesh

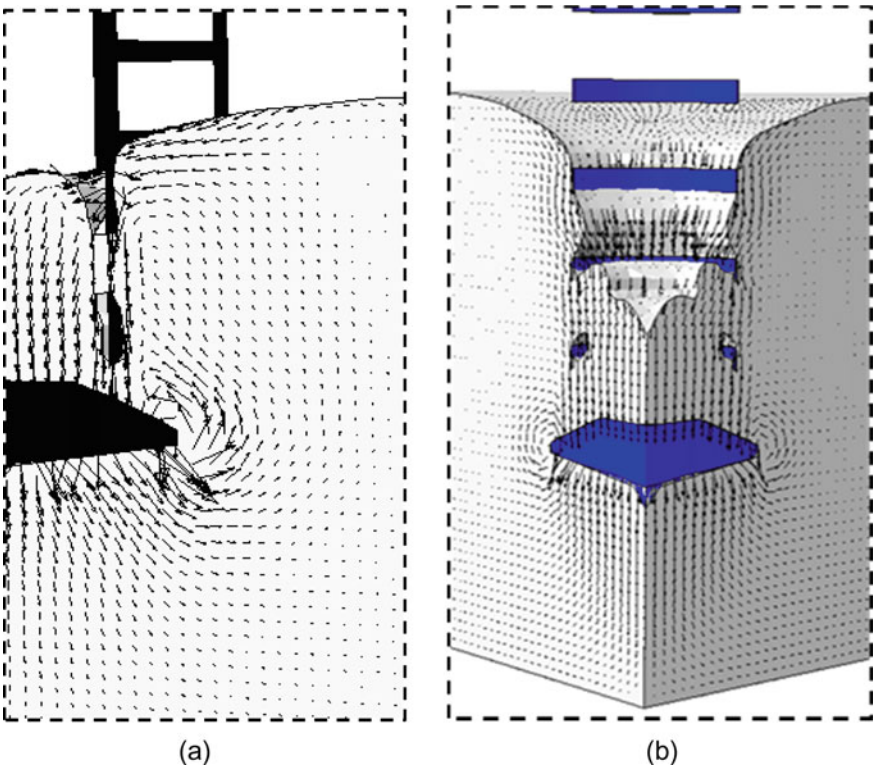

Fig. 3 Soil flow into the lattice cage for **a** normally consolidated soil and **b** clay with over-consolidation ratio of 2

cavity, Fig. 3b. Hence, the main effect of the lattice leg is to restrict soil backflow just behind the spudcan and restrain cavity collapse in the shallower regions, thereby allowing a deeper cavity to be formed. Li et al. (2017) used two parameters to characterize the lattice leg, namely the opening ratio and area ratio. The opening ratio is the ratio of the area of the openings to the area of the lattice cage. The area ratio is the ratio of the footprint area of the lattice to that of the spudcan. They noted that the brace arrangement of the lattice cross-section does not significantly influence the soil flow and cavity depth provided the opening and area ratios of the lattice leg are the same. Furthermore, lattice leg interference on soil flow was observed even at very high opening ratio.

The effect of the lattice chords and braces on penetration resistance and short-term bearing capacity has also been examined by Aagesen et al. (2018), who proposed a simplified method for estimating the additional resistance arising from chord– and brace–soil interaction. The method involves summing the resistance contributions from all the chords and braces, assuming that there is no interaction between them. Each chord and brace is treated as an individual member bearing against the soil.

Members which are oriented perpendicular to the direction of load are treated similarly to piles moving laterally through clay. Members which are oriented parallel to the loading direction are assumed to be subjected only to shearing resistance. The resistance of members which are oriented at oblique angles to the loading are obtained by an elliptical interpolation relationship. Their results indicate that the contribution of the chords and braces to penetration resistance can be significant for depth penetration exceeding one time the spudcan diameter.

Aagesen et al.'s (2018) method applies only to the short-term undrained condition. Over the longer term, complex time-dependent behaviour may also result due to changes in pore pressure. Menzies and Roper (2008) reported additional spudcan settlements under the maximum preloading at seven locations in the Gulf of Mexico, which did not appear to be caused by punchthrough. They attributed this to the unaccounted for loading due to soil backflow. If this is true, then delayed backflow may indeed occur in real spudcan, due to the collapse of the cavity through the lattice openings.

Li et al. (2018) examined some of the possible reasons for the large settlement observed by Menzies and Roper (2008). The deeper cavity caused by the lattice leg is not necessarily beneficial for the spudcan since the propensity for the cavity to collapse after installation is also greater. Their back-calculations indicate that the settlement caused by the additional soil weight due to cavity collapse is too small to explain observed settlement. Consolidation settlement is also only able to account for a small proportion of the spudcan settlement, indeed probably less significant than that caused by cavity collapse. However, centrifuge cyclic rocking tests demonstrate that large spudcan settlement can still occur if the spudcan is subjected to large amplitude cyclic loading, even after removal of 50% of the maximum preloading, Fig. 4. This motivates the possibility that stiffness and strength degradation of the soil in the vicinity of the spudcan footing and the leg might have occurred due to cyclic loading.

All these indicate that interaction between lattice leg and soil in deeply penetrated spudcan is not only significant but may also be complex. So far, research has only touched on the short-term, relatively undrained, leg–soil interaction. However, there are indications that there may be other facets of behaviour such as long-term as well as cyclic loading effects.

3 Punchthrough

The issue of punchthrough is closely related to that of penetration resistance since it is essentially a loss of penetration resistance. Current methods of mitigating punchthrough include downward skirted spudcan (Yu et al. 2010a, b; InSafeJIP 2011; Hossain et al. 2014), extended suction-piled spudcan (Thomas et al. 2007) and perforation drilling (Hossain et al. 2014; InSafeJIP 2011). Amongst these methods, the most widely studied is probably downward skirts. All these methods have their limitations. The mitigating effect of downward skirt usually comes at the cost of reduced

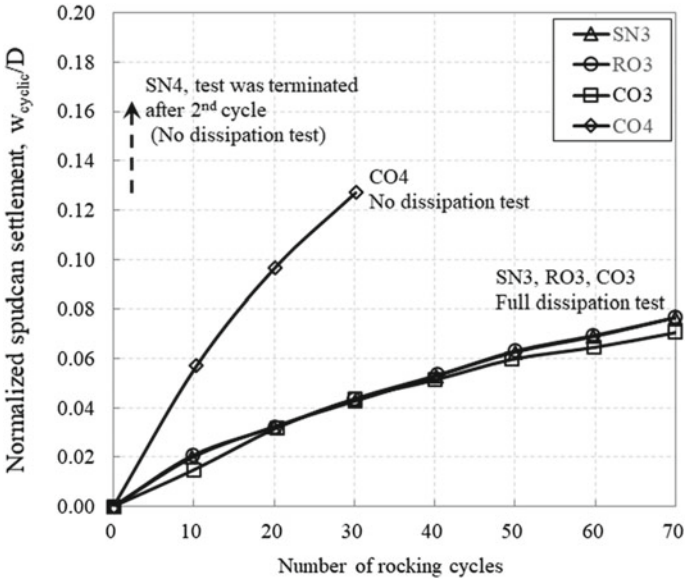

Fig. 4 Cyclic settlement of spudcans in clay

foundation bearing capacity (Yu et al. 2010a; Hossain et al. 2014). There is also an operational constraint on the length of the downward skirt; skirts which protrude beyond the cone tip of the spudcan have been noted to degrade the hydrodynamic stability of the jack-up rig during towing (Li et al. 2019). For this reason, the length of downward skirts is typically kept short. However, this also limits their effectiveness in mitigating spudcan punchthrough (e.g. Hossain et al. 2014).

Appendages have also been attached to the base of the spudcans to improve their performance in other special circumstances. For instance, it is known that, for operations in sites known to be underlain by thick layer of soft clay, enlarged base slabs have been attached to the bottom of the spudcan to increase the bearing area and reduce spudcan penetration. However, such appendages are also subjected to a similar constraint that they cannot protrude beyond the conical tip of the spudcan.

Extended suction-piled spudcans may also compromise spudcan fixity (Thomas et al. 2007); while perforation drilling is likely to require increased time and effort in installation and is more suitable for stiff clay than sand deposits overlying soft clay (InSafeJIP 2011).

Less is known about the effect of lattice legs on punchthrough than penetration resistance. However, more recently, Li et al. (2019) proposed the use of upward sleeves, which is a segment of the lattice leg that is fully enclosed, Fig. 5 to mitigate punchthrough effects. Li et al. (2019) compared the punchthrough behaviour of plain, skirted and sleeved spudcans, using centrifuge model tests, Fig. 5, and coupled Eulerian-Lagrangian finite element analyses, Fig. 6.

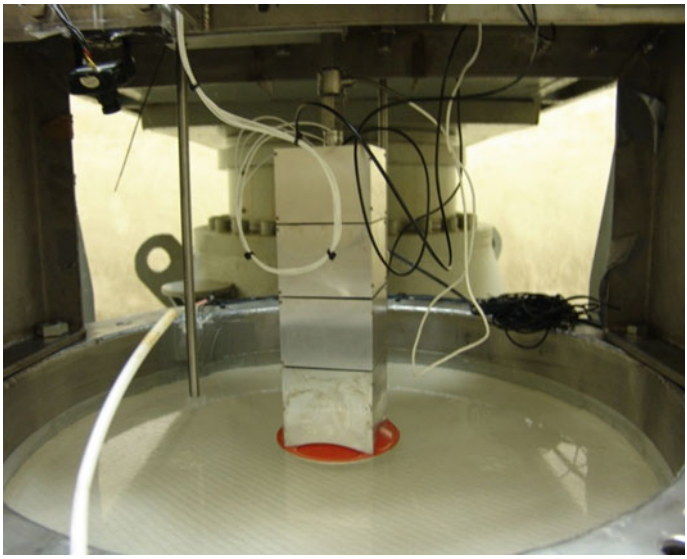

Fig. 5 Centrifuge model of a sleeved spudcan

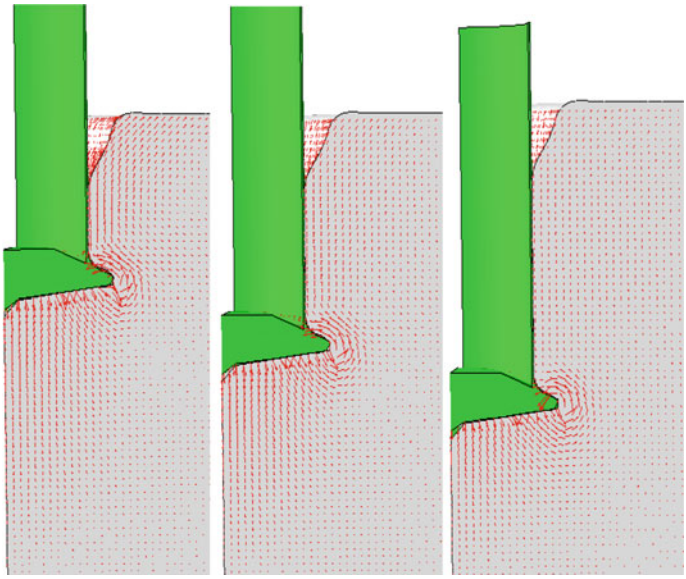

Fig. 6 Soil flow around a sleeved spudcan at different depths of penetration

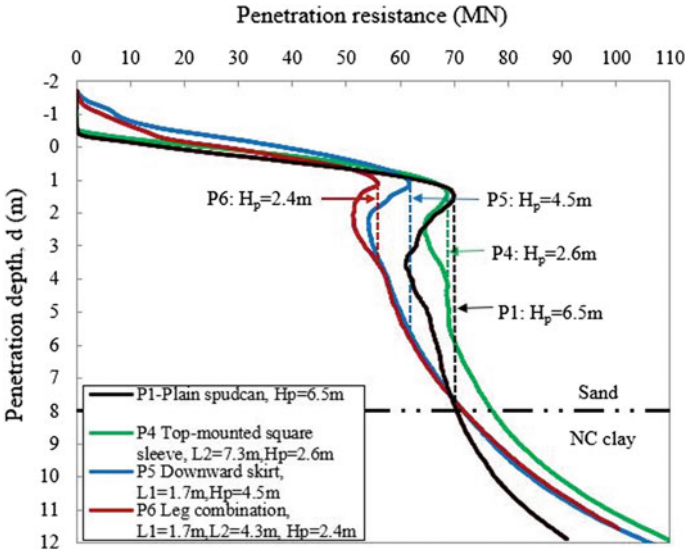

Fig. 7 Penetration resistance curves of plain, skirted and sleeved spudcan

As Fig. 7 shows, the effect of the downward skirt is to reduce the peak penetration resistance, and thereby the magnitude of the punchthrough distance, that is, the distance between the depth at peak resistance and the depth at which the resistance is fully recovered to the peak value. In other words, the presence of the skirt allows the spudcan to detect the soft layer beneath the stiff soil and prepares itself in advance by lowering the peak resistance. In contrast, the sleeve increases the peak penetration resistance and reduces both the loss of penetration resistance during punchthrough as well as punchthrough distance, by obstructing the soil flow behind the spudcan. This brings the spudcan closer in configuration to a large diameter pile foundation and demonstrates the important role that soil flow plays in the penetration behaviour of the spudcan foundation.

4 Bending Moment and Fixity

If the lattice legs can have a significant effect on the penetration and bearing behaviour of the spudcan, one can surmise that, they should also have a significant effect on the fixity of the leg and spudcan. Springman and Schofield (1998) conducted centrifuge model tests on a laterally loaded lattice leg with deeply penetrated spudcan in a soft clay layer. They reported that almost all the lateral load is transferred to the clay via the lattice leg, resulting in minimal moment at the spudcan connection. Temperton et al. (1999) also postulated that lattice legs may have an important effect on spudcan fixity.

Yi et al. (2019) examined the effect of lattice leg on spudcan fixity and settlement under cyclic loading through centrifuge modelling. As Figs. 8 and 9 show the centrifuge model apparatus consists of a vertical actuator system which can operate in both displacement- and load-controlled modes, and a displacement-controlled cyclic lateral actuator system. The vertical closed-loop servo-controlled actuator system was attached to a loading frame which was overslung above the cylindrical model container housing the model clay bed. The vertical load and displacement of the spudcan were measured by a load cell and linear variable differential transformer (LVDT), respectively.

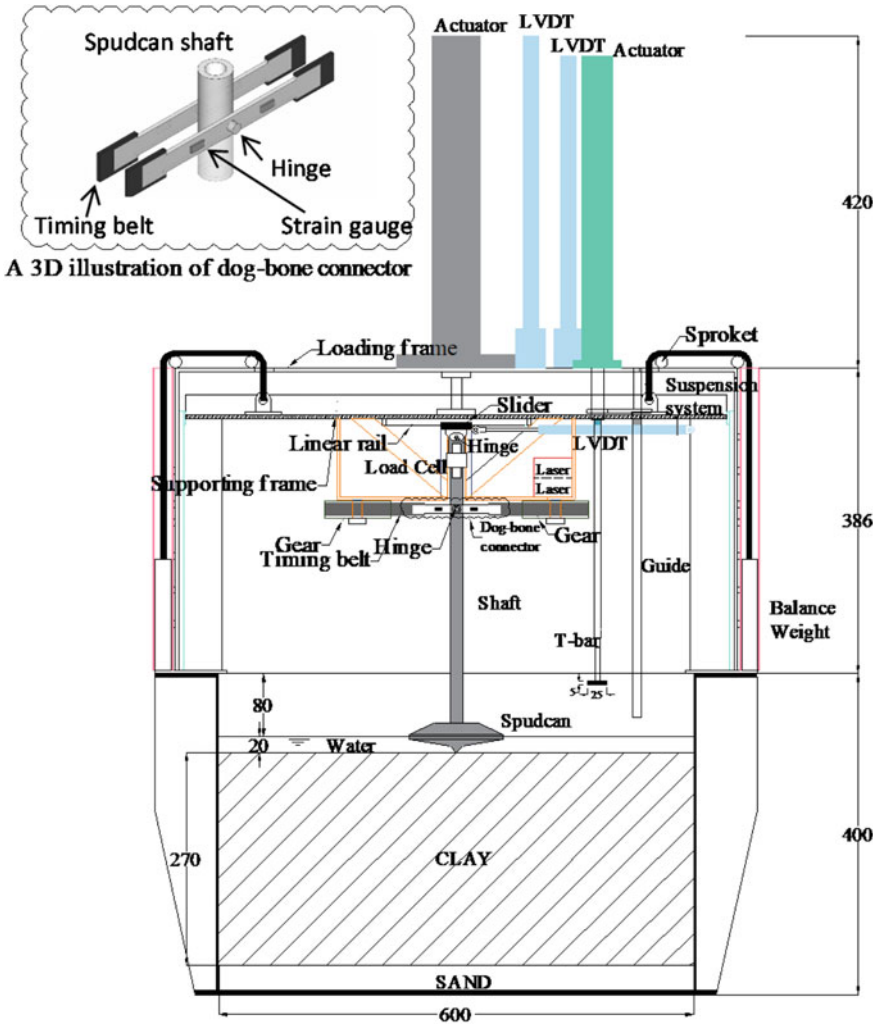

Fig. 8 Front view of vertical and lateral actuator systems

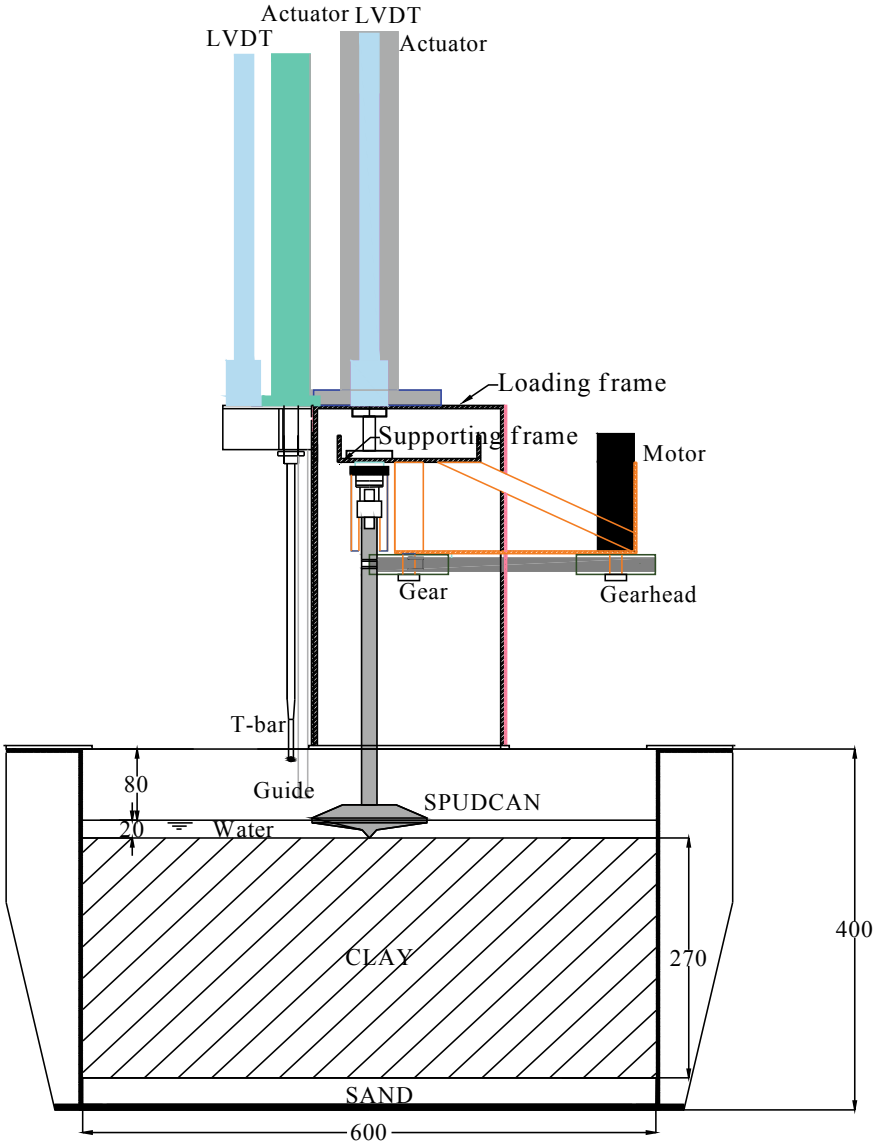

Fig. 9 Front view of vertical and lateral actuator systems

The displacement-controlled cyclic lateral actuator system was mounted onto a supporting frame which was attached to the main shaft of the vertical actuator system and is therefore able to move vertically. This allowed the lateral actuator system to be raised or lowered together with the model spudcan and lattice. Lateral rocking motion was actuated by an electric servo-motor through a timing belt looped over two spur gears. This allowed back-and-forth sliding of the timing belt to take place within the desired plane of rocking of the spudcan shaft. The speed and direction of the electric servo-motor were controlled by a motion controller which received command signals from the computer. The timing belt was connected to a point along the upper segment of the spudcan shaft via a strain-gauged aluminium dog-bone connector, through a central hinge (see the inset in Fig. 8). This transferred and measured the lateral force on the spudcan shaft, without inducing any moment.

The top end of the spudcan shaft was attached to the main supporting frame via a slider block on a linear rail. This allowed the combined weight of the spudcan, shaft and lattice to be supported by the frame. The decrease in the vertical distance between the supporting frame and the soil surface arising from the tilting of the shaft was compensated for by the vertical servo-actuator acting through the slider block, enabling the vertical loading to be kept constant during rocking motion. Relative rotation between the slider block and spudcan shaft was facilitated by a hinge connection. The lateral displacement and rotation of the shaft were measured using two sets of vertically offset laser transducers which were mounted to the supporting frame as well.

Figure 10 shows leg configurations used in centrifuge model tests, with additional information provided in Table 1. The SNN-series of tests are only spudcans with a bare shaft, without any lattice legs, Fig. 10a. The RON series is on spudcans with a rectangular lattice leg, with an opening ratio of 0.75, which is similar to those used in prototype spudcans, Fig. 10b. The RFN-series features fully enclosed rectangular legs, Fig. 10c, which are similar in overall shape to RON series, but without any openings. For each leg configuration, two sets of test were conducted, Table 1. In the "no-dissipation" tests, the legs were subjected to cyclic lateral loading immediately after penetration; this leaves virtually no time for penetration-induced excess pore pressure to dissipate. In contrast, in the "full-dissipation" tests, excess pore pressure due to spudcan penetration was allowed to dissipate prior to cyclic loading.

In this research, the bending moment was determined by two methods. The first method is by measurements from the strain gauges, hereafter termed "measured bending moment". The second method is by inference from the lateral force and the corresponding lever arms to each gauge location, hereafter termed "inferred bending moment". The inferred bending moment is the bending moment, which the shaft would have to sustain if there is no load transfer between lattice leg and soil. The discrepancy between the inferred and measured bending moments is thus an indication of the load transfer between soil and lattice.

Figure 11 shows the normalized measured and inferred bending moment along the spudcan shaft for various configurations. The normalized bending moment is defined, herein as the actual bending moment divided by the largest inferred bending moment. The latter is calculated moment at the lowest strain gauge position (i.e. B1,

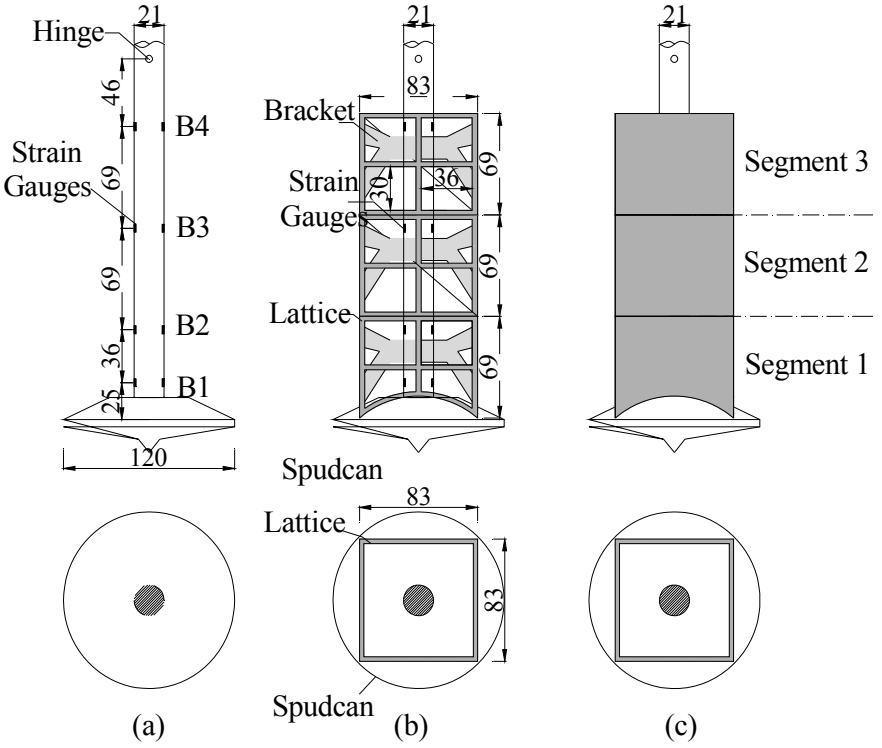

Fig. 10 Spudcan-leg configurations used in centrifuge model tests. **a** No lattice leg, **b** open rectangular lattice with opening ratio $e = 0.75$, **c** fully enclosed rectangular lattice

Table 1 Spudcan-leg configurations

Test ID	Lattice	Test type	Opening ratio e	Area ratio a_s
SNN1	None	No dissipation	1	
SNN2	None	Full dissipation	1	
RON1	Rectangular	No dissipation	0.75	0.61
RON2	Rectangular	Full dissipation	0.75	0.61
RFN1	Rectangular	No dissipation	0	0.61
RFN2	Rectangular	Full dissipation	0	0.61

see Fig. 10a). As Fig. 11 shows, for the spudcans without lattice legs (SNN-series), the difference between the inferred and measured moments is generally small, typically less than 10% of the maximum inferred moment. This indicates that, as expected, much of the bending moment was generated at the spudcan level due to spudcan-soil interaction. The spudcan with open lattice leg shows significantly lower normalized measured bending moment, especially along lattice segment 3 and the lower half of

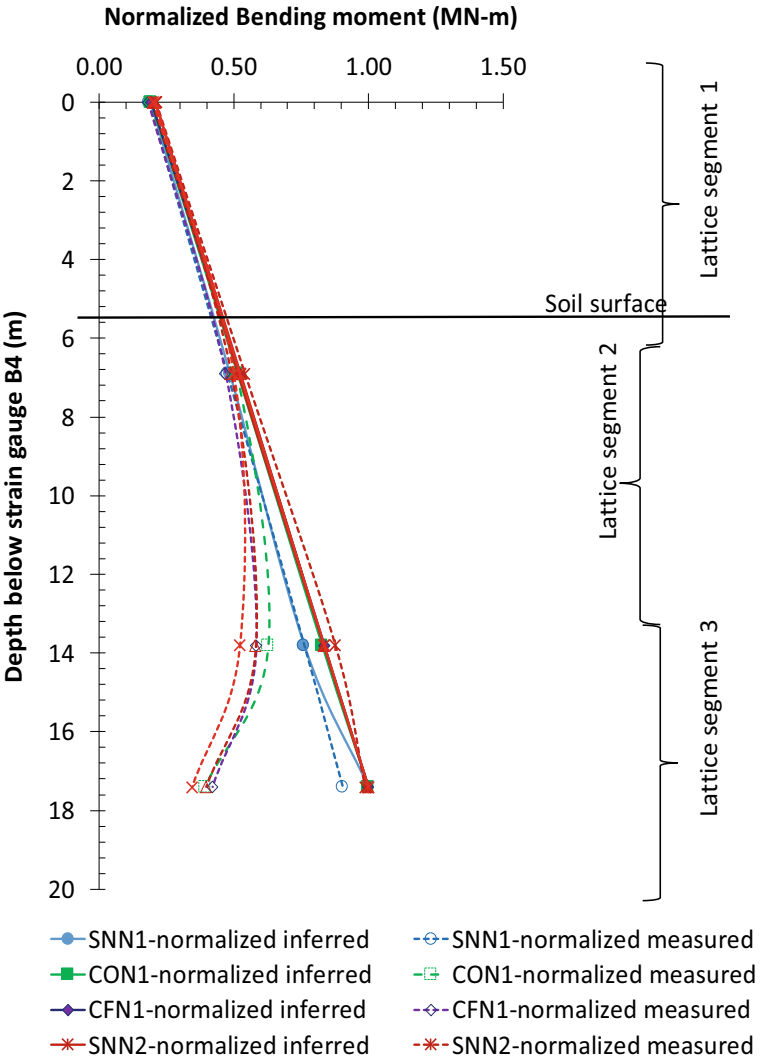

Fig. 11 Normalized measured and inferred bending moment along spudcan shaft for various leg configurations

lattice segment 2. The full-dissipation case RON2 also shows much lower bending moment than the no-dissipation case RON1. This can be readily attributed to the gain in strength of the soil around the spudcan leg as excess pore pressure dissipates and indicates that the effect of the lattice leg on the moment distribution is likely to be most pronounced after excess pore pressure dissipation. Of the three configurations tested, the fully enclosed rectangular leg (RFN-series) gives the lowest normalized bending moment. All these indicate a significant transfer of load between lattice leg and soil, resulting in a decrease in bending moment at the spudcan level. This transfer remains significant even with relatively high opening ratio of 0.75.

The measured bending moment profiles also show that the moment at the spudcan-leg connection is not necessarily the largest. One effect of the lattice leg is thus to shift the point of maximum moment upwards along the lattice leg. This observation is consistent with Temperton et al. (1999)'s postulate that lattice can help to reduce the footing moment at the spudcan-lattice connection. Moreover, bending moment measurements made using spudcan models without lattice legs may not accurately reflect bending moments on real spudcan which has lattice leg installed.

The foundation fixity of the different leg configurations was estimated from the curve of the inferred moment at the spudcan-leg connection against rotation angle curve of the spudcan foundation in the first loading cycle, as illustrated in Fig. 12. The inferred moment is not the real bending moment experienced by the lattice leg or spudcan, but it allows the lateral load experienced by the different leg configurations to be compared on a common basis, since the lever arm, i.e. length of the spudcan leg, is the same for all cases. The foundation fixity was evaluated as the gradient of the diagonal joining the two ends of the load cycle, as illustrated by the dash lines in Fig. 12. This is equivalent to a secant fixity or a rotational secant stiffness

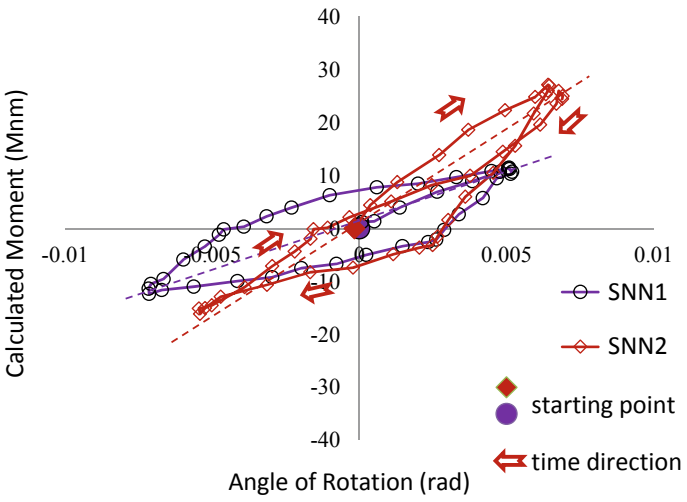

Fig. 12 Moment versus rotation angle for the first loading cycle in tests SNN1 and SNN2 (without lattice legs)

Table 2 Ratio of short-term spudcan-only fixity to total foundation fixity for open and fully enclosed lattice legs

Leg configuration	Ratio of spudcan-only secant fixity to foundation fixity	
	1st loading cycle	1000th loading cycle
RON1 open lattice	0.52	0.48
RFN1 fully enclosed lattice	0.43	0.41

(BSI 2012; SNAME 2008). Table 2 summarizes the ratio of spudcan-only fixity to total foundation fixity for open and fully enclosed lattice legs in the first cycle and after 1000 cycles of loading, in "no-dissipation" tests. This will be designated as short-term fixity ratio. As Table 2 shows the spudcan-only fixity is typically about 40–50% of the total foundation fixity and does not change appreciably over the first 1000 cycles. This indicates that the lattice leg can significantly enhance spudcan foundation fixity.

5 Extraction

Spudcan extraction has been widely studied (e.g. Purwana, et al. 2005; Zhou et al. 2009; Kohan et al. 2014). Purwana et al. (2009) reported that the spudcan breakout force consists of three parts, namely a top resistance, a base resistance and the submerged weight of the spudcan, Fig. 13. The top resistance comprises the weight of soil above the spudcan footing and the shear resistance along a shear plane formed above the spudcan, while the base resistance refers to the suction beneath spudcan footing. Purwana et al.'s (2005) results indicate that base resistance increases from about 40% of its breakout force in the short-term after penetration to about 60% in the long-term.

Water jetting (e.g. Gaudin et al. 2011; InsafeJIP 2011; BSI 2012; Kohan et al. 2014) has been proposed as a method for mitigating extraction difficulties. Other measures include excavation of soil above spudcan footing to reduce the overburden and cyclic loads on the spudcan footing (InsafeJIP 2011) to reduce the soil strength. On the other hand, downward skirts have been known to exacerbate extraction difficulty of deeply embedded spudcans with substantial soil backfill (BSI 2012).

The effect of upward sleeve on spudcan extraction remains largely unknown. However, one can surmise that it should not have any material effect on base suction. Furthermore, by constraining soil backflow and restricting the accumulation of soil on top of the spudcan, weight of overburden can be reduced. The shear plane resistance is more uncertain and much will depend on the sleeve-soil interface sliding resistance vis-à-vis the shearing resistance of the soil itself. However, one may surmise that, in principle, if the sleeve-soil interface sliding resistance exceeds the soil shearing resistance, shearing will take place within the soil. Hence, the soil shearing resistance

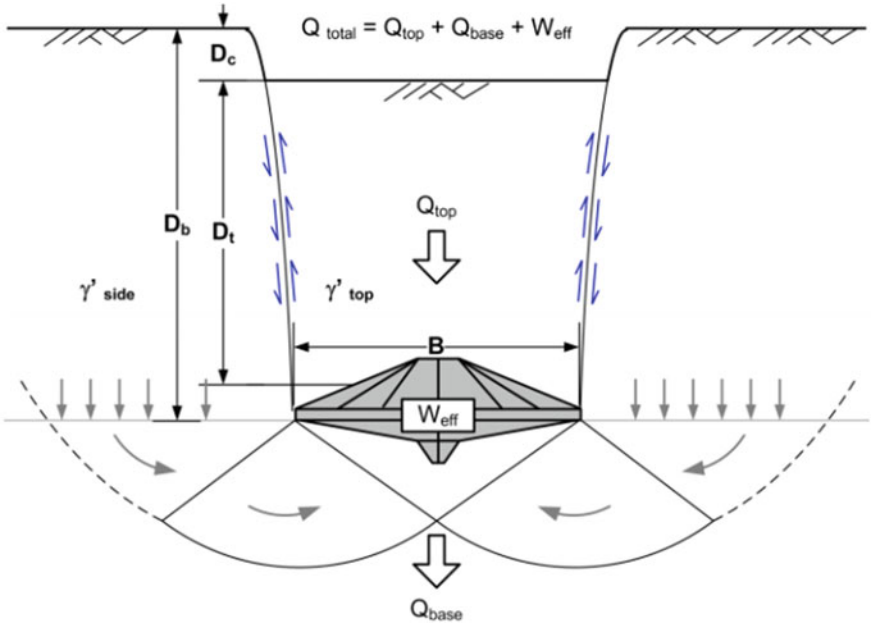

Fig. 13 Breakout force components from observed breakout failure mechanism (after Purwana et al. 2009)

is likely to set an upper bound on the sliding resistance. Figure 14 shows the penetration and extraction resistance profiles for a plain (i.e. without leg) spudcan and a spudcan with the open lattice replaced by a sleeve of same shape and overall size. As can be seen, for the same depth of penetration, both spudcans have similar extraction loads, but the sleeved spudcan has a significantly higher penetration resistance. This implies that, for the same penetration resistance, fully sleeved spudcans will have a smaller depth of penetration and presumably, a smaller extraction breakout force.

6 Conclusion—Re-Thinking the Spudcan Foundation?

The spudcan is conventionally regarded to be the only foundation elements in the jack-up rig for which geotechnical design is required. The lattice leg is often assumed to have no interaction with the soil. This assumption is used even when the spudcan is penetrated deeply into soft seabed deposits. As such, the lattice leg is often regarded as a purely structural element, with no geotechnical implications. Indeed, this may well be one of the reasons why lattice legs are designed as such. Lattice trusses are highly efficient structures for axial load transmission. Spudcan improvements to date consist largely of adding appendages to the spudcan itself rather modifying the leg.

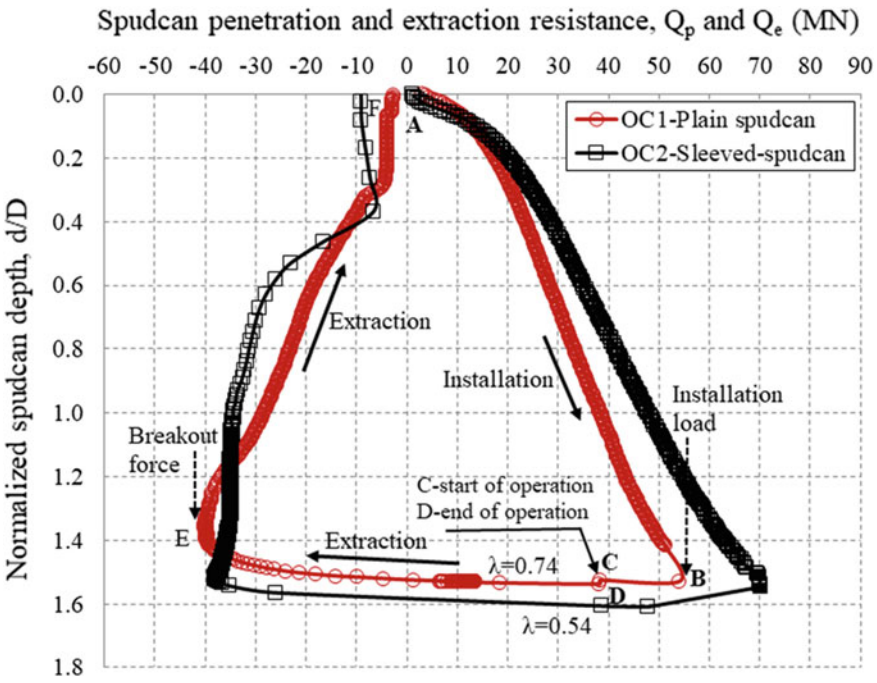

Fig. 14 Penetration and extraction curves for plain and sleeved spudcans

However, the foregoing discussion shows that deeply penetrated lattice leg does interact significantly with the surrounding soft soil, in terms of soil backflow and cavity formation, bearing capacity, lateral load and moment transfer, as well as, possibly, extraction. Furthermore, the degree of interaction is dependent upon the configuration of the lattice; a fully enclosed leg typically interacts much more than open lattice. However, even open lattices similar to those generally used in practice have been demonstrated to interact significantly with the surrounding soft soil.

This opens up the possibility that geotechnical design of spudcan foundations can be further improved by considering lattice–soil interaction. However, one can perhaps go even further by recognizing the fact that the part of the leg that is embedded in the soil will interact with the ground and therefore should be regarded as a foundation element too. By making use of their geotechnical capabilities, it may be possible to bring about substantial improvements to the overall performance of the spudcan foundation.

The fully enclosed upward sleeve is one example. The above discussion shows that penetration resistance (and thus bearing capacity), fixity and punchthrough performance are all improved. Furthermore, there is issue with hydrodynamic stability during towing since the sleeve will be fully retracted together with the leg. As illustrated in Fig. 15, it is unnecessary to sleeve the entire leg; only the region which is expected to be embedded in the ground needs to be sleeved. Furthermore, if a top

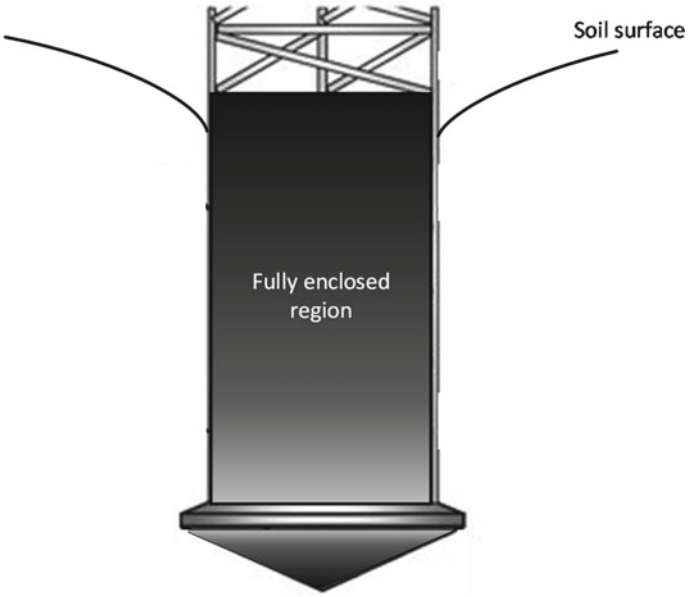

Fig. 15 Possible implementation of an upward sleeve in the form of a fully enclosed ballast tank

cap can be incorporated onto the sleeved region so that the entire enclosed region can be made watertight, then it can be used as a ballast tank. By pumping air into the ballast tank to displace the water within during extraction, addition buoyancy force can be brought into play to assist in the uplift. Some re-engineering of the leg, including the rack-and-pinion system, may be required. However, it should be noted that cylindrical hollow steel tubes have been used on jack-up rigs for water depths less than about 100 m (e.g. Elsayed 2013; Drilling Formulas 2018), as shown in Fig. 16. Drilling Formulas (2018) noted that "…*Cylindrical legs can vary slightly but the basic premise involves hollow steel tubes. However, some units will have internal stiffening and others may have rack teeth or small holes to allow the some units will have internal stiffening and others may have rack teeth or small holes to allow the hull to move up and down the legs. Generally, these cylindrical legs are used on units that stay shallower than 300 feet of water depth. With the newer units that are designed to work in environment deeper than 300 feet, they tend to use trussed legs and this is because trussed legs require less steel for the same resistance and same elevated response*". Hence, the choice of lattice over cylindrical legs is based on the lesser amount of steel required, rather than intractable engineering challenges.

Since the proposal sleeve covers only the lowest part of the legs, then difference in steel requirement between this proposed sleeve and a lattice leg is likely to be smaller that the difference between a full length cylindrical leg and lattice leg. It may be possible to just this increased cost by the advantages to be gain by thinking of the entire spudcan-leg system, rather than just the spudcan itself, as a foundation system.

Fig. 16 Cylindrical leg jack up (after Drilling Formulas 2018)

References

Aagesen R, Dean ETR, Lee FH, Li YP (2018) Simplified analysis of chord and brace effects on jackup leg penetration for preloading in soft clay. Can Geotech J 55(12):1900–1907

Bennett & Associates LLC & Offshore Technology Development Pte Ltd (2005) Jackup units: a technical primer for the offshore industry professional. Keppel FELS, Singapore

BSI (2012) BS EN ISO 19905-1:2012: Petroleum and natural gas industries. In: Site-specific assessment of mobile offshore units—part 1: jack-ups. BSI, London, UK

Drilling Formulas (2018) Basic information about jack up rig legs. http://www.drillingformulas.com/basic-information-about-jack-up-rig-legs/

Elsayed K (2013) The road to Saqqara—Jack-up units and move. https://www.slideshare.net/kemo44/the-road-to-saqqara-jackup-units-and-move

Endley SN, Rapoport V, Thompson PJ, Baglioni VP (1981) Prediction of jack-up rig footing penetration. In: Proceedings of the offshore technology conference, Houston, TX, USA, Paper OTC4144

Gaudin C, Bienen B, Cassidy MJ (2011) Investigation of the potential of bottom water jetting to ease spudcan extraction in soft clay. Geotechnque 61(12):1043–4054

Hossain MS, Hu Y, Keaputra D (2014) Skirted foundation to mitigate spudcan punch-through on sand-over-clay. Geotechnique T.027:1–8

InSafeJIP (2011) Improved guidelines for the prediction of geotechnical performance of spudcan foundations during installation and removal of jack-up units, Joint Industry-Funded Project, RPS Engergy Ltd.

Kohan O, Gaudin C, Cassidy M, Bienen B (2014) Predicting spud can extraction resistance in soft clay. Geotech Eng J SEAGS AGSSEA 45(4):53–62

Li YP, Yi JT, Lee FH, Goh SH, Liu Y, Yang Y, Zhang XY, Wu JF (2017) Effects of the lattice leg on cavities and bearing capacity of deeply embedded spudcans in clay. Géotechnique 67(1):1–17

Li YP, Yang Y, Yi JT, Ho JH, Shi JY, Goh SH, Lee FH (2018) Causes of post-installation penetration of jack-up spudcan foundations in clays. PLoS ONE 13(11):e0206626

Li YP, Liu Y, Lee FH, Goh SH, Zhang XY, Wu J-F (2019) Effect of sleeves and skirts on mitigating spudcan punch-through in sand overlying normally consolidated clay. Géotechnique 69(4):283–296

Menzies D, Roper R (2008) Comparison of jackup rig spudcan penetration methods in clay. In: Proceedings of the offshore technology conference, Houston, TX, USA, Paper OTC19545

Purwana OA, Leung CF, Chow YK, Foo KS (2005) Influence of base suction on extraction of jack-up spudcans. Géotechnique 55(10):741–753

Purwana OA, Quah M, Foo KS, Nowak S, Handidjaja P (2009). Leg extraction/pullout resistance—theoretical and practical perspectives. In: Proceedings of 12th jack up conference, London

SNAME (The Society of Naval Architects and Marine Engineers) (2008) Guidelines for site specific assessment of mobile jack-up units. The Society of Naval Architects and Marine Engineers, Jersey City, NJ, USA

Springman SM, Schofield AN (1998). Monotonic lateral load transfer from a jack-up platform lattice leg on soft clay deposit. In: Kimura T, Kusakabe O, Takemura J (eds) Centrifuge 98: proceedings of the international conference centrifuge 98. Balkema, Rotterdam, the Netherlands, pp 563–568

Temperton I, Stonor RWP, Springett CN (1999) *Measured spudcan fixity: analysis of instrumentation data from three North Sea jack-up units and correlation to site assessment procedures.* Marine Structures 12:277–309

Thomas PA, Cherniguin NT, Maconochie A, Oliphant J, Technip (2007) Retractable pile: a new solution for jack-up platform. In: OTC 18684 offshore technology conference, Houston, TX, USA

Yi JT, Yang Y, Li YP, Zhang XY, Lee FH (2019) Centrifuge study of lattice legs effect on spudcan fixity under cyclic combined loading conditions. Acta Geotechnica (Published online at time of writing)

Yu L, Kumar A, Hossain MS, Hu YX (2010a). Mitigation of punch-through failure of spudcan using skirted footing on sand over clay soils. In: Proceedings of the twentieth international offshore and polar engineering conference (ISOPE), Beijing, China. pp 564–569

Yu L, Ramadan C, Liu J, Hu YX (2010b) Numerical analysis of offshore skirted footings on double layer clays. In: Proceedings of the twentieth international offshore and polar engineering conference, ISOPE-I-10-559, Beijing, China

Zhang YH, Bienen B, Cassidy MJ, Gourvenec S (2011) The undrained bearing capacity of a spudcan foundation under combined loading in soft clay. Marine Struct 24(4):459–477

Zhou XX, Chow YK, Leung CF (2009) Numerical modelling of extraction of spudcans. Geotechnique 59(1):29–39

Developing Screw Piles for Offshore Renewable Energy Application

Michael J. Brown, Craig Davidson, Benjamin Cerfontaine, Matteo Ciantia, Jonathan Knappett, and Andrew Brennan

1 Introduction

Screw piles or screw anchors have been recognized as having the potential to develop from their small current onshore size with low pile central core diameters (D_c) and larger helix diameters (D_h).This development for offshore application will require the upscaling of size and general geometry to carry significantly greater loads than they are currently used for onshore as well as a more complex loading regimes with combinations of tension and compressive loading (Davidson et al. 2018a), lateral loading (Al-Baghdadi et al. 2015, 2017a; Pavan Kumar et al. 2019) and cyclic loading (Newgard et al. 2019; Schiavon et al. 2019). This may be as a result of use as anchors in aquaculture or future floating offshore wind or as alternative foundations to driven piles in jacket structures.

The use of screw piles in jacket structures offshore is being motivated by the strict requirements to mitigate or minimize noise during installation of wind farms in Europe (Koschinski and Lüdemann 2013) with similar restrictions being imposed in emerging wind developments in other areas of the world (Huisman et al. 2020). This could result in costs as high as $1 M US for noise mitigation per wind turbine jacket structure. As well as direct costs the environmental credentials of noise mitigation systems may be called into question with the need for constant DP vessel presence and compressor operation resulting in significant fuel use to create bubble curtains.

This paper outlines some of the work undertaken at the University of Dundee which has been designed to bring the use of large screw piles in an offshore setting closer to a realistic prospect. Investigation to date has focused on sands only.

M. J. Brown (✉) · C. Davidson · B. Cerfontaine · M. Ciantia · J. Knappett · A. Brennan
University of Dundee, Dundee, Scotland, UK
e-mail: m.j.z.brown@dundee.ac.uk

S. Haldar et al. (eds.), *Advances in Offshore Geotechnics*, Lecture Notes in Civil Engineering 92, https://doi.org/10.1007/978-981-15-6832-9_5

1.1 *Historical Research on Screw Based Piling Systems at the University of Dundee*

Research on various forms of screw piles in sand has been ongoing at the University of Dundee since 2007. Initially, this was for a form of cast in situ screw pile referred to as the continuous helical displacement pile or CHD (Knappett and Craig 2019). This investigation focused on the development of compressive capacity calculation techniques (Jeffrey et al 2016) and verification of operational or effective pile diameters through 1g testing (as centrifuge refurbishment for earthquake capabilities were underway, Brennan et al. 2014). Based on these works and field database investigation, a method of simulating CHD installation effects was also developed for Plaxis 2D to allow this process to be simulated numerically by industry (Knappett et al. 2014).

To undertake these works, 1g equipment was developed that allowed pitch matched or perfect installation (Lutenegger 2019) to occur with the ability to inject grout on removal of the CHD bullet. This system also included measurements of axial loads as well using a dedicated torque cell during installation and injection (Jeffrey 2012).

This equipment was then utilized over several years to service undergraduate and MSc projects but in a simpler form to install solid steel screw piles. This was done to service the ever-present need for student projects. Often these screw piles were fabricated in a modular manner to allow various elements of behaviour to be investigated. Projects looked at a range of things including cyclic performance, optimizing helix spacing (*s/D*), (Fig. 1) for compressive and tensile performance (Knappett et al. 2014) and inclined loading Fig. 2 for use as offshore or aquaculture anchoring systems (Caton 2016; Horvath 2018).

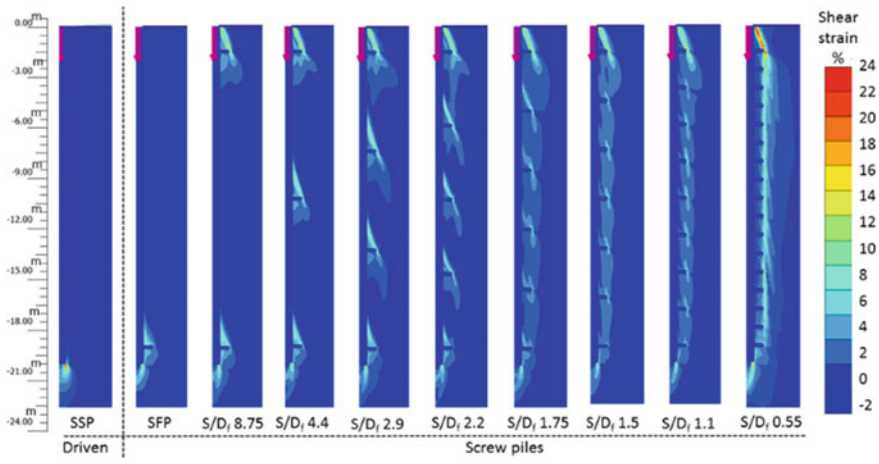

Fig. 1 FEA study of optimization of helix spacing for compressive loading (Al-Baghdadi 2018)

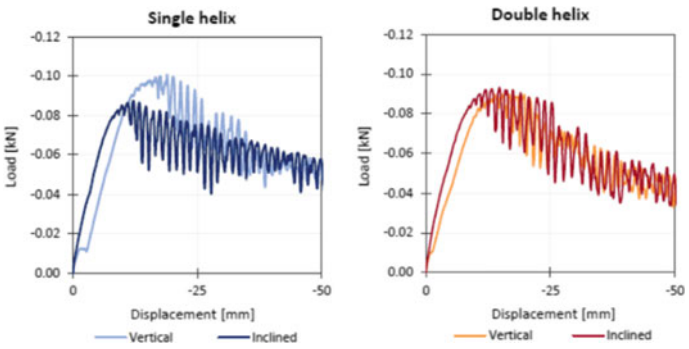

Fig. 2 1g model testing of vertical and inclined screw pile anchors (Horvath 2018)

The first full time study of screw piles as replacement for driven piles for offshore wind jacket structures began in 2013 and was undertaken by Al-Baghdadi. Al-Baghdadi (2018) wanted to undertake numerical modelling of screw piles and had an interest in renewable energy foundations. With a need for validation of the numerical work (as there were little useful detailed field test case studies in existence for installation requirements), it was also decided to undertake scaled physical modelling at appropriate stress levels. This required the development of a bespoke centrifuge rig with the additional requirement that installation and testing could be undertaken all at an appropriate g level as many previous studies installed at 1g and tested at g, or partially installed at 1 g and g (Al-Baghdadi et al. 2016; Davidson et al. 2018a).

2 Areas of Screw Pile Development

2.1 Structural and Load Carrying Capacity

2.1.1 Lateral Loading and Capacity

From an early stage of investigation of screw piles for offshore renewable energy development, it was obvious that considerable upscaling of the currently used onshore piles was required with an increase in helix diameter to allow increased tensile and compressive capacity as well as increased core or steel cross-sectional area to allow the pile the large lateral capacity required in offshore applications. Initially, Al-Baghdadi (2018) focused on axial compressive load performance in sands as this part of screw pile behaviour had seen little attention as they are normally designed to be used in tension. This resulted in a multi-helix pile design similar to that shown in Fig. 1 where the helix plates were spaced between 2 and 3 D_h for optimal capacity whilst inducing soil-soil shear. Al-Baghdadi (2018) also considered the optimum core (D_c) to helix diameter ratio (D_h) so that piles could still perform well (also

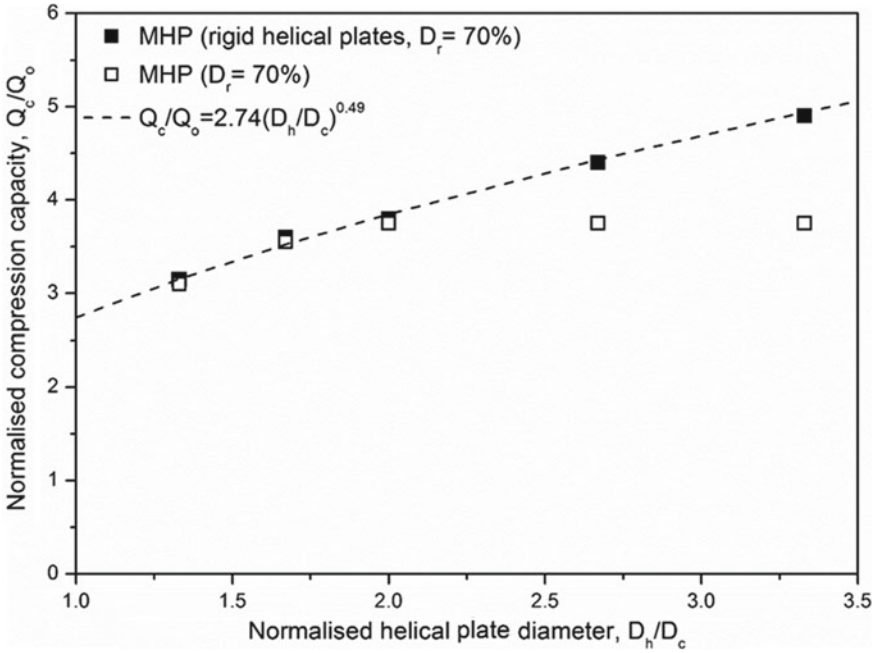

Fig. 3 Effect of varying helix to core diameter ratio (Al-Baghdadi 2018)

approximately 2) with less stick out of the helix plates to improve offshore handling and vessel storage (Fig. 3).

Then, attention turned to attempts to increase lateral performance firstly through the use of near surface helix plates (Al-Baghdadi et al. 2015). This seemed a viable option initially based on FEA modelling but it was found that although the lateral resistance with large near surface plates could be increased by up to 22% when compared to a straight shafted pile the helix plate had to be placed very close to the seabed surface for greatest efficiency (Fig. 4). On the grounds that this near seabed zone would be subjected to scour this proposed method of increasing lateral capacity seems unlikely to be adopted without appropriate scour protection (Fig. 4).

Further investigation of combined lateral and vertical loading (both compression and tension) affects were modelled using Plaxis 3D validated against a number of field studies (although field study case histories for lateral loading are limited in the literature, Sakr 2010; Zhang, 1999). Similar combined loading was investigated by Karthigeyan (2008). The study by Al-Baghdadi et al. (2017a) showed that the lateral performance of both straight shafted and screw piles is enhanced under compressive vertical loading, with greater enhancement for screw piles. For both pile types the lateral performance degraded under vertical tension loading (below a zero vertical load situation). Interrogation of the radial stresses and earth pressures mobilized during modelling suggested that the presence of screw pile helical plates has the potential to increase the vertical compressive stresses below the helical plates

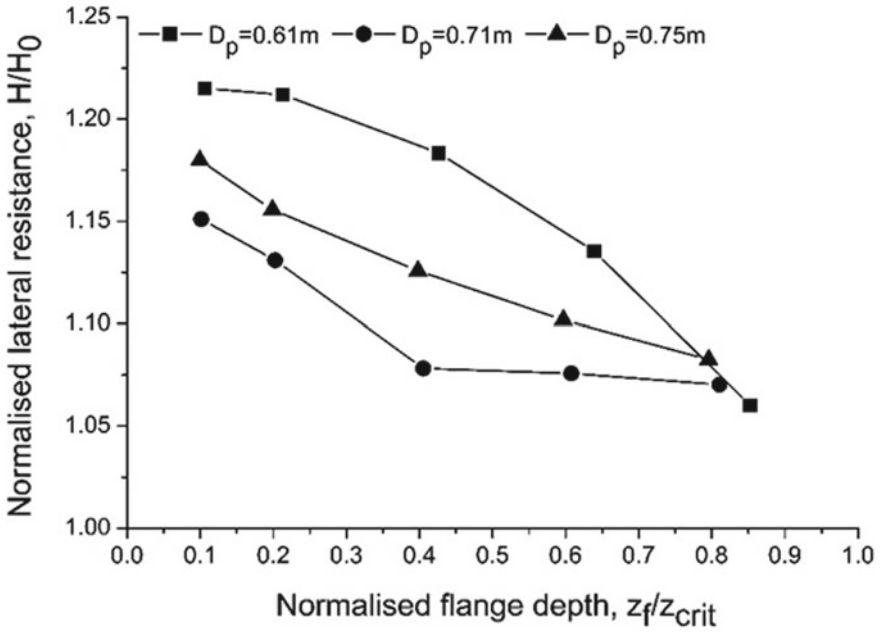

Fig. 4 Results of 3D Plaxis simulation to identify the potential of near surface helix plates ability to deal with lateral loading demands (Al-Baghdadi 2018)

and the resulting radial stresses, which in turn increases lateral pile resistance and vertical capacity of the pile core. Screw piles potentially offer good performance when used in jacket or tripod arrangements where the horizontal loading can be shared and where moments acting on the jacket can be carried principally in axial tension/compression, superimposed on the static self-weight. These will be particularly effective if the screw piles can remain (just) in compression under maximum environmental horizontal loads. The main drawback of the enhanced lateral capacity of screw piles with increasing vertical compressive loads is that greater bending moment is induced in the core of the pile. This implies a need to carefully consider the central core to ensure it has sufficient moment capacity so as not to yield under the combined effects of vertical and lateral loading.

2.1.2 Axial Capacity

Although a multiple helix pile configuration may be logical, where axial compressive capacity is required and helix spacing can be optimized to induce soil-soil shearing between the helix plates the same cannot be said for axial tension. As has been shown by many previous authors the axial tensile capacity is dominated by the either a shallow (uplifting wedge from top surface of the plate to the seabed) or a deep mechanism (flow around the helix plate or a local bearing capacity mechanism).

This behaviour is dependent on the soils density and the ratio of the depth of the upper plate (*H)* to the diameter of the helix (Fig. 5).

Figure 5 only considers the shallow mechanism behaviour where transition may occur at $H/D = 7–9$. Whilst undertaking numerical modelling (Cerfontaine et al. 2019a) of this uplift process to understand shallow mechanism controls it was found that the position of the upper helix (where multiple helices were installed) tended to determine the initiation point for any uplifting wedge (Cerfontaine et al. 2019a). Based on this finding it would suggest that for a pile installed to a "shallow" level (which may be relatively deep for a pile with a large diameter helix plate and *H*/*D*) a single helix plate may be superior in tension to a multi-helix design which was contrary to the findings or direction of investigation for early compressive performance studies by Al-Baghdadi (2018).

This work also showed that the failure plane that the shallow mechanism followed was defined by the dilation angle of the sand as found in other applications such as the uplifting of pipelines. It also suggested how existing analytical techniques could be improved to include the findings from FE analysis to give better predictions of screw pile uplift capacity (Cerfontaine et al. 2020).

At the same time, as undertaking these numerical studies Davidson et al (2018a) began centrifuge testing on a series of piles designed to have the structural and load

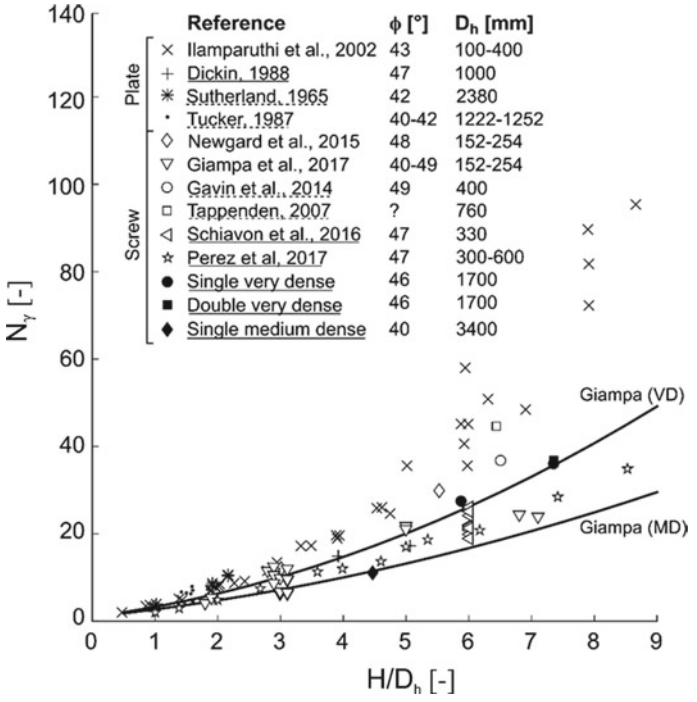

Fig. 5 Variation of uplift resistance with increasing depth for shallow mechanisms

carrying capabilities to support a large jacket and wind turbine system designed to be installed in 80 m of water depth. This resulted in a pile that would be required to carry 6.28MN in lateral loading, 26.14MN tensile loading and 34.85MN compressive loading. The resulting piles were designed based on classic onshore screw pile methodologies: tensile resistance from the multi-helix method in Das and Shukla (2013); cylindrical shear method in Perko (2009) for compressive capacity; and analytical methods in Fleming et al. (2008) for the lateral capacity.

The first design had uniform core and helix dimensions, while the second (upper), optimized design, and had reduced core and bottom helix diameters (Fig. 6 and Table 1) which were designed to give reduced installation requirements whilst maintaining axial and lateral capacity requirements. Santos Filho et al. (2014) demonstrated a substantial reduction in installation torque of small diameter onshore screw piles with a reduced core diameter over designs with a uniform core diameter.

It is clear in considering the piles in Fig. 6 that at this stage the findings on limiting uplift performance by the upper helix were unknown as the pile had two helices although a single helix pile was also tested at the same time of similar length.

Results from compressive and tension capacity testing showed that the existing design techniques for tension and compressive capacity were not able to capture the

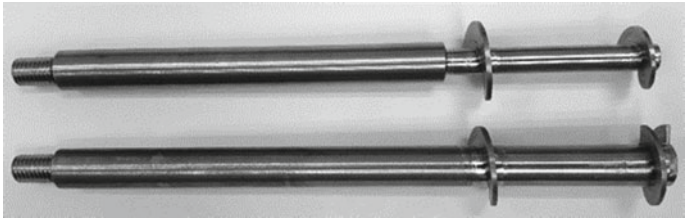

Fig. 6 Examples of the 80th scale model piles designed to operate in very dense soil. The upper pile is the optimized pile

Table 1 Screw pile dimensions in metres at prototype scale (mm at model scale), see Fig. 6

Parameter		Uniform screw pile	Optimized screw pile
Length, L		13 (162.5)	
Core diameter	Upper	0.88 (11)	
	Lower	0.88 (11)	0.60 (8)
Helix diameter,	Upper	1.70 (21.25)	
	Lower	1.70 (21.25)	1.34 (16.75)
Pitch, p	Upper	0.56 (7)	0.56 (7.5)
	Lower		
Thickness, t	Upper	0.11 (1.4)	0.11 (1.4)
	Lower		
S/D_h		2	2

behaviour of the piles sized for offshore deployment and performed particularly badly (overprediction of true capacity 34–77%) in the case of tensile capacity predictions (Davidson et al. 2020). Much better prediction of compressive capacity was achieved using the approaches developed by Jeffrey et al. (2016) and in tension lower uplift factors as per Fig. 5 coupled with the use of the uplifting failure wedge defined by the dilation angle of the sand.

Historically screw pile capacity (Q) (in tension or compression) has been linked to the torque (T) required to install the piles via a torque factor (K):

$$Q = KT \tag{1}$$

$$K_t = 1433/D_c^{0.92} \tag{2}$$

where K is a torque correlation factor which may be selected based on the core diameter of the screw pile (Eq. 2) (D_c) by Perko (2009). This approach though shows significant scatter in the selection of the K value even over the limited core diameters used onshore. Perko (2009) recommended that similar K values could be used in both tension and compression but this advice would seem problematic as it does not recognize in tension, for instance, that the uplift mechanism may vary between a deep and shallow mechanism and torque measurements would not be influenced by this in-service behaviour. For instance, an offshore pile geometry is more likely to be operating in a shallow mechanism due to its large helix diameter (i.e. H/D), whereas a small diameter onshore pile may be more likely to operate in a deep mechanism mode.

Davidson et al. (2020) showed that adopting the approach for tensile capacity prediction resulted in over prediction of 283%. Lutenegger (2019) highlights that correlations of torque to capacity are often assumed to be the same whether one or two helices are included (i.e. the inclusion of additional helix plates is ignored) and goes onto show that the torque encountered during installation is also affected by the pitch of a helix plate, while the capacity is unaffected. Thus, non-unique values of K_t can be observed for screw piles with the same shaft diameter. It is also assumed that K is unaffected by relative density and that piles are always installed in the same manner (pitch matched) which seems unlikely based on the apparent vertical force requirements which may not be encountered in the field (based on existing rig reaction mass) and that in-service performance is unaffected by installation approaches.

2.2 Installation Requirements

The initial centrifuge testing by Al-Baghdadi (2018) and Davidson et al. (2018a) highlighted at an early stage that significant torques were required for installation (Fig. 7) and thus the need to experiment with reduced cross-sectional area piles (Fig. 6) as the torque required is a function of the piles surface area.

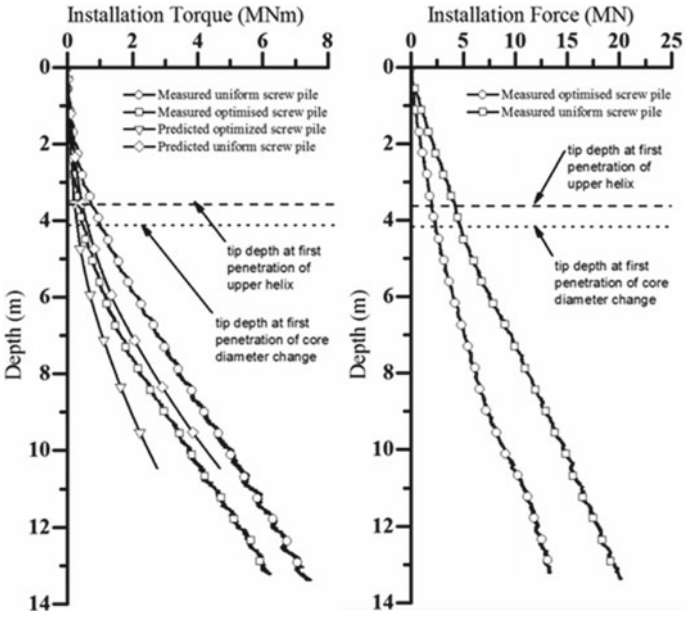

Fig. 7 (L) vertical installation force and (R) installation torque required for uniform and optimized screw pile designs

Figure 7 highlights that there is the potential to reduce torque in a limited fashion but Davidson et al. (2020) found that the optimized pile design did not perform in tension or compression as expected and gave lower capacities than the non-optimized form.

What was possibly more concerning was that for the pitch matched (or perfect) installation adopted here, and as per common guidance on installing screw piles to minimize disturbance and ensure in-service capacity, the vertical forces (or crowd force) measured during installation were also very high. Possibly to the level where they could not be installed, or very significant reaction force would be needed which would be difficult to create in an offshore setting. This vertical force requirement also came as somewhat of a surprise as crowd force is not normally measured during onshore screw pile operations and onshore rigs may have high torque capacity but relatively low self-weight making it appear impossible to supply the apparent vertical forces required for installation. This suggests that screw piles may not be installed in the pitch matched or perfect installation procedure recommended. Again, this is difficult to verify for onshore installation as only installation torque is normally measured directly (or indirectly). Records of advance rates and rotation rates are not normally made and rigs do not capture this information automatically.

2.2.1 Predicting Installation Requirements

Due to the significant size and surface area of the screw piles required for offshore deployment it is likely that significant torque (and possibly vertical force) installation will be required (Fig. 7). In order to install these piles, specialist plant will have to be developed with appropriate capabilities and at significant cost. Therefore, certainty over predicting installation requirements is necessary for offshore development.

Throughout the centrifuge works of Al-Baghdadi (2018) and Davidson et al. (2018a) cone penetration testing (CPT) have been undertaken in parallel with screw pile installation and load testing. CPT was adopted as this is the preferred offshore site investigation tool in sand and there are correlations with other common design parameters as well as direct methods of using CPT to determine in-service pile capacity. There are also examples of both analytical and CPT-based predictions of screw pile torque requirements in the literature (Ghaly and Hanna 1991; Sakr 2015; Gavin et al. 2013; Spagnoli 2016). For example, Eq. 1 could be used for this but it would require an accurate prediction of in-service capacity and would be subject to the uncertainties in this approach as already discussed above.

Al-Baghdadi (2018) initially proposed an improved CPT-based torque and vertical installation method that allowed for different geometry piles and multiple helices (previous methods had only incorporated a single helix). This was further corrected and improved by Davidson et al. (2018b, 2020). The torque which develops from the installation of a screw pile into sand is assumed to be created by the frictional resistance between the soil and the entire surface area of the pile. In terms of the proposed CPT-torque correlation method, the torque contribution from the upper surface of the helical plates(s) to the total torque is negligible and can be ignored. The torque from the shaft area of the core is calculated based on the UWA 05 method (Lehane et al. 2005) where a stress drop index equal to the CPT friction ratio divided by the interface friction was used to compute the radial stress acting on the screw pile. This CPT prediction method as mentioned can deal with complicated pile geometry and the inclination of the screw pile helix, the pitch angle and the interface frictional properties. In a similar fashion based on the UWA 05 method (Lehane et al. 2005), a CPT screw pile prediction method was defined to predict vertical installation force requirements for pitch matched installation. These methodologies are not given here due to space limitations and more detail can be found in Al-Baghdadi et al. (2017b), Al-Baghdadi (2018), Davidson et al. (2018b, 2020).

The results as shown in Fig. 8 highlight the ability of the proposed CPT methods to predict the installation torque for offshore geometry piles and that they offer better predictions than exiting in situ-based techniques. Similar good performance of the prediction techniques was obtained when used for real case study sites. Comparison is only shown for single helix piles as although the method developed here can handle complex pile geometries existing techniques by others only work for single helix piles.

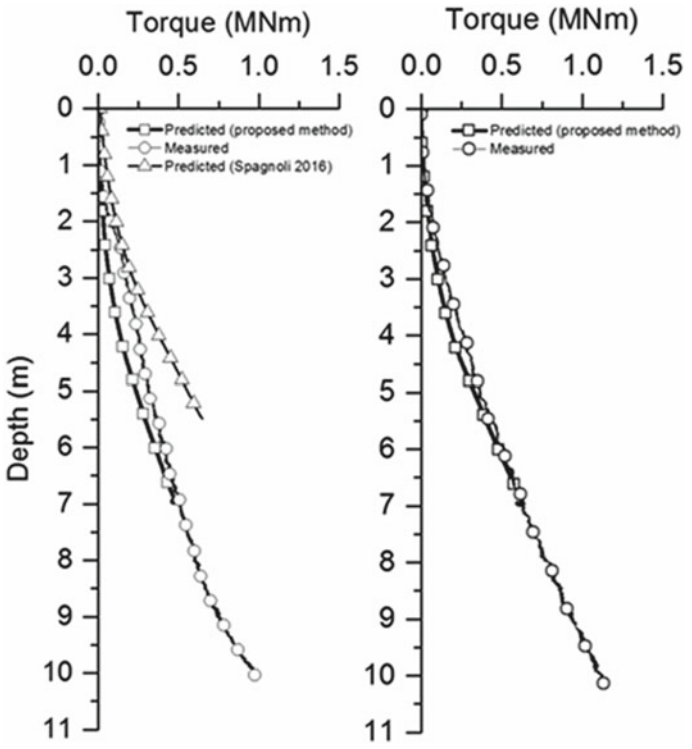

Fig. 8 Predicted and measured prototype installation torque from centrifuge tests of: (L) single helix screw pile; (R) multi-helix (2 No.) screw pile. Symbol notation: square—predicted torque from the proposed method; triangle—predicted torque from (Spagnoli 2016); circle—measured torque

2.3 Other Areas of Development

2.3.1 Numerical Techniques

Development in numerical techniques has focused on the use of Plaxis FEA and discrete element modelling. FE studies have been used to investigate the uplift failure mechanism and the effect of soil density and multiple or single helices as already mentioned and has been used to inform improved tensile capacity models as already discussed (Cerfontaine et al. 2019a). The other aim was to develop the use of FE such that as an industrially available and regular used approach it could be used in a non-specialized manner to simulate large deformation problems (without the need for less user-friendly LDFE, MPM or DEM). A similar ethos was employed by Knappett et al. (2016) to allow FE to simulate CHD pile performance based on the effect of installation seen in model tests with comparison to field study data.

The approach adopted for screw piles is outlined in Cerfontaine et al. (2019b) and is a push and replace or push and retain type methodology. In this approach, a screw pile geometry is wished in place at some depth above the final installation position. It is then subjected to the vertical load measured in a parallel centrifuge test at the corresponding depth (or as could be predicted from the CPT-based vertical load prediction method). The stress and strains associated with this loading are captured and retained for the next step of analysis which is repeated until the pile reaches the final penetration depth. The pile can then be loaded as it would be in-service under displacement control. The method also includes observed strain softening along the failure plane of the uplifting wedge.

Figures 9 and 10 show the potential for improvements in simulation-based prediction of screw pile uplift capacity where informed attempts are made to incorporate installation effects. The results show a much better prediction of low displacement stiffness and general form of pile behaviour. The figures also show investigation of whether or not uplift failure occurs as a straight cylinder or an uplifting wedge defined by the dilation angle. The results would suggest that the latter is more appropriate as previously found in FE simulations and by others undertaking work on uplift behaviour of buried pipelines.

As well as utilizing FE with simulation of installation effects for screw pile modelling much work has been undertaken using discrete element modelling DEM (PFC 3D). Historically, this approach may not have been seen as practical based on the times required to create large enough soil beds or chambers for simulation

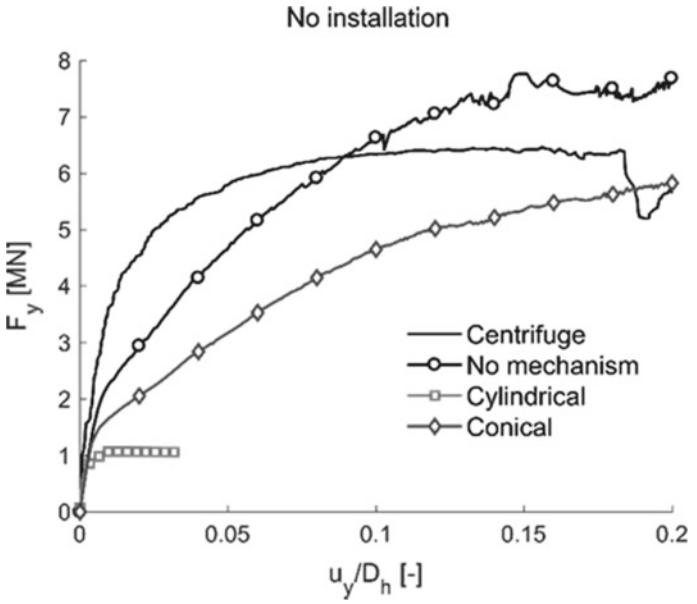

Fig. 9 FE prediction of measured centrifuge screw pile test for a simple wished in place model

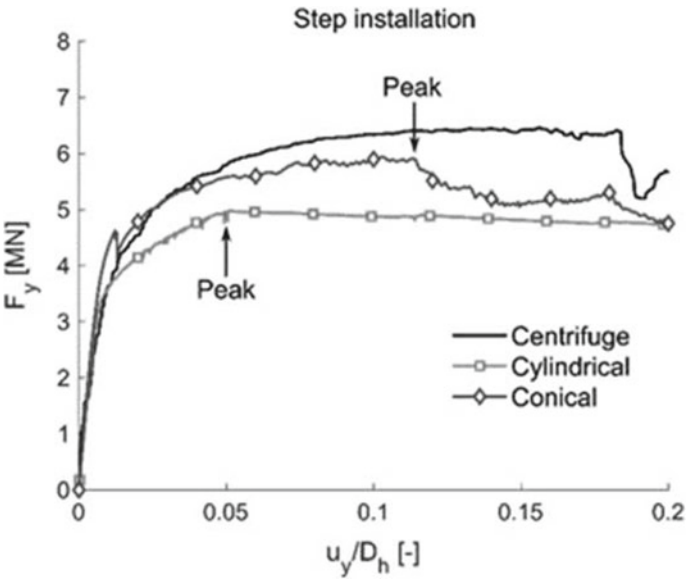

Fig. 10 FE prediction of measured centrifuge screw pile test based on simulations containing strategies to incorporate installation effects

and the general run time of events. This has been overcome with advances in soil bed preparation (Ciantia et al. 2018; Sharif et al. 2019) using the particle refinement method (PRM) and periodic boundary replication method (PBRM) and the reducing computational costs where a £2500–5000 GBP desktop work station can be adequate and allow simulations at speeds comparable to 3D FE (Fig. 11).

The results of DEM simulation of screw pile loading and installation can be calibrated against similar centrifuge tests or in a commercial environment against actual triaxial tests or CPT tests where the same triaxial or CPT test can also be simulated in DEM and the parameters controlling the DEM simulation adjust to suit the laboratory or field measurements.

The results in Fig. 12 show the DEM simulation of installation of the optimized pile (Fig. 6) compared to that measure in centrifuge testing. The consistency of the DEM simulation with the measured results is very good if not a little noisy. The noise itself in the main is due to the size of the balls used to optimize runtimes and could be reduced with smaller balls close to the pile at the expense of computational time.

The use of DEM in screw pile or displacement pile simulation shows great promise as results are fully repeatable (same soil chamber repeatedly used) and the geometry or the installation approach for the pile can easily be modified making it quicker than fabricating new piles for centrifuge testing.

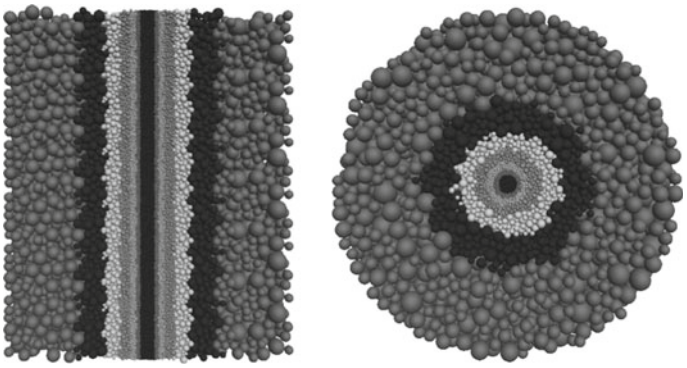

Fig. 11 Example sample made using PRM and PBRM methods, shading indicates different particle scaling applied to the PSD. (L) cross-sectional view of sample, (R) top view of sample

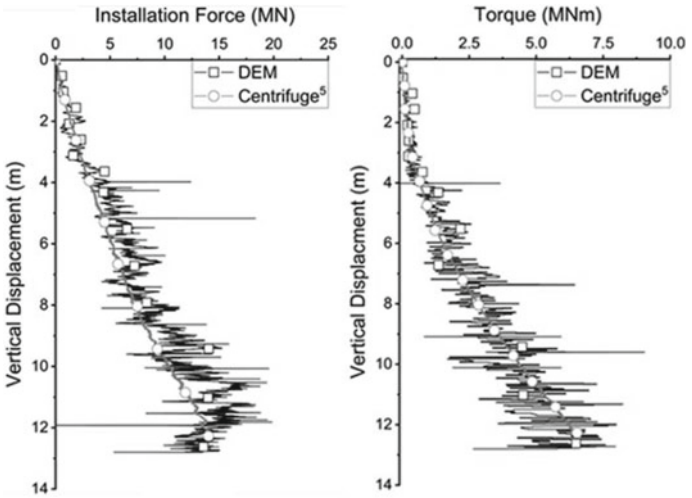

Fig. 12 Comparison of DEM screw pile installation with measured centrifuge results

3 Future Research Direction

Research with a view to bringing the industrial deployment of screw piles for offshore renewable energy deployment will continue at the University of Dundee (UoD). This will occur through ongoing projects looking at the performance of screw piles in clays and recent industrial funding to accelerate the technology readiness level (TRL) with a view to full scale or reduced scale demonstrator deployment in the near future. This forms part of a wider project using both centrifuge scaled model testing and DEM simulation to develop a variety of "silent" piling techniques for offshore

use (Huisman et al. 2020). Further information on these techniques can be seen by watching the videos via the following links:

Push-in piles:

https://go.hmc-heerema.com/visuals/1501810.80844-HE-136-333-20/.

Helical piles:

https://go.hmc-heerema.com/visuals/1501810.80844-HE-136-333-03/.

To date, the work has focused on installation and requirements and monotonic in-service performance. The large torque and vertical compressive force required to install the piles needs to be reduced where possible through either geometry modification, for example, different tip geometries or open and closed piles. The work outlined in Huisman et al. (2020), Garcia Galindo et al. (2018) and Bradshaw et al. (2019) suggests that installation requirements can be reduced through over rotation or overflighting (i.e. ignoring the advice to install pitch matched or perfect installation). For example, Huisman et al. (2020) showed from centrifuge testing that vertical installation forces can be reduced to zero by overflighting (or over rotating), although the effects on in-service compressive performance require further investigation.

The work at UOD to date has focused on in-service monotonic performance but it is acknowledged that further work is required with respect to cyclic performance, although work has been done in this area as previously mentioned (Newgard et al. 2019; Schiavon et al. 2019). This previous work must be repeated for the pile geometries being developed for offshore use and with further focus on the potential for cyclic ratcheting through for instance DEM with varying particle sizes. The existing UoD centrifuge actuation rig will be upgraded to allow both displacement and stress-controlled loading to allow validation of DEM studies.

Further ongoing apparatus developments include the fabrication of a fully instrumented pile that measures both axial loads and bending moments at various points along its length (again for DEM validation). This has resulted in the need for classic slip rings to be used again local to the pile to get the many channels of data past the rotating connections. The other design change is that this pile and the connections to the loading rig are designed to be rotated in both directions such that decommissioning, or removal of screw piles can also be investigated.

Much of our recent work has been undertaken in partnership with the Durham University (DU) and the University of Southampton. DU have focused on developing new or refined computational techniques (material point method, MPM) and applying them to the challenges of screw pile installation (Wang et al. 2019). The University of Southampton have been undertaking a series of field investigations in sand to

validate the work at UoD and DU whilst creating an important case study data set on screw pile installation and in-service performance (Richards et al. 2019). Their work is also ongoing.

4 Summary and Conclusions

The University of Dundee have been undertaking research since 2007 on a variety of screw piles. Initially, these were cast in situ continuous helical displacement piles (CHD). This allowed equipment to be created that was later used to undertake undergraduate and MSc projects on steel screw piles normally used onshore for underpinning and guyed supports. Due to their silent installation properties and the need for deeper water alternatives to monopiles, it was decided to investigate upscaling of these pile types to allow deployment offshore.

This has been done through a variety of research studies using both physical modelling techniques and numerical approaches (FEA, DEM, MPM). The results to date have resulted in:

- CPT-based methods for predicting installation requirements for complex geometry screw piles.
- Improved methods of predicting and designing both in-service tensile and compressive capacity for large screw pile geometries.
- Insights on how to optimized offshore screw piles and what optimized pile designs might look like.
- Development of the use of DEM for screw pile simulation.
- Identification of how screw pile installation requirements may be significantly reduced through different approaches to installation.

Although much has been achieved, further work is required to bring this foundation system to a higher technology readiness level for offshore deployment in the applications identified.

Acknowledgements We would like to thank Roger Bullivant Limited (RBL) and particularly Jon Ball for their support, help and guidance throughout our many years of looking at piles. RBL continue support our work through sponsorship of current PhD student Yaseen Sharif. We would like to acknowledge the support of EPSRC for funding over many years that has contributed to our current level of understanding: EPSRC CASE for New Academics, EPSRC Supergen Windhub Call 2015: Grand Challenge project EP/N006054/1., EPSRC NPIF funded studentship with industry contribution—Screw piles in clay soils. More recently, facilities and staff have been supported by the EU through LUPS/ERDF/2013/10/1/0075 to create the Scottish Marine Renewables Test Centre for Materials & Foundations (SMART), 2017, EU H2020 Marie SkŁodowska-Curie Actions Individual Fellowships SAFS – Development of Screw Anchors for Floating marine renewable energy System arrays incorporating anchor sharing. H2020-MSCA-IF-2016, Grant no. 753156 (08/17-07/19). We would also like to thank many colleagues, students, technicians and research partnerships (Durham University and the University of Southampton, Industry: Cathie Associates, SMD, RBL, In Situ SI, Lloyd's Register, Hereema Marine Contractors) that have contributed to the success of our ongoing work.

References

Al-Baghdadi T, Brown MJ, Knappett JA, Ishikura R (2015) Modelling of laterally loaded screw piles with large helical plates in sand. In: Meyer V (ed) 3rd International symposium on frontiers in offshore geotechnics, Oslo, Norway, 10–12 June 2015. Taylor & Francis Group, London, pp 503–508

Al-Baghdadi T, Brown MJ, Knappett JA (2016) Development of an inflight centrifuge screw pile installation and loading system. In: Thorel L, Bretschneider A, Blanc M, Escofier S (eds) In: 3rd European conference on physical modelling in geotechnics (Eurofuge 2016), Nantes, France, 1–3 June, pp 239–244

Al-Baghdadi T, Brown MJ, Knappett JA, Humaish A (2017a) Effects of vertical loading on lateral screw pile performance. Proc Inst Civil Eng Geotechn Eng J 170(GE3):259–272

Al-Baghdadi T, Brown, MJ, Davidson C, Knappett J, Brennan A, Wang L, Coombs WM, Augarde CE, Richards D, Blake A (2017b) CPT based design procedure for installation torque prediction for screw piles installed in sand. In: 8th International conference on offshore site investigation & geotechnics (SUT OSIG), vol 1, 12–14th Sept, London, UK, pp 346–353

Al-Baghdadi T (2018) Screw piles as offshore foundations: numerical and physical modelling. Ph.D. thesis, University of Dundee, Dundee, UK

Bradshaw AS, Zuelke R, Hildebrandt L, Robertson T, Mandujano R (2019) Physical modelling of a helical pile installed in sand under constant crowd. In: Proceedings of the 1st international symposium on screw piles for energy applications (ISSPEA), 27–28th May. University of Dundee, Dundee, UK, pp 109–115

Brennan AJ, Knappett JA, Brown MJ, Bertalot D, Loli M, Anastasopoulos I (2014) Dynamic centrifuge modelling facilities at the University of Dundee and their application to studying seismic case histories. In: 8th International conference on physical modelling in geotechnics ICPMG'14, Perth, Western Australia, 14–17th Jan, pp 227–233

Caton A (2016) Examining the behaviour of screw anchors under varying load inclinations. M.Sc. thesis. University of Dundee. Dundee, UK

Cerfontaine B, Knappett JA, Brown MJ, Bradshaw AS (2019a) Effect of soil deformability on the failure mechanism of shallow plate or screw anchors in sand. Comput Geotech 109:34–45

Cerfontaine B, Brown MJ., Knappett JA, Davidson C (2019b) Finite element modelling of the uplift behaviour of screw piles in sand. In: Proceedings of the 1st international symposium on screw piles for energy applications (ISSPEA), 27–28th May. University of Dundee, Dundee, UK, pp 69–75. https://doi.org/10.20933/100001123

Cerfontaine B, Knappett JA, Brown MJ, Davidson C, Al-Baghdadi T, Sharif Y, Brennan AJ, Augarde C, Coombs W, Wang L, Blake A, Richards DJ, Ball JD (2020) A finite element approach for determining the full load-displacement relationship of axially-loaded screw anchors, incorporating installation effects. Can Geotech J. In Press

Ciantia MO, Boschi K, Shire T, Emam S (2018) Numerical techniques for fast generation of large discrete-element models. Proc Inst Civ Eng Eng Comput Mech 171(4):147–161

Das BM, Shukla SK (2013) Earth anchors. J. Ross Publishing

Davidson C, Al-Baghdadi T, Brown MJ, Knappett J, Brennan A, Augarde CE, Wang L, Coombs WM, Richards D, Blake A (2018a) Centrifuge modelling of optimised screw piles for offshore wind energy foundations. In: Proceedings of 9th international conference on physical modelling in geotechnics (ICPMG 2018), 17–20th July, London, UK. Taylor & Francis Group, London, UK, pp 695–700

Davidson C, Al-Baghdadi T, Brown MJ, Knappett J, Brennan A, Augarde CE, Coombs WM, Wang L, Richards D, Blake A, Ball J (2018b) A modified CPT based installation torque prediction for large screw piles in sand. In: 4th International symposium CPT'18—Cone penetration testing. 21–22 June 2018, Delft, Netherlands. CRC Press, pp 255–261

Davidson C, Brown MJ, Cerfontaine B, Knappett JA, Brennan AJ, Al-Baghdadi T, Augarde C, Coombs W, Wang L, Blake A, Richards DJ, Ball JD (2020) Feasibility of screw piles for offshore jacket structures. Geotechnique. Submitted for consideration

Fleming K, Weltman A, Randolph M, Elson K (2008) Piling engineering, Taylor and Francis
Gavin K, Doherty P, Spagnoli G (2013) Prediction of the installation torque resistance of large diameter helical piles in dense sand. In: Proceedings of 1st international geotechnical symposium of helical foundations, Amherst, USA
Garcia Gallindo P, Davidson C, Brown MJ (2018) Installation behavior of open ended and closed ended piles with torque application. In: Proceedings of the 1st international conference on press-in engineering 2018, 19–20th Sept Kochi, Japan. International Press in Association, Japan, pp 379–386
Ghaly A, Hanna A (1991) Experimental and theoretical studies on installation torque of screw anchors. Can Geotech J 28:353–364
Horvath A (2018) Examining inclined installation of screw anchors scaled up for offshore renewable energy deployment. M.Sc. thesis. University of Dundee. Dundee, UK
Huisman M, Ottolini M, Brown MJ, Sharif Y, Davidson C (2020) Silent deep foundation concepts: push-in and helical piles. In: 4th International symposium on frontiers in offshore geotechnics, Austin, Texas, USA. 16–19 Aug. Taylor & Francis Group, London. Submitted for consideration
Jeffrey J (2012) Investigating the performance of continuous helical displacement piles. Ph.D. thesis, University of Dundee, Dundee, UK
Jeffrey J, Brown MJ, Knappett JA, Ball J, Caucis K (2016) CHD pile performance, Part I: physical modelling. Proc. Inst. Civil Eng: Geotechn Eng J 169(5):421–435
Karthigeyan S (2008) Numerical investigation of the effect of combined loading on the lateral response of piles in sand. In: Challenges and applications of mathematical modeling techniques in building science and technology (CAM2TBST). Central Building Research Institute, Roorkee, India, pp 420–429
Knappett JA, Brown MJ, Brennan AJ, Hamilton L (2014) Optimising the compressive behaviour of screw piles in sand for marine renewable energy applications. In: International conference on piling & deep foundations, Stockholm, Sweden, 21st–23rd May. Article #1904; Publication #100 (IC-2014)
Knappett JA, Caucis K, Brown MJ, Jeffrey J, Ball J (2016) CHD pile performance, Part II: numerical modelling. Proc Inst Civil Eng Geotech Eng J 169(5):436–454
Knappett J, Craig RF (2019) Craig's soil mechanics, 9th edn. CRC Press, Boca Raton, FL
Koschinski S, Lüdemann K (2013) Development of noise mitigation measures in offshore wind farm construction 2013. Report commissioned by the Federal Agency for Nature Conservation (Germany), p 102
Lehane BM, Schneider JA, Xu X (2005) The UWA-05 method for prediction of axial capacity of driven piles in sand. In: Gourvenec S, Cassidy M (eds) Frontiers in offshore geotechnics. Taylor & Francis
Lutenegger A (2019) Screw piles and helical anchors—What we know and what we don't know: an academic perspective—2019. In: Proceedings of the 1st international symposium on screw piles for energy applications (ISSPEA) 27–28th May. University of Dundee, Dundee, UK, pp 15–28
Newgard JT, Mccartney JS, Schneider JA, Thompson DJ (2019) Static and cyclic axial loading of single and multiplate helical anchors in sand. In: Proceedings of the 1st international symposium on screw piles for energy applications (ISSPEA). 27–28th May 2019. University of Dundee, Dundee, UK, pp 81–86
Pavan Kumar PV, Patra S, Haldar S (2019) A critical review on design aspects of screw piles for renewable energy devices. In: Proceedings of the 1st international symposium on screw piles for energy applications (ISSPEA), 27–28th May. University of Dundee, Dundee, UK, pp 59–66
Perko HA (2009) Helical piles: a practical guide to design and installation. Wiley, Hoboken, NJ
Richards DJ, Blake AP, White DJ, Bittar EM, Lehane BM (2019) Field tests assessing the installation performance of screw pile geometries optimised for offshore wind applications. In: Proceedings of the 1st international symposium on screw piles for energy applications (ISSPEA), 27–28th May. University of Dundee, Dundee, UK, pp 47–54

Sakr M (2010) Lateral resistance of high capacity helical piles—case study. In: Proceedings of the 63rd Canadian geotechnical and 6th Canadian permafrost conference, Calgary, Alberta, pp 402–412

Sakr M (2015) Relationship between installation torque and axial capacities of helical piles in cohesionless soils. Can Geotech J 52:747–759

Santos Filho JMSM, Silva Oliveira Morais T, Hollanda Cavalcanti Tsuha C (2014) A new experimental procedure to investigate the torque correlation factor of helical anchors. Electron J Geotech Eng (EJGE) 19(2014):3851–3864 (Bund)

Schiavon JA, HC, Tsuha C, Thorel L (2019) Behaviour of a single helix anchor in sand subjected to cyclic loading: centrifuge modelling. In: Proceedings of the XVI Pan-American conference on soil mechanics and geotechnical engineering (XVI PCSMGE*),* Cancun, Mexico, 17–20 Nov, pp 493–500

Sharif Y, Brown M, Ciantia M, Knappett J, Davidson C, Cerfontaine B, & Robinson S (2019) Numerically modelling the installation and loading of screw piles using dem. Proceedings of the 1st international symposium on screw piles for energy applications (isspea) 27-28th may 2019. University of dundee, dundee, uk. Pp. 101-108. https://doi.org/10.20933/100001123

Spagnoli G (2016) A CPT-based model to predict the installation torque of helical piles in sand. Marine Georesour Geotechn 1–8

Wang L, Coombs WM, Augarde CE, Cortis M, Charlton T, Brown MJ, Knappett J, Brennan A, Davidson C, Richards D, Blake A (2019) On the use of domain-based material point methods for problems involving large distortion. Computer Methods Appl Mech Eng J. 355:1003–1025

Zhang DY (1999) Predicting capacity of helical screw piles in Alberta soils. M.Sc. thesis, University of Alberta, Edmonton, Canada

Challenges in the Design and Construction of Offshore Wind Turbine Foundations Including Sites in Seismic Areas

Subhamoy Bhattacharya, Georgios Nikitas, Muhammad Aleem, Liang Cui, Ying Wang, Saleh Jalbi, and Joseph Hilton

1 Climate Change and Wind Power

The United Nations recently declared that we are facing a grave climate emergency and this one of the grand technological challenges in our times. Continuous ocean and atmospheric warming, heat waves and rising sea levels are some of the most common manifestations of climate change. The recent floods in Venice (Italy) and the ongoing forest fires in Australia are attributed to the effects of climate change. It is not an understatement that island and coastal cities and towns will be disproportionately affected. Developed nations are taking decisive actions, and in this context, it is important to highlight that the UK Committee on Climate Change has set an ambitious target to reduce greenhouse emission to net-zero by 2050. This must involve decarbonising the economy, the backbone of which is energy. A practical way to achieve net-zero target is to run the country mostly on electricity produced from renewable sources without burning much fossil fuel.

Offshore wind power is one the major renewable energy technologies and can tackle many of the current technological and societal challenges by providing green energy and thus reducing the air pollution and improving life-long health. Wind power has an established track record in the sense that it has been used for centuries for sailing ships, sawing wood, grinding grains and many more.

It is one of the oldest sources of '*machine*' power which fits the definition of machine as laid out in Cambridge Dictionary, i.e., a piece of equipment with several moving parts, that uses wind power to carry out a particular type of work such, i.e., sawing a wood. The invention of wind-powered sawmills by Dutchman Cornelis Corneliszoon van Uitgeest in the late sixteenth century helped Holland increase ship

S. Bhattacharya (✉) · G. Nikitas · M. Aleem · L. Cui · Y. Wang
University of Surrey, Guildford, Surrey, UK
e-mail: S.bhattacharya@surrey.ac.uk

S. Jalbi · J. Hilton
Sea and Land Project Engineering, New Malden, UK

S. Haldar et al. (eds.), *Advances in Offshore Geotechnics*, Lecture Notes in Civil Engineering 92, https://doi.org/10.1007/978-981-15-6832-9_6

Fig. 1 Wind mill in Zaanse Schans (the Netherlands) where the sawing of wood can be seen. *Photo* Prof. Bhattacharya

production through automated wood cutting, outcompeting their European rivals who were relying on slow manual processes. It can also be said that offshore wind turbine machines are also the largest moving machine. A typical 10 MW turbine will have three 80 m long blades and each weighing circa 35 tonnes turning at average of 8–10 RPM.

Figure 1 shows a wind mill for sawing wood still conserved in the Netherlands and is a tourist attraction. The readers are referred to various aspects of climate change in relation to offshore wind in Nikitas et al. (2018, 2020) in the edited books on Managing Climate Change: Human intervention and Future Energy.

1.1 Offshore Wind Energy

Modern-day wind power is harvested through wind farms, either onshore or offshore. As compared to onshore, an offshore wind farm is scalable and relatively easy (not necessarily cheaper) to construct due to the sea routes and vessels available to transport parts from manufacturing sites to turbine locations. Further details of comparison between offshore and onshore turbines can be found in Chap. 1 of Bhattacharya (2019).

A typical offshore wind farm can generate 1 GW of power, approximately equivalent to two standard nuclear power plants. A typical turbine can produce 8–10 MW of power, and therefore, 1 GW of offshore wind farm power involves 100–125 offshore turbines.

Figure 2 illustrates a typical layout of an offshore wind farm, annotating all the different components (turbine generator through the electricity cables to the offshore substation and finally to the onshore power grid). The design of an offshore wind farm requires extensive and comprehensive input from geotechnical engineers. Figure 3 shows an aerial view of the Dudgeon wind farm, with a capacity 400 MW, located off the coast of Norfolk showing the turbines and a substation.

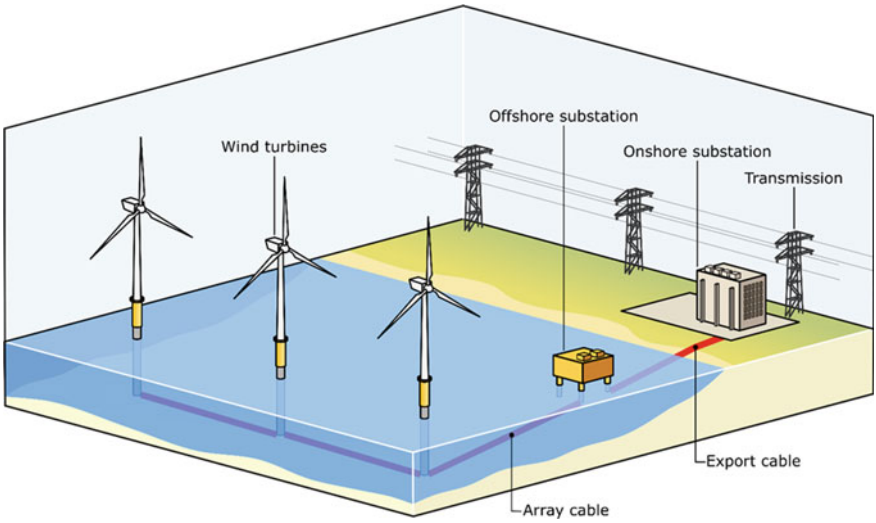

Fig. 2 Layout of an offshore wind turbine

Fig. 3 Aerial view of Dudgeon wind farm. *Photo* Jan Arne Wold, Equinor

1.2 *Sustainability of Wind Farm and Tackling Intermittency of Wind Power*

In a nutshell, wind will blow as long as the sun is shining. The sun is the ultimate source of energy and responsible for wind. Due to the radiation of the sun reaching the earth, a continuous warming of the earth's surface is caused. Out of this radiation, the largest amount is sent back to space, and only a small amount is transformed into heat. Due to the surface characteristics of the earth and having different materials (water and land), its surface is not heated evenly resulting in the equator getting more energy than the poles. As a result, there is a continuous heat transfer from the equator to the poles.

The atmospheric air consists of nitrogen and oxygen, and they expand when heated and contract when cooled. The solar radiation causes the air to get warmer and lighter and less dense than cold air. This also results in the rise of warm air in higher altitudes and the creation of areas of lower atmospheric pressure, where the air is warmer. Due to the variance in pressure, the air will move from a high pressure to a lower pressure area, in an attempt to reach equilibrium.

Wind is essentially atmospheric air in motion and is very complex, see Fig. 4. At 30° and 60° latitude, there is a major change in atmospheric pressure creating zones of high and low pressure, respectively. The air circulation within these zones is known as cells and the major winds created as trade winds. Due to the diurnal motion of the earth, the wind deflects to the right in the Northern Hemisphere and to the left in the Southern one, leading to a spiral movement of the air mass, and this phenomenon is known as Coriolis effect. Figure 4 describes the mechanism of

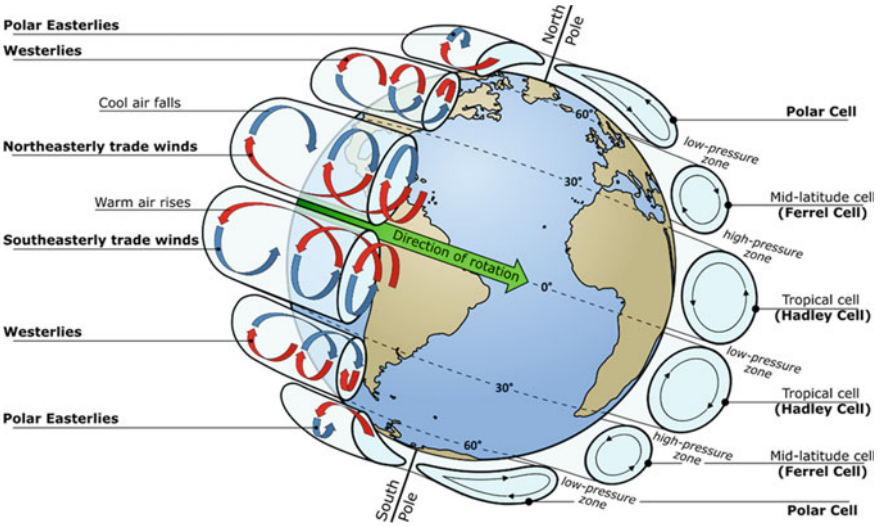

Fig. 4 Global circulation of wind

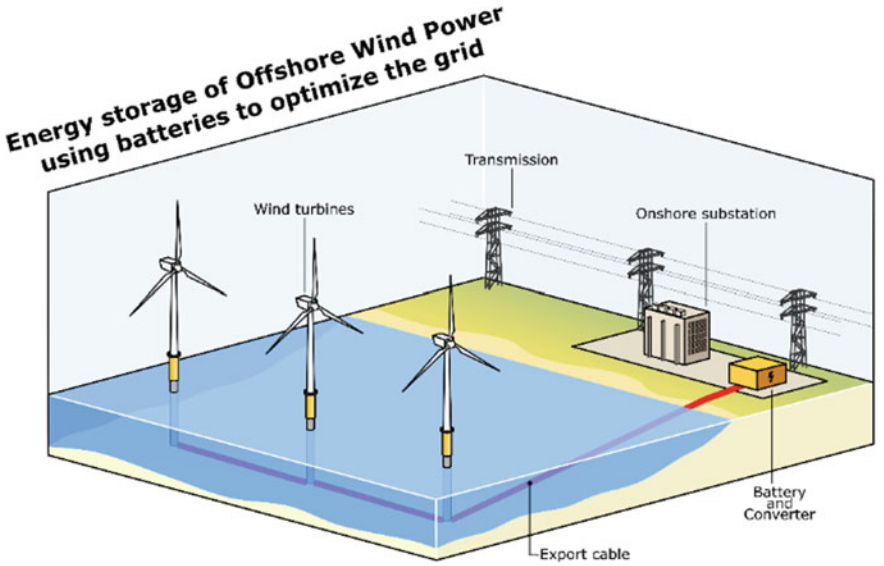

Fig. 5 Combining offshore wind with battery storage

the global wind system. In addition to the global wind system, there are localised influences as well and are mostly related to the terrain of an area and its proximity to water bodies. Further details of wind energy engineering can be found in the edited book by Letcher (2017).

A power curve from a typical turbine will show that a turbine can generate power from a wind speed starting from as low as 3 m/s and reach the rated power at about 12 m/s. It is believed by many that wind does not blow constantly, and therefore, when you need power, it will not be available or when the wind is blowing there may not be the need for the power. To face these problems, technologists have manufactured systems that can store the energy generated by wind in batteries and thus optimising the grid. The synergy of offshore wind along with storage technologies such as batteries will become necessary in order to secure grid's stability. However, such technologies often need rare earth metals for battery production which needs extensive mining and the effects of commodity trading (similar to oil and gas trading). The next section shows another technology that may avoid some of the above effects (Fig. 5).

1.3 Hydrogen Production Using Offshore Wind—The Japanese 'Jidai' Concept

The 2011 Fukushima Daiichi Nuclear Power Plant (NPP) disaster was a devastating moment in the history of mankind, see Bhattacharya et al. (2019). Following

the disaster, many countries such as Germany and Japan reduced their reliance on nuclear power and compensated with fossil fuels and renewables. Within the framework of global warming, and amongst others such as energy security, Japan aims to become a carbon-free country through a 'hydrogen society'. The main idea is to generate hydrogen from water through renewable energy sources such as wind, solar and hydroelectricity. Japan named it as the Jidai concept. Similar attempts are also ongoing in major European economies. These attempts have been boosted by other technology developments, i.e., the invention of hydrogen-powered cars, trains, ships and even aircrafts (Fig. 6).

The Jidai concept is a four-step process: (a) seawater is desalinated; (b) electrolysis is used to produce hydrogen and oxygen from water; (c) hydrogen gas is compressed to 700 bar to reduce storage volume; (d) high-pressure hydrogen gas is stored in a module-based tank system (Fig. 7).

The potential of hydrogen is huge: through the existing offshore infrastructure of pipe networks, hydrogen can be transported for distribution. With the advent of hydrogen cars and trains, the economy can be transformed without the need for expensive metals that are needed for battery production. For example, lithium and nickel, unlike hydrogen, can be seen as a trading commodity like oil and gas.

Studies are being conducted to demonstrate that a 100% hydrogen gas network is equally as safe as the existing natural gas. It is worth noting that burning natural gas to heat homes and businesses accounts for approximately a third of the UK's

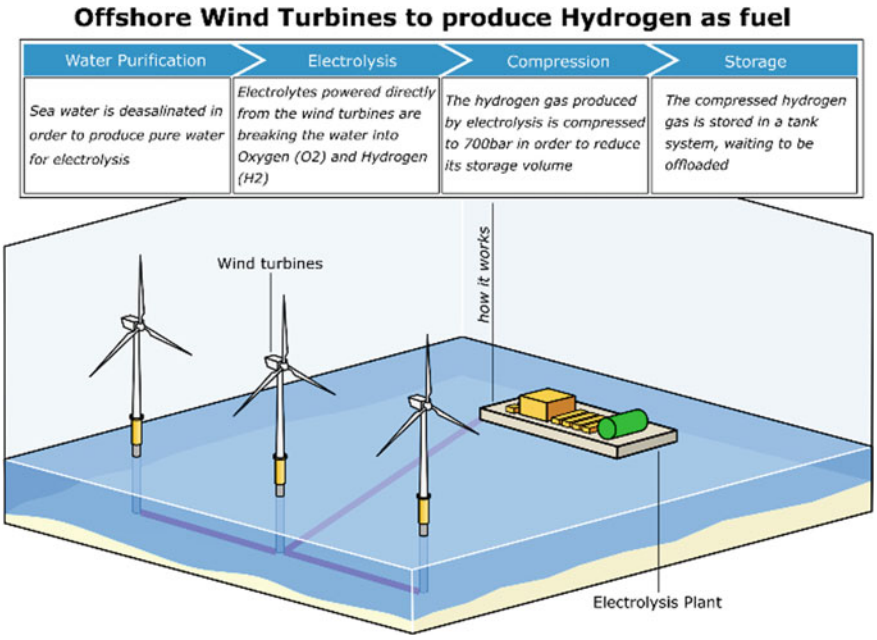

Fig. 6 Use of offshore wind to produce hydrogen

Fig. 7 Hydrogen-powered buses in Tokyo (photo taken in September 2019)

carbon emissions. Hydrogen-powered commuter trains are available, and it has been reported in New Civil Engineer that 30% of the UK rail fleet could be suitable for running hydrogen-powered trains. In summary, wind power has the potential to carry the transition to low carbon energy, transforming the fossil fuel energy landscape to a more sustainable energy future.

1.4 Opportunity for Increasing Resilience of Nuclear Power Plant Through the Use of Offshore Wind Turbines

Following the 2011 Fukushima Nuclear Power Plant disaster, one of the main technological challenges is the seismic resilience of existing nuclear power plant, so that similar incidents may not happen. Table 1 shows the summary of the main three nuclear accidents, and it appears that cooling power for the reactor is vital for safety.

Table 1 Case studies of major global NPP disasters

Name of NPP	Cause of failure
Three-mile island (USA)	Damage to reactor core due to cooling loss
Chernobyl (Russia)	Overheating, steam explosion and meltdown
Fukushima (Japan)	Failure of emergency cooling caused an explosion after the shutdown of reactor during the cascading events of Tohoku earthquake

Bhattacharya (2009), Bhattacharya and Goda (2016) and Bhattacharya et al. (2018) described the Fukushima NPP incident, and it was inferred that seismic resilience of NPP is directly linked to resilience of the cooling power.

In the context of offshore wind, it is of interest to describe the performance of near-shore offshore wind turbines in Japan during the 2011 Tohoku earthquake.

1.4.1 Case Study: Performance of Near-Shore Wind Farm During 2011 Tohoku Earthquake

A devastating earthquake of moment magnitude 9.0 struck the Tohoku and Kanto regions of Japan on 11th March at 2:46 p.m. which also triggered a tsunami, see Fig. 8 for the location of the earthquake and the operating wind farms. The earthquake and the tsunami caused effects such as: liquefaction, economic loss, loss of life, damage to national infrastructures but very little damage to the wind farms. Extensive damage was also caused by the massive tsunami in many cities and towns along the coast. Figure 9 shows photographs of a wind farm at Kamisu (Hasaki) after the earthquake, and Fig. 10 shows the collapse of a pile-supported building at Onagawa where for the first time the world saw complete uprooting of piled foundations. At many locations (e.g., Natori, Oofunato and Onagawa), tsunami heights exceeded 10 m, and sea walls and other coastal defence systems failed to prevent the disaster.

The earthquake and its associated effects (i.e., tsunami) also initiated the crisis of the Fukushima Daiichi nuclear power plants (NPP). The tsunami, which arrived

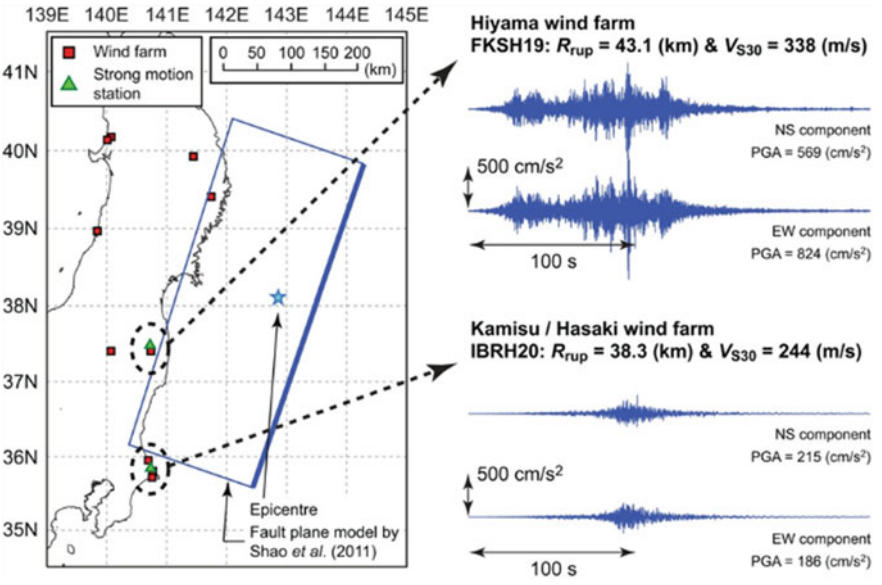

Fig. 8 Details of the 2012 Tohoku earthquake and locations of the wind farms

Fig. 9 Photograph of the Kamisu (Hasaki) wind farm following the 2012 Tohoku earthquake

Fig. 10 Collapse of the pile-supported building following the same earthquake

around 50 min following the initial earthquake, was 14 m high which overwhelmed the 10 m high sea walls, flooding the emergency generator rooms and causing a power failure to the active cooling system.

Limited emergency battery power ran out and subsequently led to the reactor heating up and the subsequent meltdown leading to the release of harmful radioactive material to the atmosphere. Power failure also meant that many of the safety control

systems were not operational. The release of radioactive materials caused a large-scale evacuation of over 300,000 people, and the clean-up costs are expected to be of the order of tens of billions of dollars. On the other hand, following/during the earthquake, the wind turbines were automatically shut down (like all escalators or lifts), and following an inspection, they were restarted.

1.4.2 Why Did the Wind Farm Stand Up?

Recorded ground acceleration time-series data in two directions [North–South (NS) and East–West (EW)] at Kamisu and Hiyama wind farms [FKSH19 and IBRH20] are presented in Fig. 11 in frequency domain. The dominant period ranges, of the recorded ground motions at the wind farm sites, were around 0.07–1 s, and on the other hand, the periods of the offshore wind turbine systems are in the range of 3 s. Due to non-overlapping of the vibration periods, these structures will not get tuned in, and as a result, there are relatively insensitive to earthquake shaking. However, earthquake-induced effects such as liquefaction may cause some damages. Further details of the dynamics of wind turbine structures together with the effects of foundation can be found in Bhattacharya (2019).

Forward Outlook: One may argue, had there been few offshore wind turbines operating, the disaster may have been averted or the scale of damages could have certainly been reduced. The wind turbines could have run the emergency cooling system and prevented the reactor meltdown. In this context, it is interesting to note that there are plans to replace the Fukushima NPP by a floating wind farm.

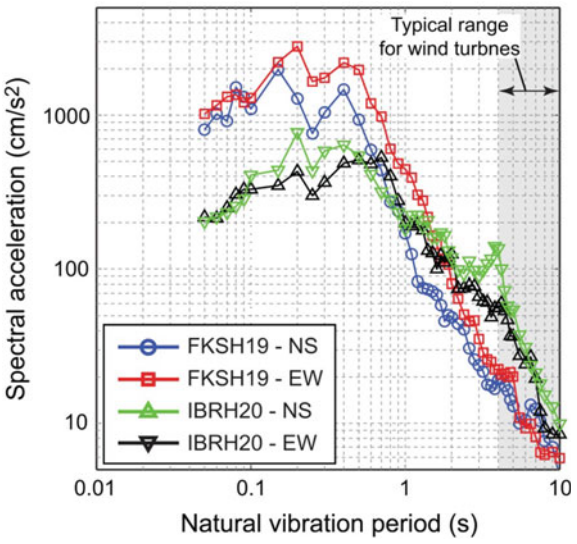

Fig. 11 Power spectra of the earthquake and natural frequency of wind turbines

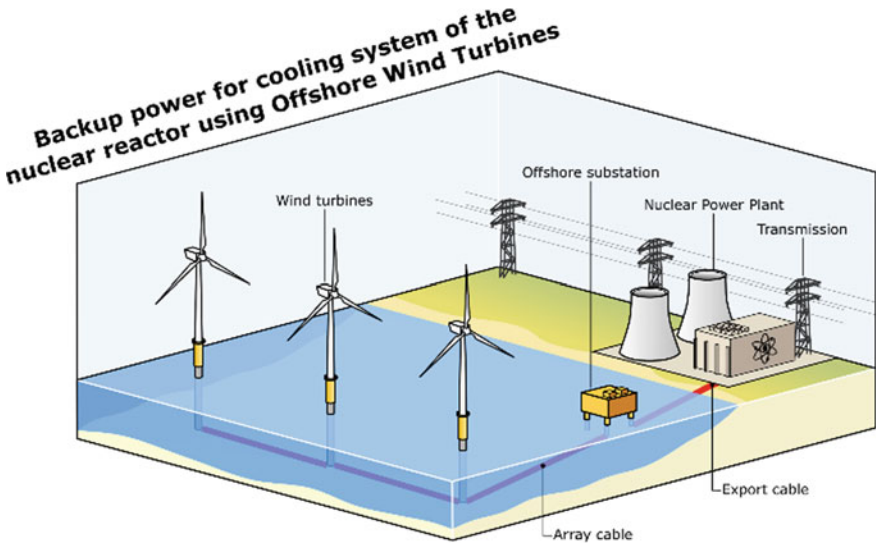

Fig. 12 Proposition of additional backup power for resilience of NPP

The proposition is therefore to have few offshore wind turbines in seismic locations close to the existing NPP so as to have an additional cooling system backup, see Fig. 12 for schematic. To summarise, the primary system of cooling is the grid (external source), and backup systems are offshore wind turbines and diesel generator as well as battery power. Figure 13 shows locations of NPP (either planned or operating) in four countries (India, China, UK and Japan), and it is interesting to note that many of these are near the coastline. One of the risks are therefore Tsunami effects where seismically-qualified OWT's can be easily installed to add resilience. An alternative way to increase resilience against Tsunami is by developing a very long robust sea-wall (along the external boundary) based on the prediction of tsunami wave height, which can be very expensive (Fig. 14). Furthermore, if due to local variation if one part of the sea-wall fails, the whole resiliency is lost. Use of offshore wind turbines may provide a viable, economic and equally (if not higher) robust alternative. Figure 15 shows the aerial view of Fukushima Daiichi NPP sea-defence before the disaster, taken from National Land Information Division.

Installation of wind turbines are therefore crucial even in seismic zones, and for this to happen, design methodology must be developed. This paper also highlights such issues. Figure 16 shows the expansion of offshore wind farms in seismic zones, further details can be found in De Risi et al. (2018).

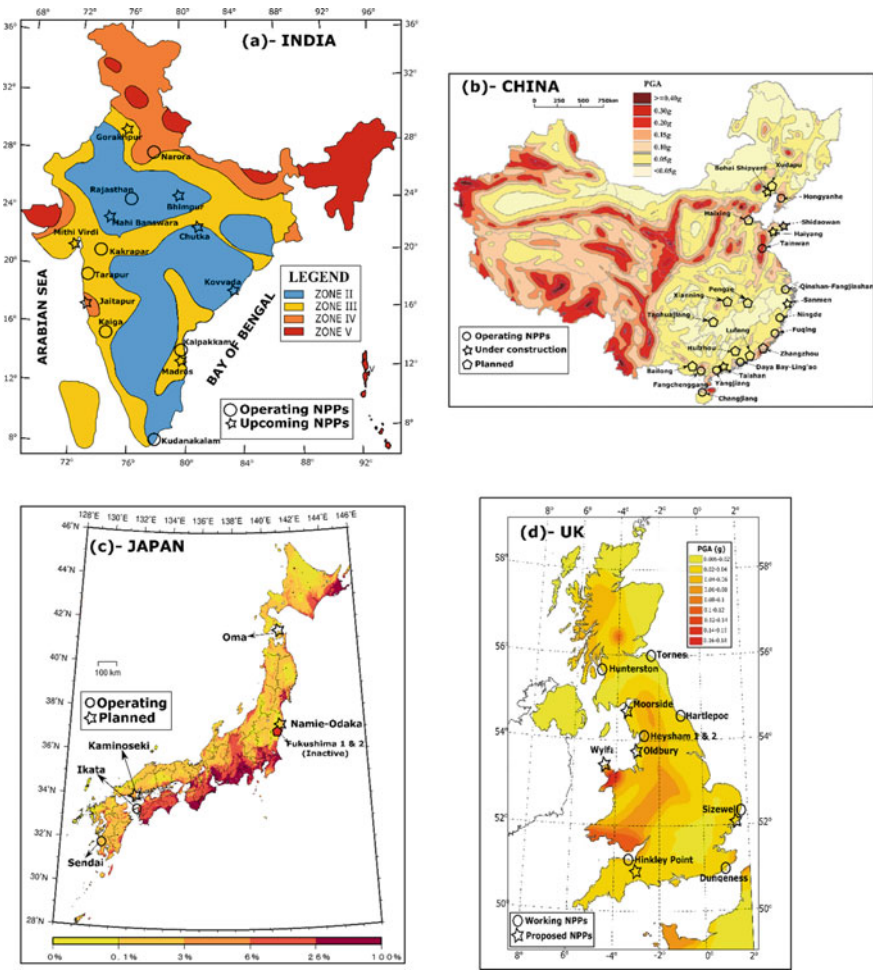

Fig. 13 Locations of offshore wind turbines for four countries together with seismic hazard

1.5 Research Needs in Offshore Wind Turbines

The aim of this lecture is to highlight some of the challenges related to design and construction of offshore wind farms. The paper is structured in the following way:

1. Section 2 discusses the uniqueness of offshore wind turbine structure together with loading complexities.
2. Considerations for analysis and design in different seas around the world.
3. Issues with long-term performance prediction.
4. Additional considerations for construction and maintenance.
5. Emphasis is given for seismic considerations.

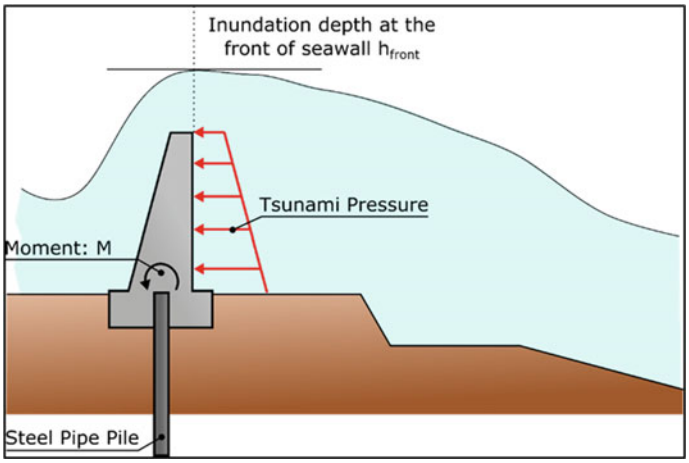

Fig. 14 Robustness concept of resiliency of sea-wall for safe-guarding NPP

2 Uniqueness of Offshore Wind Turbine Structure

Figure 17 shows a schematic diagram showing the loads on the structure which must ultimately be carried by the foundations. There are four main loads apart from the self-weight of the whole system: wind, wave, 1P (rotor frequency) and 2P/3P (blade-passing frequency) loads. Figure 17 shows a schematic representation of the time history (wave form) of the main loads. The salient points of the loads are discussed here:

1. Each of these loads has unique characteristics in terms of magnitude, frequency and number of cycles applied to the foundation. Figure 18 shows a plot where the various frequencies of the loads are shown. The example of 3 MW turbine is taken together with the fundamental frequency of the wind turbines in two wind farms.
2. The loads imposed by the wind and the wave are random in both space (spatial) and time (temporal), and therefore, they are better described statistically.
3. Apart from the random nature, these two loads may also act in two different directions (often termed as wind-wave misalignment) to have a steady power output.
4. 1P loading is caused by mass and aerodynamic imbalances of the rotor, and the forcing frequency equals the rotational frequency of the rotor.
5. On the other hand, 2P/3P loading is caused by the blade shadowing effect, wind shear (i.e., the change in wind speed with height above the ground) and rotational sampling of turbulence. Its frequency is simply two or three times the 1P frequency. Further details on the loading can be found in Arany et al. (2015a, b, 2017) and Chap. 2 of Bhattacharya (2019).

Fig. 15 Sea-defence system for Fukushima NPP

Figure 18 presents a schematic diagram of the main frequencies of these four types of loads, so that the dynamic design constraints can be visualised where three design space may be noted: soft-soft, soft-stiff and stiff-stiff. These terms are essentially concerned based on relative flexibility of the tower with respect to the foundation. Figure 19 shows a schematic view of the definition.

Few points may be noted from the design choices available:

1. In the 'soft-stiff' design, the natural frequency or the resonant frequency is very close to the upper end of 1P (i.e., frequency corresponding to the rated power of

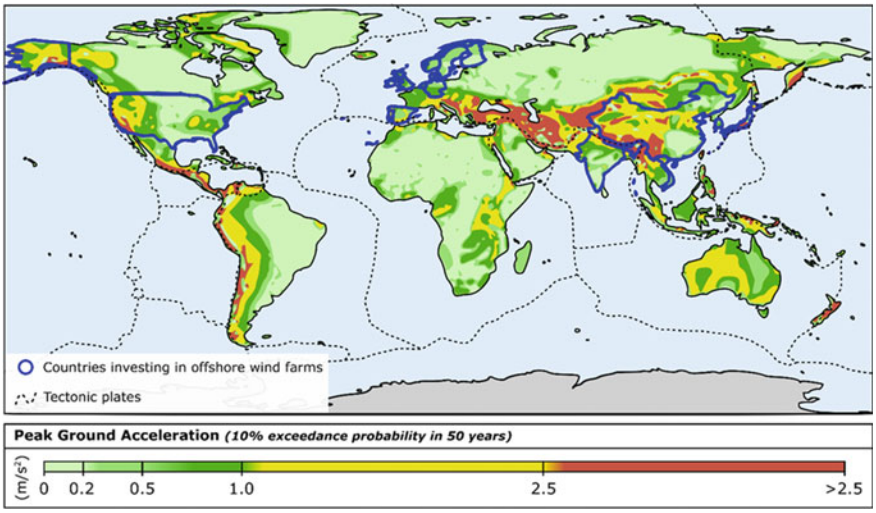

Fig. 16 Expansion of offshore wind is seismic locations

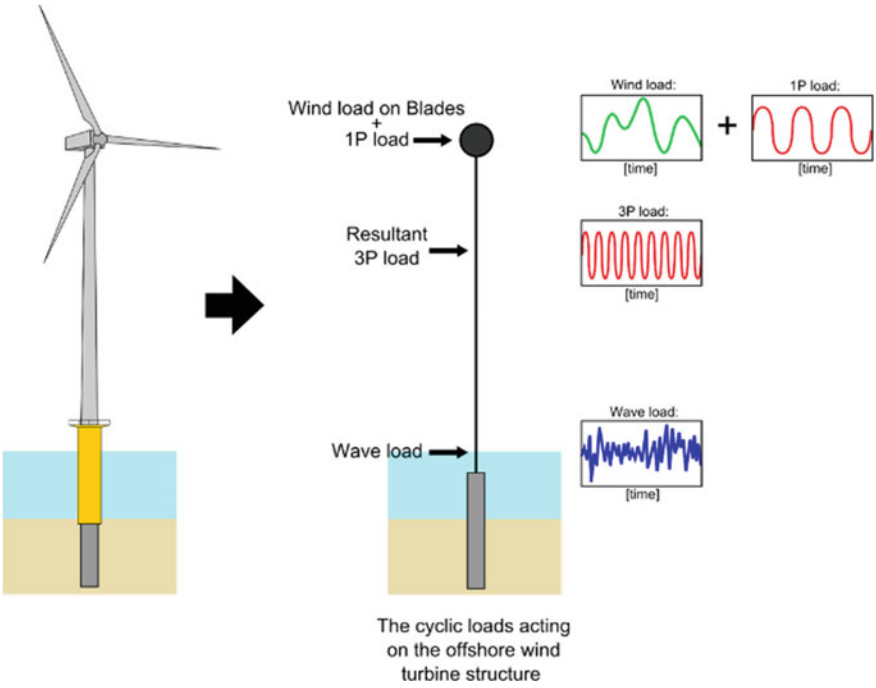

Fig. 17 Loads on offshore wind turbine foundations

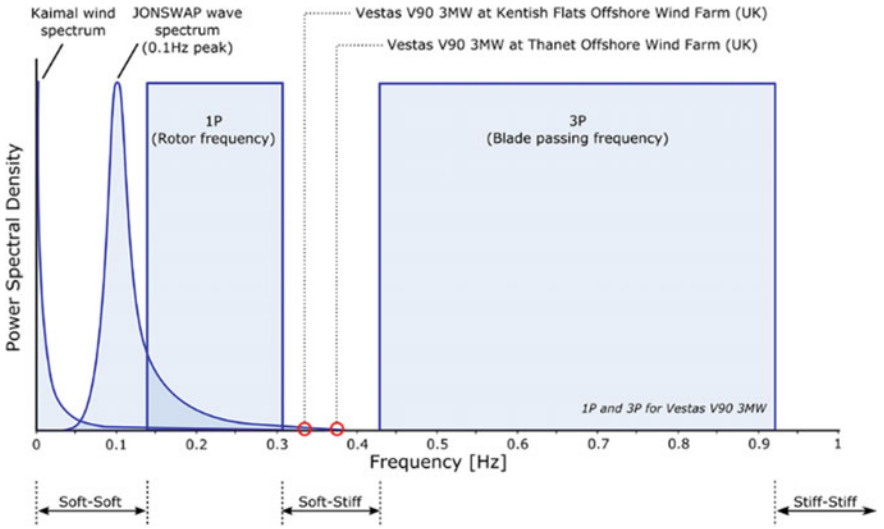

Fig. 18 Frequency range of the loads along with natural frequency of the turbines for 3 MW turbines

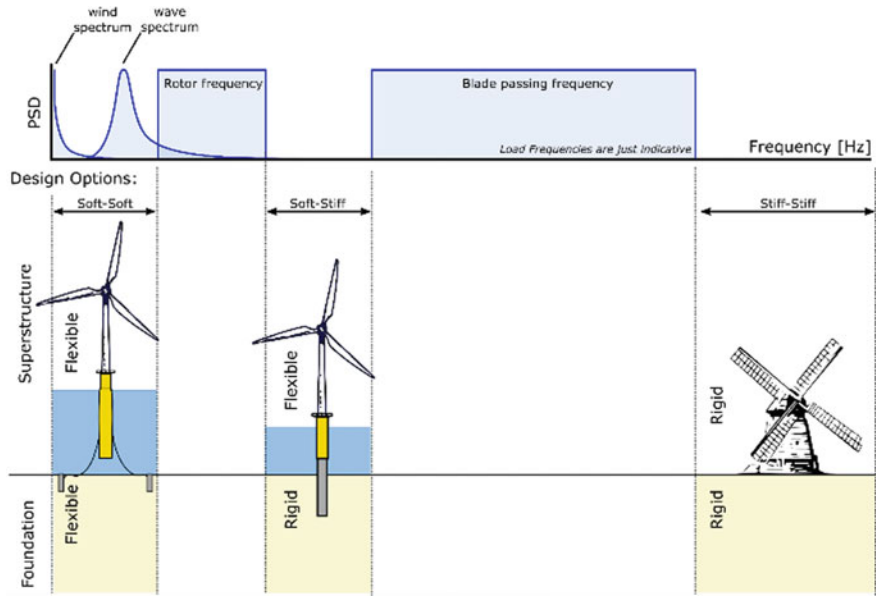

Fig. 19 Schematic shows the different structural systems

the turbine) and lower bound of the 3P (i.e., cut-in speed of the turbine). This will inevitably cause vibration of the whole system as the ratio of forcing to natural frequency is very close to 1. It is worth noting that resonance under operational condition has been reported in the German North Sea projects, see Hu et al. (2014).

2. For a soft-stiff 3 MW WTG system, 1P and 3P loading can be considered as dynamic (i.e., ratio of the loading frequency to the system frequency very close to 1). Most of the energy in wind turbulence is in lower frequency variations (typically around 100 s peak period), which can be considered as cyclic. On the other hand, 1P and 3P dynamic loads change quickly in comparison with the natural frequency of the WTG system, and therefore, the ability of the WTG to respond depends on the characteristics, and dynamic analysis is therefore required.
3. As a rule of thumb, if the natural frequency of the WTG structure is more than five times the forcing frequency, the loading can be considered cyclic, and inertia of the system may be ignored. For example, for a 3 MW wind turbine having a natural frequency of 0.3 Hz, any load having frequency more than 0.06 Hz is dynamic. Therefore, wave loading of 0.1 Hz is dynamic.

Current design aims to place the natural frequency of the whole system in between 1P and 3P in the so-called 'soft-stiff' design. In the plot in Fig. 18, the natural frequency of two Vestas V90 3 MW wind turbines from two wind farms (Kentish Flats and Thanet) are also plotted. Though the turbines are same, the variation in the natural frequency is due to the different ground and site conditions.

2.1 Can the Foundations Design Code for Oil and Gas Platforms Be Directly Used for Design of Offshore Wind Foundations?

Often to explain the problem of foundation design of wind turbines to school children, an analogy may be used. It is effectively a large washing machine on the top of a flagpole, see Fig. 20. The flagpole is supported on a fence post. The whole challenge is how to design the fence post. Figure 20 also shows a typical offshore oil and gas structure. There are, however, obvious differences between those two types of foundations, see Chap. 1 of Bhattacharya (2019), and they are listed below:

1. Offshore oil and gas platforms are supported on many small diameter piles. Piles for offshore platform structures are typically 60–110 m long and 1.8–2.7 m in diameter, and monopiles for offshore wind turbines are commonly 30–40 m long and 3.5–9 m in diameter.
2. The fixity or the boundary condition of oil and gas platform piles is very different than from that of the monopiles. The oil and gas platform piles can under lateral loads translate laterally but cannot rotate. Therefore, degradation in the upper

Fig. 20 Analogy of OWT and offshore oil and gas structure

soil layers resulting from cyclic loading is less severe for offshore piles, which are significantly restrained from pile head rotation, whereas monopiles are free-headed. Free-headed piles allows more deformation and, as a result, high strain levels in the soil.

3. Beam on nonlinear Winkler springs (known as 'p-y' method in American Petroleum Institute, API code or Det Norske Veritas, DNV code) is used to obtain pile-head deflection under cyclic loading for offshore oil and gas piles, but its use is limited for wind turbines application because for two reasons: (a) The widely used API model is calibrated against response to a small number of cycles (maximum 200 cycles) for offshore fixed-platform applications. In contrast, for a real offshore wind turbine, 10^7–10^8 cycles of loading are expected over a lifetime of 20–25 years; (b) under cyclic loading, the API or DNV model always predicts degradation of foundation stiffness in sandy soil. However, foundation stiffness for monopiles in sandy soil will actually increase as a result of densification of the soil next to the pile.

Foundation choice is very important as it affects in many ways including economics. Figure 21 shows a typical guidance in this regard based on water depth. Further details on the different design considerations can be found in Bhattacharya (2019). Typically for water depths more than 60 m, floating foundations are likely to be used. The first floating wind farm is located in Scotland and is known as Hywind concept which is essentially is floating spar. The type of foundation dictates the loads on it—see Figs. 22 and 23. As may be observed, for a monopile (or a single foundation type such as gravity base, suction caisson), the foundation (H). For a jacket type of structure (or Tripod on piles), the loads are push-pull action, i.e., mainly axial load on the foundation. For floating and anchor type, the load on the foundation is pull, i.e., snatch type of load, see Fig. 23, and acts when one mooring line is broken.

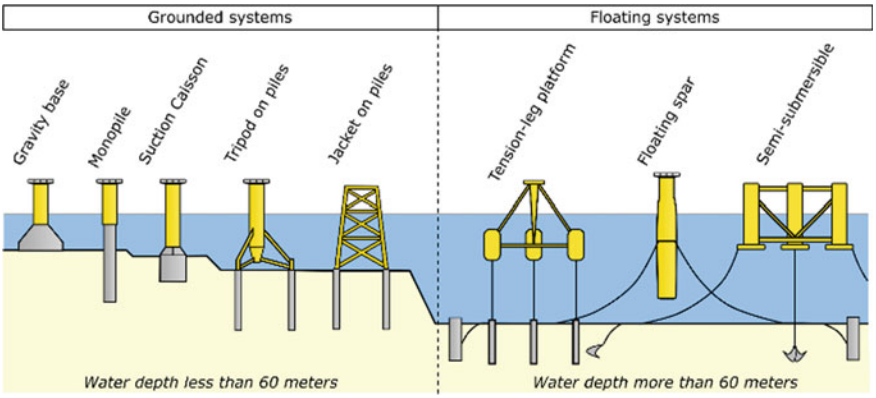

Fig. 21 Foundation choices based on water depth

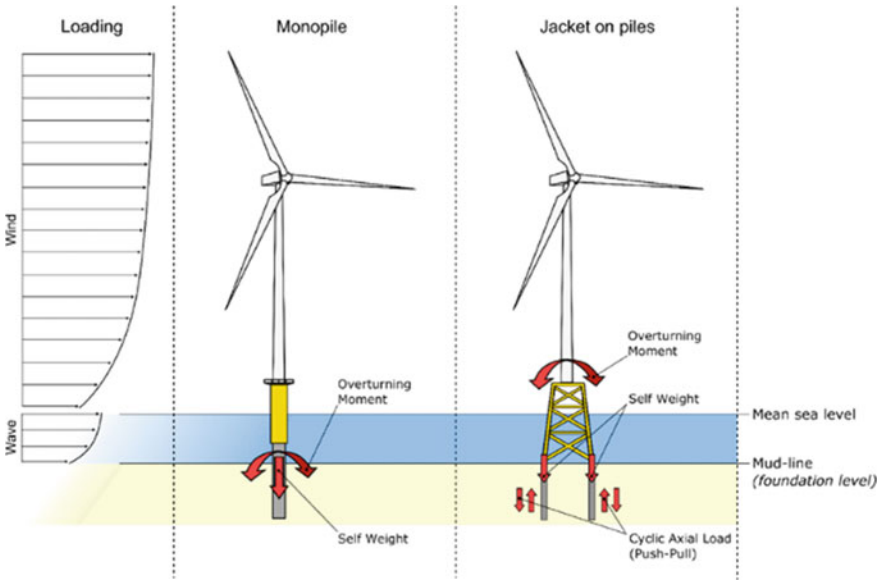

Fig. 22 Loads on foundation for grounded systems

3 Known Challenges in Design

This section of the paper highlights some of the known engineering challenges in design which are identified so far.

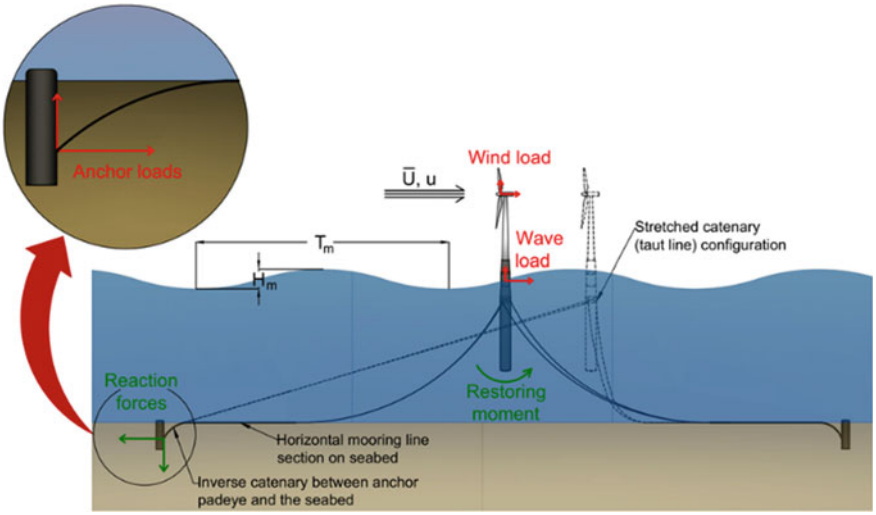

Fig. 23 Loads on foundation for a floating system

3.1 Load Complexities in Monopile Type of Foundation

Figure 24 shows the four main loads on foundations in a simplified model which can be estimated based on closed form solution, see Arany et al. (2016, 2017) and

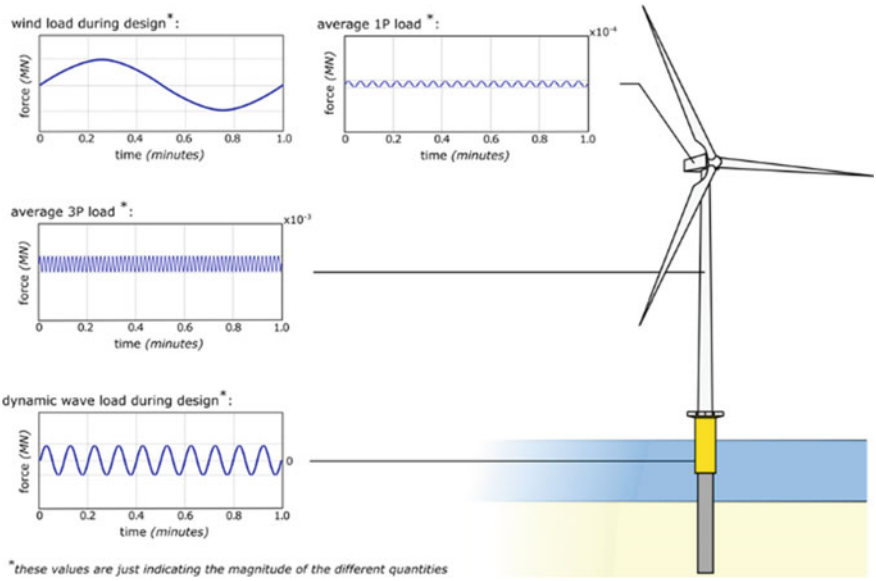

Fig. 24 Instantaneous description of load on a foundation

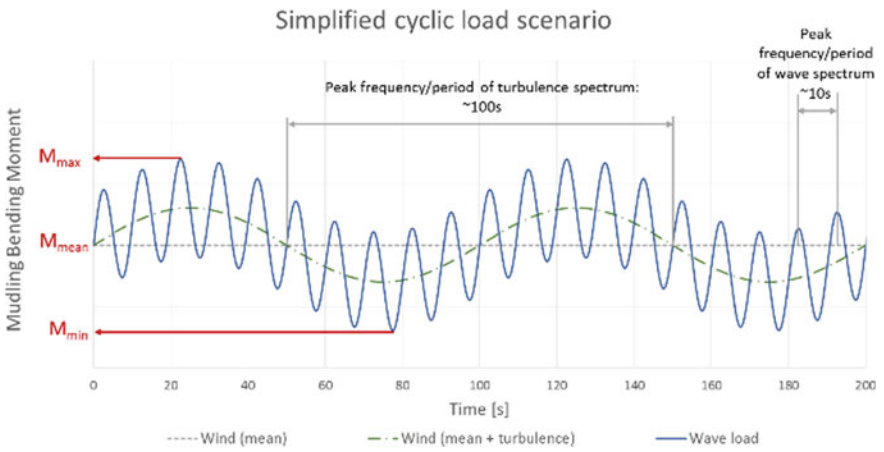

Fig. 25 Simplified load on monopile foundations

Chap. 6 of Bhattacharya (2019) without needing to recourse to expensive aero-servo-hydro-dynamic-soil-structure-interaction (ASH-DSSI) Code. For obtaining preliminary sizes of foundations for economic viability and tender document preparation, these methods are adequate. Figure 25 shows a simplified version of the load scenario which can be estimated for different design load cases (known as DLC's). The method is explained in Jalbi et al. (2019) from where minimum and maximum over-turning moment can be obtained. These values depend not only on the turbine size (3.6 or 10 MW), water depth (10 m water or 21.5 m water) but also on the wind and wave climate (wind turbulence and sea states), i.e., extreme turbulence model (ETM), normal turbulence model (NTM) and extreme wave height (EWH), see Figs. 26 and 27 for two examples. It is clear that there may be a bias in the foundation load and one of the challenges is to predict the long-term tilt due to this type of loading for the entire design life time of 25–30 years. The problem is schematically shown by Fig. 28 and is a highly nonlinear soil-structure interaction (SSI) problem. Theoretical understanding of the problem based on discrete element method (DEM) where each sand particle is modelled has been carried out by Cui and Bhattacharya (2016) and Cui et al. (2017, 2019).

3.2 Impact of Technological Advancements (i.e., Long Blades, Large Turbines) and Deeper Water Installations

Figure 29 shows technological progress since 1980s, where it may be noted that the turbine capacity increased from 0.01 to 20 MW with 9.5 MW currently available commercially. Figure 30 shows the top rotor-nacelle assembly (RNA) mass and the tower height. With both RNA mass and turbine height increasing, the natural

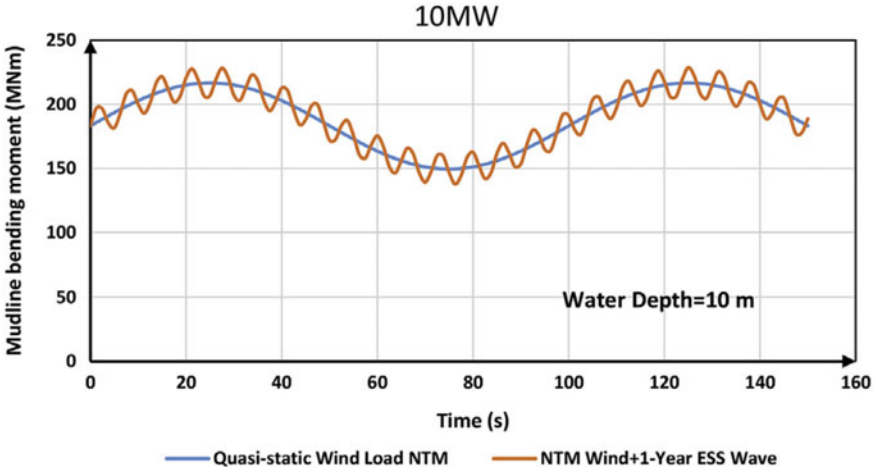

Fig. 26 Loading scenario for a typical 10 MW turbine in 10 m water depths

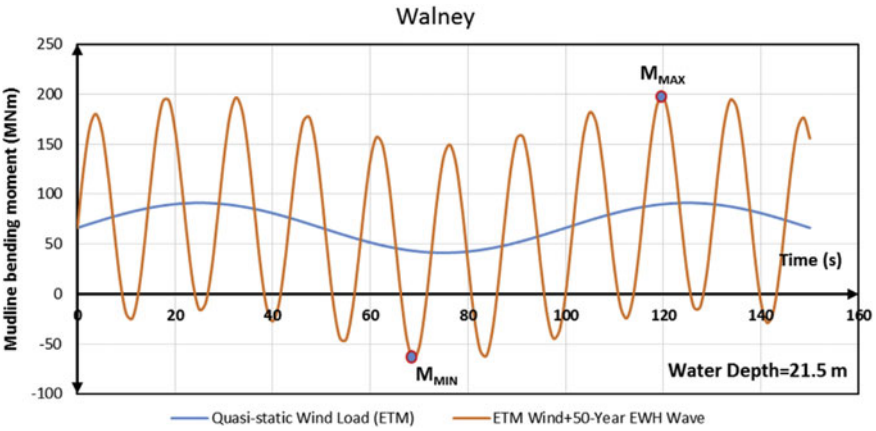

Fig. 27 Loading scenario for 3.6 MW turbine in 21.5 m water depths

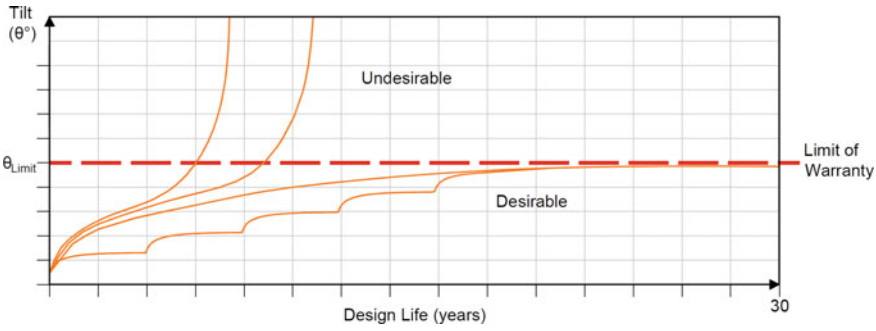

Fig. 28 Prediction of long-term tilt over 30 years life time for a complex load scenario

frequency is reducing due to increased flexibility of the system. For example, the target frequency (which is provided by the turbine manufacturer) of a typical 3.6 MW is circa 0.33 Hz and that of 8 MW is 0.22 Hz. As the target frequency reduces, it may come close to wave frequencies causing higher fatigue damages. Figure 31 shows the impact of turbine sizes on the target natural frequency.

Table 2 shows the wave frequencies for different Chinese seas, and it is clear that some of the predominant wave period is very close to the target frequencies of large turbines which poses significant design challenges from the point of view of fatigue and long-term tilting.

3.3 Modes of Vibrations of the Wind Turbine System

Vibration characteristics play a significant role in choosing a particular structural system to support wind-turbine-generator (WTG), i.e., four-legged suction caisson or three-legged pile (Tri-pile) Bhattacharya and Adhikari (2012). There are mainly two types of vibrations for grounded wind turbines: (a) Sway-bending; (b) Rocking. Readers are referred to Bhattacharya (2019) for the modes of vibration. Due to lack

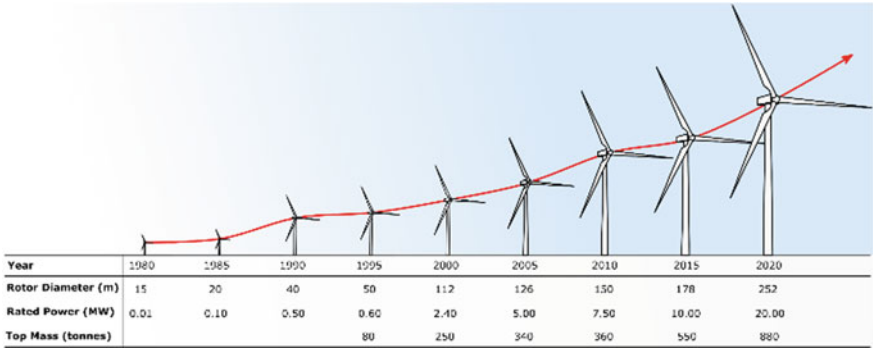

Fig. 29 Technological progress of turbines

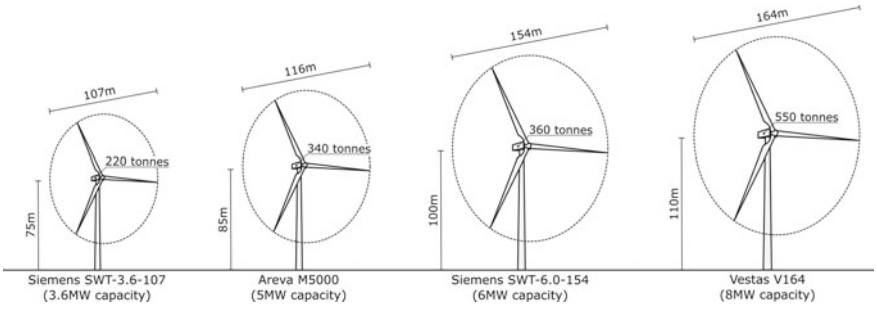

Fig. 30 Future of turbines showing the top mass and tower height

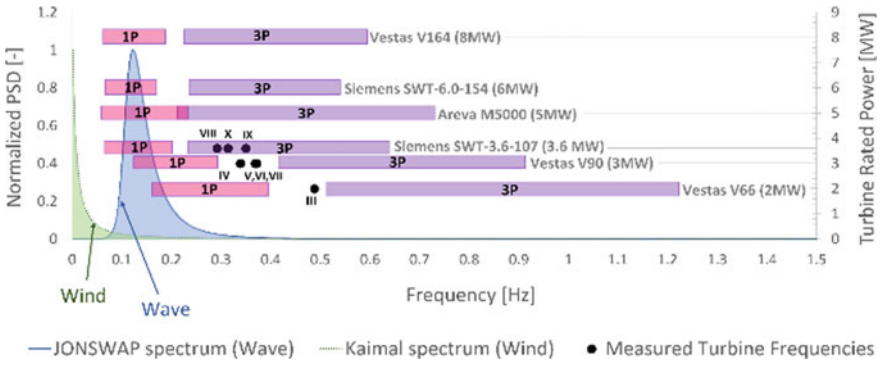

Fig. 31 Target frequencies for a range of turbines

Table 2 Typical wave period for various Chinese seas

China Sea	Region	Wave height (m)	Wave period (s)
Bohai Sea	Bohai Strait	1.2	4.8
	Others	<1	<4.5
Yellow Sea	North	1.2	5
	Centre	1.4	5
	South	1.6	6
East China Sea	Shanghai coastline	1.6	6
	Zhejiang coastline	1.8	7
	Taiwan Strait	2.4	9
South China Sea	Luzon Strait	2.8	10
	Indo-China Peninsula	2.6	8
	Others	<2	6

of space, the non-trivial case is discussed here: If the foundation is rigid compared to the flexibility of the tower, sway-bending mode is expected. On the other hand, if the foundation is not sufficiently rigid, rocking modes combined with flexible modes of tower may occur (Fig. 32). Bhattacharya (2019) and Jalbi et al. (2019) showed that rocking modes must be avoided at any cost for offshore wind turbine structures as low-frequency rocking mode may interact with the rotor frequency. There is therefore a requirement of minimum vertical stiffness of suction caissons as is described in Jalbi et al. (2019). Often, surprising type of vibration modes may be encountered, either in field records or scaled testing. Figure 33 shows one such case, a '*beating*' modes of vibration observed in a scaled model testing of a symmetric tripod on shallow foundation. Theoretical studies revealed that this is typical of two

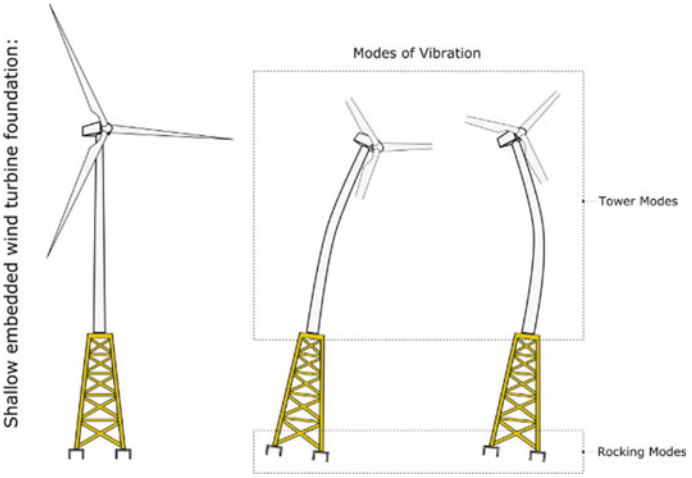

Fig. 32 Rocking modes of vibration

closely spaced vibration modes with low damping. The main point to highlight is the importance of damping for performance prediction.

3.4 Scour

Figure 34 shows the observed scour in few turbines of Robin Rigg Offshore Wind farm leading to early decommissioning. The observation was a rapid change in

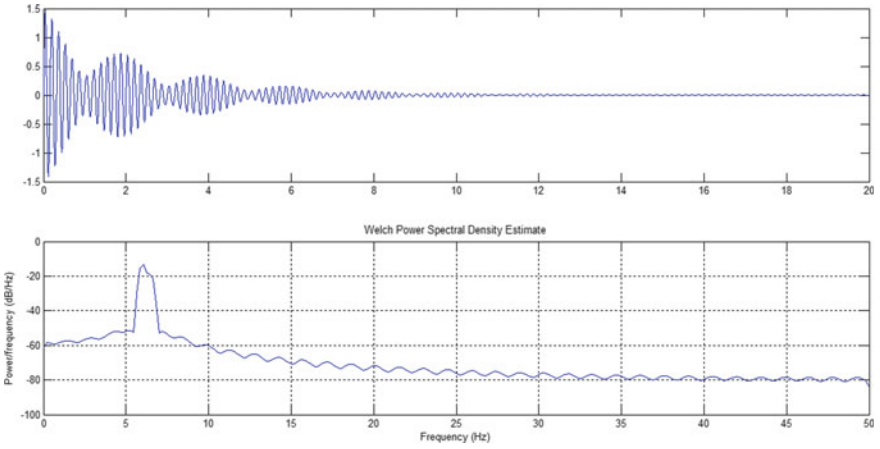

Fig. 33 'Beating' type modes of vibration

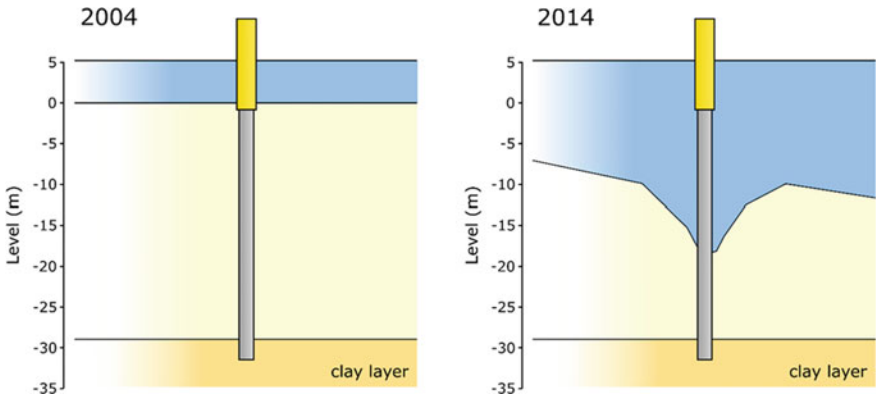

Fig. 34 Observed scour of wind turbine foundations

frequency leading to investigation and then shut down. Further details can be found in Cassie (2017). This highlights the importance of site investigation.

3.5 Soft Soil and Typhoon Challenges for Chinese Offshore Wind Development

One of the challenges in Chinese offshore wind development is that the soft soils are encountered in the seas together with typhoon. Figure 35 shows the ambition of offshore wind development in China, and Fig. 36 shows a typical profile in Fujian sea. It is therefore not surprising that unconventional (from the point of view of European offshore win development) innovative type of foundations are being used in Chinese developments. Some details are provided in the next section.

3.6 Specific Challenges Due to Seismic Actions

Design of OWT structures in seismic regions required additional considerations and detailed discussions are carried out in Chap. 2 of Bhattacharya (2019). This section is relevant to the ongoing developments in Taiwan and some parts of China and Korea, India and USA. The steps in the design process are summarised as follows:

1. **Seismic hazard analysis (SHA):** This is carried out to assess the seismic risk in the lifetime of the offshore wind turbines. The work can be carried out in deterministic framework. The required outcome of the analysis that will be sensitive to the design choices are: types of faults, expected peak ground acceleration (PGA) and earthquake moment magnitude. Another aspect is the identification

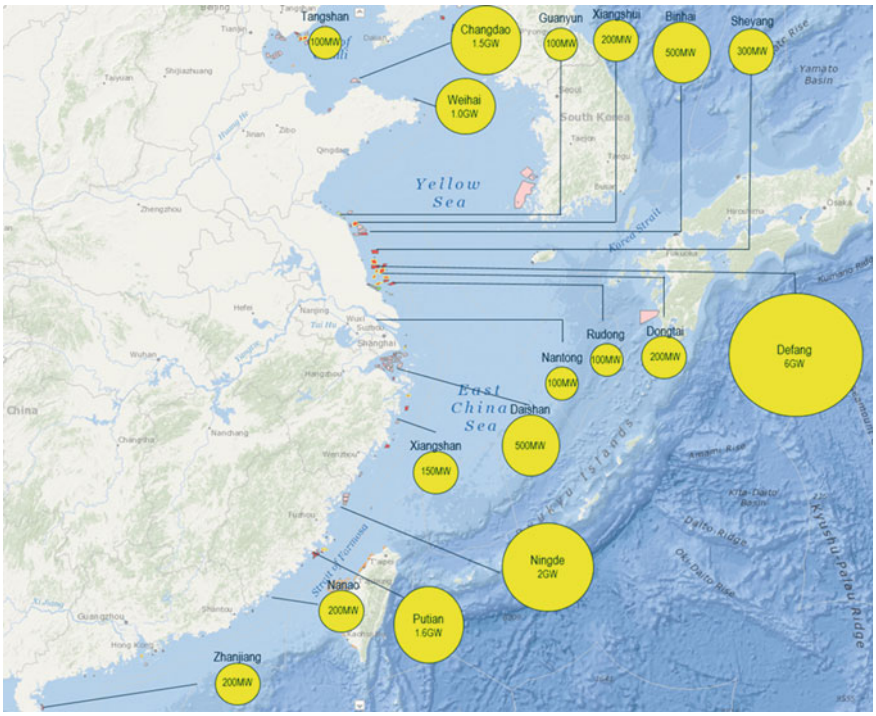

Fig. 35 Development of offshore wind in Chinese seas

of potential seismic hazards at the site and must also include potential cascading events. Some examples are:

(a) Impact of large fault movements and specially on the inter-array cables and export cables.
(b) Effect of strong shaking on the structure. One needs to also consider shaking without the effects of liquefaction of the subsurface. Therefore, inertial effects on the structure and inertial bending moment on the foundation piles.
(c) Effect of shaking coupled with effects of subsurface liquefaction. Liquefaction may lead to a rather long unsupported length of the pile and elongate the natural vibration period of the whole structure. The ground may liquefy very quickly or may take time (and is a function of ground profile and type of input motion). In such scenarios, the transient effects of liquefaction need to be considered, as it will affect the bending moment in the piles.
(d) The combined effects of shaking followed by liquefaction and subsequently tsunami.
(e) Effects of shaking and submarine landslides.
(f) The effects of earthquake sequence and suitable combinations of foreshock, mainshock and aftershock.

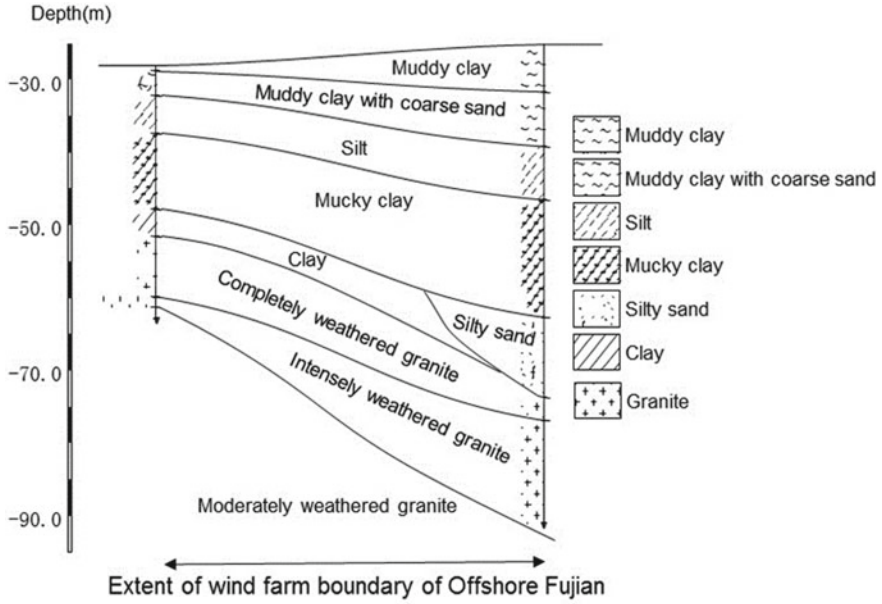

Fig. 36 Example from ground profile in Fujian Sea

2. Generation of site-specific input motion for the site and further details can be found in Chap. 3 of Bhattacharya et al. (2019). The input motion depends on the seismo-tectonics of the faulting region area. Some of the factors are: faulting pattern, distance of the site from earthquake source, wave travelling path, and the geology of the area. Strong motions generated can be either synthetic (artificially generated through spectrum compatibility) or recorded ground motion from previous earthquakes in that area.
3. Site-specific response analysis will predict how the ground will behave under the action of the input motion. This requires site-specific soil testing.
4. Dynamic SSI analysis incorporates the knowledge of the site response into the calculations.

Figure 37 shows a mechanical model of the problem where the foundation is replaced by a set of springs (K_L, K_R and K_{LR}) (Bhattacharya, 2014). During earthquake liquefaction, these springs will degrade substantially. Figure 38 shows p-y model for ULS and SLS calculations. Methods to calculate p-y springs for liquefied soils can be found in Lombardi et al. (2017a), Bhattacharya et al. (2019) and Dash et al. (2017).

Often new challenges are encountered while designing and constructing these structures. In many cases, standard foundations such as monopile or caissons are not suitable, and some form of hybrid foundations are necessary. In other cases, different structural systems are adopted. For example, in one of the Chinese developments, a group of eight piles were used, and it is named as high-rise pile cap (HRPC) as

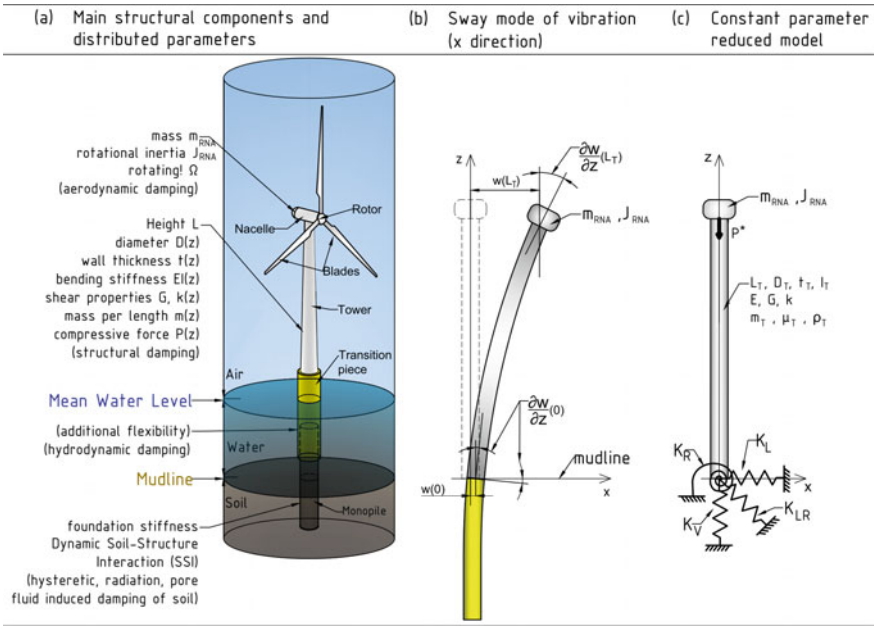

Fig. 37 Mechanical model of the structure

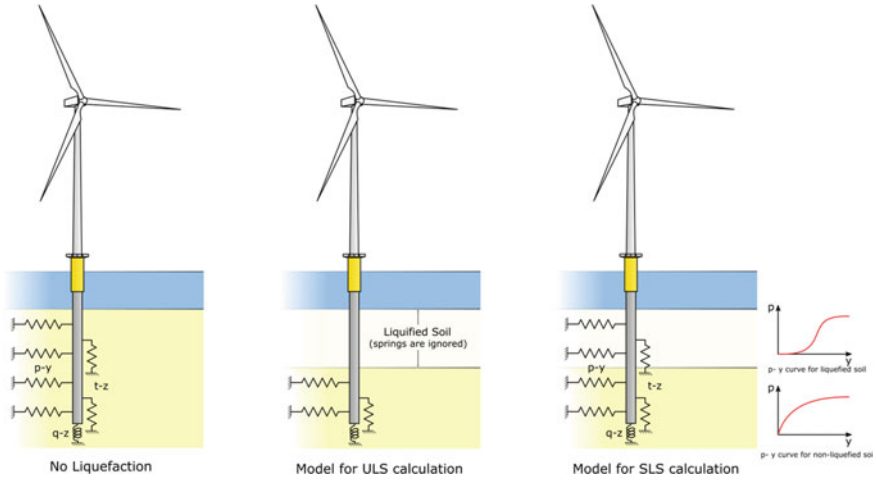

Fig. 38 p-y model for ULS and SLS calculations

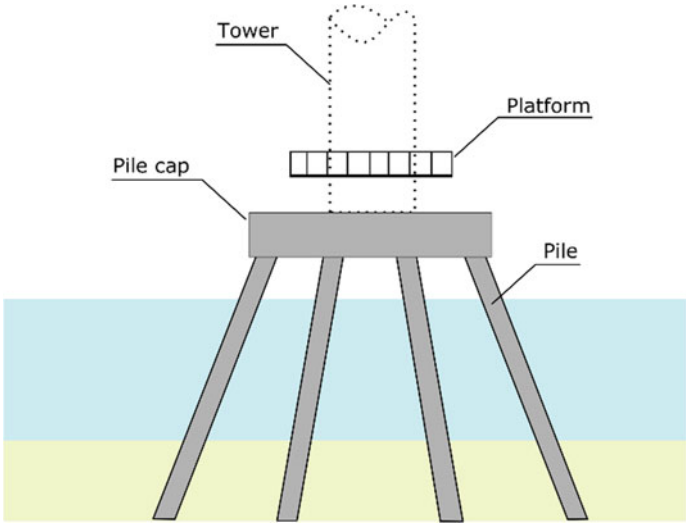

Fig. 39 HRPC type of foundation used in a Chinese offshore development project

shown in Fig. 39. As in many of the innovative cases, there will be no codes of practice or best-practice guide, and therefore, model tests (physical modelling) are often carried to verify the various design assumptions and establish reliability of the chosen method. The next section of the paper discusses various aspects of physical modelling highlighting the subtleties.

4 Physical Modelling of Offshore Wind Turbine Foundations

Foundations typically cost 25–35% of an overall offshore wind farm project, and in order to reduce the levelised cost of energy (LCOE), new innovative foundations are being proposed. However, before any new type of foundation can actually be used in a project, a thorough technology review is often carried out to de-risk it.

European Commission defines this through technology readiness level (TRL) numbering starting from 1 to 9, see Table 3 for different stages of the process together with the meanings.

One of the early studies that needs to be carried out is technology validation in the laboratory environment (TRL and 4), and in this context of foundations, it would mean carrying out tests to verify the failure mechanism, modes of vibration and long-term performance under the action of cyclic loads.

It must be realised that it is very expensive and operationally challenging to validate in a relevant environment, and therefore, laboratory-based evaluation has to

Table 3 Technology readiness level (TRL)

TRL level as European Commission	Interpretation of the terminology and remarks
TRL-1: Basic principles verified	In this step, the requirement is to show that mechanics principles are obeyed. For example, in the case of foundation, it must be checked whether the whole system is in equilibrium under the action of environmental loads
TRL-2: Technology concept formulated	In this step, it is necessary to think about the whole technology starting from fabrication to methods of installation and finally operation, maintenance (O&M) and decommissioning. In this step, it is expected that method statements will be developed
TRL-3: Experimental proof of concept	In this step, small-scale models will be developed to verify steps in TRL-1 and TRL-2. In terms of foundation, this would correspond to checking the modes of failure in ultimate limit state (ULS) and identifying the modes of vibration
TRL-4: Technology validated in laboratory	Once TRL-3 is satisfied and business decision is taken to go ahead with the development/design, it is necessary to check the technology for further details. This may correspond to long-term performance under millions of cycles of loading and checking the dynamic performance over the lifetime in relation to fatigue limit state (FLS)
TRL-5: Technology validated in relevant environment	Relevant environment may mean numerical simulation whereby close to reality analysis can be carried out. In the context of foundation, this step may use advanced soil constitutive models to verify the performance under extreme loading
TRL-6: Technology demonstrated in relevant environment	In this step, a prototype foundation is constructed and tested in an offshore environment. Critical aspects are verified
TRL-7: System prototype demonstration in operational environment	In this step, the foundation is subjected to operational loads, and the performance are monitored
TRL-8: System completed and qualified	Based on the results in TRL-7, the system can be classified as qualified or not-qualified or changes are required
TRL-9: Actual system proven in operational environment	Technology may be used in energy generation with contingency plans

be robust so as to justify the next stages of investment. From the point of view of assessment, the main issues are:

1. Verification of safe load transfer from the superstructure to the supporting ground,
2. Modes of vibration of the structural system adopted.
3. Long-term change in dynamic characteristics, i.e., change in natural frequency and damping.
4. Long-term deformation so that SLS requirements are not violated.

4.1 Suitability on Different Methods of Testing

Behaviour of offshore wind turbines involves complex dynamic-wind–wave–foundation–structure interaction, and the control system onboard the RNA hub adds further interaction. There are different established methodology, see Table 4 for carrying out testing for some part of the problem to a scientifically acceptable level:

1. Wind Tunnel can model the aerodynamics and aeroelasticity of the problem.
2. Wave tank can model the hydrodynamics part.
3. Geotechnical Centrifuge testing can identify soil-structure interaction problem.
4. Shaking table at 1-g or in a centrifuge can model the seismic soil-structure interaction (SSI).

In wind tunnel tests, aerodynamic effects are modelled efficiently and correctly (as far as practicable), and as a result, the loads on the blade and towers can be simulated. On the other hand, in the wave tank, the hydrodynamic loads on the sub-structure and scouring on the foundation can be modelled. In a geotechnical centrifuge, one

Table 4 Different forms of testing for offshore wind turbines

Types of testing	Remarks on the understanding
Wind tunnel testing	Example: Blades can be tested to show the importance of profile
Wave tank testing	Wave tank of different forms can be used to study scour, hydrodynamic loading, tsunami. In this type of testing, the wave loads on the foundations can be understood
Geotechnical centrifuge	In a geotechnical centrifuge, the stress levels in a soil can be modelled accurately (as far as practicable). However, the whole model is spun at a high rate which creates unwanted small vibrations. Therefore, the subtle dynamics of the problem is difficult to study as filtering of signals are inevitable during processing of data
Whole system modelling	Small-scale whole system modelling which can be considered as a very scale prototype pioneered by Bhattacharya et al. (2011) is one of the ways to study the overall system. This type of modelling was used to carry out TRL of self-installing wind turbine (SIWT), asymmetric tripod and details are provided in Bhattacharya et al. (2013a, b). As the system is tested in a stable floor, dynamics of the problem can be studied very well

can model the stress level in the soil, but the model package is spun at a high RPM which will bring in unwanted vibrations in the small-scale model. Ideally, a tiny wind tunnel together with a tiny wave tank onboard a geotechnical centrifuge may serve the purpose, but this is not viable and will add more uncertainty to the models than it tries to unearth. Each of the techniques has its own limitations, and these aspects must be taken into consideration while scaling the observations. Therefore, the focus of the experiments needs to be on the governing laws or mechanics or process.

A model need not be more complex, and often simple experiments can unearth the governing laws. In every type of experiments, there will be cases where the scaling laws/similitude relationships will not be satisfied (rather violated), and these must be recognised while analysing the test results. Therefore, results of scaled model tests for offshore wind turbine problems involving so many interactions (examples include: aerodynamics, hydrodynamics, damping from three different mediums: air, water and soil, control system intervention affecting misalignment of wind and wave) should not be extrapolated for prototype prediction through scaling factors (N^a where N is typically geometrical scale ratio and a is the scaling factor) (Lombardi et al. 2017b). The tests must be carried out to identify trends and behaviours and upscaling must be carried out through laws of physics through numerically or analytically or through soil-element tests (Nikitas et al. 2017). Figure 40 shows a method laid out in Bhattacharya (2019) for such purpose and also shows the usefulness of small-scale tests and its application in developing design methods.

Based on the literature of physical modelling and in the context of predicting foundation behaviour, the experimental test setup can be classified as follows:

1. '*Foundation only modelling*' referred to as Type 1 as shown schematically in Fig. 41. In this modelling, cyclic loads (symmetric or asymmetric or a combination) can be applied. The limitation of this method is that the effects of vibration of the whole system, i.e., the effects of inertia is not modelled. In other words, using the analogy (from Fig. 20), the vibration of the washing machine is not considered. If we were to translate in the context and bring the understanding of soil mechanics, the small strain vibration is ignored. For sandy soil, this phenomenon will definitely densify the soil around the foundation.
2. '*Whole system modelling with an actuator (attached with the model with rigid link)*' referred to as Type 2 as shown in Fig. 42. In this case, actuator provides lateral stiffness to the overall system, and the effect is distorting the modes of vibration.
3. '*Whole system modelling with eccentric mass actuator*' referred to as Type 3 as shown in Fig. 43. This is currently the most appropriate physical modelling technique, and details can be found in Nikitas et al. (2016). Type 3 modelling technique is scalable, can model wind-wave misalignment, can be used in field testing and can also study fatigue-related issues. Examples of testing using Type 3 technique can be found in Yu et al. (2015) and Guo et al. (2015) where long-term performance of monopiles have been studied. Xu et al. (2019) using the apparatus studied the fatigue problem.

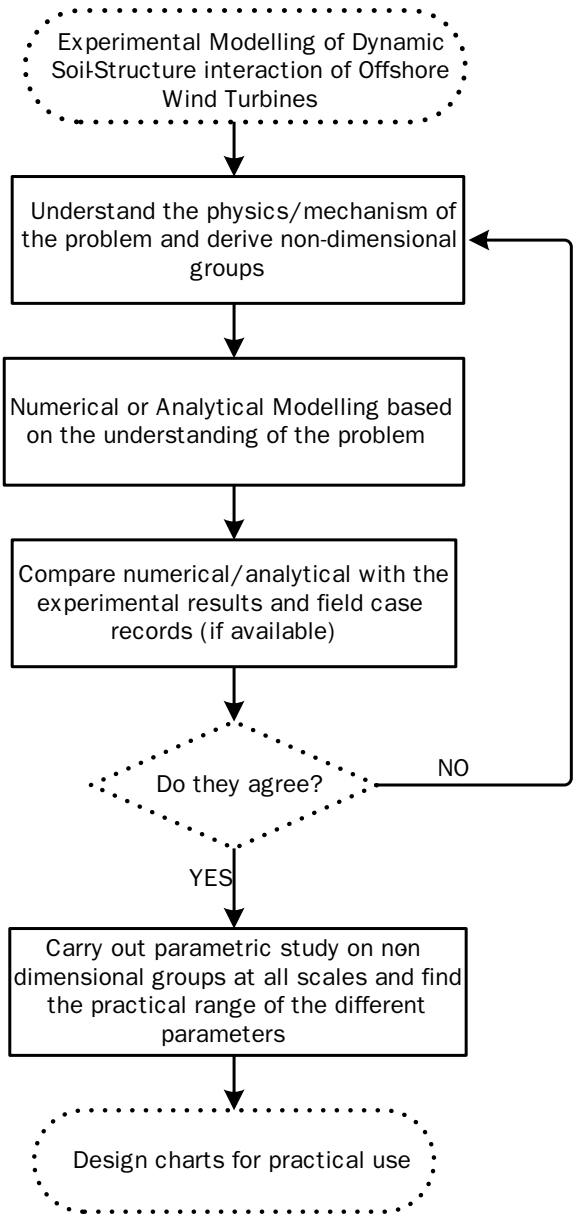

Fig. 40 Flowchart showing the usefulness of scaled laboratory testing

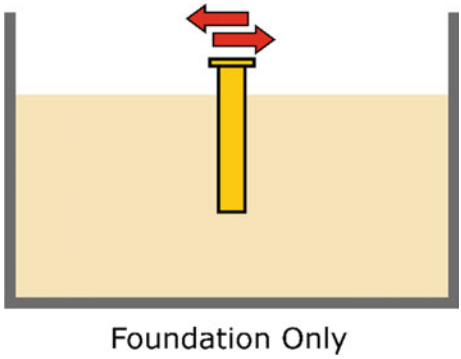

Fig. 41 'Foundation only modelling'—Type 1 technique

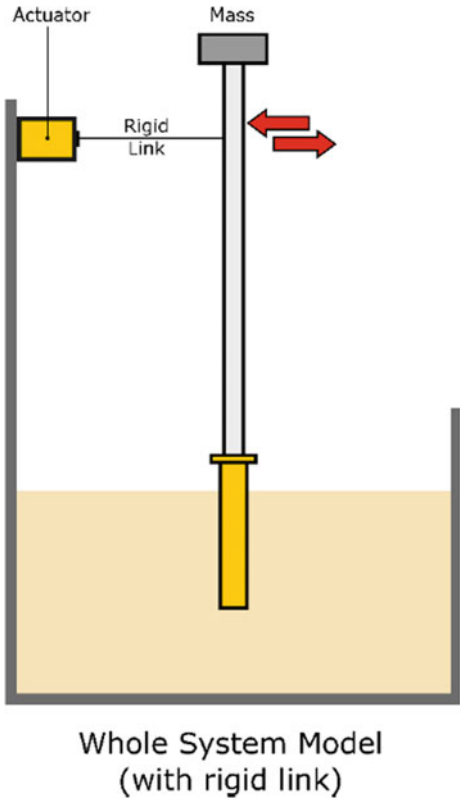

Fig. 42 Whole system model with an actuator connected to the model through a rigid link (Type 2 technique)

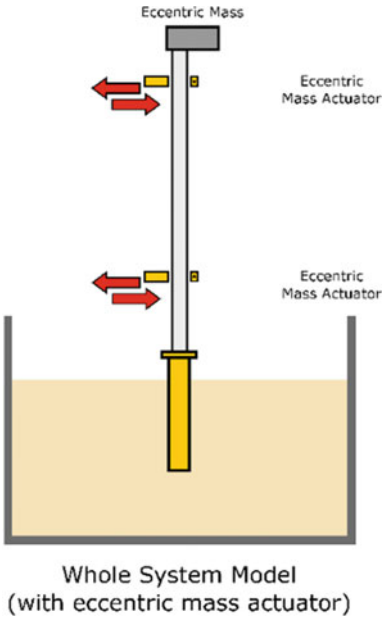

Fig. 43 Whole system modelling with eccentric mass actuator (Type 3 technique)

4.1.1 Example Application of Study of Failure Mechanisms Using Physical Modelling

One example of usefulness of physical modelling is taken here in relation to spar type floating wind turbine (see Fig. 23). Physical modelling was conducted to understand the optimum location of the padaye, i.e., where the chain will be attached to the anchor piles and what failure mechanism may be invoked, see Figs. 44 and 45. A second purpose was to see the deformation mechanism of soil around the foundation. Figure 46 notes the observed modes of failure. Knowledge from this understanding was used (without scaling any numbers) to develop a design method and can be found in Arany and Bhattacharya (2018). The method was calibrated and compared with Hywind Wind Farm project.

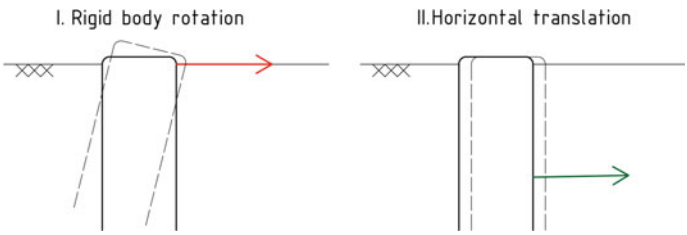

Fig. 44 To verify the above hypothesis of failure mechanism

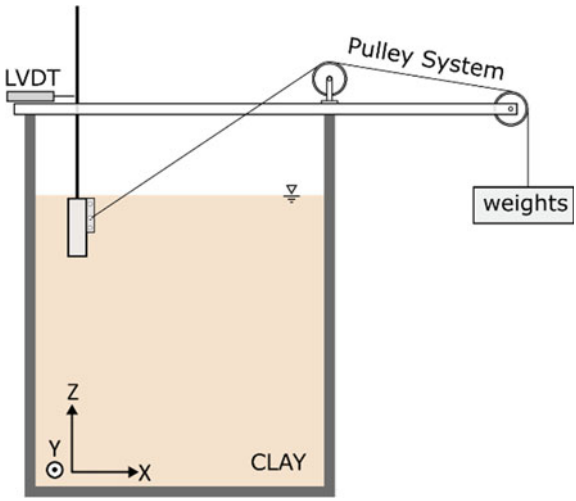

Fig. 45 Schematic of the test setup

5 Concluding Remarks

The paper provides a summary of the outlook of offshore wind in relation to tackling the grave climate change crisis. The paper summarises the challenges faced in design and construction together with potential way forward.

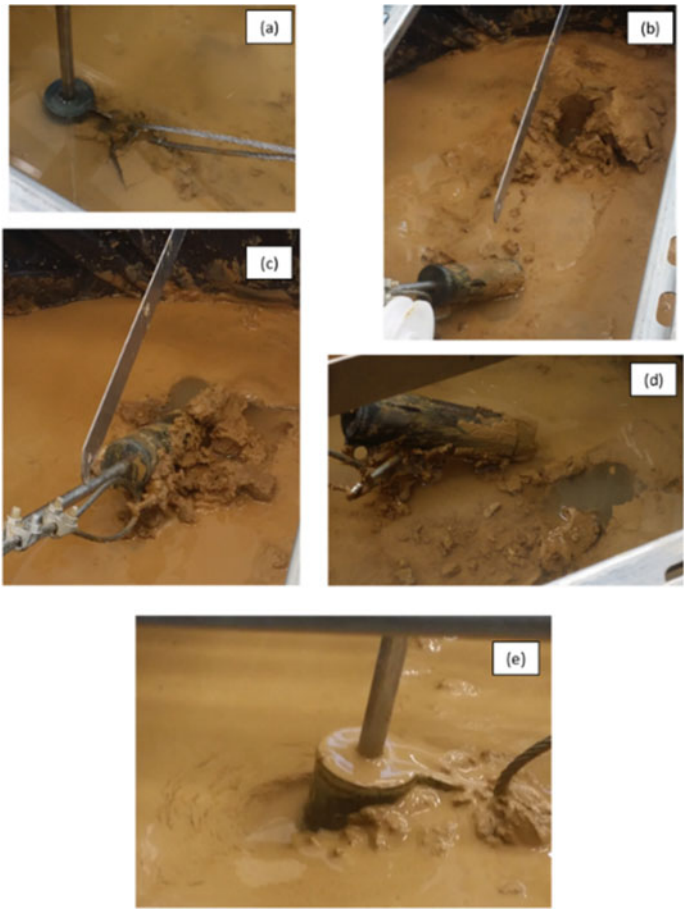

Fig. 46 Example of understanding failure mechanism of anchor for different location of padaye

References

Arany L, Bhattacharya S (2018) Simplified load estimation and sizing of suction anchors for spar buoy type floating offshore wind turbines. Ocean Eng 159:348–357

Arany L, Bhattacharya S, Adhikari S, Hogan SJ, Macdonald JHG (2015a) An analytical model to predict the natural frequency of offshore wind turbines on three-spring flexible foundations using two different beam models. Soil Dyn Earthq Eng 74:40–45. https://doi.org/10.1016/j.soildyn.2015.03.007

Arany L, Bhattacharya S, Macdonald J, Hogan SJ (2015b) Simplified critical mudline bending moment spectra of offshore wind turbine support structures. Wind Energy 18:2171–2197

Arany L, Bhattacharya S, Macdonald JHG, Hogan SJ (2016) Closed form solution of eigen frequency of monopile supported offshore wind turbines in deeper waters incorporating stiffness of substructure and SSI. Soil Dyn Earthq Eng 83:18–32. https://doi.org/10.1016/j.soildyn.2015.12.01

Arany L, Bhattacharya S, Macdonald J, Hogan SJ (2017) Design of monopiles for offshore wind turbines in 10 steps. Soil Dyn Earthq Eng 92:126–152
Bhattacharya S (2014) Challenges in the design of offshore wind turbine foundations. Engineering and Technology Reference, IET
Bhattacharya S (2019) Design of foundations for offshore wind turbines. Wiley
Bhattacharya S, Adhikari S (2012) Experimental validation of soil–structure interaction of offshore wind turbines. Soil Dyn Earthq Eng 31(5–6):805–816
Bhattacharya S, Goda K (2016) Use of offshore wind farms to increase seismic resilience of nuclear power plants. Soil Dyn Earthq Eng 80:65–68. https://doi.org/10.1016/j.soildyn.2015.10.001
Bhattacharya S, Lombardi D, Wood DM (2011) Similitude relationships for physical modelling of monopile-supported offshore wind turbines. Int J Phys Model Geotech 11(2):58–68
Bhattacharya S, Orense RP, Lombardi D (2019) Seismic design of foundations: concepts and applications. Text book. ICE Publications
Bhattacharya S, Cox J, Lombardi D, Muir Wood D (2013a) Dynamics of offshore wind turbines supported on two foundations. Geotech Eng Proc ICE 166(2):159–169
Bhattacharya S, Nikitas N, Garnsey J, Alexander NA, Cox J, Lombardi D, Muir Wood D, Nash DFT (2013b) Observed dynamic soil–structure interaction in scale testing of offshore wind turbine foundations. Soil Dyn Earthq Eng 54:47–60
Cassie P (2017) Robin Rigg-WTG decommissioning project: decommissioning project review and lessons learnt. Presentation on 25/01/2017. Renewables UK
Cui L, Bhattacharya S (2016) Soil–monopile interactions for offshore wind turbines. Proc Inst Civ Eng Eng Comput Mech 169(4):171–182
Cui L, Bhattacharya S, O'Kelly BC (2017) Discussion: soil–monopile interactions for offshore wind turbines. Proc Inst Civ Eng Eng Comput Mech 170(4):174–176
Cui L, Bhattacharya S, Nikitas G, Bhat A (2019) Macro- and micro-mechanics of granular soil in asymmetric cyclic loadings encountered by offshore wind turbine foundations. Granul Matter 21(3):73
Dash S, Rouholamin M, Lombardi D, Bhattacharya S (2017) A practical method for construction of p-y curves for liquefiable soils. Soil Dyn Earthq Eng 97:478–481
De Risi R, Bhattacharya S, Goda K (2018) Seismic performance assessment of monopile-supported offshore wind turbines using unscaled natural earthquake records. Soil Dyn Earthq Eng 109:154–172
Guo Z, Yu L, Wang L, Bhattacharya S, Nikitas G, Xing Y (2015) Model tests on the long-term dynamic performance of offshore wind turbines founded on monopiles in sand. ASME J Offshore Mech Arct Eng 137(4). https://doi.org/10.1115/1.4030682
Hu W-H, Thöns S, Said S, Rücker W (2014) Resonance phenomenon in a wind turbine system under operational conditions. In: Proceedings of the 9th international conference on structural dynamics, EURODYN 2014 Porto, Portugal, 30 June–2 July 2014, pp 3619–3626
Jalbi S, Nikitas G, Bhattacharya S, Alexander N (2019) Dynamic design considerations for offshore wind turbine jackets supported on multiple foundations. Marine Structures 67:102631
Jalbi S, Arany L, Salem A, Cui L, Bhattacharya S (2019) A method to predict the cyclic loading profiles (one-way or two-way) for monopile supported offshore wind turbines. Marine Structures 63:65–83
Lombardi D, Dash SR, Bhattacharya S, Ibraim E, Muir Wood D, Taylor CA (2017a) Construction of simplified design—curves for liquefied soils. Géotechn 67(3):216–227
Lombardi D, Bhattacharya S, Nikitas G (2017b) Physical modelling of offshore wind turbine model for prediction of prototype response, Chap 17. In: wind energy engineering: a handbook for onshore and offshore wind turbines. Academic Press. ISBN 9780128094518
Letcher T (2017) Why wind energy?, Chap 1. In: Wind energy engineering: a handbook for onshore and offshore wind turbines. Hardcover. Elsevier. ISBN: 9780128094518
Nikitas G, Vimalan NJ, Bhattacharya S (2016) An innovative cyclic loading device to study long term performance of offshore wind turbines. Soil Dyn Earthq Eng 82:154–160

Nikitas G, Arany L, Aingaran S, Vimalan J, Bhattacharya S (2017) Predicting long term performance of offshore wind turbines using cyclic simple shear apparatus. Soil Dyn Earthq Eng 92:678–683

Nikitas G, Bhattacharya S, Vimalan N, Demirci HE, Nikitas N, Kumar P (2018) Wind power: a sustainable way to limit climate change, Chap 10. In: Managing global warming. Academic Press. ISBN 9780128141045

Nikitas G, Bhattacharya S, Vimalan N (2020) Wind Energy, Chap 16. In: Future energy (3rd Edition): Improved, sustainable and clean options for our planet. Academic Press. ISBN 9780081028865

Xu Y, Nikitas G, Zhang T, Han Q, Chryssanthopoulos M, Bhattacharya S, Wang Y (2019) Support condition monitoring of offshore wind turbines using model updating techniques. In: Structural health monitoring

Yu L, Wang L, Guo Z, Bhattacharya S, Nikitas G, Li L, Xing Y (2015) Long-term dynamic behavior of monopile supported offshore wind turbines in sand. Theor Appl Mech Lett 5(2):80–84

Evaluation of Offshore Pile Capacity and Pile Integrity Using Dynamic Pile Monitoring Services

Ramesh Gangisetti and C. R. Parthasarathy

1 Introduction

Offshore installation contractors often limit the pile monitoring scope to one or two piles in a foundation system of several piles and might end up with refusal on a pile with no dynamic measurements due to unexpected well-cemented soils or rock presence. Hindcast of soil model for pile capacity of refused pile can be done by using either shaft resistance from CAPWAP of adjacent monitored piles or reduced soil static strength model and matching the observed blowcounts in GRLWEAP. Another important aspect at the time of refusal driving through rock is the evaluation of driving stress at toe to be able to terminate the driving without overstressing, which otherwise might cause buckling. This is more critical if a rock is present at shallow depths with little or no shaft resistance. Pile driving termination in cemented soil/rock without toe buckling is possible by dynamic pile monitoring so that pile advancing methods such as drill-drive-drill and insert pile can be employed to advance the pile to the intended final penetration.

Substrata at offshore sites in the Middle East predominantly consist of dense to very dense calcareous silica sands, calcarenite, gypsum, and hard calcareous clays. For granular soils, empirical equations (Dutt et al. 1985; Kolk 2000) are available based on $CaCO_3$ content to modify limiting skin friction and limiting end bearing values. The SRD in such soils may be more than ten times the static capacity (Stevens and Al-Shafei 1996), and for static capacity calculations, the limiting unit skin friction and end bearing values are increased if $CaCO_3$ and fines content is less than 25% and 15%, respectively.

R. Gangisetti (✉) · C. R. Parthasarathy
Sarathy Geotech and Engineering Services Pvt. Ltd., Bengaluru, Karnataka, India
e-mail: ramesh@sarathygeotech.com

S. Haldar et al. (eds.), *Advances in Offshore Geotechnics*, Lecture Notes in Civil Engineering 92, https://doi.org/10.1007/978-981-15-6832-9_7

2 Jacket A

This jacket in offshore Southeast Asia is supported by eight (8) steel skirt piles (4 nos each of gripper and non-gripper piles). The skirt piles are 106.7 m long with 2.134 m OD and uniform wall thickness of 50 mm. A 2 m long and 60 mm wall thick driving shoe is provided. The design target penetration is 85 m below seabed. The impact hammers mobilized are IHC S-500 and IHC S-800. The substrata at the location are summarized in Table 1.

Except one (1 nos) gripper skirt pile which refused initially with IHC S-500 at 44 m and again with IHC S-800 at 63.5 m, all the other skirt piles were driven to the design penetration without any incident. The gripper pile, refused at 63.5 m during continuous driving with IHC S-800 at 95% efficiency, was not instrumented for dynamic pile monitoring as the scope of pile monitoring had been complete with the monitoring of adjacent non-gripper pile driven to design penetration without any incident. In the absence of pile monitoring data, the gripper pile acceptance at the refused depth of 63.5 m became an issue. The soil plug was jetted out and found to be consisting of conglomerate rock pieces at about 40 m depth. After the plug removal up to 40 m, the pile was re-struck with IHC S-800 with 95% efficiency and found "Nil" pile movement resulting in refusal again. It was reasoned that the pile might have got plugged with the rock pieces at some penetration after 40 m and eventually

Table 1 Substrata, Jacket A location

Sl. No.	Layer depth (m)		Soil type	Undrained shear strength (kPa)		Effective unit weight (kN/m^3)	Φ (°)
	From	To		From	To		
1	0.00	6.70	Clay	2	15	4.9	–
2	6.70	17.20	Sand	–	–	9.5	20
3	17.20	19.40	Clay	40	40	10.5	–
4	19.40	24.30	Sand	–	–	8.7	20
5	24.30	26.80	Clay	60	60	10.3	–
6	26.80	30.70	Clay	110	110	10.3	–
7	30.70	33.00	Sand	–	–	10.3	35
8	33.00	34.00	Clay	80	80	10.3	–
9	34.00	36.10	Clay	110	110	10.3	–
10	36.10	38.90	Sand	–	–	10.2	25
11	38.90	70.00	Clay	120	150	10.1	–
12	70.00	72.00	Sand	–	–	11.3	30
13	72.00	78.00	Clay	200	200	9.9	–
14	78.00	80.00	Sand	–	–	9.0	30
15	80.00	94.30	Sand	–	–	9.0	30

Fig. 1 Conglomerate rock pieces

refused at 63.5 m due to high end bearing. The pictures of rock pieces found in the soil plug are presented in Fig. 1.

Hindcast of soil model for pile capacity of refused gripper pile using pile monitoring data of adjacent non-gripper pile and hammer console readings was proposed. The unit skin friction profile computed using CAPWAP on the pile monitoring data of the adjacent non-gripper pile was input to GRLWEAP. The gripper pile was modeled with the unplugged toe up to 44 m and plugged toe from 44 to 63.5 m. The observed blowcounts of gripper pile were then matched by adjusting the unit end bearing values for the hammer efficiencies obtained from hammer console. A 10% reduction in energy transfer to the pile, as observed from pile monitoring data of non-gripper pile, was considered. The observed versus computed blowcounts with the pile penetration graph is presented in Fig. 2.

The back-calculated shaft and toe resistances from GRLWEAP at 63.5 m are 7.7 and 63.2 MN. The shaft resistance represents the continuous driving as the unit skin friction profile obtained from continuous driving of adjacent non-gripper was used for blowcount matching. Therefore, a setup factor of 2.59, measured on non-gripper during restrike test after 1.92 days of delay, can be applied to shaft resistance of gripper pile to include setup effects. It is known that, during pile refusal, it is possible to mobilize a resistance more than the impact force at the pile top. The maximum imparted pile force measured from pile monitoring on non-gripper during restrike was about 40 MN with S-800 at 50% efficiency. Apparently, the IHC S-800 could have mobilized at least 40 MN of end bearing on gripper pile at 63.5 m during refusal with 95% efficiency. After applying a setup factor of 2.59 to computed shaft resistance (2.59×7.7 MN) and limiting the computed toe resistance of 63.3–40 MN, the total computed resistance of 60 MN was found to be more than the required ultimate pile capacity in compression. The piles at this location are not required to support tension loads.

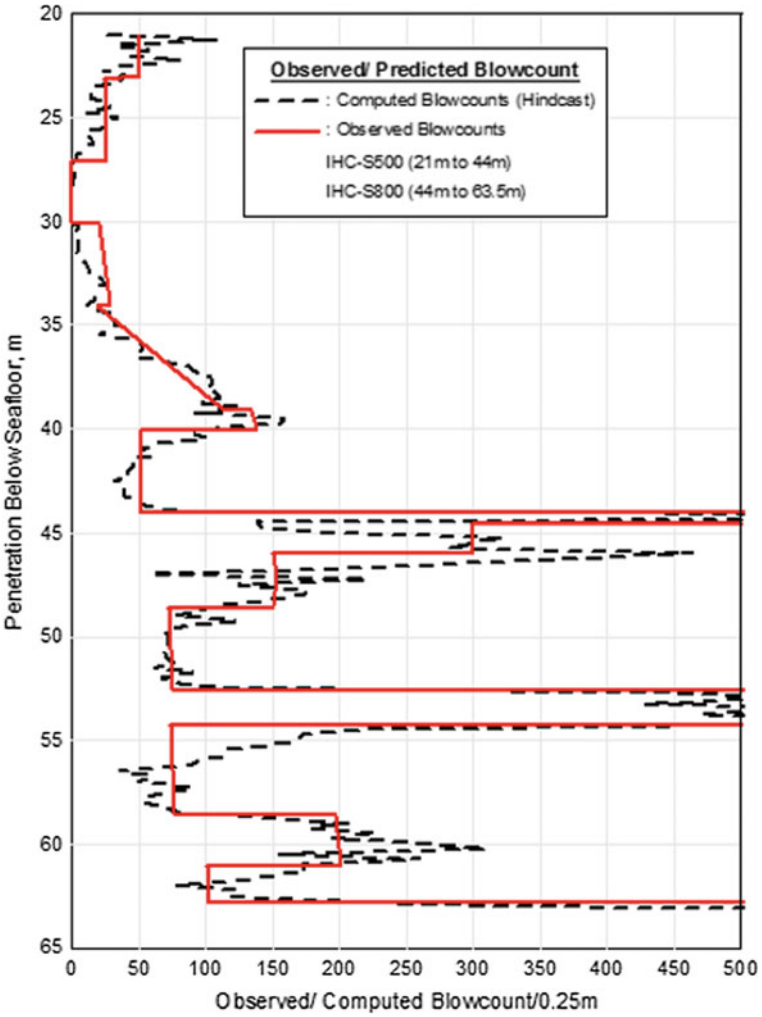

Fig. 2 Observed/computed blowcounts

3 Jacket B

This jacket in the offshore Middle East is supported on four steel piles. The 1.214 m OD steel pipe piles with uniform wall thickness of 38.1 mm and a 3 m long, 44.4 mm thick driving shoe, were planned to be driven in two sections to a designed vertical penetration of 67 m. The substrata at this location consist of carbonate sands, calcareous clays and very weak to weak gypsum layers at 9, 14.6 and 22.8 m. The gypsum layer at 14.6 m is 4.5 m thick. The substrata are summarized in Table 2.

Table 2 Substrata, Jacket B location

Sl. No.	Layer depth (m)		Soil type	Undrained shear strength (kPa)		Effective unit weight (kN/m^3)	Φ (°)
	From	To		From	To		
1	0.00	1.30	Sand	–	–	7.6	30
2	1.30	1.80	Sand	–	–	9.9	40
3	1.80	2.30	Sand	–	–	9.9	25
4	2.30	4.50	Sand	–	–	9.7	32.5
5	4.50	6.70	Sand	–	–	9.3	27.5
6	6.70	9.00	Clay	185	185	9.7	–
7	9.00	10.50	Rock	–	–	12.0	30
8	10.50	11.00	Sand	–	–	9.0	32.5
9	11.00	12.20	Clay	195	195	9.8	–
10	12.20	14.60	Clay	265	265	8.9	–
11	14.60	19.10	Rock	–	–	10.3	30
12	19.10	20.60	Clay	395	395	9.0	–
13	20.60	22.80	Clay	350	350	8.0	–
14	22.80	24.30	Rock	–	–	12.0	30
15	24.30	40.00	Clay	425	425	10.0	–
16	40.00	42.80	Clay	235	235	10.0	–
17	42.80	52.30	Clay	235	235	9.2	–
18	52.30	55.60	Sand	–	–	10.0	35
19	55.60	59.10	Clay	300	300	10.0	–
20	59.10	60.30	Sand	–	–	10.0	40
21	60.30	63.60	Clay	200	200	8.4	–
22	63.60	67.00	Clay	300	300	10.0	–

Premature pile refusal at any of these gypsum layers was predicted. It was planned to drill-out and insert smaller diameter pile up to the design penetration and grout the annulus if premature refusal occurred during pile driving. Pile monitoring was employed with a primary objective to monitor the pile driving stresses while driving through gypsum layers and terminate the driving safely without toe buckling if refusal had occurred. The impact hammer IHC S-500 was used to drive the piles. There was some increased driving resistance while driving in gypsum layer at 9 m, but the pile could pass through. However, as predicted, all piles experienced very high end bearing in gypsum layer felt at about 14.25 m with an abrupt increase in blowcounts from 30 to 530 bl/0.25 m at 14.75 m. The blowcounts versus penetration graphs for all piles are presented in Fig. 3.

As the driving behavior of all piles is similar, pile monitoring parameters of one pile A1 is discussed here. Pile monitoring indicated a sharp increase in-pile bottom stress from about 75 to 140 MPa at 14.25 m, while the pile top stress was about

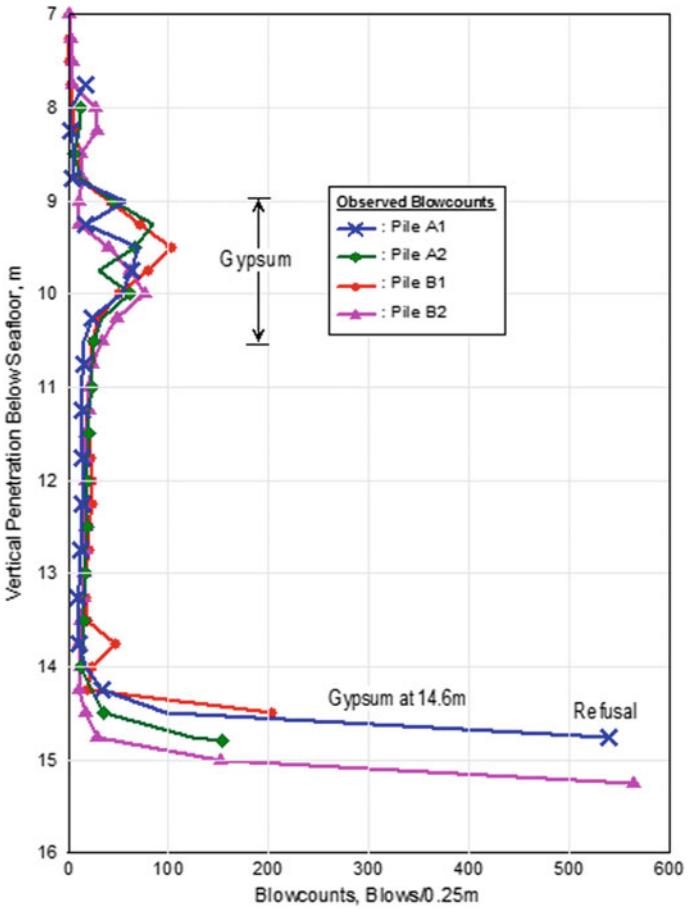

Fig. 3 Observed blowcounts

160 MPa, when the energy transferred was about 250 kJ. Since the measured stresses were far below the allowable driving stress of 310.5 MPa (90% of yield strength of pile material), it was decided to increase the energy of hammer blows gradually. Further increase in-pile bottom stress from 140 to 240 MPa and pile top stress from 160 to 210 MPa was observed over another 0.25 m penetration, when the hammer energy gradually increased from 250 to about 450 kJ in 500 blows. Pile driving was stopped at this point as the pile bottom stress was about 77% of the 310.5 MPa. The sharp increase in bottom stress indicated the presence of gypsum. Although the driving stresses at pile top and bottom are within the limit, it was required to check if the stresses were exceeding the limit elsewhere along the pile. Also, the pile bottom stress from PDA may be an overestimate as the CASE method uses an empirical equation to estimate compression force at the bottom. For an accurate estimation of in-pile stresses throughout the length, CAPWAP computer program was

used to determine the soil system along the shaft and toe that caused the resistance. The CAPWAP estimated maximum in-pile driving compression stress of 290 MPa occurred at about 4 m from pile toe. The measured pile top and pile bottom stresses versus penetration and the estimated in-pile compression stresses versus pile length graphs are presented in Figs. 4 and 5.

The compression reflection waves due to very high end bearing and increase in impedance at pile shoe would have been added to the incident impact compression waves resulting in high compression stress near the pile bottom. As the maximum estimated driving stress was close to the allowable limit, it was decided to terminate the pile driving and proceed with the pile advancing method of plug drill-out and insert the smaller diameter pile up to the design penetration and grout the pile annulus.

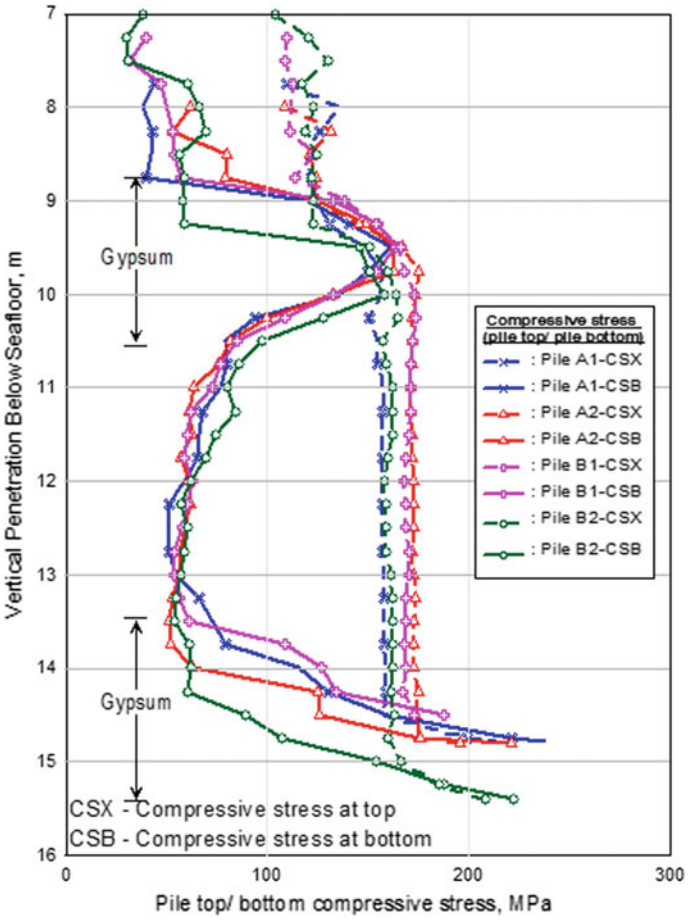

Fig. 4 Measured compressive stress at pile top and bottom

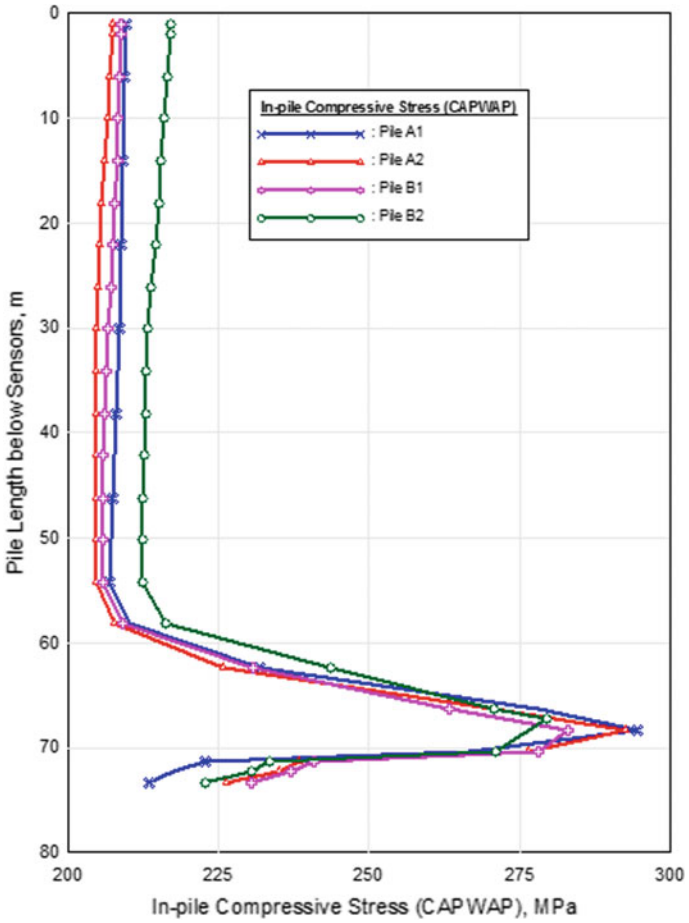

Fig. 5 In-pile compressive stress (CAPWAP)

4 Jacket C

This jacket in the offshore Middle East is supported on 4 steel piles. The 1.214 m OD steel pipe piles with uniform wall thickness of 38.1 mm and a 3 m long, 44.4 mm thick driving shoe, were planned to be driven in two sections to a designed vertical penetration of 61 m and 50 m, respectively, for Row-A and Row-B piles. The substrata at this location consist of alternate dense to very dense calcareous silica sand and very stiff to hard calcareous clay up to 25.4 m followed by hard calcareous clay up to 75 m. The substrata are summarized in Table 3.

Static pile capacity was estimated using API RP2A (2000) with increased limiting unit skin friction and end bearing as per Rastanajib method and considering the effect of $CaCO_3$ (Dutt et al. 1985; Kolk 2000). The observed blowcounts were more than

Table 3 Substrata, Jacket C location

Sl. No.	Layer depth (m)		Soil type	Undrained shear strength (kPa)		Effective unit weight (kN/m^3)	Φ (°)
	From	To		From	To		
1	0.00	1.10	Clay	1	2	9.9	–
2	1.10	4.79	Sand	–	–	9.9	21
3	4.79	7.21	Clay	70	70	9.0	–
4	7.21	11.82	Clay	310	310	9.0	–
5	11.82	13.82	Sand	–	–	9.9	32.5
6	13.82	16.13	Clay	330	330	9.7	–
7	16.13	20.64	Sand	–	–	9.0	32.5
8	20.64	22.99	Clay	180	180	10.6	–
9	22.99	25.44	Sand	–	–	10.5	35
10	25.44	29.25	Clay	400	400	9.4	–
11	29.25	35.06	Clay	350	350	9.5	–
12	35.06	39.97	Clay	220	220	8.8	–
13	39.97	42.49	Clay	340	340	10.2	–
14	42.49	54.7	Clay	340	430	9.7	–
15	54.7	61.1	Clay	430	430	10.4	–

the predicted blowcounts for 100% static capacity up to about 40 m. The CAPWAP estimated capacity exceeded the static pile capacity at the end of driving of P1 section. The blowcounts were found to be falling within the predicted blowcounts range for continuous driving from about 50 m to final penetration of 61 m. The CAPWAP estimated capacity at final penetration was about 50% of static capacity, and during the restrike conducted after 20 h delay, the CAPWAP estimated capacity was found to be slightly more than the static capacity. The predicted versus observed blowcounts and the predicted versus CAPWAP SRDs graphs are presented in Figs. 6 and 7.

5 Jacket D

This jacket located in Southeast Asia is supported by a caisson pile driven in three sections. The 1.524 m diameter and 35–60 mm wall thick caisson pile was driven to a design penetration of 98 m below seabed successfully using impact hammer IHC S-280. Pile monitoring was performed for the last two caisson sections CN-2 and CN-3. The substrata at this location consist of soft to firm clay layers up to 48 m followed by very stiff to hard clay layers up to 101.2 m. The substrata are summarized in Table 4.

Pile monitoring data of both CN-2 and CN-3 showed a beta line, indicating structural damage (Likins et al. 2014) , with beta values ranging from 77% to 82% and

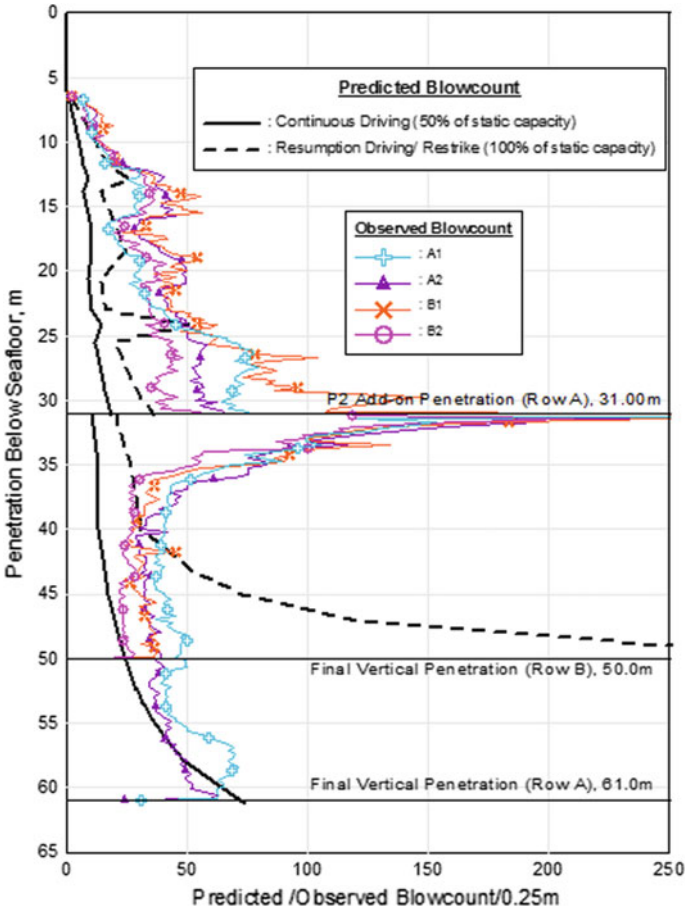

Fig. 6 Predicted/observed blowcounts

84% to 86%, respectively, during continuous driving at a depth of about 15.5–17.5 m from top of CN-1 section. The beta value further improved to 87–90% during restrike test. Pile makeup drawing indicated no planned change in wall thickness at the location where beta line was shown. Also, the beta line was shown right from the initial blow on CN-2 indicating the damage was not due to high pile driving stresses. The improved beta value as the driving progressed was attributed to increased soil resistance, which may have partially masked the wave reflections from the damage. The

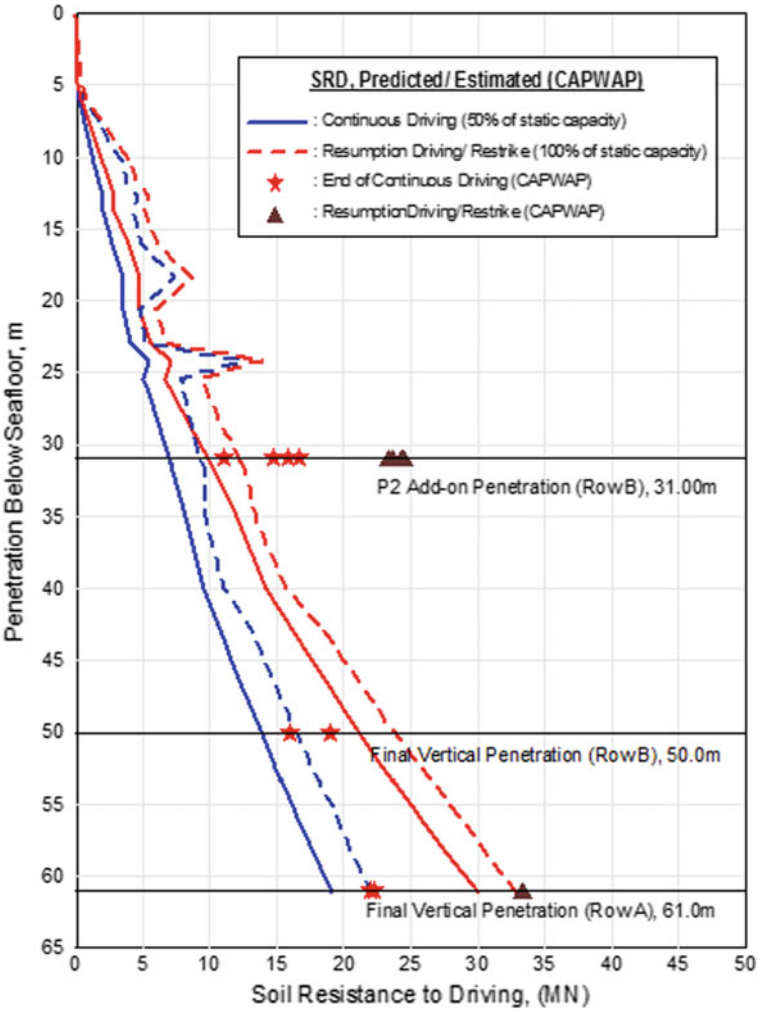

Fig. 7 Static resistance to driving (predicted/CAPWAP)

magnitude of beta value (77–82%) during CN-2 driving classifies the damage as moderate. The structural damage (possibly, a girth weld defect) may have happened during the fabrication stage. The force-velocity curves from PDA indicating beta line during continuous driving of CN-2 and CN-3, and during restrike test are presented in Figs. 8, 9 and 10.

Table 4 Substrata, Jacket D location

Sl. No.	Layer depth (m)		Soil type	Undrained shear strength (kPa)		Effective unit weight (kN/m^3)
	From	To		From	To	
1	0.00	2.60	Clay	0	2	6.2
2	2.60	15.0	Clay	6	12	7.0
3	15.0	18.3	Clay	19	21	9.9
4	18.3	23.0	Clay	26	28	9.2
5	23.0	25.2	Clay	26	28	8.9
6	25.2	33.1	Clay	25	29	8.4
7	33.1	41.3	Clay	27	30	8.0
8	41.3	44.00	Clay	40	42	9.6
9	44.00	48.00	Clay	37	39	9.4
10	48.00	52.00	Clay	210	210	10.5
11	52.00	68.20	Clay	130	130	8.9
12	68.20	77.20	Clay	100	100	9.4
13	77.20	81.8	Clay	140	140	7.8
14	81.8	89.30	Clay	160	160	8.0
15	89.30	96.8	Clay	145	145	8.2
16	96.8	101.2	Clay	190	190	9.3

6 Conclusions

Hindcast of soil model for pile capacity estimation for the refused pile, which is not dynamically monitored, can be done by using adjacent pile monitoring data, observed blowcounts and hammer console readings for pile acceptance or rejection.

Pile toe stresses during driving in cemented soils or rock can be monitored and in-pile stresses along the pile can be estimated using CAPWAP for pile termination.

Pile damage occurred in the fabrication stage can be evaluated during pile driving for damage location and its quantification for quality assurance.

Offshore sites in the Middle East, unlike the sites in Southeast Asia, may offer an SRD up to static capacity during continuous driving for shallow penetrations up to 35 m. And, during resumption driving and restrike test, the SRD may exceed the static capacity.

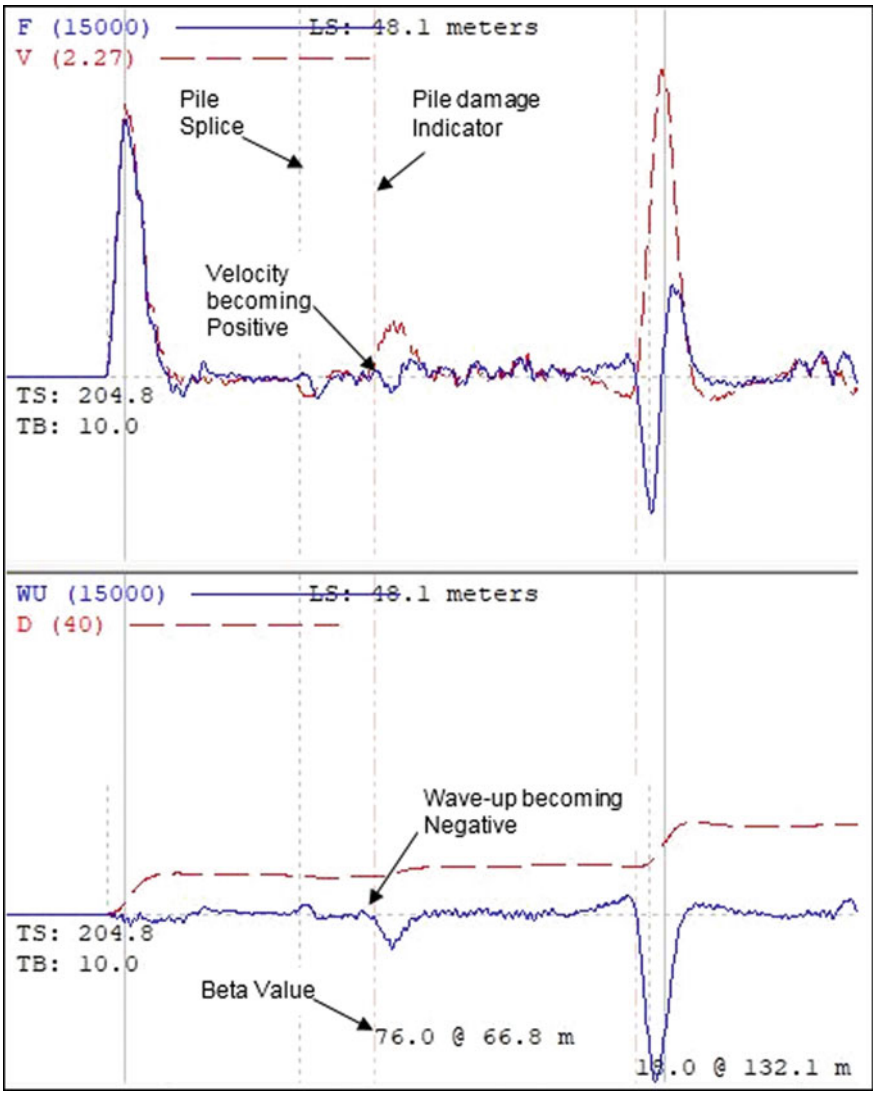

Fig. 8 F-V curve, begin of drive, caisson pile (CN-2)

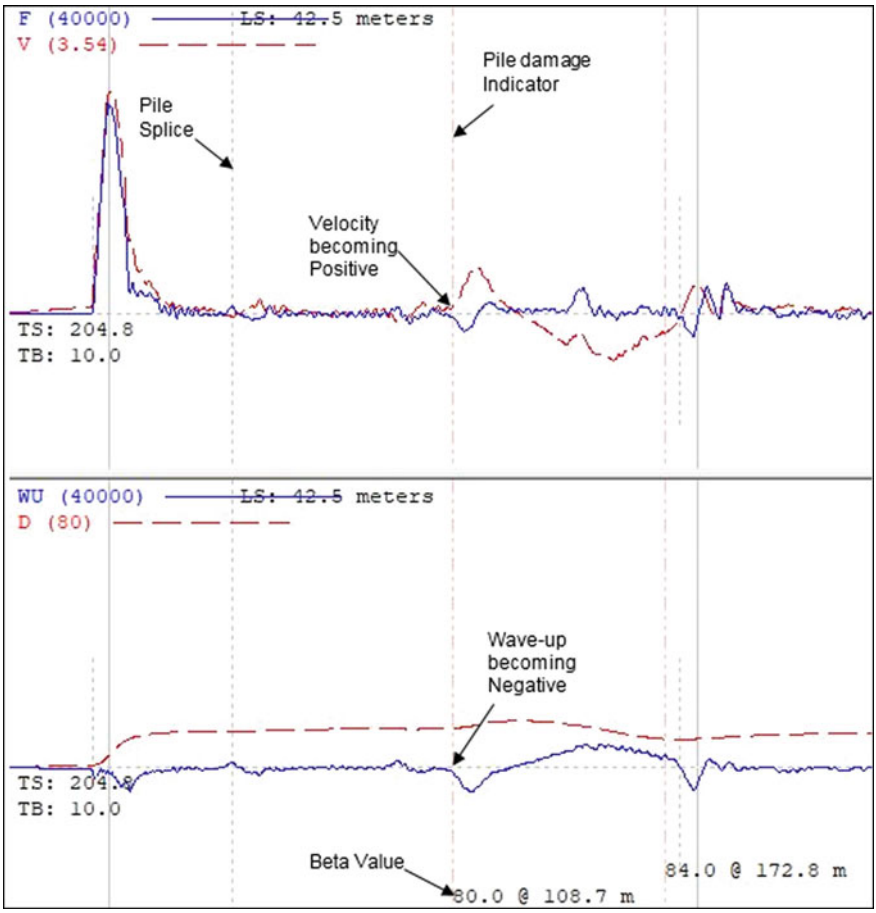

Fig. 9 F-V curve, begin of drive, caisson pile (CN-3)

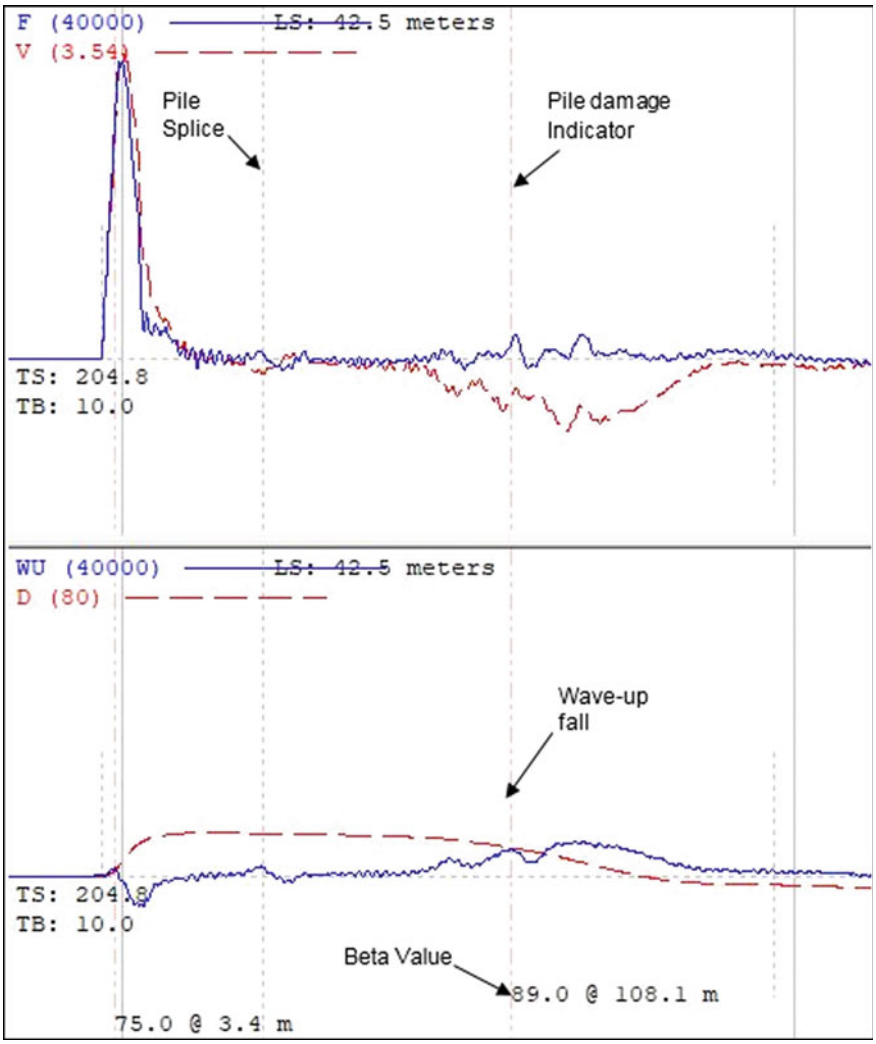

Fig. 10 F-V curve, restrike, caisson pile (CN-3)

References

API RP-2A (2000) Recommended practice for planning, designing and constructing fixed offshore platforms—working stress design

Dutt RN, Moore JE, Mudd RW, Rees TE (1985) Behaviour of piles in granular carbonate sediments from offshore Philippines. In: Proceedings, 17th offshore technology conference, vol 1, Houston, pp 73–82

Kolk HJ (2000) Deep foundations in calcareous sediments. In: Al-Shafei KA (ed) Proceedings of the 2nd international conference on engineering for calcareous sediments, vol 2, Bahrain, pp 313–344

Likins G, Rausche F (2014) Pile damage prevention and assessment using dynamic monitoring and the beta method. In: From soil behavior fundamentals to innovations in geotechnical engineering. ASCE geo-institute geotechnical special publication no 233. Reston, pp 428–442

Stevens RF, Al-Shafei KA (1996) The applicability of the Ras Tanajib pile capacity method to long offshore piles. In: 28th annual offshore technology conference, Houston, 6–9 May 1996. Proceedings, vol 1, OTC paper 7974, pp 171–180

Geotechnical Characterisation of Krishna Godavari Basin Sediments, Offshore Eastern India

T. M. Chang, X. Long, R. K. Ghanekar, S. Gamidi, A. Srivastava, R. Gunasekharan, P. Lakshminarayana, and S. Namburi

1 Introduction

A recent offshore geotechnical site investigation was carried out offshore India to evaluate the nature and mechanical properties of the soil to aid the design and future installation of subsea structures for a future development in the Krishna Godavari (KG) Basin, Bay of Bengal. This paper presents the key results and findings of the site investigation and subsequent comprehensive onshore laboratory testing and interpretation.

2 Geological Setting

The study area is located in the Krishna Godavari (KG) Basin off the east coast of India, which is within the eastern extended margin of India's peninsular stable continental region (SCR). The NNW-SSE-oriented Pranhita-Godavari Graben (PGG) or Godavari Rift is to the north of the study area and terminates at a NE-SW trending extended crustal terrane that forms the KG basin. The area is characterised by low rates of seismic activity. The Indian eastern continental margin within 500 km of

T. M. Chang (✉)
Fugro, Perth, WA, Australia
e-mail: t.chang@fugro.com

X. Long
Fugro, Houston, TX, USA

R. K. Ghanekar · S. Gamidi · A. Srivastava
Institute of Engineering and Ocean Technology, Navi Mumbai, Maharashtra, India

R. Gunasekharan · P. Lakshminarayana · S. Namburi
Oil and Natural Gas Corporation, East Offshore Asset, Kakinada, Andhra Pradesh, India

S. Haldar et al. (eds.), *Advances in Offshore Geotechnics*, Lecture Notes in Civil Engineering 92, https://doi.org/10.1007/978-981-15-6832-9_8

the site has seen only moderate magnitude earthquakes (Mw < 6) and low levels of seismic activity.

The submarine physiography offshore the Godavari Delta is subdivided into four major provinces: Shelf and Shelf Break, Slope, Toe-Thrust and Anticline, and Lower Slope. The Shelf and Shelf Break Province, as well as the upper slope within the Slope Province, are considered very dynamic areas due to the proximity of the Godavari River and Delta. The Godavari River is a monsoon-driven system and exhibits a very high sedimentation rate. This river has one of the largest sediment loads in India and is also considered one of the most turbid rivers. Subsidence onshore is comparable to that observed in other large rivers, such as the Nile or Yangtze; however, it is important to note that hundreds of dams have been constructed on the river over the past four decades, which has decreased the sediment discharge to the delta. Based on the analysis of satellite imagery and onshore coring data by Rao et al. (2015), there has been considerable coastal erosion of the Godavari Delta during the past four decades. Monsoon, cyclone/typhoon, and tsunami events have all affected the area in the recent past.

The site traverses a wide range of geologic features and conditions that are prevalent within each of the physiographic provinces. Water depths within the study area ranged between approximately 13 and 1559 m. The study area seafloor is generally characterised by the following types of features: sediment pathways, minor channels, moderate seafloor amplitudes, seafloor expression of blocky mass transport deposit, slumps, pathway margin mass movement, undulating seafloor, area of failures related to subsurface gas front, sediment wave areas, seafloor scarps, erosional scars, gullies, scoured irregular seafloor, seafloor and near seafloor fault scarps (normal and reverse), pockmark clusters, seafloor hydrate mounds, mud volcanoes, and elongated depressions. Several man-made features were also present in the area, consisting of drag scars, well mud splays, existing wells, possible wellheads and seafloor debris.

3 Summary of Fieldwork

The site investigation fieldwork was carried out from an 83 m, dynamic positioning (DP) Class 2 dedicated geotechnical drilling vessel capable of working in both downhole drilling and seabed modes in water depths up to 3000 m.

The investigation comprised offshore geotechnical and geological data acquisition through seabed and downhole mode sampling and in situ testing techniques. The drilling method consisted of a straight flush rotary system. Drilling was performed through a centre moonpool using a top drive power swivel with 5½″ standard drill pipes. Sampling was conducted through the open centre bit. Seawater was used to clean and stabilise the borehole when drilling in cohesive layers, while a mixture of bentonite or barite and drill water was used to flush or clean the hole.

For the seabed mode sampling, box corer (BC) and large gravity piston corer (LGPC) were deployed from an A-frame. Seabed mode piezocone penetrometer tests (PCPT), T-bar tests (TBT) and cyclic T-bar tests (CTBT) were conducted.

The soil samples from downhole mode were recovered by wire line push (WIP) or piston sampling (PIS) techniques either by using thin-walled tubes (76 mm OD, 72 mm ID) or thick-walled tubes (80 mm OD, 72 mm ID). Very soft to soft surficial clays were sampled using thin-walled tubes, fitted with 3 m PVC sample liner with 70 mm OD and 67 mm ID. The downhole PCPTs were performed using a 10 cm^2 base area, 60° cone with a 150 cm^2 cylindrical sleeve.

4 Summary of Laboratory Test Programme

A comprehensive soil testing programme was formulated to evaluate pertinent soil indices and engineering properties and was conducted in two phases; offshore laboratory tests performed on-board and onshore laboratory tests in several soil laboratories.

The offshore soil tests were performed concurrently with the drilling operations and were performed either while the sample was still inside the sample tube, or immediately after extrusion. Test types include laboratory (miniature) vane (intact and residual), unit weight determination, water contents and unconsolidated undrained (UU) triaxial compression (intact and remoulded).

After reviewing the field test results, an extensive onshore laboratory (static and cyclic) test programme was performed to characterise the sediments found across the study site. A study into the effect of strain rate on the monotonic shear strength was also included as part of the cyclic/dynamic test programme. The laboratory testing programme included monotonic and cyclic simple shear tests, monotonic and cyclic triaxial tests, bender element and resonant column tests. X-ray scans were also performed to ensure the best available samples were selected for strength testing.

The principal objectives of the laboratory test programme were to allow development of a site-wide monotonic undrained strength model, a strain rate effect model, a generalised cyclic undrained strength degradation model and generalised shear modulus degradation curves.

5 Geotechnical Soil Units

Interpretation of site-specific stratigraphy was performed by integrating geotechnical and geohazard core logging data with the AUV subbottom profiler (SBP) and 3D seismic geophysical data. This process involved (1) identifying general trends in the geotechnical data, (2) reviewing detailed geohazard core logging descriptions and then (3) integrating these data with the geophysical data to identify potential geophysical horizons. A geophysical horizon was mapped within the study area

Table 1 Geotechnical units across the site

Geotechnical unit	Generalised description	Geologic features
G1/G1a	Very soft to soft clay	Fine-grained stratified sediments (drapes)
G1b	Very soft to stiff clay	Fine-grained stratified sediments (drapes)
G2	Firm to stiff clay	Parallel-bedded, fine-grained sediments with the presence of localized mass transport deposits and/or channels
G3	Firm to stiff clay	Parallel-bedded, fine-grained sediments or fine-grained mass transport deposits
G4	Stiff clay	Parallel-bedded, fine-grained sediments or mass transport deposits
G5	Stiff to very stiff clay	Parallel-bedded, fine-grained sediments or mass transport deposits
G6	Very stiff to hard clay	Unit disrupted by numerous faults and characterised by chaotic seismic reflectors indicative of mass transport deposits

if it represented a significant geotechnical and/or geohazard core logging trend, unconformity, or other clear stratigraphic break, and it could be regionally mapped between different geotechnical exploration locations using available geophysical data. Five main horizons were identified across the study areas, dividing the shallow section into six geophysical units.

Geotechnical units which are systematic three-dimensional groupings of soils, with similar geotechnical properties and generally similar boundary elevations, were also defined for the study areas and shown in Table 1. Generally, good agreement was found between the geotechnical and geophysical units. The maximum depth of investigation across the site was 150 m below mudline (BML).

6 Index Properties

Although index properties including water content, plasticity index, liquidity index and submerged unit weight for the defined geotechnical units were generally consistent within each unit, there was, however, a large range of values within the units and in particularly in the surficial units. Furthermore, the depth dependency of soil parameter values was more obvious in the surficial units; for example, there was a clear depth-related increase in submerged unit weight in Unit G1a/G1, whereas in Units G2 to G6, depth-related increases were less obvious and so these units were treated as effectively independent of depth. In reality, a general increase in submerged unit weight would be expected, as there was a general trend of increasing strength with depth in all units and because increasing strength is nonlinearly related to a decrease in voids ratio (and a decreasing voids ratio leads to increasing submerged

Table 2 Characteristics of tested soils

Index property	Geotechnical unit	P15	P50	P85
Submerged unit weight	G1a/G1	4.0	4.8	5.7
	G1B	5.3	5.9	6.9
	G2	5.2	6.0	6.7
	G3	5.3	6.2	6.9
	G4	5.5	6.3	6.9
	G5	6.3	7.2	7.9
	G6	7.2	7.8	8.8
Plasticity index (PI) (%)	G1a/G1	53	63	75
	G1B	42	59	69
	G2	43	57	70
	G3	44	59	73
	G4	47	58	71
	G5	38	47	57
	G6	35	44	53
Specific gravity	All units	2.71	2.79	2.86

unit weight). This discrepancy highlights the important issue that geotechnical units are simplifications of observed soil properties to enable efficient geotechnical design.

The statistical P15, P50 and P85 values of the submerged unit weight, plasticity index and specific gravity for the defined geotechnical units are shown in Table 2, where P15, P50 and P85 are defined as the values below which lie 15%, 50% and 85% of the data values, respectively.

The organic contents of the soils encountered at the study site were generally between 1 and 10% with some values slighter higher than 13% at discrete depths suggesting the presence of localised organic matter from terrestrial plant fragments transported by streams offshore, or from marine phytoplankton. The carbonate contents were generally less than 10% with some local values up to 38% likely associated with localised occurrence of relatively high concentrations of foraminifera and/or shell fragments or occurrence of gassy soils and a platy/blocky structure in sediments. The soil salt content values were between 23 and 32 ppt which were lower than the global average of approximately, 35 ppt indicative of the marine deltaic origin.

7 Stress History and Consolidation Characteristics

Controlled-rate-of-strain (CRS), one-dimensional consolidation tests were performed on selected intact specimens recovered from the saved tube samples to evaluate the stress history of the soil formation across the whole study site.

Table 3 Statistical assessment of k_{ocr}

Location	P15	P50	P85
Site-wide facility locations	0.23	0.28	0.33

The preconsolidation pressures ($\sigma'_{v,m}$) were also estimated from the PCPT data, using the empirical correlation described in Lunne et al. (1997):

$$\mathrm{OCR} = k_{ocr}(q_{net}/\sigma'_{vo}) \tag{1}$$

where OCR is the over consolidation ratio and defined as the ratio of the maximum preconsolidation pressure and the present effective overburden stress. k_{ocr} is a correlation factor and q_{net} is a net piezocone resistance from PCPT. Typically, k_{ocr} is in a range of 0.2–0.5; higher values of k are recommended in aged heavily overconsolidated clays (Powell et al. 1988).

Statistical assessment of k_{ocr} across the whole study site based on sixty-three (63) good quality CRS test results was performed with the P15, P50 and P85 values given in Table 3. These values are within the range from Powell et al. (1988).

The soils across the study site comprised of underconsolidated soils (in situ vertical effective stress less than hydrostatic pressure with OCR < 1) and overconsolidated soils with OCR more than 4 as shown in Fig. 1 using methods proposed by Casagrande (1936) and Becker et al. (1987).

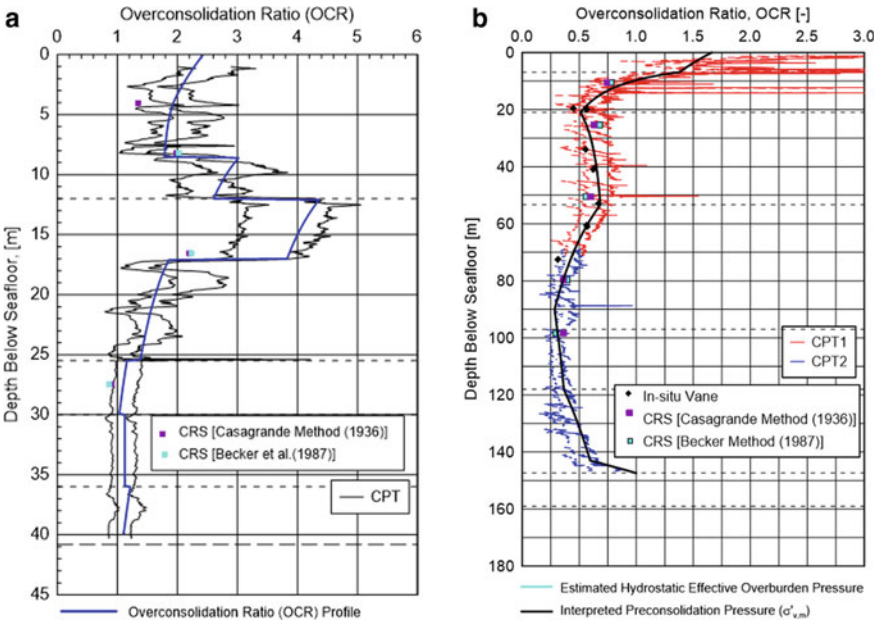

Fig. 1 **a** Example OCR profiles at the study site (OCR > 4). **b** Example OCR profiles at the study site (OCR < 4)

The coefficient of consolidation, c_v, was generally in the range of 0.6–6.4 m^2/year across the study site. c_v inferred from the remoulded CRS tests generally range between 0.4 and 1.0 m^2/year, which suggest that there are some soil fabric effects for the site and the excess pore pressures are expected to take longer to dissipate in remoulded soil than in intact soils.

Swelling index (c_s) describes the slope of the one-dimensional consolidation prior to preconsolidation pressure while compression index (c_c) defines the slope of virgin loading, i.e. post-preconsolidation pressure. c_c values between 0.3 and 1.5 were determined for intact specimens across the site and values between 0.5 and 0.7 were derived for remoulded specimens. c_s values were within the range of 0.03–0.15 for intact specimens with the ratio of c_s/c_c between 0.07 and 0.23.

8 Monotonic Undrained Shear Strength

The undrained shear strengths of the cohesive soils were evaluated by conventional laboratory strength tests (laboratory vane (LV), Fallcone, and UU triaxial compression tests), in situ PCPT, seabed T-bar and mini T-bar, and a suite of advanced static laboratory tests (static direct simple shear (CKoU′ DSS) and Ko-consolidated-undrained (CKoU) triaxial compression or extension tests). However, the T-bar, PCPT and advanced testing results are considered more reliable for assessing in situ conditions, due to concerns relating to the effect of unavoidable drilling disturbance on the index strength results.

The site-specific cone factor (N_{kt}) values can be developed from the PCPT net cone tip resistance (q_{net}) and the undrained shear strength (s_u). The advantage of using N_{kt} is that it normalises the data, thus effectively removing the depth dependency of the shear strength profile. Taking account of the fact that undrained shear strength is not an intrinsic measurement, separate assessments of N_{kt} as given in Table 4 were performed for UU triaxial, DSS and CKoU triaxial compression (CKoUC) and extension tests (CKoUE).

The derived N_{kt} values for the study site based on triaxial tests and DSS tests are comparable to those recommended by Andersen et al. (2008) as shown in Table 5.

An example plot of the interpreted intact shear strength profiles for a facility location is shown in Fig. 2. For this site, recommended characteristic trend lines of low estimate (LE) and high estimate (HE) UU triaxial shear strength s_{uu} interpreted from PCPT were provided as s_{uu} shear strength which is the reference shear strength for

Table 4 Statistical N_{kt} distribution

Test type	P15	P50	P85
DSS	11.4	13.2	15.1
UU	13.2	15.5	18.6
CKoUC	9.7	11.4	12.8
CKoUE	13.4	15.3	17.9

Table 5 Andersen et al. (2008)'s recommended N_{kt} values

Application	Based on $S_{u,CAUC}$[a]	Based on $S_{u,av}$ or $S_{u,DSS}$[a]
1. Overall, if limited previously experience	11.5 (9.5–13.5)	13 (11–15)
2. Gulf of Guineas	12.5 (10.5–14.5)	13.5 (11.5–15.5)
3. Norwegian Sea	11.5 (9.5–13.5)	14.5 (12.5–16.5)

[a]Mean (range)

ISO 19901-4 (2016) main text pile calculations. The interpreted DSS shear strength s_{ud} profile is also presented for suction pile design purpose.

Site-wide database of soil sensitivity S_t was generated by unit and on overall basis. The S_t statistics was developed based on intact and residual laboratory vane (M_v and $M_{v,re}$) values, intact and remoulded laboratory vane measurements (M_v and $M_{v,r}$), intact and remoulded UU triaxial test data and intact and remoulded fall cone test results. By the examination of the results for individual units, it was deemed reasonable to adopt the overall statistical values for all units. A sensitivity S_t value of 2.6 was generally adopted to derive LE and HE remoulded shear strength profiles. This value is comparable to the typical sensitivity S_t of Gulf of Mexico clays in the order of 2.5–3.0 (note that for Drammen clay, the sensitivity is typically in the range of 6–10). It should be noted, however, that site-specific adjustments to the remoulded shear strength profiles were occasionally deemed necessary particularly close to the unit boundaries.

9 Strain Rate Effects

The strain rate effects on the undrained shear strength were investigated by performing monotonic DSS tests at different shearing rates (0.6–85,493%/h). Figure 3 presents the measured undrained shear strengths normalised against the undrained shear strength from the corresponding tests conducted at the standard loading rate of ~5%/h, plotted as a function of strain rate and also plotted on Fig. 3 as background data for comparison purposes are the Drammen clay and other clay results published in Lunne and Andersen (2007). Although there is significant scatter in the range of measured results, the general trend of the test results is observed to be in reasonable agreement with the published data, but with a tendency to a slightly lower strain rate effect than for the other clays. A best-fit trend line through the test data is also shown in Fig. 3. The equations which define this trendline are as follows.

For strain rate (SR) $\geq$ 0.6%/h:

$$s_{ud\text{-}fast}/s_{ud} = 0.944\ SR^{0.0389} \quad (2)$$

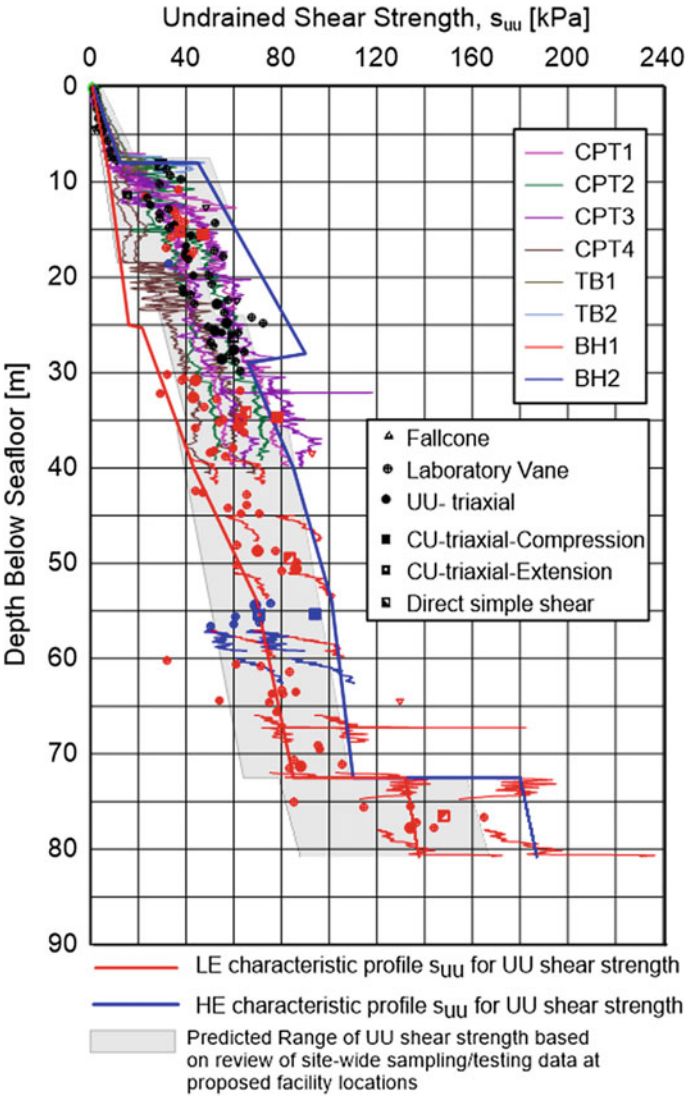

Fig. 2 Example intact shear strength profile for a facility location at the study site

For strain rate (SR) < 0.6%/h:

$$s_{\text{ud-fast}}/s_{\text{ud}} = 0.928\ \text{SR}^{0.0106} \tag{3}$$

where $s_{\text{ud-fast}}$ is the undrained shear strength measured from a test performed at a particular strain rate (note that in this equation $s_{\text{ud-fast}}$ can apply to strain rates higher or lower than the standard rate of 5%/h), s_{ud} is the undrained shear strength measured

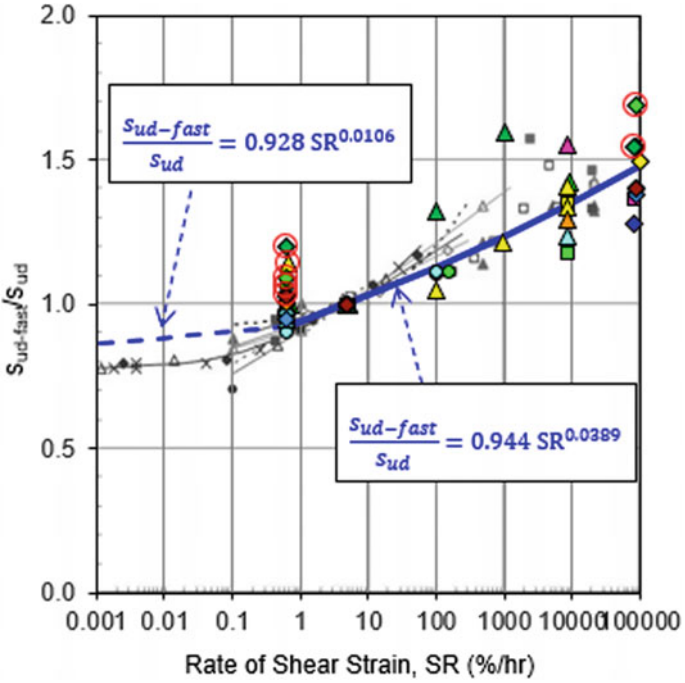

Fig. 3 Strain rate effects (background data in grey from Lunne and Andersen 2007). Unusual test results are circled and given less emphasis in fitting

from a test conducted at the standard loading rate of ~5%/h and SR is the strain rate (in % per hour).

For engineering design, the above relationship can be used to adjust the monotonic undrained shear strength profiles based on tests conducted at the standard strain rate of 5%/h, to the actual shear strain rate of interest for the problem under consideration. Although the strain rate effect has been specifically developed from simple shear data, the same equations and parameters can be adopted for assessing the strain rate effect for any other stress path.

10 Cyclic Undrained Shear Strength

10.1 Generalised Cyclic Strength Degradation Model

For engineering design at this development site, it was necessary to develop a generalised model which holistically considered all of this collected data, and from which an appropriate prediction of cyclic strength could be made for any element of soil, subject to any combination of cyclic loading and for any combination of monotonic

strength and in situ vertical effective stress. The cyclic response of the sediments was thoroughly investigated by conducting a large suite of cyclic DSS tests which was designed to test clusters of samples from different depths and reflecting a range of normalised shear strengths (s_{ud}/σ'_{vo}).

Classical S-N curves were constructed from individual sets of 2-way and 1-way test results, which enabled a site-specific generalised cyclic degradation model to be established for any combination of monotonic strength and in situ vertical effective stress in accordance with the following general expression:

$$s_{u\text{-}cyc}/s_{ud\text{-}fast} = a\exp(bs_{ud}/\sigma'_{vo}) + c < 1.0 \quad (4)$$

where a, b and c are empirical parameters.

For this study, trendlines for cyclic shear strains of 5, 10 and 15% each with $N =$ 5, 10, 15, 20 and 100 were fitted with the a, b and c parameters. An example of these parameters fitted with trendlines for $N = 10$ for 1-way and 2-way cyclic loading regimes are summarised in Tables 6 and 7 and shown in Fig. 4.

In Fig. 4, the ratio of cyclic undrained shear strength ($s_{u\text{-}cyc}$) to the monotonic undrained shear strength at the applicable cyclic loading rate ($s_{ud\text{-}fast}$) is presented as a function of s_{ud}/σ'_{vo} where s_{ud} is defined at the standard rate of shearing (5%/h). Although there is some scatter in the data, the fitted lines using Eq. (4) have been defined such that they closely follow the overall trends shown in the data, erring on the conservative side where there is any doubt. The form of Eq. (4) and ranges of appropriate values for the empirical parameters a, b and c are consistent with Fugro's extensive database of cyclic test results. This invariably indicates increasing degradation for higher normalised monotonic strengths (i.e. for higher s_{ud}/σ'_{vo}).

Table 6 Cyclic undrained shear strength parameters: 1-way, $N = 10$

Cyclic strain, γ_{cyc} (%)	Number of cycles, N	Empirical parameters		
		1-way strength		
		a	B	C
5	10	0.5	−7	0.63
10	10	0.5	−7	0.70
15	10	0.5	−7	0.76

Table 7 Cyclic undrained shear strength parameters: 2-way, $N = 10$

Cyclic strain, γ_{cyc} (%)	Number of cycles, N	Empirical parameters		
		2-way strength		
		a	b	c
5	10	0.4	−5	0.54
10	10	0.4	−5	0.60
15	10	0.4	−5	0.66

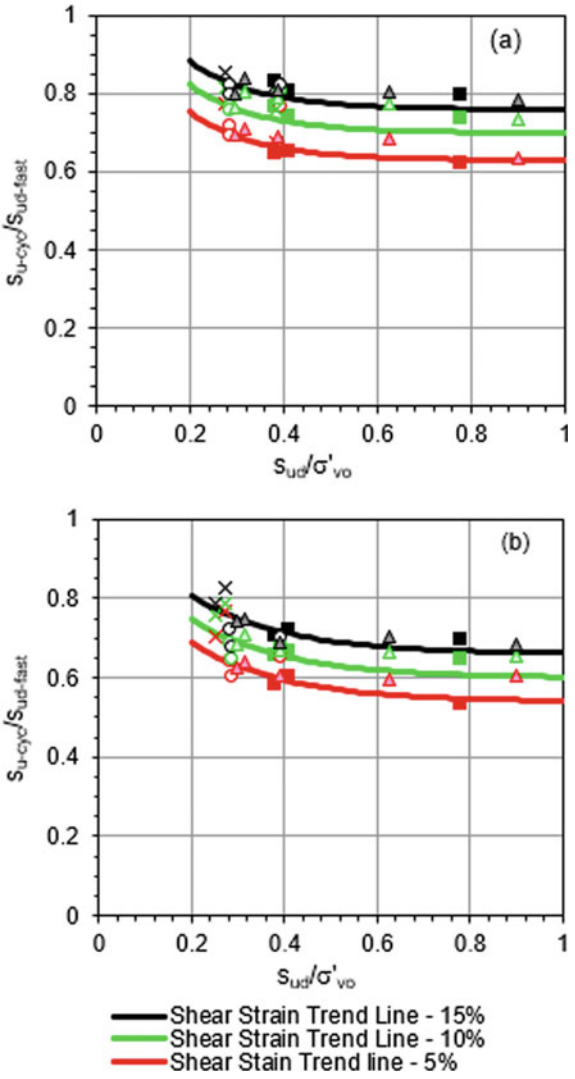

Fig. 4 **a** Cyclic strength 10 cycles 1-way, **b** cyclic strength 10 cycles 2-way

10.2 Failure Interaction Diagrams

In order to compare the predictions of the generalised cyclic strength degradation model presented in this study (based on tested material with a plasticity range of 34–81%) with existing clay models, such as Drammen Clay (Andersen 2004), failure interaction diagrams (FID) have been developed which present contours of the number of cycles to failure as a function of the average and cyclic shear stresses. An example of the comparison is present in Fig. 5 (original figure adopted from Andersen 2004) where $s_{ud}/\sigma'_{vo} = 0.25$ from this study is compared with OCR = 1

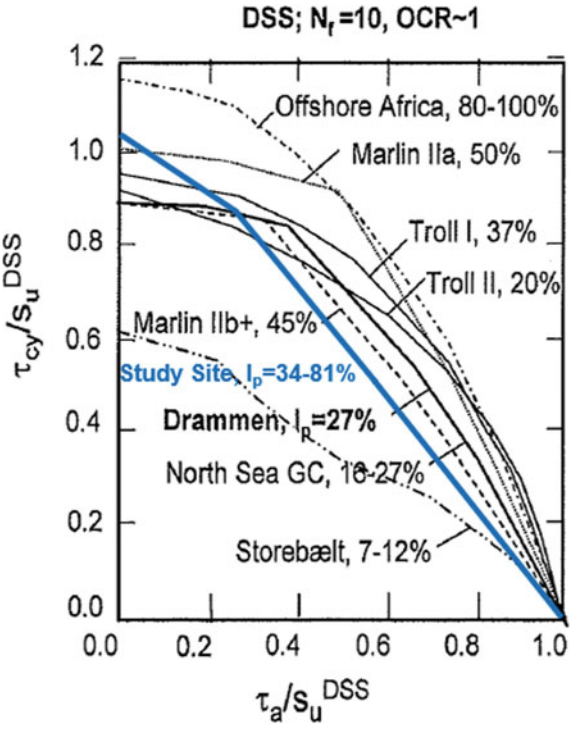

Fig. 5 Normalised shear stresses in simple shear causing failure after $N = 10$ for various clays (from Andersen 2004)

clays. Based on the DSS FID comparison shown in Fig. 5, the soils from this study appear to be more degradable than Drammen Clay and also more degradable than most of the presented clays under 1-way cyclic loads but is comparable or slightly less degradable under 2-way cyclic loads.

11 Shear Modulus and Shear Modulus Degradation

11.1 Shear Modulus and Cone Resistance Correlation

The maximum (or "small strain") shear modulus (G_{max}) was determined from a number of bender element and resonant column tests. The measured values of G_{max} are presented as a function of the corresponding cone resistance (q_c) on Fig. 6a. Also plotted in Fig. 6a, as background data and for comparison purpose, are other clay results published in Mayne and Rix (1993). As shown in this Fig. 6b, the site-specific test results are sensibly encompassed within the range of the published data. The site-specific measured G_{max} values are also plotted as a function of the corresponding net cone resistance (q_{net}) in Fig. 6b. Constant ratios for G_{max}/q_{net} of 20 and 50 were

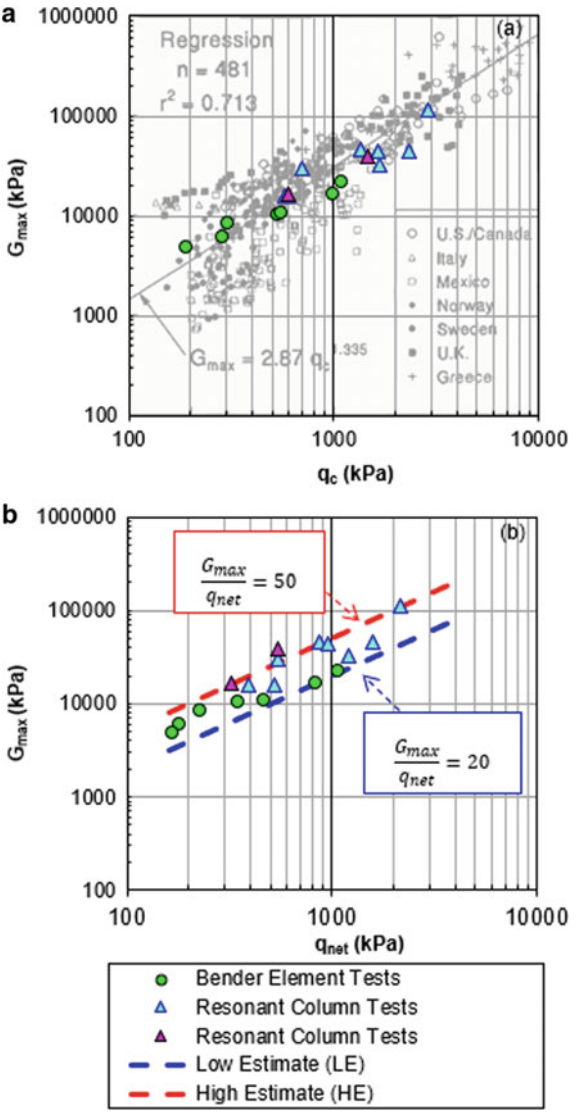

Fig. 6 **a** Comparison of test results with database of different clays (from Mayne and Rix 1993). **b** Correlation of maximum shear modulus and net cone resistance

proposed as the low estimate (LE) and high estimate (HE) design lines, respectively. As shown in Fig. 6b, the proposed relationship envelopes over 90% of the interpreted data. These design lines when combined with the appropriate q_{net} profiles can be used to derive the G_{max} profiles as input to assessing dynamic properties to use in seismic analysis.

11.2 Shear Modulus Degradation and Damping Ratio Curves

Analysis of nonlinear seismic ground response requires information on stiffness (shear modulus degradation) and material damping (damping curves) throughout the soil profiles at each location. In order to allow general application in a seismic analysis in a relatively simple way, the required seismic soil parameters for a range of soil conditions were developed using a generalised model pegged to the cone factor, N_{kt}. Having defined G_{max} as a fixed proportion of q_{net} (i.e. $G_{max}/q_{net} = 20$ or 50 for LE and HE stiffness, respectively) and since the undrained strength is also defined as a proportion of q_{net}, via the cone factor N_{kt}, for any fixed value of N_{kt}, there will be fixed values of G_{max}/s_{ud} (i.e. 20 N_{kt} for the LE G_{max} and 50 N_{kt} for the HE G_{max}). For each unique value of $G_{max}/s_{ud,}$ a single stress–strain curve can be derived that encompasses the full response from small to large strain. However, since G_{max}/s_{ud} varies with different values of N_{kt} separate stress–strain relationships must be defined for each potential value of N_{kt}.

Accordingly, modulus reduction curves (G/G_{max}) for seismic design were developed and are presented in Fig. 7 for different values of N_{kt} (covering the range found at the site) and for the proposed LE and HE G_{max}/q_{net} ratios and also shown in Fig. 7 are the results from the resonant column tests. In terms of G/G_{max}, it can be seen that the recommended design curves sensibly encompass the range of measured data, particularly for the most common range of expected N_{kt} values.

The damping ratio (D) defines the energy dissipated by the soil and is generally assessed based on the soil stress–strain hysteresis loops. The stress–strain hysteresis loops are defined using two functions: one describing the "backbone curve" and the other describing the "unload/ reload" behaviour. In this study, the backbone curve was defined using the relationship between τ and γ obtained from the generalised stress–strain curves from the DSS results. The "unload/ reload" behaviour was modelled using the Masing rule (Pyke 1979), since this is the most common assumption built into nonlinear site response analysis software. The resulting damping ratio curves are presented in Fig. 8, and it may be noted that the recommended design curves typically slightly underpredict the measured damping ratio for very low strains (γ less than about 0.05%), but thereafter generally provide a sensible fit up to the limit of the resonant column data (γ about 0.4%). At larger strains, it is commonly found that Masing rule-based models tend to overestimate the actual damping ratio, as has been previously reported in the literature (e.g. Lo Presti et al. 2006). For engineering design, alternative strategies such as using engineering models that do not employ the Masing rule or utilising a reduced or equivalent shear modulus (Yamamoto et al. 2015) may be adopted.

For seismic analysis conducted using a simplified equivalent linear approach (e.g. SHAKE), the damping ratio can be defined independently of the shear modulus degradation curves, and in such software adopting the damping response recommended by Vucetic and Dobry (1991), for plasticity index of 50% may be appropriate. This relationship is also shown in Fig. 8.

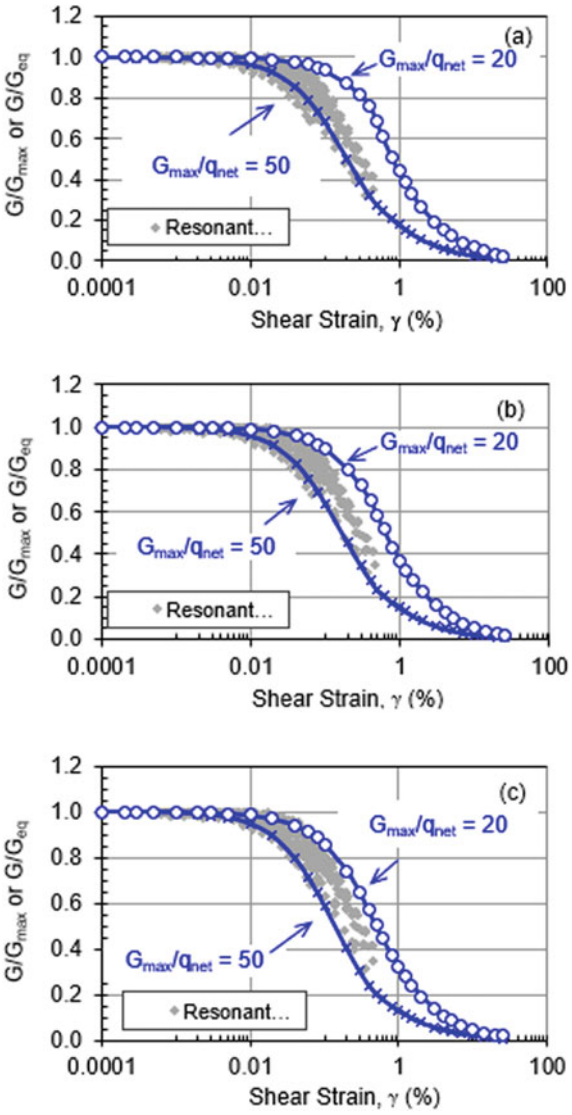

Fig. 7 Shear modulus degradation curves cone factors, **a** $N_{kt} = 11$, **b** $N_{kt} = 13$ and **c** $N_{kt} = 15$

12 Conclusion

This paper presented key results from a recent offshore geotechnical site investigation and subsequent comprehensive onshore laboratory testing and interpretation carried out for an offshore development in the Krishna Godavari (KG) Basin, Bay of Bengal. The interpretation was carried out using a consistent framework leveraging site-wide data to characterise the recovered sediments. The undrained shear strength, shearing

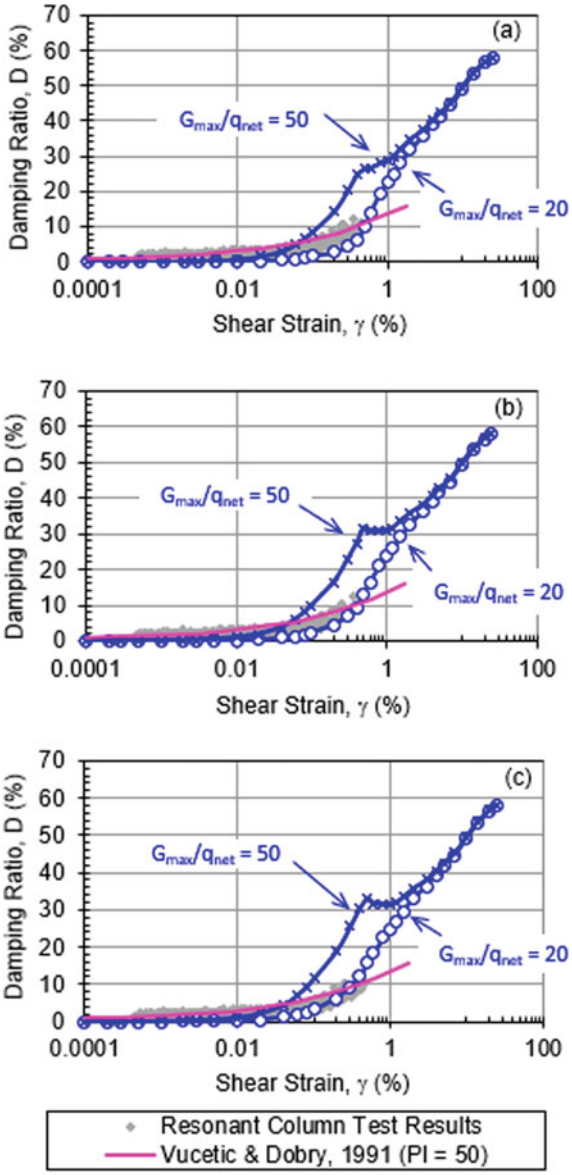

Fig. 8 Damping ratio curves, **a** cone factors, $N_{kt} = 11$, **b** cone factors, $N_{kt} = 13$ and **c** cone factors, $N_{kt} = 15$

rate effect and the cyclic and seismic behaviours of the range of materials recovered across the site are found to be different but comparable to other clays in the literature.

References

Andersen KH (2004) Cyclic clay data for foundation design of structures subjected to wave loading. In: International conference on cyclic behaviour of soils and liquefaction phenomena, CBS04, Bochum

Andersen KH, Lunne T, Kvalstad TJ, Forsberg CF (2008) Deep water geotechnical engineering. In: Proceedings of XXIV national conference of Mexican society of soil mechanics, Aguascalientes, 26–29 Nov 2008

Becker DE, Crooks JHA, Been K, Jefferies MG (1987) Work as a criterion for determining in situ and yield stresses in clays. Can Geotech J 24:549–564

Casagrande A (1936) Determination of the preconsolidation load and its practical significance. In: Proceedings, first international conference on soil mechanics and foundation engineering, vol 3, Cambridge, pp 60–64

ISO 19901-4 (2016) Petroleum and natural gas industries—specific requirements for offshore structures—part 4: geotechnical and foundation design considerations, 2nd edn

Lo Presti DC et al (2006) ONDA: computer cone for nonlinear seismic response analyses of soil deposits. J Geotech Geoenviron Eng ASCE 132(2):223–236

Lunne T, Andersen KH (2007) Soft clay shear strength parameters for deepwater geotechnical design. In: Proceedings of the 6th OSIG, London, pp 151–176

Lunne T, Robertson PK, Powell JJM (1997) Cone penetration testing in geotechnical practices. Blakie Academic Professional, New York

Mayne PW, Rix GJ (1993) G_{max}-qc relationships for clays. Geotech Test J GTJODJ 16(1):54–60

Powell JJM, Quaterman RST, Lunne T (1988) Interpretation and use of the piezocone test in UK clays. In: Proceedings of penetration testing in the UK, London, pp 151–156

Pyke R (1979) Non-linear soil models for irregular cyclic loading. J Geotech Eng ASCE 105(GT6):715–726

Rao NK, Saito Y, Nagakumar KCV, Demudu G, Rajawat AS, Kudo S, Li Z (2015) Palaeogeography and evolution of the Godavari delta, east coast of India during the Holocene: an example wave-dominated and fan-delta settings. Palaeoogeogr Palaeoclimatol Palaeoecol 440:67–74

Vucetic M, Dobry R (1991) Effect of soil plasticity on cyclic response. J Geotech Eng Div ASCE 117(1):89–107

Yamamoto N, Sharma S, Erbrich CT (2015) Suitability of Masing rules for seismic analysis of offshore carbonate sediments. In: Frontiers in offshore geotechnics, ISFOG 2015, Oslo, 10–12 June 2015

Back Analyses of Jack-up Rig Penetration for Punch Through Case

Y. Nanda Kishore, M. Pradeep, R. K. Agrawal, K. Faris, and T. Oussama

1 Introduction

Jack-up barges are used extensively in shallow water depths for various installation and hook-up activities. The hull of the jack-up rig is in floating condition during the transportation and rests on the extendable legs during the positioning. Installation rigs have wide range of capacities 150–750 T and pre-loads of the barges are in the range of 5–35 MN. The legs of jackups are equipped with a hexagonal or circular '*spud can*' at the bottom. Spudcan acts as a temporary shallow foundation for both vertical and horizontal loads such as self-weight, wind and wave loads of the barge.

Prediction of the spudcan penetrations for maximum pre-load conditions is very crucial for mobilization of jack-up rig. For each setup of the jack-up barge, spudcan penetration analysis is to be performed to check the safe bearing of the spudcan. '*punch through*' and rapid penetrations of the spudcan are major risks for the stability and equilibrium of the jack-up rig structure.

Parker et al. (2008) compared predicted bearing capacities versus field measurements over 15 offshore sites. Relatively simple closed form bearing capacity formulas are shown to provide good predictions for real behavior of these large-scale foundations. Kellez and Stromann (2003) carried finite element modeling for the comparison of convention methods and finite element analysis. Conventional analysis was modified based on finite element analysis and field observations to suit actual field behavior.

Accuracy of the geotechnical parameters is vital in the assessment of spudcan penetration analyses. This paper presents case study of barge where 'punch though' was predicted due to consideration of conservative soil parameters. Final approval of the barges was obtained based on back analysis from penetration records.

Y. Nanda Kishore (✉) · M. Pradeep · R. K. Agrawal · K. Faris · T. Oussama
National Petroleum Construction Company, Abu Dhabi, United Arab Emirates
e-mail: nanday@npcc.ae

S. Haldar et al. (eds.), *Advances in Offshore Geotechnics*, Lecture Notes in Civil Engineering 92, https://doi.org/10.1007/978-981-15-6832-9_9

2 Methodology for Spudcan Penetration Analysis

The bearing capacity of the spudcan foundation is evaluated for a number of possible penetration depths and the resulting curve of foundation capacity versus spudcan penetration, '*leg penetration curve*' is plotted. Maximum pre-load of the barge is compared with the predicted capacity to determine the expected spudcan penetration depth. Industry standard approach follows the site specific assessment of jack-up rigs, SNAME (2008) guidelines which are derived from conventional bearing capacity formulae with some modifications. The ultimate vertical bearing capacity (F_v) is defined as the maximum vertical load which the footing can support at a given penetration. F_v is computed from following equations for sand and clayey soils.

2.1 Bearing Capacity Estimation in Sand

Ultimate bearing capacity of circular footing resting on silica sand can be estimated by below equation

$$F_V = \left(0.5\gamma' B N_\gamma s_\gamma d_\gamma + p'_o N_q s_q d_q\right) A \tag{1}$$

where

F_v = ultimate bearing capacity
γ' = submerged unit weight of the soil
B = width/diameter of the footing
p'_o = overburden pressure
A = area of the footing.

2.2 Bearing Capacity Estimation in Clay

Ultimate bearing capacity of circular footing resting in clay can be estimated by below equation

$$F_V = \left(C_u \cdot Nc \cdot s_c \cdot d_c + p'_o\right) A \tag{2}$$

where

C_u = undrained shear strength
d_c = depth of the footing below the ground
N_γ, N_q, N_c—bearing capacity factors
s_γ, s_c, s_q—shape factors
d_c, d_γ, d_q—depth factors.

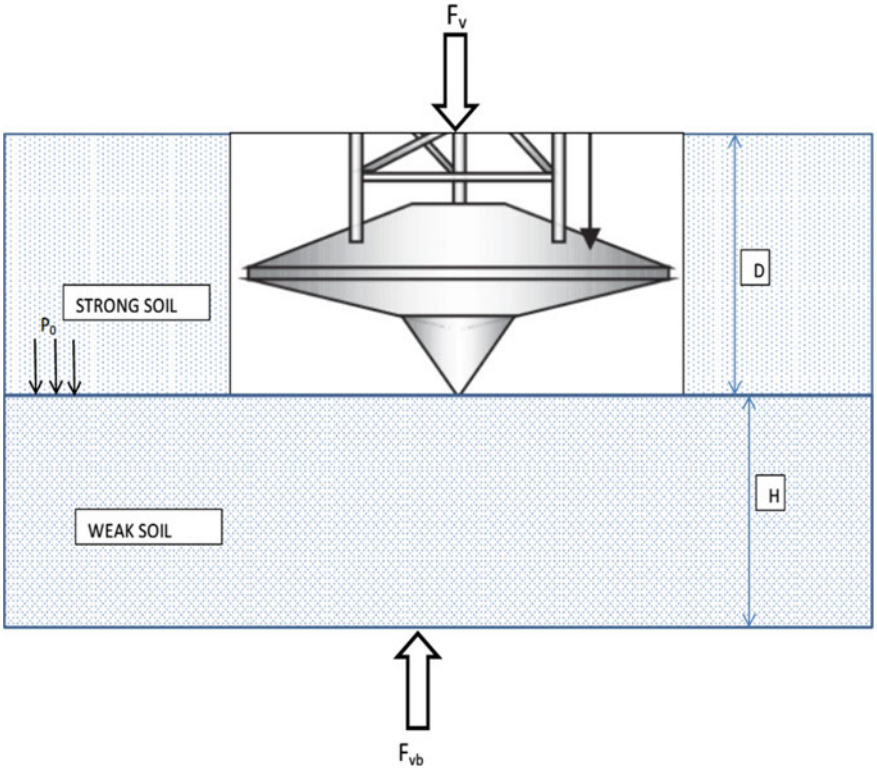

Fig. 1 Punch through sand over soft clay

In case of the layered soils, if strong layer overlain weak layer chances of the 'punch through' risk need to be assessed by Eq. (3) (Fig. 1).

$$F_{\mathrm{V}} = F_{\mathrm{vb}} - AH\gamma' + 2H/B\left(H\gamma' + 2p'_{\mathrm{o}}\right)K_{\mathrm{s}} \tan \Phi A \tag{3}$$

where

F_{vb} = bearing capacity of underlying layer
H = thickness of the sand layer
Φ = angle of internal friction
K_{s} = coefficient of the punching shear.

3 Case Study of the Installation Jack-up Barge

One of the locations in Arabian Gulf, SEP 450 jack-up was mobilized for platform modification works. Geotechnical investigation was carried out up to 50.0 m borehole depth. Rock and soils types have been classified based on Clark and Walker (1977) for the description of Middle East Sedimentary rocks. Strength tests on the rocks were carried out as point load test and unconfined compressive strength (UCS) test. In situ test, cone penetration test (CPT), was conducted in the borehole on the sand/clay layers. Classification tests, for example, water content, unit weight, particle size distribution, Atterberg limits, and carbonate content tests were carried out. Soil stratum was defined as top 0.5 m as Calcarenite followed by medium dense to dense sands up to 4.60 m and loose sands from 4.6 to 13.0 m. Generalized stratigraphy of the borehole is presented in Table 1.

Design parameters for low, best, and high estimation of spudcan penetration were provided in the geotechnical report as presented in Tables 2, 3, and 4. Basis of extraction of design parameters is defined below

1. Angle of internal friction for sand is considered from low and high estimation of CPT profiles and relative densities.
2. For rock, low, and best estimation is conservatively considered as 'dense sand' and for high estimation as clay with UCS/2.

Table 1 Generalized stratigraphy of the borehole

Unit	Depth below seabed (m)		TCR (%)	RQD (%)	Description
	From	To			
1	0	0.5	95	90	Calcarenite
2	0.5	3	–	–	Dense sand
3	3	4.6	–	–	Dense sand
4	4.6	13	–	–	Loose to medium dense sand
5	13	16	–	–	Dense sand

TCR = total core recovery; RQD = rock quality designation

Table 2 Low estimation design parameters

Soil strata	Depth (m)		Unit weight, γ' (kN/m^3)	Angle of internal friction, Φ (°)
	From	To		
Calcarenite	0	0.5	10.5	30
Dense sand	0.5	3	9.0	30
Dense sand	3	4.6	9.5	30
Loose to medium dense sand	4.6	13	10.0	20

Table 3 Best estimation design parameters

Soil strata	Depth, m		Unit weight, γ' (kN/m^3)	Angle of internal friction, Φ (°)
	From	To		
Calcarenite	0	0.5	10.5	35
Dense sand	0.5	3	9.0	30
Dense sand	3	4.6	9.5	30
Loose to medium dense sand	4.6	13	10.0	25

Table 4 High estimation design parameters

Soil strata	Depth (m)		Unit weight, γ' (kN/m^3)	Angle of internal friction, Φ (°)	Undrained shear strength, C_u (kN/m^2)
	From	To			
Calcarenite	0	0.5	10.5	–	500
Dense sand	0.5	3	9.0	35	–
Dense sand	3	4.6	9.5	35	–
Loose to medium dense sand	4.6	13	10.0	30	–

Spudcan penetration analyses were carried on based on SNAME (2008) guidelines by considering the soil parameters reported in Tables 2, 3, and 4.

3.1 Jack-up Rig Details

The spudcan of the jack-up barge is in hexagonal shape with equivalent diameter of 6.2 m. Spudcan details are presented in Fig. 2 and Table 5.

3.2 Leg Penetration Analysis

Soil resistance versus spudcan penetration curves are plotted for low, best and high estimation parameters as shown in Figs. 3, 4 and 5.

Expected leg penetration for low and best estimation is 2.2 m and high estimation is 0.1 m. For high and best estimation, punch through was not anticipated and low estimation analysis indicated punch through failure. Jack-up barge mobilization at this site was not approved by marine warranty surveyor (MWS) and company due to the risk of punch through in low estimate. Company was advised to mobilize another barge with higher bearing pressure which can suit to this location. This

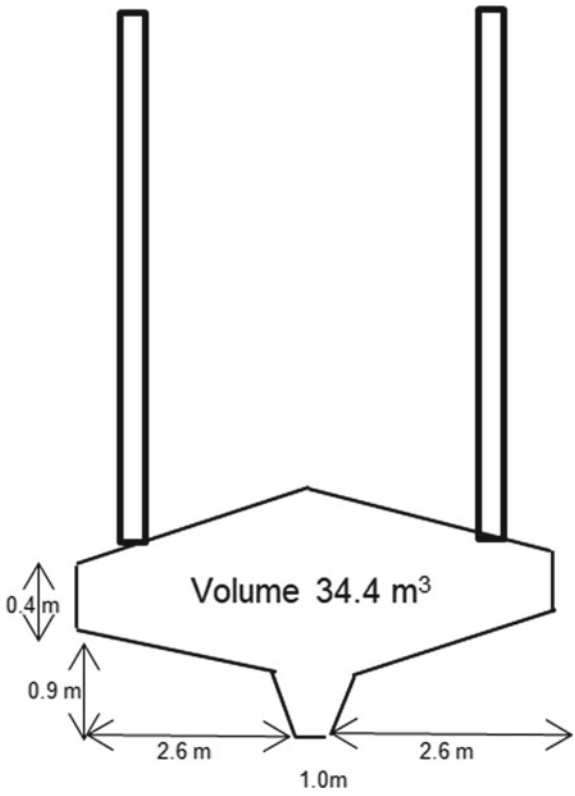

Fig. 2 Spudcan configuration

Table 5 Spudcan details

Spudcan description	Details
Circular diameter of the leg	6.20 m
Weight of each leg	2705 t/leg
Distance from base to maximum spudcan area	0.9
Surface base area	30 m^2
Volume of the leg	34.3 m^3
Maximum pre-load (excluding leg weight)	29.85 MN

was an additional burden to the project and also impact on the schedules due to non-availability of the suitable barge.

Punch through possibility at this location is meager since progressive failure in underlying dense sands is less likely. Hence, existing penetration records were used to back estimate the soil parameters to assess the real behavior of spudcan penetration.

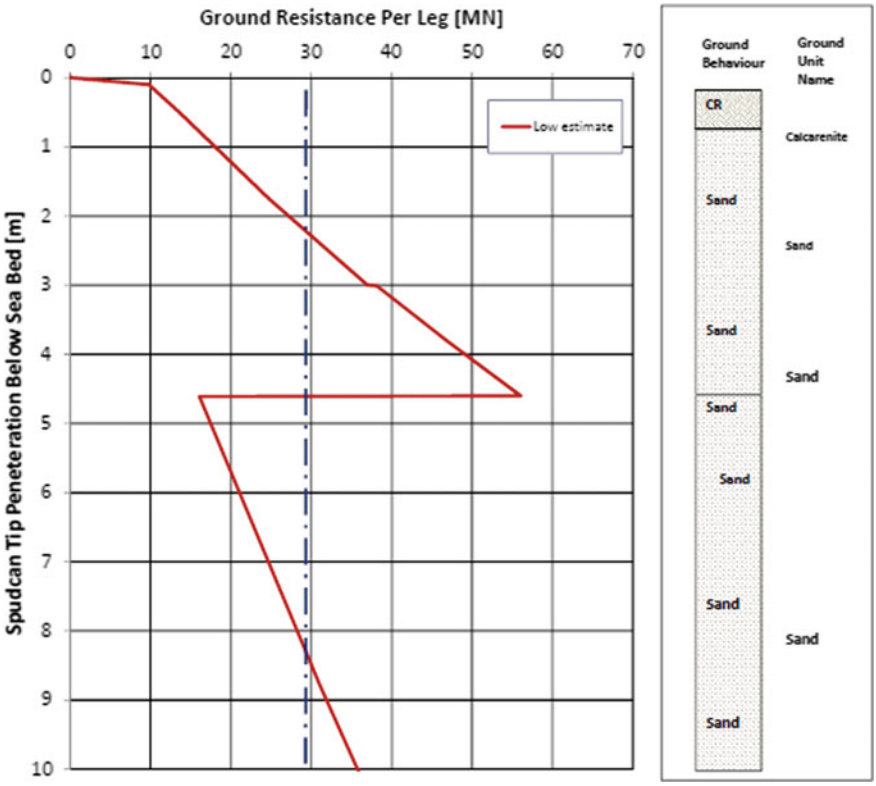

Fig. 3 Low estimate-soil resistance versus spudcan penetration

3.3 Back Estimation Using Existing Records

Penetration records of the barges mobilized at this location are collected. SEP-650 jack-up barge of pre-load in the range of 30.2 MN was mobilized near the platform and recorded spudcan penetration is 1 ft. Using this data, back analysis of the design parameters was carried out since bearing pressures of the both barges are in the same range. From the back analysis, angle of internal friction of top layers was arrived as 36°. With this, spudcan penetration analysis was revised and results are presented in Fig. 6.

Spudcan penetration of 0.35 m is predicted as per Fig. 6 and punch through is not noticed. With this justification, revised spudcan penetration was submitted to company and obtained approval for the barge setup.

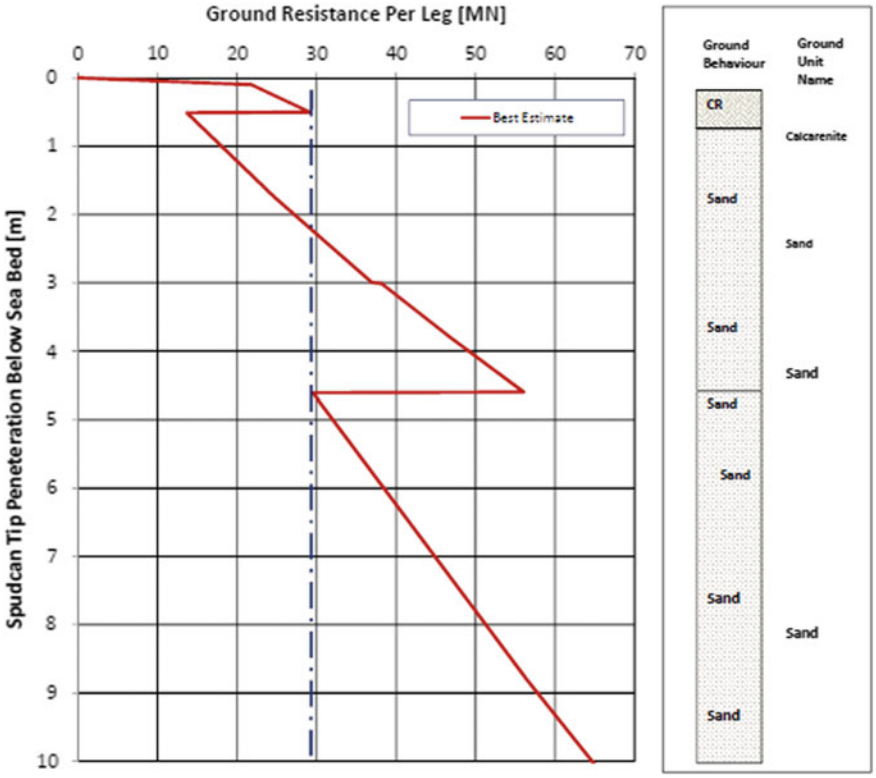

Fig. 4 Best estimate-soil resistance versus spudcan penetration

4 Finite Element Analysis

Finite element analysis was carried out using finite element software, PLAXIS-2D to simulate actual field conditions and check the risk of punch through.

4.1 Soil Model

Mohr-Coulomb model is considered for finite element soil model. Parameters considered for finite element analysis are tabulated in Table 6. Finite element mesh is generated by 15-node triangular elements.

Spudcan is modeled as elasto-plastic element with equivalent circle of 3.0 m radius. FEM model of spudcan and soil layers is shown in Fig. 7.

For the pre-load of 29.5 MN, maximum settlement of 0.3 m was predicted. Punch through was not noticed in FEM analysis. Deformed mesh of soil is shown in Fig. 8. Comparison of field data with FEM analysis is presented in Fig. 9.

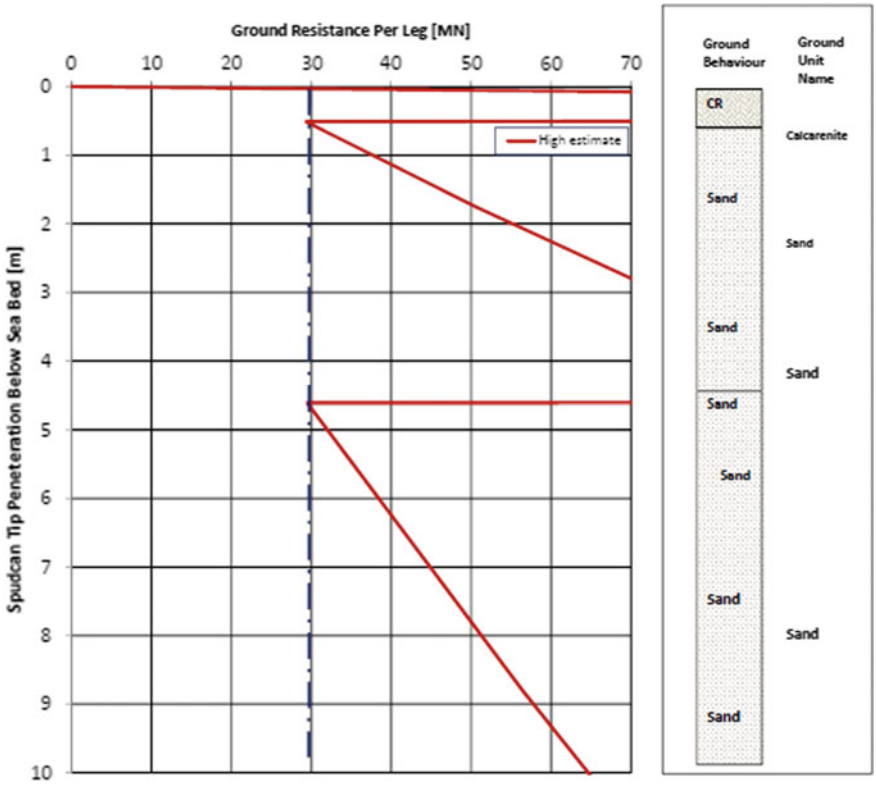

Fig. 5 High estimate-soil resistance versus spudcan penetration

5 Conclusions

From the back analysis, in situ soil parameters were analyzed to simulate actual spudcan penetration. With this method, punch through risk was disregarded. FEM analysis also proved that risk of punch was negligible at this location. Revised analysis facilitated the barge approval and eliminated the risk of '*punch through*.' Barge was mobilized at this site and leg penetration readings were reported as 0.2 m.

Similar approach was implemented for other locations where risk of punch through was predicted in the analyses and penetration records were available. More than 20 locations, leg penetration analyses were approved with back-analysis approach for similar field conditions and barges were pinned down without any excess settlement or punch through.

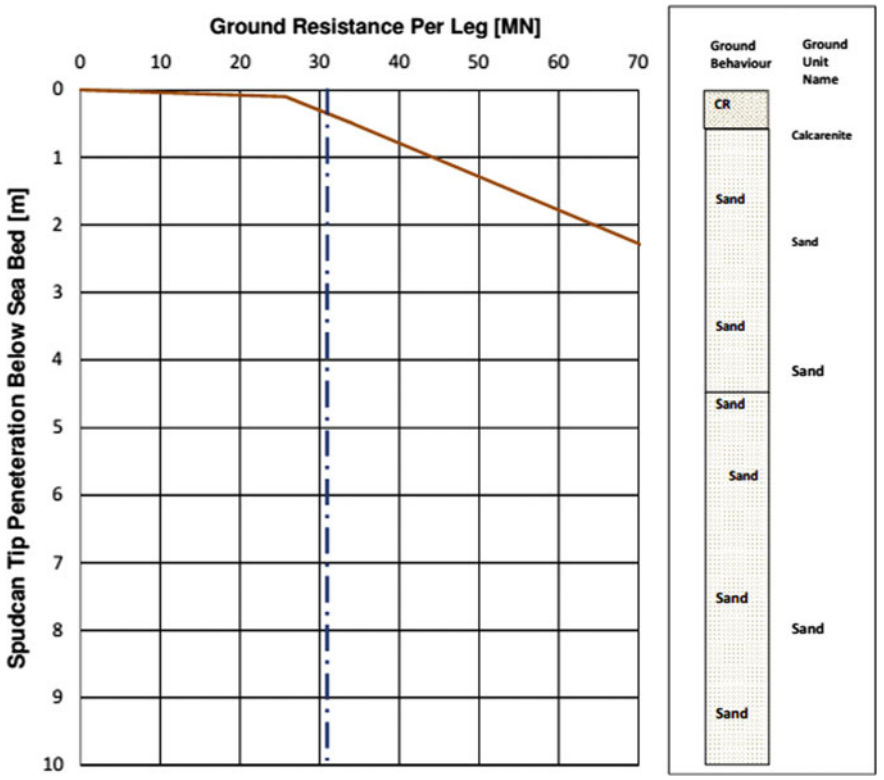

Fig. 6 Soil resistance versus spudcan penetration based on back estimation parameters

Table 6 Soil input parameters for FEM analysis

Parameters	Rock	Sand-1	Sand-2
Depth (m)	0–0.5	0.5–4.6	4.6–13
γ (kN/m^3)	10.5	9	10.0
E (kN/m^3)	40,000	20,000	18,000
υ	0.4	0.3	0.15
Φ (°)	36	30	25

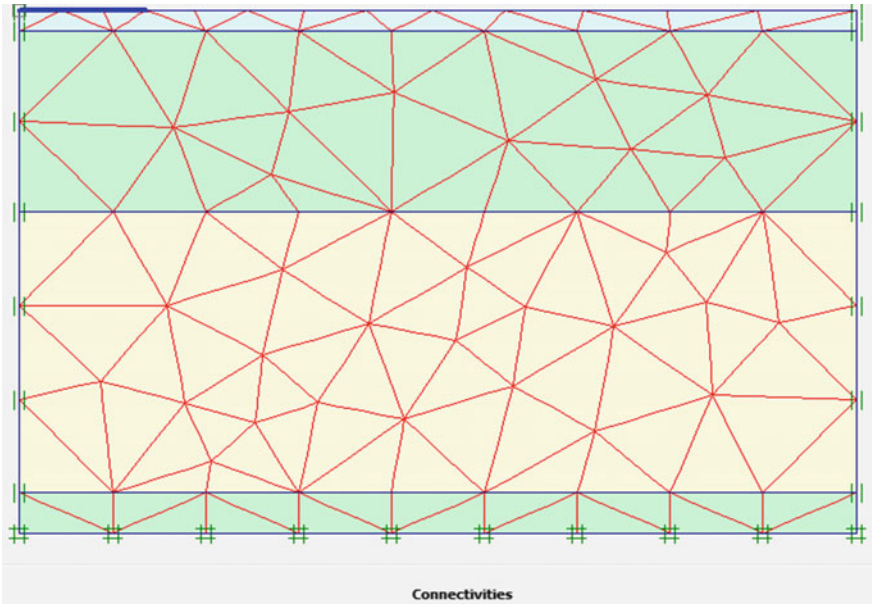

Fig. 7 FEM model of spudcan and soil layers

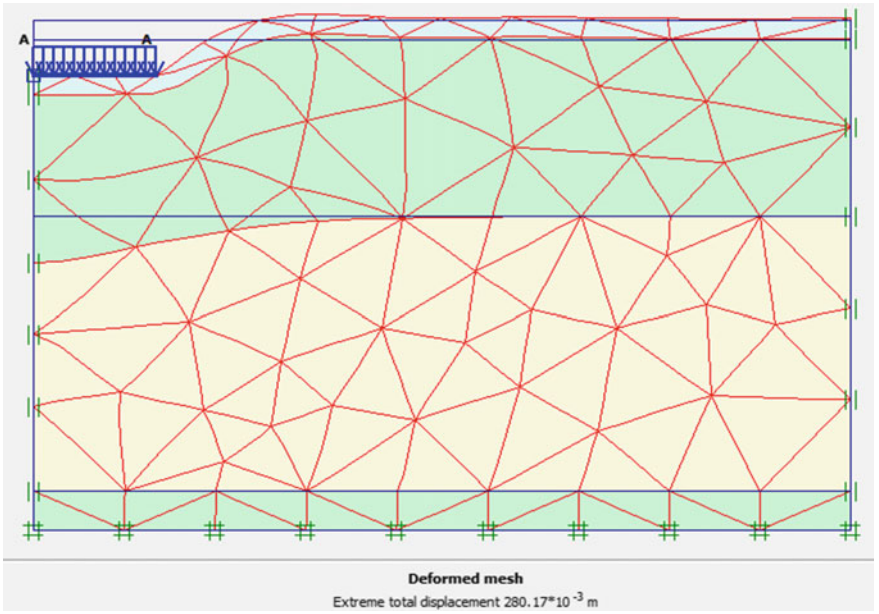

Fig. 8 Deformed mesh of soil after pre-loading

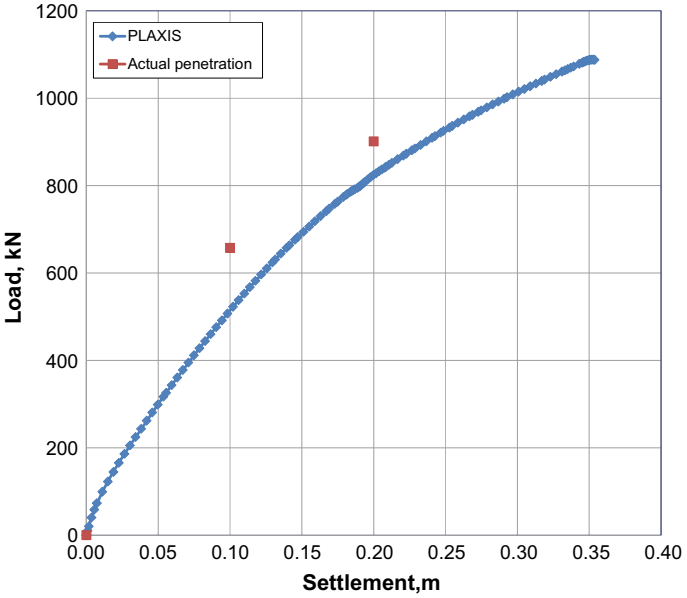

Fig. 9 Comparison of field data with FEM analysis

References

Clark AR, Walker BF (1977) A proposed scheme for the classification and nomenclature for use in the engineering description of Middle Eastern sedimentary rocks. Géotechnique 27(1):94–99

Kellez L, Stromann H (2003) FEM analysis of jack-up rig spudcan penetration analysis for multi-layered critical soil conditions. In: BGA international conference on foundations: innovations, observations, design and practice, Denmark, pp 411–420

Parker EJ, Farncesco M, Lorenzo P (2008) Case histories-jack-up rig spudcan penetrations—a 6,000 ton load test. In: Sixth international conference on case histories in geotechnical engineering, 9.09, Missouri, pp 1–7

Society of Naval Architects and Marine Engineers (SNAME) (2008) Recommended practice for site specific assessment of mobile jack-up units, 1st edn. New Jersey

Foundation Failure and Instability of an Offshore Jacket Structure During Installation—A Case Study

Rupam Mahanta and R. K. Ghanekar

1 Introduction

Mudmats play an important role as temporary foundations for fixed offshore jacket structures for their stability during the initial period of their installation before they are secured to the seabed by piling. Geometry of mudmat is primarily governed by the soil condition at the site and design load combinations. Soil strength near the seafloor plays a significant role on the design, especially when the soil near seafloor is soft clay. At sites, where the soil is relatively weak up to a substantial depth below the seafloor, the required size of mudmats may be quite large. There are many offshore areas in Indian offshore where weak soil condition, i.e. very soft clay, exists near seafloor (gradually increasing in strength as the depth below seafloor increases). In some of these sites, the mudmats had to be designed to cover the entire footprint of the jacket at the seafloor or even beyond it. Mudmats may be designed with or without skirts. Generally, the mats are designed without skirts for ease of fabrication and installation. For operational reasons, mats are generally designed to remain on the seafloor without penetration.

Assessment of bearing capacity for a large mudmat requires good quality assessment of soil properties below the seafloor up to a significant depth. In offshore installation of jacket structures, various load combinations need to be examined, e.g. gravity loads, installation time wind and wave loading. The vertical, horizontal and moment components of the loads vary at various phases of the installation (as one-by-one the pile segments are placed and subsequently driven) in combination with different directions of environmental loading. Therefore, proper assessment of load combination, resulting bearing stress and bearing capacity are essential for safe installation of jackets supported by mudmat foundation.

R. Mahanta (✉) · R. K. Ghanekar
Geotechnical Section, Institute of Engineering and Ocean Technology, ONGC, Panvel, Navi Mumbai, Maharashtra, India
e-mail: rupam.mahanta@gmail.com

S. Haldar et al. (eds.), *Advances in Offshore Geotechnics*, Lecture Notes in Civil Engineering 92, https://doi.org/10.1007/978-981-15-6832-9_10

During one of the installations of offshore jacket structure, the mudmat failed leading to instability of the jacket structure. The case was analysed for finding the root causes of the failure. Details of the case and the results of analysis are presented in this paper.

2 Design Requirements

The design needs to take into account many load combinations for the installation condition. In the present case, the combination included gravity (self-weight) as well as installation environmental loads (wind, wave and current) from different directions along with loads resulting from sequential placement and driving of various pile segments of the four main corner piles driven through the jacket legs. Therefore, many combinations of vertical, horizontal and moment loading were needed to be examined. The mudmat was to be designed to remain stable under any of the design load combinations without penetration into the seabed.

Three modes of foundation failure needed to be examined: bearing, sliding and overturning. The codal provision, i.e. American Petroleum Institute guideline (API RP 2GEO 2011, with addendum 2014), on minimum factors of safety to be met with respect to these modes of failure was:

1. For safety against bearing failure: 2.0 for gravity loading and 1.5 for combination of gravity and environmental loading.
2. For safety against sliding failure: 1.5
3. For safety against overturning failure: 1.5.

Analysis and design of the mat foundation were carried out by consultant of the EPC contractor based on the soil data provided by the company.

3 Soil Condition

The soil near the seafloor was very soft clay, and the undrained shear strength increased gradually as the depth below seafloor increased. Recommended soil parameters were derived from available results from laboratory tests and in situ test, i.e. Cone Penetration Test with pore pressure measurement (CPTU).

The geotechnical investigation was carried out at the platform location using two boreholes—one up to about 40 m, where CPTU was carried out in 3 m strokes, and the other, about 5 m apart, where sampling was carried out up to 40 m and alternate sampling and CPTU at depths greater than 40 m up to the end of the borehole, i.e. 125 m. The undrained shear strength for the first layer up to a depth of 15 m was measured in laboratory using index tests torvane and motor vane since the soil was very soft near seafloor; towards the end of the layer, two triaxial tests (unconsolidated

Table 1 Relevant soil parameters for top layers

Layer	Soil type	Depth (m)	s_u (kPa)	ϕ' (deg.)	γ' (kN/m^3)
1	Clay	0–15	3–18		4.5
2	Sand	15–25	–	25	9.5
3	Clay	25–37	85–100	–	8.0

Note Depth of 0 m starts at seafloor; s_u = undrained shear strength; ϕ' = effective angle of internal friction; γ' = effective unit weight

undrained) were also carried out. Key soil parameters used for the design of the mudmat are presented in Table 1.

4 Plan of Piles at Seafloor and Geometry of the Mudmat

The plan of piles at the seafloor is shown in Fig. 1. Two of the piles were designed as single battered and the other two as double battered. The platform was designed to be permanently supported by four main piles having an outer diameter of 2.134 m. The piles were open-ended steel tubes to be installed by driving with pile driving hammer. Water depth at the site was about 58 m.

Single battered pile on one face of the platform was to make it convenient for deployment of jack-ups for drilling wells in the platform subsequent to installation of the jacket platform.

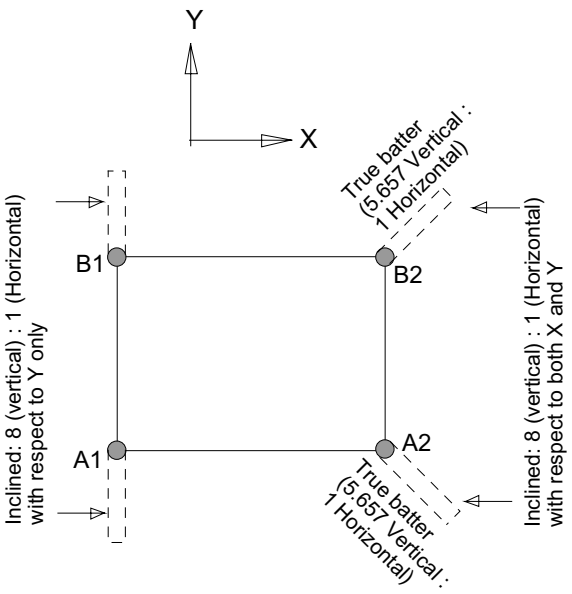

Fig. 1 Pile positions with inclinations at seafloor (not to scale)

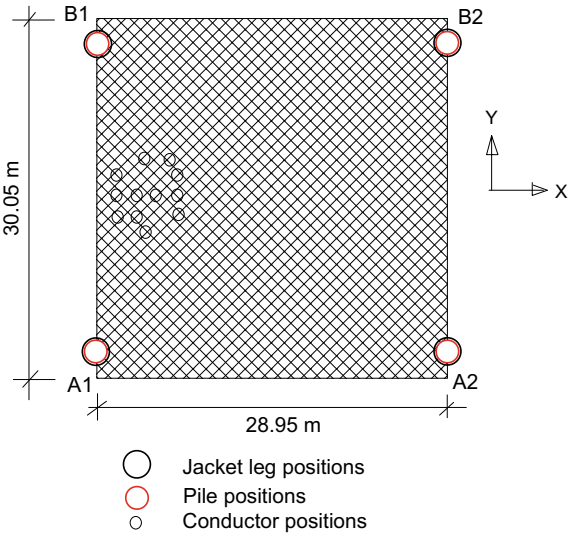

Fig. 2 Mudmat plan (not to scale)

The mudmat was fabricated using steel plates stiffened with steel structural members. The shape of the mudmat was rectangular having the dimension of 28.95 m $\times$ 30.5 m (without skirt). The mudmat (Fig. 2) was designed to be on the seafloor, i.e. without penetrating into the seafloor. The net area of the mat was 864.5 m^2 (excluding area of slots for drilling conductors which is less than 1% of the gross area), and the second moment of area with respect to *X*-*X* and *Y*-*Y* axes is 65,464 m^4 and 60,167 m^4, respectively.

5 Installation and Description of Failure

As per the design and installation plan, at first, the jacket was positioned slowly on the seafloor and supported by the mudmat. Total length of each pile includes the design depth of penetration below seafloor, the batter, the water depth and the distance from water surface to the elevation where the decks of the platform are connected with the pile. Such long piles are installed in segments where the bottom of subsequent segments are stabbed and welded to the top of the previously installed segment.

In this case, after the positioning of the bare jacket, the first segments of piles were placed inside jacket legs at the corners A2 and B1 (Fig. 2). At that stage, the pile load is fully borne by the mudmat. The second segment of pile was then added in jacket leg A2, and the pile was released to penetrate the ground under self-weight. On releasing, the combined segment 1 and segment 2 of the pile at A2 corner penetrated 14 m below the seafloor. There was no sign of impending failure of foundation up to this stage.

After this, pile segment 2 was placed over the first segment of pile B1. At this stage, the jacket structure started tilting and settling. Tilting was towards the corner B1. Despite all efforts to arrest the tilting, the jacket finally toppled.

6 Post-Failure Review and Analysis

Post-failure, the soil parameters and consultant's design were reviewed and analyses were performed to find out the root cause of the failure. Mudmat was analysed with respect to the design loads, resistance of soil and capacity of the foundation as per its geometry. Load combinations calculated during design were used to verify the adequacy of the design of the mudmat.

6.1 Review of Soil Parameters

First, the pre-engineering shallow geophysical survey record was studied. Spatial variation of soil strata over the mudmat footprint was not observed in survey results.

Soil properties were then reviewed for their reasonability before post-failure analysis. Statistical analysis was performed on undrained shear strength (s_u) for the relevant soil zone, i.e. up to 15 m below seafloor. The soil property assigned in the soil report for the design is generally conservative with respect to the mean. In case of very soft clay, the soil sampling process and handling of samples in laboratory are likely to cause some disturbance, and the impact of such disturbance is expected to be manifested in measured values of undrained shear strength. As such, measured strength in laboratory for such soft soils is expected to be conservative with respect to in situ strength. It is well known that the interpretation of undrained shear strength from CPTU for very soft to soft clays is not very reliable. Therefore, shear strength interpretation based on CPTU was not considered.

A statistical analysis was carried out to examine the mean undrained shear strength (s_u) profile vis a vis the strength profile used for the design. Only the first layer of soil is relevant for bearing capacity of the mudmat in this case. Since the soil is very soft near the seafloor, test data is comprised of undrained shear strength measured mostly by index tests using torvane and motor vane. There are two data points of triaxial (unconsolidated undrained) tests towards bottom of this soil layer. The data for the relevant depth (up to 15 m) is presented in Fig. 3. The statistical analysis was carried out using DNV-recommended procedure (DNV-RP-C207 2012) and the results are shown in Fig. 3.

It was observed (Fig. 3) that the soil strength profile recommended for the design was on the conservative side within the range of '−1 standard deviation' from the 'mean'.

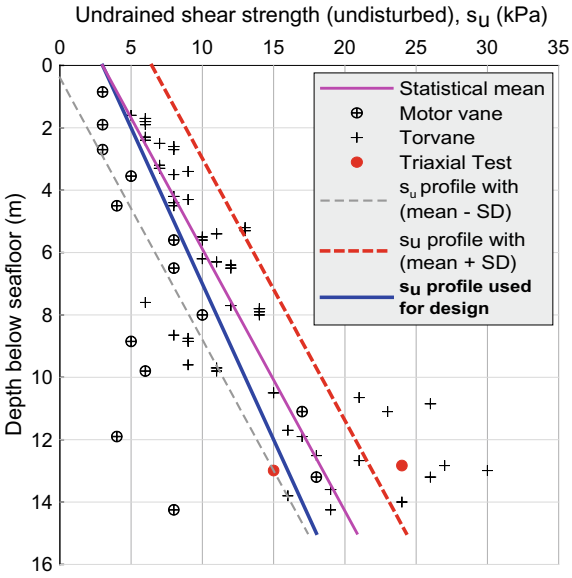

Fig. 3 Statistical analysis of shear strength of soil up to 15 m depth

Figure 4 shows the CPTU cone resistance (q_c) up to a depth of 30 m. The mean line of q_c up to 15 m depth is plotted in Fig. 4. The data clearly indicates the trend of increasing shear strength of clay up to a depth of about 15 m below the seafloor.

In view of the above, the same set of soil design parameters as given for initial design provided to the contractor was considered for post-failure analysis as well.

6.2 *Bearing Capacity of the Mudmat*

Bearing capacity of the mudmat was assessed with both conventional and finite element analysis. For conventional analysis, the guidelines for bearing capacity of shallow foundation in clay were followed as per API RP 2GEO (2011, with addendum 2014).

6.2.1 Post-failure Conventional Analysis

The latest version of the standard API RP 2GEO (2011, with addendum 2014) has significantly revised recommendations compared to the previous version. In view of the size of the mudmat, soil property of the first layer of soil was considered for the assessment of bearing capacity since the significant zone of stress is limited to this layer.

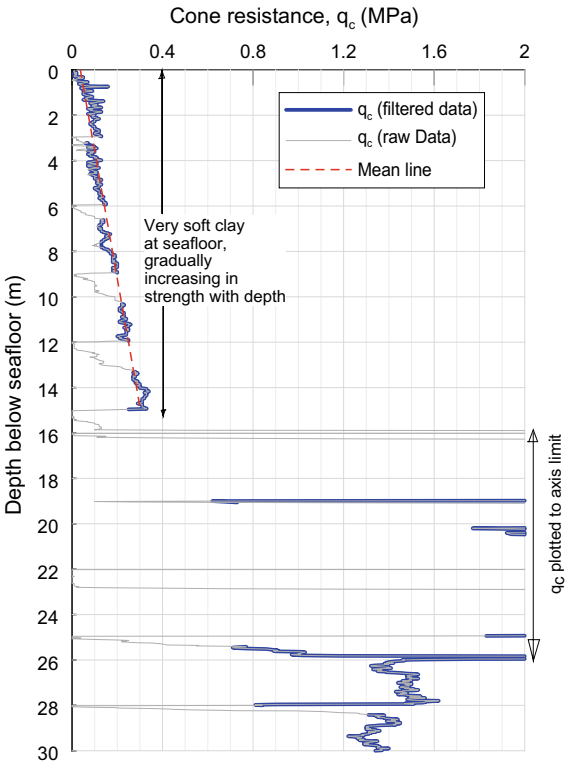

Fig. 4 CPTU cone resistance (data limited by axes for depths exceeding 2 MPa and 15 m)

Analyses were also performed with respect to combined vertical, horizontal and moment loading. In analysing bearing capacity affected by overturning moment, effective area method (American Petroleum Institute 2014) was applied.

The bearing stress was examined from the results of all design load combinations and compared with corresponding bearing capacity. Software SACS was used by the designer for analysis of the loads with respect to installation loading taking into account eight directions of environmental loads.

6.2.2 Post-failure Finite Element Analysis

In addition to assessment of bearing capacity using the conventional method (API RP 2GEO, 2011, with addendum 2014), 3D finite element analysis (PLAXIS 2019) was also performed to examine it. The geometrical model is shown in Fig. 5.

The software PLAXIS was used for the purpose. Mohr–Coulomb soil model was used for the assessment where shear strength of clay was modelled as undrained. The 3D model was made sufficiently large in geometrical dimensions so that the accuracy of calculation is not influenced by lateral or vertical boundary constraints.

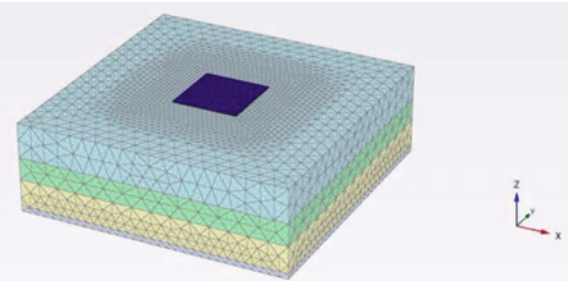

Fig. 5 Finite element model of the mudmat and soil

Finite element mesh was refined appropriately near the foundation. The mudmat was modelled as rigid.

The bearing capacity of the mudmat for purely vertical load was first estimated and compared with the conventional analysis. Capacity from finite element analysis was found to be matching reasonably well with capacity calculated as per API RP 2GEO (2011, with addendum 2014) which was about 4% higher than the value from conventional analysis.

After validation of the bearing capacity (for purely centric and vertical load) derived from finite element analysis with respect to API RP 2GEO (2011, with addendum 2014), finite element analysis was further carried out by applying combined vertical, horizontal and moment loading.

7 Results of Analysis and Discussion

The area of drilling conductor slots (less than 1% of gross mudmat area) in the mudmat was neglected in the geometrical model used in finite element analysis. The load-displacement data for the mudmat based on 3-D finite element analysis with respect to purely vertical and centric load is shown in Fig. 6.

The load-displacement data in arithmetic plot did not show any clear value on the ultimate bearing capacity. Therefore, in order to find the ultimate capacity, a log–log plot was made and the appropriate value was selected. The comparison of bearing capacity with purely vertical and centric load using the two approaches is shown in Table 2.

On applying the most critical load combination which included vertical, horizontal and moment loading, the bearing failure of the mudmat as per the finite element analysis is shown in Fig. 7.

Figure 8 shows the soil movement at failure, and Fig. 9 shows the plastic soil zone. These figures also indicate propagation of the failure after application of the most onerous load combination. The failure started from the expected corner as the mudmat started inclining towards the B2 corner of the mudmat. The load eccentricity increased with inclination of the structure. Increasing eccentricity reduces the ultimate bearing capacity further as effective bearing area as well as the mobilized shear resistance

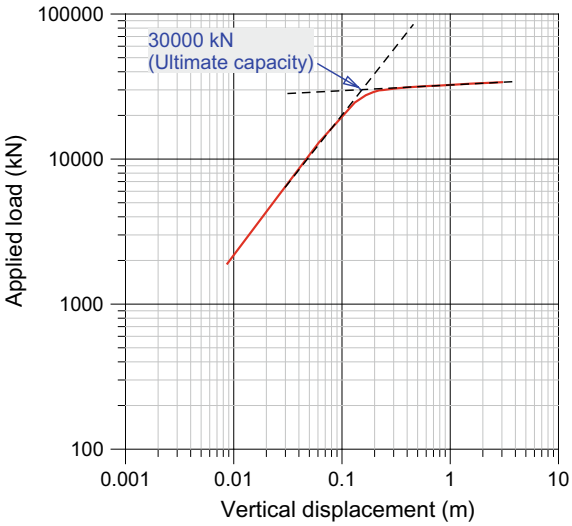

Fig. 6 Ultimate bearing capacity result of 3D finite element analysis (for centric vertical loading)

Table 2 Comparison of bearing capacity (vertical load)

Analysis method	Ultimate bearing capacity (kN)
API RP 2GEO (2011, with addendum 2014)	29,692
3D finite element (PLAXIS)	30,000

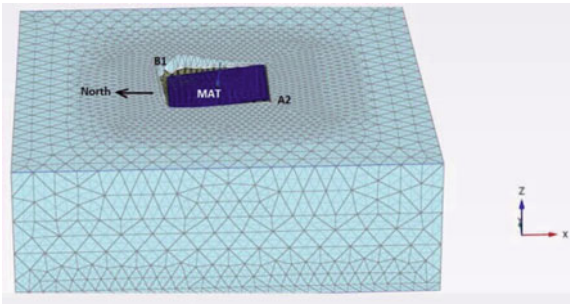

Fig. 7 Failure of the mudmat when subjected to most critical load combination of vertical, horizontal and moment

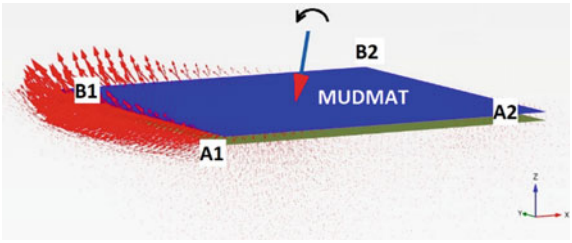

Fig. 8 Soil movement at failure of the mudmat (from finite element analysis)

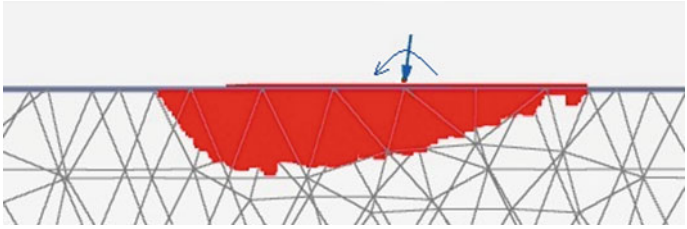

Fig. 9 A vertical section of the mudmat and soil at failure (finite element analysis)

of the soil is reduced, causing more settlement. Finally, the complete collapse of the foundation happened.

The analysis showed that the average maximum foundation (bearing) stress caused by the most critical combination of loading with gravity as well as with combination of gravity and design environmental forces were significantly higher than what was considered for the design. Table 2 shows the comparison.

The estimated bearing stress calculated by the designer was less than the values found in the post-failure analysis. The underestimation of bearing stress was 10% and 28%, respectively, for gravity and combined gravity with design environmental loading.

Post-failure analysis of bearing capacity has been compared with the values used in the design. The comparison (applicable for the most onerous load combinations) is shown in Table 4.

The bearing capacity values shown in the Table 4 were calculated as per API RP 2GEO (2011, with addendum 2014). However, the values which were used for design were found to be over-estimated.

From Tables 3 and 4, it may be observed that the available factors of safety were actually less than required as per terms of design that was same as per the referred API recommendation. Therefore, the mudmat was actually susceptible for significant settlement and bearing failure with the design load combinations. The

Table 3 Comparison of maximum of average bearing stress from all load combinations

Type of loading	Actual (kPa)	Design (kPa)	Underestimation (%)
Gravity	21.6	19.3	10
Gravity + env.	30.1	21.8	28

Note 'env.' means environmental loading

Table 4 Comparison of bearing capacity

Type of loading	Actual (kPa)	Design (kPa)	Actual safety factor	Required safety factor
Gravity	32.3	40.4	1.5	2.0
Gravity + env.	27.5	37.3	0.91	1.5

critical combinations of loading are plotted using the V-H bearing capacity envelops. Figures 10 and 11 show the design critical loads versus the bearing capacity envelops.

It may be observed that the ultimate bearing capacity envelops encompass reduced areas when the overturning moments act on the foundation. The safe zone of loading in Figs. 10 and 11 was derived using the procedure given in API RP 2GEO (2011, with addendum 2014).

It is generally observed from experience of the previous successful installation of many platforms in similar soil conditions that when the recommended factors of

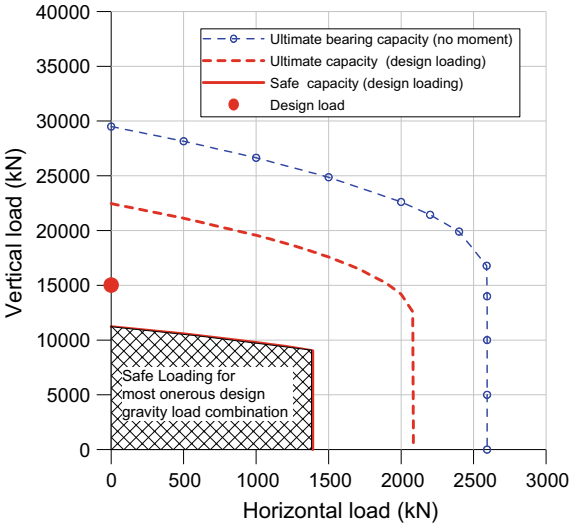

Fig. 10 Capacity envelops for V-H loading (gravity load combination)

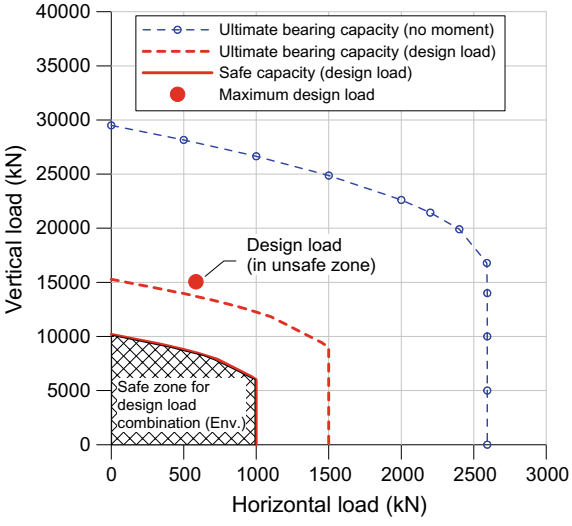

Fig. 11 Capacity envelops for V-H loading (environmental load combination)

safety are ensured in design, no problem of excessive settlement or failure of mudmat occurs.

The failure modes viz. overturning and sliding were also examined with respect to the design loading, soil data and mudmat geometry. Post-failure analysis showed that the designed area of mudmat was adequate to meet the required safety margins with respect to these failure modes. Therefore, these two analyses have been kept out of further discussion.

The review and analysis of the case led to the conclusion that the geometry of the mudmat was inadequate to prevent the bearing failure. Failure began when the gravity load along with eccentricity increased after application of the segment 2 of pile in B1 corner. The factor of safety provided in the design was obviously inadequate. Actual factors of safety with respect to bearing were less since there was underestimation of bearing stress and overestimation of bearing capacity.

It was a progressive failure of the foundation. After a certain stage of loading, the failure started from the B1 corner of the mudmat as expected from analysis. As the tilting of the structure increased, the load eccentricity increased on the mudmat causing further reduction in bearing capacity of the mudmat which finally led to toppling of the jacket.

Subsequently, the structure was successfully installed near the original site after fabricating a larger mudmat satisfying the required factors of safety with proper analysis. The same set of soil parameters as used for the original design was used, and the required factors of safety were met in the revised design.

8 Conclusion

A foundation failure of the jacket structure occurred during installation in western Indian offshore resulting in toppling of the jacket. The post-failure review and analysis of the case led to the following conclusions:

1. During post-failure review, the prescribed soil parameters used for initial analysis and design of the mudmat were found to be reasonable.
   Post-failure successful re-installation of the structure (near the original site) with a newly designed and fabricated mudmat (larger in size than the original) using the same set of soil parameters also proves that the soil parameters were appropriate for the design.
2. Assessment of bearing capacity of mudmat using the current API guidelines matched quite well with 3D finite element analysis in the case. Both conventional bearing capacity and 3D finite element analyses established clearly the susceptibility to failure of mudmat under the design load combinations.
3. Bearing capacity was overestimated, and the bearing stress was underestimated during design by the consultant, thus creating a false sense of adequacy of the required factors of safety.

4. Available factor of safety for design environmental loading was in fact less than 1.0. The factor of safety with respect to gravity loading was 1.5 which was also much less than the required minimum value of 2.
5. The presented case study highlights the importance of scrupulously following the codal requirements and appropriate analysis methodology during the design stage of offshore platforms to prevent avoidable mishaps during installations.

Acknowledgements Authors are grateful to ONGC for permission to publish the paper. Views expressed in the paper are authors' own and not necessarily those of ONGC.

References

API RP 2GEO (2011) (Addendum 2014). Geotechnical and foundation design considerations, , 1st edn. American Petroleum Institute. API, Washington DC, USA

DNV-RP-C207 (2012) Recommended practice, statistical representation of soil data, Det Norske Veritas AS

PLAXIS (2019) User manual for software Plaxis 3D suite. Plaxis, Delft, The Netherlands

Numerical Study on Torpedo Anchor

S. Keerthi Raaj, R. Sundaravadivelu, and Nilanjan Saha

1 Introduction

Traditional anchor system used in offshore energy exploration is challenging and costlier as the water column depth increases. In recent decades, the Dynamically Embedded Anchors (DEAs) are successfully used in Brazilian and Norwegian deep waters (Medeiros 2002; Lieng et al. 2010; Sturm et al. 2011). Though the recent research on DEAs through experiment, field and numerical investigation was carried out considerably, the codal provisions for the design and analysis of these anchors are yet to be established. In order to understand the pullout behavior of the torpedo anchor, earlier using Plaxis 3D, a parametric study was conducted (Keerthi Raaj et al. 2018). The parameter considered in the analysis is the effect of ballast weight, number of fins and tilt angle. In this paper, the parametric study was extended by considering other influencing parameters like effect of loading direction, diameter ratio and fin ratio. The fins/flukes attached laterally to the shaft of the anchor provide stability during anchor free fall in the water column, and later also, these flukes aid in increasing in both the horizontal and vertical pullout resistances. The length and width of these fins play a significant role in pullout capacity estimations. The diameter ratio and fin ratio are the parameters used to investigate the influence of the length and width of the fins.

Mooring lines used to anchor the offshore structure may be catenary, semi-taut or taut lines, as shown in Fig. 1. In the catenary system, mooring lines are connected horizontally to the anchor, and part of anchor line rests over the seabed. Tension in the mooring line at the anchor will be lesser than the tension in the mooring line at the mud line, due to skin friction around part of mooring line resting on/in the seafloor. But, in case of taut or semi-taut, tension at the mud line and tension at the anchor are approximately equal. In this analysis, the torpedo anchors are subjected

S. Keerthi Raaj · R. Sundaravadivelu · N. Saha (✉)
Indian Institute of Technology Madras, Chennai, Tamil Nadu, India
e-mail: nilanjan@iitm.ac.in

S. Haldar et al. (eds.), *Advances in Offshore Geotechnics*, Lecture Notes in Civil Engineering 92, https://doi.org/10.1007/978-981-15-6832-9_11

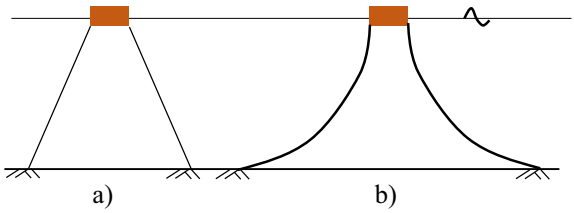

Fig. 1 Mooring line systems **a** taut **b** catenary

to inclined loads, and the effect of loading direction on the pullout capacity was investigated numerically using Plaxis 3D, a finite element commercial package. The scope of the paper is to evaluate the pullout capacity torpedo anchors with a different configuration of loading direction, diameter ratio and fin ratio.

2 Anchor and Soil Properties

The details of the anchor and the soil properties are discussed here concisely (for more details Keerthi Raaj et al. 2018). The top pad eye, bottom conical tip and lateral fins are connected to the hollow shaft, which was usually ballasted with heavy materials. The torpedo anchor numerical model geometry is chosen similar to prototype tested by Medeiros (2002), in Campos Basin, Brazil, and the validation is made to the field tests. These 12-m-long anchors weighing 24 tonnes have an embedment depth of 20 m in the seafloor of undrained shear strength varying $s_u = 5 + 2z$, increase linearly with depth. In the earlier studies, the parameters considered are ballast amount, fin configuration and anchor tilt. For four different ballast conditions (20, 40, 60 and 80%) and three fluke configurations (without a fin, 3 fins, and 4 fins), the anchor tilt was varied ($\beta = 0°$, 2.5°, 5°, 7.5° and 10°). From this analysis, the following conclusions are made: (i) stable torpedo anchors have tilt angle less than 2.5 (ii) anchors with more ballast weight are more stable (iii) increased number of fins offers lateral stability to the anchor. Thus, the torpedo anchors with lesser tilt angle, more ballast weight and with fin are more stable and observed to offer maximum pullout resistance. In this paper, this study was extended by considering the effect of loading direction (0°–90°), diameter ratio (1.02, 1.07 and 1.13) and fin ratio (0, 25, 50 and 75%) of torpedo anchor.

3 Test Condition

The earlier analysis was based on three parameters only (ballast amount, fin numbers and anchor tilt); here, the parametric study was extended by considering three more features like diameter ratio (D_e/D_a), fin ratio (L_f/L_s) and loading direction (α). The diameter ratio (D_e/D_a) is the ratio between the equivalent diameter of the anchor at

the fin cross section (D_e) and the diameter of the anchor at the shaft cross section (D_a).The diameter ratio represents the fluke width of the anchor and their significance in the pullout behavior. Three diameter ratios, 1.02, 1.07 and 1.13, are used to evaluate the fluke width contributions, and the corresponding fluke width is 0.15 m, 0.45 m and 0.95 m, respectively (as shown in Fig. 2f–h). The fin ratio (L_f/L_s) is the ratio between the height of the shaft (L_s) and the height of the fins (L_f). This parameter evaluates the height of the fins and varied from 0 to 75% (as shown in Fig. 2a–d). The last parameter was the loading direction (α), the angle at which the anchor will be moored to the floating offshore structure. This parameter was used to evaluate the best mooring line system to be used to anchor the torpedo anchor, and the loading

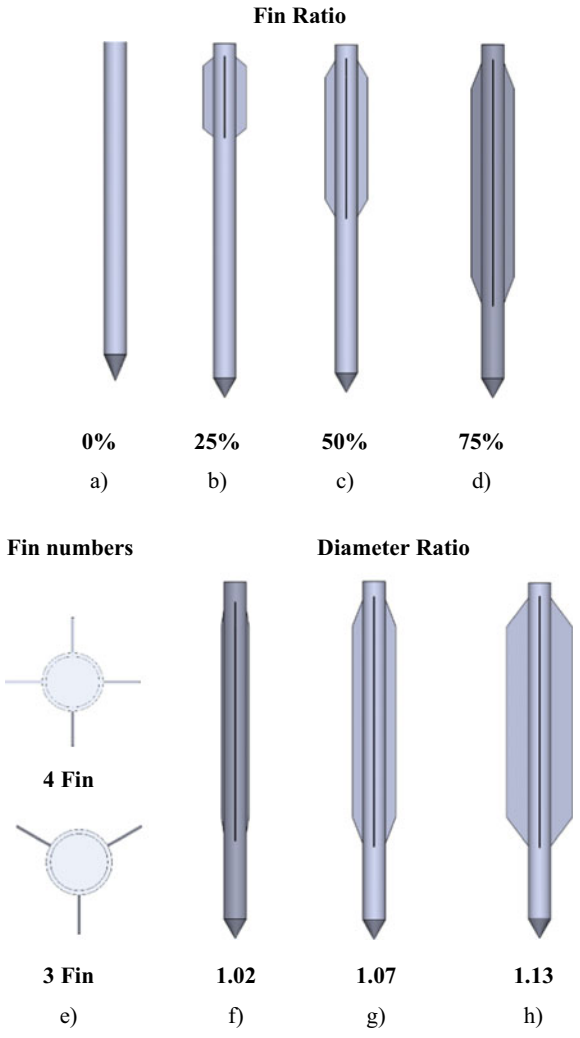

Fig. 2 Torpedo anchor models **a**–**d** fin ratio (0–75%) **e** fin numbers and **f**–**h** diameter ratio (1.02–1.13)

direction was varied from 0°–90° at 30° intervals. The test is also conducted for varying number of fins (3 and 4), but ballast weight was kept constant to 20%. Thus, the tensile load test was conducted for constant ballast weight, varying fin numbers, fin ratio, diameter ratio and the loading direction. The anchor in the analysis is denoted by B20FxDRyyFRzzLDaa, for example, B20F3DR13FR75LD90 which means the model anchor was ballasted for 20% has 3 fins, diameter ratio of 1.13, fin ratio of 75% was subjected to the loading direction of 90°.

4 Numerical Model

A finite element tool, Plaxis 3D, was used to perform the tensile load test on the torpedo anchor (Brinkgreve et al. 2016). The torpedo anchor was modeled as a rigid body and allowed to translate about their respective axis. The tensile load is applied at the top of the anchor (as in Fig. 3) and translated about the x- and z-axis. Hence, the anchor is pulled along the resultant and required loading direction. The soil is modeled using modified Cam-Clay (MCC) model and defined by normal consolidation line slope (λ) and swell line slope (κ). The torpedo anchor was modeled as a non-porous linear elastic material. Installation and pullout are simulated numerically in Plaxis through different stages: the initial sage, anchor embedment stage, pore pressure dissipation stage and finally pullout loading in the particular direction. The in situ field

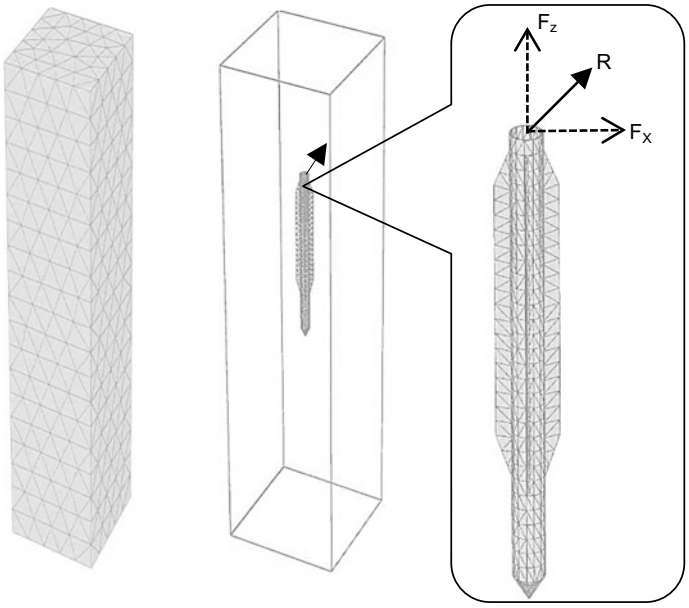

Fig. 3 Plaxis 3D model of total domain with embedded torpedo anchor (in-detail)

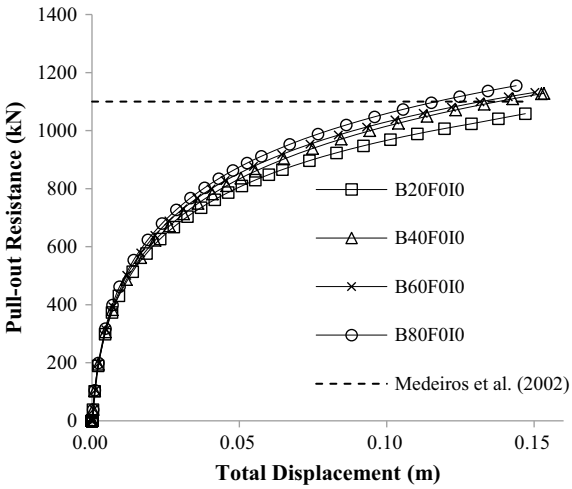

Fig. 4 Validation—pullout resistance of finless torpedo anchor

conditions are simulated in the initial stage, where the anchor and loading conditions are deactivated. In the second and third stages, the anchor is activated as a rigid body, and the excess pore pressure is allowed to drain, respectively. Figure 3 shows the "wished in place" embedded anchor in the soil domain. In the last stage, the embedded rigid anchor was subjected to inclined loads. The resultant total displacement of 0.15 m was applied for a time span of 1 min (Raie 2009).

The field trials performed by Medeiros (2002) in the Campos Basin were validated with the current numerical modeling. The prototype offered 1.1 MN pullout resistances for the horizontal tensile load when the anchor was embedded for 20 m deep. The load–displacement curve shown in Fig. 4 was obtained numerically by inputting the above conditions. These results are close to the prototype in the field test. The difference in the field and the numerical result is about 4.6%, and thus, the Plaxis numerical simulation results are validated by established full-scale field test results. Consequently, for 20%, 40% and 60% ballast condition, the ultimate pullout resistance is 1058 kN, 1126 kN and 1131 kN, respectively, and the difference is within 5%. From Fig. 4, it is also noted that with an increase in ballast weight, the pullout capacity of the anchor increases.

5 Result and Discussion

In this section, the extended parameter study was discussed in detail by analyzing the effect of loading direction (0°–90°), diameter ratio (1.02, 1.07 and 1.13) and fin ratio (0, 25, 50 and 75%) of torpedo anchor. All the above-mentioned parameters are evaluated for the varying ballast and fin configurations (0, 3 and 4), but here, the results for 20% ballast weight are discussed for convenience.

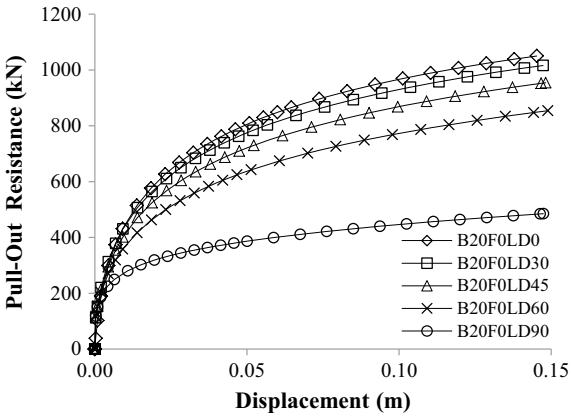

Fig. 5 Effect of loading direction

5.1 Effect of the Loading Directions

Figure 5 represents the typical load–displacement curve for finless torpedo anchor with 20% ballast conditions for different loading directions. It was clear to notice that with an increase in the loading direction the pullout capacity decreases. For the 0°, the pullout capacity was maximum, and with increase in the loading direction, the pullout capacity reduces gradually and reaches minimum value when the anchor was pulled vertically. The reduction in the pullout capacity is 3%, 9%, 18% and 53% for 30°, 45°, 60° and 90°, respectively. Hence, it was proven that the torpedo anchor is good enough to anchor the offshore structures by catenary mooring lines. In this case, the anchor is subjected purely to the horizontal loads only, and the anchor has the ability to withstand more tensile load. But, in the case of taut mooring lines, they offer minimal resistances and undergo failure. If semi-taut mooring lines are used, then mooring line angles at the mud line should not be more than 60°.

5.2 Effect of the Fluke Numbers

Figure 6 shows the typical load–displacement curve for different loading directions for finless and 3- and 4-finned torpedo anchor. From the figure, it could be noted that with an increase in the loading directions, there is an initial gradual decrease in the pullout capacity and followed by a steep decline after 60°. This trend is observed in all three types of fin configurations (0, 3 and 4). For torpedo anchor with 4 fins, the pullout capacity is maximum and followed by 3-finned anchor and finless anchor. With an increase in loading direction from 0° to 90°, the pullout capacity drops for all the cases of fin configurations. Further, the reduction in pullout capacity is in the ratio of nearly 2%, 7%, 16% and 41% for 30°, 45°, 60° and 90°, respectively, for

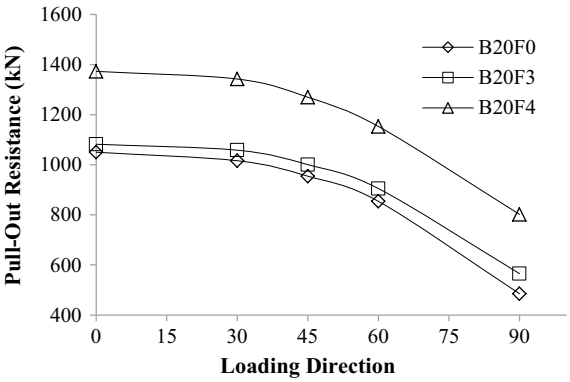

Fig. 6 Effect of fluke numbers

all fin configurations. Therefore, the torpedo anchors with more number of fins have maximum pullout resistances for all loading directions.

5.3 Effect of Diameter Ratio

The diameter ratio (D_e/D_a) is the ratio between the equivalent diameter of the anchor at the fin cross section (D_e) and the diameter of the anchor at the shaft cross section (D_a). Figure 7 represents the load–displacement curve for different diameter ratios of 3- and 4-finned torpedo anchor. It is interested to note that with increase in the loading direction, there is a gradual decrease in the pullout capacity for all the diameter ratios and fin configurations. In the case of 3- and 4-finned anchors with diameter ratio of 1.02 they are closer to each other, which signifies that the fluke width of 0.15 m was not sufficient enough to hold the lateral soil resistances. Also, its worth to note that the gap between the diameter ratio of 1.02 and 1.07 for 3 finned anchors they are more

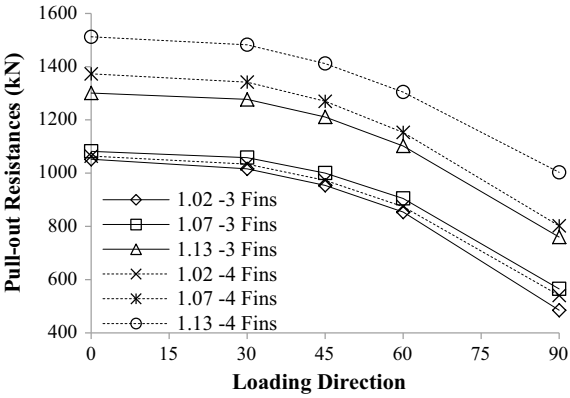

Fig. 7 Effect of diameter ratio

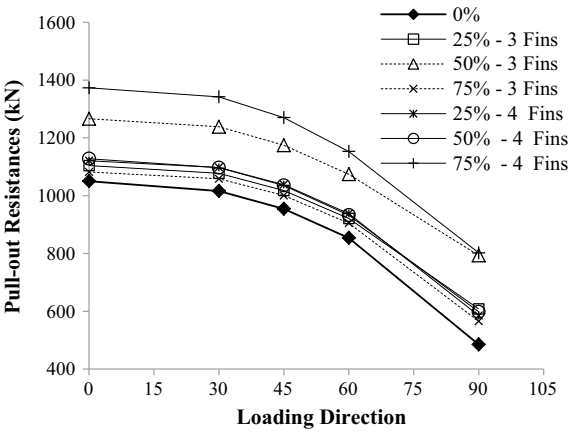

Fig. 8 Effect of fin ratio

closer, while for 4 finned anchors they were separated long enough. This is due to the included angle between fins; for 4 finned, they are perfectly perpendicular which enables to resist the lateral movement more effectively than the 3-finned anchors. A torpedo anchor with diameter ratio of 1.13 has maximum the pullout capacity. Therefore, the increase in diameter ratio increases the pullout resistance, and at the same time, with an increase in loading direction, these resistances decrease gradually.

5.4 Effect of Fin Ratio

The fin ratio (L_f/L_s) is the ratio between the height of the shaft (L_s) and the height of the fins (L_f). Figure 8 represents the load–displacement curve for different fin ratios of 3- and 4-finned torpedo anchor (with same diameter ratio of 1.07) and also a finless anchor. The finless anchor has minimum pullout resistance for all the loading direction cases, which is as expected. But, for 3- and 4-finned anchors, the fin ratio was not as expected since the consistency of results between the 3- and 4-finned anchors are not well matched. The numerical simulations are checked for several times, but the consistency was not uniform for 3- and 4-finned anchors. The 3-finned anchor with 75% fin ratio offers minimum resistances compare to 25 and 50%, which is not as expected. Also, for 4-finned anchors, the fin ratio of 25 and 50% has nearly equal pullout resistances. The inconsistency between the results should be verified through scaled model laboratory experimental studies. Furthermore, this might have occurred due to change in the orientation of the anchor during pull-out. This could be the possible way, even though proper experimental studied will offer more confidence and reliable method of mooring the torpedo anchor.

6 Conclusions

This paper made a complete analysis of the design and loading methods of a torpedo anchor. The previous numerical study was extended by considering additional parameters like the effect of loading direction, diameter ratio and fin ratio. The inference of the present study is:

1. Torpedo anchor is good enough to anchor the offshore structures by catenary mooring lines. But, in the case of taut mooring lines, they offer minimal resistances and undergo failure. If semi-taut mooring lines are used, then mooring line angles at the mud line should not be more than 60°.
2. For all types of fin configurations (0, 3 and 4), with an increase in the loading directions there is an initial gradual decrease in the pullout capacity and followed by a steep decline after 60°.
3. The growth in diameter ratio increases the pullout resistance, and at the same time, with an increase in loading direction, this resistances decrease gradually.
4. Scale down experimental model studies may offer a good understanding of the fin ratio.

Acknowledgements The authors gratefully acknowledge the support from the Ministry of Human Resources and Development, Government of India through Indian Institute of Technology Madras, Chennai. The author also thanks to the Department of Ocean Engineering of IIT Madras for the research facilities.

References

Brinkgreve RBJ, Swolfs WM, Engine E (2016) PLAXIS user's manual. PLAXIS bv, The Netherlands

Keerthi Raaj S, Sundaravadivelu R, Saha N (2018) Stability analysis of torpedo anchors for mooring operations. In: Proceedings of Indian geotechnical conference IGC-2018. Indian Institute of Science, Bangalore

Lieng JT, Tjelta TI, Skaugset K (2010) Installation of two prototype deep penetrating anchors at the Goja field in the North Sea. In: Proceedings of the 2010 offshore technology conference, paper OTC 20758

Medeiros CJ (2002) Low cost anchor system for flexible risers in deep waters. In: Proceedings of offshore technology. Offshore technology conference. Texas, U.S.A. https://doi.org/10.4043/14151-ms

Raie MS (2009) A computational procedure for simulation of torpedo anchor installation, set-up and pull-out. Ph.D. Thesis. The University of Texas—Austin

Sturm H, Lieng JT, Saygili G (2011) Effect of soil variability on the penetration depth of dynamically installed drop anchors. In: Offshore technology conference. Rio de Janeiro, Brazil. https://doi.org/10.4043/22396-ms

Sensitivity and Remoulded Shear Strength of Indian Marine Clays from Eastern Offshore—Evaluation and Correlations

Rohit Sinha, Louis Doley, and R. K. Ghanekar

1 Introduction

A part of shear strength of cohesive soils is lost upon remoulding. The effect of remoulding on shear strength of cohesive soils is expressed by the parameter called sensitivity. Primarily, the cause of this loss is destruction of clays' natural structure, i.e. inter-particle arrangement and inter-particle bonds that develop through natural processes in its geological history. Quantitatively, sensitivity is defined as the ratio of peak undisturbed shear strength and the remoulded shear strength at the same water content.

Sensitivity or remoulded shear strength of clays is an important parameter for the analysis and design of offshore foundation systems. The remoulded shear strength (S_{ur}) profile is important for computing self-weight penetration of piles and suction caissons. Moreover, the knowledge of S_{ur} is useful in computing the soil resistance to installation of these foundation elements. In case of preliminary analysis, low-budget investigations or when data gaps exist in the field or laboratory measurements of these parameters, empirical correlations, either site specific or from literature, can be used. Such correlations for Indian eastern offshore area have not been established so far.

The objective of the study was to review the correlations available in the literature for remoulded shear strength/sensitivity and evaluate them on Indian eastern offshore soil data to arrive at a methodology to assess the remoulded shear strength/sensitivity from other parameters measured in the laboratory or in situ. A second objective of the project was to develop new region-specific correlations for Indian eastern offshore clays, if the selected correlations reported in literature are found not to predict the remoulded shear strength or sensitivity reasonably well.

R. Sinha · L. Doley · R. K. Ghanekar (✉)
Geotechnical Engineering Department, Institute of Engineering and Ocean Technology, ONGC, Panvel, Maharashtra, India
e-mail: rkghanekar@gmail.com; ghanekar_rk@mail.ongc.co.in

S. Haldar et al. (eds.), *Advances in Offshore Geotechnics*, Lecture Notes in Civil Engineering 92, https://doi.org/10.1007/978-981-15-6832-9_12

2 Data Used

The data used in this study have been taken from ONGC's recent eastern offshore deepwater project which also had some installations in shallower waters. The remoulded shear strength has been measured using laboratory vane (LV).

Soil samples were recovered using a piston sampling techniques by using thin walled Shelby steel tubes. To assess the quality of the samples, X-rays of the samples were taken and the best-quality samples were selected for testing. Moreover, quantitative assessment of the sample quality was done using Lunne et al. (2011) method (ISO 19901-8, 2014). Sample quality of majority of samples was found to be "good to fair" or "better". The test results were available from 28 locations in the area. Water depth within the study area ranged approximately from 13 to 1559 m. Majority of the cohesive samples were high-plasticity clays with plasticity index ranged from 40 to 88 and generally have very high clay fraction reaching up to 100%. The water content varied from 40 to 135%. The activity of clays was predominantly in the range of 0.7–1.65, which suggests that the predominant clay mineral is Illite or Illite with some Montmorillonite.

3 Comparison with Existing Correlations

3.1 Remoulded Shear Strength and Liquidity Index

The following correlations between remoulded shear strength and corresponding liquidity index (I_L) have been taken from the literature and evaluated on eastern Indian offshore data. Table 1 summarizes the correlations used for the comparison.

Figure 1 shows the evaluation of the correlation proposed by Yang et al. (2006). Figure 2 depicts the evaluation of the correlation proposed by Worth and Wood (1978). Figures 3 and 4 show the evaluation of the correlation proposed by Terzaghi et al. (1996) and NGI (2002), respectively. It is observed that the proposed correlations are close to the data, but there is a scope of developing area-specific similar correlation for the eastern Indian offshore data.

Table 1 Existing correlations chosen for comparison with Indian eastern offshore data

SL. No.	Correlation proposed by	Correlation	R^2
1.	Yang et al. (2006)	$S_{ur} = 159.6 * \exp(-3.97 I_L)$	0.813
2.	Wroth and Wood (1978)	$S_{ur} = 170 * \exp(-4.6 I_L)$	–
3.	Terzaghi et al. (1996)	$S_{ur} = 2(I_L)^{-2.8}$	–
4.	NGI (2002)	$S_{ur} = 4.2(I_L)^{-1.6}$	–

Note S_{ur} is the remoulded shear strength (kPa), I_L is the liquidity index. R^2 is coefficient of determination

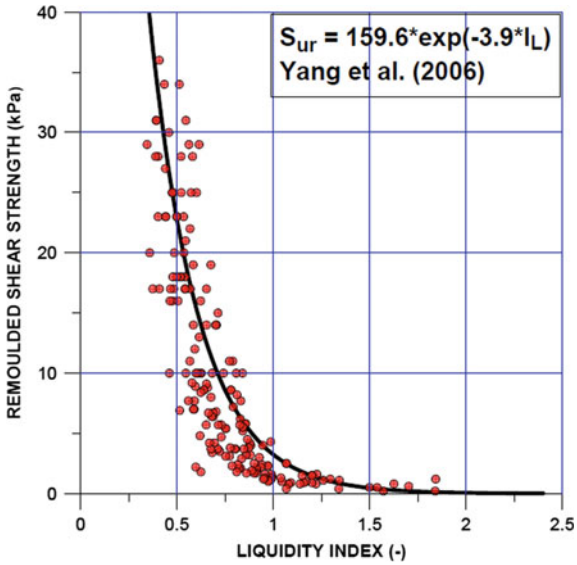

Fig. 1 Evaluation of correlation for remoulded shear strength by Yang et al. (2006)

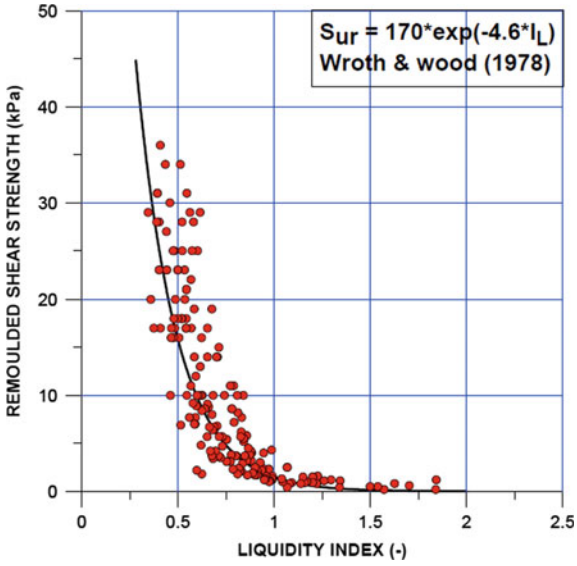

Fig. 2 Evaluation of correlation for remoulded shear strength by Worth and Wood (1978)

To get a clearer view of the comparison, predicted remoulded shear strength using the above discussed correlation has been plotted against the measured remoulded shear strength. Variation of ± 20% has also been shown in Figs. 5, 6, 7 and 8.

It is clearly shown in Figs. 5, 6, 7 and 8 that majority of the data fall outside the ±20% error envelop. Hence, it can be concluded that none of the selected correlations predict very well for the eastern offshore Indian clays.

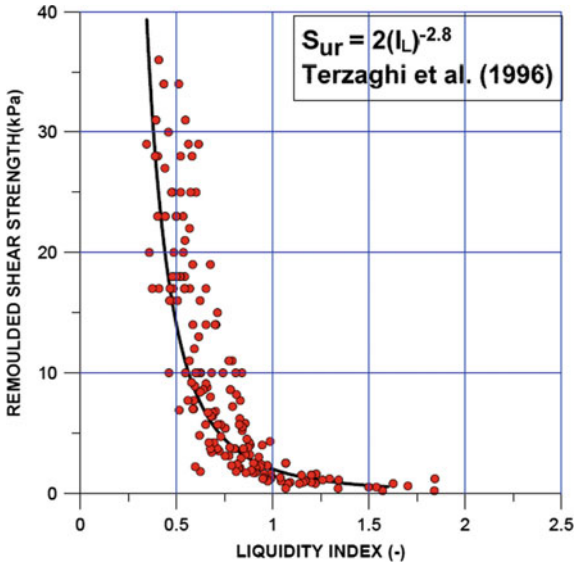

Fig. 3 Evaluation of correlation for remoulded shear strength by Terzaghi et al. (1996)

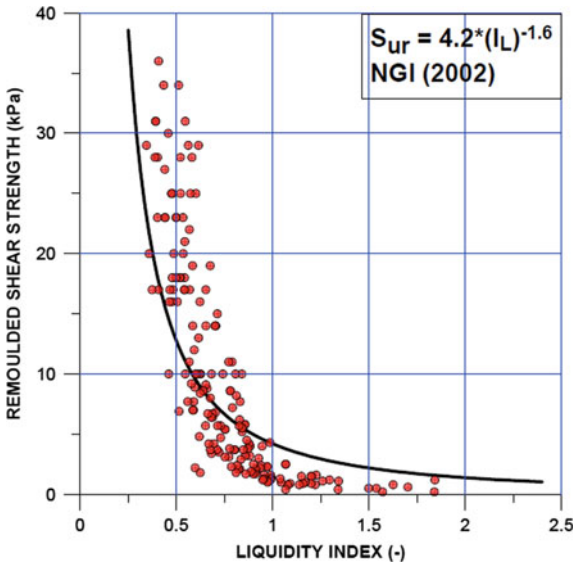

Fig. 4 Evaluation of correlation for remoulded shear strength by NGI (2002)

3.2 Remoulded Shear Strength and CPT Sleeve Friction

The sleeve friction (f_s) values measured by CPT are considered representative of remoulded shear strength of fine-grained soil (Lunne et al. 1997). Hence, the remoulded shear strength is also evaluated in relation to CPT sleeve friction on

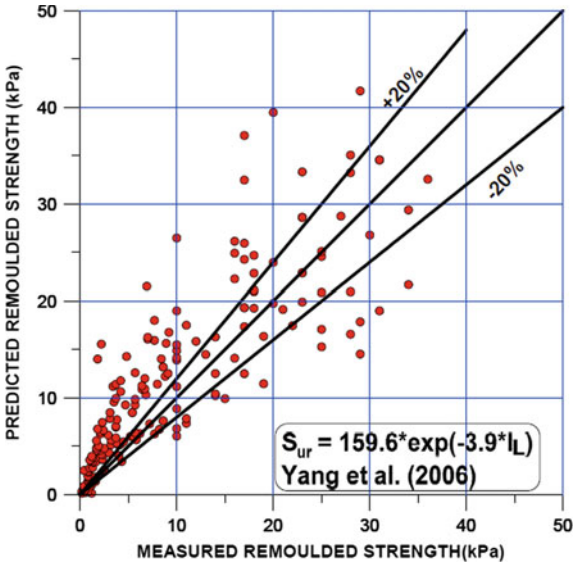

Fig. 5 Predicted remoulded shear strength from Yang et al. (2006) versus measured remoulded shear strength

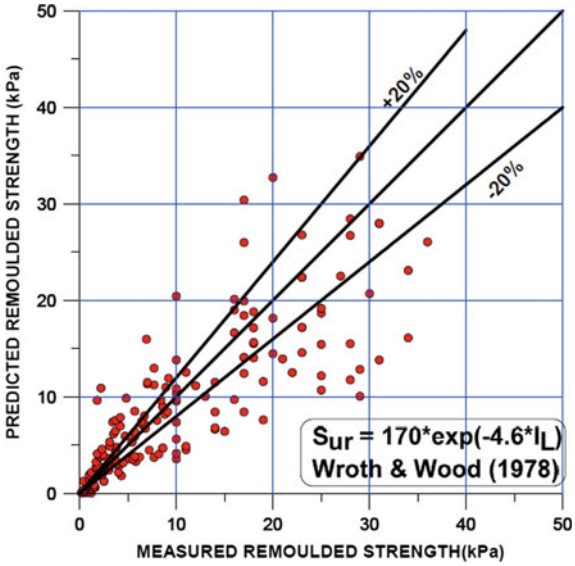

Fig. 6 Predicted remoulded shear strength from Worth and Wood (1978) versus measured remoulded shear strength

Indian eastern offshore area. The existing correlations selected for the evaluation are summarized in Table 2.

Figures 9 and 10 show comparison of the two correlations with the measured data from eastern Indian offshore. It can be seen that both the correlations plot above the data obtained from Indian eastern offshore clays.

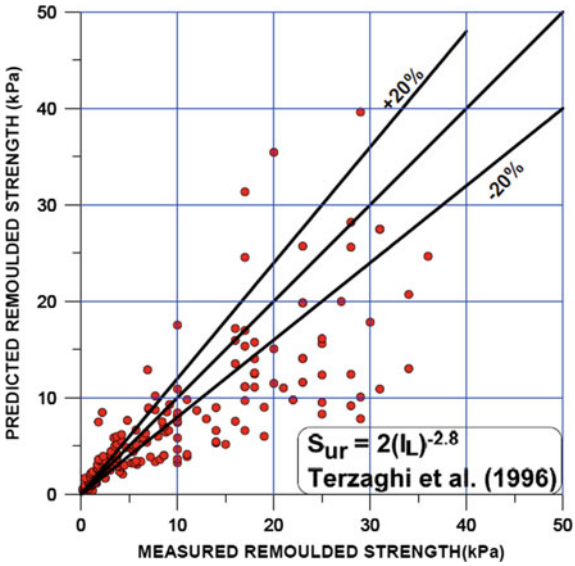

Fig. 7 Predicted remoulded shear strength from Terzaghi et al. (1996) versus measured remoulded shear strength

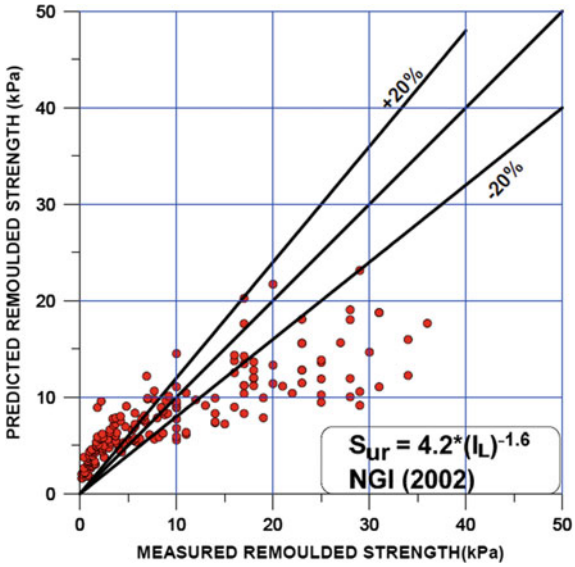

Fig. 8 Predicted remoulded shear strength from NGI (2002) versus measured remoulded shear strength

3.3 Remoulded Shear Strength and Sensitivity

Existing correlations were evaluated on the sensitivity data obtained from Indian eastern offshore, and some attempts to develop new correlations were also made, but it was found that the scatter is too large to make any meaningful conclusion or

Table 2 Existing correlations chosen for comparison with Indian eastern offshore data

Sl. No.	Correlation proposed by	Correlation	R^2
1.	Nayak et al. (2016)	$S_{ur} = 2.254 + 0.6191 * (f_s)$	0.685
2.	Ramsey (2010)	$S_{ur} = 2/3 * (f_s)$	–

Note S_{ur} is the remoulded shear strength (kPa), f_s is the sleeve friction (kPa). R^2 is coefficient of determination

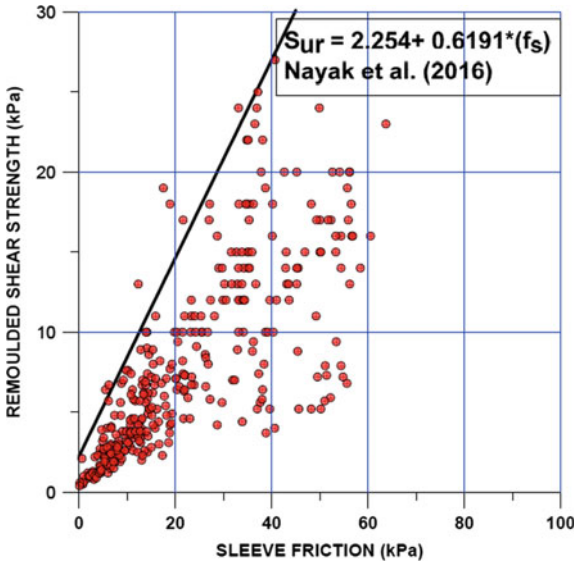

Fig. 9 Evaluation of correlation for remoulded shear strength by Nayak et al. (2016)

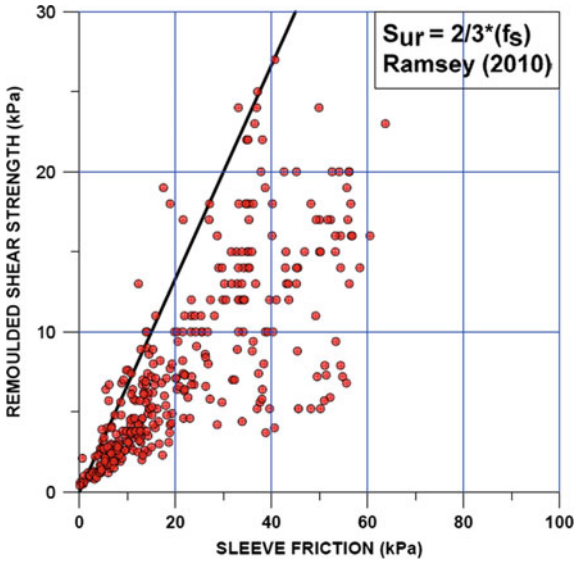

Fig. 10 Evaluation of correlation for remoulded shear strength by Ramsey (2010)

Table 3 Results of regression analysis

Equation	Results of regression analysis	R^2	n
A	$S_{ur} = 2.0624 * I_L^{-3.102}$	0.8058	184
B	$S_{ur} = 95.305 * \exp(-3.682 * I_L)$	0.7763	184
C	$S_{ur} = 31.711 * I_L^2 - 83.552 * I_L + 52.798$	0.7085	184
D	$S_{ur} = -49.307 * \log(I_L) + 2.9101$	0.6460	184
E	$S_{ur} = -23.153 * I_L + 27.621$	0.5164	184
F	$\ln(S_{ur}) = 0.81 * \ln(f_s) - 0.49$	0.7691	328

Note n is number of data points, R^2 is coefficient of determination, S_{ur} is the remoulded shear strength (kPa), I_L is the liquidity index, f_s is the sleeve friction (kPa)

develop any worthwhile correlation. It was hence decided that it is not worthwhile to pursue such correlations at present.

4 Regression Analysis

From the discussion in the previous sections, it is evident that there is a scope to develop area-specific correlation for eastern Indian offshore. Development of a few new correlations was attempted using regression analysis. Single-variable regression analysis was performed between the remoulded shear strength and the corresponding liquidity index and CPT sleeve friction.

The results of the regression analysis are presented in Table 3.

5 Results and Discussion

The evaluation of soil data from eastern Indian offshore revealed that although the plot between remoulded shear strength and liquidity index conforms to the trends proposed by researchers worldwide, a significant error in the predicted values from these correlations is observed.

A possible reason of this deviation could be the method of measurement of remoulded shear strength.

The measurement method for remoulded shear strength in most of the published correlations is fall cone test, but the Indian eastern offshore data used in this study have been primarily measured via laboratory vane test.

The statistical analysis between remoulded shear strength and liquidity index is represented by Equations A–E in Table 3. Equations A and B show a reasonable strength with R^2 of 0.8058 and 0.7763, respectively. Figures 11 and 12 show the evaluation of Equations A and B, respectively.

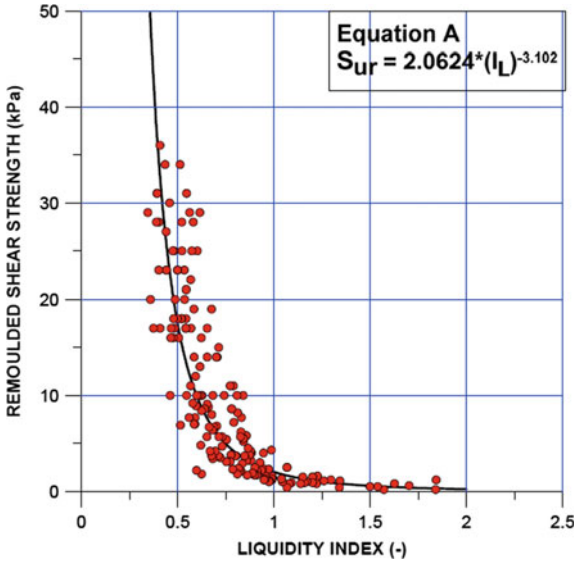

Fig. 11 Evaluation of correlation for remoulded shear strength by Equation A

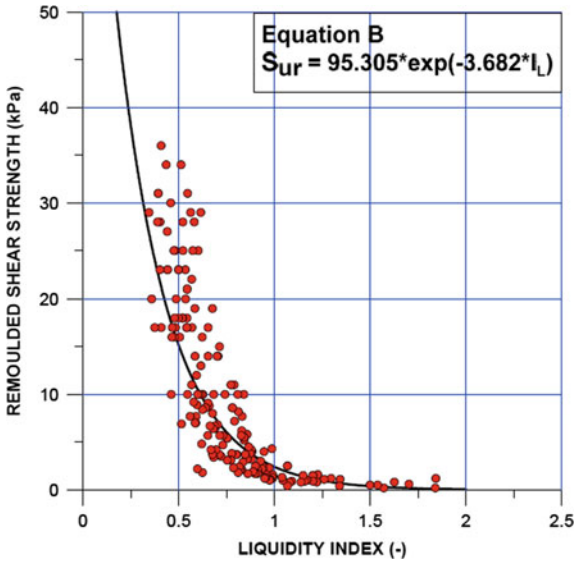

Fig. 12 Evaluation of correlation for remoulded shear strength by Equation B

A correlation attempted between remoulded shear strength and sleeve friction measured by CPT shows a reasonably good correlation with R^2 value of 0.7691. The evaluation for equation F is presented in Fig. 13.

However, when these correlations are applied practically, a lot of scatter is observed. Plots between measured remoulded shear strength and the predicted remoulded shear strength using Equations A to F show that the calculated and

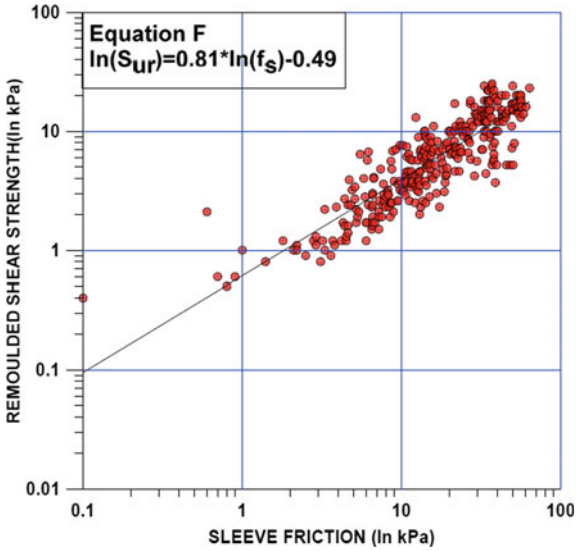

Fig. 13 Evaluation of correlation for remoulded shear strength by Equation F

measured values do not agree well. Figures 14, 15 and 16 depict the same for Equations A, B and F, respectively.

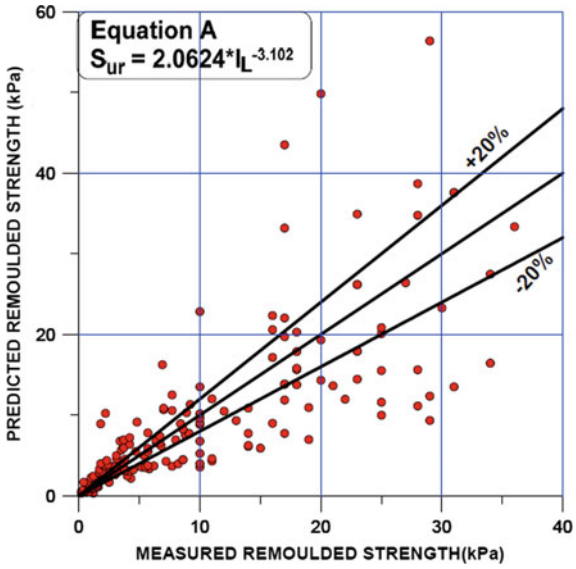

Fig. 14 Predicted remoulded shear strength from Equation A versus measured remoulded shear strength

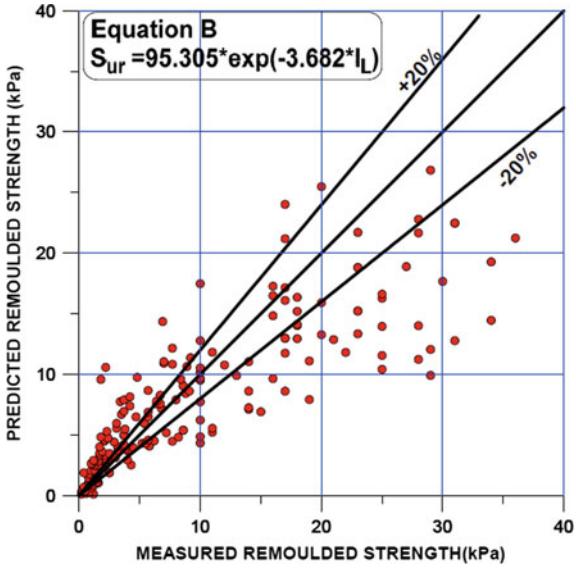

Fig. 15 Predicted remoulded shear strength from equation B versus measured remoulded shear strength

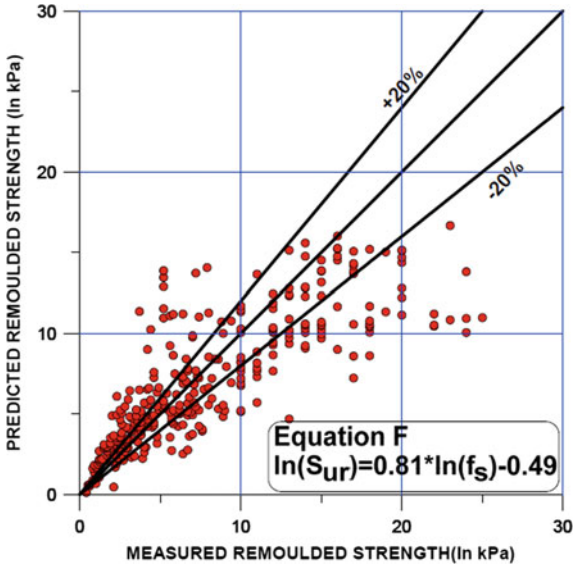

Fig. 16 Predicted remoulded shear strength from Equation F versus measured remoulded shear strength

6 Conclusion

To evaluate the applicability of the published correlations for remoulded shear strength and sensitivity for Indian eastern offshore clayey soils, in this study, soil data from 28 offshore locations of Indian eastern offshore area were selected. It is

concluded that none of the published correlations predict very well for the clays found in the selected site. Attempts were hence made to derive some new area-specific correlations by performing regression analysis between remoulded shear strength and corresponding liquidity index and CPT sleeve friction.

It is observed that the sensitivity data from the soil investigation site show considerable scatter when plotted against liquidity index. Hence, no further attempts to develop correlations were made for the same. For the remoulded shear strength data, a total of six correlation equations have been derived with strength of R^2 ranging from 0.51 to 0.80. Statistically, Equations A, B and F show comparatively better strength with R^2 of 0.806, 0.776 and 0.769, respectively. The best correlation statistically for the data is represented by Equation A ($R^2 = 0.806$). However, when the correlations are evaluated for their applicability by plotting the measured values against calculated values of remoulded shear strength, it is observed that a good amount of data fall outside the error envelop of $\pm 20\%$.

It is hence proposed that, at present, for preliminary engineering, the best-available correlations reported in this paper, i.e. Equations A, B and F (Table 3), should be used to arrive at a reasonable assessment. The present data will be augmented with data from future investigations in eastern Indian offshore area, and the issue will be re-evaluated.

Acknowledgements Authors are grateful to the management of ONGC for granting permission to publish the paper. Views expressed are those of authors only.

References

Lunne T, Robertson PK, Powell JJM (1997) Cone penetration testing in geotechnical practice. Blackie Academic and Professional, London

Lunne T, Berre T, Andersen K, Strandvik S, Sjursen M (2011) Effects of sample disturbance and consolidation procedures on measured shear strength of soft marine Norwegian clays. Can Geotech J 43:726–750

Nayak B, Ghanekar RK, Ajit A (2016) Appraisal of sensitivity correlations on data from clays of western Indian offshore. Geotech Appl Lecture Notes Civil Eng 13. Springer, Singapore

NGI (2002) Early soil investigations for "fast track projects", Report 521553. Norwegian Geotechnical Institute, Oslo, Norway

Ramsay N (2010) Some issues related to applications of CPT. In: 2nd international symposium on cone penetration testing. Huntington Beach, CA, USA

Terzaghi K, Peck RB, Mesri G (1996) Soil mechanics in engineering practise, 3rd edn. Wiley, NY

Wroth CP, Wood DM (1978) The correlation of index properties with some basic engineering properties of Soils. Can Geotech J 15:137–145

Yang SL, Kvalstad T, Solheim A, Forsberg CF (2006) Parameter studies of sediments in the Storegga slide region. Geo-Mar Lett 26(4):213–224

Application of Reliability-Based Methodology in Determining Risk on Offshore Stationary Platforms Due to Regional Geohazards

Kaushik Mukherjee and M. Sapihie B. Ayob

1 Introduction

By definition, geohazards are the results of the long-term or short-term geological processes which give rise to several geological and environmental conditions. Geohazards can appear in a large magnitude enough to affect local or regional engineering and economy to a great extent. For the structures particularly constructed in a subsea environment, prior detection of such conditions is essential to ensure future stability and integrity.

The significant geohazards in subsea condition are earthquake, shallow gas and subsidence among the few. The most common earthquakes are of tectonic nature causing ground shaking due to various intensities of released energy at the plate boundary. The uncertainty model of the earthquake lies in its treatment of data through probabilistic seismic hazard analysis [PSHA] to determine the energy spectrum. The designed structure is generally equipped with the energy attenuation mechanism. The uncertainty modeling lies in developing a variable load surface depending on the most likely range of intensities.

The subsidence is a deep reservoir geologic phenomenon mainly caused due to reservoir compaction during oil and natural gas extraction. This normally happens to the reservoirs with some particular oil-bearing rock properties. In most of the cases, the subsidence is not associated with any differential movement of the platform structure. The uncertainty lies in the magnitude and extent of subsidence that may cause wave-in-deck scenario and potential jacking up operation. A little or no changes in the soil condition anticipated.

Shallow gas is essentially a natural gas which is accumulated at a very shallow depth from earth's surface. Shallow gas may be of biogenic or petrogenic origin trapped within the pore water of shallow soils. In situ natural gas can exist either

K. Mukherjee (✉) · M. S. B. Ayob
Global Technical Solutions, PETRONAS, Kuala Lumpur, Malaysia
e-mail: mukherjee_km@hotmail.com

S. Haldar et al. (eds.), *Advances in Offshore Geotechnics*, Lecture Notes in Civil Engineering 92, https://doi.org/10.1007/978-981-15-6832-9_13

in gaseous form or bonded with water to form a solid, known as gas hydrate. The entrapped shallow gas may not always be detectable prior to construction by a routine survey. It may appear during operating stages of the offshore structures. Shallow gas seeping upward through the soil deteriorates the soil strength, which effects foundation capacity. This is a dynamic phenomenon, whereas soil properties keep on changing due to continuous scouring because of seepage of gas. Uncertainty in prediction of soil strength subsequently may lead to many studies, surveys and analyses after detection of shallow gas. The reliability study revolves around this uncertainty modeling of soil or foundation resistance.

The previous reliability studies were performed by other researchers to determine the pile capacity in shallow gas-dominated site. This paper concentrates on devising a standardized methodology through a case study [on shallow gas geohazard] to perform a detailed structural reliability assessment (SRA) used to predict the probability of failure (POF) for the platform structures subjected to various geohazards and random load–resistance conditions.

Traditional structural analysis has been based on deterministic analysis. Nevertheless, in real cases, many of these analysis parameters inherit certain degree of uncertainties, e.g., fluctuation of loads, variation of material properties, different analysis models and others, which requires reliability analysis to predict failure probability of the structures.

The SRA determines the structural probability of failure (POF) considering various possible uncertainties in load and resistance responses. Various uncertainties affecting structural performance have been considered which arise from the effect of gas seepage in the soil properties, material properties, environmental and gravity loading parameters. These parameters form the load and resistance response surface. The POF is established by adopting first-order reliability method (FORM). Measuring the safety of a structure by its POF value makes the reliability analysis a useful decision tool. Fulfillment of requirement to this reliability is then necessary in order to ensure a sufficient safety level (i.e., target reliability or POF) as called by the code has been met. The target POF is normally calibrated for the region and it assumes different values for different types of facilities.

The POF for this study is calculated for two (2) conditions: one addresses the structural collapse of the jacket due to soil failure which involves the soil around the upper layers of the piles, bending of the piles and global horizontal displacement of the substructure and the other addresses the structural collapse due to buckling of the structural members. Subsequently, the results are presented to establish the methodology.

2 Background Theories

Structural reliability analysis (SRA) is a tool to quantify probability of failure (POF) of a structure due to time-variant or -invariant damage or natural processes. The load

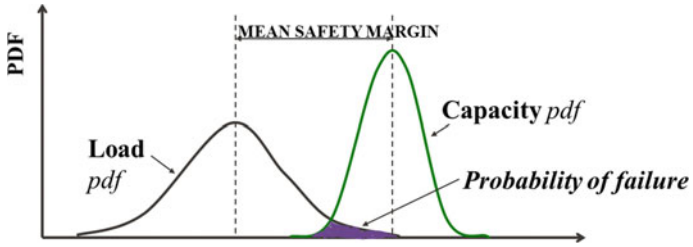

Fig. 1 Probability distribution function of load and capacity

and resistance or strength uncertainty will affect the mean safety margin and chances of failure as per Fig. 1.

To estimate the overall system failure probability, the parameters which are significant for component failure need to be identified. The identified parameters will then be segregated either deterministic or stochastic. A deterministic or stochastic parameter may be considered as a function of time-variant or time-invariant. When a random variable assumes values as a function of time, the variable is called a stochastic variable. The probabilistic study of a stochastic variable is called stochastic process or random process. Data collected in the random process is simulated using Monte Carlo technique.

The failure criterion has to be described by a mathematical function, known as the limit state function, in a structural reliability analysis, which must fulfill the following condition:

$$g(x) = \begin{cases} > 0, \text{ when } x \text{ is in the safe set} \\ = 0, \text{ on the failure surface} \\ < 0, \text{ when } x \text{ is in the failure set} \end{cases} \tag{1}$$

where the limit state function is denoted by $g(\ )$ and x is the vector of stochastic variables involved in the behavior of the system. When the limit state function fulfills these requirements, the probability of failure can be written as:

$$P_F = \int_{g(x)<0} f_x(x)\, \mathrm{d}x \tag{2}$$

where the integration is carried out over the failure set of the joint probability density function of the stochastic variables $f_x(x)$. The limit state function is often expressed as the difference between the capacity of the structure, R and the load applied to the structure, L, i.e., $g = R - L$.

In more general problems, the probability of failure can be expressed as follows (Gilbert 2011):

$$P_F = P\left[g\left(\vec{X}\right) \leq 0\right] \tag{3}$$

where $g\left(\vec{X}\right)$ is a function that indicates the performance of the foundation and $\vec{X}$ is a vector on 'n' random variables upon which the performance depends.

First-order reliability method (FORM) provides a useful technique to approximate the probability of failure analytically for complex cases where the performance function can be a nonlinear.

$$P_F \cong \phi(-\beta) \tag{4}$$

where the reliability index β takes the form of:

$$\beta = -\frac{\overrightarrow{\frac{\partial g}{\partial s}\Big|_{s^*}}^T \overrightarrow{s^*}}{\left(\overrightarrow{\frac{\partial g}{\partial s}\Big|_{s^*}}^T [C_s] \overrightarrow{\frac{\partial g}{\partial s}\Big|_{s^*}}\right)^{1/2}} \tag{5}$$

The key to this method is finding the realization of input variable $\overrightarrow{X^*}$ such that the equation for P_F provides a reasonable approximation. This point in the n-dimensional space of $\vec{X}$ is found by minimizing β with respect to $\vec{X}$ subject to $g(\vec{X}) = 0$. The set of values in $\overrightarrow{X^*}$ is referred to as the most probable point, and it physically represents the most likely combination of input variables that will lead to the event of failure. Figure 2 depicts a typical joint probability distribution of two independent normal variables with different failure criteria (Beacher and Christian 2003).

The salient features of FORM are as follows (Gilbert 2011):

- The standardized limit state failure surface is linearized.

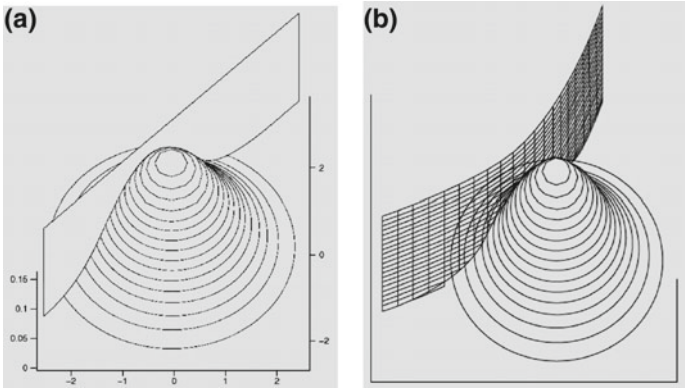

Fig. 2 Joint probability distribution of two independent normal variables and **a** linear [FORM]; **b** nonlinear failure criterion [SORM]

- Only the first-order terms are used of the failure function.
- Therefore, the method is called first-order reliability method (FORM) which uses mean and standard deviation values.
- The 'design point' or the 'beta point' is the 'point of maximum likelihood' of failure.
- The failure surface is rarely linear, and it will have some curvature, but at the point closest to the origin (beta point), its first-order linearization is valid for most cases.

In second-order reliability method (SORM), the limit state surface is approximated by a second-order quadratic surface in the design point (Fig. 3). The analytical methods give approximate results and should only be applied for failure probabilities less than 0.05. For larger failure probabilities, simulation methods should be used (Gilbert 2011).

Another alternative solution is described by expanding ellipsoidal perspective of reliability procedure as described by Bak Kong Low (Phoon 2008). The matrix formulation (Veneziano 1974; Ditlevsen 1981) of the Hasofer-Lind (FORM) index β is expressed as:

$$\beta = \min_{x \in F} \sqrt{(x-\mu)^{\mathrm{T}} C^{-1} (x-\mu)} \tag{6}$$

or, equivalently,

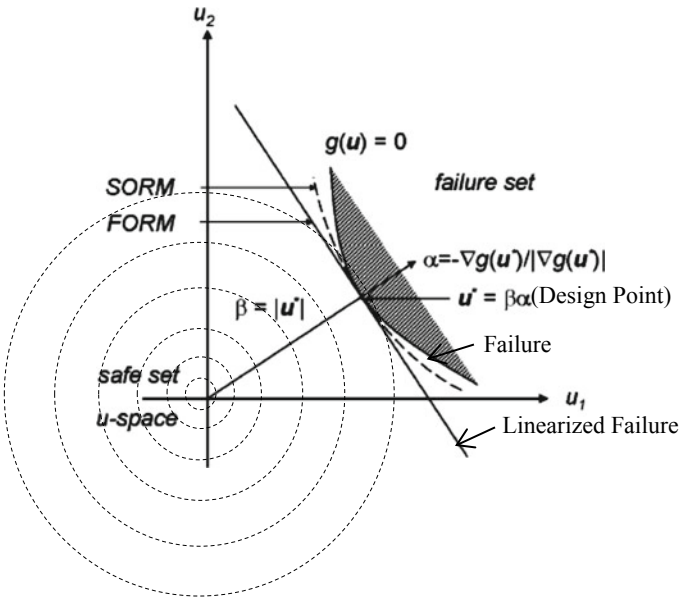

Fig. 3 FORM/SORM approximation to failure surface

$$\beta = \min_{x \in F} \sqrt{\left[\frac{x_i - \mu_i}{\sigma_i}\right]^{\mathrm{T}} [R]^{-1} \left[\frac{x_i - \mu_i}{\sigma_i}\right]} \tag{7}$$

where x is representing random variable, μ is the mean value, C is the covariance matrix, R is the correlation matrix, σ is the standard deviation and F is the domain of failure. The method requires the setup of the correlation matrix R between various random variables constituting the load–resistance uncertainty model. The solution centers around the minimization of β to satisfy the performance function $g(x)$.

3 Methodology

In a pilot study, a standard offshore platform is considered for its reliability against environmental loading resisted by uncertain soil environment under complex shallow gas effect. Here, the capacity is defined as the base shear force at ultimate collapse [calculated in terms of Reserve Strength Ratio or RSR], and the load is the resultant base shear force due to applied environmental loads. The performance function will check the cases where the applied load surface overtakes the capacity to define a failure.

In this case, a simplified in-place model is adopted for the ease of multiple pushover run required for the generation of resistance or capacity Surface. The applied gravity loads include self-weight of structures, appurtenances, equipment and piping loads, etc. Wind loads from modules are also applied at respective points of topsides module supports. The environmental loads have been applied on substructure. The maximum wave and current load for 100-year return period [extreme storm case] have been considered and the worst combination of the loading direction.

3.1 Parametric Sensitivity

The computation of uncertainty importance factors is not a must but provides a measure of the relative contribution from the uncertainty in each variable to the failure probability or reliability index β. The factor indicates the importance of modeling the random variable(s) as a distributed variable rather than as a fixed variable, the median of the distribution being the fixed value.

$$\boldsymbol{\alpha}_{\boldsymbol{\mu}} = \frac{\partial \boldsymbol{\beta}_{\boldsymbol{R}}}{\partial \boldsymbol{\mu}} \tag{8}$$

The typical importance factors for a shallow gas uncertainty modeling, based on basic stochastic variables, are as per Table 1. In this case, the random variables fall into two main groups:

Table 1 Uncertainty importance factors [typical]

Description	Relative importance (%)
Environment: wave height, current and wind speed	86
Load effect: model uncertainty in the calculated environmental load effect	7
Soil condition: intercept value of static, undrained, soil shear strength	1
Soil condition: cyclic loading factor	~0
Soil condition: soil strain at 50% strength	~0
Soil condition: excess pore pressure	2
Capacity: model uncertainty factor on the calculated capacity	3

1. Environmental Variable
2. Soil Variable.

Table 1 indicates that the failure probability is strongly influenced by uncertainties of environmental loadings. Uncertainties in resistance from foundation stiffness lead to the remaining percentage due to shallow gas effect. Other variable will be treated as deterministic variables.

3.2 Load Surface Modeling

With the importance factors above, a typical set of variables is specified by the following parameters:

- Water Depths—uncertainties of MSL changes due to various factors such as subsidence, differences of HAT and LAT.
- Maximum Wave Height—uncertainties with assigned COV of 15, 20, 25 and 30%.
- Peak Wave Period—associated with the significant wave height fitting correlation curve from raw data fitted with log-normal distribution function.
- Surface Current Speed—uncertainties with assigned COV of 15, 20, 25 and 30%.
- Bias factor on marine growth from observed inspection data on the variation of marine growth.

The water depth and marine growth variations follow the data from respective region and standards. The other parameters specified above are derived using the respective distribution function as explained in Table 2. As for the wind speed, initial analysis confirms that the wind load is a small component of the total base shear for the particular region. Thus, it is modeled as conditional on the wave and current loads. It is also assumed that dynamic response of the jacket structure contributes to approximately 10–15% of the base shear for 100-year return period at the critical

Table 2 Distribution function of variables

Description	Distribution function
Short-term maximum wave height	Weibull
Long-term maximum wave height	Weibull
Short-term total current speed	Gumbel
Long-term total current speed	Weibull
Wave period	Log normal

direction, for the structures in general in the region [with a natural frequency varying between 2.5 and 3.0 s].

The maximum wave height is based on hindcast data of 56 years from 1956 up to 2012 hourly data in the region. This data was originally developed by Oceanweather Inc for the SEAMOS (2012) joint industry project. This hindcast data is applicable for description of general features of the metocean condition; thus, it is used to develop the uncertainty model parameters of the distribution of maximum wave height that is based on 56 years hourly data.

The waves that have dominant load effects on the platform are waves approaching from northeast (NE) compass direction. The scatter plots from the hindcast data in Fig. 4 confirm that the highest waves approach from the compass sector between 22.5° and 67.5° or heading toward compass sector between 202.5° and 247.5°.

The wave and current approaching from northeast direction generate maximum base shear, and thus for this analysis, only NE direction has been considered for environmental loading. Using Weibull distribution, the short-term distribution for 56 years maximum wave height was plotted to get the mean value of the distribution. Extreme value analysis was conducted to plot the long-term distribution, and the value for 100-year maximum wave height was obtained. The mean of the 100-year distribution is then used to plot the distribution uncertainties with COV of 15, 20, 25

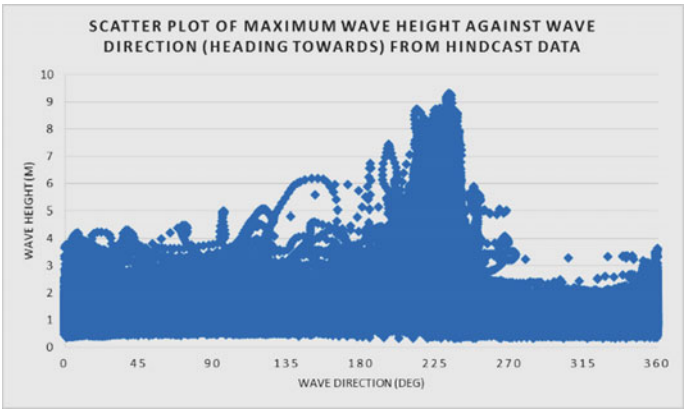

Fig. 4 Scatter plot of maximum wave height

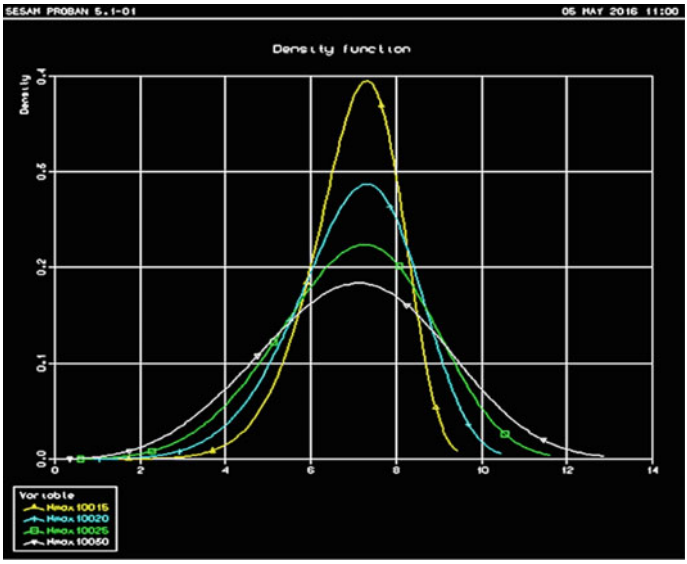

Fig. 5 100-year wave load distribution with COV of 15, 20, 25 and 30% [typical from PROBAN]

Table 3 Maximum wave height from different COV

COV (%)	Maximum wave height, H_{max} (m)
15	9.02
20	9.83
25	10.73
30	11.69

and 30% as per Fig. 5. The 100-year maximum wave height values obtained are as per Table 3 and were used to obtain the base shear for the load response surface.

The current speed is based on hindcast data of 20 years from 1992 up to 2012 hourly data. The data taken is in the same direction, which is from northeast (NE) toward southwest (SW) direction, with compass sector between 22.5° and 67.5°. The scatter plots of the hindcast data in Fig. 6 confirm that the total current speed is highest heading from the compass sector between 22.5° and 67.5° or heading toward compass sector between 202.5° and 247.5°.

Using Gumbel distribution, the short-term distribution for 20-year current speed was plotted to get the mean value of the distribution. Using values for 20 years, extreme value analysis was conducted to plot the long-term distribution and the value for 100-year total current speed using Weibull distribution was obtained. The mean of the 100-year distribution is then used to plot the distribution uncertainties with COV 15, 20, 25 and 30% as per Fig. 7. The 100-year total current speed values obtained are as per Table 4 and were used to obtain the base shear for the load response surface.

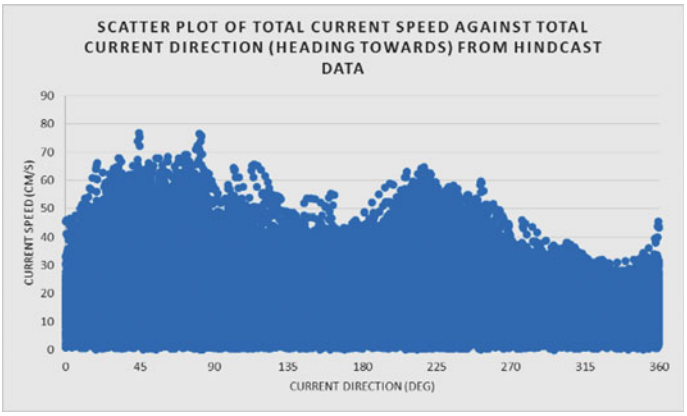

Fig. 6 Scatter plot of total current speed

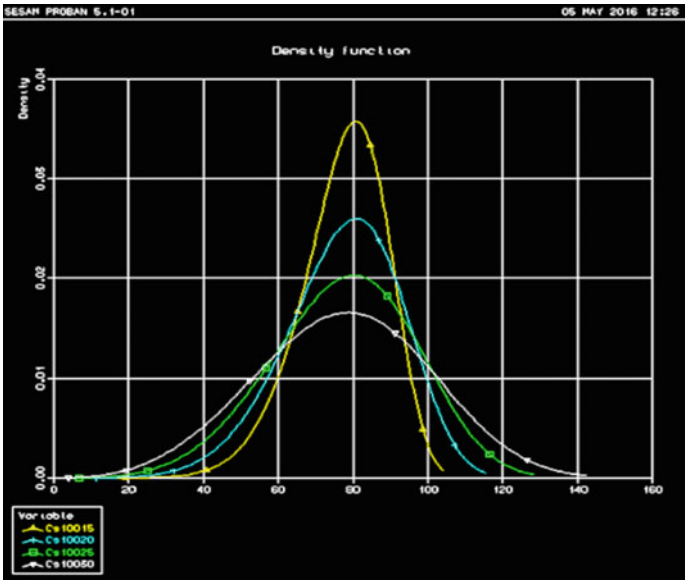

Fig. 7 100-year current load distribution with COV of 15, 20, 25 and 30% [typical from PROBAN]

Table 4 Total current speed from different COV

COV (%)	Total current speed, C_T (m/s)
15	0.99
20	1.08
25	1.18
30	1.29

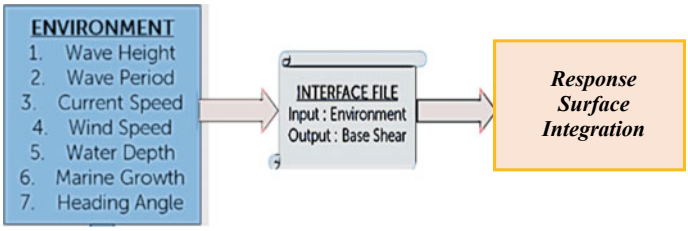

Fig. 8 Load response surface development

The hydrodynamic loads due to wave and current are calculated by Morrison equation. Stoke's fifth-order wave theory is applied. The analyses input comprises all the 100-year loading, and the hydrodynamic properties are specified accordingly. The output is the loading in terms of base shear force and overturning moment. Since the base shear is expected to be the dominant load effect, it is normally selected for the interface file.

The calculation of environmental loads and the reliability analysis is decoupled by inserting a response surface module between the two sets of calculations. A systematic series of calculation of loads is carried out, and the results are arranged on the interface file. The response surface module is developed fitting in Weibull distribution and provides load variables by interpolating on the interface file. Development of response surface is shown schematically in Fig. 8.

The response surface module is based on sequential application of spline interpolation for each input variable and requires that the interface file is defined for a full grid of data points. The typical summary of input data is as per the following:

- A single collinear heading from compass direction northeast (NE)
- Maximum wave height
  9.02, 9.83, 10.73 and 11.69 m
- Associated wave period
  9.96, 10.40, 10.86 and 11.34 s
- Total current speed
  0.99, 1.08, 1.18 and 1.29 m/s
- Water depths
  74.7, 72.87 and 76.46 m
- Bias factor on marine growth
  1.0, 1.1, 1.2 and 1.3

This implies a total combination of 192 data points (4 wave height × wave period × 4 current speed × 3 water depth × 4 marine growth).

Wind forces on the structure above the mean sea level are included in the analysis as a fixed value, which is the 1-min mean wind speed for 100 years. Thus, the total base shear loads are taken as the sum of hydrodynamic and wind loads.

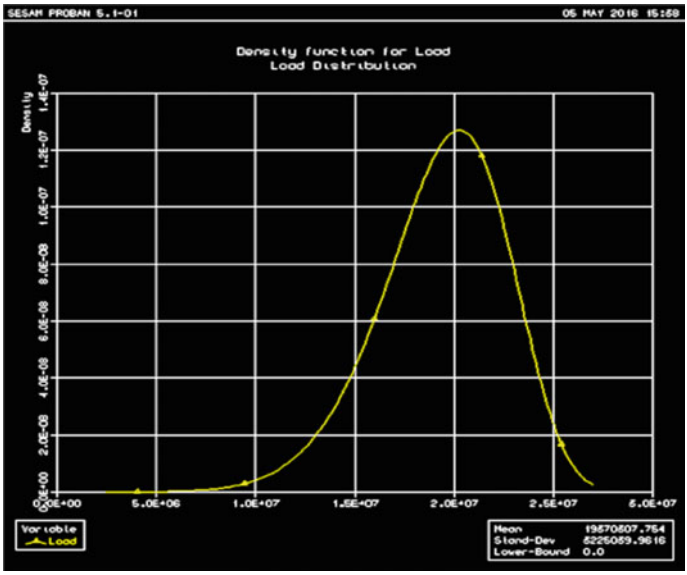

Fig. 9 Load response surface [typical from PROBAN]

The 192 runs were conducted (using SESAM 2016) to determine the base shear load with different combinations of environmental condition. The results are then collected to develop the best-fit load response surface. The resultant load response surface is shown in Fig. 9.

3.3 Probabilistic Model for Capacity Surface

Based on the findings from the site and the soil analysis report, the recommended upper bound, lower bound and best estimate variations with depth for undrained shear strength, submerged unit weight and soil strain at 50% strength were extracted. The effect of excess pore water pressure may or may not be negligible, but the range of recommended parametric value should include this effect.

The typical site soil profile consists of twelve (12) clay layers. Depending on the survey confirmation, any visible effect of shallow gas on top soil, e.g., formation of craters, loosening of soil, etc., and these effects should be catered for in the recommended strength and other parameters. The soil variables are estimated based on geological, geophysical, geotechnical and survey reports. Soil parameters include the value of static, undrained soil shear strength, cyclic loading factor, soil strain at 50% strength and excess pore pressure. The typical soil profile summary example is presented in Table 5. This data will be used as the input to establish the strength distribution or capacity surface.

Table 5 Typical soil profile example summary [clay]

Depth (m)	S_u top (kPa)			S_u bot (kPa)		
	Low	Best	High	Low	Best	High
0–2.1	0	0	0	30	41	47
2.1–4.0	30	41	47	31	43	49
4.0–18.9	31	43	49	43	59	67
……	……	……	……	……	……	……
69.2–120	111	153	174	187	257	293
Depth (m)	Submerged unit weight, γ (kN/m^3)			Eps 50 (%)		
	Low	Best	High	Low	Best	High
0–2.1	5.66	7.24	8.82	0.13	0.75	1.4
2.1–4.0	6.96	7.72	8.48	0.3	1.59	2.9
4.0–18.9	6.96	7.72	8.48	0.3	0.5	0.6
……	…..	……	……	……	……	……
69.2–120	7.18	7.79	8.40	0.3	0.5	0.6

The soil resistance is represented by nonlinear springs attached to the pile nodes distributed at certain intervals along the pile. Nonlinear springs are generated in the center of each defined layer. The presence of shallow gas has reduced the effective stresses at a certain depth and impacted the shear strength in principal.

The calculation of resistance load or strength variable and the reliability analysis is decoupled by inserting a response surface module between the two sets of calculations. A systematic series of calculation of loads is carried out in the form of RSR, and the results are arranged on the interface file. The response surface module is developed using best-fit distribution and provides strength variables by interpolating on the interface file. Development of strength surface is shown schematically in Fig. 10.

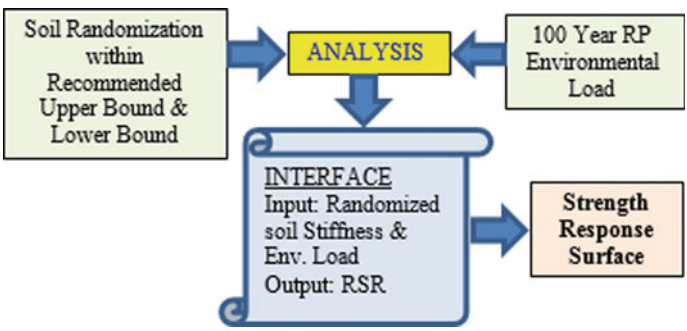

Fig. 10 Strength response surface development

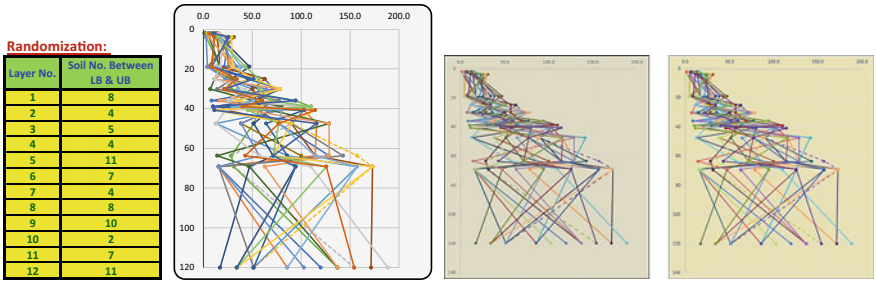

Fig. 11 Typical randomized soil strength profile between recommended upper bound and lower bound

Using the 100-year return period environmental parameters as the basis, the structure is then subjected to nonlinear pushover runs with several random combinations of soil parameters derived by ranging out from the upper and lower bound and best-fit values to capture random effect of the presence of shallow gas at any random depth along the length of the piles. Set of the piles are also separated from worst-affected to least-affected piles in the area. A spreadsheet program is used to create the random soil combination profiles as shown in Fig. 11.

The Reserve Strength Ratio (RSR) which is the collapse base shear divided by the design base shear at 100-year storm condition is then determined by pushover analysis (SESAM 2016). The input of the analysis is the different soil resistance profile randomly generated and the collapse base shear and RSR are the outputs for the analysis which is finally used for the development of strength response surface. The model pushed with the same 100-year storm load but with different random combinations of resistance from the soil condition. The resultant strength response surface is shown in Fig. 12.

4 Reliability Analysis

When two response surfaces of load and capacity are developed and subjected to the limit-state function applying FORM procedure as described in Sect. 2 earlier, that results in the reliability Index 'β' which in this particular example is 4.092. This corresponds to the probability of failure [POF] of 2.13E-05. As this analysis was performed for 100-year return period storm condition, the resulting annual POF is 2.13E-07, i.e., a failure return period of 4,694,835 years. Normally, this POF is checked against the acceptance criteria or a target reliability developed for the region as explained by ISO (2007) and API (2007) requirement. The present result meets the target reliability in Malaysian waters. The reliability curves are as illustrated in Fig. 13.

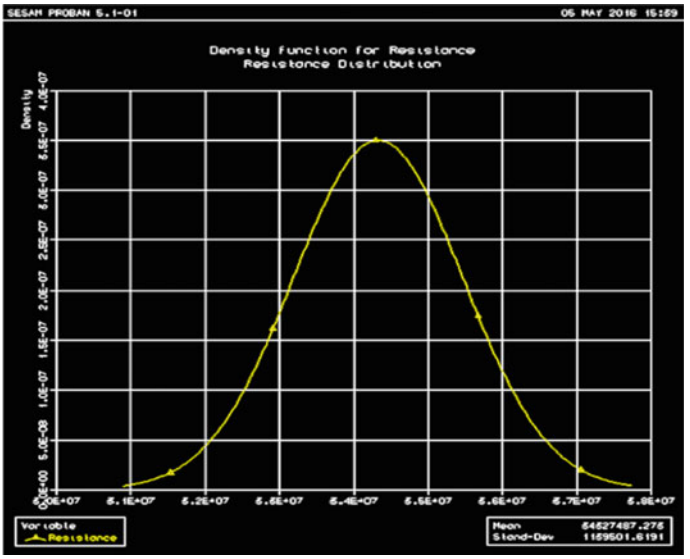

Fig. 12 Strength response surface [typical from PROBAN]

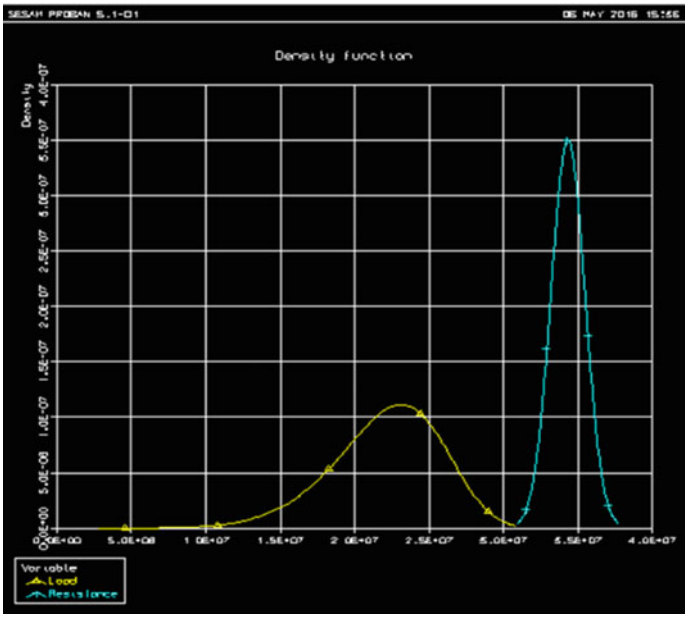

Fig. 13 Probability of failure by FORM [PROBAN]

4.1 The Matrix Approach

The matrix approach to the reliability problem as discussed in Sect. 2 above requires a covariance matrix C or a correlation matrix R. Normally, the correlation matrix R is easier to set up and establishes the correlation structures between the parameters more explicitly (Low 2008).

The contours of decreasing probability as the multivariate dispersion ellipsoid expands, the minimization of β is obtained as shown in Fig. 3. The governing function connected with all relevant parameters is called the 'Performance Function' presented as $g(x) = \mathrm{BS}_{\mathrm{Col}} - \mathrm{BS}_{100}$. The base shear [BS] at collapse and at 100-year return period is calculated through a statistical model or by the deterministic method as suited. This method requires the establishment of correlation matrix R between the relevant important parameters in determining β.

4.2 Results and Discussion

The capacity or strength response surface for the offshore platforms represented by Reserve Strength Ratio (RSR) is normally further defined on the failure mode judged from the pushover analyses results, segregated based on either soil failure or member failure. The prominent failure mode may either be a pile or member failure as a result of formation of plastic hinges due to bending action or a weaker soil particularly toward the top causing a soil failure often to look like a rigid body movement of the main structure laterally.

When shallow gas affects the platform foundation, in all probability, it may affect one particular area of the platform unless it is reported to be widespread. In this situation, the soil response needs to be studied separately for each pile in the system. Action of the environmental force depends on the direction, and it may prove to be worst if the critical environmental direction is coupled with the worst-affected compression end of the platform.

5 Conclusions

The generalized methodology described here to deal with reliability assessment of a stationary jacket structure in a shallow gas environment comprises the following basic steps:

- Establishment of comprehensive procedure, variable uncertainty model and selection of major variables contributing to the system should be detected.
- Parametric sensitivity analysis in determining the uncertainty importance factors.
- Load response surface—development of probabilistic model for environmental loads.

- Develop probabilistic model for structural capacity or strength response surface—requires randomization of soil parameters and defining various soil strength distributions along the depth.
- Perform reliability assessment [in terms of probability of failure (POF)] for load and capacity surfaces using FORM/SORM from the first principles.

Important parameters to be adopted as stochastic variables in this reliability analysis are environmental, resistance from soil foundation and model uncertainty. These parameters provide significant relative contribution to the eventual probability of failure value.

The results produced by this methodology indicate a good prediction potential of risk level against similar geohazards at any location. The uncertainties related to other geohazards should be treated separately by identifying major contributing parameters and associated uncertainties. The numerical techniques like the matrix approach may also be used as an alternate analysis tool.

References

American Petroleum Institute (2007) Recommended practice for the structural integrity management of fixed offshore structures. API RP 2 SIM

Beacher GB, Christian JT (2003) Reliability and statistics in geotechnical engineering. Wiley, England

Ditlevsen O (1981) Uncertainty modeling: with application to multidimensional civil engineering systems, McGraw-Hill, New York

Gilbert RB, Najjar SS, Choi YJ, Gambino SJ (2008) Practical Application of reliability based design in decision making, in reliability based design in geotechnical engineering; computations and applications, Phoon edn. Taylor and Francis Books, London

ISO 19902 Petroleum and natural gas industries—Fixed Steel Offshore Structures (2007)

Low BK (2008) Practical reliability approach using spreadsheet, reliability based design in geotechnical engineering, Taylor and Francis, London

Phoon KK (2008) Reliability based design in geotechnical engineering. Taylor and Francis, London

PROBAN (2004) General purpose probabilistic analysis program, Version 4.4. Developed and Marketed by Det norske Veritas

Robert B, Gilbert (2011) Relliability of Offshore foundations. The University of Texas at Austin. In Deepwater Foundations and Pipeline Geomechanics, McCarron Ed., J. Ross Publishing

SESAM (2016) Structural and hydrodynamic analysis of ships and offshore structures, Version 7.2-07. Developed and Marketed by Det norske Veritas

South sea Asia meteorological and oceanographic study [SEAMOS] (2012) A JIP for South China sea and contiguous basins by oceaweather Inc., USA

Veneziano D (1974) Contributions to second moment reliability, research report No. R74–33, Department of civil engineering, MIT, Cambridge, MA

WEAP Analysis and HSDPT for Steel Piles for Transmission Line Project Across River Hooghly

Sujan Kulkarni and Ravikiran Vaidya

1 Introduction

High Strain Dynamic Pile Testing (HSDPT) is popular worldwide for more than four decades. HSDPT is primarily used to assess the capacity of pile foundation (Vaidya 2006). The testing is standardized by several codes worldwide (Beim and Likins 2008). Reliability of HSDPT has been rigorously investigated and its correlation with static load testing has been summarized by Likins and Rausche (2004).

The test can be used to evaluate various pile parameters, important of these are static capacity of the pile at the time of testing, simulated static load test curve, total skin friction and end bearing of the pile, skin friction variation along the length of the pile, stresses developed in the pile during driving, net and total displacement of the pile, pile integrity and hammer Performance.

HSDPT is now very common in India for bored piles, however its application for driven piles has been proved to be extremely beneficial to piling industry. The biggest advantage of HSDPT for driven piles is no separate test setup is required for the testing. With the pile driving hammer and regular operation only, pile testing can be performed while in case of static load testing especially in marine conditions, preparation of test setup is challenging and requires significant time.

Another powerful tool associated especially with driven piles is the WEAP software. The main objective of the software is to assess whether a pile can be driven to required penetration with the proposed hammer or not. The input includes hammer parameters, pile profile details and soil details either in terms of soil classification and SPT blow counts or in terms of layer wise unit skin friction and end bearing. The software then simulates the pile response to hammer impact forces. The input also requires careful selection of several other parameters such as gain/loss factors, damping and quake values etc.

S. Kulkarni (✉) · R. Vaidya
Geo Dynamics, Vadodara, Gujarat, India
e-mail: sujan@geodynamics.net

S. Haldar et al. (eds.), *Advances in Offshore Geotechnics*, Lecture Notes in Civil Engineering 92, https://doi.org/10.1007/978-981-15-6832-9_14

The following sections present a case study of a marine project for which WEAP and HSDPT was utilized successfully for driving of steel piles and resulted in significant cost and time savings for the project.

2 Project Information

A 400 kV Transmission tower was to be constructed across Hooghly River. For transmission towers, steel piles were chosen as preferred choice considering its ease of installation.

Each of the transmission towers was supported on four legs and for each of the legs 14 raker piles were designed. The center to center distance between adjacent legs was 55 m. The steel piles were open ended having diameter of 1219 mm of variable thickness and raked in 1:5. The High tide level was 9.5 m above mudline and maximum scour depth was 15 m. Four 12 m steel pipe segments were planned to be mobilized so as to achieve target penetration level of −42 m (Pile founding level). The thickness of steel pile section varied from 25 mm (bottommost segment) to 40 mm (topmost segment). Figure 1 presents the layout of foundation for the transmission tower.

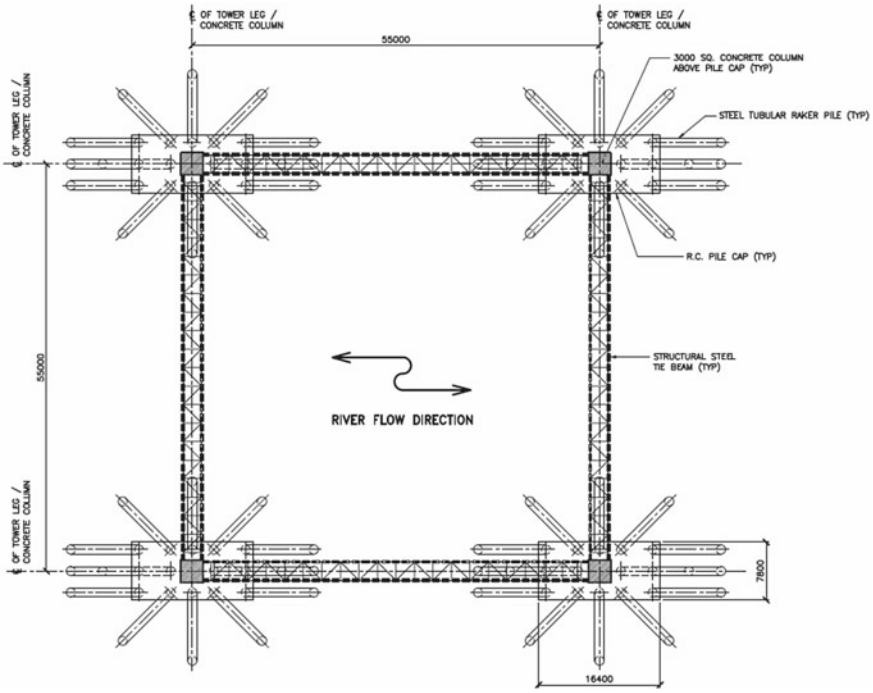

Fig. 1 Layout of foundation for transmission tower

3 Subsurface Conditions

Five boreholes were drilled up to depth of 55 m in order to assess the subsurface conditions at the site. Two boreholes (BH-3 and BH-4) were drilled on either side of river banks and three boreholes (BH-1, BH-2 and BH-5) were drilled in the river bed. Figure 2 presents the subsurface exploration in progress in river bed.

Typical subsurface conditions were consist of loose to medium dense silty sand, underlain by soft to stiff silt and silty clay. Medium dense to very dense silty sand was encountered below the silt layer underlain by very stiff to hard silty clay layer. Bottommost layer was again medium dense to very dense silty sand. The subsurface profile was highly variable for each boring and typically found to be layered profile of silts, sands and clays. Figure 3 presents the SPT blowcount for all five boreholes along the depth which indicates the consistency of each soil layer encountered in all boreholes along with the variation in subsurface condition across site.

Fig. 2 Subsurface exploration in progress

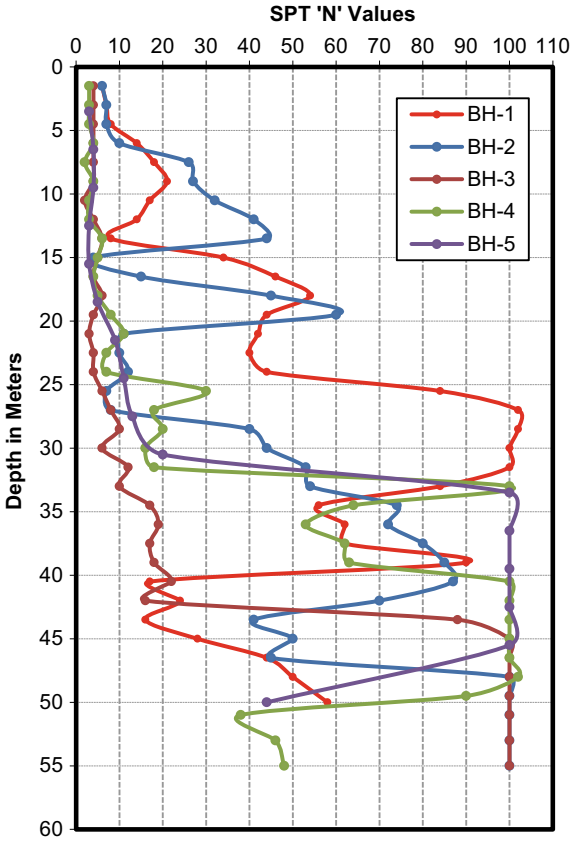

Fig. 3 SPT (N) blowcount versus depth

4 Weap Analysis

Based on information obtained from subsurface investigation program, detailed design study was undertaken and it was proposed to install driven steel piles as foundation for towers. Delmag D100-13 hammer was available with the client and hence it was the preferred choice for driving the piles. However, before mobilizing hammer to the site, it was necessary to confirm that the hammer is suitable to drive the piles to required penetration. Hence WEAP analysis was performed for two borehole locations (BH-1 and BH-3).

Since the early 1970s wave equation analysis of pile driving (WEAP) has become a standard tool for the preparation of pile installations by impact driving. The original concept had been developed by E.A.L. Smith of Raymond International. Basically, the analysis simulates what is happening in hammer, pile and soil during and immediately after the ram impact. It does this by replacing the system's components with masses, springs and dashpots and calculating the displacements and velocities of the

masses and the forces in the springs. Stresses are determined from forces divided by cross sectional area at points that are roughly 1 m apart. This method of calculating the pile movements and stresses is an accurate solution of the wave equation (a differential equation).

Based on available information, WEAP was performed to determine whether Delmag D100-13 diesel hammer is capable to drive open ended pipe piles of 1219 mm diameter to a tip elevation of −42.0 m. The pile was proposed to be driven 37 m into mudline at BH-1 location and 44 m at BH-3 location.

Static analysis was performed by contractor which was used as input into WEAP to define soil parameters. Friction angle for sandy soil was varying from 30° to 35° in case of BH-1 and 36°–37° in case of BH-3. Cohesion for silts and clays were ranging from 3.5–20 ton/m^2 in case of BH-1 and 2.1–9 ton/m^2 in case of BH-3. The setup factor was considered as 1.2 for sands and 2.5 for silty clays. In order to model the SRD, i.e. the static resistance to driving based on the above setup factors, analysis was performed with shaft Gain/Loss Factor of 0.4 (full loss of resistance) and 1.0 (no loss of shaft resistance, i.e., full long term resistance or restrike situation). It was considered that there will be no change in End Bearing with time and hence a toe Gain/Loss Factor of 1.0 was used for the analyses.

A shaft damping factor of 0.65 s/m for clays and 0.16 for sands were used and a toe damping factor of 0.5 s/m have been considered based on the soil type, GRLWEAP recommendations and some conservatism. Shaft quakes were set to 2.5 mm which are standard assumptions for open ended pipe piles. It was expected that such large diameter piles will be driven unplugged and hence toe quakes were also set to 2.5 mm.

For each of the analysis of BH-1, two cases of hammer performance were evaluated; the lowest fuel setting of the hammer for an efficiency of 80% and 3rd fuel setting of hammer for an efficiency of 60%. For each of the analysis of BH-3, similar two cases of hammer performance were evaluated; the 2nd fuel setting of the hammer for an efficiency of 80% and highest fuel setting of hammer for an efficiency of 60%.

For BH-1 analysis, static analysis of piles ignored the upper 15 m soil resistance to account for scouring. However, during driving operations this soil was present and expected to offer some resistance to driving and hence was modeled accordingly. The ultimate static capacity ignoring the upper 15 m of soil was estimated to be around 837 tons. It was estimated that upper 15 m of soil will offer approximately 73 tons and the total ultimate capacity of the pile was expected to be 910 tons. Around 95% of resistance was expected to be contributed by skin friction. Although plugging at pile bottom was not anticipated, for conservatism as far as driveability is concerned, it was considered that friction inside the pile would be present and would offer resistance to driving. For BH-3 analysis, it was assumed that there will be 48 h interruption after driving two sections of the piles i.e. after 24 m (20.2 m into the ground). It was assumed that the piles will be driven continuously without any other significant interruptions like hammer breakdown or any other site related unforeseen issues.

WEAP analysis performed for both locations i.e. BH-1 and BH-3 indicated that, under the assumption of no plugging, the Delmag D100-13 hammer would successfully drive the piles to the required depth. It was expected that driving stresses would be within allowable limits as the estimated compressive stresses were around

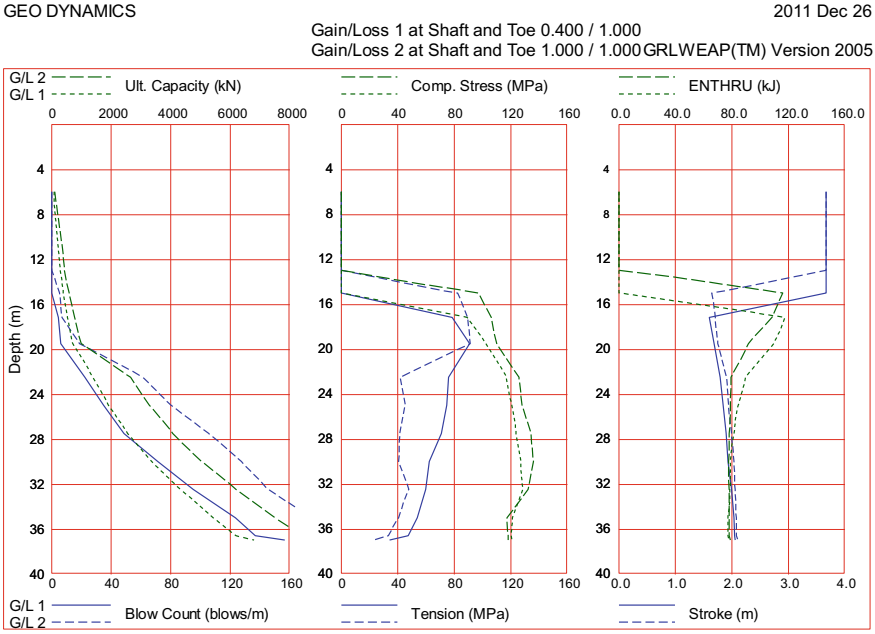

Fig. 4 WEAP output (BH-1) 80% efficiency with lowest fuel setting

135 MPa and allowable limit was 216 MPa. Figure 4 presents typical output obtained from WEAP analysis for BH-1 location which summarizes variation of blowcounts along the depth, expected compressive and tensile stresses, energy as well as predicted pile capacities along the depth.

5 HSDPT of Steel Piles

WEAP analysis confirmed that Delmag D100-13 hammer is capable to drive the steel piles to required penetration and hence hammer was mobilized to the site for pile driving operations. All the piles were driven successfully and no issues were encountered. Piles were not monitored during initial driving operations. However, few piles were selected and HSDPT was performed after wait period of few days (ranging from 5 days to 28 days) in order to assess pile capacities and to confirm that piles can carry the required test load.

Four piles were tested in marine condition after wait period ranging from 5 days to 11 days and one land pile was tested after wait period of 28 days. Marine piles were driven up to depth of around 33 mm and land pile was driven up to a depth of 46 m. The required test load was 454 tons for marine piles and 600 tons for land

piles. Restrike tests were performed by providing 10 blows to the pile from a height of approximately 3.5 m (i.e. 4th fuel setting).

After performing HSDPTs set observed during HSDPT was in the range of 1–3 mm indicating the piles are not loaded till their ultimate capacities and piles have more capacities which were not needed to be mobilized. CAPWAP analysis was performed for selected blow for each of the HSDPT for evaluating the pile capacities. CAPWAP analysis indicated that all piles achieved much more capacities than required test load. For all piles estimated capacities were more than 800 tons. Skin friction component was 85% while the end bearing was 15% which matched fairly well with the static analysis results. Also the capacity estimated by static analysis proved to be conservative based on HSDPT results. Maximum measured compressive stresses were around 150 MPa which were close to the predicted compressive stress of 135 Mpa from WEAP. Small variations to the stresses as estimated by WEAP to the actual measurement can also be attributed to fuel setting which was 4 during actual restrike testing. Figure 5 presents results for typical CAPWAP analysis which summarizes skin friction distribution, simulated load settlement curve and force-velocity data.

6 Concluding Remarks

WEAP, HSDPT and CAPWAP are routinely used tools in piling industry and have resulted in tremendous assistance to entire fraternity. It is always riskier to mobilize pile driving hammer to the site before making sure its suitability to drive the piles. WEAP is powerful software addresses this issue and for a transmission tower project hammer was mobilized after confirming that Delmag D100-13 is suitable hammer to drive the open ended steel piles. Actual compressive stresses measured during restrike testing were nominally higher than predicted by WEAP but which is justified as the testing was performed with the 4th fuel setting. Static capacity from computation was a conservative estimate and actual measured capacities were higher than estimated although friction components as predicted from WEAP and actual measurements were within 10%. Thus assumptions of damping and quake and other parameters can be largely justified and can be said within acceptable range as the pile could be driven to the estimated depth at similar compressions stresses. Performing static load tests in marine conditions is always a crucial activity. A proper planning and check with wave equation analysis followed by HSDPT provided viable and reliable option for speedier completion of project.

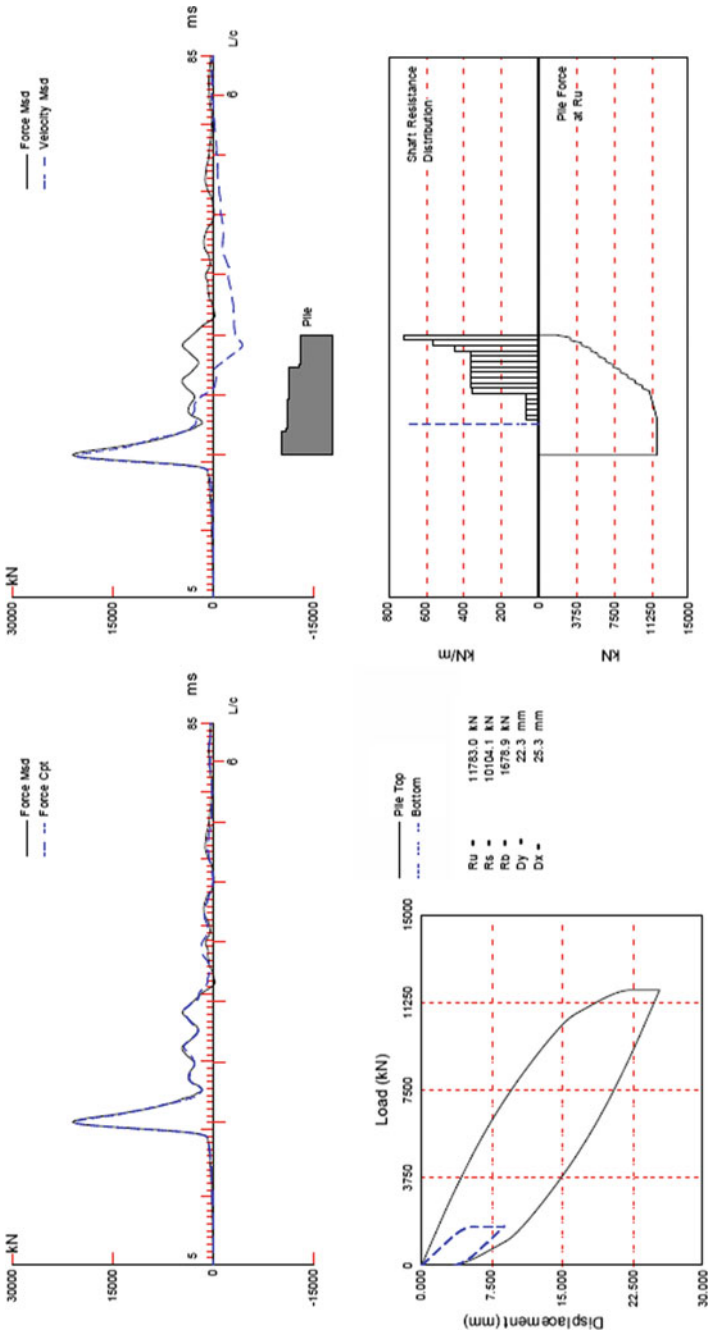

Fig. 5 Typical CAPWAP output

References

Beim G, Likins G (2008) Worldwide dynamic foundation testing codes and standards. In: Proceedings of the eighth international conference on the application of stress-wave theory to piles, pp 689–697. Lisbon, Portugal

Likins G, Rausche F (2004) Correlation of CAPWAP with static load tests. In: Proceedings of the seventh international conference on the application of stresswave theory to piles. pp 153–165. Petaling Jaya, Selangor, Malaysia

Vaidya R (2006) Introduction to high strain dynamic pile testing and reliability studies in Southern India. IGC 2006, Chennai, India

Long Term Capacity Estimation of Steel Pipe Piles in the Neelam Field, West Coast of India

Prasad Hiremath and Vivek Dhandapani

1 Introduction

In the recent years, a large number of offshore oil platforms are being installed in the Indian waters. In the wake of optimizing this process, the design and installations of jackets is becoming complex owing to the difficult soil strata and the loads to be carried by these structures. One such grey area in pile design is the setup or the strength gain the pile undergoes with time. This region- specific study is intended to account for such strength gains and thereby to optimize the design process.

In the last 50 years, extensive research has been put into increase the accuracy of assessment of the bearing capacities of the piles by the dynamic methods and static methods. The pile capacities have been observed to increase with time which is termed as setup. This is more prominent in the driven piles where significant increase in capacities within a short span of time has been witnessed. The mechanism contributing to this phenomenon is still an area of research. Moreover, a rational approach to account for the increase in driven pile capacity with time in design has not yet been developed. If the expected increase in bearing capacity with time can be utilized in design, it has the potential in significantly upgrading of existing piled foundation designs, especially for piled foundations that need to support higher loads in the future than those they were originally designed for (Lied 2010).

During the pile driving process, soils around the pile shaft and below the pile tip are highly disturbed. As a result of driving, excess pore water pressure builds up. Based on the permeability properties of the subsoil, the duration for the complete dissipation of excess pore water pressure varies. The pile capacity could be underestimated if pile

P. Hiremath (✉) · V. Dhandapani
Geotechnical Engineer, Fugro Survey (India) Pvt. Ltd, Fugro House, D-222/30, TTC Industrial Area, MIDC, Nerul, Navi Mumbai 40076, India
e-mail: p.hiremath@fugro.com

V. Dhandapani
e-mail: v.dhandapani@fugro.com

S. Haldar et al. (eds.), *Advances in Offshore Geotechnics*, Lecture Notes in Civil Engineering 92, https://doi.org/10.1007/978-981-15-6832-9_15

load test was carried out while significant excess pore water pressure still remains. The pile capacity increases as the strength of the surrounding soil increases by re-consolidation. This is common phenomenon for low permeability soils such as silt and clay. For granular soil which has higher permeability, the complete dissipation of excess pore water pressure is normally within few hours to few days. However, literatures have shown that there is a tendency of increase in pile capacity even after complete dissipation of excess pore pressure has been achieved (Chen et al. 2009).

The various reasons for soil setup to take place can be listed as below or a combination of these:

- An increase in the earth pressures against the pile surface on the long term, due to creep of the soil structure
- A long-term build-up of new diagenic bonds between soil particles, after the complete destruction of the soil structure due to the severe displacements and disturbance resulting from the driving of the pile into the ground
- Chemical bonding due to the interaction between the steel pile surface and the soil minerals (cat ion exchange)
- The effects of sustained loads on the piles, gradually causing a more stable soil structure and increased strength
- The effects of previous loading and unloading cycles of the piles, which can have similar effects as sustained loading.

HSDT has been used for more than 40 years to monitor pile installation, measure the hammer performance, measure the SRD and various other factors. HSDT also helps in predicting the LTSR and thereby helps in calculating the setup achieved by the pile. There are several other methods available to determine the bearing capacity of a driven pile, such as static load test and rapid load test. These methods cannot be used to determine driving stresses, evaluate the hammer performance, and have rarely been used in offshore environment due to lack of feasibility. These methods cannot be used for underwater test (Liang et al. 2014).

In the present study the pile installation was monitored by the HSDT and real-time SRD were calculated based on the CAPWAP analysis. Out of these 16 piles, a certain number of piles were selected for restrike at certain intervals of time to evaluate setup ratio and thus to arrive at LTSR. The method proposed by Bullock et al. (2005) to estimate the LTSR based on the setup calculated by the End of Driving (EOD) capacity and the Beginning of Restrike (BOR) test capacity was relied upon to estimate the LTSR. Suitable damping values have been selected relevant to the site while running the analysis.

2 Location Geology

The soil profile at the location is predominantly clayey with few intermittent layers of sand. The soil in this field is further classified as clay, calcareous clay or carbonate clays mainly. The average water depth in the Neelam field is between 55 and 60 m.

Table 1 Representative soil profile

Depth (m)		Description
From	To	
0.00	9.00	Calcareous clay silty very stiff
9.00	15.00	Calcareous clay very silty
15.00	18.90	Siliceous carbonate sand
18.90	27.80	Calcareous clay silty sandy
27.80	33.00	Calcareous silica sand
33.00	53.50	Calcareous clay very stiff
53.50	55.00	Siliceous carbonate sands
55.00	67.00	Calcareous clay, silty
67.00	82.00	Calcareous clay, sandy
82.00	88.00	Calcareous silica sand, clayey
88.00	100.00	Calcareous clay, silty
100.00	125.75	Calcareous clay, silty

The sample borehole depths at various locations were in the range of 125 m. Borehole data of a representative borehole conducted at one of the locations in the Neeelam field has been presented in Table 1.

As evident from Table 1 the design of piles will be completely based on the clay-pile interaction and the capacity anticipated will be mainly from the shaft resistance.

2.1 Pile Dimensions

In the Neelam field a total of 4 jackets were installed with each jacket being pinned down to the sea floor with 4 skirt piles. These 4 pile-set for each jacket are referred to as Set 1, Set 2, Set 3 and Set 4. In the present study.

Based on these soil profiles the design indicated that the piles are required to achieve an LTSR ranging from 44 to 60 MN. Prior to the installation of the piles, the wave equation analyses were also performed to check for the driveability and stresses that could be encountered by the piles. To account for the uncertainty in SRD, a hammer efficiency of 85% was assumed and a combination of skin friction and toe resistance distribution were used for clay and sand strata.

The pile penetration length, diameter and thickness of the pile for each set are as mentioned in Table 2.

The Piles, through-out their length have a varying thickness. The thickness is highest at the bottom of the pile and it acts as a driving shoe.

Table 2 Pile dimensions

	Pile	Diameter (mm)	Penetration depth (m)	Thickness (mm)
Set 1	A1	2438	91.00	63–95
	A2	2438	82.00	63–95
	A3	2438	91.00	63–95
	A4	2438	82.00	63–95
Set 2	A5	2438	98.00	63–95
	A6	2438	98.00	63–95
	A7	2438	98.00	63–95
	A8	2438	98.00	63–95
Set 3	A9	2438	90.00	63–95
	A10	2438	90.00	63–95
	A11	2438	90.00	63–95
	A12	2438	90.00	63–95
Set 4	A13	2438	105.00	63–95
	A14	2438	105.00	63–95
	A15	2438	105.00	63–95
	A16	2438	105.00	63–95

3 Piling and Data Collection

The piling work for all the 4 set of piles were carried out successfully without any hindrance such as pile refusal. With the pile weights ranging between 400 and 600 MT the piles had a self-weight penetration of 7–22 m. The piles were then hammered using the MENCK MHU 800 s and MHU 1200 hydraulic hammers. During hammering, some piles also underwent a pile-rundown for few meters due to the presence of intermittent soft-layers.

The piles were monitored while being driven with the use of under-water (UW) strain gauge and accelerometers. Two piles from each jacket that is from each set were also tested during the restrike driving after appropriate wait time from end of initial driving. The piles for which the restrike tests were carried out are listed in Table 3. The monitoring of piles was done by fixing the strain gauge and accelerometers at 4.2 m below the pile top. Two UW strain gauge and two UW accelerometers were fixed on the diametrically opposite sides of the piles. In the Pile Driving Analyzer (PDA) the strain and acceleration signals thus measured are then turned into force and velocity of the wave travelling through the pile when pile is given a blow by the hammer. For each hammer blow, the PDA calculates various parameters and indicators and also estimates the pile capacity by the Case method (Goble et al. 1975).

Table 3 Pile monitoring result summary

Pile	Blow count (m)	CSX (MPa)	EMX (kJ)	ETR (%)
A1	16/0.25	165.95	655.60	81.95
A2	15/0.25	155.82	532.60	66.58
A3	15/0.25	164.05	613.50	76.68
A3-RE	136/0.50	180.88	649.20	81.15
A4	19/0.25	150.91	489.90	61.23
A4-RE	168/0.50	161.28	576.50	72.06
A5	31/0.25	168.78	382.70	47.83
A6	35/0.25	246.03	417.60	52.20
A7	27/0.25	132.19	356.20	44.52
A7-RE	236/0.50	137.40	523.20	65.40
A8	27/0.25	211.84	395.60	49.45
A8-RE	215/0.50	262.84	570.50	71.31
A9	23/0.25	253.90	596.60	74.57
A10	22/0.25	136.50	410.20	51.27
A10-RE	225/0.50	153.30	550.70	68.83
A11	26/0.25	141.80	443.50	55.43
A12	25/0.25	196.60	439.30	54.91
A12-RE	300/0.50	233.30	565.60	70.70
A13	25/0.25	141.43	465.60	58.20
A13-RE	250/0.50	172.84	908.30	75.69
A14	27/0.25	150.85	462.20	57.77
A15	30/0.25	147.42	383.80	47.97
A16	31/0.25	125.75	454.70	56.83
A16-RE	230/0.50	175.02	907.40	75.61

4 Results and Analysis

During hammering, the PDA records and analyses measured dynamic blow to evaluate hammer and driving system performance, compression stresses at the pile top and structural integrity of the pile. The SRD is also computed based on the Case method equations which are widely used to calculate the soil resistance (Rausche et al. 1972). The PDA logs each hammer blow with a sequential blow number at that particular pile penetration. Table 3 gives a summary of the dynamic data analyses for each pile at the end of drive and at restrike test for all the 4 sets of piles.

The blow counts are mentioned for the last 0.25 m of penetration during the EOD of continues driving and for 0.50 m for the BOR test. The piles with "RE" suffix are the piles subjected to restrike testing after certain wait period. The terms CSX, EMX and ETR stand for the maximum compressive stress at the pile top, maximum

energy transferred by the hammer to the pile, and the hammer energy transfer ratio respectively. The ETR is the ratio of the Hammer energy rating and the energy transferred to the pile that is recorded by the sensors.

The compressive stresses near the pile head as can be read from Table 3 are well below the API recommendation of 90% of the 345 MPa which is approximately 310 MPa of the yield strength of the steel thus eliminating the chances of pile damage or pile yielding. Figure 1 shows the recorded EMX, CSI the maximum compressive stress recorded by individual sensors and the recorded blow-count throughout the pile driving. The figure also shows the variation of the ETR, CSX and FVP the ratio of the reading of the sensors from both side of the pile, till it reaches the target penetration for the pile A1. These curves are produced for all the 16 piles. This is a typical graph produced by the PDA and also shows any interruptions that occurred during continuous driving.

The stress recorded at the pile top may not be the maximum in the pile body for that certain blow. The stresses reported thus are averaged over the over-all cross-sectional area of the pile. The maximum stress in the pile body can only be analyzed by the CAPWAP by selecting that individual blow.

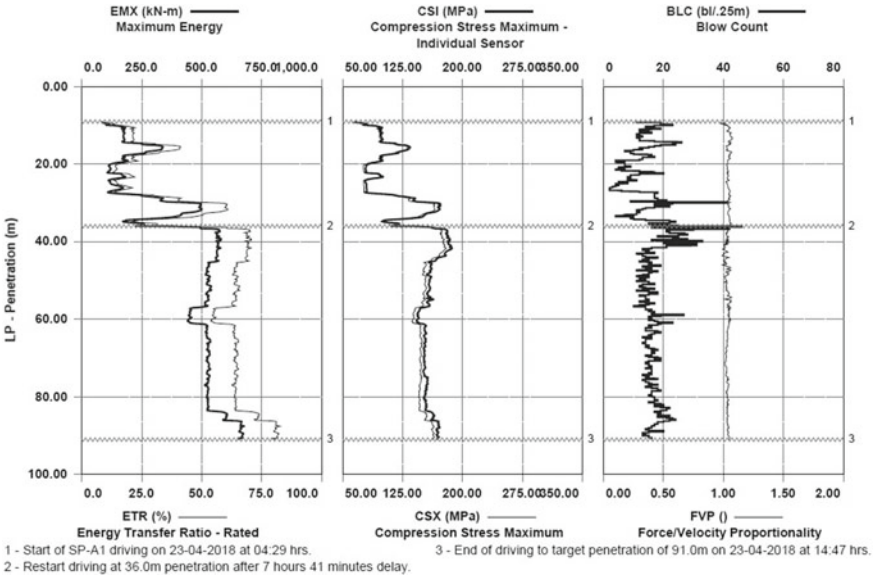

Fig. 1 Typical graph produced by the PDA based on the readings of the sensors indicating EMX, CSI, Blow-Count, ETR, CSX and FVP for pile A1

4.1 CAPWAP Results

CAPWAP is a signal matching procedure which, based on pile top force and velocity measurements during hammer impact, extracts static and dynamic soil resistance parameters for pile shaft and pile toe.

The blows near the EOD for continuous driving and from the BOR for the restrike were selected to run CAPWAP analyses. The pile capacities computed using CAPWAP are then compared to the capacities estimated using Case method of capacity estimations. The RMX capacity which represents the Case method capacity is noted besides the CAPWAP capacities in Table 4 to draw a clear comparison between these two quantities. The Case damping factor for RMX capacities in the Neelam field is assumed to be 0.60 (JC = 0.60).

Table 4 Capacities computed from Case method (RMX) and from the CAPWAP analysis

Pile	RMX (MN) JC = 0.60	Ultimate capacities (MN)		
		Shaft	Toe	Total
A1	19.48	17.36	3.39	20.75
A2	9.48	11.08	2.87	13.95
A3	15.77	15.07	3.71	18.78
A3-RE	44.14	37.97	4.96	42.93
A4	16.73	10.50	3.92	14.42
A4-RE	30.65	30.11	4.62	34.73
A5	18.73	19.09	2.46	21.55
A6	20.66	19.21	3.23	22.44
A7	19.75	20.25	2.43	22.68
A7-RE	37.80	40.19	5.09	45.28
A8	18.63	19.42	3.04	22.46
A8-RE	37.01	43.58	5.02	48.60
A9	16.20	18.22	2.25	20.47
A10	16.65	17.04	2.17	19.21
A10-RE	28.24	36.65	3.91	40.56
A11	23.82	18.21	2.30	20.51
A12	16.77	19.04	2.50	21.54
A12-RE	38.67	38.92	3.89	42.81
A13	19.50	21.84	2.82	24.66
A13-RE	36.63	45.13	5.14	50.27
A14	25.43	23.78	3.03	26.81
A15	19.90	22.13	3.12	25.25
A16	24.94	21.68	2.94	24.62
A16-RE	41.45	44.63	5.13	49.76

The Case damping factor, JC, is a dimensionless damping factor which is predominantly related to the type of soil. For clays soils the recommended range is higher than 0.70. The value of JC = 0.60 in the current study is thus justified, as the ground is having predominantly clayey soil with few layers of other soil types.

From Table 4 it is observed that the RMX capacities and the CAPWAP computed capacities are close to each other in agreement with the selection of JC = 0.60 for this field.

CAPWAP overcomes the limitations that Case method has and gives a better estimation of the capacities. It matches the soil resistance profiles computed and soil resistance profiles measured. The adjustments in the soil resistance distribution along the pile length in the measured curve improve the match quality and give the best soil resistance capacities.

The CAPWAP results are based on the "best possible match" between a computed pile top variable, say the pile top force and its measured equivalent. One such measure of the degree of matching is Match quality (MQ) number. MQ number in CAPWAP is effectively a "mismatch" indicator; the higher its value, the worse the match between the measured and the computed pile parameters. Generally, a match quality number below 5 for any analysis is considered acceptable considering that the other parameters are in feasible range. In the current study all the CAPWAP analysis have MQ numbers well below 5. The shaft damping and shaft quake as well as the toe damping and toe quake are adjusted to meet the site-specific criteria and to have a best match. The final output shall have a soil resistance distribution and corresponding soil damping and quake parameters and an equivalent static resistance profile. Table 5 gives the damping and quake parameters for all the 16 piles. The time elapsed after the initial driving till the restrike test is also mentioned in Table 5.

As per the standards, a minimum wait period of 24 h after the end of initial driving to conduct restrike test to assess the long-term capacity is recommended. But any wait period longer than this time is always good to have a better assessment of the long-term capacity as the piles will achieve greater capacities with elapsed time. However, the operational and time restrictions in the field usually do not allow for greater wait periods than 24 h. In the present study as it can be seen from Table 5 the wait periods for the restrike tests are well above 24 h.

The CAPWAP outputs for the pile A1 are as shown in Fig. 2. CAPWAP outputs generally comprises of a graph showing the match between measured force and computed force along the pile length, static load-set curve, resistance distribution along the pile length when it has completely reached its target penetration and curves showing various other parameters. Similar outputs are produced for all the piles.

However, when the capacity is estimated from the blows of the last 0.25 m of the pile penetration during continuous driving will be comparatively less than the actual capacities at the place. These capacities are often lesser than the required capacities for that particular structure. This is because while the pile is being driven the amount of soil equivalent to the pile volume is being displaced. This remoulds the soil around the pile creating a remoulded zone. Given time, the soil regains its strength and hence an increase in the capacities. To account for the time-related gain in strength restrike tests are conducted after a certain wait period from the end of initial driving.

Table 5 Shaft damping, shaft quake, toe damping and toe quake from the CAPWAP results

Pile	Smith damping (s/m)		Soil quake (mm)		Restrike wait period (Hours)
	Shaft	Toe	Shaft	Toe	
A1	0.50	0.88	1.00	1.00	–
A2	0.43	1.31	1.88	1.96	–
A3	0.43	0.41	1.00	1.94	–
A3-RE	0.75	1.31	1.07	1.00	28.10
A4	0.54	1.31	1.00	3.64	–
A4-RE	0.65	1.31	1.19	1.73	29.90
A5	0.64	0.76	1.19	1.40	–
A6	0.65	0.90	1.38	1.00	–
A7	0.52	0.65	1.08	1.00	–
A7-RE	0.77	0.87	1.00	1.00	52.50
A8	0.53	0.85	1.20	1.00	–
A8-RE	0.59	1.10	2.40	1.14	55.00
A9	0.56	1.31	1.00	2.54	–
A10	0.47	0.91	1.40	1.75	–
A10-RE	0.46	0.89	1.00	1.00	27.45
A11	0.55	1.13	1.89	1.05	–
A12	0.52	1.31	1.47	1.00	–
A12-RE	0.54	1.10	1.00	1.00	31.21
A13	0.50	0.95	1.88	2.13	–
A13-RE	0.49	1.31	1.20	1.03	27.50
A14	0.55	1.30	1.26	2.00	–
A15	0.51	0.98	2.08	2.03	–
A16	0.59	1.31	1.54	1.00	–
A16-RE	0.45	1.31	1.00	1.99	29.40

The ratio of EOD of the initial driving capacities and the restrike test capacities is the setup ratio of the soil. In certain events, even the restrike capacities fall short of the required capacities. Limitation on the wait period of only 24 h for restrike also hinders the proper capacity estimations. With higher wait period higher restrike capacities can be expected. Therefore, based on the EOD capacities, restrike capacities and the set-up ratio, the long-term capacities are estimated. The method and the analogy are explained further.

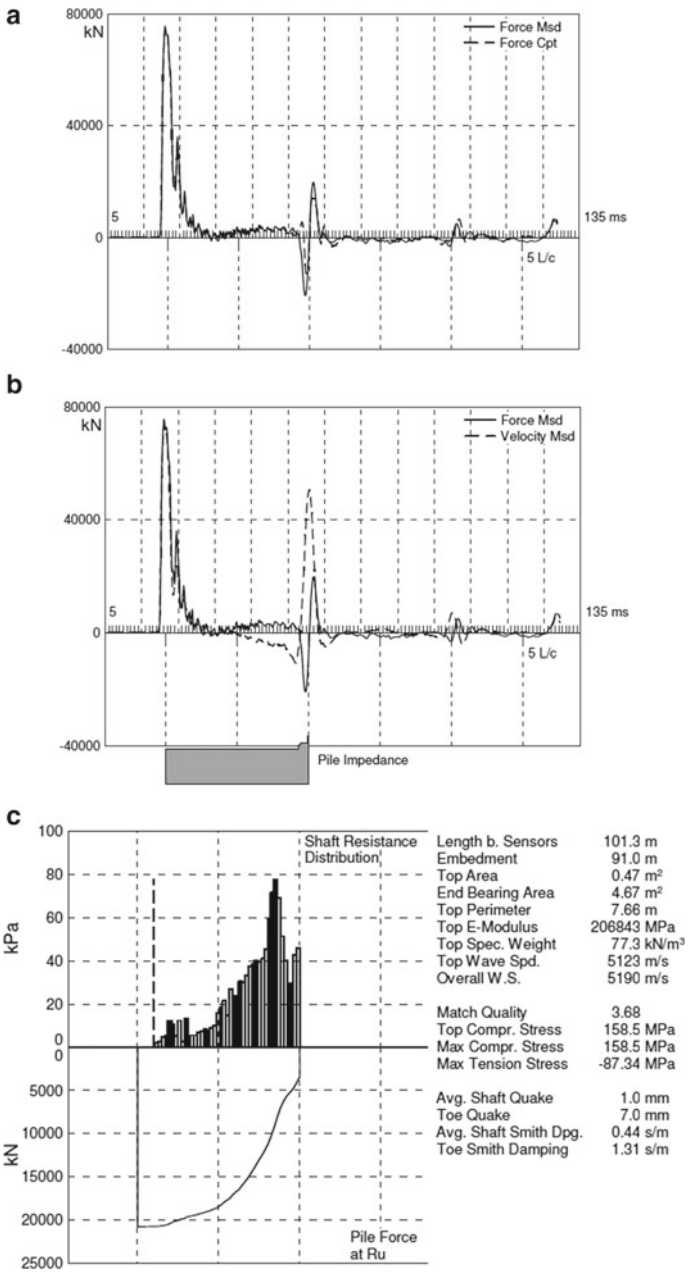

Fig. 2 CAPWAP output curves **a** measured force versus computed force, **b** measured force and velocity (impedance), **c** soil resistance distribution along the pile length and **d** static load-set curve

Fig. 2 (continued)

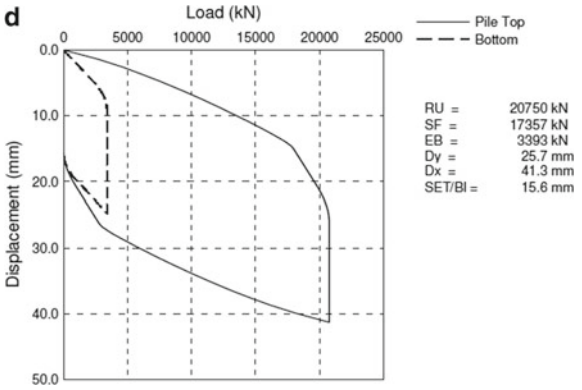

4.2 Side Shear Setup

As stated previously setup takes place in the shaft of the pile as indicted by Kehoe (1989). Previously the end bearing and side shear were both clubbed together as "Pile End Bearing" to estimate LTSR. However, it has been observed that the end bearing changes very little with time (Samson and Autheir 1986; Skov and Denver 1988; Preim et al. 1989; Shioi et al. 1992). Static test presented by Airhart et al. (1967) and Axelsson (1998) also confirms this observation. This large change in the side shear compared to the end bearing could be attributed to the fact that the large shear strains along the shaft compared to the end of the pile and also due to the larger contact are of the shaft and thereby resulting in a bigger restructuring recovery producing a greater side shear setup.

The pile setup is observed to be having a linear correlation with the time elapsed after the EOD. Based on the four case histories from the driven piles around various locations Skov and Denver (1988), proposed a dimensionless setup factor, '*A*', that represents the relative increase in pile capacity per log cycle of elapsed time. The Eq. 1 gives us the long-term capacity estimate formula

$$\frac{Q}{Q_0} = A\log\left(\frac{t}{t_0}\right) + 1 = \left(\frac{m_Q}{Q_0}\right)\log\left(\frac{t}{t_0}\right) + 1 \tag{1}$$

where A = Dimensionless setup factor, Q = Whole pile capacity at time t, Q_0 = Whole pile capacity at reference time t_0, t = Time elapsed since EOD, t_0 = Reference time elapsed since EOD and m_Q = Semilog-linear slope of Q versus log-t plot. As per the data presented by the Svinkin et al. (1994) a semilog-linear slope m_Q is shown in Fig. 3.

Skov and Denver (1988) defined t_0 as the elapsed time at the beginning of the semilog-linear capacity increase. The determination of onset reference time t_0 is difficult as it affects the value of '*A*'. Choosing a common reference time for all soil

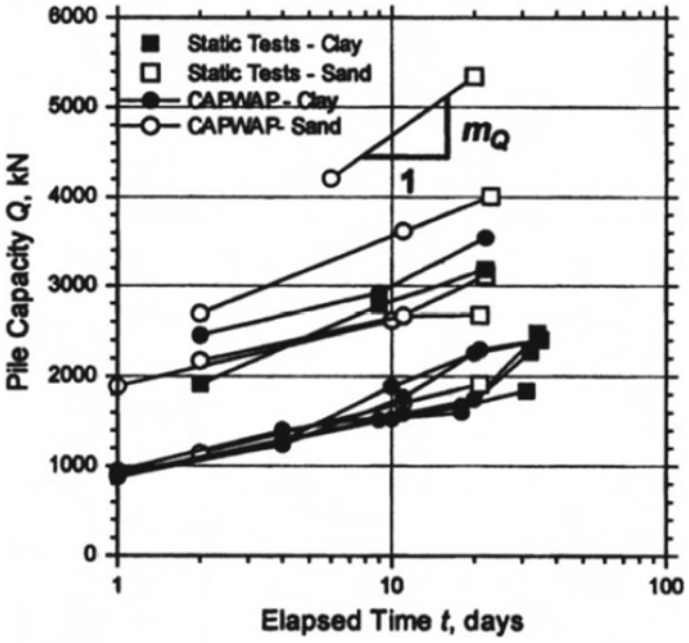

Fig. 3 Pile capacity data from Svinkin et al. (1994)

types still within the semilog-linear graph helps in defining a range for the value of '*A*'.

4.3 Long-Term Capacity Estimates

In the present study out of the 16 piles no pile could achieve the required capacities in the initial EOD. Even after the restrike test after sufficient wait period, the capacities fell short of the required capacities. This led to the estimation of the long-term capacity for reach pile and to predict the time frame within which the piles are going to achieve the required capacities. Table 6 gives us the total capacity at EOD, total capacity at restrike, setup ratio and the required capacities for each pile.

To estimate the LTSR, initially the value of '*A*' is evaluated. '*A*' being the ratio of m_Q and Q_0. To estimate the value of m_Q the semilog-linear setup graph was drawn for all the piles and then the slopes of the lines were measured which is the value of m_Q. The Q_0 and Q values used in the estimation of LTSR are not the total capacities but the shaft capacities of each pile as the end bearing has little change with time hence omitted from the LTSR estimations. Therefore, the shaft frictions of EOD and restrike tests f and f_0 are used in place of Q and Q_0. The reference time t_0 in the present case is taken as 1 min for all the piles. Figure 4 shows the semilog-linear

Table 6 Capacity achieved and capacity required for each pile

	Pile	Total capacity at EOD (MN)	Total capacity at restrike (MN)	Setup ratio	Required capacity (MN)
Set 1	A1	20.75	46.69	–	48.23
	A2	13.95	35.13	–	43.31
	A3	18.78	42.43	2.5	51.7
	A4	14.42	34.73	2.9	44.61
Set 2	A5	21.56	45.03	–	54.24
	A6	22.44	46.07	–	54.24
	A7	22.68	45.28	1.98	54.24
	A8	22.46	48.6	2.23	54.24
Set 3	A9	20.47	41.42	–	45.84
	A10	19.22	40.56	2.15	45.84
	A11	20.51	41.45	–	45.84
	A12	21.54	42.81	2.04	45.84
Set 4	A13	24.66	50.27	2.07	54.76
	A14	26.81	52.16	–	63.84
	A15	25.25	48.84	–	57.29
	A16	24.62	49.76	2.05	61.13

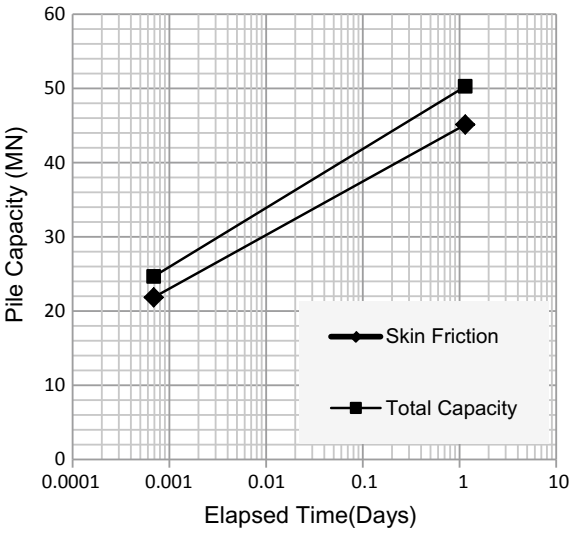

Fig. 4 Semilog-linear capacity curve to find the slope m_Q for pile A1

capacity curve for pile A1.

Using the Eq. (1) LTSR is further calculated. LTSR is then projected for a suitable period of time. Figure 5 gives us the LTSR estimations of all the 4 sets. Different piles are taking different setup times to achieve the LTSR. There is logarithmic increase in the pile capacities. There is a rapid rise in the capacities in the initial few days indicating that the soil displaced by the pile is setting rapidly. After this initial rapid rise in the capacity the increment becomes almost flat with time. The predicted time taken by the piles to achieve the required capacities in terms of days is as shown in Table 7. The analyses are done mainly considering clay soil profile in the region ignoring the small layers of sand present at the locations. No pile out of 16 showed any signs of relaxation or loss of setup.

The LTSR is calculated only for the shaft as discussed earlier and then the toe capacity is added to it to arrive at the total capacities. The required capacities and the predicted capacities in Table 7 are sum of the long-term estimation of the shaft resistance and the toe capacity achieved during the restrike test. For some piles where it was observed that the hammer could not mobilize the complete capacity of the pile during restrike, a sum of shaft capacity recorded during restrike and toe capacity during EOD was used. This method is termed as superposition and can be used

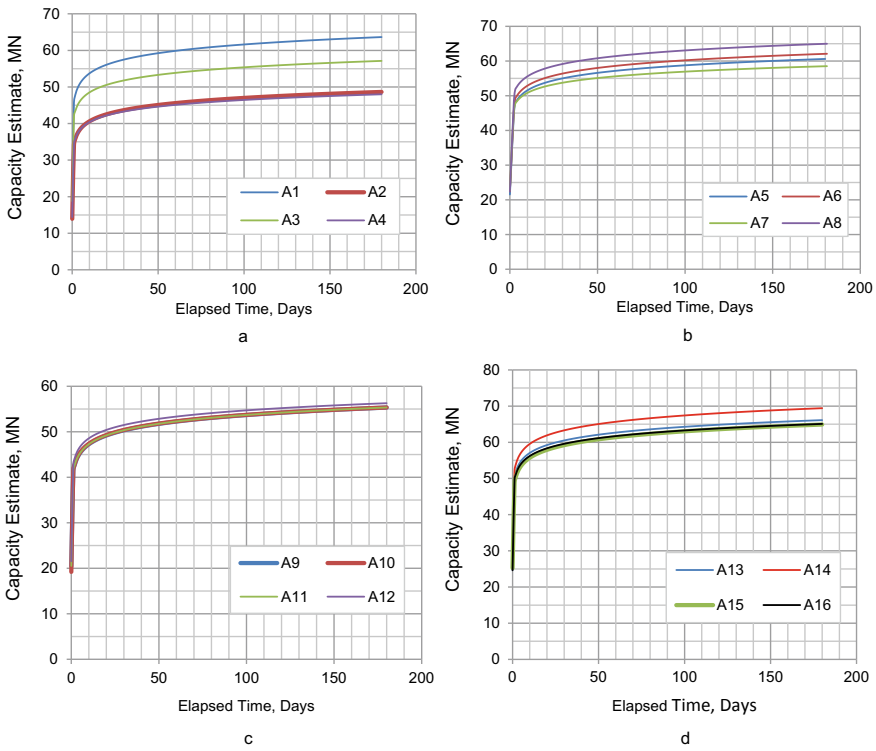

Fig. 5 LTSR with elapsed time for piles of **a** set 1, **b** set 2, **c** set 3 and **d** set 4

Table 7 Required capacities and the predicted capacities with the time required

	Pile	Required capacity (MN)	Predicted capacities (MN)	Time required (days)
Set 1	A1	48.23	49.57	3.00
	A2	43.31	43.37	27.00
	A3	51.70	51.79	30.00
	A4	44.61	44.62	50.00
Set 2	A5	54.24	54.29	24.00
	A6	54.24	54.38	16.00
	A7	54.24	54.29	37.00
	A8	54.24	55.23	9.00
Set 3	A9	45.84	46.24	7.00
	A10	45.84	46.38	7.00
	A11	45.84	46.27	7.00
	A12	45.84	46.69	5.00
Set 4	A13	54.76	55.45	6.00
	A14	63.84	63.93	36.00
	A15	57.29	57.40	17.00
	A16	61.13	60.00	61.16

whenever the pile capacity is not fully mobilized. The pile capacity not being fully mobilized could be due to usage of a smaller hammer or due to higher soil setup achieved by the soils within a shorter span of time i.e. a quick setup rate.

In the present study, due to the sufficient wait period to conduct restrike tests good setup were observed for all the piles and with the estimation of LTSR the piles were observed to be reaching the required capacities within a short span of time.

5 Summaries

From the results stated above the following excerpts can be drawn

- It was observed that the piles did not achieve the required capacities at the end of the drive during continues driving.
- So as to determine the long-term capacities, restrike tests were carried out on 2 piles from each pile set.
- The restrike tests were carried out at intervals more than 24 h for all the piles.
- Since the toe capacities change very little with time, only the shaft capacities were subjected to the long-term capacity estimation.
- The ratio of shaft capacity of the pile at the end of the drive at initial driving and the shaft capacity of the pile at restrike is calculated which is nothing but the setup ratio.

- The final capacities are then calculated as a sum of shaft capacities and toe capacities.
- However, the capacities even after the restrike test were well short of the required capacities.
- The long-term capacity estimation method as suggested by Bullock et al. (2005) is used to predict the long-term capacities.
- To evaluate the value of '*A*', a dimensionless setup factor, the semi log-linear capacity slope was estimated.
- Then using the Eq. 1, and reference time as 1 min the long-term capacities are estimated and the durations, the piles were taking to achieve the required capacities were estimated.

6 Conclusions and Recommendations

One of the major advantages of using HSDT to estimate the pile capacities is that the chances of underestimating the pile capacities are very minimal. In the current study after the end of initial driving no pile achieved the required capacities. Even the capacities after the restrike test with sufficient wait time were short of the required capacities which made the pile acceptance difficult. When the capacities were projected with the long-term capacity estimation the piles were observed to be achieving LTSR values well above the required capacities within a short period of time thereby aiding in making the pile acceptance decision without hassles.

In the offshore environment where it is impractical to carry out traditional pile testing procedures such as static pile load test, HSDT gives a reliable and real-time pile data, thereby saving time and costs effectively. The LTSR estimated even for the piles which have achieved the required capacities could help in loading the structure with loads additional to which they were originally designed for.

If the increase in capacity is accounted for while designing the piles it could significantly reduce the pile diameter, pile penetration depth, reduction in pile driving hammer sizes and various other benefits. There have been many efforts made to develop a method to incorporate the setup in the design in the past. Alawneh et al. (2009) have tried to develop empirical correlations to predict the magnitude of setup during the pile design phase itself. However, a thorough study in this regard and a proper method to incorporate the increase in capacity at certain time in the future into the pile design is yet to be arrived at.

References

Airhart TP, Hirsch TJ, Coyle HM (1967) Pile-soil system response in clay as a function of excess pore water pressure and other soil properties. Research representation number. Texas Transportation Institute, pp 33–38

Alawneh AS, Nusier OK, Awamleh MS (2009) Time dependent capacity increase for driven piles in cohesionless soils. Jordan J Civ Eng 3:01–31

Axelsson G (1998) Long-term setup of driven piles in noncohesive soils evaluated from dynamic tests on penetration rods. In: Proceedings of 1st international conference on site characterization, pp 895–900

Bullock PJ, Schmertmann JH, McVay MC, Townsend FC (2005) Side shear setup I: test piles driven in Florida. J Geotech Geoenviron Eng ASCE 292–300

Chen CS, Liew SS, Tan YC (2009) Time effects on the bearing capacity of driven piles. In: Proceedings of the 11th Asian regional conference on soil mechanics and geotechnical engineering, p 36. South Korea

Goble G, Likins G, Rausche F (1975) Bearing capacity of piles from pile measurements. Case Western Reserve University, Cleveland, USA

Liang L, Webster S, Yuan R, Tian H, Han Y, Wang C, Yu L (2014) Prediction of long-term capacity using dynamic testing for underwater Skirt Pile foundation. In: Proceedings of the 24th international ocean and polar engineering conference, pp 660–667. Korea

Lied EW (2010) A study of time effects on pile capacity. In: Proceedings of European young geotechnical engineers conference. Czech Republic

Preim MJ, March R, Hussein M (1989) Bearing capacity of piles in soils with time dependent characteristics. In: Proceedings of the 3rd international conference on Piling and deep foundations, pp 363–370. USA

Rausche F, Moses F, Goble G (1972) Soil resistance predictions from pile dynamics. J Soil Mech Found Div Am Soc Civ Eng 418–440

Samson L, Authier J (1986) Change in pile capacity with time case histories. Can Geotech J 23(2):174–180

Shioi Y, Yoshida O, Meta Y, Homma M (1992) Estimation of bearing capacity of steel pipe pile by static loading test and stress wave theory. In: Proceedings of 4th international conference on the application of stress-wave theory to piles, pp 325–330. USA

Skov R, Denver H (1988) Time-dependence of bearing capacity of piles. In: Proceedings of the 3rd international conference on the application of stress-wave theory to piles, pp 879–888. Canada

Svinkin MR, Morgano CM, Morvant M (1994) Pile capacity as a function of time on clayey and sandy soils. In: Proceedings of the 5th international conference on piling and deep foundations, pp 1.11.1–1.11.8. USA

Semi-analytical Estimation of Surface Subsidence During Gas Recovery from Hydrate Reservoirs Under Indian Conditions

Rahul Yadav, Raghavendra P. Singh, and Malay K. Das

1 Introduction

Methane hydrates are potential sources of methane gas present under the deep-sea environment. Their abundance and gas holding capacity have attracted the attention of the researchers to consider them as a future energy source. For instance, even in very relaxed measures, the amount of organic carbon available with such reservoirs worldwide is estimated to be 10^{16} kg (Kvenvolden et al. 1993). The ever-building energy need of the civilization demands the exploration of such hydrate-rich sites. Many of the countries such as USA, France, Japan, Netherlands and India have expedited their efforts in identification of hydrate reservoirs and are investigating the ways to extract the methane gas from the same. Hydrate has a crystalline structure, where a methane gas molecule is surrounded by several molecules of water in solid form. On dissociation from the equilibrium state, the ice converts to water leaving the trapped methane gas free. This methane gas can be efficiently stored and used for energy extraction. The dissociation requirement, therefore, suggests to break down the methane-hydrate equilibrium either by lowering the pressure or by providing external heating. In some cases, injection of an inhibitor may also enhance hydrate dissociation. Out of these, the primary method to extract gas from the hydrate reservoirs is depressurization, where the equilibrium conditions in the reservoir are disturbed by lowering its pressure. As the depressurization process takes place, the pore pressure inside the gas hydrate bearing sediments may reduce to a significant extent. This pore pressure reduction, in turn, may result in changes in the overall stress equilibrium of the reservoir. This can lead to the compaction of the reservoir and ultimately ground subsidence. In many of the reservoirs, where significant ground subsidence has been reported, the reduction in pore pressure was cited as one of the important factors. For instance, in the Ekofisk gas field, production-induced pore

R. Yadav (✉) · R. P. Singh · M. K. Das
Indian Institute of Technology Kanpur, Kanpur, Uttar Pradesh, India
e-mail: yrahul@iitk.ac.in

S. Haldar et al. (eds.), *Advances in Offshore Geotechnics*, Lecture Notes in Civil Engineering 92, https://doi.org/10.1007/978-981-15-6832-9_16

pressure reduction was held accountable for the observed subsidence (Hermansen et al. 2000). A similar case is of Lacq gas field, where the ground displacements measured by continuous spirit levelling over a period of 20 years were found linearly related to the changes in the pore pressures (Segall et al. 1994). Therefore, the correct estimation of probable ground subsidence due to a proposed production activity is a crucial information to plan and execute the gas recovery in a safe manner.

Some of the early models to predict the subsidence during gas production have derived their analogies from the theory of thermo-elasticity. The nucleus of strain concept, which relates the vertical displacement of the surface to a confined source of pressure change located at a certain depth from the surface, was used by Geertsma (1973) and following the poro-elastic assumptions, the expressions for radial and vertical displacements of the surface due to such sources were derived. Segall (1992) represented the nucleus of strain solutions in a more general form by deriving the displacement and stress Green's functions for a disc-shaped reservoir. These formulations were then applied to estimate the subsidence at the surface of Lacq gas field in France by the same authors (Segall et al. 1994). The predicted and the measured subsidence data matched closely. Over the years, Geertsma and Segall formulations have proved to be important tools in getting initial estimates of the reservoir subsidence and to underline the contributing factors. Their extensions and applications are widely discussed among the researchers (Du and Olson 2001; Walsh 2002; Mendoza-Molina et al. 2015; Muñoz and Roehl 2017; Jayeoba et al. 2019). Although these models suffer from the drawback of assuming homogenous mechanical properties for the rock and the reservoir, their prediction in some cases have proved to be fairly accurate (Segall et al. 1994; Taherynia et al. 2013). With the rise of excellence in scientific computing, the advanced methods such as finite difference, finite element and boundary element have provided more sophisticated ways to solve this problem. However, the major concern with them is the need of high computing resources and time. On the other hand, the semi-analytical models come with the advantages of ease of implementation and lesser computational time. Therefore, the significance of these models cannot be ruled out completely as they can give a fair idea of the reservoir response to any proposed production activity. The first approximations provided by these models may certainly help in localizing the domain of interest for carrying out detailed computations using advanced tools.

In this study, we focus on obtaining the geomechanical response of hydrate reservoir sites governed by Indian conditions when subjected to depressurization-based gas recovery. To characterize the Indian reservoirs, the site-specific data from the recent National Gas Hydrate Program (NGHP-02) has been taken (Lin et al 2018; Jang et al 2018; Kim et al 2018). The depressurization of the hydrate reservoirs is modelled using a multi-component, multi-phase flow solver typically tuned to simulate Indian conditions. For the calculation of the subsidence, a semi-analytical model based on nucleus of strain theory has been considered and a numerical code to perform these computations has been developed. The estimates are obtained at different time scales, different production pressures and by varying reservoir depth and Poisson's ratio.

2 Mathematical Formulation

2.1 Flow Problem

The dissociation of gas hydrates at the reservoir site is accomplished by setting up a production well. At the well, a constant depressurization pressure lower than the hydrate equilibrium pressure is maintained. The hydrate at the reservoir starts to dissociate into methane gas and water, the gas flows through the production well and is collected at the sea surface. The dissociation physics is modelled considering a non-isothermal, multi-component, multi-phase flow problem, where the mobile phases are water and methane, while the hydrate phase is assumed to be immobile. The governing equations include mass, momentum and energy conservation and their general representation is as given below,

$$\frac{\partial}{\partial t}\left(\phi \sum\left(\rho_\alpha S_\alpha \omega_\alpha^i\right)\right) + \nabla.\left(\sum_\alpha\left(\rho_\alpha \bar{V}_\alpha \omega_\alpha^i - D_\alpha^i \nabla \omega_\alpha^i\right)\right) = \dot{m}^i \tag{1}$$

$$\bar{V}_\alpha = \frac{K k_{r\alpha}}{\mu_\alpha}(\nabla P_\alpha - \rho_\alpha \bar{g}) \tag{2}$$

$$\frac{\partial E}{\partial t} + \nabla. \sum\left(\rho_\alpha \bar{V}_\alpha H_\alpha\right) - \nabla.(\lambda_m \nabla T) = \dot{m}^h \Delta H \tag{3}$$

where the superscript i denotes the water and methane species and α denotes the phase index. ϕ is porosity, S is phase saturation, V is phase velocity, D is phase diffusion constant, ω is mass fraction of α phase of i specie and m is mass generation rate. The second equation denotes the velocity of phases governed by Darcy's law, where K is reservoir permeability, $k_{r\alpha}$ is the relative permeability and μ_α is phase viscosity. The third equation corresponds to energy conservation, where E is total energy accumulation term combining contribution from all the phases and H is phase enthalpy. The above set of equations are highly coupled and nonlinear. These governing equations along with a set of constitutive relations in terms of relative permeability, capillary pressure and hydrate kinetics provide closure to the problem. The solution produces the evolutions of gas pressure, temperature and velocity of different phases in the reservoir domain. A well-established, two-dimensional solver, hydrate reservoir simulator (HydReSim) has been utilized in this study to solve the above set of equations in the reservoir domain. The details on the development, validation and accuracy of HydReSim is available in Gamwo and Liu (2010).

2.2 Geomechanical Problem

The pore pressure distributions obtainable from the flow solver serve as an input to the geomechanical model. As discussed, a semi-analytical model based on nucleus of strain theory has been considered for subsidence estimation. The nucleus of strain theory is based on considering a point source located in the reservoir, which undergoes a pressure change in the poro-elastic half space. The disturbance at the nucleus may propagate at any other point in the domain. The contribution of such a disturbance to the overall subsidence at a point depends on its strength, which in this case is the pressure change. Following this, the expression for the subsidence at any location x due to pressure source located at ξ can be written as:

$$u_i(x) = f * \int_V \Delta P(\xi) g_i(x, \xi) \mathrm{d}V_\xi \tag{4}$$

where $f = -2 * C_m * (1 - \nu)$, here C_m is the compaction coefficient and ν is Poisson's ratio of the reservoir sediment. The term $\Delta P(\xi)$ represents the pressure source located at ξ and $g_i(\xi, x)$ is the displacement Green's functions relating to the disturbance at the source point ξ to the observation point x. If the reservoir domain is discretized into N sources of dilatation representing homogenous pressure change, then the displacement at any point on the surface x is simply the superposition of the contribution of all such sources weighted by their strength, i.e. pressure change, therefore,

$$u_i(x) = f * \sum_{k=1}^{N} \Delta P_k \int_{V_k} g_i(x, \xi) \mathrm{d}V_k \tag{5}$$

The Green's functions expressions for a thin disc- shaped reservoir to calculate the displacements at the surface in the vertical and radial directions are available as given by Geertsma (1973),

$$g_z(r, z = 0, \xi) = \int_0^\infty e^{-\mathrm{d}k} J_1(kR) J_0(kr) \mathrm{d}k \tag{6}$$

$$g_r(r, z = 0, \xi) = \int_0^\infty \mathrm{e}^{-\mathrm{d}k} J_1(kR) J_1(kr) \mathrm{d}k \tag{7}$$

where J_0 and J_1 are the Bessel functions of first and second kind, d is the depth of the source and R is radius of the reservoir. The set of Eqs. (4)–(7), along with pore pressure distribution $\Delta P(r, z)$ available from flow solver at any time step enables us

to calculate subsidence of the reservoir surface induced by changes in pore pressures. The integral in Eqs. (6) and (7) must be accomplished numerically. Therefore, such a procedure falls in the category of semi-analytical estimation. As discussed, the primary input in these semi-analytical models is the reservoir pore pressure distribution. Detailed information on the localized pore pressure changes due to a production activity is difficult to obtain experimentally and one has to resort to numerical tools for the same. As the pore pressure change takes place, due to increase in effective stress, the properties governing the flow problem such as porosity and permeability also change, which in turn changes the pressure evolution in subsequent computations. Thus, this is an inherently coupled problem. However, such a solution is both time-consuming and resource intensive and therefore can only be considered for the specialized studies. For the first approximations of the nature of geomechanical response due to a production activity, an uncoupled analysis can be considered and explicit effect of one on the other can be examined. For this purpose, the accurate pressure distribution from the reservoir simulations is mapped into a geomechanical domain to monitor the subsidence of the upper rock surface.

3 Schematic of the Problem

The problem geometry considered here is a two-dimensional axisymmetric layer of hydrate reservoir surrounded by rocks as shown in Fig. 1. The figure shows an axisymmetric plane of the reservoir, with z axis pointing downwards from the top and r axis originating at the well. The hydrate bearing layer (HBL) of 25 m thickness is bounded by 237.5 m of overburden and underburden rock. The bounding reservoir rocks are assumed to be impermeable and non-porous. At the left end of the reservoir, a production well is set up to carry out the depressurization of the reservoir. The hydrate layer is extending in radial direction up to 1500 m.

On depressurizing, the hydrate in the reservoir layer dissociates and the released gas moves toward the production well. The pressure in the reservoir decreases, which in turn increases the vertical effective stress on the reservoir sediments leading to their compaction. Our interest here is to estimate the probable subsidence of the ocean floor due to such a compaction triggered by prolonged gas withdrawal. The two-dimensional pressure distribution at different time steps is obtainable from ‘HydReSim’, the hydrate dissociation and flow simulator. The focus here has been laid on Indian conditions. The Indian gas hydrate reservoirs, primarily located in Krishna--Godavari basins are ultra-deep, segmented layers of hydrates hosted with sediments of varied morphologies. Several studies conducted on the characterization of the Indian reservoirs under the National Gas Hydrate Program (NGHP-02) have been considered as the source of obtaining the required parameters for the simulations. The characteristic dimensions of the reservoir along with its representative flow and mechanical properties are presented in Table 1.

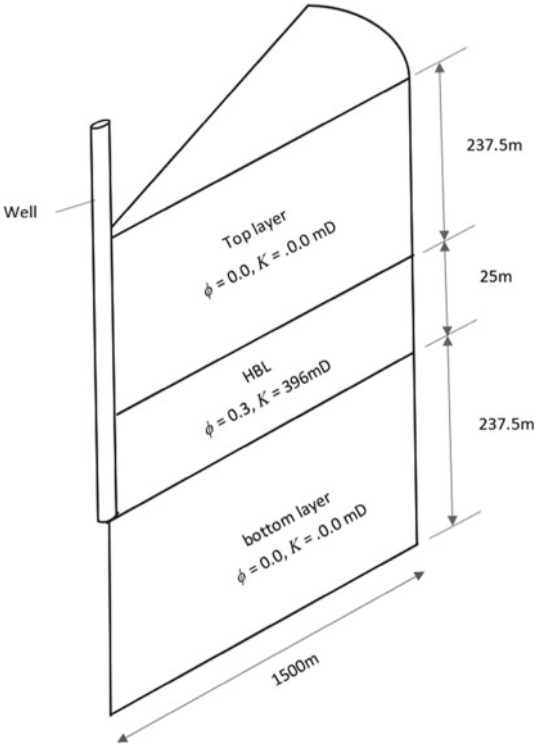

Fig. 1 Schematic of the hydrate layer surrounded by impermeable rocks

Table 1 Important characteristics of Indian reservoirs (from Lin et al. 2018; Jang et al. 2018; Kim et al. 2018 and Helgerud et al. 2009)

Properties	Values
Initial pressure	28 MPa
Initial porosity	0.3–0.4
Depth	250 m
Hydrate saturation	0.5
Poisson's ratio	0.3–0.35
Shear modulus	3.54 GPa
Reservoir thickness	25 m

4 Validation of the Model

The flow solver based on hydrate dissociation modelling is extensively validated with various test cases and the results of the same can be found in Gamwo and Liu (2010). Since this is a decoupled analysis, it remains to reason that appropriate validation of the geomechanical part of the solver should be performed independently. Therefore, in this section, we present the validation of the geomechanical solver developed upon

the nucleus of strain theory to estimate the surface subsidence by numerically integrating the displacement Green's functions. The numerical integration is performed using Gauss Lehster method in MATLAB (2015). We consider two standard cases for validation as discussed below.

The first case corresponds to a hypothetical reservoir of equal depth and radius. The reservoir is assumed to undergo a unit pore pressure change at multiple locations. Each of these locations can be considered as a nucleus of strain whose contribution will be superimposed to determine the subsidence at any location on the top of the surface as given by Eq. (5). The non-dimensional vertical and horizontal displacements of the reservoir surface are calculated at 20 and 40 observation points on the surface. These results are plotted against the radial distance from the well as shown in Figs. 2 and 3. The results are compared with the numerical results of Du and Olson (2001) and analytical estimations by Geertsma (1973). It can be observed from the figure that the present solution exactly matches with the previous published works and hence it proves the credibility of numerical integration scheme and its implementation.

Another case considered here is the measured subsidence at the Lacq gas field. The gas reservoir of Lacq, situated in south western France, is an interesting case to study as far as surface subsidence is considered. The data for fluid withdrawal and pore pressure change is acquired over a period of 20 years and the subsidence of the surface has been measured using spirit levelling (Segall et al. 1994). Several researchers in the past have considered this data for validation of their analytical or numerical models and fine-tuning their approximations. The reservoir is located at a depth of 7 km and has a radius of 3.5 km. The mechanical properties of the reservoir are listed in reference (Segall et al. 1994). The pore pressure drop over the monitored period is assumed to follow the equation,

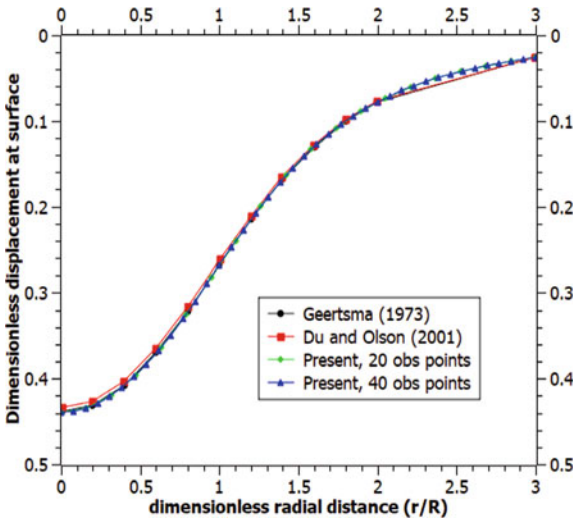

Fig. 2 Calculation of surface subsidence in vertical direction for unit pressure distribution using present code, comparison with solutions of Geertsma (1973) and Du and Olson (2001)

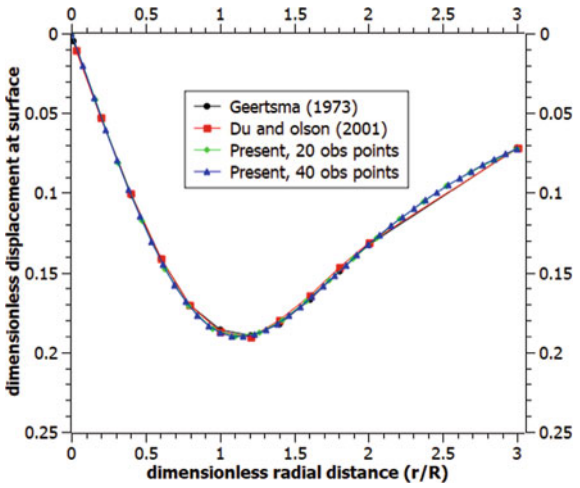

Fig. 3 Calculation of displacement in radial direction for unit pressure distribution using present code, comparison with solutions of Geertsma (1973) and Du and Olson (2001)

$$P(r,t) = P_0 e^{-\left(\frac{r}{r_c}\right)^4}$$

where P_0 is the pressure change at the well (i.e. $r = 0$) and r_c is the characteristic radius of the reservoir. This pressure change is introduced in the present geomechanical solver and the values of the vertical displacement at the surface are estimated at 10 and 20 observation points. The result is compared against the measured subsidence as reported by Segall (1992) and the numerical simulation results presented by the same author. The subsidence values are plotted against the reservoir radial location as shown in Fig. 4. It can be seen from the figure that the present solution matches closely with the analytical calculations of Segall (1992) as well the measured values.

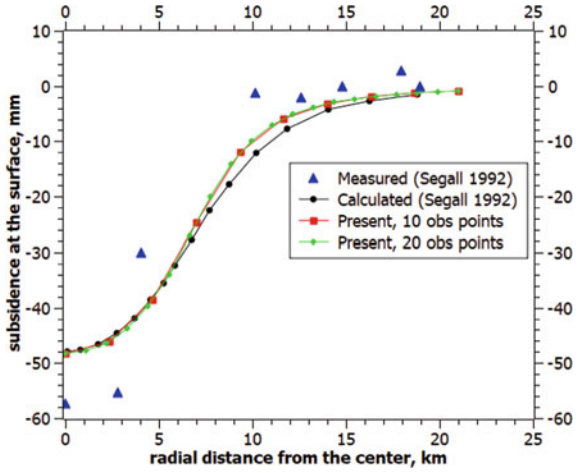

Fig. 4 Calculation of surface subsidence at Lacq gas field with a fourth-order pressure distribution using present code and comparison with solutions of Segall (1992)

These results certainly prove the credibility of the present solution scheme and opens vistas to perform subsidence analysis for Indian reservoir cases.

5 Results and Discussion

For the reservoir schematic as shown in Fig. 1, the flow problem is set up as follows. The porosity of the reservoir is taken as 0.3, the Possion ratio is assumed to be 0.3 and all other parameters are taken as mentioned in Table 1. Near the well, the minimum grid spacing of 0.02 m is taken while at the other end of the reservoir, a maximum grid spacing of 500 m is considered. In between 0 to 1000 m, a logarithmically increasing grid spacing is considered and total grid elements for the flow simulations is 3720. The gas production is carried out for 4 years and the pore pressure data is monitored in terms of gas pressure within the pores at the time scales of 6 months, 1, 2, 3 and 4 years. Using the reservoir simulator data, the pore pressure distribution within the reservoir is mapped into geomechanical domain for estimation of probable subsidence. A total of 20 elements in radial and 20 elements in axial direction within the reservoir domain are considered for mapping the pressure change to carry out geomechanical studies. Further increment in the number of elements did not show any change in the obtained subsidence values. The subsidence of the surface is monitored at 20 observation points. At first, the depressurization pressure is set at 24 MPa and the values of the vertical displacement at the surface (or subsidence) is calculated and plotted at various time scales along the length of the domain as shown in Fig. 5. From the figure, it can be seen that as the time progresses the pore pressure drops continuously and observable subsidence occurs. As usual, the maximum subsidence occurs near the wells. The rate of maximum subsidence is observed to be of the

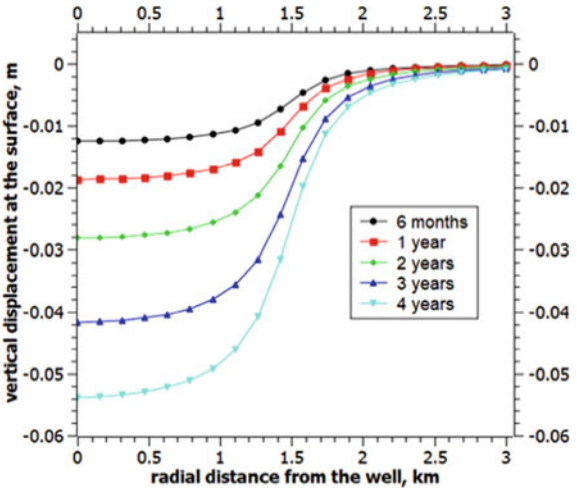

Fig. 5 Calculation of subsidence for a pore pressure distribution obtained from the reservoir simulator for the case of Indian reservoir simulated at depressurization pressure of 24 MPa and plotted at different time scales

order of 10–15 mm per year. Subsidence revokes its well-known bowl shape and the volume of this subsidence bowl increases for the longer production runs.

5.1 Effect of Depressurization Pressure

In the subsequent simulations, the value of depressurization pressure is further lowered from 24 to 22 MPa and 20 MPa. The pore pressure data for these three depressurization pressures has been obtained after a production run of 4 years. The change in subsidence values at this instant is then calculated and compared. The results are plotted in Fig. 6. It can be seen from the figure that the subsidence values are considerably higher for the case of 20 MPa depressurization pressure due to higher changes in pore pressures observed during the given time scale of production. The observed behaviour of previously modelled reservoirs clearly shows up in the results as the subsidence values are directly proportional to the changes in pore pressure. We shall now look the effect of location of reservoir and its mechanical properties such as Poisson's ratio. This analysis is expected to be insightful since Indian hydrate reservoir sites are identified at varied depths and occur in varied host conditions. Therefore, the information about how a particular site may behave in terms of subsidence modelling may give preliminary idea of vulnerability of these reservoirs.

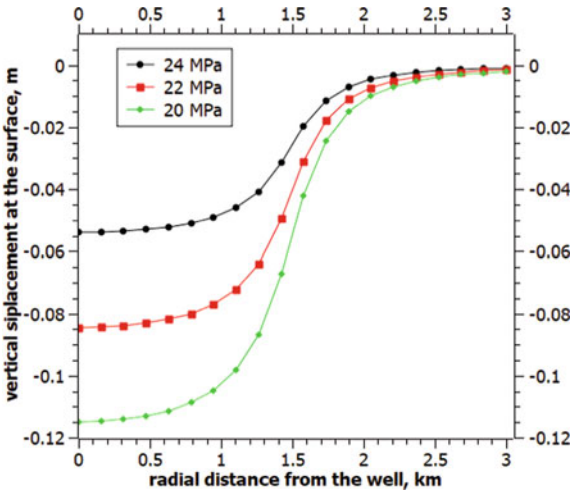

Fig. 6 Calculation of subsidence with pore pressure distribution obtained from reservoir simulator after a production run of 4 years for Indian reservoir case simulated at three different depressurization pressures

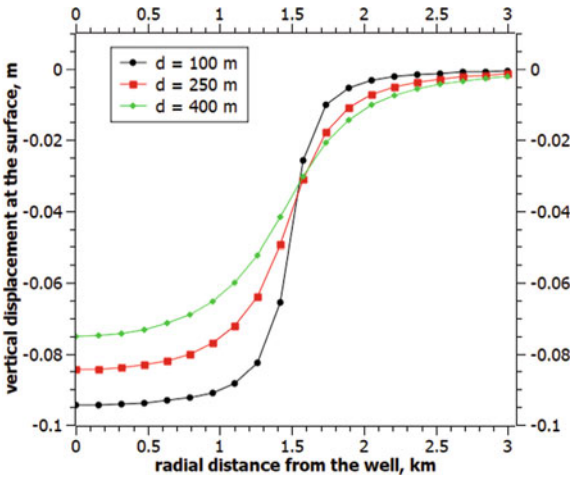

Fig. 7 Calculation of subsidence with pore pressure distribution obtained from reservoir simulator after a production run of 4 years for Indian reservoir case simulated at different values of depth of reservoir

5.2 *Effect of Depth of Reservoir*

The accumulated data after the National Gas Hydrate Program suggests that gas hydrate reservoir sites occur at varied depths from the seafloor. Therefore, it is necessary to know the subsidence response of production activity when the reservoir is located at various depths. With this motivation, we choose three representative values of the depth of reservoir, viz. 100, 250 and 400 m. The subsidence results for these three different depths of reservoir are highlighted by carrying out the production for 4 years with a depressurization pressure of 22 MPa. The values of vertical displacement at the surface are calculated and plotted against the radial location from the well as shown in Fig. 7. From the figure, it can be seen that the depth of reservoir plays an important role in overall subsidence of the surface and the values are higher for lower depth. The maximum subsidence was observed to be 10.5% and 20.6% lower when the depth of the reservoir is increased from 100 m to 250 m and 400 m, respectively. This supports the intuitive results, also highlighted by others (Segall 1992) that the shallow reservoirs are more prone to subsidence than the deeper ones for same depressurization pressure.

5.3 *Effect of Poisson's Ratio*

In the next analysis, we highlight the effect of Poisson's ratio on the reservoir surface subsidence. It is customary to note that exact value of the reservoir Poisson's ratio, in particular to gas hydrate reservoirs is not known, instead a range is always suggested. This is because of the inhomogeneity of the host sediment and its varying morphology across the reservoir domain which changes the mechanical response of the reservoir. To highlight the effect of Poisson's ratio, three values of the same, lying in the specific

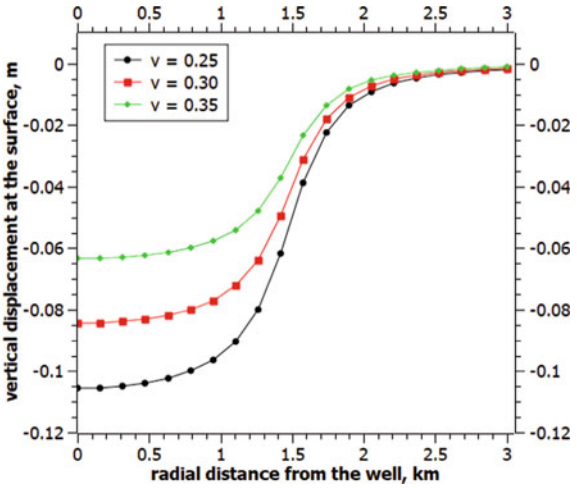

Fig. 8 Calculation of subsidence with pore pressure distribution obtained from reservoir simulator after a production run of 4 years for Indian reservoir case simulated at different values of Poisson's ratios

range of interest has been considered, viz. 0.25, 0.3 and 0.35. The gas production is then performed for a period of 4 years at a depressurization pressure of 22 MPa. The subsidence response of the surface is estimated using the geomechanical model at the end of 4 years. The results are plotted against the radial location from the well as shown in Fig. 8. From the figure, it is clear that even a small change in the values of Poisson's ratio gives a large change in the subsidence predictions. On increasing Poisson's ratio from 0.25 to 0.3 and 0.35, a relative decrease of 20% and 40% in the value of maximum subsidence is observed, respectively. Thus, the subsidence is higher for a lower Poisson's ratio which is intuitive because of the fact that the reservoirs with higher Poisson's ratios are more elastic and the increase in vertical load as a result of pore pressure drop induces significant lateral displacements in this case. On the other hand, lower value of reservoir Poisson's ratio indicates a clayey behaviour for which lateral displacements are not so pronounced and therefore are more prone to vertical displacements.

6 Conclusion

Subsidence in case of a gas hydrate reservoir has been estimated using semi-analytical model based on nucleus of strain theory. A decoupled analysis is performed where the realistic pore pressure data is obtained using a multi-phase, multi-component flow solver tuned to model hydrate dissociation physics. Depressurization is considered as the primary production process, and the evolution of gas pressure in the pores at different time scales is input to the semi-analytical subsidence model. The value of depressurization pressure, depth of reservoir and reservoir Poisson's ratio are seen to impact the subsidence prediction by a large margin. The subsidence values are more for a shallow reservoir than for a deep one. It is also observed that even

small changes in the value of Poisson's ratio changes the subsidence values to a considerable extent and hence, the correct estimation of reservoir Poisson's ratio is quite necessary in order to accurately capture the subsidence response. This analysis, therefore, opens up new windows to perform a detailed analysis of geomechanical response in case of shallower and inelastic reservoirs. This also highlights the need to estimate geomechanically safe operating conditions to minimize the subsidence.

References

Du J, Olson JE (2001) A poroelastic reservoir model for predicting subsidence and mapping subsurface pressure fronts. J Petrol Sci Eng 30(3–4):181–197

Gamwo IK, Liu Y (2010) Mathematical modeling and numerical simulation of methane production in a hydrate reservoir. Ind Eng Chem Res 49(11):5231–5245

Geertsma J (1973) Land subsidence above compacting oil and gas reservoirs. J Petrol Technol 5:734–744

Helgerud MB, Waite WF, Kirby SH, Nur A (2009) Elastic wave speeds and moduli in polycrystalline ice Ih, sI methane hydrate, and sII methane-ethane hydrate. J Geophy Res Solid Earth 114(B2)

Hermansen H, Landa GH, Sylte JE, Thomas LK (2000) Experiences after 10 years of water flooding the Ekofisk field, Norway. J Petrol Sci Eng 26(1–4):11–18

Jang J, Dai S, Yoneda J, Waite WF, Stern LA, Boze LG, … Kumar P (2018) Pressure core analysis of geomechanical and fluid flow properties of seals associated with gas hydrate-bearing reservoirs in the Krishna-Godavari Basin, offshore India. Mar Petrol Geol (In press)

Jayeoba A, Mathias SA, Nielsen S, Vilarrasa V, Bjørnarå TI (2019) Closed-form equation for subsidence due to fluid production from a cylindrical confined aquifer. J Hydrol 573:964–969

Kim J, Dai S, Jang J, Waite WF, Collett TS, Kumar P (2018) Compressibility and particle crushing of Krishna-Godavari Basin sediments from offshore India: Implications for gas production from deep-water gas hydrate deposits. Marine Petrol Geol (In press)

Kvenvolden KA, Carlson PR, Threlkeld CN (1993) Possible connection between two Alaskan catastrophes occurring 25 years apart (1964 and 1989). Geology 21:813–816

Lin JS, Uchida S, Myshakin EM, Seol Y, Rutqvist J, Boswell R (2018) Assessing the geomechanical stability of interbedded hydrate-bearing sediments under gas production by depressurization at NGHP-02 Site 16. Mar Petrol Geol (In Press)

MATLAB, version 8.5 (R2015a) (2015) The MathWorks Inc., Natick, Massachusetts

Mendoza-Molina JF, Mercado-Montes CA, Calderón-Carrillo ZH (2015) New approach for compaction prediction in oil reservoirs. CT&F Ciencia, Tecnología y Futuro 6(1):5–16

Muñoz LFP, Roehl D (2017) An analytical solution for displacements due to reservoir compaction under arbitrary pressure changes. Appl Math Model 52:145–159

Segall P (1992) Induced stresses due to fluid extraction from axisymmetric reservoirs. PAGEOPH 139(3/4):535–560

Segall P, Grasso JR, Mossop A (1994) Poroelastic stressing and induced seismicity near the Lacq gas field, southwestern France. J Geophys Res Solid Earth 99(B8):15423–15438

Taherynia MH, Aghda SFM, Ghazifard A (2013) Modeling of Land Subsidence in the South Pars Gas Field (Iran). Int J Geosci 4:1095–1100

Walsh JB (2002) Subsidence above a planar reservoir. J Geophy Res Solid Earth 107(B9):ETG-6

Fatigue Damage After Installation of an Offshore-Driven Pile-Back Analysis from Pile Monitoring Data

Viet Nguyen, C. R. Parthasarathy, and Vikas Goel

1 Introduction

Open ended steel pile is often used as foundation of offshore structures such as jacket platform. It is often driven into the seabed by means of adequate hammer. The design of the pile needs to ensure the stability of the structure under operational load cases and to make sure that the piles would not be damaged by fatigue phenomenon during its design life.

A high number of stress cycles applied could cause the fatigue failure of the steel, especially in the weld joints. The fatigue damage of the pile could be caused during both installation operation and inplace condition.

In general, the grand total fatigue damage that the pile might have will be the sum of the installation and inplace fatigue damages. For design purpose, a margin of safety should be established to ensure the long-term performance of the pile. A general design format that accounts for each contribution independently can be expressed as:

$$\mathrm{DF}_{\mathrm{inplace}} \cdot \mathrm{SF}_{\mathrm{inplace}} + \mathrm{DF}_{\mathrm{install}} \cdot \mathrm{SF}_{\mathrm{install}} \leq 1.0 \tag{1}$$

$\mathrm{DF}_{\mathrm{inplace}}$, $\mathrm{DF}_{\mathrm{install}}$ are the fatigue damage factors estimated for inplace condition and for installation operation, respectively, and SFs are their associated safety factors.

The process to predict the fatigue damage for inplace condition of a driven pile involves the structure analysis of an offshore structure under periodic actions such as wind, wave, or current.

V. Nguyen
Geotechnical Consultant, Paris, France

C. R. Parthasarathy (✉) · V. Goel
Sarathy Geotech and Engineering Services Pvt Ltd., Bangalore, India
e-mail: partha@sarathygeotech.com

S. Haldar et al. (eds.), *Advances in Offshore Geotechnics*, Lecture Notes in Civil Engineering 92, https://doi.org/10.1007/978-981-15-6832-9_17

The fatigue damage due to installation can be predicted by using 1D wave equation theory: After doing a classic driveability study, the expected dynamic stress range at a specific position along pile shaft will be combined with the "predicted" blowcount number to access the cumulate fatigue damage at this location.

The safety factors (SFs) should be commensurate with the uncertainty of the process to evaluate the fatigue damage, the criticality of the pile, the ability to inspect it, repair it, or replace it, and the potential consequence of the failure of the pile. General practice for primary structural components that are not inspectable and are critical to the structural performance of the system, a safety factor of 10 is recommended for fatigue damage. However, no code nor standard differentiate the safety factor for "inplace" or "installation" case. Therefore, it can be understood that same SF should be considered for both situations. However, applying SF of 10 for both types of fatigue damage might be struggling in the design stage as very often the predicted fatigue damage due to driving itself is already greater than 0.1.

It is to note that the "inplace" fatigue damage is mostly from natural causes. Its prediction is therefore highly uncertain and it cannot be measured afterward. In contrary, the fatigue damage from installation partially depends on the human decision (i.e., hammer energy setting strategy when driving the pile). The uncertainty in its prediction methodology would be less and so the corresponding safety factor. Also, if the fatigue damage due to pile installation can be quantified once the operation is done, it will be a valuable information that can shed light on the uncertainty of the prediction method. Also, it will help to reduce the conservatism in fatigue damage verification where only the inplace condition will be concerned:

$$\mathrm{DF}_{\mathrm{inplace}} \cdot \mathrm{SF}_{\mathrm{inplace}} \leq 1.0 - \mathrm{DF}_{\mathrm{install}}^{\mathrm{measured}} \tag{2}$$

Nowadays, it becomes mandatory in several specifications and codes that the offshore-driven piles should be monitored/instrumented during installation. The pile instrumentation (or dynamic measurement) can be carried out by means of PDA analyzer. Their main application and objectives are to help evaluating hammer performance, control dynamic stress generated during driving, and to determine the pile bearing capacity by means of signal matching study (i.e., CAPWAP) (Pile Dynamics, Inc.)

In addition to above objectives, the pile monitoring data can be also used to quantify the pile fatigue damage because of following reasons:

- Stress cycles are induced by the dynamic effect during the pile driving process. For each blow, the magnitude of stress cycle at a specific position along pile shaft is often taken as the difference between the maximum compressive stress and maximum tensile stress caused by a single choc wave passing through it. The blowcount number is considered as number of cycles. By knowing the magnitude of stress cycle (or stress range) and the number of cycles, the fatigue damage factor of a material can be theoretically estimated.
- The pile monitoring operation discloses the maximum compressive stress (CSX) at sensor location and records the blowcount number. So, the fatigue damage factor

of pile material at sensor location can be estimated accordingly. However, it is more interested to know the fatigue damage factor at other locations, especially in the weld joints where the crack growth could be faster than in the pile base material. To do so, the dynamic stress at other locations along pile shaft will be estimated by calibrating with the measured values at sensor location. To do the calibration, a 1D wave equation numerical driveability model which is fully representative for the driving situation on site will be built.

2 Procedure to Estimate the Pile Fatigue Damage Based on Pile Monitoring Data

2.1 Step 1: Rebuild the Ground Model

The 1D wave equation numerical driveability model can be considered as fully representative for a given driving condition if it can capture the properties of the driving system (i.e., hammer--pile--soil system) and yield the same results with the site observation such as blowcount numbers and maximum dynamic stress. With help of GRLWEAP software, the hammer-pile system is quite simple and straightforward to model. However, the soil behavior during driving is not easy to simulate as it requires a separation of dynamic soil resistance and static soil resistance along with the determination of appropriate parameters for each part.

According to wave equation theory developed by Smith (Smith 1960), the dynamic behavior of the soil can be represented Smith damping model with associated damping and quake parameters both for pile shaft and pile toe. Those parameters need to be determined for representing soil dynamic behavior. Also, the static soil resistance often referred to soil resistance driving (i.e., SRD) with correct distribution of shaft and toe resistance need to be estimated for static part.

2.1.1 Step 1a: Estimation of Soil Static Resistance at Particular Depths---CAPWAP Analysis

The signal matching analysis using CAPWAP software is a reliable analysis for assessing the pile capacity (i.e., soil static resistance). It is also powerful tool to help separating the dynamic and static contribution of soil resistance [PDI (Pile Dynamics, Inc.)].

The signal matching analysis uses the measured hammer generated downward wave as an input and iteratively adjusts a numerical soil model by comparing the computed reflected upward force wave to the measured upward force wave reflected by the pile/soil interface.

In order to accurately reproduce the soil resistance, the pile actual geometry need to be correctly modeled in CAPWAP (influence of diameter and thickness changes in waves propagations are thus taken into account in the calculations).

It is to be noted that the solution disclosed by CAPWAP® software is not unique and the friction/tip resistance distribution is one order of magnitude less accurate than the disclosed total resistance. It is because it will be difficult to differentiate the contribution of shaft resistance near to the pile toe and the pile toe resistance itself. Current practice recommends to account only the contribution of shaft resistance from the pile elements that are 1–2 diameter away from the pile toe. Also, the experienced user can also provide quite reliable judgment on shaft/toe resistance distribution through their matching process with respect to the soil information from borehole logs.

The CAPWAP analysis need to be carried out at different depths of pile penetration. It is recommended for each sudden change in soil properties which is often related to different geological formation or every 10 m for long offshore pile.

2.1.2 Step 1b: Estimation of Soil Dynamic Parameter-Adjusted Analysis

In addition to the soil static resistance or pile capacity, the CAPWAP solution provides also the dynamic soil parameters such as damping and quakes. However, those parameters might not yield the same results when directly feed into the 1D Wave equation numerical simulation (i.e., GRLWEAP). That is because of the following reason (see Rausche et al. 2009):

- The measured pile force and velocity do not match the calculated curves at all points in time although the single peak points of transferred energy and stress match. Reasons include hammer--pile alignment problems and nonlinearly behaving hammer and driving system components.
- CW (i.e., CAPWAP) uses a pile model consisting of continuous sections while the GRLWEAP code works with a lumped mass model.
- The GRLWEAP software normally uses the Smith soil model with few exceptions. In order to achieve a good-quality signal match, PDA-CW, on the other hand, works with many extensions to the basic Smith model such as viscous damping, variable unloading quakes, variable negative shaft resistance levels, and other extensions of the basic Smith soil model. PDA-CW has to use a more detailed model in order to achieve a reliable capacity result.

The goal of the adjusted analysis is to determine the soil dynamic model (dynamic parameters) for 1D wave equation numerical simulation which will produce the best match between the pile capacity determined by "so-called" bearing graph and pile capacity determined by CAPWAP® study. The last one is the standard for assessing the pile capacity issued from dynamic load tests, then considered as reference value.

The goal of adjusted analysis is therefore quite similar to refined wave equation analysis (REWE) recommended by Rausche et al. (2009) but with different approach. Details of this approach can be found in (Ta and Martin 2012).

2.1.3 Step 1c: Estimation of Soil Static Resistance to Driving (SRD) Over Depth

The soil resistance to driving or static resistance to driving (SRD) is the static part of the total soil resistance experienced at time of driving. It is equal to the total resistance, reduced by the purely dynamic (or viscous) resistance, also called damping. The SRD corresponds to the static capacity of the pile if a static test could be performed immediately after an interruption of driving.

The SRD can be back-calculated from the driving data by using the global method. This method is based on the numerical model of 1D wave equation (GRL WEAP software) where the hammer--pile--soil system is established using true hammer--pile properties and some assumptions on the soil behavior. These assumptions are mostly the soil dynamic behavior (shaft and toe damping, shaft and toe quake), and the percentage of shaft resistance.

In order to accurately reproduce the driving condition, the pile geometry is modeled in GRL WEAP® according to the real pile geometry (influence of diameter and thickness changes in waves propagations are thus taken into account in the calculations). Hammer model is selected according to the hammer used on site. The soil dynamic parameters are taken from the adjusted analysis (step 1b) and the percentage of shaft resistance is taken from the CAPWAP study (step 1a).

The wave equation analysis results in the so-called bearing graphs. Based on these bearing graphs, the collected driving parameters such as blowcount BLC (bl/m) and transferred energy EMX (kJ) can be converted for each driving increment into the so-called back-analyzed SRD (or back-SRD).

2.2 Step 2: Back Analysis of Stress Range at a Specific Location (x)

The fatigue damage factor (DF) of pile material at sensor location can be estimated based on the measured compressive dynamic stress and the recorded blowcount number. However, the sensor location is often not the one has potential risk to fatigue damage. Other locations along the pile shaft such as welds, connectors or where the pile material suffer a treatment process are much more dangerous. To assessment the DF at these locations, their corresponding compressive dynamic stress experienced during driving must be known. As these stresses are not directly measured, they need to be correlated to the measured stress at sensor location, usually assumed as measured stress at the pile top σ_{top}.

The correlation can be carried out by using a 1-D wave equation simulation (i.e., GRLWEAP) step by step as detailed here below.

For a given pile makeup, the dynamic stress along pile shaft generated during driving depends on the force delivered to the pile and the reaction from the soil. These two main factors can be pictured by applied hammer energy and the soil dynamic--static behavior to driving. By knowing the soil dynamic behavior (from step 1 above), the dynamic compressive stress at a specific location x (x is the distance from the location in question and the pile top) can be expressed as a function of soil static resistance and the applied hammer energy:

$$\sigma(x) = F(x, E_{\text{thru}}, \text{SRD}) \tag{3}$$

Taking the dynamic compressive stress at sensor location as a reference value, the normalized stress function can be written as:

$$\frac{\sigma(x)}{\sigma_{\text{top}}} = N(x, E_{\text{thru}}, \text{SRD}) \tag{4}$$

where

E_{thru} is the energy delivered to the pile;
SRD is the static soil resistance to driving;
σ_{top} is the dynamic compressive stress at sensor location

In a real driving situation, the pile makeup is known, the delivered energy E_{thru} is fully recorded by mean of monitoring equipment. Also, the details of SRD including shaft percentage distribution can be estimated as per step 1c. Therefore, a 1D wave equation numerical model created with above parameters will be fully representative the driving condition on site.

The representative numerical driveability model discloses also the dynamic stress at any location along the pile shaft during driving. The normalized stress function $N(x)$ is then determined accordingly.

The dynamic stress at a location x can be therefore determined by correlating with the one measured at the pile top by the following equation:

$$\sigma(x) = \sigma_{\text{top}}^{\text{measured}} \cdot N(x) \tag{5}$$

2.3 Step 3: Estimate Damage Factor at Specific Location (x)

2.3.1 Damage Factor for a Single Blow

At a specific location x, a single hammer blow i could cause an amount of fatigue damage which can be determined by the following formula:

$$\mathrm{DF}_i = \frac{1}{N^i_{\mathrm{limit}}} \tag{6}$$

N^i_{limit} is the limit number of stress cycles to cause fatigue failure for a blow i. According to the latest version of DNV RP C203 (DNV 2011), it can be estimated as follows:

$$\log N^i_{\mathrm{limit}} = \log \bar{a} - m \log\left({}_i\left(\frac{t}{t_{\mathrm{ref}}}\right)^k \right) \tag{7}$$

where

N_{limit}	Predicted number of cycles to failure for stress range $\Delta\sigma$, also called N_{limit}
$\Delta\sigma_i$	Stress range experienced at location x, taken as $\sigma_i(x) \cdot \mathrm{SCF}$, where $\sigma_i(x)$ is dynamic compressive stress experienced at the location x caused by blow i. It is determined by the correlation with the measured pile top stress as explained in above section. SCF is the stress concentration factor depending on the nature of pile material at location x
m	Negative inverse slope of S–N curve (given in Table 2-1, 2-2, and 2-3) (DNV 2011)
$\log \bar{a}$	Intercept of log N-axis by S–N curve (given in Table 2-1, 2-2, and 2-3) (DNV 2011)
$\log a$	Intercept of mean S–N curve with the N-axis
$s_{\log N}$	Standard deviation of the log N
t_{ref}	Reference thickness equal 25 mm for welded connections other than tubular joints. For tubular joints, the reference thickness is 32 mm and for bolts 25 mm
T	Thickness through which a crack will most likely grow. $t = t_{\mathrm{ref}}$ is used for thickness less than t_{ref}
k	thickness exponent on fatigue strength as given in Table 2-1, 2-2, and 2-3 (DNV 2011)

2.4 Total Damage Factor After Driving

The total fatigue damage at a specific location x after driving operation can be estimated by:

$$\mathrm{DF}_{\mathrm{total}} = \sum_{i=1}^{\mathrm{BN}_{\mathrm{total}}} \mathrm{DF}_i \tag{8}$$

3 Case Study

A case study will be performed in order to better understand the methodology described above.

3.1 Problem Description

An offshore monopile named A04 of 6 m of diameter and 48 m of length with variable pile wall thicknesses has been driven up to 26.25 m into the soil. This offshore monopile serves as foundation of a wind turbine in the offshore wind farm located in North Sea area. The soil condition consists of mainly medium dense to very dense sand. For confidential reason, the site condition and soil properties are not explicitly reported in the present paper.

The pile was driven with hydraulic hammer IHC S2500 up to required depth in a single run without any interruption. In total, about 3000 blows have been recorded.

During driving, the pile was monitored with four strain transducers and two accelerometers piezo-resistive. The use of four strain gases is often recommended in large diameter piles in which the advised distance between sensors location and pile top (often taken as 1.5OD to 2.0OD) cannot be fulfilled. One accelerometer PR should be enough for data interpretation, however two have been used for redundancy purpose.

The monitoring data quality is considered as good for post-installation studies including back analysis of fatigue because of following observations:

- Good proportionality of F and V at start of signal;
- F and V start from zero at the beginning of signal and fade down to zero at the end;
- Absence of electrical instability;
- Repetitiveness: similarity of signals recorded from successive blows;
- Similarity of individual force measure: Bending is limited and good alignment between hammer and pile is observed.

The thickness of the pile is highly variable because the pile was made from different shorter sections with butt welding.

3.2 Rebuild the Ground Model

Signal Matching Study

The CAPWAP® analyses were performed for four different pile penetrations. The results are summarized in Table 1.

Adjusted Analysis

Table 1 Pile capacity results based on signal matching analyses

Pen. (m)	BN	Set/blow (mm)	E_{thru} (kJ)	$R_{c,m}$ (MN)	MQ	(%) shaft
8.0	589	6.5	730	57	1.98	30
15.0	1501	7.9	1060	68	2.62	45
20.0	2124	6.7	1180	80	2.05	60
26.25	3032	7.3	1478	100	2.53	65

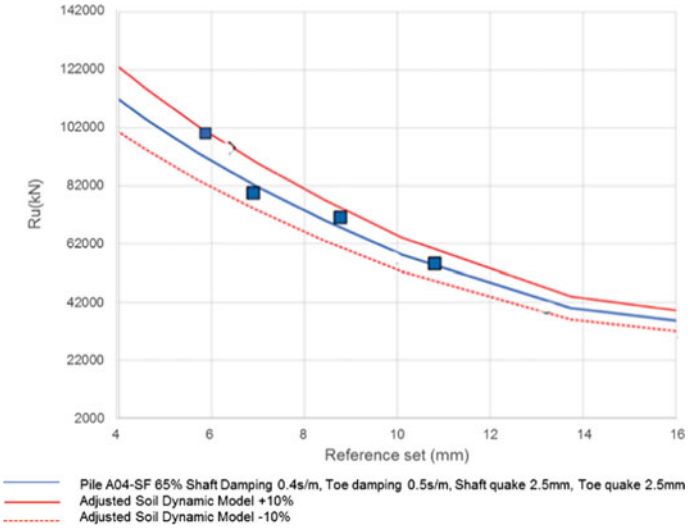

Fig. 1 Adjusted bearing graph based on pile capacity determined by CAPWAP® using set and energy reference criterion

Adjusted bearing graph based on pile capacity determined by CAPWAP®, were presented in Fig. 1.

The adjusted soil dynamic parameters applicable for the instrumented monopiles are shown in Table 2.

Table 2 also shows that the shaft damping factor in sand can be also higher than the standard recommendation. It means that higher energy losses due to soil viscosity might occur when driving big diameter pile. The assumed soil dynamic parameters in Table 2 is valid for all pile penetration depths.

Back analysis of SRD

The adjusted soil dynamic parameters as presented in Table 2 were used to create a series of bearing graphs which required for back-calculating SRD.

Also, the assumed shaft friction percentage of these bearing graphs is estimated based on the CAPWAP results presented in Table 1. The back analysis of static soil resistance to driving (SRD) is presented in Fig. 2.

Table 2 Adjusted dynamic soil parameters

Monopile		A04
Quake	Toe, Q_p (mm)	2.5
	Shaft, Q_s (mm)	2.5
Damping	Toe, J_p (s/m)	0.5
	Shaft, J_s (s/m)	0.4
Shaft resistance (%)[a]		65

[a]it is to note that as the quake and damping parameter for shaft and toe resulted from adjusted study are quite similar, the effect of shaft resistance distribution on bearing graph is quite limited. For illustration purpose, the normalized bearing graph in Fig. 1 is for the shaft distribution at final depth only

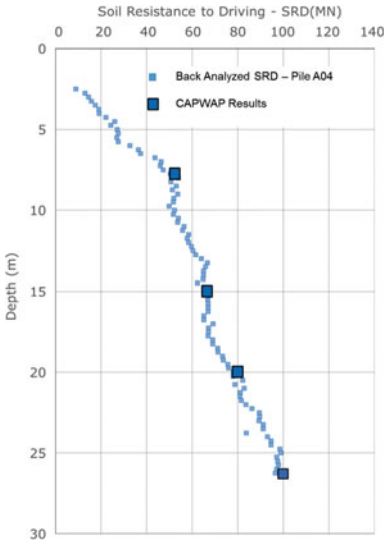

Fig. 2 Back analysis of SRD with adjusted soil parameters

3.3 Back Analysis of Stress Range at a Specific Location

3.3.1 Representative 1D Wave Equation Model

The representative 1D wave equation model for this piling operation can be created by using the driveability analysis option in GRLWEAP software with below considerations:

- The pile makeup is fully modeled;
- In addition to hammer model selection (IHC S2500), the variation of hammer efficiency in the model will be defined so that the model discloses the same calculated enthru energy EMX with the with measured EMX during driving;
- Soil dynamic parameters are as per Table 2;

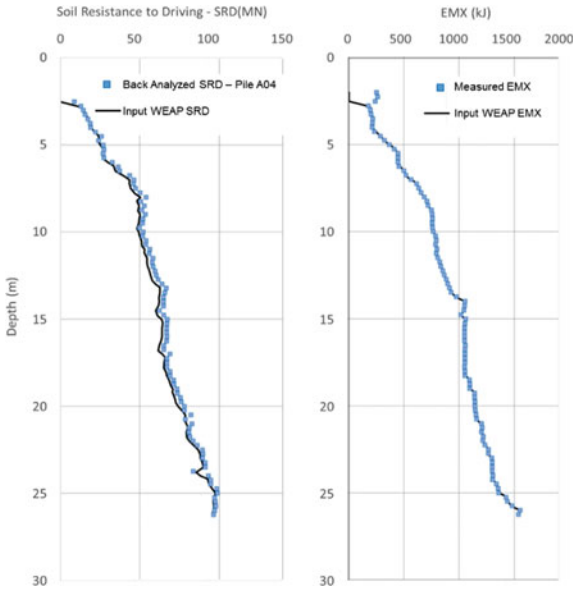

Fig. 3 Input for representative GRLWEAP driveability model

- Soil static resistance to driving SRD is as per Fig. 2, and the shaft/toe resistance distribution is roughly assumed as per Table 1.

The input data in GRLWEAP driveability model can be seen in Fig. 3 which is fully representative for the monopile driving condition. However, the validity of GRLWEAP driveability model should be checked so that it will yield similar blowcounts with site observation and other computed quantities such as CSX should be comparable with the field measurements. Both conditions are fully satisfied as shown in Fig. 4.

3.3.2 Normalized Stress Function $N(x)$

Now, we have a driveability numerical model which is fully representative for the driving condition of the monopile. By accepting that, we can perform the standard fatigue study with this representative driveability model and state that the derived fatigue damage at different locations along the pile will be the same or close for the true fatigue damage obtained at those locations. However, if we look at Fig. 4, we might see that unlike the predicted blowcount number which well fits the field records, the computed dynamic compressive stress (CSX) disclosed by representative model is slightly higher than the measurements. Therefore, direct calculation of fatigue damage from the stress ranged given by representative GRLWEAP model is not recommended. Instead, the GRLWEAP model can be used to estimate the normalized stress function $N(x)$. This function clearly depends on the monopile

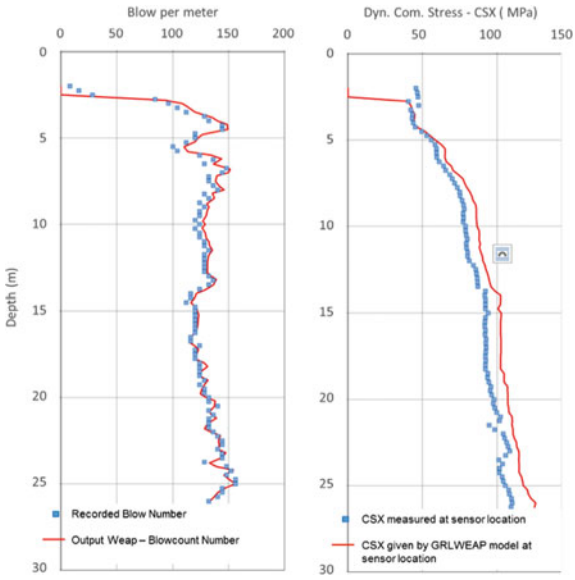

Fig. 4 Output of representative GRLWEAP driveability model

penetration depth and will be used to extrapolate the stress at other locations of the pile from the measurement at pile top (Fig. 5).

3.4 Estimation of Fatigue Damage (DF)

Thanks to the normalized stress function, the maximum compressive dynamic stress can be estimated for all other positions along the pile shaft under each hammer blow. It can be done by multiplying the normalized stress function with pile top measurement (CSX). The maximum tension stress at those locations is not as important as compressive value, they can be therefore directly estimated from representative driving model. The stress range can be then determined accordingly. It is to note that at the location of the welds, the stress range needs to be multiplied by a stress concentration factor (SCF). This factor depends on the characteristic of the welds and welding members. In the present study, the location of the fabrication welds of this offshore monopile and their associated SCFs are summarized in Table 3

Due to the SCFs, it is very likely that the welds will be more exposed to fatigue damage than other location along the pile.

By knowing the stress range and the stress cycle, it is often taken as the observed blowcount number, and the fatigue damage at any location of the monopile after driving can be assessed. Table 4 summarizes the fatigue damage factor at weld locations. Figure 6 presents the fatigue damage factor estimated for all position along the monopile.

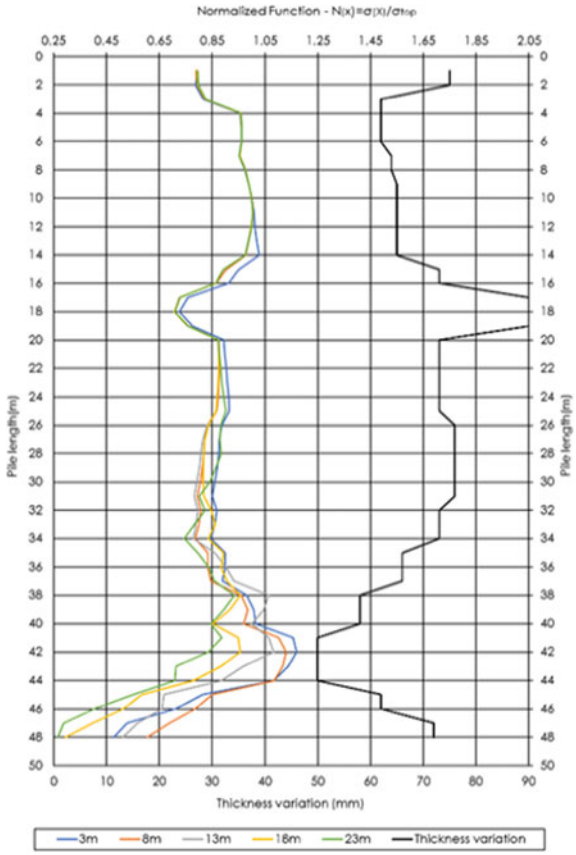

Fig. 5 Normalized stress function at different depths

4 Conclusion

This paper has outlined a methodology to assess the pile fatigue damage of an offshore pile after installation based on the pile monitoring data. This state of the art is combined of different types of post-installation studies such as signal matching analysis, adjusted or refined wave equation analysis, and back analysis of soil static resistance to driving. The basic idea is to recreate a representative numerical drive-ability model in 1D wave equation software GRLWEAP which can fully capture the characteristics of a hammer--pile--soil driving system and give the output results comparable with the measurements on site. This representative numerical driveability model will help to indirectly determine the maximum dynamic stress experienced at a specific location along pile shaft other than the measured value (CSX) at pile top (i.e., sensor location). The fatigue damage of this specific location can be then quantified by considering the interpolated maximum dynamic stress and the recorded blowcount number on site.

Table 3 Weld position and associated stress concentration factors

Weld position from top (m)	Name	Inside SCF	Outside SCF
0.28	W02	1.349	1.079
2.8	W04	1.526	1.165
5.8	W06	1.272	1.165
8.4	W08	1.238	1.184
11.4	W10	1.235	1.181
14.4	W12	1.371	1.165
16.27	W14	1.542	1.165
18.77	W16	1.497	1.165
22.21	W18	1.18	1.24
25.4	W20	1.29	1.204
28.4	W22	1.175	1.175
31.4	W24	1.252	1.165
34.4	W26	1.341	1.165
37.4	W28	1.427	1.165
40.4	W30	1.466	1.149
42.4	W32	1.246	1.246
44.32	W34	1.547	1.149
46.32	W36	1.44	1.165

Table 4 Weld position and associated stress concentration factors

Name	Inside damage factor	Outside damage factor
W02	0.0032	0.0017
W04	0.0047	0.0021
W06	0.0043	0.0033
W08	0.0044	0.0039
W10	0.0045	0.0040
W12	0.0058	0.0036
W14	0.0061	0.0027
W16	0.0043	0.0020
W18	0.0029	0.0034
W20	0.0039	0.0032
W22	0.0025	0.0025
W24	0.0027	0.0022
W26	0.0036	0.0024
W28	0.0058	0.0032
W30	0.0059	0.0029
W32	0.0034	0.0034
W34	0.0042	0.0017
W36	0.0012	0.0006

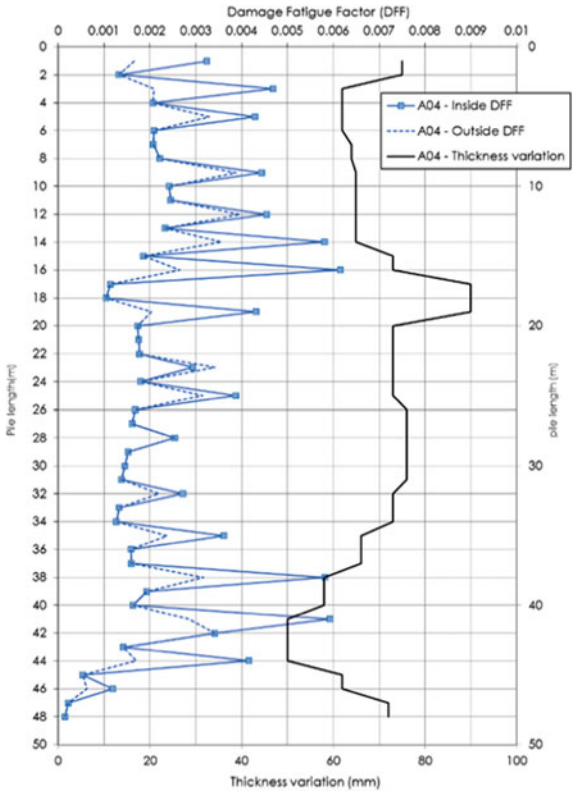

Fig. 6 Damage factors at any location along pile shaft

The most important task when recreating a representative numerical driveability model is to rebuild the ground model which requires several signal matching studies (i.e., CAPWAP analysis). The signal matching analysis requires a deep knowledge of wave equation theory, and the quality of this study highly depends on the performance of the engineer who carries out the work. Therefore, the results of this study should be always revised by an experienced person. It is also recommended to compare the disclosed soil static resistance and shaft distribution percentage with the classic prediction method using available soil properties.

A case study has been also performed for a better understanding of the methodology. The back analysis of fatigue damage of a monopile disclose a maximum damage factor of 0.0059 obtained at weld W30 located at 40.4 m from the pile top. This value is relatively small because the stress range generated by the hammer during driving is not so important (less than 120 MPa) and the total blowcount number of this piling operation is also limited (less than 3200 blows).

References

DNV (2011) DNV-RP-C203 Fatigue design of offshore steel structures. Det Norske Veritas
PDI (Pile Dynamics, Inc.) (n.d.) CAPWAP for windows manual. 2006
Rausche F et al (2009) CAPWAP and refined wave equation analyses for driveability predictions and capacity assessment of offshore pile installations. In: Proceedings of the ASME 28th international conference on ocean, offshore and arctic engineering. Honolulu, Hawaii, USA: OMAE2009
Smith EAL (1960) Pile driving analysis by the wave equation. J Soil Mech Found Div ASCE 86
Ta AN, Martin H (2012) Pile acceptance criteria based on driving parameters using adjusted wave equation analysis. In: 10th international conference on stress wave theory and testing methods for deep foundations. Kanazawa, Japan

A Study on Lateral Resistance of Finned Piles in Sands

Pankaj Bariker, K. S. Rajesh, and K. V. S. B. Raju

1 Introduction

Generally jetties, transmission towers, bridges, heavily loaded buildings, and many offshore structures are supported by piles. These are subjected to larger lateral loads due to winds and water tides. For all these loads, the lateral resistance will be smaller for regular piles and thus needed improvement. This work has been motivated by economic concerns over the large diameter and length of traditional monopile foundations with the associated costs. Usually, offshore pile foundations transmit larger vertical loads through weaker subsoil, and they are also subjected to very significant lateral loads from wind, wave, current, and tide. Lateral loads acting on the pile can exceed one-third of the gravity load. The increase in EI due to the fins at pile head can increase the lateral capacity, thus reducing the pile diameter and length.

There have been model tests on single piles, to investigate the lateral capacity (Broms 1964a, b; Reese et al. 1974; Prasad and Chari 1999) effect of rigidity, and modern pile foundations are tapered piles and finned piles (EI Naggar and Wei 1999), (Peng, 2006). Many researchers dealt with the single pile under lateral loads and recommended many facts in improving the lateral pile capacity. (Peng 2006) stated that the lateral resistance of the model piles increased significantly by introducing the fins. Many researchers dealt with the lateral capacity of single-individual pile (Peng 2006; Peng et al. 2010; Rollins et al. 2005; Babu and Viswanadham 2018; Nassar 2014) and acknowledged the use of finite element methods, such as PLAXIS, LPILE, and ABAQUS in the study of laterally loaded piles.

Peng et al. (2010) presented the 3-D analysis of laterally loaded finned piles. The improvement in the lateral resistance of piles on placing fins on pile is illustrated by plotting the lateral resistance versus pile head deformation.

P. Bariker (✉) · K. S. Rajesh · K. V. S. B. Raju
Civil Engineering Department, University Visvesvaraya College of Engineering (U.V.C.E), Bangalore University, Bengaluru 560056, India
e-mail: pankajbariker@gmail.com

S. Haldar et al. (eds.), *Advances in Offshore Geotechnics*, Lecture Notes in Civil Engineering 92, https://doi.org/10.1007/978-981-15-6832-9_18

Duhrkop et al. (2010) acknowledged the concept of increase in the lateral stiffness and capacity by the attachment of wings to the pile head. The stiffness of the fins or wings should be higher in loose sand than the dense sand and also recommended the procedure to account for the wings in common design methods and guidance on location of the wings or fins.

Bienen et al. (2012) presented results from a series of model test, in which the performance of a winged pile was evaluated and compared with that of regular monopiles. And pile head deformation decreases with introduction of fins on pile head.

Babu and Viswanadham (2018) conducted the finite element analysis using Abaqus and studied the improvement in lateral resistance of finned files for varying fin position, fin orientations, fin numbers and acknowledged the large improvement for fin with pile head position and diagonal orientation.

In the present study, the load capacities of finned piles that are embedded in sand were studied in comparison to piles without fins. The study is extended to study the behavior by varying the pile length, shape of fins, position of fin, number of fin wings, dimensions of fins, and type of pile that are embedded in sand of varying relative densities.

2 Experimental Investigation

2.1 Model Tank and Loading Frame

A series of model tests was conducted in a test tank made of mild steel with inside dimensions of 1200 mm long × 750 mm wide × 1500 mm height. These tank dimensions were chosen to ensure that the failure wedge around the models did not extend till walls.

Balachandran (1996) stated that the peak friction angle between sand and painted wall surfaces of model box decreases by 65% compared to that of unpainted wall surfaces. Hence, the smoothly polished model tank was used to minimize the possible friction between the wall sides and the sand. The raining device consisting of steel mesh attached to the model box was employed to attain the desired density. A schematic elevation of the test setup is as shown in Fig. 1.

Lateral loads were applied to the model scaled down piles in increments by using smaller diameter high-tension steel wire attached to the pile head. The other side of the wire ran over a smooth adjustable pulley and attaching the hand-winch passing through the proving ring. To record the pile head deflection, the sensitive dial gauge with the measurement of at least 0.01 mm is used.

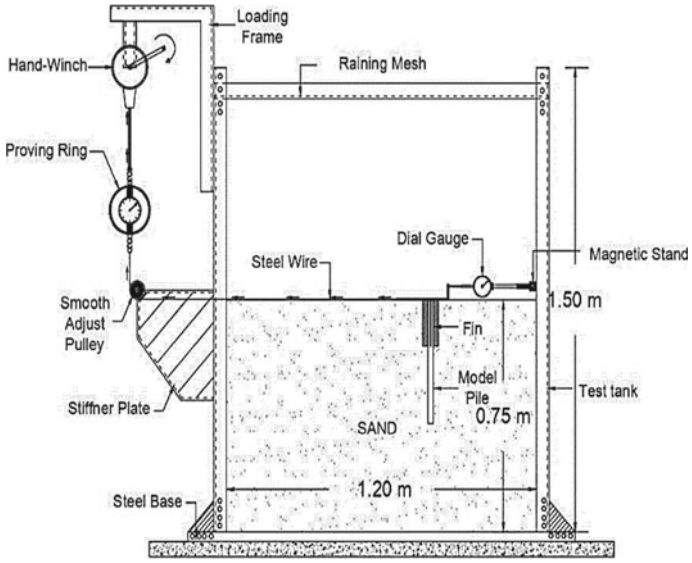

Fig. 1 Elevation of model tank and test setup

2.2 *Soil Preparation and Characterization*

The experimental model tests are carried out on dry, commercially available Bangalore sand, and the grain size distribution is as illustrated in Fig. 2. It can be noticed that the material hardly comprises of any fraction of silt. The specific gravity (G) of the sand particles was found to be 2.61. The maximum and minimum unit weights of this sand were found to be 16.019 kN/m^3 and 15.60 kN/m^3, respectively, and were classified as poorly graded.

The sand was placed to achieve two relative densities, a loose state ($D_r = 35\%$) and dense state ($D_r = 68\%$) and experiments were conducted at two unit weights:

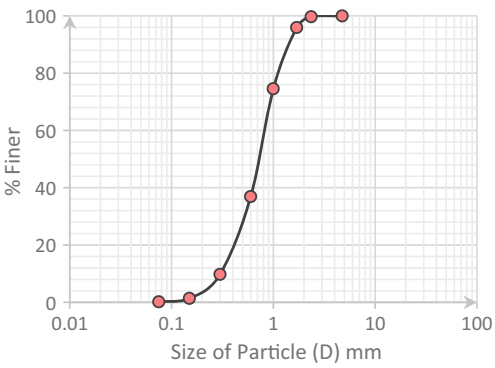

Fig. 2 Grain size distribution curve of sand

Table 1 Physical properties of sand used in tests

Property	Value
Effective grain size, D_{10} (mm)	0.3
Average grain size, D_{50} (mm)	0.7
Uniformity coefficient, C_u	2.67
Coefficient of curvature, C_c	1.5
Maximum dry unit weight, Y_{max} (kN/m^3)	16.019
Minimum dry unit weight, Y_{min} (kN/m^3)	15.600
Maximum void ratio, e_{max}	0.641
Minimum void ratio, e_{min}	0.598
Specific gravity, G	2.61
Classification (IS 1498–1970)	SP
Water content, WC (%)	0.0

15.74 and 15.89 kN/m^3 for loose and dense conditions, respectively. The direct shear tests were performed to evaluate the friction angles (ϕ) and are 34° and 40° for the loose and dense states, respectively. Other physical properties of the sand are as listed in Table 1.

The density of the sand is achieved by rainfall technique. Turner and Kulhawy (1987) stated that the unit weight of the sand deposit using the rainfall technique depends primarily on the drop height of the sand. Therefore, to simulate loose and dense conditions, the sand was allowed to freely fall at heights of approximately 100 and 400 mm, respectively.

2.3 Model Piles, Pile Cap, and Fins

In this study, the model piles were made of smooth aluminum pipe. The outer diameter and wall thickness of the piles were 21 mm and 2 mm, respectively, that were used for all the tests. Embedment lengths (L_p) of the piles were 600 mm, 380 mm, and 290 mm. The length to diameter ratios of the piles were 28.6, 18, and 13.8 corresponding to long, intermediate, and short pile, respectively.

As shown in Fig. 3, two different shapes of fins were used in the experiments. Triangular and rectangular fins with different sizes were made of 2.0 mm thick steel sheets. For all pile sections, fins were welded at 90° to the lateral loading direction and were located on pile head.

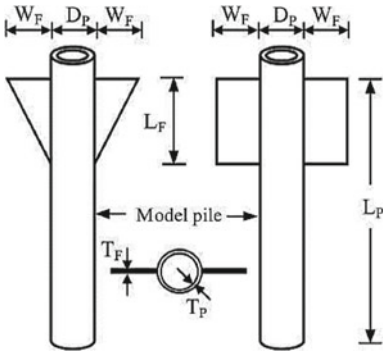

Fig. 3 Schematic dimensions of triangular and rectangular finned piles

3 Experimental Setup

At the beginning of testing, the raining device box was positioned directly above the model tank and was followed by deposition of the sand by the raining technique. Leveling of the sand surface was then completed with a straight edge. On reaching the level of the pile base, the pile was placed in position and was held vertical using a special clamp and the next layer of sand was deposited up to the desired height. This method represents no displacement in the soil around the pile during installation to maintain the sand relative density at desired values during the experimental tests.

Finally, dial gauges were placed on the pile cap/head and corrected at zero lateral displacement. Then, the incremental lateral load was applied until failure. The lateral load was applied to the pile cap with a flexible wire attached to the pile cap. The other end was attached to the loading handle of the hand-winch apparatus. A lateral load was applied approximately at the soil surface. For each load increment, the lateral deformation of the dial gauge was recorded and was taken for plotting the load-deformation graphs.

4 Test Program

The testing program presented in this paper is a parametric study that investigated different variables. To study the effect of fins on the lateral behavior of piles, regular piles (without fins) were also tested under lateral load as a reference. The total of 102 tests was conducted to study the behavior of finned piles under lateral loads at different relative densities.

Initially, the behavior of model piles, i.e., long flexible pile ($L_p/D_p = 28.6$), intermediate pile ($L_p/D_p = 18$), and short rigid pile ($L_p/D_p = 13.8$) without fins at two relative densities was determined (series I). In series II, an investigation on the effect of fin position was conducted at three positions along the length of pile, i.e., pile head, mid-length, and pile tip for all the three types of piles (long, intermediate, and short

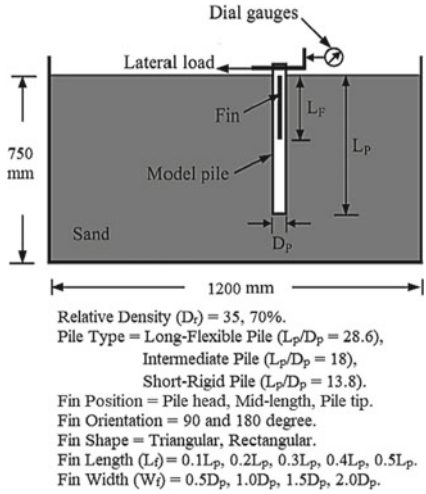

Fig. 4 Variable parameters used in the experimental study

piles). In series III, the finned piles were tested at two relative densities to study the influence of fin orientation, i.e., two-finned and four-finned piles with orientation of 180° and 90°, respectively. In series IV, an investigation on effect of fin shape on the lateral behavior of finned piles was conducted for two shapes of fins, i.e., triangular and rectangular fins. In series V, the finned piles were tested to study the influence of length of fins (L_f) on the behavior of finned piles under lateral loads. Series VI, involved study of the effect of the fin width on the lateral capacity of rectangular finned piles. All parameters and their notations are shown in Fig. 4.

5 Interpretation and Discussion of Results

Pile head lateral load and lateral deformation (P–Y) curves from the results of the experimental model pile tests are shown in Fig. 5. From the above-mentioned curves, the pile head lateral displacement (y) is expressed in mm. In the discussion of the effect of the different parameters, the ultimate lateral load (H_u) for different cases has been estimated from (P–Y) curves. In the present study and according to (Peng et al. 2010), the lateral load corresponding to the lateral displacement equal to 10% of the pile diameter at the pile head was defined as the ultimate lateral load capacity, H_u.

The increase in pile resistance due to fins is represented using a non-dimensional factor "fin efficiency factor." This factor is expressed as a ratio of the ultimate lateral load of a finned pile to ultimate lateral load of a regular pile without fins.

$$\text{Fin Efficency} = \frac{H_{u(\text{finned pile})}}{H_{u(\text{regular pile})}} \tag{1}$$

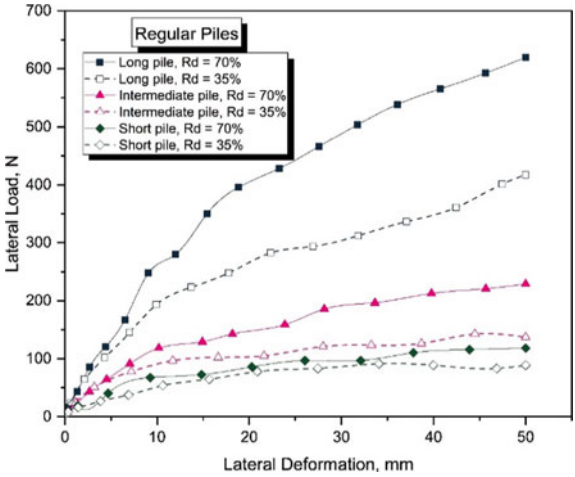

Fig. 5 Behavior of regular piles under lateral loads

5.1 Behavior of Regular Pile Subjected to Lateral Load

Initially, investigations on the behavior of regular piles are done for long flexible, intermediate, and short rigid pile with L/D ratios of 28.6, 18.0, and 13.6, respectively, subjected to lateral loads. Thereafter, these provide the necessary reference data for the purpose of comparisons.

Figure 5 shows the results of model tests for regular piles embedded in loose and dense sand, from which it can be observed that the piles resist maximum lateral load when embedded in dense sand than loose sand. Figure 6 shows the ultimate lateral loads.

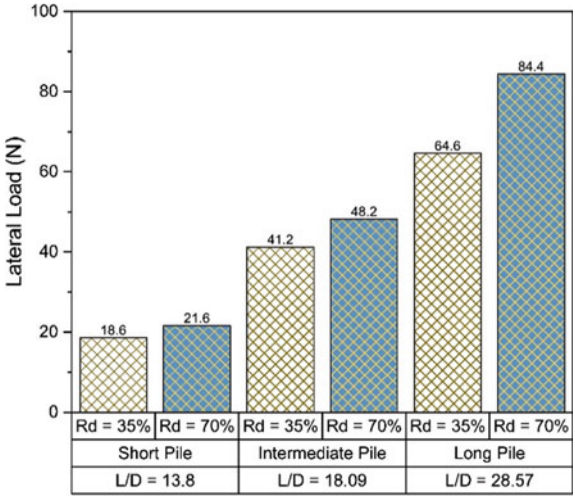

Fig. 6 Ultimate lateral resistance for regular piles

On embedding the piles in dense soils ($R_d = 70\%$), the ultimate lateral resistance for long, intermediate, and short pile increases by 30%, 17%, and 16%, respectively. Due to the increase in relative density of the sand, the sliding friction of the sand increases along with the interlocking of the particles which develop larger resistance for pile deformation. Hence, the piles sustain larger lateral loads when embedded in dense sand than in loose sand. The same reason is valid for all the remaining tests conducted for varying fin parameters.

5.2 *Effect of Fin Position on Lateral Resistance of Finned Pile*

To investigate the effect of fin position on the lateral resistance of the finned pile, the model tests are conducted on the piles with fin parameters of $L_f/L_p = 0.4$ and $W_f/D_p = 1.0$ for the three fin positions along the length of the pile, i.e., pile head, mid-length, and pile tip (top, middle, bottom), respectively, to each of the pile at their respective relative densities.

Figure 7 shows the behavior of long pile to different fin positions from which it is revealed that, the pile head (top) position of the fin will have larger lateral resistance than the other two positions, for both the relative densities. Figure 8 shows the fin efficiencies for the long pile with different fin positions. The trend and behavior were also found to be same for intermediate and short piles.

It is found that the ultimate lateral resistance of the pile is maximum for top fin position than the other two positions. Since the lateral loads on pile acts at its pile tip, any increase in the stiffness of the pile at the point of application of the lateral load will lead to the increase in its ultimate lateral resistance. The same reason is valid for all the remaining tests conducted for varying fin parameters (Figs. 9 and10).

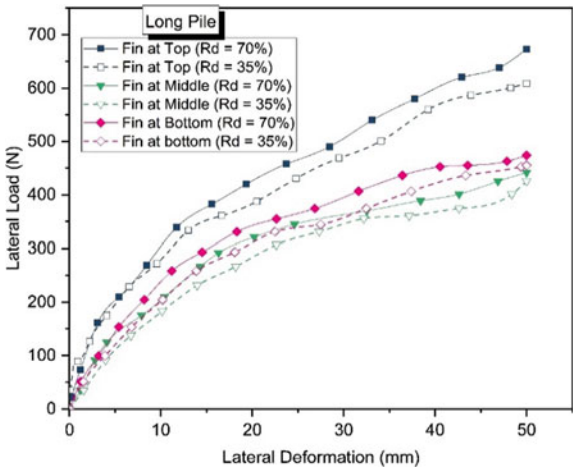

Fig. 7 Behavior of long pile with different fin positions under lateral loads

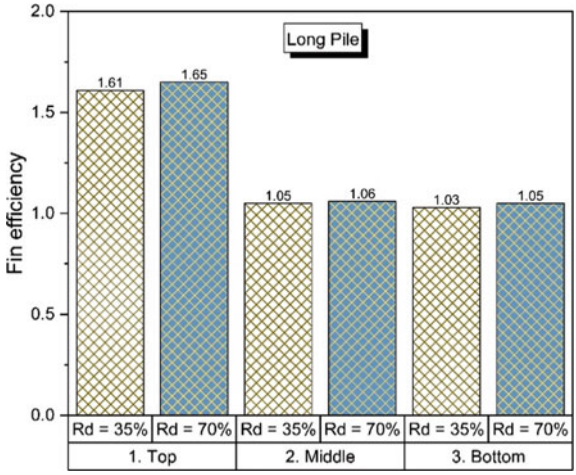

Fig. 8 Fin efficiencies of long pile with different fin positions

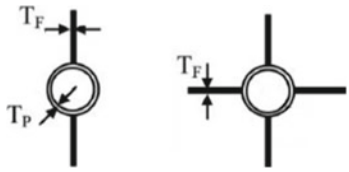

Fig. 9 Schematic representation of two-finned and four-finned arrangement

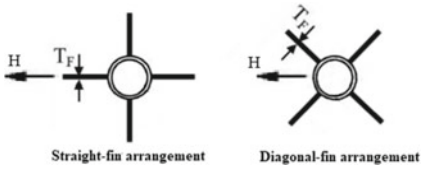

Fig. 10 Schematic representation of different four-finned arrangement

5.3 Effect of Fin Numbers on the Lateral Resistance of Finned Piles

To investigate the effect of fin numbers on the lateral resistance of the finned pile, the model tests are conducted on the piles with fin parameters of $L_f/L_p = 0.4$ and $W_f/D_p = 1.0$ and for top fin location, i.e., at pile head for the two fin numbers, i.e., orientations of fin forming plates at 90° and 180° which will form the four-finned and two-finned arrangement, respectively (Fig. 9), to each of the pile at their respective relative densities.

The behavior of long pile with two fin orientations, i.e., two-finned and four-finned oriented piles is as represented in Fig. 11. The fin efficiencies of long pile corresponding to two fin orientations are as shown in Fig. 12. Similar trend was observed for remaining two pile lengths.

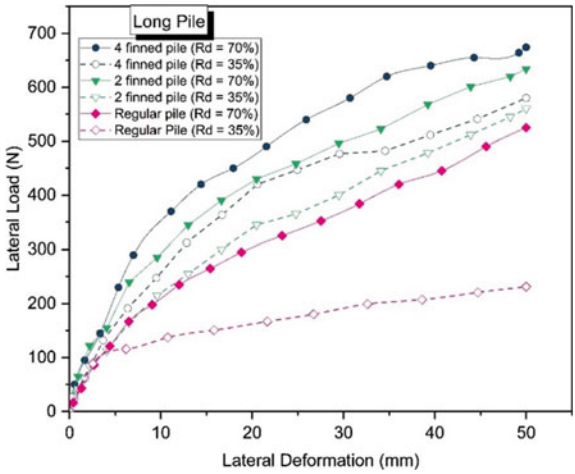

Fig. 11 Behavior of long pile for varying fin numbers under lateral loads

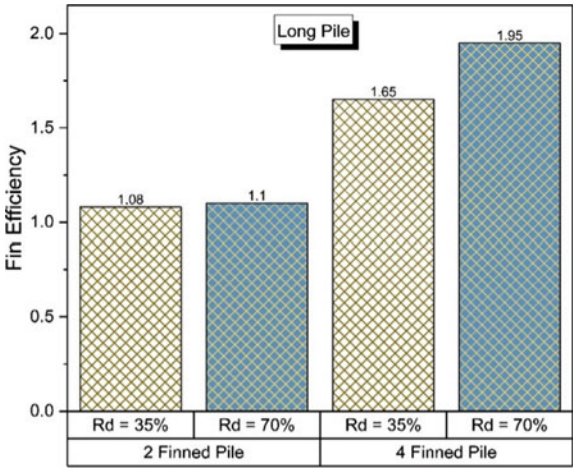

Fig. 12 Fin efficiencies of long pile with different fin numbers

Since the stiffness increases with the introduction of fins at the top position of the pile, the contribution of stiffness is maximum for four-finned pile, than two-finned pile which lead to the increase in the ultimate lateral resistance of the pile. The improvement in ultimate lateral resistance is also due to the fin orientation when dealing with four-finned feature. In present work, diagonal finned feature is used rather than straight finned and star finned feature (Fig. 10), which will activate more volume of the sand surrounding the pile, leading to increase in the lateral resistance of the pile. Hence, in all the remaining tests, the piles will be tested for four-finned (90° orientation) with diagonal finned feature.

5.4 *Effect of Fin Shape on Lateral Resistance of Finned Piles*

To investigate the effect of fin shape on the lateral resistance of the finned piles, the piles are tested for two fin shapes, namely triangular and rectangular fins. With top fin position, $L_f/L_p = 0.4$, $W_f/D_p = 1.0$, and four-finned diagonal feature (90° orientation) at the respective relative densities.

The behavior of long pile with two fin shapes, i.e., triangular and rectangular fins is as represented in Fig. 13. The fin efficiencies of each of the long pile corresponding to two fin shapes are as shown in Fig. 14. Similar behavior was observed for remaining two pile lengths.

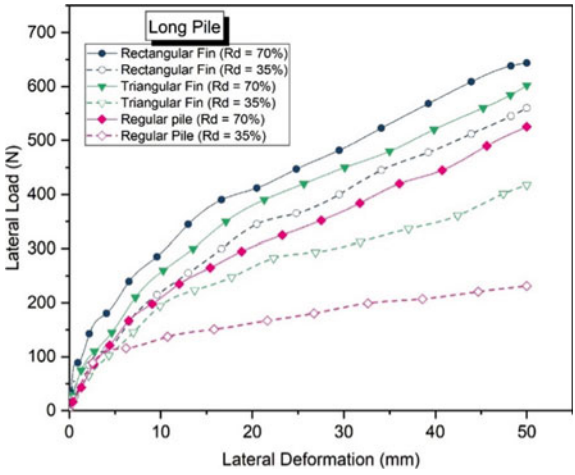

Fig. 13 Behavior of long pile for varying fin shapes under lateral loads

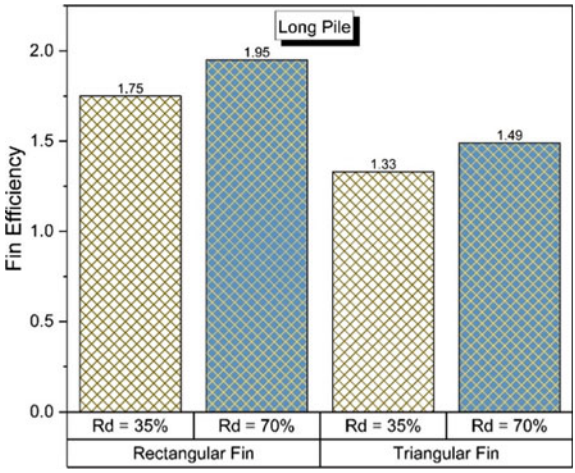

Fig. 14 Fin efficiencies of long pile with different fin shapes

Since the stiffness increases with the introduction of fins at the top position of the pile, the contribution of stiffness is maximum for rectangular-shaped fin than triangular-shaped fin. Because, the resisting surface area of the fin is maximum for rectangular-shaped fins than the triangular-shaped fins by almost two times, which lead to increase in the ultimate lateral resistance of the pile. Hence, rectangular-shaped fins are employed for all the remaining study for the purpose of increasing the lateral resistance of piles.

5.5 *Effect of Fin Length on Lateral Resistance of Finned Piles*

The upper part of the soil around the pile is the most critical part in the case of laterally loaded pile because of the greater deflection than that of lower part. Therefore, to investigate the effect of fin length on the behavior of laterally loaded finned piles, a series of experimental model tests are performed for 90° orientation, i.e., four-finned rectangular-shaped fin with top (pile head) position for various fin length to pile length ratios (L_f/L_p) of 0.1, 0.2, 0.3, 0.4, and 0.5 by keeping the fin width (W_f/D_p) of 1.0, for respective relative densities.

The ultimate lateral resistance of piles for varying fin lengths is as represented in Figs. 15, 16 and 17 for long, intermediate, and short piles, respectively.

For all piles, tested at varying fin lengths (L_f/L_p). The ultimate lateral resistance of the pile increases with increase in L_f/L_p, but it can be observed from above figures that until L_f/L_p value of 0.4, increase in ultimate lateral resistance of the pile was substantial. But, for $L_f/L_p > 0.4$, the increase in the ultimate lateral resistance was diminished, as reflected by the lateral bending of the fin wings which may affect the serviceability of the large-scale pile at field conditions.

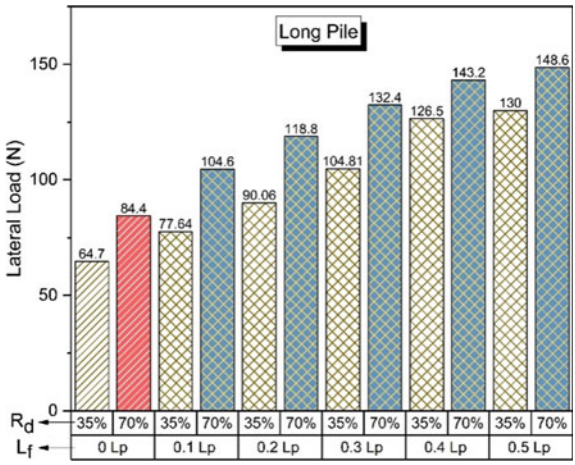

Fig. 15 Ultimate lateral resistance of long pile for varying fin lengths

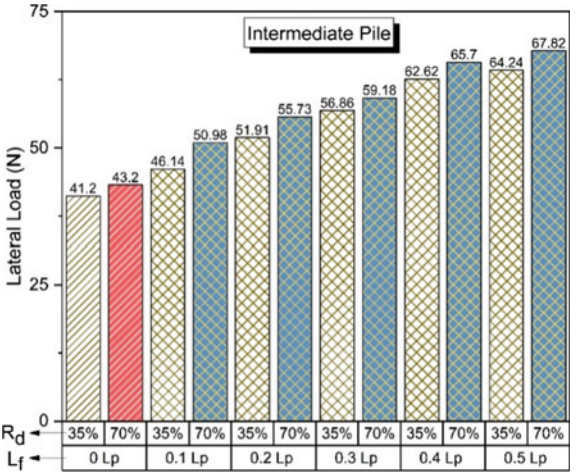

Fig. 16 Ultimate lateral resistance of intermediate pile for varying fin lengths

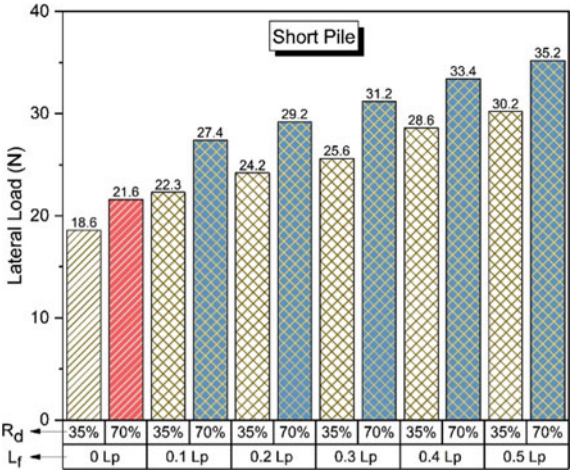

Fig. 17 Ultimate lateral resistance of short pile for varying fin lengths

Hence, $L_f/L_p = 0.4$ is considered as the optimum fin length at which both strength and serviceability satisfy resulting to the ultimate lateral resistance. The same optimum L_f/L_p will be used for the remaining model tests.

The increase in the lateral resistance of the finned piles for varying L_f/L_p values are compared to that of the optimum L_f/L_p value of 0.4 to each of the case at respective relative densities with the help of fin efficiency as shown in Fig. 18.

From Fig. 18, it can be observed that with increase in the L_f/L_p values, the ultimate lateral resistance of the finned piles increases due to the increase in stiffness of the pile system at the pile head at which the lateral loads are acting.

For short piles, on providing the piles with optimum L_f/L_p, the ultimate lateral resistance of the piles increases by 53% and 55% when embedded in loose and dense

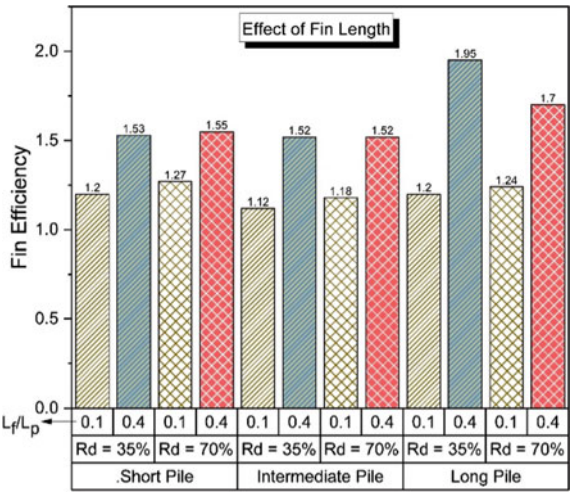

Fig. 18 Fin efficiencies of piles at varying fin length relative to pile length values

sand, respectively. For intermediate piles, it increases by 52% and 52%. For long piles, it increases by 95% and 70%, respectively.

The increase in the fin efficiency, i.e., the ultimate lateral resistance of the pile is maximum for long piles when provided with optimum L_f/L_p than that of the short piles. It is because the flexible behavior of the long piles will sustain some load in addition with the fin effect but the rigid behavior of the short pile does not do so leading to the minimum increase in the ultimate lateral resistance than long piles.

5.6 Effect of Fin Width on Lateral Resistance of Finned Piles

The upper part of the soil around the pile is most critical part in the case of a laterally loaded piles. Hence, an attempt is made to decrease the pile head deflection, i.e., increase the lateral resistance of the pile by varying the values of fin width relative to pile diameter (W_f/D_p).

To investigate the effect of W_f/D_p on lateral resistance of the piles subjected to lateral loads a series of model tests are performed for 90° orientation, i.e., four-finned rectangular-shaped fin with top (pile head) position, with optimum L_f/L_p, for various W_f/D_p of 0.5, 1.0, 1.5, and 2.0, at their respective relative densities.

Increase in the fin width will provide a considerably higher soil resistance and a stiffer behavior due to an increase of the passive area of earth pressure in front of the pile compared with regular piles (reference piles). This leads to an increase in the ultimate lateral load for finned piles, which increases the fin efficiency. Furthermore, by increasing the fin width, the effect of the fins can be observed directly at the ground surface. While the soil flowed around the regular pile, further increase in the width of the fins in excess of D_p will improve the fin efficiency with a reduced rate. The

ultimate lateral resistance of piles for varying W_f/D_p is as represented in Figs. 19, 20 and 21 for long, intermediate, and short piles, respectively.

According to Stewart, the necessary range around the pile to resist lateral loads can be set as a three-dimensional inverted cone shape centered on the pile and formed near the soil surface. The lateral resistance of the pile depends significantly on the deformation of soil within the inverted cone shape. In the case of $W_f/D_p < 1.0$, the fin width was located within the range of the inverted cone shape (soil resistance zone). On the contrary, by increasing the fin width $W_f/D_p < 1.0$, the fin width was located out of the zone of soil resistance. Hence, the fin efficiency increased by a small rate.

For practical reasons, the fin width equal to pile diameter ($W_f/D_p = 1.0$) can be considered the best fin width, i.e., optimum for several reasons, such as when the fin

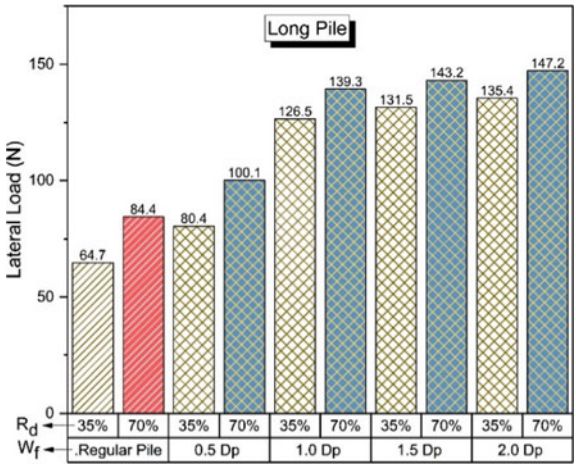

Fig. 19 Ultimate lateral resistance of long pile for varying fin widths

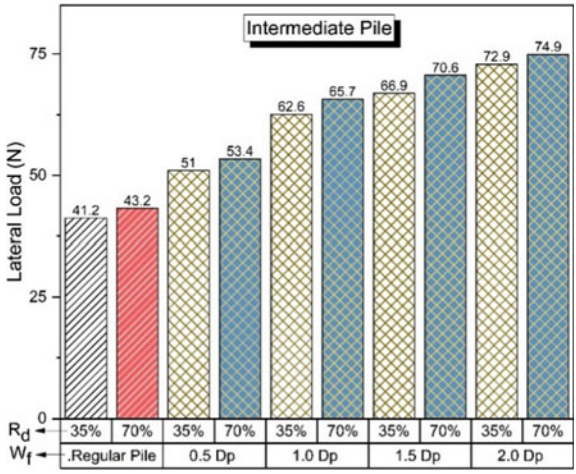

Fig. 20 Ultimate lateral resistance of intermediate pile for varying fin widths

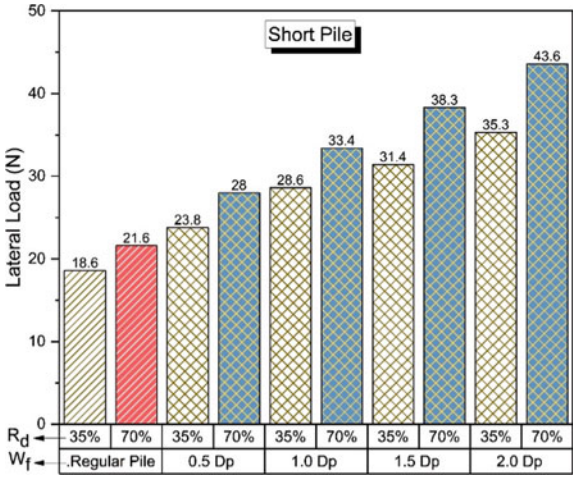

Fig. 21 Ultimate lateral resistance of short pile for varying fin widths

width increases, it becomes less rigid. Thus, for larger fins, the fin's thickness has to be increased to provide the required stiffness. Consequently, it will cost more and perhaps reduces the benefit of using such fins. On the other hand, increasing the size without maintaining the stiffness within reasonable limits causes larger deformation of the fins, which reduces the advantages of their behavior. In this study, for aluminum fins and at $W_f/D_p \leq 1.0$, it is recommended that the fin's thickness be larger or equal to the wall thickness of the steel pile to insure attainment of a sufficient level of rigidity to allow mobilization of the soil's passive resistance.

The increase in the lateral resistance of the finned piles for varying W_f/D_p values are compared to that of the optimum W_f/D_p value of 1.0 to each of the case at respective relative densities with the help of fin efficiency as shown in Fig. 22.

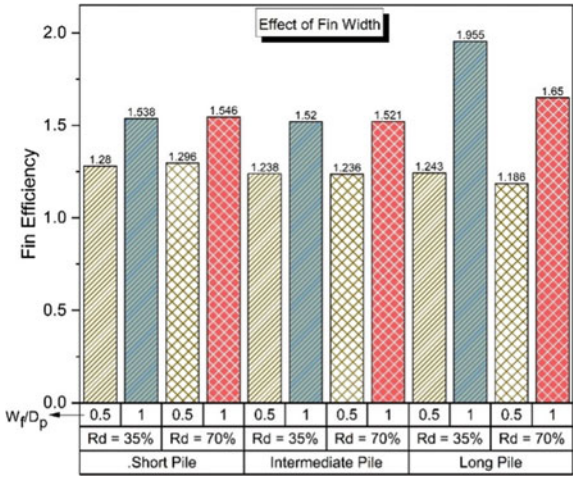

Fig. 22 Fin efficiencies of piles at varying fin width relative to pile diameter values

From Fig. 22 it can be observed that with increase in the W_f/D_p values the ultimate lateral resistance of the finned piles increases due to the increase in stiffness of the pile system at the pile head at the zone in which the lateral loads are acting.

For short piles, on providing the piles with optimum W_f/D_p, the ultimate lateral resistance of the piles increase by 53% and 54% when embedded in loose and dense sand, respectively. For intermediate piles, it increases by 52% and 52%. For long piles, it increases by 95% and 65%, respectively.

6 Conclusion

The behavior of finned piles subjected to a lateral load in sand deposits of different densities was investigated through model test studies. Based on the investigations, the following main conclusions can be drawn:

1. Finned piles provide considerably higher ultimate lateral loads and lateral resistance behavior compared with a regular reference pile.
2. Fins help to increase the lateral load-carrying capacity of piles significantly, compared to regular piles. Increase in lateral load depends on fin orientation, fin position, and sand relative density. This will in turn help to reduce overall pile length and diameter.
3. Fins placed near the pile head provide more resistance than those placed near the pile bottom. Long piles with fins placed at top, in loose and dense sand carries 61% and 65%, respectively. Intermediate piles carry 29% and 45%, whereas short piles carry 47% and 55% more compared to regular pile.
4. Four-finned piles provide more lateral resistance when compared to two-finned piles. On embedding long piles in loose and dense sands carry 65% and 95% more load than regular piles, respectively, when provided with four-finned arrangement, whereas piles carry 8% and 10% more load than regular piles for two-finned arrangement.
5. When a pile is finned with triangular and rectangular fins, the ultimate lateral load of the pile increases by about 33% and 75%, respectively, than that of a regular pile, when embedded in loose sands, and lateral load increases by 49% and 95% when embedded in dense sands. At the same time, the lateral head deflection decreases significantly. Hence, using rectangular fins is more effective in improving the lateral behavior of piles.
6. Ultimate lateral load improvement depends greatly on length of the fins and increases significantly to the value of $L_f/L_p = 0.4$. Any further increase in the fin length does not show any noteworthy contribution to the pile capacity.
7. Lateral head deflection decreases with the increase in length of the fins. At $L_f/L_p = 0.4$ and 0.5, the lateral head deflection decreased by about 70% and 74%, respectively, than that of a regular pile ($L_f/L_p = 0.0$). For practical purposes, the maximum benefit of reduction in the lateral head deflection is obtained when $L_f/L_p = 0.4$.

8. For both short and long piles, the fin efficiency increases with the increase in fin width. When fin width equals the pile diameter ($W_f/D_p = 1.0$), the fin efficiency increased by about 54% and 95% for short and long piles, respectively. Therefore, to maintain the rigidity and stiffness of the fins within reasonable limits, a fin width equal to the pile diameter can be considered as the best fin width.
9. With the application of fins, the length of a finned pile can be reduced relative to a regular pile and still manage to gain lateral resistance.
10. It can be concluded that the present study can be useful in foundations for offshore structures where large lateral loads are expected, and in such offshore environments, the length of prototype piles can be significantly reduced by employing fins to pile which leads to overall economy.

References

Babu K, Viswanadham B (2018) Numerical investigations on lateral load response of fin piles. In: Numerical analysis of nonlinear coupled problems, sustainable civil infrastructures, pp 317–329

Balachandran S (1996) Modeling of geosynthetic reinforced soil walls. University of Cambridge, Cambridge

Bienen B, Dührkop J, Grabe J, Randolph MF, White DJ (2012) Response of piles with wings to monotonic and cyclic lateral loading in sand. J Geotech Geoenviron Eng 138(3):364–375

Broms B (1964a) Lateral resistance of piles in cohesionless soils. J Soil Mech Found Div 90(3):123–158

Broms B (1964b) Lateral resistance of piles in cohesive soils. J Soil Mech Found Div 90(2):27–64

Duhrkop J, Grabe J, White D (2010) Centrifuge experiments on laterally loaded piles with wings. In: Springman SL (ed) Proceedings of the 7th international conference on physical modeling in geotechnics (ICPMG), vol 2, 919–924

EI Naggar M, Wei J (1999) Response of tapered piles subjected to lateral loading. Can Geotech J 36(1):52–57

Nassar A (2014) Experimental and theoretical studies of laterally loaded finned piles in sand. Can Geotech J 51:381–393

Peng J (2006) Behavior of finned piles in sand under lateral loading. University of Newcastle Upon Tyne, School of Civil Engineering and Geosciences. University of Newcastle upon Tyne, Tyne

Peng JR, Rouainia M, Clarke BG (2010) Finite element analysis of laterally loaded fin piles. Comput Struct 88(21–22):1239–1247

Prasad Y, Chari T (1999) Lateral capacity of model rigid piles in cohesionless soils. In: Proceedings of geotechnical society. Soils and Foundations, Canada, pp 21–29

Reese LC, Cox WR, Koop FD (1974) Analysis of laterally loaded piles in sand. In: 6th annual offshore technology conference. Tex. Offshore Technology Conference, Houston, vol 2, pp 95–105

Rollins KM, Gerber TM, Lane JD, Ashford SA (2005) Lateral resistance of a full-scale pile group in liquefied sand. J Geotech Geoenviron Eng 131(1):115–25. ISSN: 1090-0241/2005/1-115–125/

Turner J, Kulhawy F (1987) Experimental analysis of drilled foundations subjected to repeated axial loads under undrained conditions. Palo Alto, California

Uplift Capacity Determination for an Under-Reamed Pile in Non-homogeneous Clay

Ajay Kumar, Vishwas N. Khatri, and S. K. Gupta

1 Introduction

The piles either with or without under-ream were have been successfully used in the past for various onshore and offshore structures. However, the provision of one or more bulbs along the length of the pile can generate a greater bearing and uplift resistance. Till date, limited research studies are available to evaluate the capacity of the under-reamed piles in clay, especially for the uplift condition (Martin and DeStephen 1983; Annie Peter et al. 2006; Shrivastava and Bhatia 2008; George and Hari 2016; Vali et al. 2017). The research carried out by Martin and DeStephen (1983) suggested the use of a double under-reamed pile with a spacing of 1.5–2 times the bulb diameter between them as a suitable foundation option in overconsolidated stiff clay. On the basis of extensive tests, a safe compression and uplift capacity is reported by Central Building Research Institute (C.B.R.I. 1978), Roorkee. Their observations for the design and construction of under-reamed piles in clay and sand were integrated into IS 2911 Part-III (1980). Recently, George and Hari (2016) conducted a finite element analysis of the under-reamed piles in the homogeneous clay and reported an enhancement in uplift capacity for the single under-reamed pile and double under-reamed pile up to 119% and 204%, respectively. It is worth noting here that the above studies only dealt with estimating the potential of the under-reamed pile in the

A. Kumar (✉) · V. N. Khatri
Department of Civil Engineering, Indian Institute of Technology (Indian School of Mines), Dhanbad, Jharkhand, India
e-mail: aj.2013DR1091@cve.iitism.ac.in

V. N. Khatri
e-mail: vishwas@iitism.ac.in

S. K. Gupta
Department of Environmental and Sciences Engineering, Indian Institute of Technology (Indian School of Mines), Dhanbad, Jharkhand, India
e-mail: sunil@iitism.ac.in

S. Haldar et al. (eds.), *Advances in Offshore Geotechnics*, Lecture Notes in Civil Engineering 92, https://doi.org/10.1007/978-981-15-6832-9_19

Table 1 Soil and pile properties used in the analysis

Name of element	Model	E (MPa)	Unit weight (kN/m^3)	Poisson's ratio
Soil	Tresca	30	16	–
Pile	Linear elastic	25,000	25	0.15

homogeneous clay. In the present study, the uplift capacity of the under-reamed pile in clay is investigated with the consideration of the increase of soil cohesion with depth (Bishop 1966; Khatri and Kumar 2009; Khatri et al. 2019) by conducting a numerical analysis using finite element methodology. The results obtained from this analysis were presented in a normalized form and compared with literature wherever applicable.

2 Problem Definition and Finite Element Model

A pile embedded in clay whose undrained cohesion (c) at any depth below ground surface (h) is expressed in terms of cohesion at the ground surface (c_o), a parameter m and pile stem diameter (D) as $c = c_o\,(1 + mh/D)$. In the present study, the pile stem diameter (D) was taken as 0.3 m, $c_o = 15$ kPa and $m = 0$–5. The length of the pile was taken as 4.5 m while the diameter of the bulb (D_u) was taken as 0.75 m (2.5D) in accordance with IS 2911 Part-III (1980). The numerical study in the present work is performed by using Optum G2 software. The selected soil and pile properties for the sake of analysis are shown in Table 1.

The generated mesh for the pile without bulb (P), pile with single bulb (PSUR) and pile with two bulbs (PDUR) were shown in Fig. 1a–c, respectively. A six nodded element was used to model the soil domain and pile both.

It is pertinent to mention that in the analysis the pile base was not allowed to sustain any tension, i.e., immediate breakaway condition (Khatri and Kumar 2011) was assumed valid. The magnitude of uplift load (Q) at failure was computed for various soil and pile properties.

3 Results and Discussion

The parametric evaluation was performed by varying m from 0 to 5 and taking the values of the adhesion coefficient along the shaft as (α_s) as 0.25, 0.5 and 1. The results of this analysis were presented below.

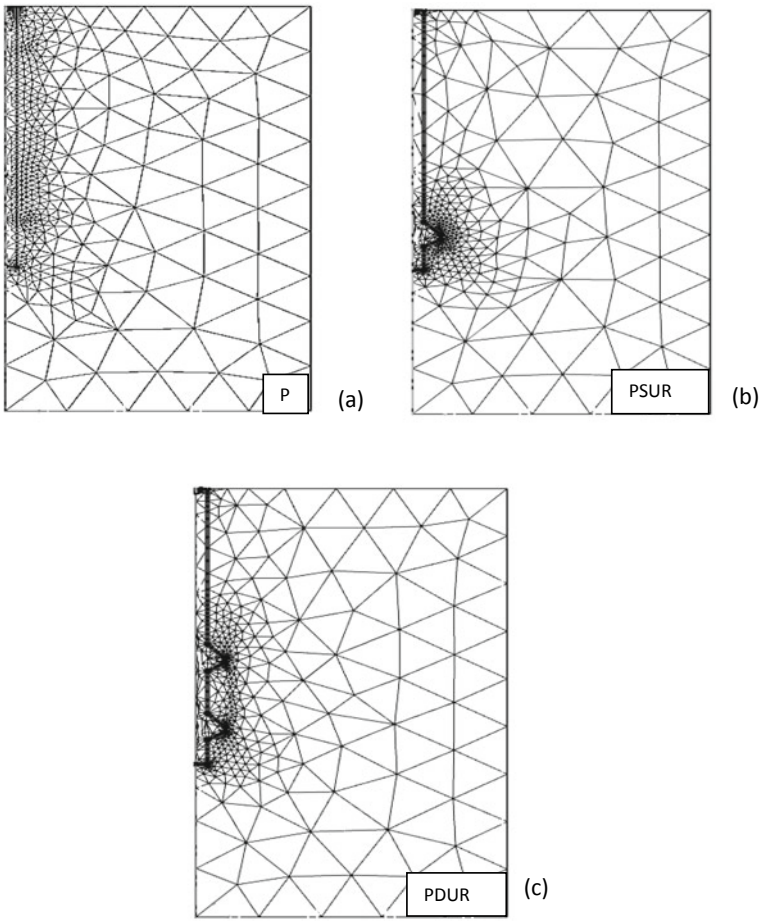

Fig. 1 Generated mesh for **a** P, **b** PSUR and **c** PDUR

3.1 Effect of m on Load-Deformation Behavior

The load-deformation curves developed from the analysis in various cases are shown in Fig. 2a–c. For the sake of general applicability, the load (Q) and the upward deformation (δ) were normalized with respect to $A_b c_b$ and D, respectively; wherein A_b and c_b bearing area and cohesion at pile base. In these figures, $m = 0$ implies piles in homogeneous clay, whereas other cases relate to piles in non-homogeneous clay. The study of Fig. 2a–c suggests that that the addition of the bulb or the under-ream to a pile improves its load-deformation behavior quite significantly. In all the cases, computed load was highest for double under-reamed pile followed by single under-reamed pile and pile without under-ream. Further, the observed deformation

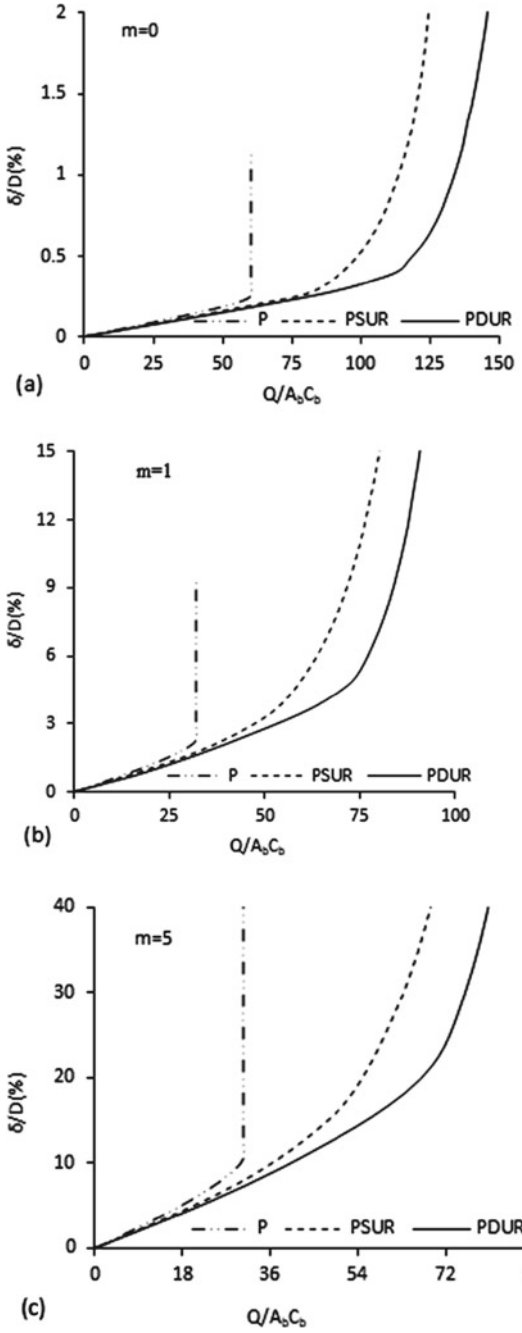

Fig. 2 Normalized load $Q/(A_b c_b)$-deformation (δ/D) variation for **a** $m = 0$, **b** $m = 1$ and **c** $m = 5$

was the smallest for the pile with two bulbs. With the use of load-deformation data, the safe load and that corresponding to a failure state were estimated.

3.2 Safe Capacity and Uplift Factor (F_{ct}) Variation with m

The safe uplift capacity was determined in the present study in compliance with IS 2911 Part-III (1980), i.e., 2/3 of the load corresponding to 12 mm deformation. On this basis, the variation of safe load expressed in the normalized form as $Q_{\text{safe}}/(A_b c_b)$ with m is shown in Fig. 3. From this figure, it can be noticed that with the increase in the value of m though the magnitude of safe load increases, on account of an increase in the cohesion at the base of the pile (c_b), the normalized safe load will keep on decreasing.

Further from the evaluated collapse load (Q_u), the uplift factor F_{ct} was defined as $F_{ct} = Q_u/(A_b c_b)$. The variation of F_{ct} in different cases is presented in Fig. 4a–c. In Fig. 4a, comparison of present F_{ct} with Khatri and Kumar (2011) is also presented for pile P. Note that Khatri and Kumar (2011) reported F_{ct} values for fully bonded condition. However, by subtracting the contribution of base resistance from the total capacity, the F_{ct} values for the present case of the pile under immediate breakaway condition have arrived. A study of Fig. 4a suggests that the present value of F_{ct} matches well with that reported by Khatri and Kumar (2011). A further study of Fig. 4a–c indicates that the presence of bulb or under-reamed section leads to a nonlinear variation of F_{ct} and also the F_{ct} value becomes constant beyond $m > 1$. As anticipated, the computed F_{ct} was highest for a pile with two bulbs followed by a pile with a single bulb and pile without bulb.

3.3 Effect of Bulb Addition on the Uplift Capacity of the Pile

To evaluate the effect of the addition of under-reamed section (bulb) to the pile P in a quantitative manner a percentage increase in uplift capacity of under-reamed pile was defined as

$$\text{Percentage increase in capacity} = \frac{Q_{\text{uPSUR/PDUR}} - Q_{\text{Up}}}{Q_{\text{Up}}} \times 100$$

where Q_{u_P}, $Q_{u_{PSUR}}$ and $Q_{u_{PDUR}}$ were the ultimate capacity of pile P, PSUR and PDUR, respectively. To evaluate the percentage increase in safe capacity, all the ultimate capacity was replaced by the safe capacity of P, PSUR and PDUR in the above equation. The variation of percentage increase in safe and ultimate capacity for different values of m is shown in Figs. 5 and 6.

From these figures, one can notice that for pile in homogeneous soil ($m = 0$), the addition of bulbs leads to the same enhancement in the safe and ultimate uplift

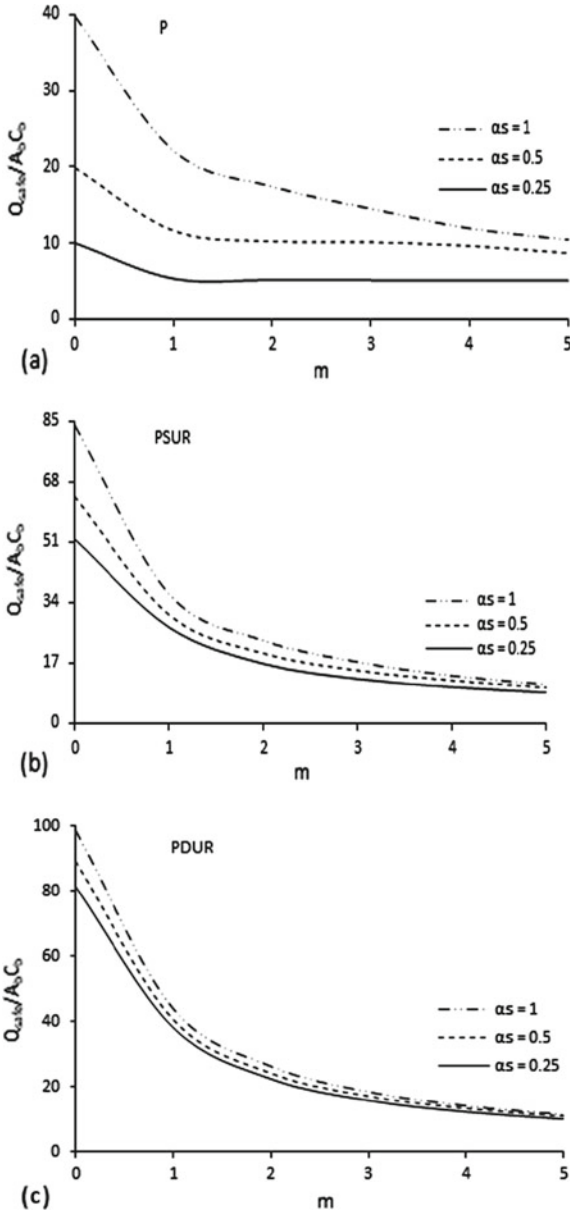

Fig. 3 Variation of normalized safe load with m for **a** P, **b** PSUR and **c** PDUR

capacity by 111.44% and 147.33% for PSUR and PDUR, respectively. It is due to the fact that deformation at the failure in each pile was less than 12 mm. The percentage increase in safe uplift capacity decreases with m remains maximum for $m = 0$ and almost becomes constant beyond $m = 2$. In the case of ultimate uplift capacity, the percentage increase in uplift capacity increases with the increase of m and the

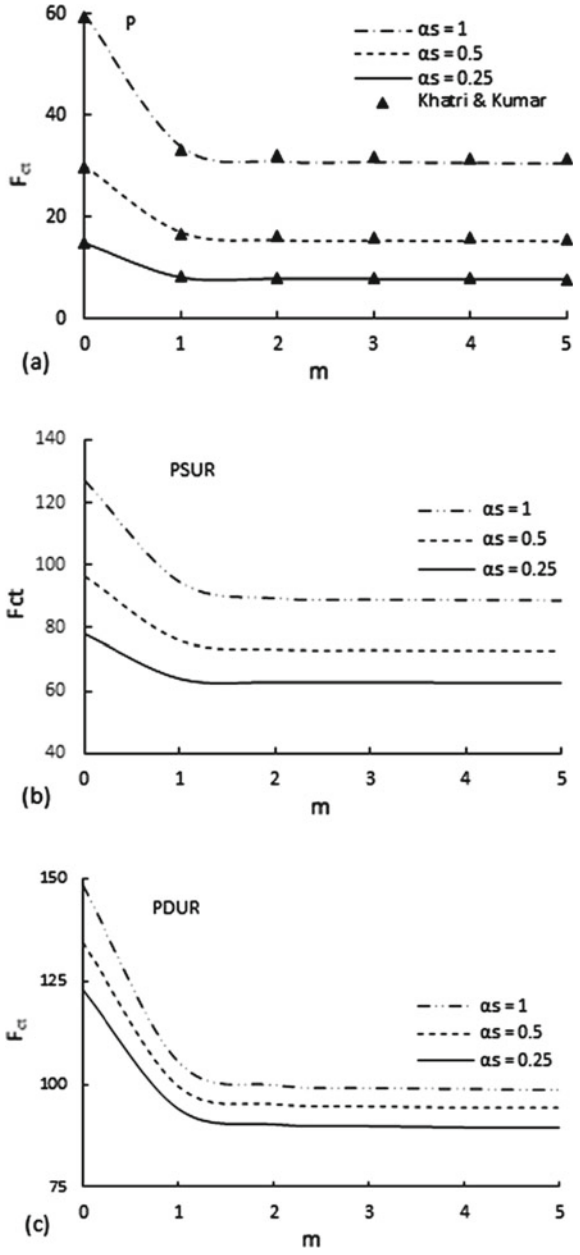

Fig. 4 Variation of F_{ct} with m for **a** P, **b** PSUR and **c** PDUR

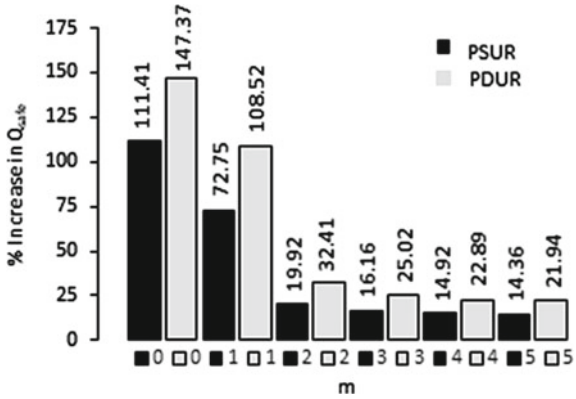

Fig. 5 Percentage increase in safe capacity (Q_{safe}) of PSUR and PDUR over P for different value of m

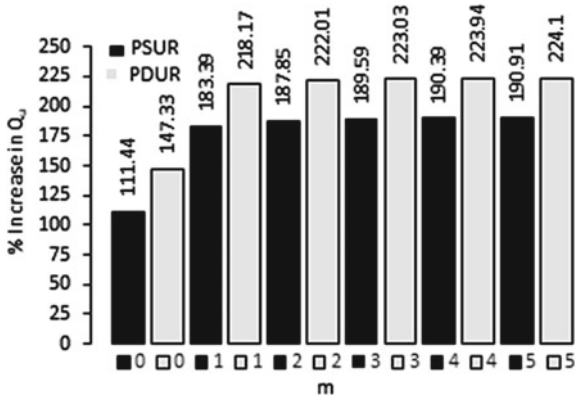

Fig. 6 Percentage increase in ultimate capacity (Q_u) of PSUR and PDUR over P for different value of m

maximum increase was 190.39 and 223.94% at $m = 4$. Thereafter, the percentage increase in uplift capacity becomes constant. Therefore, the percentage increase in safe uplift capacity due to bulbs addition is less sensitive with increasing cohesion.

4 Conclusion

The effect of linearly increasing cohesion on the uplift capacity of pile either with or without under-ream is investigated by numerical analysis. The findings of the analysis communicate the following conclusions.

The inclusion of the bulb results in a major change in the load-deformation behavior of the pile as in the case of the pile with one or two bulbs also for a given load smaller deformation was observed.

Further for a given deformation highest load was observed for pile with two bulbs followed by pile with one bulb and pile without bulb. This observation was consistent for different values of *m*.

With an increase in m, the safe and ultimate uplift capacity of all three types of piles increases, but the improvement for piles with two bulbs was quite substantial.

References

Annie Peter J, Lakshmanan N, Devadas Manoharan P (2006) Investigations on the static behaviour of self-compacting concrete under-reamed piles. J Mater Civil Eng 18(3):408–414

Bishop AW (1966) The strength of soils as engineering materials. Geotechnique 16:89–128

Central Building Research Institute (C.B.R.I) (1978) Handbook

George BE, Hari G (2016) Numerical investigations of under reamed piles in clays with application of finite element method. IGC

IS 2911(Part III-1980): 1980 Indian standard of Practice for Design and construction of pile foundations, under-reamed piles (first revision). Bureau of Indian Standard

Khatri VN, Kumar J (2009) Bearing capacity factor N_c under $\varphi = 0$ for piles in clays. Int J Numer Anal Meth Geomech 33(9):1203–1225

Khatri VN, Kumar J (2011) Uplift capacity of axially loaded piles in clays. Int J Geomech 11(1):23–28

Khatri VN, Kumar A, Gupta SK, Dutta RK, Gnananandarao T (2019) Numerical study on uplift capacity of under-reamed piles in clay with linearly increasing cohesion. Int J Geotech Eng. https://doi.org/10.1080/19386362.2019.1660527

Martin RE, DeStephen RA (1983) Large diameter double under-reamed drilled shafts. J Geotech Eng ASCE 109(8):1082–1098

Shrivastava N, Bhatia N (2008) Ultimate bearing capacity of Under Reamed Pile- Finite Element approach. In: 12th International conference of international association for computer methods and advances in Geomechanics (IACMAG), Goa, India, pp 1–6

Vali R, Mehrinejad KE., Saberian M, Li J, Mehrinejad M, Jahandari S (2017) A three-dimensional numerical comparison of bearing capacity and settlement of tapered and under-reamed piles. Int J Geotech Eng 1–13

Influence of Seabed Soil Characteristics on Eigenfrequency of Offshore Free Spanning Pipeline

Goutam Sarkar and Pronab Roy

1 Introduction

Pipelines are generally used to transport oil or gas from the offshore platform to the onshore processing unit or storage unit. However, due to various uncertainties, offshore pipelines are subjected to high risk. As at high water depth, there is an extreme environment, thus the inspection and maintenance of subsea pipelines are very difficult. If any failure occurs on the subsea pipelines, it will cause economic loss as well as environmental deserters.

One of the major causes of failure in the offshore pipeline is the formation of the free spans. A free span of submarine pipelines is a common and inevitable phenomenon in offshore oil and gas engineering, due to seabed unevenness, change of topology, scouring or sand waves (Vedeld et al. 2013). When water flows across a free span, the flow separates, the vortex sheds, and a periodic vibration will be generated. This vibration is well known as vortex-induced vibration (VIV). This periodic oscillation will cause fatigue damage to pipeline welds. On the other hand, the pipeline has its own natural frequency or eigenfrequency based on its geometry and material properties. When VIV frequency synchronised with one of its eigenfrequencies, then resonance will occur. This resonating span will experience significant deflections and associated stresses, and as a result, fatigue damages will occur to the pipeline. This fatigue failure can be prevented if VIV frequency is sufficiently far from eigenfrequencies. Thus, the eigenfrequencies of free span pipelines are vital parameters associated with the vibration response and also govern the allowable free span length.

Figure 1 shows a typical free span scenario, where L_{sh} is the contact length or shoulder length of pipe with the seabed soil and L_s is the free span length. The

G. Sarkar · P. Roy (✉)
Department of Civil Engineering, National Institute of Technology Durgapur, Durgapur, West Bengal 713209, India
e-mail: pronab.roy@ce.nitdgp.ac.in

S. Haldar et al. (eds.), *Advances in Offshore Geotechnics*, Lecture Notes in Civil Engineering 92, https://doi.org/10.1007/978-981-15-6832-9_20

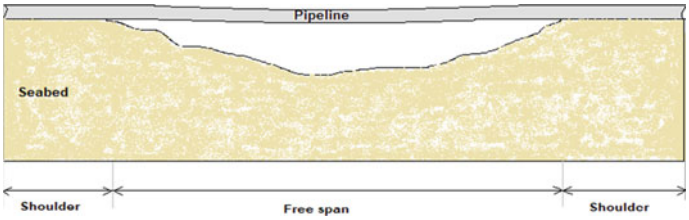

Fig. 1 A typical sketch of free spanning pipeline

middle unsupported portion of the free span pipeline will not remain straight due to the submerged weight.

1.1 Literature Review

Previously, the pipe-soil interaction was ignored by the researchers, and they were using only simplified boundary conditions, i.e., pin-pin, fix-fix and fix-pin. Later, it is found out that the soil in both ends of the pipe has significant effects on eigenfrequencies of free span pipeline. Hobbs (1986) analysed the effects of seabed elasticity on the effective length and eigenfrequencies of the free span subsea pipeline and expressed a non-dimensional graph of effective length. Choi (2001) investigated the effect of axial force on free span analysis, and it was concluded that during the operation and installation stage, its effect could not be neglected. Fyrileiv and Mørk (2002) investigated the lowest eigenfrequency and mode shape of free spanning offshore pipeline for different free span lengths, pipe diameters, wall thickness and soil conditions by using improved beam theory and developed a semi-empirical approximate expression for determining eigenfrequencies. The Det Norske Veritas recommended practice DNV-RP-F105 (2006) which is a guideline of free span pipeline used this semi-empirical approach to update the expressions of the effective length, eigenfrequency. Bakhtiary et al. (2007) used modal analysis with Euler--Bernoulli beam equation to investigate the effect of real seabed conditions and axial force on eigenfrequencies of offshore free spanning pipelines. It has been concluded that the effect of axial force has less influence on the pipeline lays on rock than lays on clayey soil. Ruby and Hartvig (2008) used transmitting boundary elements to analyse free span pipeline by including various environmental conditions, structural data, soil parameters, damping parameters and safety factors. Xiao and Zhao (2010) studied the eigenfrequencies of single and multiple free spanning pipelines based on different boundary conditions, axial force and mass of the hydrocarbon. Finally, it has been concluded that the pipeline frequency decreases with the increase of span length and increases with the fixity against rotation at ends. Mehdi et al. (2012) examined the influence of the different types of soil on the fundamental eigenfrequency of free spanning pipeline and concluded that eigenfrequencies of the pipeline increased with increase in the soil stiffness. Gamino (2013) used a 3D fluid-structure interaction (FSI) simulation

to incorporate the damping effects from the pipe-soil interaction at the ends of the free span oscillation due to VIV. They found out that the pipeline embedment during free span oscillation will lower the maximum stress. Vedeld et al. (2013) developed semi-analytical method to carry out modal analysis of free span offshore pipelines by applying Rayleigh-Ritz method, and the limitations of semi-empirical method given by Fyrileiv and Mørk have been overcome with better accuracy. Forbes and Reda (2013) examined the effect of axial boundary condition on the eigenfrequencies of free spanning pipeline and concluded that axial restrained and initial imperfection had significant effects on the first cross-flow mode. Sollund et al. (2015) used dimension analysis to investigate the modal response of an axially loaded infinitely long pipeline resting on semi-infinite elastic supports on either side of free span by applying Buckingham Pi theorem. They proposed a new expression to calculate the effective length of free span pipeline, which expands the validity range of eigenfrequencies, given by DNV-RP-F105. Guha et al. (2016) proposed a new form of axial soil stiffness depended on the embedment of pipe or degree of soil non-homogeneity. Finally, they concluded that pipeline laying, buckling, walking and on-bottom stability problems could be analysed more rigorously by the proposed expression of soil stiffness. Li et al. (2018) investigated the modal response of free span pipeline by using general integral transform technique (GITT) and concluded that GITT was a fast and accurate approach for analysing the dynamic response of free spanning submarine pipelines.

1.2 Objective

In this present paper, the dynamic behaviour of a free span offshore pipeline is analysed, and the effect of various factors or parameters on its dynamic behaviour is studied. The dynamic behaviour of the single-span pipeline is analysed in terms of extracting the eigenfrequencies of the free spanning pipeline by using DNV guidelines and FEM modeling.

This paper focuses on the effects of pipeline specifications and seabed soil characteristics on the determination of the eigenfrequencies. Here, six different types of seabed soil conditions (such as very soft clay, soft clay, firm clay, stiff clay, loose sand and dense sand) are considered. A parametric study of D/t (outer diameter to the wall thickness of pipe) ratio carried out to analyse the influence of the ratios on the eigenfrequencies of free spanning pipelines with different types of seabed soils. To do this, D/t ratio varies from 20 to 53 for a 508 mm outer diameter pipe.

The influence of L/D (free span to outer diameter) ratio with different types of seabed soils is also carried out to study the effects. To do these, four numbers of different outer diameter pipes are selected as 1016, 813, 610 and 508 mm with L/D ratio varying from 49 to 98.

2 Methodology

2.1 Structural and Functional Data of Pipeline

The geometry of the pipeline is modeled as a free span in the middle and two equal-sized shoulders, which are supported on the soil. The shoulder length on each side of the free span is taken as three times the free span length according to Vedeld et al. (2013). The geometry of the pipeline is given in Table 1. The pipeline has an initial static deflection due to its submerged weight and also a compressive axial force acting on the pipeline. In the operating stage, the pipeline carries high-temperature and high-pressure fluid. As a result, the pipeline is in compression. The pipe is coated with a concrete coating to increase the submerged weight, drag forces, added mass and buoyancy.

API 5L X65 grade of stainless steel is used for modeling the pipeline, which is taken from API 5L (2004) specification. In this study, the material of the pipe is assumed to be isotropic throughout the length. The material properties of the pipeline are given in Table 2.

Six different types of soil (sandy as well as clayey) are considered in the shoulders of the free span pipeline. Very soft clay, soft clay, firm clay, stiff clay, loose sand and dense sand are considered in this analysis. It is assumed that axial stiffness is equal

Table 1 Geometric properties of pipeline

Variable	Symbol	Unit	Value
Free span length	L	m	50
Shoulder length	L_{sh}	m	150
Outer diameters	D	mm	508, 610, 813 and 1016
Wall thickness	T	mm	9.5,12.7, 15.9,19.1 and 25.4
Concrete coating thickness	t_c	mm	67.7
Effective axial force	S_{eff}	kN	(−)50

Table 2 Material properties of pipeline

Variable	Symbol	Unit	Value
Modulus of elasticity for steel	E_{st}	GPa	206
Modulus of elasticity for concrete	E_c	MPa	$10{,}000 f_{ck}^{0.3}$
Grade of concrete	–	–	M35
Poisson's ratio for steel	ν	–	0.3
Density of steel	ρ_s	kg/m^3	7850
Density of concrete	ρ_c	kg/m^3	3040
Density of hydrocarbon	ρ_h	kg/m^3	900
Density of water	ρ_w	kg/m^3	1025

Table 3 Soil properties of seabed

Type of soil	Undrained shear strength (kN/m^2)	Angle of internal friction (degree)	Poisson's ratio	C_V (kN/m$^{5/2}$)	C_L (kN/m$^{5/2}$)
Very soft clay	<12.5	–	0.45	600	500
Soft clay	12.5–25	–	0.45	1400	1200
Firm clay	25–50	–	0.45	3000	2600
Stiff clay	50–100	–	0.45	4500	3900
Loose sand	–	28°–30°	0.35	10,500	9000
Dense sand	–	36°–41°	0.35	21,000	18,000

to lateral stiffness. The properties of soil are taken from DNVGL-RP-F114 (2017) and given in Table 3.

2.2 DNVGL-RP-F105 (2017) Guidelines

DNVGL-RP-F105 is a guideline for free span pipeline. A simple formula (Eq. 1) is provided in this code at clause 6.8.2 to calculate the lowest eigenfrequency of the free spanning subsea pipeline considering the pipeline specifications, seabed soil conditions, concrete coating, effective axial force and initial imperfection factor. The eigenfrequency expression in this guideline is taken from Fyrileiv and Mørk (2002). There is a limitation of this expression, the span length should be less than 140 D_s (outside steel diameter) and compressive effective axial force up to 0.5 P_{cr}, and ratio of static deflection (δ) to the outer diameter of the pipe (D) should be less than 2.5. The expression is as follows,

$$f_1 = C_1 \sqrt{\frac{EI}{m_e L_{eff}^4}\left(1 + \frac{S_{eff}}{P_{cr}} + C_3\left(\frac{\delta}{D}\right)^2\right)} \tag{1}$$

C_1 and C_3 are boundary condition coefficients. C_1 is the coefficient corresponding to end support condition, and for fix-fix support or single span on seabed condition it is 3.56. The value of C_3 is zero for inline frequency, and for cross-flow frequency with a single span on the seabed, it is 0.4. E and I are the young modulus of material and moment of inertia of steel pipe, respectively.

m_e is the effective mass of pipeline, and Eq. (2) shows the expression of m_e according to DNVGL-RP-F105 (2017) clause 6.6.6.

$$m_e = \left(\frac{\int_L m(s)\phi^2(s)\mathrm{d}s}{\int_L \phi^2(s)\mathrm{d}s}\right) \tag{2}$$

$\phi(s)$ is the assumed mode shape function satisfying the boundary condition. $m(s)$ is the mass per unit length, which is including the mass of the pipeline, the mass of the concrete coating, the mass of the hydrocarbon product and hydrodynamic added mass.

L_{eff} is the effective length of the pipeline corresponding to deferent soil types at supports. Equation (3) shows the expression of effective length according to DNVGL-RP-F105 (2017) clause 6.8.8.

$$\frac{L_{eff}}{L_s} = \begin{cases} \frac{4.73}{0.066\beta^2+1.02\beta+0.63} & \text{for } \beta \geq 2.7 \\ \frac{4.73}{0.036\beta^2+0.61\beta+1.0} & \text{for } \beta < 2.7 \end{cases} \tag{3}$$

The β is a non-dimension parameter and calculated by Eq. (4).

$$\beta = \log_{10}\left(\frac{KL_s^4}{E_{st}I_{st}}\right) \tag{4}$$

where L_s is the free span length of the free spanning pipeline, E_{st} and I_{st} are young modulus of material and moment of inertia of steel pipe, respectively.

K is dynamic seabed soil stiffness vertical or horizontal. According to Vedeld et al. (2013), a free span pipeline can be vibrated along two directions if the pipe is vibrating along with the flow of fluid and also perpendicular to pipe axis, then this frequency is called inline frequency. On the other hand, when the span pipeline is vibrating perpendicular to both pipe axis and flow of fluid, then the frequency is called cross-flow frequency. In case of inline frequency, the lateral dynamic stiffness K_L is used. Equation (5) shows the K_L according to DNVGL-RP-F114 (2017) clause 7.2.3.

$$K_L = C_L \times (1+\nu) \times \left(\frac{2}{3} \times \frac{\rho_s}{\rho} + \frac{1}{3}\right)\sqrt{D} \tag{5}$$

For cross-flow frequency, the vertical dynamic stiffness K_V is used, and it is given by Eq. (6) according to DNVGL-RP-F114 (2017) clause 7.2.3.

$$K_V = \frac{C_V}{(1-\nu)} \times \left(\frac{2}{3} \times \frac{\rho_s}{\rho} + \frac{1}{3}\right)\sqrt{D} \tag{6}$$

C_L and C_V are the coefficients with respect to the soil and taken from Tables 3 to 4 of DNVGL-RP-F114 (2017), respectively. ν is the Poisson's ratio of corresponding soil, $\frac{\rho_s}{\rho}$ is the ratio of density pipe mass and displaced water, and D is the outer diameter of pipe including the coating thickness.

In Eq. (1), the S_{eff} is the effective axial force for an axially restrained pipe, and P_{cr} is the critical buckling load given by Eq. (7) according to clause 6.8.2 of DNVGL-RP-F105 (2017). The S_{eff} is calculated according to clause 6.5.4 of DNVGL-RP-F105 (2017).

$$P_{\text{cr}} = C_2 \frac{\pi^2 EI}{L_{\text{eff}}^2} \tag{7}$$

C_2 is the boundary condition coefficient. For fix-fix support condition, it is 4.

δ is the static deflection of free span pipeline, which is ignored in case of inline frequency and given by Eq. (8) according to DNVGL-RP-F105 (2017) clause 6.8.6.

$$\delta = C_6 \frac{q L_{\text{eff}}^4}{EI} \frac{1}{\left(1 + \frac{s_{\text{eff}}}{P_{\text{cr}}}\right)} \tag{8}$$

where C_6 is the boundary condition coefficient (for fix-fix support condition, it is 1/384) and q is the submerged weight of the pipe.

2.3 Eigenfrequency Analysis with Numerical Method

Commercial finite element software Abaqus 6.12 is used for free spanning pipeline eigenfrequency analysis. The finite element analysis includes various modules for creating a model, defining the material property and specifying boundary conditions and external loads. The geometric and material properties which were used for the FEM analysis are the same as in the analytical method. The modelling details of the free span pipeline are described in the following sub-sections.

2.3.1 Pipeline and Pipe-Soil Interaction

The pipeline is considered as a beam, and its structural model consists of 3D elements. To do, these PIPE31 elements are taken, which are two-nodded 3D beam elements. The pipe-soil interaction of the pipeline lying on the seabed is taken into account by representing the seabed soil with nonlinear springs. The nonlinear springs in Abaqus incorporate with pipe-soil interaction elements (PSI34). The PSI34 is a 3D four-node pipe-soil interaction element. This PSI34 element can incorporate nonlinear soil behaviour as well as the interaction of pipe with adjacent soils. One edge of the element shares nodes with the underlying PIPE31 elements. The consecutive behaviour of the PSI element is determined using Eqs. (5) and (6). Figure 2 shows the free span model in Abaqus with PIPE31 and PSI34 elements.

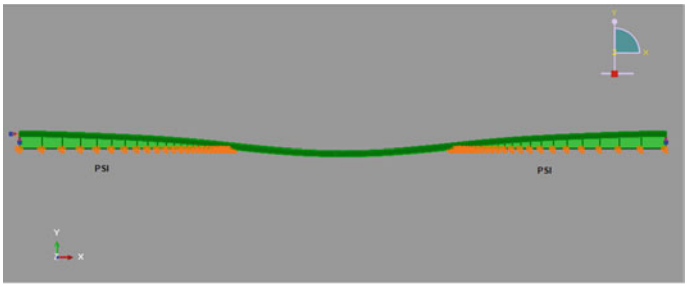

Fig. 2 FE model of the pipeline with PSI elements

2.3.2 Meshing

In FEM analysis, meshing is one of the important aspects to discrete the model into many numbers of elements. This is one of the most important modules since the accuracy of the result depends on the meshing of the assemblies. A mesh sensitivity analysis has been carried out to determine the optimum element length. For that a model was prepared with 50 m free span, 508 mm pipe outer diameter and 7.9 mm thickness on very soft clay soil. At first a 0.01 m element length is used for pipeline, and it gives a fundamental eigenfrequency of 0.42028 Hz. Next, the same model is run with 0.1 m element length for the pipeline and gives a fundamental eigenfrequency of 0.42029 Hz, and also it takes less time to run the analysis compared to the 0.01 m element model. Thus, it can be concluded that the 0.1 m element length is the optimum size of the element.

2.3.3 Boundary Conditions and Loadings

The boundary conditions for the ends of the pipeline are considered as fixed-fixed. The PSI elements are not restrained by default. The axial, lateral and vertical displacement of each node of a PSI element which is far from the pipeline is set as zero. An additional restrained is provided at the nodes of PSI elements which are not connected to the pipe (Fig. 2).

In this FE modelling mass of the hydrocarbon, concrete coating and hydrodynamic added mass are considered as non-structural mass per unit length of pipeline. A point load is applied to the right-hand end of the pipe to represent the effective axial force. The submerged weight of the pipeline is also applied to the pipeline as a uniformly distributed load acting along the pipeline vertically.

Finally, the analysis procedure of the finite element modelling in Abaqus is as follows,

1. PIPE31 and PSI34 elements are generated.

2. The hydrodynamic added mass and the mass of pipe coating are included as non-structural mass.
3. The pipe is fixed at one end, while the other end is temporarily free.
4. The axial force is applied at the free end of the pipeline, which is the first step of the static analysis.
5. The uniformly distributed load (submerge weight of pipeline) is applied over that pipeline, which is the second step of the static.
6. The temporarily free end of the pipe is subsequently fixed.
7. Lastly, the frequency analysis (dynamic) step is created to extract the eigenfrequencies.

3 Validation of Model

In order to verify the models, tests have been performed between the analytical model (as per DNVGL-RP-F105) and the numerical model in Abaqus. A free span is considered with a span length of 50 m, 1016 mm outer diameter and 12.7 mm wall thickness. The L/D ratio of the model is 49.21. In this model, the total effective mass and submerge weight are determined as 2836 kg/m and 6879 N/m, respectively. The soil in the shoulder considered very soft clay. Table 4 shows the results of the test model for inline frequency and cross-flow frequency by FEM and DNV guidelines.

From Table 4, it is clear that inline frequency for both FEM and DNV guidelines is very close to each other with a difference of 0.2%. The same result is also observed for cross-flow frequency, but a slight increase in difference (3.3%). Thus, inline and cross-flow frequency difference for both DNV and FEM is within the permissible limit (i.e., 5% according to DNVGL-RP-F105 (2017) clause 6.7.4, and this observation validated the FE model.

Table 4 Test results

Directions	DNV (Hz)	FEM (Hz)
Inline frequency	0.490	0.491
Cross-flow frequency	0.541	0.523

4 Results and Discussion

The next step after validation of model is to study the influence of D/t and L/D on the eigenfrequencies of free span pipeline. Both the inline and cross-flow frequencies were studied in this analysis. After finding the results, Figs. 5, 6, 7 and 8 are plotted to show the effects.

Figures 3 and 4 show the enlarged first inline and cross-flow mode shapes of the free span model with pipe diameter 508 mm, the wall thickness of 9.5 mm and resting on very soft clay soil respectively.

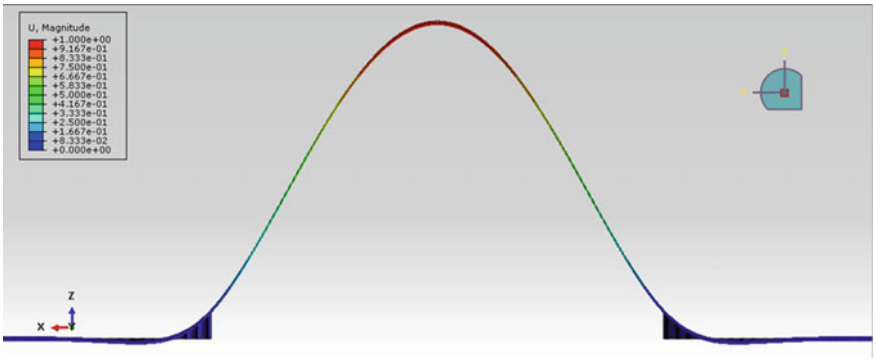

Fig. 3 Mode shape for first inline frequency

Fig. 4 Mode shape for first cross-flow frequency

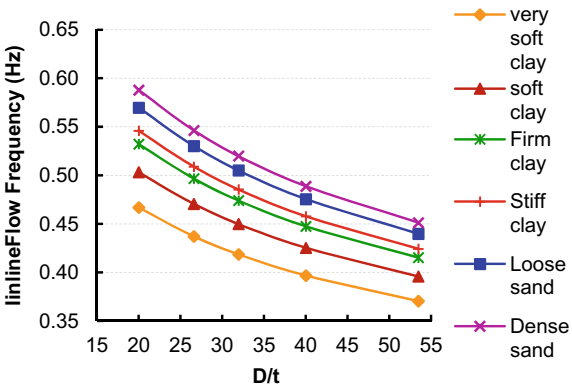

Fig. 5 Effect of different types of soil on the first inline frequency of pipelines for various (*D*/*t*) ratios

4.1 Influence of D/t

A parametric study is carried out to study the influence of outer diameter-to-thickness (*D*/*t*) ratios and soil conditions on inline and cross-flow eigenfrequencies of the free spanning subsea pipeline. A 508 mm outer diameter pipe is considered in this analysis with a 50 m free span. The *L*/*D* ratio for this case is 98.43. Five numbers of wall thicknesses are considered as 9.5 mm, 12.7 mm, 15.9 mm, 19.1 mm and 25.4 mm with *D*/*t* of 53.47, 40.00, 31.95, 26.60 and 20.00, respectively.

Figure 5 shows the plot of *D*/*t* versus inline frequencies of the free spanning pipeline. It is seen that with the increase of *D*/*t* ratio the frequency is decreasing. As the *D*/*t* ratio increases, the wall thickness of the pipe getting reduced, thus the structural stiffness of pipe is also getting reduced. Now, the frequency is proportional to stiffness, so the frequency will be reduced as the *D*/*t* ratio increases. It is also seen that very soft clay soil having the lowest stiffness gives the lowest frequency, and dense sand having the highest stiffness gives the highest frequency.

Figure 6 shows the plot of *D*/*t* versus cross-flow eigenfrequencies of the free spanning pipeline. The same observation is also shown as in the case of inline flow. The same study is also done for other outer diameter pipelines (610, 813 and 10,106 mm) with various wall thicknesses. The *D*/*t* versus eigenfrequency graph also plots for those pipe diameters, and the same nature of the graph as Figs. 5 and 6 were observed.

4.2 Influence of L/D

A parametric study is also carried out to study the influence of free span length to the outer diameter (*L*/*D*) ratios and soil conditions on fundamental inline and cross-flow eigenfrequencies of the free spanning subsea pipeline. The free span length of the model is fixed as 50 m. Four different outer diameter pipes are selected as 1016 mm,

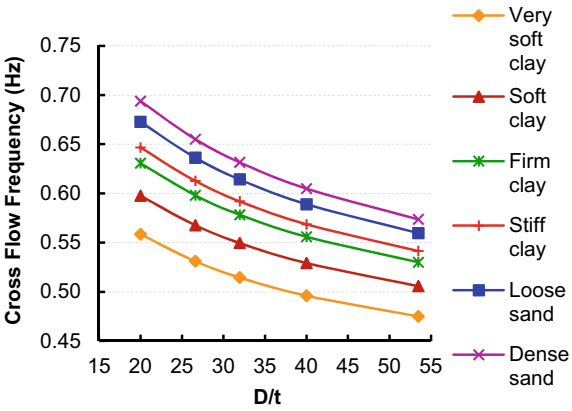

Fig. 6 Effect of different types of soil on the first cross-flow frequency of pipelines for various (D/t) ratios

813 mm, 610 mm and 508 mm with L/D ratio varying of 49.21, 61.5, 81.97 and 98.43, respectively. Here, the wall thickness of the pipe is fixed as 12.7 mm.

Figure 7 shows the plot of L/D ratio versus inline frequencies of the free spanning pipeline. Very soft clay soil having the lowest stiffness gives the lowest frequency, and dense sand having the highest stiffness gives the highest frequency for a fixed L/D ratio. This figure (Fig. 7) also shows that as the L/D ratio is increasing, the frequency is decreasing.

Figure 8 shows the plot of L/D ratio versus cross-flow frequencies of the free spanning pipeline. Just like inline flow, the very soft clay soil gives the lowest frequency, and dense sand gives the highest frequency. However, it is seen that the cross-flow frequency is decreasing initially, but later, it is increasing. In cross-flow mode, the pipe will vibrate in the vertical plane (perpendicular to both pipe and flow of fluid). Thus, when the L/D ratio is increasing, the sagging is also increased on the free span. This sagging will resist the free span pipe to vibrate in the vertical plane, so the frequency increases again.

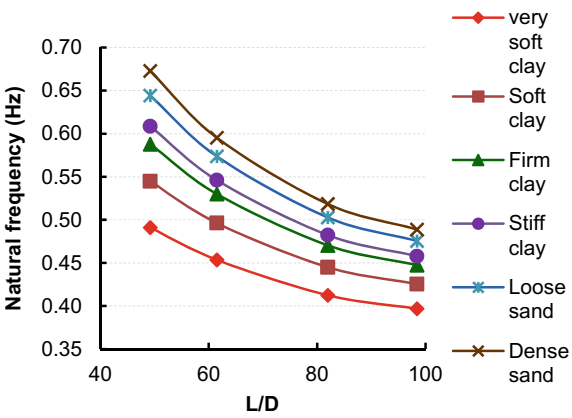

Fig. 7 Effect of different types of soil on the first inline flow frequency of pipelines for various (L/D) ratios

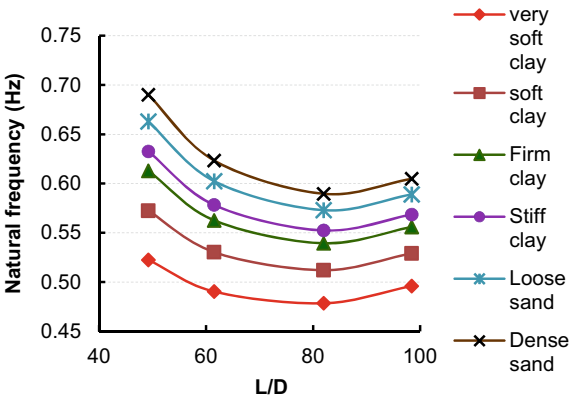

Fig. 8 Effect of different types of soil on the first cross-flow frequency of pipelines for various (*L*/*D*) ratios

5 Conclusion

The lowest inline and cross-flow eigenfrequencies have been calculated numerically by considering various factors such as pipeline specifications and seabed soil conditions. Validation of the FEM model is also performed with the DNVGL-RP-F105 (2017) guidelines. From this study, the following conclusions can be drawn:

- With the increase of the pipeline wall thickness, the eigenfrequency of free spanning subsea pipeline increases for a particular diameter and seabed soil condition. Both inline and cross-flow eigenfrequencies decrease with the increase of *D*/*t* ratio.
- With the increase of the soil stiffness, the eigenfrequencies of the free spanning subsea pipeline increase.
- The eigenfrequency will decrease with the increase of *L*/*D* ratio for a particular seabed soil condition.
- The deflection of the midspan will reduce cross-flow vibration. Due to increased *L*/*D* ratio, the cross-flow frequencies initially decrease after that they increase gradually due to increased sagging of the pipeline.

References

API 5L (2004) Specification for line pipe. American Petroleum Institute, USA
Bakhtiary YA, Ghaheri A, Valipour R (2007) Technical note on: analysis of offshore pipeline allowable free span length. Int J Civ Eng 5(1):84–91
Choi HS (2001) Free spanning analysis of offshore pipelines. Ocean Eng 28:1325–1338
DNVGL-RP-F105 (2017) Free spanning pipelines. Det Norske Veritas, Norway
DNVGL-RP-F114 (2017) Pipe-soil interaction for submarine pipelines. Det Norske Veritas, Norway
DNV-RP-F105 (2006) Free spanning pipelines. Det Norske Veritas, Norway

Forbes GL, Reda AM (2013) Influence of axial boundary conditions on free spanning pipeline natural frequencies. In: Proceedings of the ASME 2013 32nd international conference on ocean, offshore and arctic engineering. Nantes, France, pp 1–9

Fyrileiv O, Mørk K (2002) Structural response of pipeline free spans based on beam theory. In: Proceedings of 21st international conference on offshore mechanics and arctic engineering. Oslo, Norway, pp 1–9

Gamino M (2013) FSI methodology for analyzing VIV on subsea pipeline free spans with practical boundary conditions. Master thesis. University of Houston, USA

Guha I, Randolph MF, White DJ (2016) Evaluation of elastic stiffness parameters for pipeline–soil interaction. J Geotech Geoenv Eng 42(6)

Hobbs RE (1986) Influence of structural boundary conditions on pipeline free span dynamics. In: Proceedings of 5th international conference on offshore mechanics and arctic engineering. Tokyo, pp 685–691

Li T, An C, Liang W, Duan M, Estefen SF (2018) Semi-analytical solution for soil constrained vibration of subsea free-spanning pipelines. J Ships Off Struct 13(6):666–676

Mehdi Y, Said M, Ebrahim J (2012) Determining natural frequency of free spanning offshore pipelines. J Persian Gulf Mar Sci 3(8):25–34

Ruby K, Hartvig PA (2008) Free span analyses of an offshore pipeline. Master thesis. Aalborg University, Denmark

Simulia Abaqus FEA (2012) User's manual, version 6.12. Dassault systems. Velizy-Villacoublay, France

Sollund H, Vedeld K, Fyrileiv O (2015) Modal response of free spanning pipelines based on dimensional analysis. J Appl Ocean Res 50:13–29

Vedeld K, Sollund H, Hellesland J (2013) Free vibrations of free spanning offshore pipelines. J Eng Struct 56:68–82 (Elsevier)

Xiao ZG, Zhao XL (2010) Prediction of natural frequency of free spanning subsea pipelines. Int J Steel Struct 1(1):81–89

Offshore Geotechnical Investigation and Design of Offshore Pile Foundations Considering Liquefiable and Non-liquefiable Soils

M. K. Pradhan, S. Chakroborty, V. S. Phanikanth, and K. Srinivas

1 Introduction

Execution strategy and methodology adopted during construction of civil engineering structures at offshore locations are very much different from onshore due to expensive site investigation, unusual soil conditions, and installation difficulties. Offshore foundations withstand complex aerodynamic and hydrodynamic loads from wind and wave. The load acting on a structure is dependent not only on the environment and location (for example wind, wave) but also on unpredictable natural hazards (like Tsunamis and earthquake and its associated effects such as liquefaction). Hence may affect the reliability and serviceability of the structure and its foundation during its operational condition, which need to be considered in offshore design. In this paper, geotechnical investigation results at a selected site proposed for construction of a facility consisting both onshore and offshore structure at Bay of Bengal, Odisha, are presented.

1.1 General Design Consideration Offshore Structures

A basic understanding of several key subject areas is essential to an engineer involved in the design of offshore structures as suggested by El-Reedy (2011) and Haritos (2007). The authors provided an overview of some of the key factors that need be considered in the analysis and design of offshore structures. Prior to design of offshore structures, soil investigation is very essential.

M. K. Pradhan (✉) · S. Chakroborty · V. S. Phanikanth · K. Srinivas
Bhabha Atomic Research Centre, Mumbai, Maharashtra, India
e-mail: mpradhan@barc.gov.in

M. K. Pradhan
HBNI, Mumbai, Maharashtra, India

S. Haldar et al. (eds.), *Advances in Offshore Geotechnics*, Lecture Notes in Civil Engineering 92, https://doi.org/10.1007/978-981-15-6832-9_21

1.2 Onshore and Offshore Site Investigations

Geotechnical information of seabed soils is essential and pre-requisite for proper design and construction of offshore structures. The first step to evaluate risks for an offshore structure is to perform site investigation. Site investigations are necessary to acquire data that will facilitate successful foundation design, choice of foundation type, dimensioning, installation, and operational integrity of the proposed structure (ISSMGE 2005).

1.3 Offshore Pile Design and Construction Philosophy

Offshore structures are generally classified as bottom-supported fixed structures or floating structures. The most common form of fixed offshore platforms (jacket structure) may be supported on piled foundations or gravity-based structures (GBS) resting on the seabed. Harbor and offshore structures use piles extensively and for both vertical and lateral loads (Bowles 1997). Piles are also drilled and grouted in calcareous sediments, and other crushable material, where the shaft friction obtained with driven piles can be extremely low (Randolph et al. 2005). A Review of Design Methods for Offshore Driven Piles in Siliceous Sand was presented by Lehane et al. (2005a). American Petroleum Institute (2011) is very useful guide for geotechnical engineers for Geotechnical and Foundation Design Considerations in offshore structures (API 2011). Matlock and Reese (1961) also presented insight about the foundation analysis of offshore pile supported structure. Randolph (1983) presented design consideration of pile foundation in offshore.

1.4 Liquefaction: Onshore and Under-Seabed

Liquefaction is a phenomenon of saturated cohesionless soil subjected to repetition of cyclic loads which loss its strength parameters and stiffness and behaves like liquid. In case of onshore area, the cyclic loads are the form of earthquake; however, in offshore/under seabed, the loads may be in the form of earthquake or sea waves. Physics of liquefaction phenomena around marine structure was briefed by De Groot et al. (2006). Mechanics of seabed liquefaction and re-solidifications along with pore pressure changes was studied by Sawicki (2014). He presented two mechanism of pore pressure changes such as caused by external excitation such as earthquake when pore pressure is gradually generated and leading to liquefaction. Another phenomenon is caused by water waves that lead to cyclic changes in pore water pressure and mean effective stress. A modified criterion for wave-induced momentary liquefaction of sand seabed was briefed by Qui and Gao (2014). Numerical modelling was developed by Chang et al. (2004) for liquefaction analysis of

seabed at near shore area. Residual liquefaction was studied by Kirca et al. (2012). Young et al. (2008) briefed that Tsunami drawdown can lead to liquefaction failure of coastal sandy slope. On account of the detrimental consequences of soil liquefaction, special attention and considerations are warranted in analysis, designing and detailing of offshore structures supported on pile foundation.

2 Methodology

In the present study, geotechnical investigation is carried out and liquefaction potential of soil is evaluated at a selected site consisting of both onshore and offshore structures. It was found that at some locations, soil is susceptible to liquefy. Further site response analysis is performed using DEEPSOIL software to investigate soil amplification.

2.1 Geotechnical Investigation

Broad objectives of soil investigations are to evaluate geological parameters of soil, to estimate bearing capacity of soil, and to provide information for design of foundation system. During process of geotechnical investigation, numbers of boreholes (Seabed boreholes designated as SBL and land boreholes designated as LBH) are drilled for in situ tests. Also, sample collections are taken for laboratory tests. Cross-borehole test is also carried out to evaluate various dynamic properties of soil. The schematic diagram showing the location of investigation points considered in the present paper is marked in Fig. 1.

2.1.1 Onshore Investigation

Details of boreholes considered in the present study are as shown in Fig. 1. It consists of four boreholes on onshore and three boreholes at offshore location. Borehole LBH-03 (at sea bank) is bored up to 25.10 m depth, LBH-01 and LBH-02 (at 500 m distance from offshore) are bored up to 15.00 m and 11.50 m below ground level, respectively. One cross-hole test is performed as per ASTM D4428/D4428M at CHT-01 up to depth 20.50 m from ground level, respectively. The results obtained from offshore geotechnical investigation are discussed in Sect. 3.1.1.

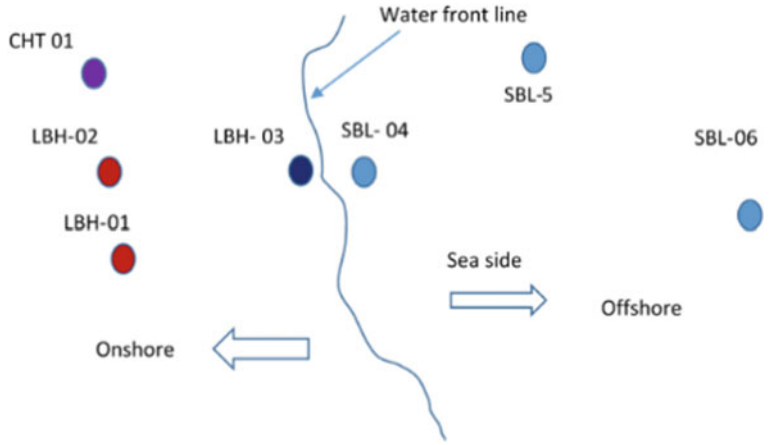

Fig. 1 Schematic diagram of borehole location during geotechnical investigation considered for present study

2.1.2 Offshore Investigation

For conducting offshore/marine geotechnical investigation, structural platform was built with the support of floating arrangement, i.e., pontoons. The drilling arrangements like rigs and all accessories are supported on the artificial structural platform. The positioning of platform at marine boreholes is established with the help of hand-held global positioning system (HGPS). For the present study, three boreholes at seabed designated as SBL-04, SBL-05, and SBL-06 were considered. The sea water depth up to seabed level at SBL 04, SBL-05, and SBL-06 are 1.5 m, 4.5 m, and 12.5 m, respectively. A typical offshore bore log details and water depth for SBL-06 are shown in Fig. 2. The results obtained from offshore geotechnical investigation are discussed in Sect. 3.1.3.

2.2 Design of Foundation System in Seabed

A suitable foundation for any structure must satisfy two basic independent criteria with respect to the underlying foundation soils. First, the foundation must have an adequate factor of safety against exceeding the bearing capacity of the foundation soils. Second, the vertical movements of the foundation due to settlement or swelling of the foundation soils must be within tolerable limits for the structure. In the present study, an attempt was made to asses the required size of pile foundation at selected site.

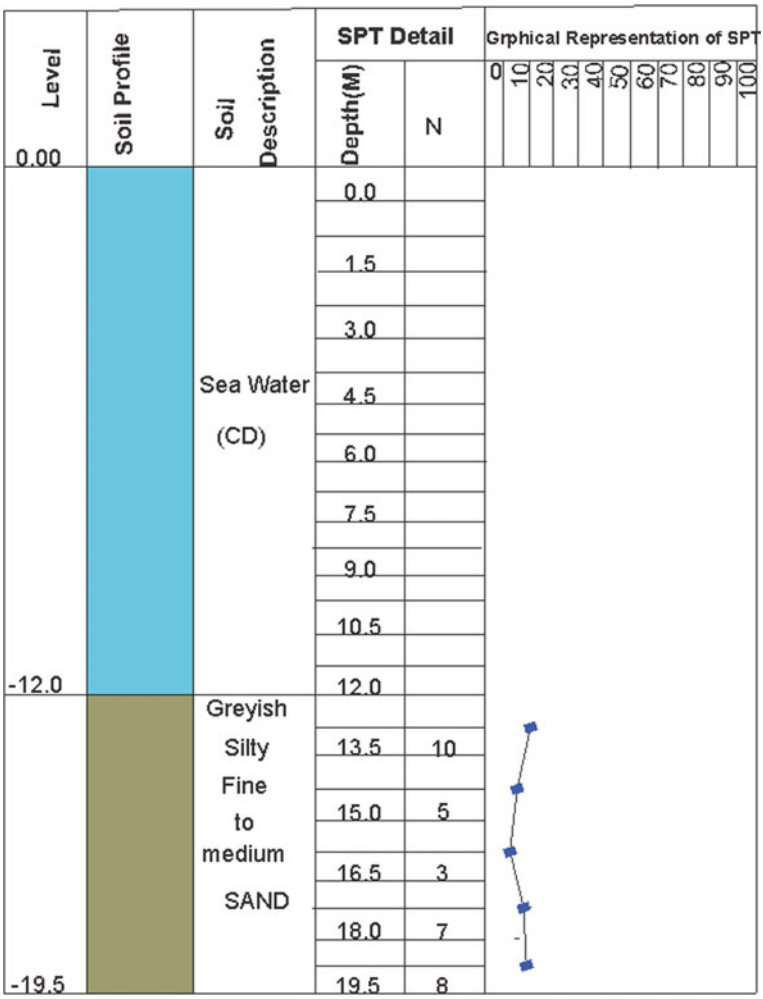

Fig. 2 Soil profile of bore log at seabed (SBH-06)

2.3 Evaluation of Liquefaction Potential

For evaluation of liquefaction potential of soils, factor of safety against initial liquefaction which is the ratio of cyclic resistance ratio (CRR) to cyclic stress ratio (CSR) is calculated. CSR is evaluated as: (Seed and Idriss 1971).

$$\mathrm{CSR} = 0.65 \times \frac{a_{\max}}{g} \times \frac{\sigma_{v0}}{\sigma'_{v0}} \times r_d \tag{1}$$

Cyclic resistance ratio (CRR) is calculated as:

$$\mathrm{CRR}_{M=7.5,\sigma_{Vv0=1}} = \exp\left(\left(\frac{(N_1)_{60cs}}{14.4}\right) + \left(\frac{(N_1)_{60cs}}{126}\right)^2 - \left(\frac{(N_1)_{60cs}}{23.6}\right)^3 + \left(\frac{(N_1)_{60cs}}{25.4}\right)^4 - 2.8\right) \tag{2}$$

where $(N_1)_{60cs}$ is standard penetration number with all standard correction, i.e., energy, overburden stress, fines content, etc. briefed as follow:

$$(N_1)_{60CS} = (N_1)_{60} + \Delta(N_1)_{60} \tag{3}$$

where

$$\Delta(N_1)_{60} = \exp\left(1.63 + \frac{9.7}{\mathrm{FC} + 0.01} - \left(\frac{15.7}{\mathrm{FC} + 0.01}\right)^2\right) \tag{4}$$

where FC is fine content.

For other moment magnitudes other than ($M = 7.5$), CRR is evaluated as

$$\mathrm{CRR}_M = \mathrm{CRR}_{7.5}\chi\mathrm{MSF} \tag{5}$$

Liquefaction potential is evaluated and details are discussed in Sect. 3.1.4.

2.4 Liquefaction Below Seabed

Catastrophic consequences like sinking, instability of offshore foundations, structures, etc., are due to result of liquefaction below seabed. Thus, in offshore engineering practices, the occurrence of soil liquefaction and its effect on the structures should be well assessed. Under the continuous action of the cyclic wave loading, the excessive pore pressure may build up gradually and the soil is liquefied when the residual pore pressure exceeds the effective overburden pressure (Chang et al. 2004).

2.5 Design of Pile Foundation in Liquefiable Site

In offshore construction, to transmit loads above the water surface through the water and into the underlying soil partially embedded piling is subjected to vertical (and buckling) as well as lateral loads (Bowles 1997). In case, pile foundation is located at site susceptible to liquefaction, the influences and adverse effects of liquefaction in pile design are emphasized. Due to loss of confinement, frictional resistance contribution of pile in load carrying capacity in liquefied zone is not considered. In case

of presence intermediate zone of liquefiable soil, top layer is considered to act with passive load on the pile section. In the zone of liquefied soil, it is considered the lateral load of 30% of surcharge load is considered as per JRA (1996).

2.6 Site Response Analysis

Soil amplification studies provide a realistic estimate of site hazard and risk involved in designing the structure and hence need to be duly considered in the design. In the present study, site responses analysis is performed using DEEP Soil software for onshore and offshore locations using site investigation results obtained for selected site (Hashash et al. 2016). Chi-Chi earthquake as input acceleration time history is considered for the present study. Details of results are discussed in Sect. 3.2.

3 Results and Discussion

Liquefaction potential of soil is evaluated at selected site. Site responses with the help of software DEEPSOIL are also discussed.

3.1 Geotechnical Investigation

The results of geotechnical investigation conducted as per IS 1892 (1979) at various location as shown in Fig. 1 are presented in subsequent subsection.

3.1.1 Results: Geotechnical Investigation Onshore

It is observed from bore logs, subsoil in the area consists of loose to very dense fine to coarse-grained sand. Observed bore log profile, SPT results of LBH-01, and CHT-01 are presented in Table 1 and of LBH-03 in Table 2.

Chemical tests were conducted on five water and based on the results, the sulfates (SO4) contents in the water were found in the range of 13,500--15,480 ppm, chloride contents in the range between 18,500 and 20,521 ppm and pH ranges from 7.6 to 7.85. According to the recommendations of IS 456 (2000), the results place the soil in the very severe category for sulfate attack (IS 456 2000). In addition to above, another point (onshore) marked as LBH-03 in Fig. 1 at a distance of 50 m from offshore (sea shore line) is selected for the study. The selected point is bored for geotechnical investigation and the SPT results of point LBH-03 presented in Table 2 after required correction.

Table 1 Observed bore log profile and SPT results of LBH-01 and CHT-01 (500 m away from sea shore)

LBH-01			CHT-01		
Depth (m)	Description	Corrected N-Value	Depth (m)	Description	Corrected N-Value
0.0-0.5	Loose to medium dense sand		0.0-0.5	Medium dense sand	
0.5-0.95		18	0.5-0.95		20
1.5-1.95		22	1.5-1.95		19
2.5-2.95		17	2.5-2.95		20
3.5-3.95		12	3.5-3.95	Medium to dense sand	22
4.5-4.95		14	4.5-4.95		30
5.5-5.95		15	5.5-5.95		34
6.5-6.95		11	6.5-6.95	Very dense sand	39
7.5-7.95	Medium to dense sand	22	7.5-7.75		R
8.5-8.95		31	8.5-8.77		R
9.5-9.9	Very dense sand	R	9.5-9.7		R
11-11.43		R	11-11.3		R
12.5-12.75		R	12.5-12.9		R
14-14.42		R	14-14.45		R
			15.5-15.95		R
			17-17.45	Dense to very dense sand	R
			18.5-18.95		R
			20-20.4		R

Table 2 Geotechnical investigation for borehole 03 (50 m away from sea line)

Depth (m)	Description	Corrected N-Value
0.0-0.5	Loose Sand	
0.5-0.95		8
1.5-1.95		9
2.5-2.95	Medium Dense Sand	29
3.5-3.95		22
4.5-4.95		23
5.5-5.95		20
6.5-6.95	Dense Sand	43
7.5-7.95		44
8.5-8.95		33
9.5-9.95		32
11-11.45		28
12.5-12.95		32
14-14.45		30
15.5-15.95		31
17-17.45		32
18.5-18.8	Very Dense Sand	R
20-20.5		R
20.5-23.3		R
23.3-25.1		R

3.1.2 Geotechnical Investigation: Seabed

Geotechnical investigation also performed at selective locations in seabed as shown in Fig. 1 marked as SBH-01, SBH-02, and SBH-03. The soil profile at boreholes SBL-06 below seabed is already presented in Fig. 2 in Sect. 2.1.1. Typical borehole data of a bore hole SBH-05 is presented in Table 3.

Table 3 Typical properties of soil-borehole SBH-05 in seabed

Depth (m)	Type of soil	SPT value	Density (t/m^3)	Phi (angle of internal friction)
1.5–7.5	Dense medium sand	32	1.79	35
7.5–18.0	Medium dense sand	21	1.78	32
18.0–27.50	Cemented lime stone		2.55	

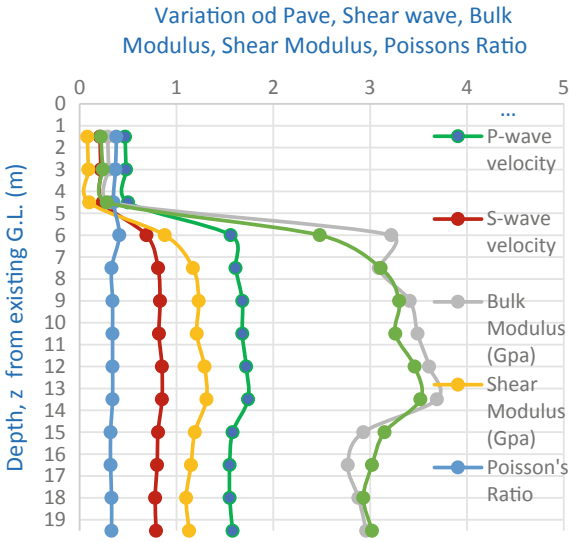

Fig. 3 Variation of *P*-wave, *S*-wave, bulk modulus, shear modulus, Poisson's ratio, Young's modulus of soil with depth

3.1.3 Cross-Borehole Test: Onshore

The average dynamic parameters of the soil, i.e., *P*-wave, *S*-wave, bulk modulus, shear modulus, Poisson's ratio, Young's modulus along the depth evaluated from cross-borehole test results (CHT 01) are presented in Fig. 3.

3.1.4 Liquefaction Potential Evaluation at Selected Site

The liquefaction potential at selected site is evaluated adopting the methods available in literatures. The cyclic resistance ratio evaluated based on the various soil properties obtained from geotechnical investigation for borehole LBH-01 is presented in Table 5. The cyclic stress ratio considering the credible earthquake at selected site is presented in Table 6. The selected site located on the bank of Bay of Bengal in Odisha site and lies in seismic zone-II as per seismic zone mapping of India (IS 1893 2016). The CSR, CRR, and factor of safety against liquefaction of soil are tabulated in Tables 4, 5 and 6 and presented in Fig. 4.

As per IS 1893 (2016) Part 1, if soil consists of submerged loose sand and SPT value is less than 15 in zone III, IV, and V or with SPT value less than 10 in zone II, occurrence of seismic event may cause the soil to liquefy. The location marked as LBH-01 at selected site consists of loose sand in intermediate layer with SPT value close to 10 ($N < 15$) as pointed in Table 1. It is also specified by IS 1893 (2016) Part 1 that factor of safety against liquefaction should be 1.2 or more. In more stringent manner, it is also further guided by AERB that factor of safety against liquefaction should not be less than 1.4 for important structure like nuclear facility (AERB guidelines). Considering generalized soil profile for location LBH-01 area,

Table 4 CRR calculations (DP borehole)

Depth from existing G.L. (m)	Average field SPT (N) value	Atmospheric pressure (Pa)	Effective vertical overburden stress (o''_{v0})	Corrected penetration resistance for fine content FC (in %)	CRR 7.5	MSF	CRR
0	0	100.000	0.000	–		0.821	
0.725	18	107.112	6.228	36	0.262	0.821	0.215
1.725	22	116.922	14.904	44	0.321	0.821	0.264
2.725	17	126.732	23.680	34	0.247	0.821	0.203
3.725	12	136.542	33.115	24	0.273	0.821	0.224
4.725	14	146.352	42.478	28	0.370	0.821	0.303
5.725	15	156.162	52.613	30	0.218	0.821	0.179
6.725	11	165.972	61.803	22	0.242	0.821	0.199
7.725	22	175.782	70.993	41	0.299	0.821	0.245
8.725	31	185.592	80.183	56	0.410	0.821	0.337

Table 5 CSR calculations

Depth from existing G.L. (m)	Stress reduction factor, r_d	Bulk density (kN/m^3)	Effective unit weight (kN/m^3)	Total vertical overburden stress, o'_{v0} (kN/m^2)	Effective vertical overburden stress, o''_{v0} (kN/m^2)	(o'_{v0}/o''_{v0})	CSR
0	1.000	9.810	0.000	–	–	–	–
0.725	0.994	18.400	8.590	13.34	6.227	2.142	0.213
1.725	0.987	18.450	8.640	31.826	14.904	2.135	0.211
2.725	0.979	18.500	8.690	50.412	23.680	2.128	0.209
3.725	0.972	18.700	8.890	69.657	33.115	2.103	0.205
4.725	0.964	18.800	8.990	88.83	42.477	2.091	0.202
5.725	0.956	19.000	9.190	108.775	52.612	2.067	0.198
6.725	0.994	19.000	9.190	127.775	61.802	2.067	0.206
7.725	0.968	19.000	9.190	146.775	70.992	2.067	0.200
8.725	0.941	19.000	9.190	165.775	80.182	2.067	0.195

the liquefaction is likely to occur as can be seen in results of Table 6 and hence ground improvement by placing an engineering fill/ compaction is desirable or foundations going to stronger strata is recommended.

Table 6 Calculations of factor of safety against liquefaction

Depth, z from existing G.L. (m)	CRR	CSR	FOS	Remarks
0.725	0.215	0.221	0.970	Soil has potential to liquefy
1.725	0.263	0.219	1.203	Non-liquefiable soil
2.725	0.202	0.216	0.936	Soil has potential to liquefy
3.725	0.224	0.212	1.056	Soil has potential to liquefy
4.725	0.303	0.209	1.447	Non-liquefiable soil
5.725	0.178	0.205	0.869	Soil has potential to liquefy
6.725	0.198	0.214	0.929	Soil has potential to liquefy
7.725	0.245	0.208	1.179	Soil has potential to liquefy
8.725	0.336	0.202	1.663	Non-liquefiable soil

Note Soil is considered liquefiable if FOS is less than 1.2 as per IS 1893 (2016)

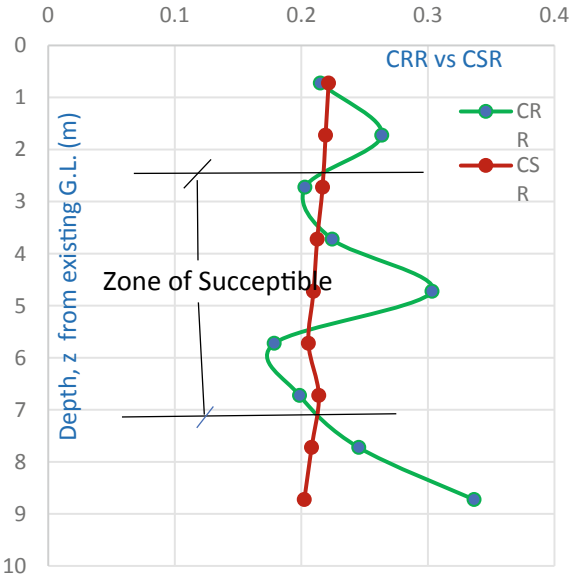

Fig. 4 Cyclic stress ratio and cyclic resistance ratio at location LBH-01

3.2 Site Responses

Site response is carried out using DEEPSOIL software based on the geotechnical investigation test results at LBH-01, LBH-02, SBH-01 and SBH-02, and Chi-Chi earthquake as input excitation. LBH is the boreholes at onshore and SBH is the boreholes in seabed, i.e., Offshore. The DEEPSOIL site response of onshore location is presented in Fig. 5.

In the case of offshore site response analysis, the depth of water above the seabed is also considered and its site response is presented in Fig. 6.

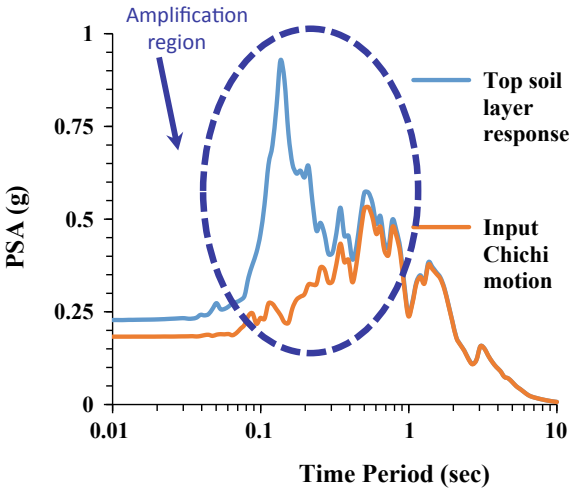

Fig. 5 Amplification study of soil at borehole location at LBH-01

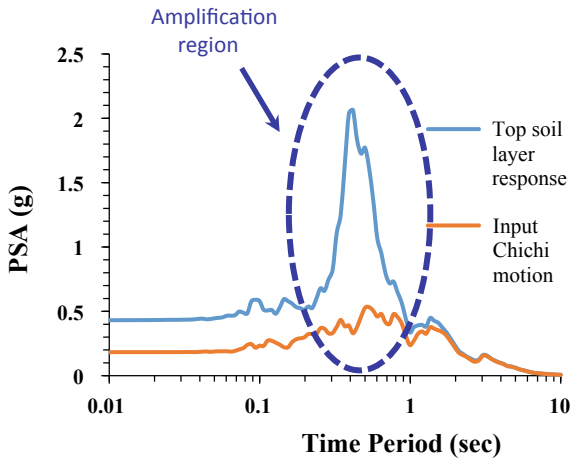

Fig. 6 Amplification study of soil at borehole location at SBH-02

It is observed the amplification of soils at top surface when subjected to earthquake loads such as Chi-Chi earthquake.

3.3 Foundation System

Considering generalized soil profile at selected site, the soil with low SPT value possessing low bearing capacity, the liquefaction is likely to occur and hence foundations going to stronger strata are recommended. Pile fFoundation may be required for supporting the heavy structure, tall and settlement sensitive structures to resist

Table 7 Vertical and lateral pile load carrying capacity

Pile diameter (m)	Pile length (m)	Vertical pile capacity (MT)	Lateral pile capacity (MT)	
		Downward	Free	Fixed
0.6	10	68.00	2.10	5.40
	12	78.00		
0.8	10	126.00	3.30	8.60
	12	164.00		
1.0	10	192.00	4.80	12.30
	12	247.00		

large uplift and lateral loads, and to limit settlement to within tolerable limits. The pile capacities are calculated based on IS 2911 (Part 1/Sec 2 2010). Considering the sub-surface soil conditions, the pile capacity for 600, 800, and 1000 mm diameter bored cast in places piles are present in Table 7. However, considering the intermediate zone of soil susceptible to liquefy, the length of pile is to be extended suitably as the frictional contribution of liquefy zone is neglected. The diameter of the pile is also to be considered against buckling instability because liquefaction of soil.

4 Conclusion

In the present paper, geotechnical investigation is performed at a selected site at Bay of Bengal, Odisha. Various dynamic properties of soil are also evaluated from cross-borehole test. Considering generalized soil profile as the soil exhibits low SPT value, possessing low bearing capacity foundations are going to stronger strata recommended. Pile foundation may be suitable option for supporting the heavy structure, tall and settlement sensitive structures. Capacity of pile foundation based on soil properties for non-liquefiable soil is evaluated. Liquefaction potential at selected site is also evaluated. As some locations, soil is found to be susceptible to liquefy, suitable engineering measures like increase the pile length pile diameter, soil stabilization, etc., are recommended. The capacity of pile shall be suitably reduced for liquefying soils based on methods available in literature.

Acknowledgements Authors would like to thank Homi Bhabha National Institute (HBNI) and BARC (Mumbai) for providing academic and research support.

References

AERB Guide No. AERB/NPP/SG/CSE-02. Geotechnical aspects and safety of foundation for building and structures important to safety of nuclear power plant

American Petroleum Institute (2011) Geotechnical and foundation design considerations. In: ANSI/API recommended practice 2GEO, 1st edn. API, Washington, Apr 2011

ASTM D4428/D4428M-14. Standard test methods for cross-hole seismic testing

Bowles JE (1997) Foundation analysis and design, 4th edn

Chang CH, Chien LK, Chang YH (2004) 3-D liquefaction potential analysis of seabed at near shore area. J Mar Sci Technol 12(3):141–151

De Groot MB, Bolton MD, Foray P, Meijers P, Palmer AC, Sandevan R, Sawicki A, Teh TC (2006) Physics of liquefaction phenomena around marine structures. J Waterw Port Coast Ocean Eng ASCE 132(4):227–243

El-Reedy MA (2011) Offshore structure design construction and maintenance. Elsevier

Haritos N (2007) Introduction to the analysis and design of offshore structures—an overview. EJSE

Hashash Y, Musgrove MA, Harmon MI, Groholski JA, Phillips DR, CA, Park D (2016) DEEPSOIL 6.1, user manual

IS 1892 (1979) Bureau of Indian Standard—code of practice for subsurface investigations for foundations

IS 1893: Part 1 (2016) Bureau of Indian Standard—criteria for earthquake resistant design of structures, general provision and buildings

IS 456 (2000) Plane and reinforced concrete: code of practice, Bureau of Indian Standard

IS 2911 (Part 1/Sec 2 2010) Design and construction of pile foundation—code of practice, Bored cast in-situ concrete pile

ISSMGE TC1 (2005) Geotechnical and geophysical investigations for offshore and nearshore developments. Technical committee 1. International Society for Soil Mechanics and Geotechnical Engineering

JRA (1996) Design specifications of highway bridges. Part V: seismic design. Japan Road Association, Tokyo, Japan

Kirca VSO, Summer BM, Fredsoe J, Summer SK (2012) Residual liquefaction under standing waves. In: International conference offshore and polar engineering, pp 1392–1398

Lehane BM, Schneider JA, Xu X (2005a) A review of design methods for offshore driven piles in siliceous sand. Report no. GEO: 05358. University of Western Australia, Perth, Geomechanics Group

Matlock H, Reese L (1961) Foundation analysis of offshore pile supported structure. In: Proceedings of 5th international conference on soil mechanics and foundation engineering. Paris, pp 91–97

Qi W-G, Gao F-P (2014) A modified criterion for wave induced momentary liquefaction of sand seabed. Theoret Appl Mech

Randolph MF (1983) Design considerations for offshore piles. In: Proceedings of the conference on geotechnical practice in offshore engineering. Austin, Texas. American Society of Civil Engineers, New York, pp 422–439

Randolph MF, Cassidy MJ, Gourvenec S, Erbrich CT (2005) Challenges of offshore geotechnical engineering. In: Proceedings of the 16th international conference on soil mechanics and geotechnical engineering. Osaka, Japan, pp 123–176

Sawicki A (2014) Mechanics of sea bed liquefaction and re-solidification. Arch Mech 66:307–328

Seed HB, Idriss IM (1971) Simplified procedure for evaluating soil liquefaction potential. J Soil Mech Found Div ASCE 97(SM9):1249–1273

Young YL, Xia OH, White JA, Borja RI (2008) Can Tsunami drawdown can lead to liquefaction failure of coastal sandy slope. In: 14th world conference on earthquake engineering

Lateral Resistance of Belled Pile Embedded in Sand

Amaresha, K. S. Rajesh, and K. V. S. B. Raju

1 Introduction

Design of foundations in offshore structures is different due to its extremely unusual site conditions with various types of soils like high spatial variation, shifting sands, hard clays and very soft to soft clayey soils. These types of soils are situated both in India Western and Eastern offshore. In offshore environment, large lateral loads are expected than when compared to axial/uplift loads.

Foundations required for transmission line towers, television tower, radar tower and multi-storey buildings have to incorporate with their self-weight and high ambitious structures like silos, overhead water tank and tall chimneys are not only concerned about transmission of large lateral loads along with uplift loads. More over, water front structures and offshore structures in hostile environment are subjected to wave action, wind gust and thrust from floating vessels result in tension in foundation.

Belled or under-reamed pile is one of the best options for these conditions. Belled piles are bored cast in situ and bored compaction concrete types having one or more bells. Belled piles are widely used in varying moisture conditions and problematic soils like expansive soil. Bell of the under-reamed pile provides anchorage against uplift due to swelling pressure apart from the increased bearing. Since base area of belled piles increases, it increases end bearing capacity and in turn it increases lateral load carrying capacity.

Amaresha (✉)
Department of Civil Engineering, Presidency University, Bengaluru, Karnataka, India
e-mail: amareshacp17@gmail.com

K. S. Rajesh · K. V. S. B. Raju
Department of Civil Engineering, Bangalore University, Bengaluru, Karnataka 560056, India

S. Haldar et al. (eds.), *Advances in Offshore Geotechnics*, Lecture Notes in Civil Engineering 92, https://doi.org/10.1007/978-981-15-6832-9_22

2 Literature Review

Previous researches on lateral load carrying capacity of belled piles are limited. Dhatrak et al. (2018) studied experimental study on belled wedge pile for different loadings in cohesionless soil. They conducted series of experiments on model single pile and group of circular-, tapered-, belled-, belled-edge-shaped piles embedded in sand. Pile load tests are also carried out in order to determine vertical load capacity and uplift capacities. From the test results, vertical and uplift load capacities of belled wedge pile and belled piles are much higher than conventional piles.

Kong et al. (2012) studied comparative analysis of single belled wedge pile with conventional piles under lateral load. They analysed models of conventional belled pile, tapered pile and uniform section pile and models of single belled wedge pile embedded on soft soils built by *p–y* curves method via *L* PILE software. It was found that belled piles behaved better than circular and tapered piles.

Dickin et al. (1990) studied Performance of piles with enlarged bases subject to uplift forces. The influence of embedment, base diameter, and backfill density on the uplift behaviour of piles with enlarged bases embedded in sand was investigated in a centrifuge. Comparative tests on straight-shafted piles are also reported. For piles in dense sand, sensible agreement was found with earlier research on anchor plates and published field data.

3 Materials and Methods

For the present experimental study, materials used are sand, model belled pile, and model monopile without bell. Model piles were made up of aluminium.

3.1 Sand

In the present work, dry clean river sand is used as foundation bed. Different tests were conducted on sand to determine its engineering properties according to relevant IS codes. The properties of sand used are summarized in Table 1.

3.2 Model Pile

Scaling of properties to choose aluminium piles was not done; however, based on stiffness consideration and based on literature studies, aluminium model piles were chosen for study. So three different piles of length 24 cm, 36 cm and 48 cm corresponding to *L*/*d* ratios of 5, 7.5 and 10, respectively. Diameter of pile used was 48 mm

Table 1 Properties of sand

Properties	Sand
Uniformity coefficient (Cu)	2.71
Coefficient of curvature (Cc)	0.91
Specific gravity (G)	2.61
Maximum unit weight (γ_{max}), e_{min}	17.5 kN/m^3, 0.49
Minimum unit weight (γ_{min}), e_{max}	15.69 kN/m^3, 0.66
D10, D30, D60	0.28, 0.44, 0.76
Angle of internal friction (φ)	32° (RD = 35%), 36 (RD = 55%)
I.S classification	SP

Table 2 Properties of model pile

Parameter	Model pile
Material	Aluminium
Modulus of elasticity, E GPa	70
Length (cm)	24 ($L/d = 5$), 36 (7.5), 48 (10)
Outer diameter (mm)	48
Thickness (mm)	5
Bell angle (°)	30, 45, 60
Bell diameter (mm)	72 ($D_b/D_s = 1.5$), 96($D_b/D_s = 2$)

for both monopile and belled pile. Bell angle of 30°, 45° and 60° are used. Along with this, bell diameter (D_b) to shaft diameter (D_s) ratios of 1.5 and 2 were used to understand the effect of bell diameter on lateral load carrying capacity. As in offshore foundations, mostly, the piles are large diameter bored cast in situ piles, and hence enlarged base will not pose much difficulty as in case of driven piles. The properties of model pile used are given in Table 2 and the model belled piles for different bell angle θ (30°, 45° and 60°) and model monopiles are shown from Figs. 1, 2, 3 and 4, respectively.

3.3 Experimental Setup

Reduced scale physical model piles are used in the present studies. The monopile of diameter 48 mm and lengths of 24, 36 and 48, cm i.e. L/d ratio of 5, 7.5 and 10 were used. Belled pile of same L/d ratio with bell diameter 72 and 96 mm and bell angles of 30°, 45° and 60° were used. Sand is poured into the tank by using rainfall technique. The lateral load is applied to the pile through hand winch with

Fig. 1 Model belled pile for $L/d = 5$

Fig. 2 Model belled pile for $L/d = 7.5$

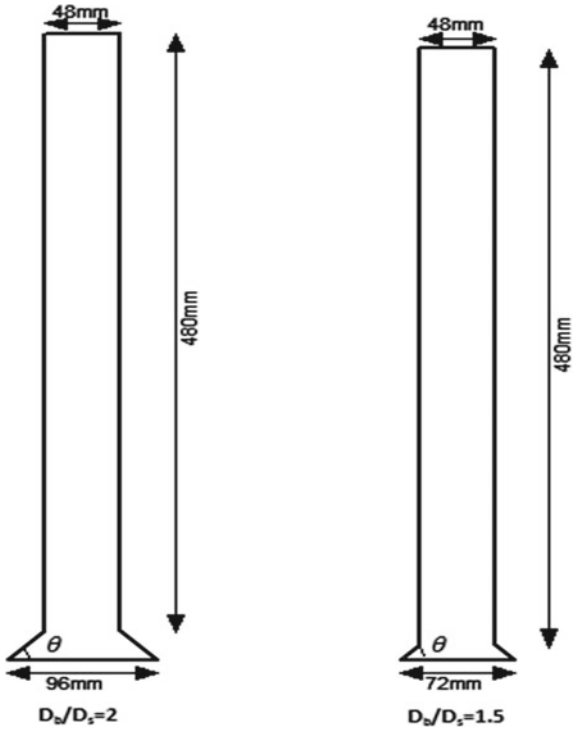

Fig. 3 Model belled pile for $L/d = 10$

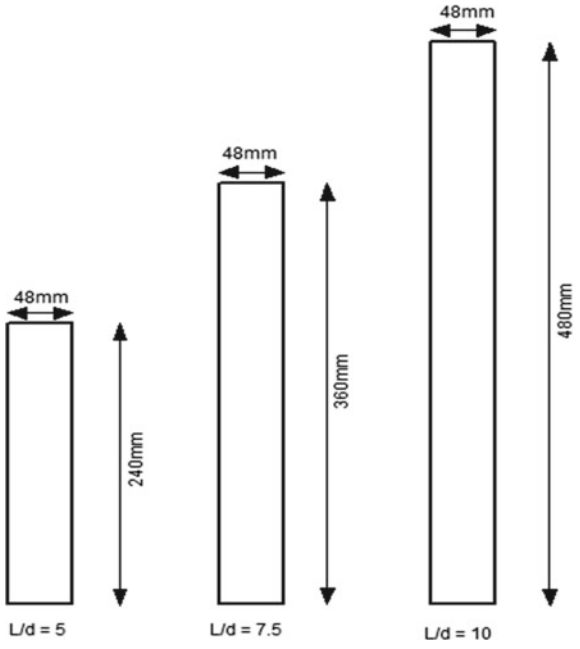

Fig. 4 Model monopiles (without bell) for different L/d ratio

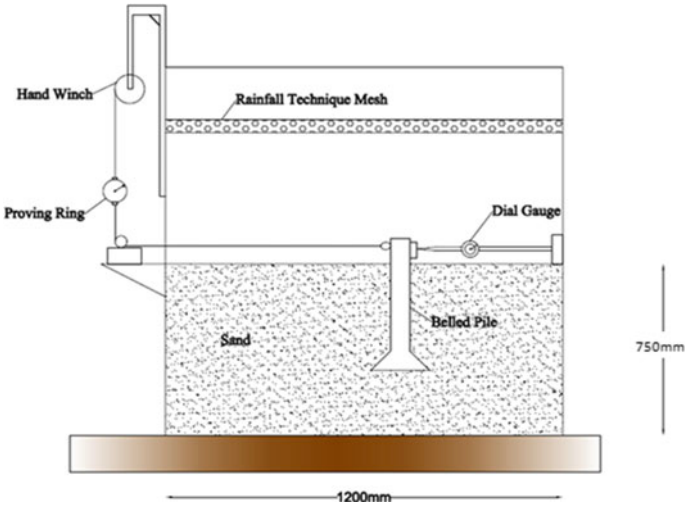

Fig. 5 Experimental setup

belt attached to saddle and displacements are monitored for applied load increment with the help of magnetic mount dial gauge. An experimental setup for the present study is shown in Fig. 5.

3.4 Experimental Procedure

The objective of the present study is to determine the lateral load carrying capacity of belled pile in comparison with monopile. The experiment consists of mild steel model tank of size (1200 × 720 × 750) mm, in which belled pile of shaft diameter 48 mm, bell diameter of 72 mm and 96 mm and thickness 5 mm are embedded. The experiment is carried out for *L*/*d* ratio of 5, 7.5 and 10 with bell angles of 30°, 45° and 60°. The experiment is also conducted for monopile of 48 mm diameter and thickness of 5 mm for the same *L*/*d* ratios of 5, 7.5 and 10. The tank is filled with sand (which is sun dried or oven dried) using rainfall technique which is achieved by pouring the sand through a raining box, and this height is maintained uniformly for subsequent increment in the height of fall to achieve required density and this density is predetermined.

In offshore environment, loads are cyclic lateral loads due to waves and water effects, but however the present study is confined to static lateral loads of model piles embedded in dry sand. However, based on mechanics of sand, the pore pressure generated will be very less as it is a clean sand and tests are conducted for drained conditions in case of sands, so the condition of testing dry sand will not cause much error. Hence, lateral/horizontal force is applied to the pile through belt in which one end of the belt is attached with a hook, which is connected to the centre of the

pile saddle and the other end is connected to the proving ring and this proving ring is connected to a manually operated hand winch. The hand winch is mounted on extension at the top of mild steel tank itself. The dial gauge with magnetic stand is rigidly mounted on to the MS tank, so as to measure the displacement of the different piles to the lateral loading. Readings are taken up to the maximum deformation of 50 mm. The above procedure is carried out different relative densities, *L*/*d* ratios and D_b/D_s ratios. Finally, lateral load v/s displacement graphs are plotted, and peak load obtained from the plot represents the ultimate lateral resistance of the sand-pile corresponding to embedment depth of piles and density of the sand.

4 Results and Discussion

The variation of the lateral load (P_L) acting on the monopile and corresponding changes in the horizontal displacement (δ) were obtained for loose sand condition (relative density of 35%) and medium dense condition (relative density of 55%) with varying *L*/*d* ratios of 5, 7.5 and 10. Static lateral load test is performed on belled pile with varying D_b/D_s of 1.5 and 2 for same *L*/*d* ratios and relative densities and corresponding results are compared with monopile.

Variations of lateral load and horizontal displacements curves are plotted for different conditions and corresponding results are shown from Figs. 6, 7, 8, 9, 10, 11, 12, 13, 14, 15, 16, 17, 18 and 19.

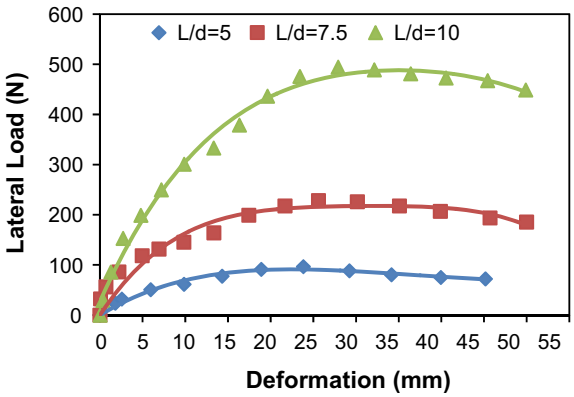

Fig. 6 Variations of lateral load and displacement curve for different *L*/*d* ratios

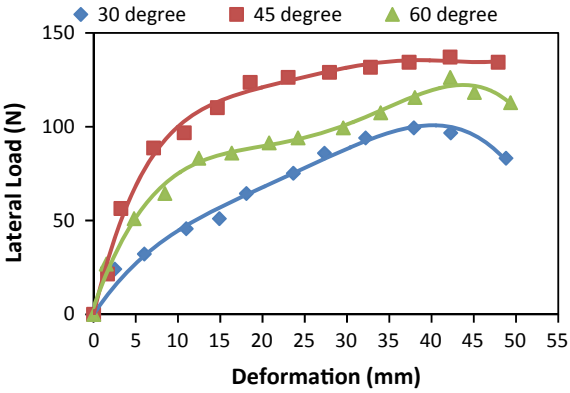

Fig. 7 Variations of lateral load and displacement curve for $L/d = 5$

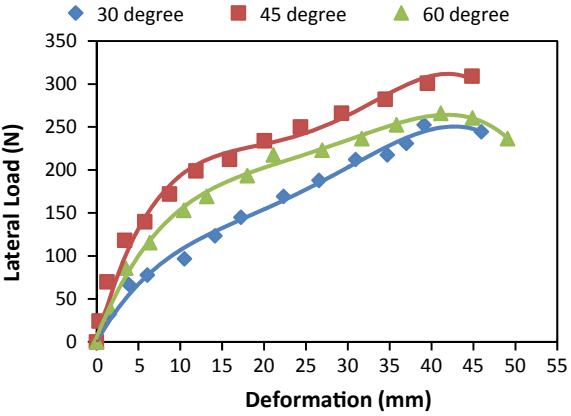

Fig. 8 Variations of lateral load and displacement curve for $L/d = 7.5$

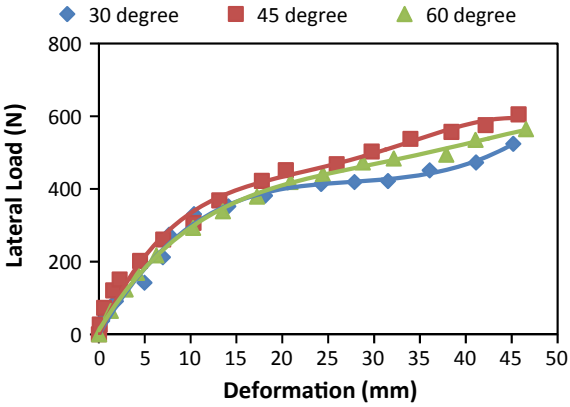

Fig. 9 Variations of lateral load and displacement curve for $L/d = 10$

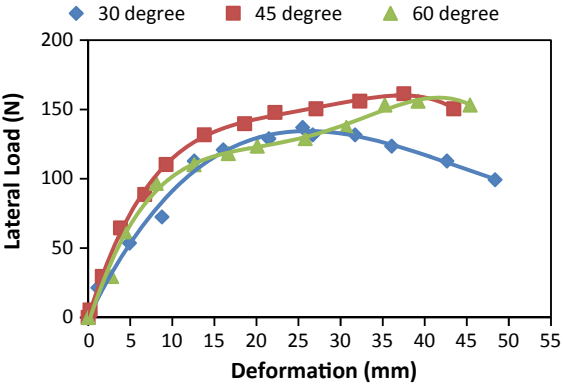

Fig. 10 Variations of lateral load and displacement curve for $L/d = 5$

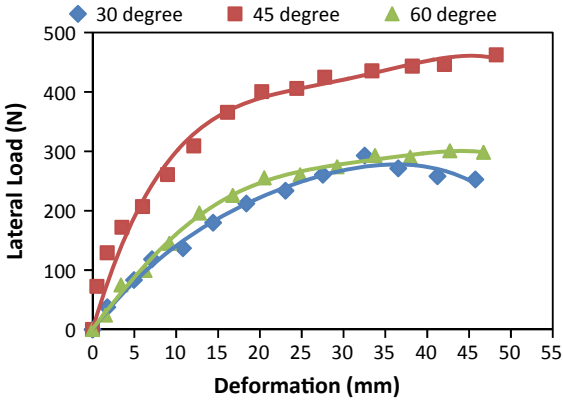

Fig. 11 Variations of lateral load and displacement curve for $L/d = 7.5$

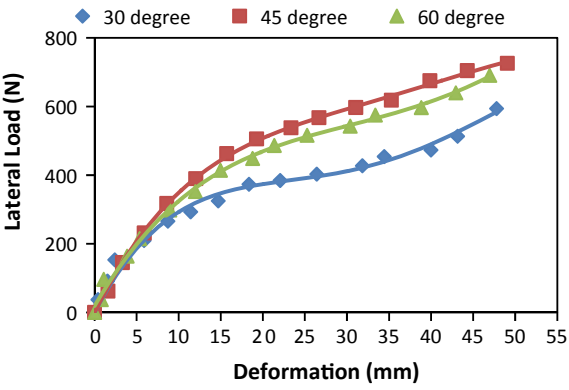

Fig. 12 Variations of lateral load and displacement curve for $L/d = 10$

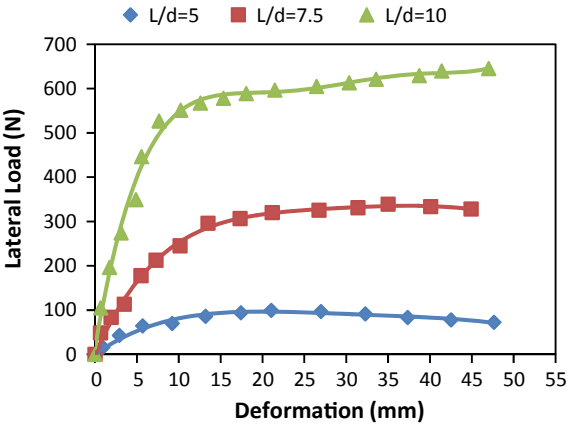

Fig. 13 Variations of lateral load and displacement curve for $L/d = 5$

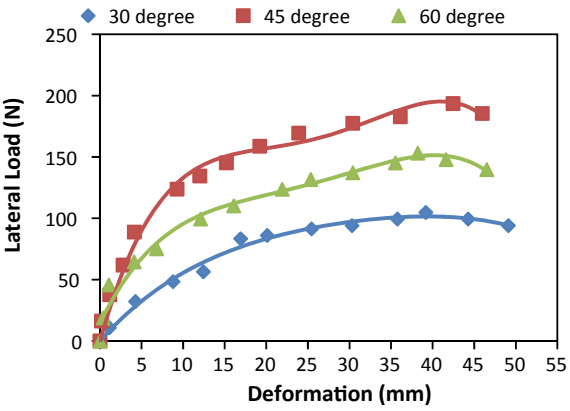

Fig. 14 Variations of lateral load and displacement curve for $L/d = 5$

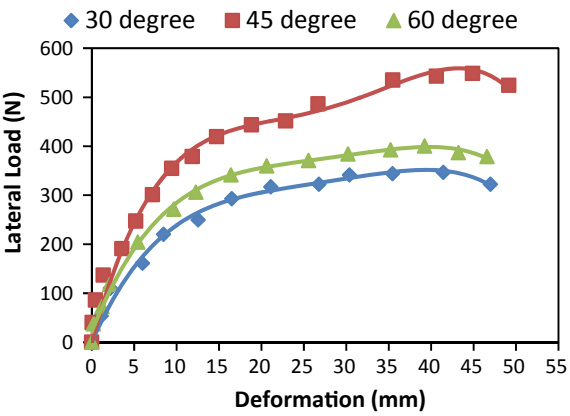

Fig. 15 Variations of lateral load and displacement curve for $L/d = 7.5$

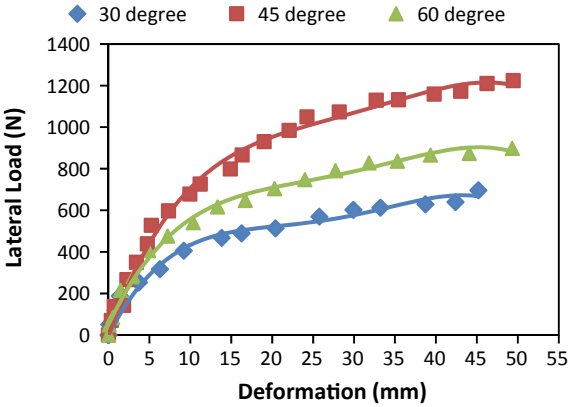

Fig. 16 Variations of lateral load and displacement curve for $L/d = 10$

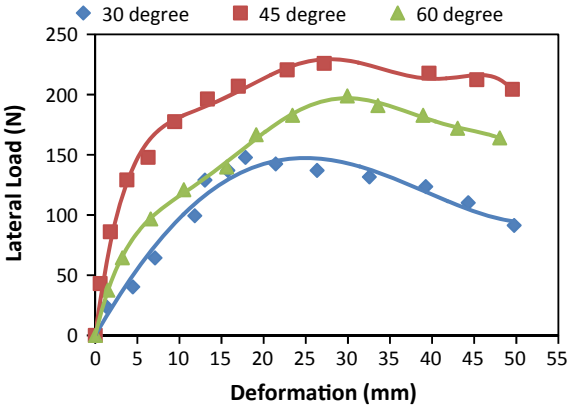

Fig. 17 Variations of lateral load and displacement curve for $L/d = 5$

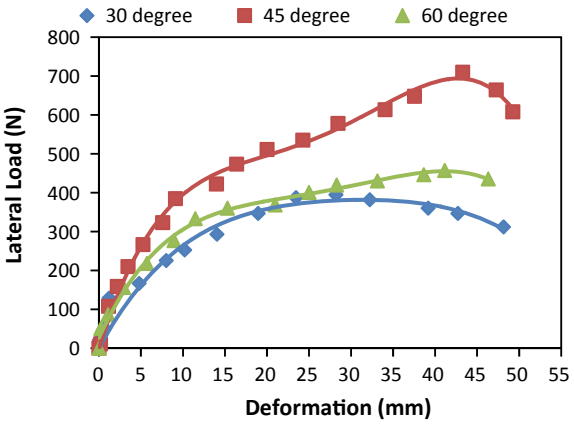

Fig. 18 Variations of lateral load and displacement curve for $L/d = 7.5$

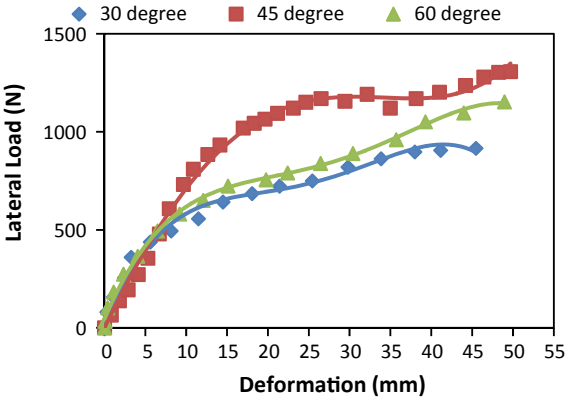

Fig. 19 Variations of lateral load and displacement curve for $L/d = 10$

4.1 Curves for Monopiles (Without Bell) with Relative Density of 35%

Figure 6 shows the variation of lateral load with displacement for a monopiles of different L/d ratios by maintaining relative density of 35%. From these figures, it is observed that, the measured displacement for the peak load of 96 N is 24 mm for L/d ratio of 5 and 235 N is found for corresponding displacement of 28 mm for L/d ratio of 7.5 and for L/d ratio of 10, the peak load of 500 N is found for corresponding displacement of 29 mm. It is clearly observed that, by increasing L/d ratio peak load as well as displacement is increased.

4.2 Curves for Belled Pile of $D_b/D_s = 1.5$ with RD = 35%

Figures 7, 8 and 9 show the variation of lateral load with displacement for different belled angles of 30°, 45° and 60° with D_b/D_s of 1.5 for different L/d ratios by maintaining relative density of 35%. From these figures, for L/d ratio of 5, the maximum measured displacement for the peak load of 136 N is 40 mm. For L/d ratio of 7.5, the maximum measured displacement for the peak load of 310 N is 42 mm and for L/d ratio of 10, the maximum measured displacement for the peak load of 600 N is 45 mm is observed for bell angle of 45°.

4.3 Curves for Belled Pile of $D_b/D_s = 2$ with RD = 35%

Figures 10, 11 and 12 show the variation of lateral load with displacement for different belled angles of 30°, 45° and 60° with D_b/D_s of 2 for different L/d ratios by maintaining relative density of 35%. From these figures, for L/d ratio of 5, the maximum

measured displacement for the peak load of 160 N is 37 mm, for *L*/*d* ratio of 7.5, the maximum measured displacement for the peak load of 460 N is 45 mm and for *L*/*d* ratio of 10, the maximum measured displacement for the peak load of 730 N is 49 mm are observed for 45° bell angle.

4.4 Curves for Monopiles (Without Bell) with Relative Density of 55%

Figure 13 shows the variation of lateral load with displacement of monopile for different *L*/*d* ratios by maintaining relative density of 55%. From these figures, it is observed that maximum values are achieved for a belled angle of 45° and for *L*/*d* ratio of 5, the maximum measured displacement for the peak load of 90 N is 20 mm, for *L*/*d* ratio of 7.5 the maximum measured displacement for the peak load of 335 N is 37 mm and for *L*/*d* ratio of 10, the maximum measured displacement for the peak load of 640 N is 47 mm. It is clearly observed that, by increasing *L*/*d* ratio peak load as well as displacement is increased.

4.5 Curves for Belled Pile of $D_b/D_s = 1.5$ *with RD = 55%*

Figures 14, 15 and 16 show the variation of lateral load with displacement for different belled angles of 30°, 45° and 60° with D_b/D_s of 1.5 for different *L*/*d* ratios by maintaining relative density of 55%. From these figures also, we can observed maximum peak load for bell angle of 45° only and for *L*/*d* ratio of 5, the measured displacement for those peak load of 195 N is 41 mm, for *L*/*d* ratio of 7.5, the measured displacement for those peak load of 560 N is 43 mm and for *L*/*d* ratio of 10, the measured displacement for those peak load of 1210 N is 46 mm.

4.6 Curves for Belled Pile of $D_b/D_s = 2$ *with RD = 55%*

Figures 17, 18 and 19 show the variation of lateral load with displacement for different belled angles of 30°, 45° and 60° with D_b/D_s 2 for different *L*/*d* ratios by maintaining relative density of 55%. From these figures, for *L*/*d* ratio of 5, the measured displacement for the maximum peak load of 230 N is 28 mm, for *L*/*d* ratio of 7.5, the measured displacement for the maximum peak load of 700 N is 43 mm and for *L*/*d* ratio of 10, the measured displacement for the maximum peak load of 1360 N is 50 mm are observed for bell angle of 45°.

The observed peak loads of monopile and belled pile for different conditions from Figs. 6, 7, 8, 9, 10, 11, 12, 13, 14, 15, 16, 17, 18 and 19 are mentioned in the Table 3.

Table 3 Peak loads for different conditions in *N*

RD = 35%				RD = 55%		
Bell angle	$D_b/D_s = 2$					
	L/*d*			*L*/*d*		
	5	7.5	10	5	7.5	10
30	134	280	590	148	380	940
45	160	460	730	230	700	1360
60	158	300	680	190	460	1140
Bell angle	$D_b/D_s = 1.5$					
	L/*d*			*L*/*d*		
	5	7.5	10	5	7.5	10
30	100	250	520	102	350	730
45	136	310	600	195	560	1210
60	124	265	560	154	400	910
Monopile	96	235	500	90	335	640

The percentage increase of peak load of belled pile w.r.t. monopile is mentioned in Table 4.

From Table 3, it is concluded that as *L*/*d* ratio increases lateral load carrying capacity increases. This is due to increase in shaft resistance along the pile. In a similar way, as D_b/D_s ratio increases, lateral load carrying capacity increases due to increase in bearing resistance at the base of bell. When relative density increases, load carrying capacity increases as expected. Because as relative density increases, relative stiffness ratio of soil and pile increases, which caused the behaviour of the

Table 4 Percentage increase of peak load of belled pile w.r.t. monopile (%)

RD = 35%				RD = 55%		
Bell angle	$D_b/D_s = 2$					
	L/*d*			*L*/*d*		
	5	7.5	10	5	7.5	10
30	40	19	18	64	13	47
45	67	96	46	156	109	113
60	65	28	36	111	37	78
Bell angle	$D_b/D_s = 2$					
	L/*d*			*L*/*d*		
	5	7.5	10	5	7.5	10
30	4	6	4	13	4	14
45	42	32	20	117	67	89
60	29	13	12	71	19	42

pile in medium dense sand to be elastic rather than rigid. When pile is tested for different bell angles like 30°, 45° and 60°, lateral load carrying capacity for bell angle 45° was more among three.

From the results, we can assume that as bell angle increases, lateral load carrying capacity increases up to certain angle, then after load carrying capacity decreases. For bell angle of 45°, shearing resistance developed within soil on the cylinder circumscribing the bell is more and resultant resistive forces on the bell are greater than other two bell angles. Hence, among three, bell angle of 45° acts as optimum bell angle. Even according to IS 2911(1980)-Part 3, bell angle used in the field is 45°.

As applied load increases, lateral load carried by the belled pile increases which results in higher peak load than monopile. From Table 3, we can conclude that peak loads for belled piles are more than the monopile for all different conditions.

The same behaviour of belled piles is confirmed by Table 4, which represents percentage increase or decrease in the allowable load and peak load of belled pile with respect to monopile, respectively.

5 Conclusions

In the present study, a series of model tests on aluminium model piles with and without bell (enlarged base) was investigated, which is embedded in dry sand at relative density of 35% and 55%. The ratio of diameter of bell to diameter of plain shaft was varied for 1.5 and 2 and bell angles of 30°, 45° and 60°.The following conclusions were drawn:

1. As the L/d ratio; (where L = length of pile, d = diameter of pile shaft) increases from 5 to 10, the lateral load carrying capacity was found to increase.
2. As the relative density of sand increases, the lateral resistance was found to increase.
3. As the ratio of D_b/D_s (Where D_b = diameter of bell, D_s = diameter of plain shaft or monopile increases from 1.5 to 2, peak lateral load was found to increase.
4. As applied load increases, lateral load carried by the belled pile increases which results in higher peak load than monopile. Further, it can be concluded that peak loads for belled piles are more than the monopile for all different conditions.
5. When pile is tested for different bell angles like 30°, 45° and 60°, lateral load carrying capacity for bell angle 45° was more among three. The same behaviour of belled piles and monopiles is confirmed by the percentage increase in peak load. The amount of increase in percentage of peak load for bell angle 45° was found to be higher than other two. Also, as D_b/D_s ratio increases from 1.5 to 2, amount of percentage increase was found more in peak load for all different conditions.

6. The present study will be useful in the study of lateral resistance of belled pile embedded in sand, where large lateral loads are expected for structures in offshore environment.

References

Dhatrak AI, Ghawd M, Thakare SW (2018) Experimental study on belled wedge pile for different loadings in cohesionless soil. In: Indian geotechnical conference. IISc Bengaluru

Dickin EA, Leung CF (1990) Performance of piles with enlarged bases subject to uplift forces. Can Geotec J 27(5):546–556

IS: 2911 (1980) (Part-3) Indian standard code of practice for design and construction of pile foundations for under-reamed piles

Kong G (2011) Performances of compressive capacity for belled wedge pile group. In: Advanced materials research. Trans Tech Publications, Switzerland

Kong G, Tan X, Deng Z, Jin Z (2012) Comparative analysis of single belled wedge pile with conventional piles under lateral load. In: Advanced materials research, vols 594–597. Trans Tech Publications, Switzerland, pp 50–55

Kong GQ, Yangb Q, Liua HL, Liangc RY (2013) Numerical study of a new belled wedge pile type under different loading modes. Eur J Env Civ Eng, Europe

Behaviour of Screw Pile Under Axial Compressive and Lateral Loading in Sand for Offshore Energy Foundations

P. V. Pavan Kumar, Shantanu Patra, and Sumanta Haldar

1 Introduction

The increase in demand for renewable energy in the offshore environment suggests moving into deeper waters for the generation of energy from wind turbines. The foundations of these structures are generally subjected to a significant amount of axial (compression and tension) and lateral loads (Al-Baghdadi et al. 2015; Byrne and Houlsby 2006). Conventionally, monopiles are widely used to support wind turbines. However, to support the higher capacity wind turbines in the deep waters (>30 m) tripod or jacket structures supported by smaller diameter driven piles are employed (Al-Baghdadi et al. 2017; Spagnoli 2017) as shown in Fig. 1.

A large deployment of these driven piles causes a significant amount of vibration during driving operations which is detrimental to marine life (Houlsby 2016). In this regard, screw piles are considered to be the potential alternative to the driven piles for jacket/tripod supported wind turbines (Byrne and Houlsby 2015; Spagnoli et al. 2015). Screw piles consist of a central shaft with one or more helixes attached to it which are installed into the ground by applying torque and vertical load with the help of hydraulic torque motor (Houlsby 2016; Spagnoli et al. 2015). Figure 2 shows the installation of screw pile in the field (Sakr 2011). Typical onshore screw piles consist of small diameter shaft and helix and are required to be upscaled to meet the loading criteria for offshore application (Al-Baghdadi et al. 2017; Houlsby 2016).

Piles supporting the offshore jacket/tripod structures are subjected to both combined axial (compression and tension) and lateral loads. Screw piles are superior in resisting this axial compression and tensile loads compared to conventional pile foundations (Spagnoli et al. 2015). Several studies in the literature were available regarding the performance of screw pile considering the installation (Spagnoli et al.

P. V. Pavan Kumar · S. Patra (✉) · S. Haldar
School of Infrastructure, Indian Institute of Technology Bhubaneswar, Argul, Khordha, Odisha 752050, India
e-mail: shantanupatra@iitbbs.ac.in

S. Haldar et al. (eds.), *Advances in Offshore Geotechnics*, Lecture Notes in Civil Engineering 92, https://doi.org/10.1007/978-981-15-6832-9_23

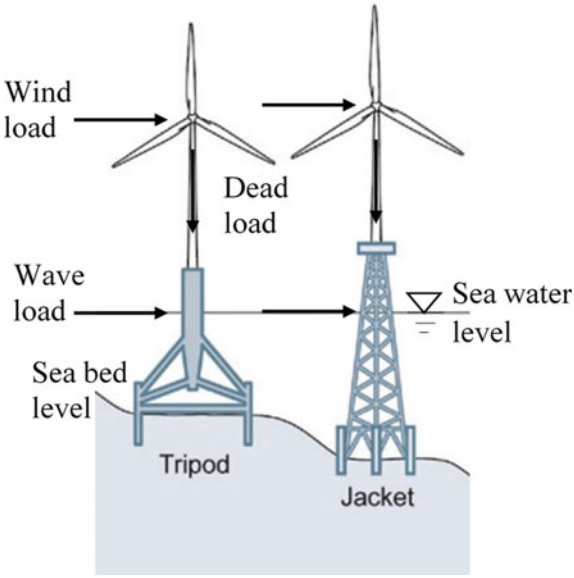

Fig. 1 Tripod and jacket structures supporting wind turbines (World Steel Association 2012)

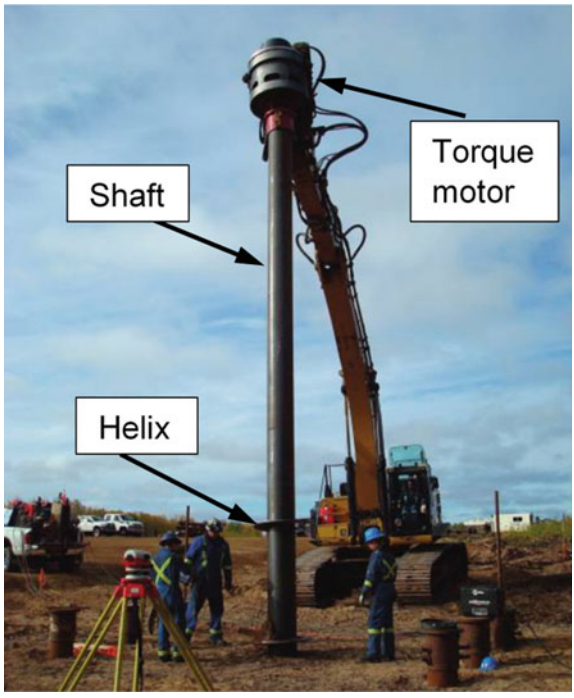

Fig. 2 Typical field installation of screw pile (Sakr 2011)

2016; Davidson et al. 2018), estimating the tensile capacity (Spagnoli et al. 2018), compressive capacity (Elsherbiny and El Naggar 2013; Knappett et al. 2014) and lateral capacity (Al-Baghdadi et al. 2015; Kumar et al. 2019a). The above studies show that the compressive and tensile capacity is significantly increased in the case of screw piles. However, to enhance the lateral capacity the geometry of the shaft plays a significant role than the helix geometry (Kumar et al. 2019b). The behaviour of the screw piles under the combined load is little known with the exception of Al-Baghdadi et al. (2017). However, the study does not present the optimum placement of the helix in the case of lateral or combined loading conditions. It is significant to know the behaviour of the screw piles under the combined loading conditions when these are used to support the renewable energy structures which incur huge amount of money.

In the present study, three-dimensional numerical analysis has been carried out using ABAQUS 2018 on the single- and double-helix screw piles under combined axial compression and lateral loads. The effect of placement of the helix in the case of screw piles is studied, and it is observed that the placement of helix place a significant role in increasing the lateral capacity. The results were also compared with that of the straight shaft piles to showcase the improved performance of the screw pile over the straight shaft piles under combined loading conditions. Preliminarily in the present study, for the case of combined loading the helixes are placed below the point of rotation of a straight shaft pile corresponding to 20-mm-pile head deflection. This placement of helix has a negligible effect in increasing the lateral capacity of the screw pile for both single and double-helix piles. Therefore, the position of the helix is changed to improve the lateral performance of the screw pile and is discussed further.

2 Soil and Screw Pile Configuration

A cohesionless soil of medium density is considered in the study, and the properties are shown in Table 1. Two types, namely single- and double-helix with open-ended hollow screw piles, were chosen with material and geometry properties as shown

Table 1 Soil properties

Property	Value
Unit weight, γ (kN/m^3)	16
Young's modulus, E (kN/m^2)	40,000
Poisson's ratio (μ)	0.3
Angle of internal friction, φ (°)	30
Dilation angle, ψ (°)	0
Cohesion, c (kN/m^2)	1

Table 2 Screw pile properties

Property	Value
Young's modulus, E (kN/m^2)	200×10^6
Poisson's ratio (μ)	0.27
Density, ρ (kg/m^3)	7850
Pile shaft diameter, D (m)	0.5
Pile shaft thickness, t (m)	0.0125
Helix thickness, t_h (m)	0.025
Helix diameter, D_h (m)	1

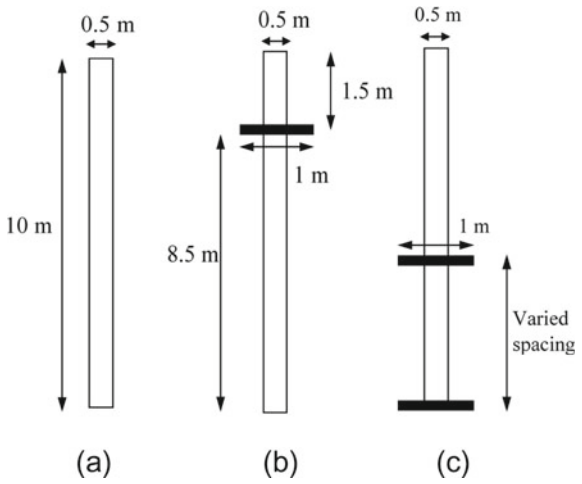

Fig. 3 Pile geometry: **a** straight shaft pile and **b** single-helix pile (helix placed at maximum lateral stress **c** double-helix pile

in Table 2. Screw pile of embedment length 10 m with a constant shaft and helix diameter of 2.5 m and 5.0 m were chosen, respectively, for the present study.

The configurations of the piles considered in the study are shown in Fig. 3. For the single-helix pile, the helix is placed at the bottom, at point of rotation (POR) and at maximum lateral stress location, and in case of double-helix pile, one-helix is placed at the bottom and the spacing is varied as 1, 2.5 and 5 times the diameter of the helix.

3 Numerical Modelling

In the present study, a three-dimensional numerical model is developed using commercially available software ABAQUS 2018. Figure 4 shows the finite element meshing and boundary extents and Fig. 5 shows the boundary and loading conditions for the model. The soil is modelled as an elasto-plastic continuum considering Mohr–Coulomb failure criteria and the screw pile as a linear elastic material. Both

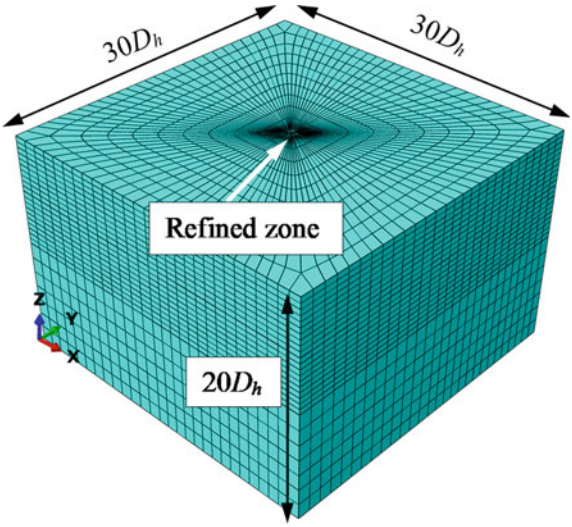

Fig. 4 Finite element mesh with boundary extents

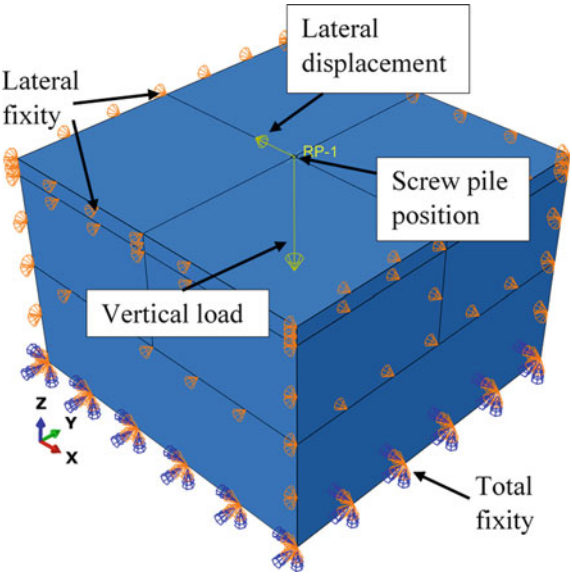

Fig. 5 Finite element model with boundary and loading conditions

the soil and the screw pile were modelled using eight-node brick with reduced integration elements (C3D8R). A total of 38,299 number of elements were generated. To minimize the complexity of the model, the screw is modelled as a flat plate, the assumption of which does not influence or have a negligible effect on the results (Al-Baghdadi et al. 2017).

The boundary conditions of the model are carefully chosen such that there is no boundary effect, which is 30 times the diameter of the helix (D_h) in plan and 20 times

the diameter of the helix along with the depth. Soil top surface is considered to be free; the bottom surface is fully fixed; and the sides of the soil are horizontally fixed. Pile–soil interface is modelled using the Coulomb frictional model considering the master–slave approach in Abaqus by providing a frictional coefficient of 0.7.

4 Loading Condition

Initial loading involves applying the gravity loading to generate the initial stresses followed by the displacement controlled load to find the ultimate compressive capacity (V_{ult}) corresponding to 10% displacement of pile shaft diameter. In the case of combined loading in addition to the compressive vertical loading (V), displacement controlled analysis (20 mm displacement) is carried out to determine the allowable lateral loading. The vertical load is considered in terms of the percentage (0, 25, 50 and 75%) of the ultimate compressive capacity. All the loads are applied through a reference point rigidly constrained to the pile head.

5 Results and Discussion

5.1 Compressive Loading

The axial compressive capacity of the straight shaft, single- and double-helix screw piles were shown in Fig. 6. It is observed that the axial capacity (V_{ult}) of the single-helix screw pile is around 2.5 times higher than that of straight shaft pile.

In the case of a double-helix screw pile, the maximum increase in the capacity is observed to be around 1.7 times that of a single-helix screw pile for the spacing of $5D_h$. However, the increase in the capacity is very minimum/almost constant when the spacing of the helix is changed from $2.5D_h$ to $5D_h$. This behaviour is observed

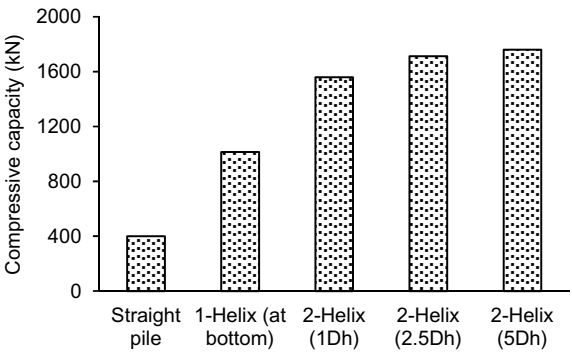

Fig. 6 Compressive capacity of the straight shaft and screw piles

as the spacing is increased the helixes behave individually in bearing leading to individual failure mechanism.

5.2 Lateral Loading

It is observed that the allowable lateral load corresponding to a lateral displacement of 20 mm (4% pile shaft diameter) at the pile head is almost constant for the straight shaft, single-helix, and double-helix piles and is shown in Fig. 7. These invariant load values are observed because of the placement of the helix/es below the point of rotation. The point of rotation corresponding to the 20-mm-lateral deflection is observed at a depth of 4 m from the ground surface. Therefore to determine the effect of the helix in improving the performance of the screw pile, it is important to note that the helix should be placed above the point of rotation.

Hence, in the present study, the placement of helix is changed in the case of the single-helix piles. Where in one case the helix is provided at the point of rotation and in another case, the helix is placed at the location of maximum lateral stress corresponding to the straight shaft pile which is observed to be at a distance of 1.5 m from the ground surface. Load control analysis (200 kN in the present study) is carried out to determine the pile head deflection.

It is observed that there is a negligible change in the lateral deflection of the pile head when the helix is placed at the point of rotation even compared to the straight shaft pile (Fig. 8). The pile head deflection is reduced around 21% compared to the straight shaft pile/helix at POR when the helix is placed at the location of maximum lateral stress. This reduction in the deflection is found as the helix could take the additional bearing resistance, thereby reducing the lateral deflection when it is subjected to lateral loading.

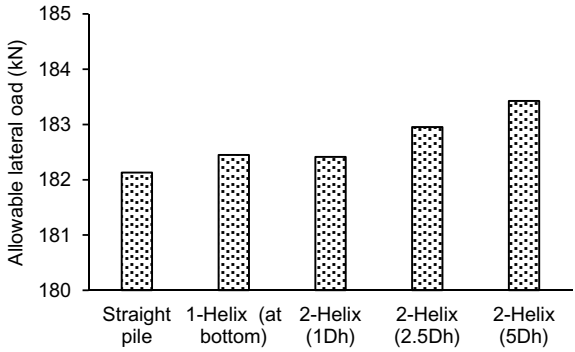

Fig. 7 Lateral capacity of the straight shaft and screw piles

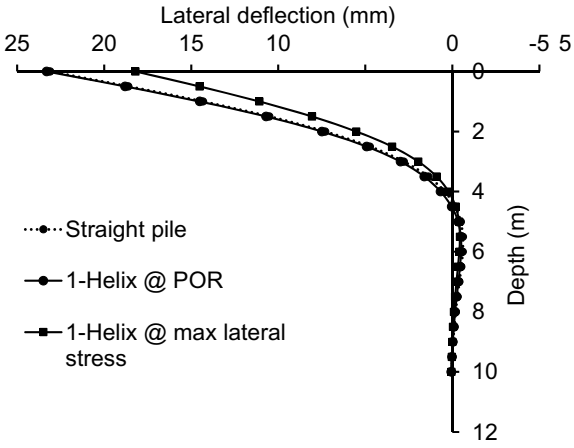

Fig. 8 Lateral deflection of pile head under lateral loading

5.3 Combined Compressive and Lateral Loading

It is observed from the above results that the placement of helix below the point of rotation does not enhance the lateral capacity of the single-helix and double-helix piles. Therefore for the combined loading conditions, the performance of the single-helix pile with helix location at maximum lateral stress is studied. Figure 9 shows the load–deflection behaviour screw pile with the change in the percentage of ultimate vertical loading. It is found that the lateral capacity of the screw pile increases with the increase in vertical compressive loading. Around 34% increase in lateral capacity is observed when the vertical load is increased from 0 to 75%. The combined loading behaviour of the straight shaft pile and the screw pile with a single helix at maximum lateral stress is shown in Fig. 10.

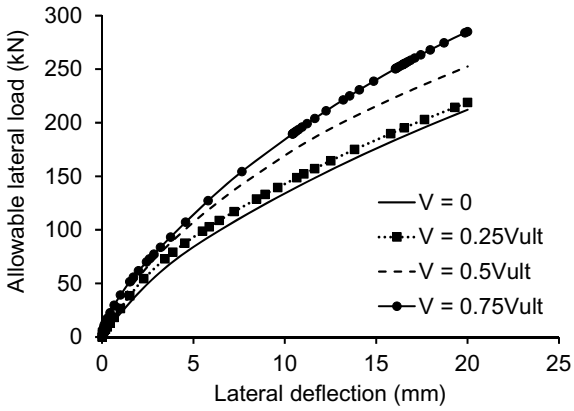

Fig. 9 Lateral load–deflection curve for combined loading condition

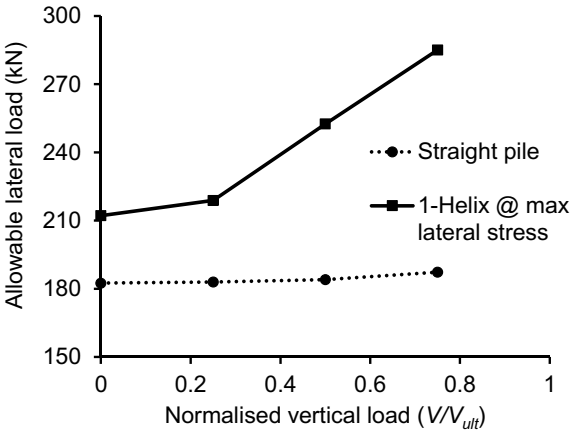

Fig. 10 Effect of the vertical loading on the allowable lateral load of the straight shaft and single-helix screw piles

It can be seen that the lateral capacity of the straight shaft pile is almost unchanged even with an increase in the compressive loading. Since the pile considered here is flexible, the lateral resistance along the pile depth is not fully mobilized in case of the straight shaft piles. This results in a negligible increase in the lateral load. Under no vertical load condition, the single-helix pile shows around a 16% increase in the lateral capacity compared to the straight shaft pile. However, the single-helix pile is showing an appreciable increase in the lateral load with an increase in compressive load. In this case, when the lateral displacement is applied under a constant vertical load, the helix contributes in enhancing the lateral capacity by having a bearing type mechanism in front of the pile. Also, the helix contributes in improving the confinement of the soil around the shaft due to the vertical loading thereby enhances the lateral capacity of the screw pile.

The reduction in the pile head deflection for a constant lateral load of 200 kN under varying compressive load is shown in Fig. 11. It is determined that pile head deflection is reduced around 39% when there is a compressive load of $0.75V_{\text{ult}}$ compared to no vertical compressive load. The confinement produced by the vertical load causes a reduction in the lateral deflection. Similarly, the lateral stress variation in the soil is shown in Fig. 12 along with the depth of soil at the contact of pile and soil for the combined loading. The lateral stresses on the soil are reduced for higher vertical loading. However, at the helix junction, the stresses are increased as the stress concentration is more at the junction.

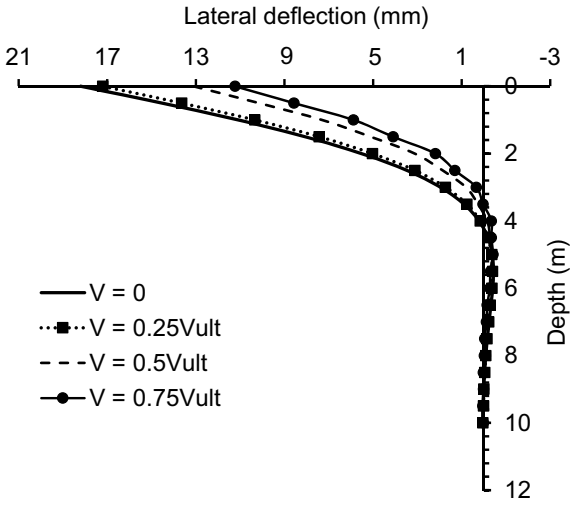

Fig. 11 Effect of the vertical loading on the lateral deflection of the pile

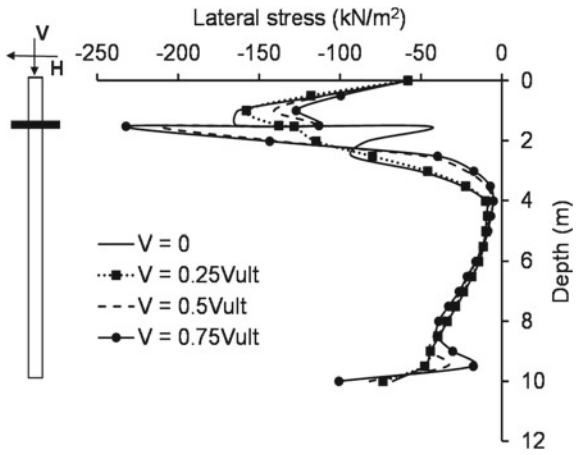

Fig. 12 Effect of the vertical loading on the lateral stresses in the soil for single-helix screw pile

6 Conclusions

In the present study, the behaviour of the screw piles under combined axial compression and lateral loading is analysed using a three-dimensional finite element method. From the study, it is found that the placement of helix is important when the screw pile is subjected to lateral loading. The lateral performance of the screw pile remains unchanged irrespective of the number of helixes (single or double) if the helix is placed below the point of rotation. The present study indicates that the best location of a single helix is at the point of maximum lateral stress. This increases the lateral capacity of about 16% and reduces the lateral deflection about 21% compared to the straight shaft pile. In the case of combined loading, the lateral capacity of the screw

pile increases as the compressive load increases, e.g. about 34% increase in lateral capacity observed at compressive load of $0.75V_{ult}$. Therefore, the present study will be helpful in the design of screw pile particularly for offshore application where they would be subjected to combined lateral (from winds and waves) and dead loads (from superstructure).

References

Al-Baghdadi TA, Brown MJ, Knappett JA, Al-Defae AH (2017) Effects of vertical loading on lateral screw pile performance. Proc Instit Civil Eng-Geotech Eng 170(3):259–272

Al-Baghdadi TA, Brown MJ, Knappett JA, Ishikura R (2015) Modelling of laterally loaded screw piles with large helical plates in sand. In: Frontiers in offshore geotechnics III: proceedings of the 3rd international symposium on frontiers in offshore geotechnics (ISFOG 2015), vol 1, pp 503–508

Byrne BW, Houlsby GT (2006) Assessing novel foundation options for offshore wind turbines. In: World maritime technology conference. London

Byrne BW, Houlsby GT (2015) Helical piles: an innovative foundation design option for offshore wind turbines. Philos Trans R Soc Math Phys Eng Sci 373(2035):20140081

Davidson C, Al-Baghdadi T, Brown M, Knappett J, Brennan A, Augarde CE, Wang L, Coombs WM, Richards D, Blake A (2018) Centrifuge modelling of screw piles for offshore wind energy foundations. In: 9th international conference on physical modelling in geoetchnics. Taylor & Francis, pp 695–700

Elsherbiny ZH, El Naggar MH (2013) Axial compressive capacity of helical piles from field tests and numerical study. Can Geotech J 50(12):1191–1203

Houlsby G (2016) Interactions in offshore foundation design. Géotechnique 66(10)

Knappett JA, Brown MJ, Brennan AJ, Hamilton L (2014) Optimising the compressive behaviour of screw piles in sand for marine renewable energy applications. In: DFI/EFFC 11th international conference on piling and deep foundations. Deep Foundations Institute, p 1904

Kumar PVP, Patra S, Haldar S (2019a) Forensic investigation of laterally loaded screw pile using finite element analysis. In: 16th Asian regional conference on soil mechanics and geotechnical engineering, Taipei, Taiwan

Kumar PVP, Patra S, Haldar S (2019b) A critical review on design aspects of screw piles for renewable energy devices. In: Proceedings of the 1st international screw pile symposium on screw piles for energy applications, Dundee, Scotland, pp 59–66

Sakr M (2011) Installation and performance characteristics of high capacity helical piles in cohesionless soils. DFI J-J Deep Found Inst 5(1):39–57

Spagnoli G (2017) A CPT-based model to predict the installation torque of helical piles in sand. Mar Georesour Geotechnol 35(4):578–585

Spagnoli G, Gavin K, Brangan C, Bauer S (2015) In situ and laboratory tests in dense sand investigating the helix-to-shaft ratio of helical piles as a novel offshore foundation system. Front Offshore Geotech III:643–648

Spagnoli G, Jalilvand S, Gavin K (2016) Installation torque measurements of helical piles in dry sand for offshore foundation systems. Geo-Chicago 2016:439–448

Spagnoli G, Tsuha CHC, Oreste P, Solarte CMM (2018) Estimation of uplift capacity and installation power of helical piles in sand for offshore structures. J Waterway Port Coastal Ocean Eng 144(6):04018019

Assessment of Uncertainty of Undrained Shear Strength of Soft Clay Using Ball Penetrometer

Dipanjan Dutta and Sumanta Haldar

1 Introduction

In present days, the ball penetrometer has drawn attention to many researchers and engineers in offshore site investigation. In this case, the cone of the conventional cone penetrometer is replaced by a ball and inserted into the soft clay soil to measure the penetration resistance. When cone is inserted into the soil, the soil is displaced laterally. With increase in depth, the overburden pressure on CPT also increases. There is a difficulty involved to determine the undrained shear strength from cone penetration resistance due to large effect of overburden pressure on it. Ball penetrometer is being used over CPT as it allows the soil to flow fully around it, thus minimizing the requirement of overburden pressure correction. Normally, the ball penetrometer of standard area ratio of 10:1 (area of ball = 100 cm^2 and area of shaft = 10 cm^2) are used in the site. The effect of different factors such as soil characteristics (Low et al. 2011), penetration rate (Zhou and Randolph 2009; Yafrate and DeJong 2007) and shaft ball area ratio (Zhou and Randolph 2011; Nguyen and Chung 2015) on undrained shear strength was studied in the past few years. The behaviour of ball penetrometer in clay layer was also studied (Zhou et al. 2013) and concept of failure mechanism and limiting cavity depth was given. The undrained shear strength is determined from penetration resistance obtained from the ball penetrometer test by dividing a suitable N factor or bearing capacity factor. Some researchers (DeJong et al. 2011; Nadir et al. 2015) suggested the range of this Nball factor based on field vane shear test (FVT) and triaxial test. However, the Nball factor of 10.5 is widely accepted (Dejong et al. 2004; Chung and Randolph 2004) and used by the researchers (Colreavy et al. 2010). Undrained shear strength determined from penetrometer effects the capacity of various anchors and foundations (suction anchor, spudcan, mudmat foundation)

D. Dutta · S. Haldar (✉)
Department of Civil Engineering, Indian Institute of Technology Bhubaneswar, Bhubaneswar, Odisha, India
e-mail: sumanta@iitbbs.ac.in

S. Haldar et al. (eds.), *Advances in Offshore Geotechnics*, Lecture Notes in Civil Engineering 92, https://doi.org/10.1007/978-981-15-6832-9_24

constructed on seabed soil as it is an important function of capacity of foundations. So any uncertainties involved in determining undrained shear strength will give inaccurate estimation of bearing capacity. For this purpose, it is very necessary to reduce this level of uncertainties as much as possible for economical design of foundation. So the focus of this paper is to determine the transformation uncertainties involved during evaluation of undrained shear strength (Su) from ball penetrometer data collected from various sites.

2 Various Uncertainties

In order to determine total uncertainties involved in any soil parameters, generally three types of uncertainties are to be considered. These are the inherent variability, transformation uncertainties and measurement uncertainties. Inherent variability is related to the soil strata and due to different geological and chemical process over the time. Inherent variability is also called spatial variability. When any other parameter is evaluated from measured soil parameter through transformation equation, then transformation uncertainties arise. Measurement uncertainties are due to condition of equipment and process of measurement. The last two uncertainties can be reduced but the spatial variability cannot be reduced.

2.1 Determination of Total Transformation Uncertainties

In this paper, total transformation uncertainties are determined. So, it automatically includes all the three uncertainties. The level of uncertainty is expressed by a dimensionless parameter coefficient of variation (COV) which is defined as the ratio of standard deviation (σ) to mean (μ).

$$\text{COV} = \frac{\sigma}{\mu} \tag{1}$$

In order to determine the random variable, (ε) the ratio of the actual target value to the predicted target value of the soil parameter is to be determined and the mean value of these values are expressed as bias factor (b).

Here, actual target value is actually measured undrained shear strength by vane shear test (VST) and the predicted target value is the evaluated undrained shear strength value from the penetrometer data through transformation equation. The random valuable is determined by the equation (Ching and Phoon 2014)

$$\varepsilon = \frac{\text{actual target value}}{b \cdot \text{predicted target value}} \tag{2}$$

where b is the bias factor which is the sample mean of the ratio of actual target value and predicted target value. Equation (2) provides an unbiased estimation on the average. The above process leads to the mean value of random variable 1. The total transformation uncertainty is expressed as the COV of the random variables (COV_ε).

3 Evaluation of Undrained Shear Strength

Undrained shear strength is evaluated from the equation,

$$S_u = \frac{q_{\text{net}(b)}}{N} \tag{3}$$

where N = ball bearing factor and $q_{\text{net}(b)}$ = net penetration resistance of the ball which is determined from the total ball resistance $q_{t(b)}$ after correcting for the overburden pressure. Total ball resistance can be evaluated from equation (Nguyen and Chung 2015).

$$q_{t(b)} = q_b + [(1-a)u_2]A_r \tag{4}$$

The net ball resistance is expressed as (DeJong et al. 2010; Randolph 2004).

$$q_{\text{net}(b)} = q_b - [\sigma_v - (1-a)u_2]A_r \tag{5}$$

where σ_v is the total overburden pressure at the level of ball. u_2 is the pore water pressure at the interface of shaft and ball and A_r is the shaft ball area ratio expressed as the ratio of area of shaft to the area of projected ball. Due to difficulties involved in the measurement of σ_v and u_2, the value of total in situ overburden pressure and equilibrium hydrostatic pressure is considered.

4 Site Description

Total of six clayey site data has been considered in this study. These are Two Japanese site Ariake and Mihara, two Korean site DIS-2 and DIS-5 (Nguyen and Chung 2017) and two Ireland site Athlone and Belfast (Colreavy et al. 2010). The soil properties are presented in Table 1.

Ariake site consists of upper and lower clay. When the level of seabed was at approximately ±0 m, then this upper clay layer was deposited under marine condition. The bottom clay layer was created by means of blackish condition when seabed level increased. The Mihara site consists of a layer of peat at top level with high water content ranging from 400 to 500% (Hayashi et al. 2012). The below soils consist

Table 1 Index properties for four clay sites (Nguyen and Chung 2017; Colreavy et al. 2010)

Site	Range of depth (m)	W_n %	I_p %	S_t	OCR
Ariake	1–14	105–190	45–90	5–12	1.2–1.6
Mihara	11–19	50–65	30–44	4–5	1.2–1.4
DIS-5	2–26	50–80	20–42	5–8	1.3–1.6
DIS-2	4–30	50–88	22–50	5–28	1.3–1.6
Athlone	2–10	25–80	30–80	–	–
Belfast	1–8	40–70	30–80	–	–

of organic clay, sandy silt and clay. In short, it is also divided in upper and lower clay layer. Ariake and Mihara both the sites are slightly over-consolidated and highly sensitive. The two sites DIS-2 and DIS-5 are situated in the Nakdong river delta flood plain and consists of upper tidal flat, inner shelf, lower tidal flat and fluvial channel. These layers were deposited 8000–5000 years before from present. These two sites are normally consolidated. Athlone site consists of peat layer over a calcium layer overlying grey clay and then brown clay. Belfast layer consists of a sandy sleech layer overlying a clayey silt sleech layer.

5 Determination and Analysis of Undrained Shear Strength

In this study, undrained shear strength from those six sites has been considered for further analysis. Undrained shear strength values with reference to ball penetrometer and field vane shear (FVT) have been collected for comparison. The data considering variation of undrained shear strength with depth have been collected for all the six sites. The data of total ball penetrometer resistance ($q_{t(b)}$) and VST variations with depth (Fig. 2) have been extracted from two Japanese sites Ariake and Mihara and two Korean sites DIS-2 and DIS- 5. The net penetration resistance $q_{\text{net}(b)}$ was determined from Eq. (5). Finally, the undrained shear strength value was determined from Eq. (3). In this work, the value of 10.5 was taken as N_{ball} factor due to its widely acceptance by many researchers (Fig 1).

Undrained shear strength determined from FVT was analysed in order to evaluate the mean Su for each site and the variations of Su in each site were studied in terms of COV. Range of Su, mean value and COV are shown in Table 2.

It is observed that the S_u values of DIS-5, DIS-2, Mihara and Belfast site are almost in the same range, whereas the other two sites, Ariake and Athlone, consist of very soft clay soil having very low S_u value. The COV_s of S_u range at Belfast site is less (17.5%) as compared to the other four sites. It indicates that variation of S_u with respect to the mean is marginal with depth. It is observed that variation of Su with depth for Athlone and DIS-2 sites is much more than the other sites which cause high uncertainty level.

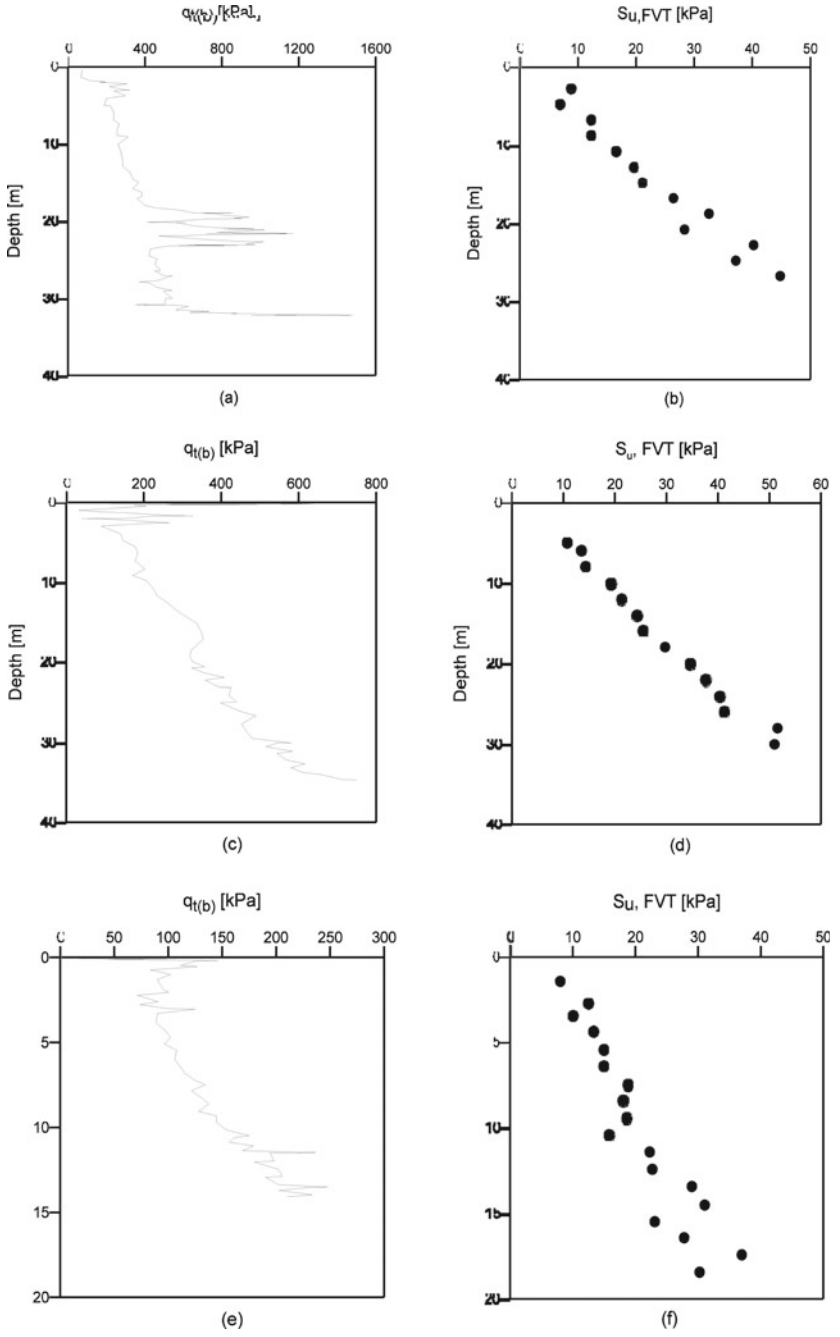

Fig. 1 Typical depth-wise variations in ball penetration resistance, q_t and field vane shear: **a**–**b** DIS-5, **c**–**d** DIS-2, **e**–**f** Ariake

Table 2 S_u range, mean value and COV for each site

Site	S_u range (kPa)	Sample mean of S_u (kPa)	COV (%)
Ariake	8–31	17.8	37.1
Mihara	18–54	29.5	36.8
DIS-5	15–45.8	28.9	34.3
DIS-2	10.7–51.6	29.6	45.4
Athlone	5.9–22	11.25	44
Belfast	19.4–34.9	24.9	17.5

6 Evaluation of Transformation Uncertainty

In this study, the transformation uncertainty is evaluated as the same procedure as Knuuti and Lansivaara (2019). At first, the predicted undrained shear strength is evaluated by Eq. (3) for all the six above sites. The values of undrained shear strength from field vane shear test (FVT) measurement are also available. Thereafter, the bias factor is determined for each site dividing the FVT undrained shear strength by the Su obtained from the ball penetration resistance. The transformation uncertainty in terms of COV is determined for each site using Eq. (1). The COV_ε for each site is given in Table 3.

A comparatively low COV_ε value was observed for Belfast and DIS-2 which are 13.8% and 14.4%, respectively. Low COV_ε indicates the low variability of the soil property. It is important to note this uncertainty that includes all types of uncertainty, which are inherent variability, model uncertainty and transformation uncertainty. A comparison between S_u obtained from FVT measurement and the predicted from ball resistance data for all the six sites is shown in Fig. 2. It is observed that the prediction of S_u from ball penetration test is reasonably good for DIS-2 and Belfast sites (Fig. 2b, f).

The COV_ε is observed to be less (13.8–14.4%) for these sites (Table 1). The predicted S_u value from ball penetrometer is significantly deviating from the S_u values obtained from VST data. Interestingly, a large COV_ε value (19.3–36.2%) is observed for DIS-5, Ariake, Mihara, and Athlone sites.

Table 3 COV_ε for each of six site

Site	COV_ε (%)
Ariake	19.3
Mihara	20.9
DIS-5	24.4
DIS-2	14.4
Athlone	36.2
Belfast	13.8

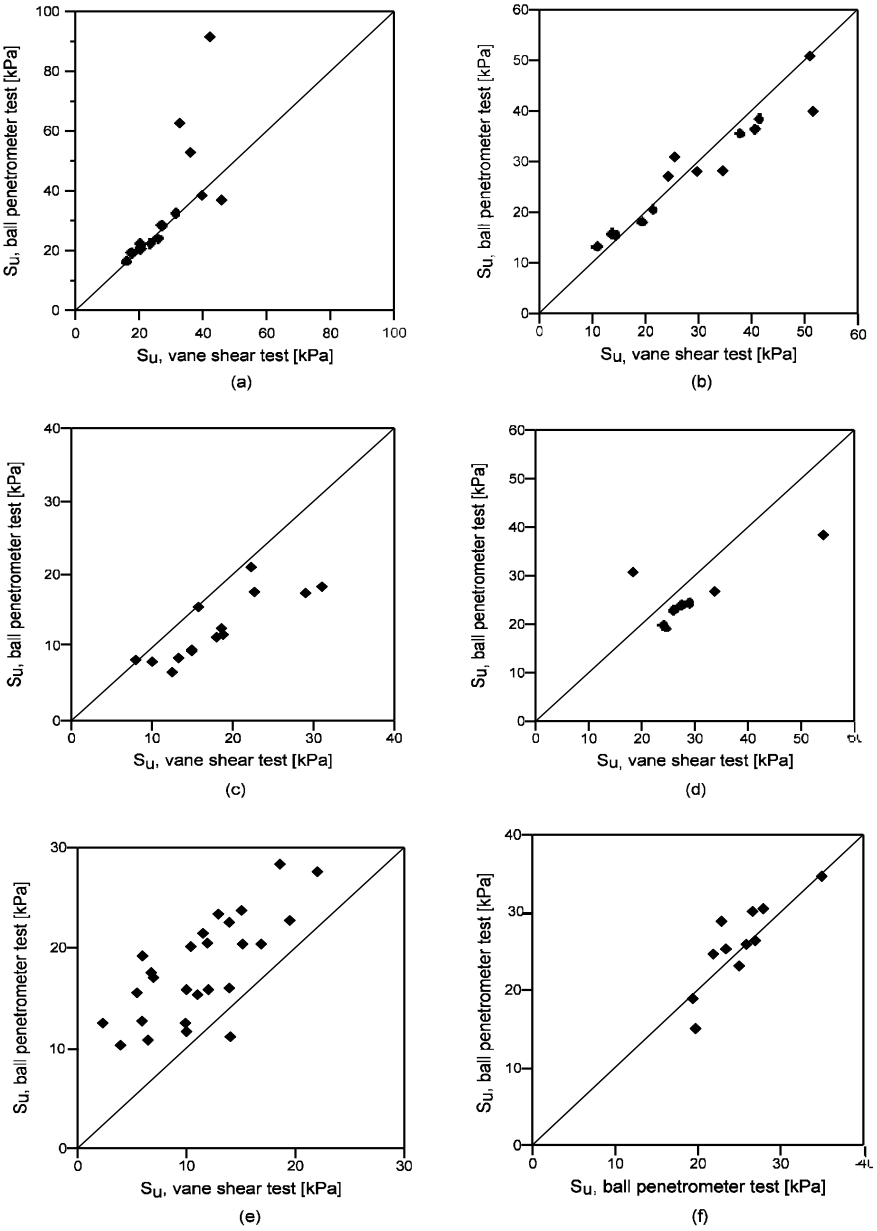

Fig. 2 Comparison between S_u, VST and S_u, BPT for all of the six sites **a** DIS-5. **b** DIS-2. **c** Ariake. **d** Mihara. **e** Athlone and **f** Belfast

The cumulative probability distribution of S_u determined from ball penetrometer, field vane shear test and the bias factor is shown in Figs. 3, 4 and 5, respectively. The sample mean of S_u for DIS-5, DIS-2, Ariake and Mihara is observed to be in the same range. Hence, the cumulative probability and uncertainty of these parameters

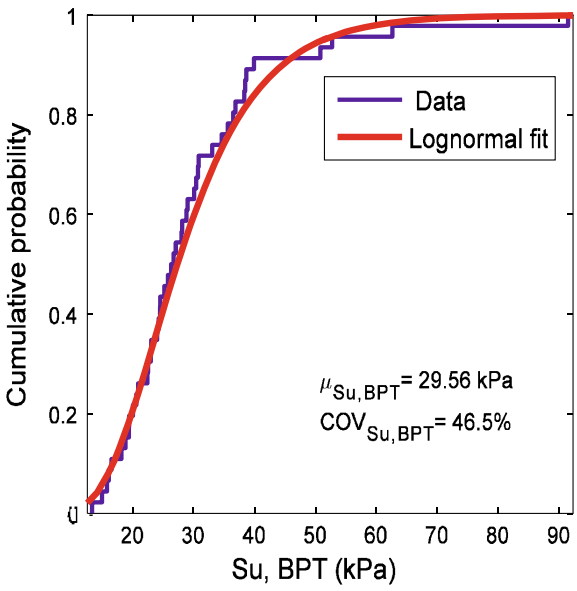

Fig. 3 Probability distribution of S_u measured from ball penetrometer

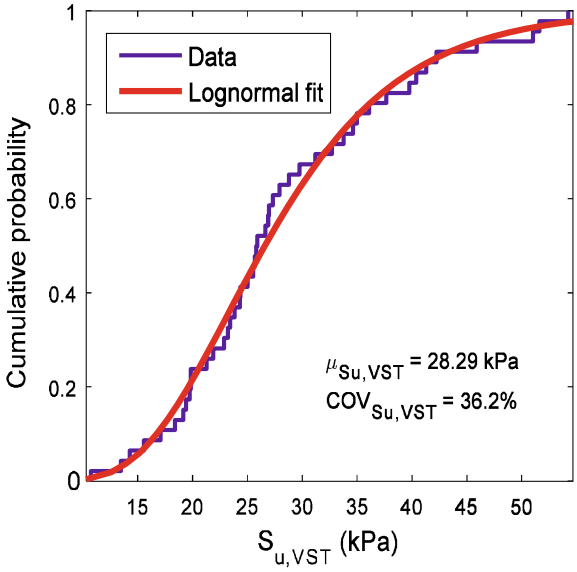

Fig. 4 Probability distribution of S_u measured from vane shear test

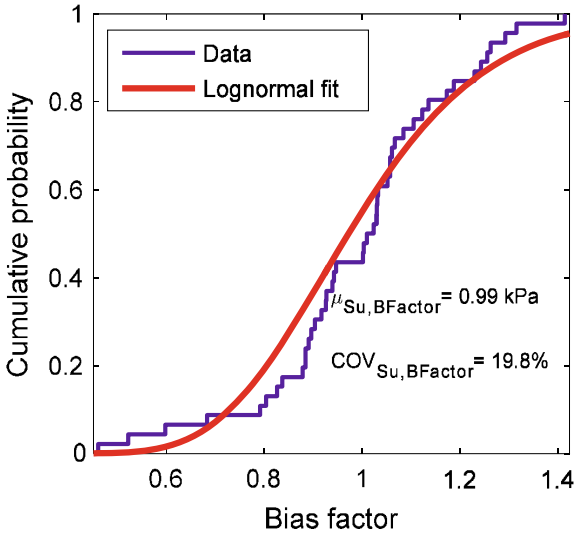

Fig. 5 Probability distribution of bias factor

are estimated considering all the data obtained from these four sites. It is observed that log-normal distribution fits well with the data for all the parameters.

The uncertainty in the predicted S_u value can affect the foundation design. Based on this uncertainty, the bearing capacity of a spudcan foundation at clay is predicted. The bearing capacity of spudcan foundation at a specific depth is expressed as (Young et al. 1984).

$$V = (S_u N_c + \sigma_v')A \tag{6}$$

where S_u is the undrained shear strength of soil. N_c is the dimensionless bearing capacity factor, $\sigma v'$ is the effective overburden pressure up to the base of footing and A is the size of the footing. The bearing capacity of a spudcan foundation is predicted considering the undrained shear strength (S_u) as deterministic and probabilistic parameter. Deterministic values were obtained directly from the data, and in probabilistic approach, the variations from the sample mean values were considered. For example, in case of Belfast site, the sample mean of S_u is 24.9 kPa is taken as deterministic S_u value. The estimated bearing capacity is 27.2 kPa. The bearing capacity for the probabilistic case is estimated considering the S_u values as sample mean ± sample standard deviation. Considering the variability of the site, estimated bearing capacity that varies from 11 to 38 kPa.

7 Summary and Conclusions

Based on the study, the following conclusions can be drawn:

1. The total transformation uncertainty involved in ball penetrometer significantly affects the predicted S_u values. Belfast and DIS-2 site possess a lesser level of uncertainty ($COV_\varepsilon = 13.8\%$ and 14.4%, respectively) as compared to the other sites. A large COV_ε value of 36.2% is observed in Athlone site. Hence, the predicted S_u value from the ball penetrometer is significantly deviating from the VST data.
2. The predicted bearing capacity of spudcan foundation at clay based on ball penetrometer data significantly alters that of deterministic case.

This preliminary study shows that the determination of transformation uncertainty for ball penetrometer is important to design foundation. A detailed study is required in this direction considering a large database.

References

Ching J, Phoon KK (2014) Correlations among some clay parameters—the multivariate distribution. Can Geotech J 51(6):686–704

Chung SF, Randolph MF (2004) Penetration resistance in soft clay for different shaped penetrometers. In: Proceedings of the 2nd international conference on geotechnical and geophysical site characterization—ISC'2, Porto, Rotter-dam: Millpress, pp 671–678

Colreavy C, Loughlin CO, Long M, Boylan M (2010) Field experience of the piezoball in soft clay. In: 2nd international symposium on cone penetration testing, Huntington Beach. https://doi.org/10.13140/2.1.3916.8000

Dejong JT, Yafrate NJ, Degroot DJ (2011) Evaluation of undrained shear strength using fullflow penetrometers Geotech Geoenviron Eng 137(1)

DeJong JT, Yafrate NJ, DeGroot DJ, Jakubowski J (2004) Evaluation of undrained shear strength profile in soft layered clay using full-flow probes. In: Proceedings 2nd international conference on geotechnical and geophysical site characterization—ISC'2, Porto, Rotterdam: Millpress, pp 679–686

DeJong JT, Yafrate NJ, DeGroot DJ, Low HE, Randolph MF (2010) Recommended practice for full flow penetrometer testing and analysis. Geotech Test J 33(2):1–13

Hayashi H, Yamazoe N, Mitachi T, Tanaka H, Nishimoto S (2012) Coefficient of earth pressure at rest for normally and overconsolidated peat ground in Hokkaido area. Soils Found 52(2):299–311

Knuuti M, Lansivaara T (2019) Variation of CPTubased transformation models for undrained shear strength of finnish clays. Georisk: Assessment Manage Risk Eng Syst Geohazards, 1–9. https://doi.org/10.1080/17499518.2019.1644525

Low HE, Randolf MF, Lunne T, Andersen KH, Sjursen MA (2011) Effect of soil characteristics on relative values of piezocone, T-bar and ball penetration resistances. Geotechnique 61(8):651–664

Nadir A, Fall A, hache R (2015) Characterization of sensitive marine clays by using cone and ball penetrometers: example of clays in eastern Canada. Geotech Geol Eng

Nguyen TD, Chung SG (2017) Ball penetration test for characterisation of soft clays. Proc Instit Civil Eng, pp 133–46

Nguyen TD, Chung SG (2015) Effect of shaft area on ball resistance in soft clays. Proc Instit Civil Eng Geotech Eng 168(2):103–119

Randolph MF (2004) Characterisation of soft sediments for offshore applications. In: Proceedings of the 2nd international conference on geotechnical and geophysical site characterization (ISC-2), Porto, Portugal pp 209–231

Yafrate NJ, DeJong JT (2007) Influence of penetration rate on measured resistance with full flow penetrometers in clays. Geotechnics

Young AG, Remmes BD, Meyer BJ (1984) Foundation performance of offshore jack-up drilling rigs. J Geotech Eng, 841–859

Zhou H, Randolph MF (2009) Resistance of fullflow penetrometers in rate-dependent and strainsoftening clay. Géotechnique 59(2):79–86

Zhou H, Randolph MF (2011) Effect of shaft on resistance of a ball penetrometer. Geotechnique 61(11):973–981

Zhou M, Hossain MS, Hu Y, Liu H (2013) Behaviour of ball penetrometer in uniform single and double-layer clays. Geotechnique 63(8):682–694

Large-Scale Dynamic Model Testing Facility for Offshore Geotechnology

Prasun Halder, Bappaditya Manna, and J. T. Shahu

1 Introduction

The use of offshore pipelines for transportation of oil and gas from offshore fields to onshore facilities and vice versa is very common throughout the world. Offshore pipelines form an integral part of the infrastructure associated with offshore oil and gas developments. Owing to their importance, offshore pipelines are also referred as the arteries of oil and gas industry. These pipelines are either laid directly on seabed or buried under seabed in trenches. During laying process, individual pipe segments are welded and then lowered in the sea using specialized lay vessels. Pipelines are placed in the trenches and covered with backfill soil. For very soft soils, pipeline may sink under the seabed under the effect of its own weight.

Pipelines undersea are subjected to several forces including large hydrostatic pressure, strong wave action, forces due to temperature and pressure, forces generated during pipe laying process, earthquake forces, etc. Depending on soil type and interface properties, pipeline can have different nature of interactions with the sea bed. Generally, surrounding soil provides longitudinal and lateral restraint to the pipeline which helps in general stability of pipeline undersea.

Generally, in offshore pipelines, transportation of oil and gas is performed amidst high temperature and pressure to prevent clogging due to wax formation. Though pipelines are laid at ambient temperature, the operating temperature of pipelines is high compared to its surrounding. As a result, it tends to undergo thermal expansion because of such temperature difference. Though the friction at interface between outer surface of the pipeline and soil prevents the longitudinal expansion of pipe, the compressive forces are setup resulting in buckling of the pipeline. Pipeline may buckle in any plane depending on the soil resistance offered. When the pipeline

P. Halder · B. Manna (✉) · J. T. Shahu
Department of Civil Engineering, Indian Institute of Technology Delhi, Hauz Khas, New Delhi, India
e-mail: bdmanna@gmail.com

S. Haldar et al. (eds.), *Advances in Offshore Geotechnics*, Lecture Notes in Civil Engineering 92, https://doi.org/10.1007/978-981-15-6832-9_25

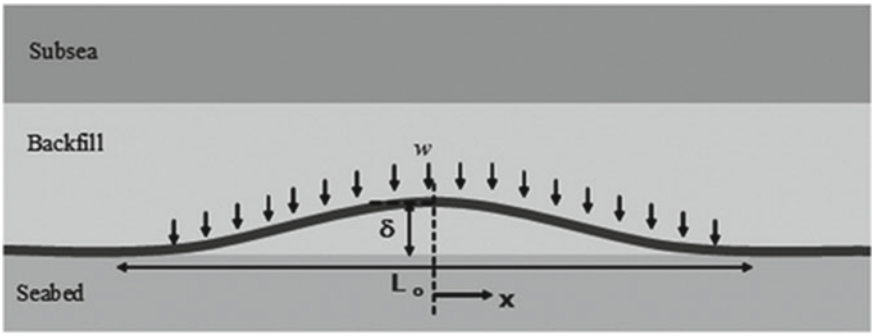

Fig. 1 Typical upheaval buckling of a buried offshore pipeline

buckles in a vertical plane, it is called as upheaval buckling (Robert and Thusyanthan 2014) as shown in Fig. 1. Similarly, when buckling occurs in a horizontal plane, it is referred as lateral buckling. For pipelines buried in a sand bed, usually upheaval buckling is most critical. Lateral buckling is resisted by the soil located on sides owing to passive resistance. However, for pipes buried in clay, the passive resistance offered is comparatively small. Hence, both upheaval and lateral buckling are critical in case of pipes buried under a clay bed. Newson and Deljoui (2006) performed FE analysis of upheaval buckling and further carried out comparative study between uplift capacity of plate anchors and pipelines. Recent researches (Maitra et al. 2016; Martin and White 2012) performed using FEM highlighted inadequacy of existing code of practice (DNV-RP-F110 2007) in the estimation of uplift capacity.

The local buckling and collapse strength of metallic pipes have been the main subjects for many studies in subsea and civil engineering, such as Murphey and Langner (1985), Gresnigt (1986), Mohareb et al. (1994), Bai et al. (1993, 1997).

Additionally, vortex-induced vibrations (VIVs) and thermal loading might cause high-cycle fatigue and fracture of the pipelines at joints and bents. Pipelines are subject to large number ($>10^3$) of relatively low range of stress cycles due to current and wave loads. The fatigue due to the high-cycle loading is designated high-cycle fatigue (HCF). The pipelines are subjected to cyclic thermal loads due to heat-ups and cooldowns of pipeline systems in the operating condition. This type of fatigue is called low-cycle fatigue (LCF). Two typical fatigue design standards for subsea pipelines and risers and subsea structures are BS7608 (1993) and DNV-RP-C203 (2005).

The problem of on-bottom stability of pipelines might play an important role during the design of the same. The main purpose of pipeline on-bottom stability design is to choose the appropriate pipeline route, materials, size and convenient manufacture, installation, and maintenance method so that the pipeline can withstand probable design current and wave loads at a low cost (Bai and Bai 2014).

Lastly, earthquake-induced ground deformation is a major concern for underground pipelines crossing an active strike-slip fault in areas vulnerable to seismic

risk. Therefore, the design of offshore pipelines under the seabed requires proper technical knowledge regarding the above-mentioned key aspects. Two typical analytical methods under certain assumptions were suggested for the fault crossing analysis, Newmark and Hall (1975) and Kennedy et al. (1977). O'Rourke and Liu (1999) report that the Kennedy model for strike-slip faulting, which results in axial tension, provides the best match to ABAQUS finite element results, based on an independent comparison of the available analytical approaches.

This paper describes the facility and procedure of large-scale geotechnical dynamic model tests at IIT Delhi for such critical conditions of offshore pipelines. With the aid of high-capacity servo-controlled hydraulic actuators, large-scale model tests can be performed to investigate the response of offshore buried pipelines addressing the various problem of offshore pipelines, e.g., upheaval and lateral buckling, fatigue and fracture of pipe, on-bottom stability, and seismic response of pipelines. Appropriate scaling law would be employed to scale down the properties and dimensions of offshore pipelines and soil as per the requirement of model testing. Various responses can be recorded using various sensors such as distribution of pressure, vertical and lateral movement of pipelines and ground movement with the help of data acquisition system. The large-scale geotechnical dynamic model testing facility established at IIT Delhi can be used for elemental testing of soil/rocks and model testing of any offshore structures for both static and dynamic conditions.

2 Geotechnical Large-Scale Dynamic Model Testing Facility

A large-scale model testing facility has been set up at the Foundation laboratory in the Department of Civil Engineering, IIT Delhi. A brief description of the testing facility along with the equipment details is presented below.

2.1 Strong Concrete Floor

A strong concrete floor is set up to enable the base to withstand high reaction of the loading frame and also the heavyweight equipment needed for the static and dynamic testing with hydraulic actuators. Blocks of mild steel are placed at a center to center distance of 0.5 m covering an area of 57 m^2 (9.5 m $\times$ 6 m) with reinforcement followed by pouring of concrete throughout the floor area as shown in Fig. 2.

Fig. 2 Strong concrete floor in the foundation laboratory

2.2 Loading Frame

Two loading frames of mild steel are established on the strong floor for holding two hydraulic actuators (Fig. 3). Strong base plates are provided at the bottom of the loading frames to anchor the system safely with the steel box placed in the strong floor. A cross-beam is also provided to hang the actuator, and necessary holes are made along the loading frame to adjust the height of the actuator during testing.

Fig. 3 Loading frames for holding hydraulic actuators

Fig. 4 Motorized lifting arrangement with crane

2.3 Lifting Arrangement (Crane)

A motorized lifting arrangement with crane is set up to move the actuator horizontally and vertically according to the need of the experiment. Figure 4 shows the lifting arrangement.

2.4 Test Tank

Two mild steel tanks of dimension 2 m × 2 m × 1.8 m are placed under the loading frames for testing. Foams are placed inside these test tanks to act as absorbing boundary for waves generated during dynamic testing as shown in Fig. 5.

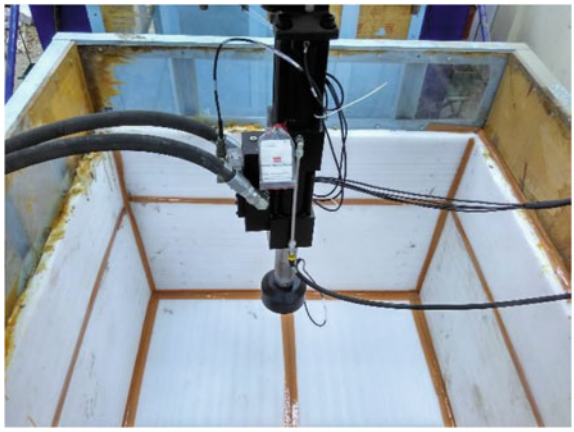

Fig. 5 Test tank with shock-absorbing boundary

2.5 Servo-controlled Hydraulic Actuators

Two MTS made servo-controlled hydraulic actuators of capacity 50 and 100 kN are hung from each of the cross beams in two loading frames as shown in Figs. 5 and 6. These are double-ended, double-acting, fatigue-rated actuators for combined balanced dynamic performance with rated load capacity of 50 and 100 kN and rated stroke of 150 mm (±75 mm double amplitude). High-capacity, non-metallic polymer bearings are bonded directly to the end caps, and piston rods are machined from a single piece of heat-treated alloy steel. Cushions are provided to protect the actuator from the effects of high-speed and high-mass forces. One servo-valve of 63 LPM capacity is provided to meet the performance criteria. Fatigue-rated axial load cell is attached (for each actuator capacity) with an overload capacity of 150% of the rated load; nonlinearity of 0.08% of full scale; hysteresis of 0.05% of full scale; repeatability of 0.03% of full scale.

One swivel head and one swivel base are attached to the actuator having adjustable bearing for clearance to eliminate backlash; dynamic force rating of ±160 kN or more(for 100 kN actuator); tilt angle of ±17° or more (for head and base); swivel angle of +90°/−75° or more. These MTS hydraulic actuators can be used for static, monotonic, dynamic, and cyclic loadings as per the requirement of the test. The actuators are capable to measure everything from high-dynamic time histories to pseudo-static creep of highly brittle materials and are also suitable for managing the smallest or most massive forces. The actuators are fitted with high-quality servo valves to deliver high-flow, quick-response, and low-distortion performance to uphold the fidelity of your test data. The actuator is equipped with a load cell and a linear variable differential transducer (LVDT) for measuring for and displacement, respectively. Dynamic testing can be done using the predefined waveforms, i.e., sine, sine

Fig. 6 MTS hydraulic actuator

Fig. 7 Hydraulic power unit (HPU)

tapered, square, etc. Additionally, user-defined dynamic input can be used with great accuracy.

2.6 Hydraulic Power Unit (HPU)

The hydraulic power unit (HPU) provides clean, quiet, and energy-efficient hydraulic power supply (Fig. 7). This unit provides extraordinary heat transfer efficiency and cleanliness with per-module polishing filtration. This filtration system minimizes energy consumption related to system cooling for the given running condition. Variable-displacement piston pumps ensure maximum hydraulic efficiency, even during times of reduced flow demand.

A corrosion-resistant stainless-steel oil-to-water heat exchanger helps to dissipate generated heat and maintains the proper temperature of the hydraulic fluid during operation. These pumps also offer optional water-shutoff valves to minimize water consumption. During operation, a hydraulic pressure of 3000 psi is maintained by the HPU. Temperature-controlled water-saver and water shutoff valves are provided to minimize water consumption. Full-flow 3-μm absolute filter is fitted in the return line to provide excellent oil cleaning. Hose pipes for actuator, i.e., pressure, return, and drain pipes of 15 m long, are attached to the HPU.

2.7 Hydraulic Service Manifold (HSM)

The MTS hydraulic service manifold (HSM) provides complete and independent control of the hydraulic pressure applied to individual stations operating from a single hydraulic power unit (HPU). Installation of the HSM (Fig. 8) between the

Fig. 8 Hydraulic service manifold (HSM)

HPU and servo-valve allows the operators to turn each hydraulic circuit on and off, as well as set the low-pressure level. Smooth, controlled transitions enhance safety and make system control more predictable.

HSM has a maximum operating pressure of 21 MPa (3000 PSI). It has a flow rate of 114 LPM or more with 3.8-l pressure and 1-l return line accumulator, and a filter of 10 μm. By minimizing the effects of rapid application and removal of high pressure, HSM reduces unexpected actuator movement that could damage test specimens. Accumulators in the pressure and return lines minimize pressure fluctuations, quieting the line, and helping ensure reliable performance.

2.8 Digital Controller

A controller (Fig. 9) is kept in the controller cabin to attach various data cards for capturing additional data from various sensors and to direct the actuators as per the requirement.

It has the facilities like digital servo control, function generation, data acquisition, hydraulic control, and digital I/O capability. Function generation is performed by 32-bit processor having standard haversine, square, and ramp waveforms and downloaded wave shapes. Automated dynamic control mode is available which can switch between any connected transducer. Any connected transducer or calculation can be selected for control (typically load, strain, or displacement) including load limited displacement during specimen loading. Three computer-selectable channels of 16-bit resolution analog output are provided for easy access to transducer signals and other critical parameters. In addition, one A/D CARD having 8-channel analogue input for data acquisition and feedback control is provided.

Fig. 9 Digital controller

2.9 Chiller and Cooling Tower

A chiller and a cooling tower are kept outside the foundation laboratory for the purpose of cooling the oil with the help of supplying cold water in the HPU and maintain a temperature suitable for testing.

A water purifier is also kept outside the Foundation Engineering Lab, IIT Delhi for serving desired and suitable water to the HUP cooler through the chiller unit (Fig. 10).

Fig. 10 Chiller, cooling tower and water purifier

3 Test Setups for Offshore Pipeline Problems

With the aid of the above-mentioned facilities, the problems related to offshore jointed rigid pipeline can be experimentally simulated in the foundation lab of IIT Delhi. Large-scale dynamic geotechnical model testing can be performed to investigate the response of offshore buried pipelines addressing the problems related to upheaval and lateral buckling, fatigue and fracture of pipe on-bottom stability and earthquake-induced ground deformation. The properties and dimensions of offshore pipelines and soil can be scaled down as per the requirement of model testing using appropriate scaling laws. Figure 11a–c shows the schematic of testing arrangement for various offshore pipeline problems.

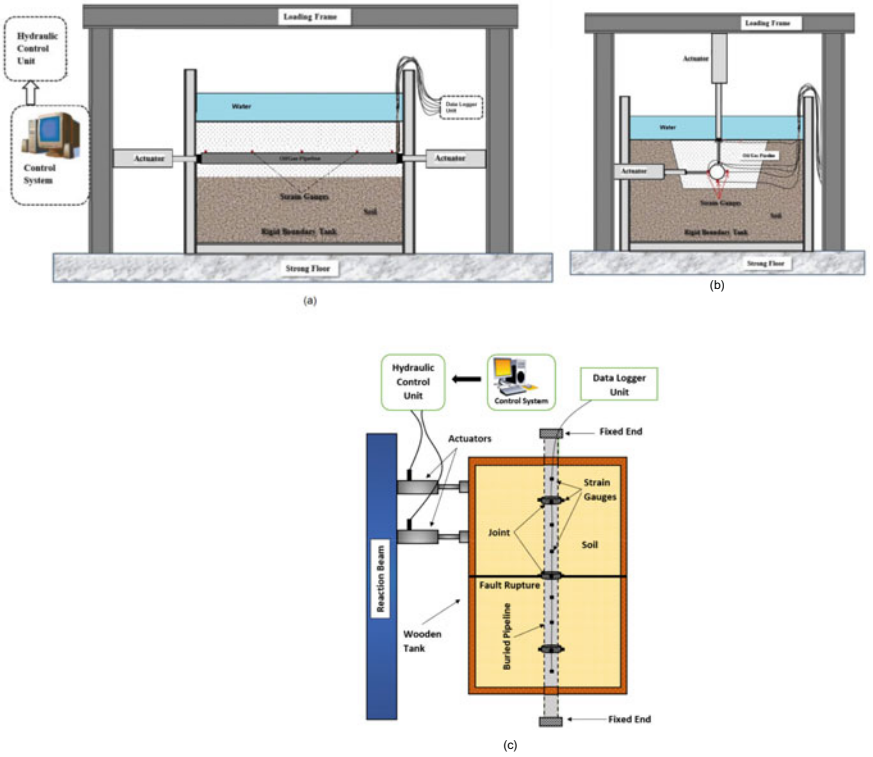

Fig. 11 Schematic diagram of large-scale dynamic model testing of underground offshore pipelines: **a** upheaval and lateral buckling test setup of pipelines; **b** test setup of on-bottom stability of pipelines; **c** split-box test setup for seismic response of pipelines

3.1 Upheaval and Lateral Buckling of Pipelines

A pipe must sustain installation and operational loads. In addition, external loads, such as those induced by waves, current, uneven seabed, trawl-board impact, pullover, expansion due to pressure and temperature changes, need to be considered. Experience has shown that the main load effect on subsea pipes is bending combined with longitudinal force while subjected to external hydrostatic pressure during installation and internal pressure while in operation. A pipe subjected to bending may fail due to local buckling, collapse, or fracture. Lateral buckling occurs if the pipeline is exposed on the seabed, or upheaval buckling may occur if it is buried or constrained in a trench. Figure 11a shows the proposed schematic diagram of experimental setup to study the buckling and collapse mechanism of metallic pipe under longitudinal forces. To study the upheaval behavior of pipeline, the actuator will be rigidly attached to a connecting steel rod at one end and other end of connecting rod will be attached to the pipeline buried in soil and underwater.

3.2 Fatigue and Fracture of Pipelines

The pipelines are subjected to cyclic thermal loads due to heat-ups and cooldowns of pipeline systems in the operating condition. The pipelines are susceptible to fatigue loads in the installation and operation conditions, which include free span vortex-induced vibrations (VIVs) and cyclic thermal loads. The actuator can be connected vertically with pipeline and cyclic load can be applied to measure the stress versus number of cycles to failure.

3.3 On-Bottom Stability of Pipelines

Pipelines resting on the seabed are subject to the forces in both the horizontal and vertical directions due to wave and current loads. When the loads are large enough, these forces can destabilize the pipe, leading to floatation or lateral movement. Figure 11b shows the experimental setup for applying combined horizontal and vertical load on pipeline to measure the stress, moment, and displacements of soils and pipeline. The actuator will be attached rigidly to a connecting steel rod through nut and bolt system at one end. In the other end, the connecting rod will be attached to a curved thick plate. The curved thick plate will be welded properly to the curved surface of the pipeline. Such an actuator-connecting rod-curved thick plate monolithic system will act integrally.

3.4 Seismic Response of Pipelines

Different kinds of seismic hazards often impose hazardous geotechnical loads on subsea pipeline systems. In some extreme situations, the loads due to those seismic hazards may be so large that the subsea pipeline system yields and suffers plastic deformation. Damage to pipeline systems during an earthquake can arise from the traveling ground waves and permanent ground deformation due to soil failures. Figure 11c shows large-scale testing setup to study the ground rupture effects on pipelines by using split-box tests controlled by the actuator. Various responses such as vertical and horizontal displacement of pipeline, ground movement and subsoil pressure distribution will be detected through sensors with high precision. These sensors will be attached to the data acquisition system to get the desired output during testing.

4 Conclusions

In this paper, the description of the large-scale geotechnical dynamic model testing facility at IIT Delhi is outlined. The problems related to offshore pipelines such as upheaval buckling, lateral buckling, vortex-induced vibrations, on-bottom stability, and earthquake-induced ground displacement can be simulated with the aid of high-capacity servo-controlled hydraulic actuators. In addition to dynamic loading, other user-defined loading can be applied through the actuators depending on the requirement of the problems. During the large-scale model testing, various responses of the pipeline and ground can be detected with the help of high precision sensors in terms of vertical and lateral displacements, subsoil pressure distribution, etc. Such model testing can be very beneficial to examine the critical issues related to any type of offshore structures. The large-scale dynamic model testing facility established at the Department of Civil Engineering of IIT Delhi can be customized as per the requirement of testing of various offshore geotechnical problems.

Acknowledgement This study was funded by the project 'Improvement of S&T Infrastructure 2015 (FIST 2015)', by Ministry of Science & Technology, Department of Science & Technology (DST), under DST Sanction No.: SR/FST/ETI-401/2015.

References

Bai Q, Bai Y (2014) Subsea pipeline design, analysis, and installation, 1st ed. Gulf Professional Publishing, Waltham

Bai Y, Igland R, Moan T (1993) Tube collapse under combined pressure, tension and bending. Int J Offshore Polar Eng 3(2):121–129

Bai Y, Igland R, Moan T (1997) Tube collapse under combined external pressure, tension and bending. J Mar Struct 10(5):389–410

BS7608 (1993) Code of practice for fatigue design and assessment of steel structures. British Standards Institution, London

DNV-RP-C203 (2005) Recommended practice for fatigue design of offshore steel structures. Det Norske Veritas

DNV-RP-F110 (2007) Global buckling of submarine pipelines–structural design to high temperature/high pressure. Dnv-Rp-F110

Gresnigt AM (1986) Plastic design of buried steel pipelines in settlement areas. HERON, Delf University of Technology, vol 31(4)

Kennedy RP, Chow AW, Williamson RA (1977) Fault movement effects on buried oil pipeline. J Transp Eng Div ASCE 103(TE5):617–33

Martin CM, White DJ (2012) Limit analysis of the undrained bearing capacity of offshore pipelines. Géotechnique 62(9):847–863

Mohareb ME, Elwi AE, Kulak GL, Murray DW (1994) Deformational behaviour of line pipe. Structural engineering report no. 202. University of Alberta, Edmonton

Maitra S, Chatterjee S, Choudhury D (2016) Generalized framework to predict undrained uplift capacity of buried offshore pipelines. Can Geotech J 53(11):1841–1852

Murphey CE, Langner CG (1985) Ultimate pipe strength under bending, collapse and fatigue. OMAE'85

Newmark NM, Hall WJ (1975) Pipeline design to resist large fault displacements. In: Proceedings of US national conference on earthquake engineering. Ann Arbor

Newson TA, Deljoui P (2006) Finite element modelling of upheaval buckling of buried offshore pipelines in clayey soils. Soil and rock behavior and modeling. American Society of Civil Engineers, Reston, VA, pp 351–358

O'Rourke MJ, Liu X (1999) Response of buried pipelines subject to earthquake effects. Monograph No. 3. Multidisciplinary Center for Earthquake Engineering Research Buffalo

Robert DJ, Thusyanthan NI (2014) Numerical and experimental study of uplift mobilization of buried pipelines in sands. J Pipeline Syst Eng Pract 6(1):04014009